Vlad Alexandru Silvestru, Dipl.-Ing.

Composite Structural Glazing Systems

Towards transparent building envelopes with composite structural behaviour between glass panes and metal framing by adhesive bonding

DOCTORAL THESIS

to achieve the university degree of

Doktor der technischen Wissenschaften

submitted to

Graz University of Technology

Reviewers

Prof. Dr-Ing. Jens Schneider
Technische Universität Darmstadt

Dr. Mauro Overend
University of Cambridge

Graz, May 2018

Affidavit

I declare that I have authored this thesis independently, that I have not used other than the declared sources/resources, and that I have explicitly indicated all material which has been quoted either literally or by content from the sources used. The text document uploaded to TUGRAZonline is identical to the present doctoral thesis.

Date

Signature

Copyright © 2018 Vlad Alexandru Silvestru

All rights reserved. No part of this publication may be reproduced, stored in a retrieval system or transmitted in any form or by any means, electronic, mechanical, by photo-copying, recording or otherwise, without written permission from the author.

Acknowledgements

Over the past few years several colleagues, professionals, companies and organisations as well as friends and family supported me both professionally and personally. Their valuable advices and the numerous very appreciated discussions helped me to successfully overcome the downs and especially enjoy the ups during this PhD research. I would like to thank every one of them, some of whom I would like to mention in particular.

First of all, I would like to express my gratitude to my scientific supervisors, Dr. Oliver Englhardt and Prof. Jens Schneider. Without their support, the completion of this thesis probably would have not been possible. I am thankful to Dr. Oliver Englhardt for providing me the opportunity to work on this research topic and especially for offering me a balanced proportion of guidance and liberty throughout the project. To Prof. Jens Schneider, I am grateful for assuming the supervision of my thesis in the final year and for the enlightening discussions on the research topic during this period. His unconditional support and encouragement after being unwillingly pushed to find a new supervisor are highly appreciated. In terms of scientific support, I am also thankful to Dr. Mauro Overend for his expertise comments on the concept dissertation and for accepting to review the submitted thesis.

I would also like to thank my colleagues at the Institute of Building Construction for providing a pleasant and friendly environment. The discussions and chats over lunch or during coffee breaks were highly appreciated alternations from the research work. I would like to thank Georg Kolany for working together with me on this research topic, despite my occasional stubbornness, and Manfred Zellinger for his uncountable encouraging advices during the past years. The collaboration with Michael Drass from the Institute of Structural Mechanics and Design of TU Darmstadt on modelling polymer materials during the last year is highly appreciated.

I am grateful to the Austrian Research Promotion Agency and Waagner-Biro for supporting this research financially in form of the FFG-Bridge project no. 838561. Moreover, the technical collaboration with the steel-glass structures division of Waagner-Biro is highly acknowledged. I would like to thank Rene Ziegler, Thomas Henriksen, Andreas Fritsch and Tobias Mähr for the numerous discussions on technical aspects and their very appreciated advices.

The support of the staff from the Laboratory for Structural Engineering at Graz University of Technology in planning and performing the experimental work was a significant contribution to the success of this thesis. I would like to thank Bernhard Freytag, Uwe Fülöp, Josef Linder, Reinhard Holzschuster and Hannes Koitz for assisting me with their technical expertise. Furthermore, I would like to thank the staff of the Laboratory for Building Physics at Graz University of Technology for providing me space and tools for preparing the test specimens. Also, I would like to thank all the students who assisted me in manufacturing the test specimens.

The input and support of the adhesive manufacturers Sika and Dow Corning are highly appreciated. These companies provided materials for experimental investigations and offered me the possibility to prepare test specimens in their laboratories in Widen (Sika) and Seneffe (Dow Corning), which is gratefully acknowledged. Moreover, I would like to thank on a personal level Florian Döbbel, Walter Leser, Sabine Erdelt, Roland Jaeggi and the laboratory staff in Widen (Sika) as well as Olaf Pretzsch, Jonathan Curon and the laboratory staff in Seneffe (Dow Corning) for their assistance and valuable advices.

I would like to acknowledge the COST Action TU0905 „Structural Glass - Novel design methods and next generation products“ and the COST Action TU1403 „Adaptive Facades Network“ for organizing training schools for young researchers and allowing them to get in contact both with other young researchers as well as with experienced professionals. I would like to thank the leading members of these networks for their indirect support and the fellow young researchers I met through these networks and with whom we met again and again at different glass conferences during the past years for the discussions and the fun we had. I would like to thank the COST Action TU0905 for financing my short term scientific mission at the University of Cambridge in 2013 and Shelton Nhamoinesu and Dr. Mauro Overend from the glass & facade technology research group for hosting me during my stay. The experience there and the investigations I assisted to have been of significant value in the beginnings of my own research.

Success on professional level can only be achieved with an appropriate compensation on private level. Therefore I would like to express a special thank you to my family and my friends for being who they are and for being in my life. Without listing names, I would like to thank my brother, my friends in Graz and in Vienna as well as all the other members of my family and all my other friends, who by having a drink, a meal, a barbecue or a simple discussion, by playing basketball, by spending our holidays together and by various other activities were part of very appreciated distractions from the ordinary.

Last, but not least, I would like to complete the acknowledgements with a very special thank you to my parents, who were always there for me with extremely appreciated advices when needed.

Abstract

Glass as a material and the associated transparency enjoy an increasing role in the architecture of recent years. At the same time, the demands for building envelopes regarding energy performance and efficient use of materials are constantly increasing. Efforts are made, especially in the area of research and development, to design systems with composite structural behaviour which benefit from the properties of different involved materials. In the case of transparent facades, a step in this direction is to activate the glass panes, which are currently only space-enclosing elements, as structural components participating to the transfer of in-plane loads. Key aspects in order to achieve this task are the solutions adopted for connections. In the field of structural glass, adhesive joints are increasingly preferred instead of mechanical fixings due to their advantages in terms of reducing local stress concentrations and avoiding thermal bridges. In this context, the use of adhesive bonding to obtain a composite structural behaviour between filigree metal frames and glass panes in transparent building envelopes is examined in the present thesis. Investigations at material level, connection level and element level are carried out focusing on the mechanical performance under room ambient conditions.

Two structural silicone adhesives (Dow Corning® 993 and Sikasil® SG-550) and one structural acrylic adhesive (SikaFast®-5221 NT) are considered. Based on results from uniaxial tensile tests, hyperelastic material models are derived for the two silicones and a strain rate dependent plastic model is proposed for the acrylic. In the case of the latter one, a novel efficient surface fitting equation is introduced to obtain stress-strain data at constant true strain rates. The influence of different substrate surfaces and their treatments as well as of different joint dimensions on the performance of adhesive connections is assessed experimentally. Double-lap shear tests on metal-metal connections and glass-stainless steel connections as well as tensile tests on glass-stainless steel connections are performed. Regarding failure modes, solely cohesive fail-

ure within the adhesive joints is noticed for the two silicones. In the case of the acrylic, failure due to loss of adhesion is observed under shear loading on too rough and too smooth metal surfaces as well as on the air surface of the glass panes.

The suitability of the material models derived for the considered adhesives is investigated by finite element simulations of selected connection tests. The hyperelastic models used for the silicones show a relatively good agreement for both tensile and shear loading. The strain rate dependent plastic model proposed for the acrylic leads to appropriate results only for shear loading. In the case of tensile loading, it is shown that existing voids, void nucleation and coalescence need to be considered for a more exact material model. Additional experimental investigations are performed for adhesive joints at the edge of laminated glass panes under tensile, compressive and shear loading. The obtained results emphasise the risk of delamination between glass panes and interlayer for such connections.

At element level, two novel concepts for glass-metal systems with composite structural behaviour to be used in large transparent facades are introduced. For the first one, a perimetrical adhesive bonding with a silicone adhesive between the glass panes and the filigree metal frames is responsible for transferring the out-of-plane loads, and grouting (or setting) blocks are used near the glass pane corners for transferring the in-plane loads. In the case of the second concept, a perimetrical adhesive bonding with acrylic adhesive between the glass panes and the filigree metal frames is responsible for transferring both the out-of-plane and the in-plane loads. For both concepts experimental tests are performed and non-linear finite element simulations are conducted. The results of the tests performed under in-plane shear loading on large-scale specimens reveal the high load-bearing capacity of both concepts and show that failure is initiated within the adhesive joints for the considered component dimensions. The developed numerical models allow a good prediction of the mechanical response of the investigated glass-metal elements. The influence of selected geometrical and material parameters as well as of different loading scenarios on the structural behaviour of the systems is assessed based on simulation results. The response of both systems is sensitive especially to the element height, the framing depth and the adhesive stiffness. The effect of the latter one is more pronounced in the case of the system with acrylic adhesive. The system with silicone adhesive and grouting exhibits additionally an increased sensitivity to different glass pane assemblies and framing corner rigidities.

The conducted investigations on novel glass-metal elements with composite structural behaviour by adhesive bonding are application driven. To encourage the further development of such elements and their consideration by engineering offices, it is shown in a final step that their mechanical behaviour can be relatively well predicted with common structural design software applications based on simplified mechanical models. Furthermore, conceptual details are proposed focusing on the resistance to weathering and on the use of insulating glass units.

Kurzfassung

Glas als Baustoff und die damit verbundene Transparenz erfreuen sich einer immer wichtigeren Rolle in der Architektur der letzten Jahrzehnte. Gleichzeitig steigen ständig die Anforderungen an Gebäudehüllen hinsichtlich Energieeffizienz und optimierten Materialeinsatz. Vor allem im Bereich der Forschung und Entwicklung werden zunehmend hybride Tragsysteme angestrebt, welche die Vorteile der verschiedenen eingesetzten Materialien gezielt ausnutzen. Ein Schritt in diese Richtung ist im Falle von transparenten Fassaden die Aktivierung der Glasscheiben, die derzeit nur eine raumabschließende Funktion haben, zur Abtragung von Lasten in Scheibenrichtung. Ein Hauptaugenmerk, um dieses zu erreichen gebührt der Fügetechnik. Im Fachgebiet des konstruktiven Glasbaus werden Klebeverbindungen, aufgrund ihrer Vorteile bezüglich Reduzierung von Spannungskonzentrationen und Vermeidung von Wärmebrücken, zunehmend den mechanischen Befestigungen bevorzugt. In der vorliegenden Arbeit wird der Einsatz von Klebeverbindungen zur Herstellung von Glas-Metall-Elementen mit Verbundtragwirkung für die Anwendung in selbsttragenden Gebäudehüllen behandelt. Untersuchungen auf Material-, Verbindungs- und Elementebene werden mit Fokus auf das mechanische Verhalten unter Raumbedingungen durchgeführt.

Zwei Silikonklebstoffe (Dow Corning® 993 und Sikasil® SG-550) und ein Akrylatklebstoff (SikaFast®-5221 NT) für tragende Verbindungen werden in Betracht gezogen. Basierend auf Ergebnisse von uniaxialen Zugversuchen werden hyperelastische Materialmodelle für die zwei Silikone abgeleitet und ein Dehnraten-abhängiges plastisches Modell für das Akrylat vorgeschlagen. Im Falle vom Letzteren wird eine neue effiziente Funktion für Flächenapproximationen eingeführt, um Spannungs-Dehnungs-Kurven bei konstanten wahren Dehnraten zu ermitteln. Der Einfluss verschiedener Substratmaterialien und Oberflächenbehandlungen sowie auch verschiedener Abmessungen der Klebefuge auf das Verhalten von Klebeverbindungen wird experi-

mentell untersucht. Zweischnittige Zugscherversuche an Metall-Metall-Klebeverbindungen und an Glas-Edelstahl-Klebeverbindungen wie auch Kopfzugversuche an Glas-Edelstahl-Klebeverbindungen werden durchgeführt. Die Ergebnisse zeigen, dass im Falle der Silikone lediglich kohäsives Versagen in der Klebefuge auftritt. Das Akrylat weist bei zu rauen oder zu glatten Metalloberflächen als auch auf der Luftseite der Glasscheiben teilweise adhäsives Versagen auf.

Die Eignung der abgeleiteten Materialmodelle wird anhand von Finite Elemente Simulationen ausgewählter Verbindungsversuche bewertet. Die hyperelastischen Modelle im Falle der Silikone führen sowohl unter Zug- als auch unter Zugscherbelastung zu einer guten Übereinstimmung der Ergebnisse. Das Dehnraten-abhängige plastische Modell liefert für das Akrylat nur unter Zugscherbeanspruchung gute Ergebnisse. Für Zugbeanspruchungen wird gezeigt, dass vorhandene und neu entstehende Poren sowie auch deren Zusammenwachsen in einem adäquaten Materialmodell berücksichtigt werden sollten. Eine weitere Reihe an Versuchen wird für Klebeverbindungen an der Kante von Verbundsicherheitsglas unter Zug-, Druck- und Zugscherbelastung durchgeführt. Die Ergebnisse zeigen, dass bei solchen Ausführungen das Risiko einer Delamination zwischen Glasscheiben und Verbundfolie besteht.

Auf Elementebene werden zwei innovative Konzepte für Glas-Metall-Systeme mit Verbundtragwirkung für den Einsatz in transparenten Fassaden eingeführt. Beim ersten ist eine umlaufende Verklebung mit Silikon zwischen Glasscheibe und filigranem Metallrahmen für die Übertragung der Lasten senkrecht zur Scheibenebene zuständig, während lokale Blöcke aus einem Injektionsmörtel (oder Klotzungen) in der Nähe der Glasecken die Lasten in Scheibenrichtung übernehmen. Das zweite Konzept sieht nur eine umlaufende Verklebung mit Akrylat zwischen Glasscheibe und filigranem Metallrahmen vor, welche die Übertragung der Lasten senkrecht zur Scheibenebene und in Scheibenrichtung sicherstellt. Laborversuche und nichtlineare Finite Elemente Simulationen werden für beide Konzepte durchgeführt. Die Ergebnisse für die unter Schublast geprüften Versuchskörper in realem Maßstab zeigen die hohe Tragfähigkeit beider Systeme und die Tatsache, dass, für die gewählten Abmessungen der Komponenten, das Versagen von der Klebeverbindung ausgeht. Die entwickelten numerischen Modelle erlauben eine gute Nachbildung des Tragverhaltens der untersuchten Glas-Metall-Elemente. Der Einfluss ausgewählter geometrischer Parameter und Materialparameter sowie auch verschiedener Belastungsszenarien auf das Tragverhalten der Systeme wird anhand von Simulationsergebnissen bewertet. Speziell die Elementhöhe, die Rahmentiefe und die Steifigkeit der Klebeverbindung haben für beide Systeme einen hohen Einfluss auf die Ergebnisse. Die Auswirkung verschiedener Klebstoffsteifigkeiten ist im Falle des Systems mit Akrylatverklebung ausgeprägter. Zusätzlich werden die Ergebnisse für das System mit Silikonverklebung und Injektionsmörtel auch von verschiedenen Glasaufbauten und Ecksteifigkeiten des Rahmens stärker beeinflusst.

Die durchgeführten Untersuchungen von innovativen Glas-Metall-Elemente mit Verbundtragwirkung durch Klebeverbindungen sind anwendungsorientiert. Um die Weiterentwicklung solcher Elemente wie auch deren Erwägung für den Einsatz durch Planungsbüros zu unterstützen, wird abschließend gezeigt dass deren mechanisches Verhalten mit üblicher Bemessungssoftware basierend auf vereinfachte mechanische Modelle relativ gut abgebildet werden kann. Zusätzlich werden konzeptuelle Details für die Gewährleistung der Dichtigkeit und für den Einsatz der zwei Systeme mit Isolierverglasungen vorgeschlagen.

Table of contents

1 Introduction 1

1.1 Background and research problem 2

1.2 Research objectives and methodology 5

1.3 Structure of the thesis 8

2 State of the art - theoretical framework 13

2.1 Selected systems for glass front facades 14

2.1.1 Post-and-beam facades 14

2.1.2 System facades 15

2.1.3 Double-skin facades 16

2.2 Properties of relevant facade materials 17

2.2.1 Glass and glass products 17

2.2.2 Frame materials for transparent facades 24

2.2.3 Structural adhesives for glass-metal connections 27

2.2.4 Materials for transferring compressive loads at the glass edge 33

2.3 Glass panes in structural applications 36

2.3.1 In-plane loaded glass beams and hybrid glass beams 36

2.3.2 Glass panes loaded in-plane by uniaxial compression 39
2.3.3 Glass panes activated as diagonal struts 42
2.3.4 Glass panes activated as shear panels 46
2.3.5 Timber-glass composite panels 48
2.3.6 Out-of-plane loaded glass panes 49

3 Transparent building envelopes with composite structural behaviour 51

3.1 Introduction to the concept 52
3.2 Fundamentals on composite action 55
3.3 Loads on transparent building envelopes 58
3.3.1 Considerations for wind loads 59
3.3.2 Considerations for temperature loads 61
3.4 Functional requirements for transparent building envelopes 64
3.5 Challenges and preliminary concepts 68
3.5.1 Load transfer within one element 70
3.5.2 Load transfer between several elements 71
3.6 Conclusions and delimitations for further investigations 73

4 Investigations on adhesives and their adhesion to metal substrates 75

4.1 Properties of the selected adhesives 76
4.2 Uniaxial tensile tests on dumbbell specimens 80
4.2.1 Specimens and procedure for the uniaxial tensile tests 80
4.2.2 Uniaxial tensile test results for Dow Corning 993 82
4.2.3 Uniaxial tensile test results for Sikasil SG-550 83
4.2.4 Uniaxial tensile test results for SikaFast-5221 NT 85
4.3 Material models for finite element simulations 88
4.3.1 Hyperelastic material models 90
4.3.2 Suitable material models for Dow Corning 993 93
4.3.3 Suitable material models for Sikasil SG-550 96
4.3.4 Suitable material models for SikaFast-5221 NT 98
4.4 Adhesion to metal substrates with different surface finishing 104
4.4.1 Substrate materials and surface finishings 105
4.4.2 Manufacturing of the test specimens 108

4.4.3 Test setup and test procedure 112
4.4.4 Failure pattern evaluation for the adhesives 113
4.4.5 Evaluation of the mechanical properties 116
4.4.6 General conclusions on the adhesion tests and outlook 118

5 Mechanical behaviour of adhesive joints between glass and stainless steel 119

5.1 Investigation procedure and experimental programme 120
5.2 Linear adhesive joints at the glass surface 123
5.2.1 Manufacturing of the test specimens 126
5.2.2 Test results for adhesive joints at the glass surface under tensile loading 130
5.2.3 Test results for adhesive joints at the glass surface under shear loading 137
5.2.4 Finite element simulations of the experimental tests 142
5.3 Linear adhesive joints at the edge of laminated glass panes 156
5.3.1 Manufacturing of the test specimens 160
5.3.2 Adhesive joints at the glass edge under tensile loading 162
5.3.3 Adhesive joints at the glass edge under compressive loading 166
5.3.4 Adhesive joints at the glass edge under shear loading 171
5.4 Evaluation of the results on linear adhesive joints 174

6 Experimental investigations on large-scale multi-component elements 179

6.1 Testing concept and objectives 180
6.2 Development of test specimens and test setup 182
6.2.1 Design of the test specimens 182
6.2.2 Assembly of the test specimens 185
6.2.3 Design of the test setup 188
6.2.4 Measurement instrumentation 192
6.3 Experimental procedure and test results 197
6.3.1 Loading scenarios and cycles 197
6.3.2 Test results from series with a single load direction 200
6.3.3 Test results from series with two combined load directions 209
6.3.4 Test results from series with three combined load directions 215
6.3.5 Failure test results for the specimen with silicone adhesive bonding 218
6.3.6 Failure test results for the specimen with acrylic adhesive bonding 223
6.4 Conclusions on the large-scale testing 229

7 Finite element investigations on large-scale multi-component elements 231

7.1 Introduction and finite element model characteristics 232

7.2 Comparison between finite element results and test results 237

7.2.1 Evaluation of eigenvalues and eigenmodes 237

7.2.2 Simulation results for the failure tests 240

7.2.3 Simulation results for other selected test series 249

7.3 Parametric study on large-scale multi-component elements 253

7.3.1 Investigation of different support conditions 255

7.3.2 Eigenmodes and eigenvalues of subsidiary systems 264

7.3.3 Variation of the glass pane height 268

7.3.4 Variation of the glass pane assembly 272

7.3.5 Variation of the metal framing depth 276

7.3.6 Variation of the metal corner thickness 280

7.3.7 Variation of the adhesive joint geometry 284

7.3.8 Variation of the adhesive stiffness 288

7.3.9 Variation of initial geometric imperfections 291

7.4 Investigation of different loading scenarios and levels 294

7.4.1 Combined wind suction and shear loading 294

7.4.2 Combined wind pressure and shear loading 296

7.4.3 Combined axial loading and shear loading 298

7.4.4 Performance under temperature loads 301

7.5 Conclusions on the large-scale finite element simulations 303

8 Approaches for structural and functional design 305

8.1 Considerations on the transfer between research and practice 306

8.2 Simplified mechanical models 307

8.2.1 Adaptation of existing mechanical models for the investigated systems 308

8.2.2 Evaluation at element level with a structural engineering software 310

8.2.3 Structural behaviour of several connected elements 315

8.3 Design approach for composite structural glazing systems 319

8.4 Conceptual extensions regarding building physics requirements 322

8.4.1 Considerations for elements with single laminated glass panes 323

8.4.2 Considerations for elements with insulating glass units 325

9 Conclusions and future research 331

9.1 Conclusions 332

9.2 Future research 338

Bibliography 343

Curriculum Vitae 359

Publication List 361

Appendices

Appendix A - Test results for uniaxial tensile tests on adhesive dumbbell specimens

Appendix B - Test results for adhesive joints between metal substrates

B.1 - Dow Corning 993 - adhesive joint dimensions: 50 mm x 12 mm x 12 mm
B.2 - Dow Corning 993 - adhesive joint dimensions: 50 mm x 60 mm x 12 mm
B.3 - Sikasil SG-550 - adhesive joint dimensions: 50 mm x 12 mm x 12 mm
B.4 - Sikasil SG-550 - adhesive joint dimensions: 50 mm x 60 mm x 12 mm
B.5 - SikaFast-5221 NT - adhesive joint dimensions: 50 mm x 12 mm x 3 mm
B.6 - SikaFast-5221 NT - adhesive joint dimensions: 50 mm x 60 mm x 3 mm

Appendix C - Test results for linear adhesive joints at the glass surface

C.1 - Adhesive joints at the glass surface under tensile loading with Dow Corning 993
C.2 - Adhesive joints at the glass surface under tensile loading with Sikasil SG-550
C.3 - Adhesive joints at the glass surface under tensile loading with SikaFast-5221 NT
C.4 - Adhesive joints at the glass surface under shear loading with Dow Corning 993
C.5 - Adhesive joints at the glass surface under shear loading with Sikasil SG-550
C.6 - Adhesive joints at the glass surface under shear loading with SikaFast-5221 NT

Appendix D - Test results for linear adhesive joints at the edge of laminated glass

D.1 - Adhesive joints at the edge of laminated glass under tensile loading
D.2 - Adhesive joints at the edge of laminated glass under compressive loading
D.3 - Adhesive joints at the edge of laminated glass under shear loading

Appendix E - Additional results from tests on large-scale multi-component elements

E.1 - Combined in-plane compressive axial loading and in-plane shear loading
E.2 - Combined in-plane tensile axial loading and in-plane shear loading
E.3 - Combined out-of-plane surface loading and in-plane shear loading
E.4 - Combined out-of-plane surface loading with both axial and shear in-plane loading

1 Introduction

Background and research problem
Research objectives and methodology
Structure of the thesis

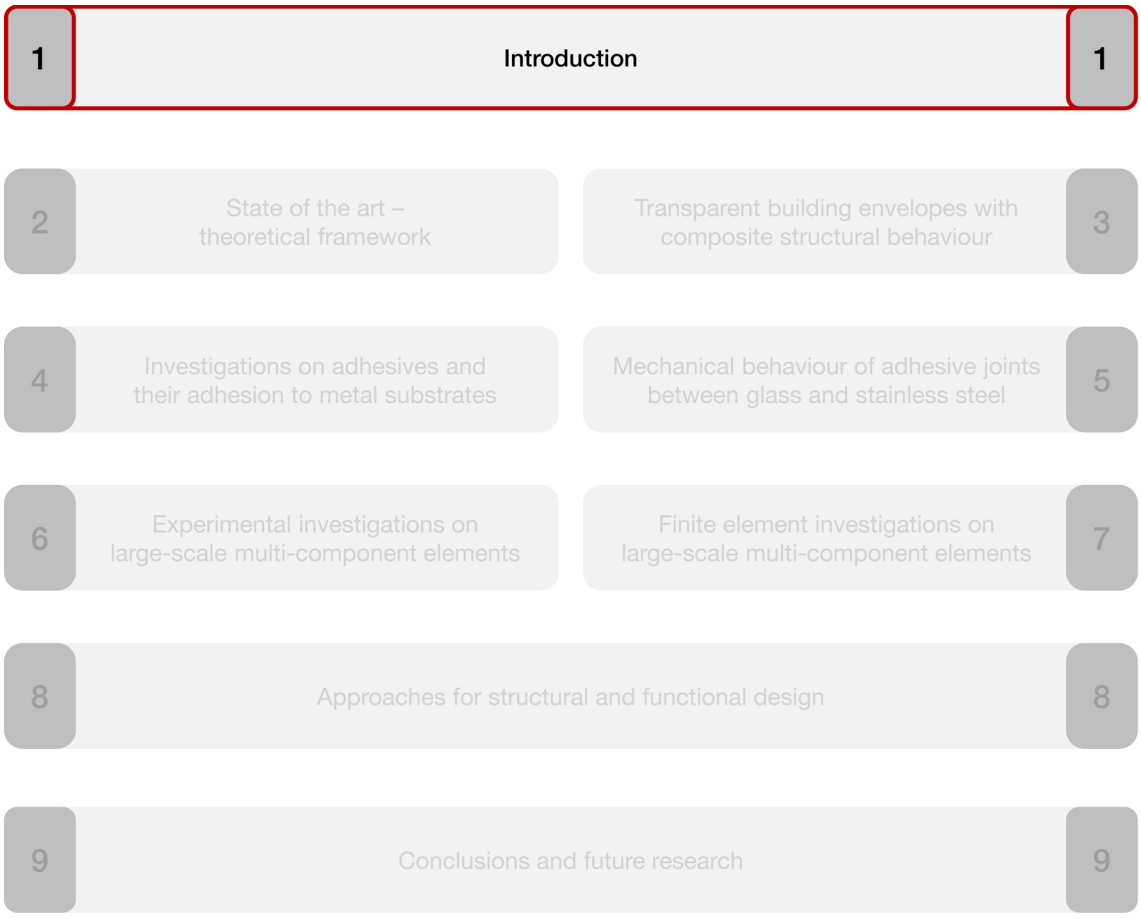

1.1 Background and research problem

The architecture of the last decades shows an increasing appreciation for transparency in facade design. This situation leads to constant developments in the glass industry and innovative applications of glass products. Highly transparent building envelopes enhance elegance in structures. The perception of this elegance however is often limited by structural elements supporting the glazing, which are generally made of opaque materials like aluminium, steel or timber and have large cross sections. In such systems, the glass panes generally act only as infill elements and are supported by either post and beam structures or prestressed cables. Additionally, diagonal metal bracings are often used to provide the facade structure with the necessary in-plane stiffness. From a structural point of view the glass panes are only subjected to out-of-plane loads, for instance by wind pressure or wind suction.

An example for this type of transparent facades is illustrated in Fig. 1.1. The innovative concept for this facade, finished in 1999, follows the objective to perform all complex assembling operations off-site, allowing for a modular erection of the system. Therefore, prefabricated panels with prestressed stainless steel rods were welded together in the field [Sinclair, 1999]. Despite the impressive appearance of the building, with the glazed facade facing the Boston skyline, the desire for maximal transparency and the latest developments in structural use of glass bring up the question, if part of the metal structural elements could be eliminated or at least reduced in their cross section dimensions by activating the in-plane load bearing capacity of the glass panes.

Fig. 1.1 *Glass facade with metal bracing at the John Joseph Moakley U.S. Courthouse in Boston, United States (© V.A. Silvestru)*

A more recent project, finished in 2016, with a transparent envelope supported by a metal structure is illustrated in Fig. 1.2. The glazed entryway to a subway station, which is planned to become a landmark, presents a rather conventional steel structure. Thin vertical steel fins and horizontal steel beams, shaped according to the expected distribution of the bending moments, are braced over large areas with round steel profiles. The glass panes are connected with point fixings exterior to the steel structure, offering a smooth appearance of the building from the outside. However, the rather obtrusive perception of the steel structure conflicts the desire for transparency. By considering the structural potential of the material glass and the current fabrication limits of glass products, a higher elegance could be achieved for a construction like this one. Adjustments in detailing and design could allow to replace some of the structural steel ele-

ments with glass elements and to remove some structural steel elements and assign their role to the existing glazing.

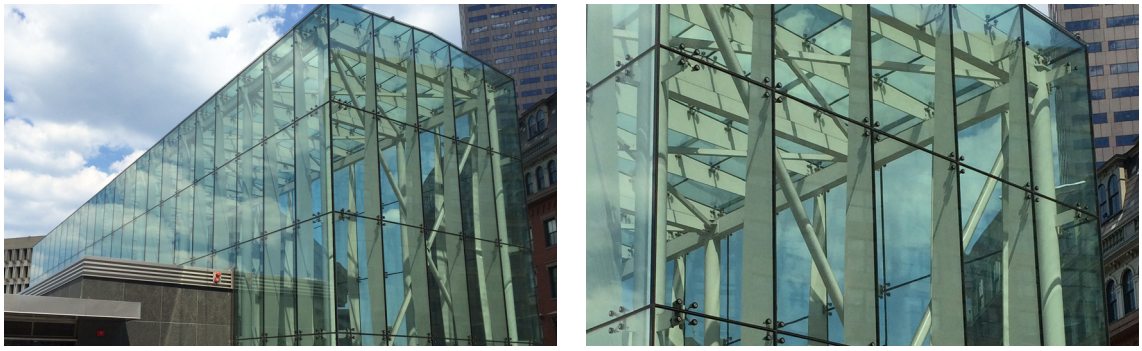

Fig. 1.2 *Glass entryway with pronounced metal structure at the Government Center Station in Boston, United States (© V.A. Silvestru)*

Leading architecture and structural engineering offices, encouraged by prosperous clients, realized during the last decade some impressive landmark projects with glass components as structurally active elements. One of the pioneering constructions in this field is the glass cube in New York (see Fig. 1.3) with an edge length of about ten metres, having only structural elements made of glass, which are connected by mechanically and aesthetically optimised metal fittings. The structure consists of eight column fins as well as two *10 m* and seven *3.3 m* long roof beams. The bracing of the structure is realised by twelve facade panels and three roof panels [O'Callaghan & Bostick, 2012]. This project illustrates the highest possible degree of transparency for a building.

Fig. 1.3 *Glass cube at the Apple Store on Fifth Avenue in New York, United States (© V.A. Silvestru)*

Glass walls with a structural role can be also noticed in some pavilion-like buildings with landmark character. Fig. 1.4 illustrates two examples, an exhibition building in Rheinbach and an entrance building in Manchester. In both cases the aim is to offer the illusion of a floating roof by using only transparent vertical elements. These glass walls have to bear additionally to out-of-plane loads, vertical in-plane loads resulting from the dead weight of the roof as well as horizontal in-plane loads resulting from their role as shear panels. While for the pavilion in Rheinbach, finished in 2000, only flat panels are used to support a 28 tons heavy roof in a height of approximately four metres [Wellershoff & Sedlacek, 2003a], in the case of the construction in Manches-

ter, completed in 2014, a 29 tons heavy monocoque roof is supported by 20 eight metres high, both flat and single-curved glass elements [Weimann et al., 2015]. These two projects demonstrate similar to the glass cube the potential of glass elements for structural use.

Fig. 1.4 *Load bearing glass walls at the glass pavilion in Rheinbach, Germany (left, © F. Wellershoff) and at the Glazed Link in Manchester, United Kingdom (right, photo by courtesy of Waagner-Biro)*

Despite the current possibilities to realize building envelopes with both transparent skin and transparent structural elements, this is not always the desired result by clients and architects. Well defined visible lines in the facade, achieved by filigree metal profiles, often lead to a higher overall elegance. Considering that in an only-glass envelope the glass pane edges are visible and the gaps between two glass panes are usually filled with non-transparent sealing materials, filigree metal profiles at the edges do not significantly decrease the overall transparency appearance and allow to avoid visible point fittings. Furthermore, linear steel profiles, which are adhesively bonded with the glass panes, improve the structural behaviour and the residual load-bearing capacity of these elements. Therefore, a possibility to design elegant transparent building envelopes with a highly efficient use of materials is to activate a composite structural behaviour between the glass panes and the metal framing.

A composite system aims to activate the advantages of its integral parts in order to obtain more efficient properties. In the case of glass-metal elements with composite structural behaviour this can be achieved by joining the metal framing with the glass pane with suitable load transfer mechanisms and materials. Although a significant amount of knowledge and data is available for the structural behaviour of the different materials, the interaction of these materials in a composite element has yet to be investigated regarding manufacturing, structural and functional performance. The work in this thesis focuses on the possibility of using adhesive bonding to obtain a composite structural behaviour between metal framing and glass panes in transparent building envelopes. The performed studies and investigations as well as the obtained results address the following two research questions:

- How can adhesive bonding be used to connect a glass pane with a filigree metal framing in order to obtain an element with composite structural behaviour?

- What are the structural performance and the failure limitations of glass-metal elements with composite structural behaviour by adhesive bonding?

1.2 Research objectives and methodology

Based on the presented background situation as well as on the defined research problem and questions in the previous subchapter, several objectives are set to be achieved with the investigations in this thesis. The structural behaviour of in-plane loaded glass panes as well as the mechanical properties of several structural adhesives for applications between glass and metal substrates were analysed in previous research projects. However, the structural performance of a combined application of in-plane loaded glass panes and structural adhesives together with a filigree metal framing has not been approached yet. The achievement of the following objectives will bring a significant contribution to this topic:

- Define possible application situations in the building envelope for glass-metal elements with composite structural behaviour by adhesive bonding.

- Identify suitable adhesives from the existing products used for structural glass applications and determine their limitations with respect to glass-metal elements with composite structural behaviour.

- Analyse different load transfer possibilities between glass pane and metal framing with focus on adhesive bonding and especially structural silicones.

- Develop and assemble a glass-metal element with composite structural behaviour by adhesive bonding, which illustrates the mechanical interactions between the different components and allows for further development to a facade product.

- Perform experimental testing on the glass-metal element with composite structural behaviour under combined in-plane and out-of-plane loading and determine the overall performance of the element as well as the performance of the adhesive in this system.

- Develop simplified modelling techniques and elaborate design recommendations in order to encourage the approach of these innovative structural systems in engineering offices.

The methodology applied to achieve these objectives is diverse and reflects the complexity of the topic. A schematic representation of the methods is illustrated in Fig. 1.5 and provides at the same time a brief insight into the performed investigations. An explicit literature review is completed at the beginning of the research and is essential for the further steps. This literature review is extended during the whole duration of the research with new publications related to the topic. The most important information obtained from this review is summarised in chapter 2, while detailed results can be found in the literature references provided in the bibliography. Another method used to obtain information on the already available knowledge, especially regarding the adhesive materials, are discussions with the adhesive manufacturers.

For determining the mechanical performance of the investigated glass-metal elements with composite structural behaviour by adhesive bonding an extensive experimental programme is carried out. This programme includes tests at material level on bulk specimens for the adhesives, tests at connection level on adhesive joints with various geometry between glass and metal substrates as well as tests at element level on real-size glass-metal elements with com-

posite structural behaviour by adhesive bonding. The methodology used for manufacturing and testing as well as the measurement instrumentations are described in detail in the respective chapters.

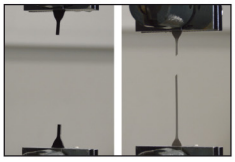

experimental testing on bulk material specimens

literature review & discussions with experts

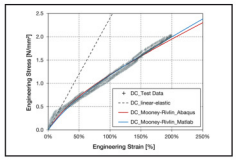

determination of material models by curve fitting

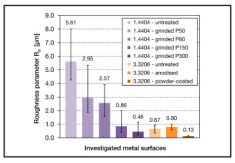

statistical evaluation of roughness measurements

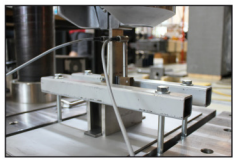

experimental testing on metal-metal adhesive joints

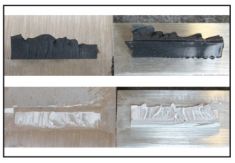

evaluation of failure types and patterns

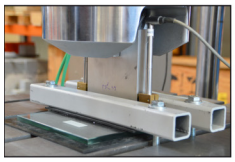

tensile tests on glass-metal adhesive joints

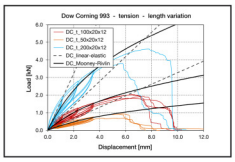

validation of the used material models

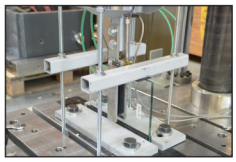

shear tests on glass-metal adhesive joints

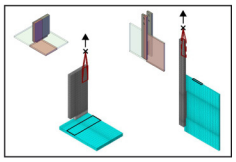

finite element simulations

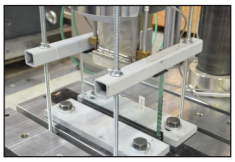

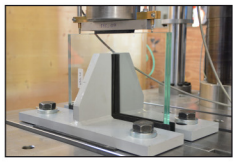

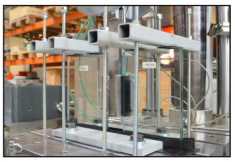

experimental testing on rectangular, L-shaped and U-shaped adhesive joints at the glass edge under tensile (left), compressive (middle) and shear loading (right)

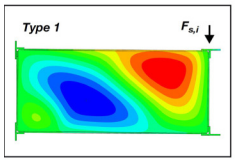

parametric studies by finite element analysis

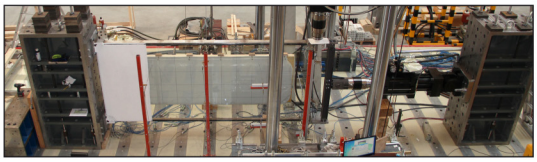

large-scale testing of elements with composite structural behaviour under combined loading

evaluation of adhesive behaviour and failure

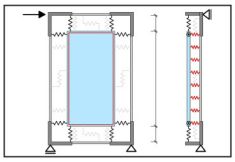

derivation of simplified mechanical models

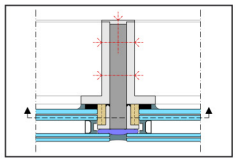

development of conceptual building construction details

Fig. 1.5 *Schematic diagram of the used methodology*

Finite element non-linear analysis with suitable material models is used to simulate all the experimental tests. The results obtained from experimental testing are evaluated by statistical methods and then compared to finite element analysis results in meaningful and clear diagrams.The objective to encourage the approach of such systems in engineering offices is achieved by elaborating design recommendations based on simplified finite element models. Furthermore, building construction details are developed with the investigated structural system on a conceptual design level by taking building physics requirements into consideration.

In this paragraph a delimitation of the research work within this thesis is formulated. The presented investigations do not have as an objective the development of a product, but to show the technical feasibility of glass-metal elements with composite structural behaviour by adhesive bonding and their potential from a structural point of view. All the performed experimental testing and finite element analysis are valid for room ambient conditions. Behaviour at high and low temperatures, resistance to moisture and ultraviolet radiation as well as other durability aspects are considered in the selection of the materials, but are not investigated within the thesis at connection and element level. Furthermore, the performance of the elements regarding building physics requirements is not analysed in this thesis, but these aspects are considered in order to be able to fulfil them by further developments.

1.3 Structure of the thesis

The research work presented in this thesis is structured in nine chapters which can be grouped as illustrated in Fig. 1.6. The order of the chapters is intended to guide the reader logically from the topic definition step by step to the formulated conclusions considering the objectives stated in subchapter 1.2. After introducing the topic, in a first step, the reader is provided with the relevant theoretical background as well as necessary conceptual aspects for the investigations to follow. Secondly, small-scale investigations performed at material and connection level are discussed. Thirdly, results from large-scale experimental testing and finite element analysis are described. In a fourth step, different aspects are emphasized which are necessary in order to approach the scientific findings to practical use. Finally, conclusions are drawn and an outlook for further necessary related research is provided. The original contribution from the author of this thesis starts with chapter 3.

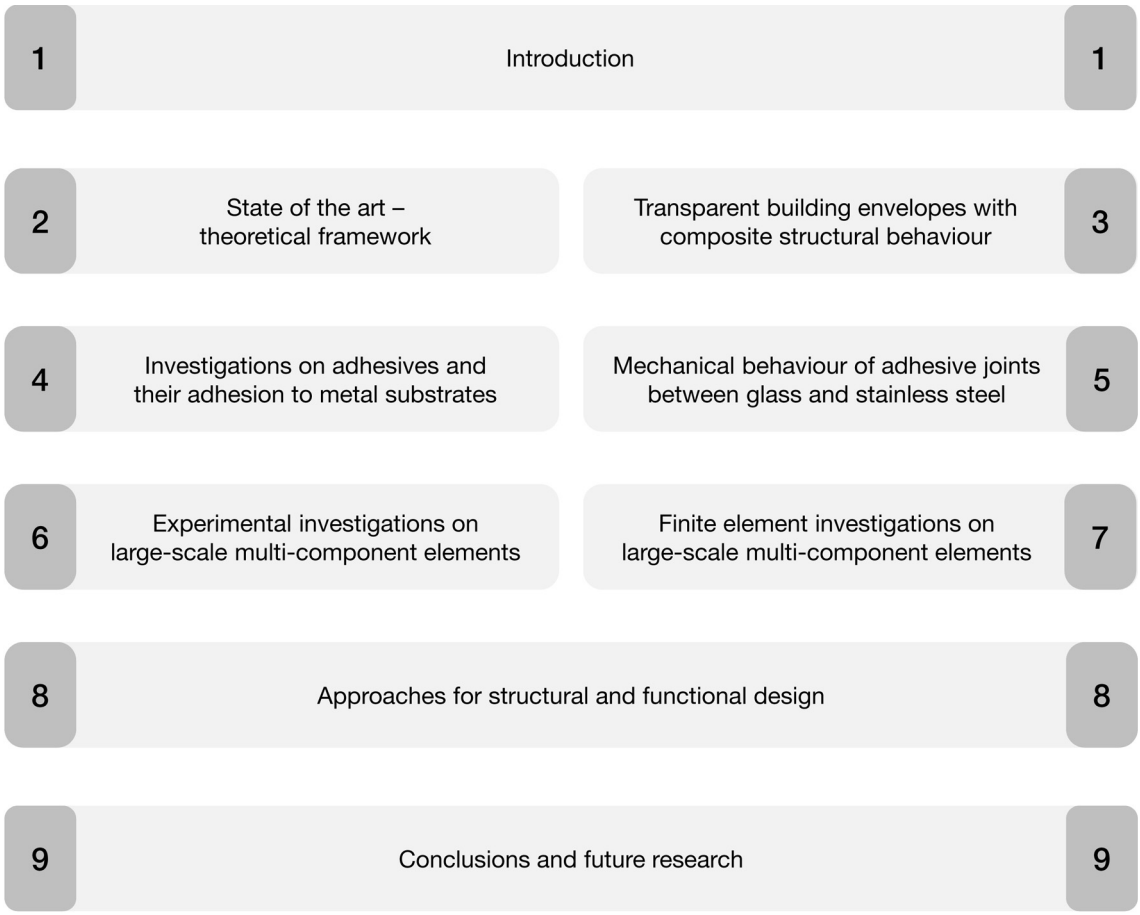

Fig. 1.6 *Structure of the thesis*

In the next paragraphs a brief description of the content of each chapter is provided in order to allow the readers to get a quick insight and decide which of the covered aspects are relevant for their interest.

1 Introduction

The motivation for investigating the composite structural behaviour between glass panes and metal framing in transparent building envelopes is illustrated by facade projects where this concept would lead to improvements regarding efficient material use and aesthetic architectural design. Further, the research topic is described, the aims of the presented investigations are specified and delimitations of the completed research are given. A description of the elaboration approach including the used methods for reaching the stated objectives and short summaries of the content of each chapter complete the introductory part of the thesis.

2 State of the art - theoretical framework

Relevant theoretical aspects are briefly covered in order to provide the reader with the necessary basic knowledge for understanding the investigations presented in this thesis as well as with references for deeper information. In a first step, structural systems for large glazed facades are described, for which an improvement is considered to be possible regarding efficiency in material use and structural performance by the investigated composite structural behaviour. In a second step, the main materials used in transparent facade structures are introduced by focusing especially on the properties relevant for the performed research. After these more general aspects, results of completed research projects dealing with composite glass-metal structural elements, with structural behaviour of glass panes under out-of-plane and in-plane loads and with load transfer concepts for out-of-plane and in-plane loads between glass panes and frame materials are summarised.

3 Transparent building envelopes with composite structural behaviour

The concept investigated in this thesis is presented in detail and aspects to be considered in the research are elaborated. Firstly, occurring actions on transparent building envelopes and their size are described. Secondly, requirements for transparent building envelopes are characterised mainly with regard to building physics and comfort expectations. Based on the occurring actions and the existing requirements, challenges for transparent building envelopes with composite structural behaviour regarding the load transfer within a single facade element as well as between several elements are defined. Finally, load transfer concepts within a single element for transferring out-of-plane and in-plane loads between the glass panes and the metal framing by using adhesives and materials for transferring compressive loads are described.

4 Investigations on adhesives and their adhesion to metal substrates

Based on the load transfer concepts for a single element with composite structural behaviour described in the previous chapter, selection criteria for suitable adhesives are defined. Considering these criteria, suitable adhesives are selected from existing products and their relevant properties are determined by experimental tests and based on data gathered from the producers. Material models to be used in finite element simulations are derived for three selected adhesives. For the two silicone adhesives, hyperelastic material models are investigated, while for the acrylic adhesive, a strain rate dependent plastic model is proposed. Additionally to these investigations on the raw material, experimental tests are performed to determine the adhesion behaviour on metal substrates with different surface conditions. Adhesive joints between stainless steel and aluminium substrates are subjected to double-lap shear tests.

5 Mechanical behaviour of adhesive joints between glass and stainless steel

In this chapter the mechanical behaviour of adhesive joints with different geometries between stainless steel and glass substrates is investigated experimentally. For joints at the glass surface, a rectangular cross-section geometry is chosen and the influence of different dimensions in length, width and thickness direction on the mechanical behaviour is analysed for the three selected adhesives. These adhesive joints are subjected to tensile and shear loading. For joints at the edge of laminated glass panes, the performance of joint geometries with rectangular, L-shaped and U-shaped cross-section is compared to each other. Tensile, shear and compressive loads are applied on the adhesive joints at the edge of laminated glass panes. Additionally to failure loads, stresses and strains, also the manufacturing process of the joints and the failure patterns are documented in detail and analysed. Finite element simulations of selected experimental tests are performed with the material models derived in the previous chapter to check their suitability for different geometry and loading conditions. Based on the evaluated results of 150 experimental tests and the performed finite element analysis recommendations for application are formulated.

6 Experimental investigations on large-scale multi-component elements

Based on the aspects presented in chapter 3 and focusing on systems with adhesive joints, simplifications are made and boundary conditions are defined in order to obtain single element systems for which the composite structural behaviour can be investigated from a mechanical point of view experimentally and with finite element methods. Two concepts are introduced: *(i)* the first one with grouting (setting) blocks near the glass pane corners for transferring the in-plane loads and a perimetrical adhesive bonding with a silicone adhesive between the glass panes and the metal framing to transfer the out-of-plane loads; *(ii)* the second one with a perimetrical adhesive bonding between the glass panes and the metal framing with an acrylic adhesive which has to transfer both the out-of-plane and the in-plane loads. Experimental testing on simplified large-scale elements for transparent building envelopes with composite structural behaviour is performed for both presented concepts. In this thesis, the focus lies on the adhesive bonding for both concepts. The mechanical behaviour of the used grouting is covered in detail in a second doctoral thesis dealing with this topic (see [Kolany, 2018]). The planning and the manufacturing of the test specimens including recommendations for possible improvements in the future are described first. Then, the test setup with all the boundary conditions and the applied loads, the experimental procedure with the driven load cycles and the used measurement techniques are presented. Finally, the test results obtained from the different loading series are evaluated and discussed. An in-plane shear load, an in-plane axial load and an out-of-plane surface load are applied separately as well as in different combinations.

7 Finite element investigations on large-scale multi-component elements

After completing the experimental programme on large-scale elements, the finite element models used for preliminary dimensioning of the test specimen components are adapted and validated by comparison to the test results. With these models, the influence of several parameters on the mechanical behaviour is then investigated. Firstly, parameters related to the glass pane dimensions and layering are varied. Secondly, the dimensions of the metal framing components are modified. Thirdly, alternative cross sections and different Young‘s moduli of the adhesive

joints are investigated. Furthermore, the influence of initial geometric imperfections on the deformation behaviour is analysed by comparing the results obtained with different eigenmodes as imperfection shapes as well as different sizes for the initial imperfection. Finally, the structural behaviour of the elements under different loading scenarios and levels is assessed in order to extend the results from the experimental series.

8 Approaches for structural and functional design

Generally, in scientific research complex methodologies and software are used to investigate the defined tasks. In order to use the obtained scientific results in practice, simplified methods and models have to be derived. In this chapter simplified mechanical models consisting of shell elements for the glass panes and the frames as well as linear elements for the load transfer materials are elaborated. These models can be implemented in software for structural design used in engineering offices. Additionally, a conceptual approach for the structural design of composite structural glazing systems, especially for early stage project phases, is proposed. Most of the investigations performed in this thesis focus on the structural behaviour of transparent building envelope elements with composite structural behaviour between glass panes and metal framing by adhesive bonding. Therefore, several simplifications are carried out, especially in neglecting building physics requirements for the investigations at element level. In this chapter, the element design used for large-scale experimental testing and finite element analysis is further developed to fulfil selected building physics requirements. An extension to insulating glass units as well as connection possibilities between several elements are illustrated and explained by conceptual sketches.

9 Conclusions and future research

In this chapter, the performed investigations and the obtained results are briefly summerised and conclusions about the essential findings related to the concept of glass-metal elements with composite structural behaviour by adhesive bonding are drawn. Finally, an outlook is provided for aspects which need to be investigated in further research projects based on the delimitations defined at the beginning of the thesis as well as on findings from this research work.

2 State of the art - theoretical framework

Selected systems for glass front facades
Properties of relevant facade materials
Glass panes in structural applications

1 Introduction 1

2 State of the art – theoretical framework

3 Transparent building envelopes with composite structural behaviour

4 Investigations on adhesives and their adhesion to metal substrates

5 Mechanical behaviour of adhesive joints between glass and stainless steel

6 Experimental investigations on large-scale multi-component elements

7 Finite element investigations on large-scale multi-component elements

8 Approaches for structural and functional design

9 Conclusions and future research

2.1 Selected systems for glass front facades

The facade has the primary role to separate the outside environment from the inside of a building and to provide a certain comfort to the users, whether it is a solid wall or a glass front. While the solid wall is part of the load-bearing structure of the building, in the case of a glass front, generally the facade function is decoupled from the load-bearing function, which is fulfilled by columns and/or solid walls. This type of facades consist of glass panes and secondary structural components which play the role of supporting the glass panes and transferring loads from the glazing to elements of the primary structure like ceilings or columns [Knaack et al., 2007]. Selected systems for glass front facades, which are considered to be suitable in particular cases for using the investigated glass-metal elements with composite structural behaviour, are explained in the next subchapters.

2.1.1 Post-and-beam facades

Glass front facades can be differentiated in single-skin and double-skin systems. Single-skin transparent facades can be further classified with regard to production and assembling into post-and-beam facades and system facades. Both types consist of a glazed outer skin which is either connected to the floor slabs or to load-bearing columns over the height of a storey. In case of large glazed atriums and entrance areas the glazed outer skin can be connected to structural elements spanning over the height of the whole building.

The conventional post-and-beam facade, also referred to as stick system curtain wall when suspended from above, consists of vertical posts (mullions) and horizontal beams (transoms), which are assembled together and glazed on site (see sketch in Fig. 2.1, right). From a structural point of view these linear elements have to bear the self-weight of the glazing and to transfer out-of-plane wind loads to the main structure. An example of a post-and-beam facade is illustrated in Fig. 2.1, left. Further information on this facade type can be found in [Herzog et al., 2004], [Knaack et al., 2007] and [Pottgiesser, 2009] while several constructive details and explosion sketches are illustrated in [Watts, 2014].

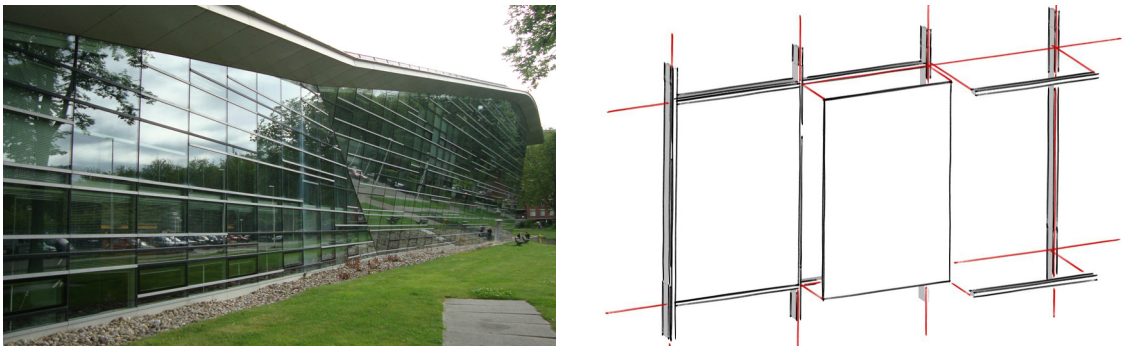

Fig. 2.1 *Example of a post-and-beam facade at the library in Delft (left; © V.A. Silvestru) and schematic illustration of a post-and-beam facade (right)*

Leading manufacturers of facade systems like [www.schueco.com] or [www.raico.de] offer in their portfolio a wide selection of post-and-beam facade systems, highly optimised regarding aesthetics, thermal and noise protection as well as regarding other requirements. The profiles

can be made out of different materials like aluminium, stainless steel or timber and show different cross section geometries depending on design concept and requirements to be achieved. The fixing of the glazing can be realised either by clamping strips or by structural sealant glazing. In the first case the posts and the beams are visible both from the inside and the outside. In the second case they are visible from the inside, but only the watertight joints between the glass panes and eventually punctual mechanical fixings are visible from the outside.

Further developments from the post-and-beam facade with the aim to increase transparency are systems only with posts or only with beams. For such systems, especially when used for facades spanning over areas higher than one storey, projects can be found where the supporting linear elements are realised out of glass in form of glass fins.

2.1.2 System facades

System facades consist of fully prefabricated elements including the framing and in-fill glazing or insulating panels, which have either the height of a storey or are even larger. This facade type is also referred to as unitised curtain wall when suspended from above. The advantage of this type of facades lies in the controlled boundary conditions during the production, which lead to high industrial automation and high accuracy as well as to rapid assembly and low labour necessity on site. The side profiles of the elements have embedded rubber-gaskets which allow for compensating tolerances and different deformations between the elements. They also help to reach the required thermal and noise protection as well as the water and air tightness. The elements are usually connected to brackets, which are already attached to the primary structure, or in particular cases just connected on top of each other and side by side. Since such systems need a higher degree of planning and more complex logistics during assembly, they are generally used for larger projects with a modular structure, like high-rise buildings for instance. A system facade during construction is illustrated in Fig. 2.2, left. For further details on this type of facade [Herzog et al., 2004], [Knaack et al., 2007], [Pottgiesser, 2009] and [Watts, 2014] are recommended as literature.

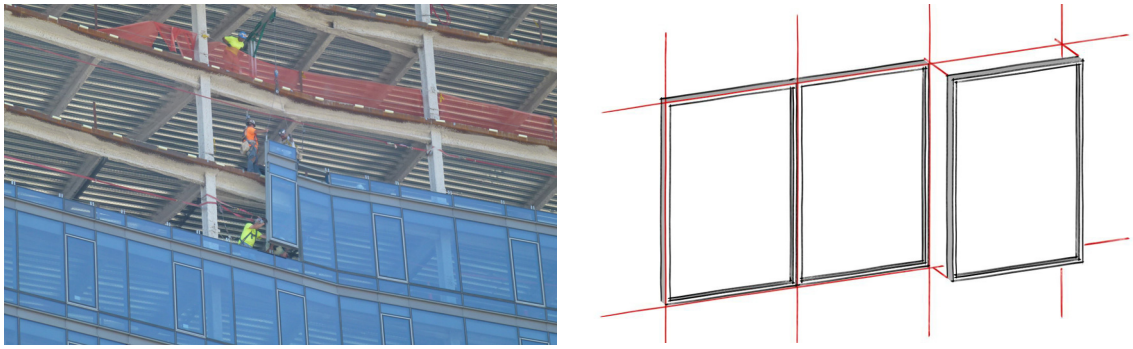

Fig. 2.2 *Example of a system facade during construction (left; © V.A. Silvestru) and schematic illustration of a system facade (right)*

Similar as in the case of post-and-beam facades, there are engineered products on the market offered by leading facade manufacturers like [www.schueco.com] and [www.wicona.com]. The difference in the case of system facades comes when non-standard projects are approached. In

such cases facade design offices elaborate new concepts for the unitised elements which are optimised to fulfil specific requirements and sometimes even show complex geometries. Specialised facade contractors then manufacture these new unique products.

2.1.3 Double-skin facades

Double-skin facades have an inner skin, which is generally a system facade but can also be a post-and-beam construction, and an additional outer skin, which in most cases is a single glazing. The purpose of the second skin is to obtain a cavity which increases the noise protection, improves the thermal performance and the ventilation during winter and offers additional protection from wind and weathering to the inner skin. Additionally, sun shading elements can be positioned within the cavity where they are protected from high wind speeds and can function continuously. However, experiences with double-skin facades show that during summer an overheating of the cavity is occurring, which makes a natural ventilation with air from the cavity difficult.

This type of facades are a suitable solution for buildings facing high levels of street noise or high wind loads, but each facade of the building showing a different orientation should be analysed separately. Double-skin facades can be classified into second-skin facades, corridor facades (see example in Fig. 2.3, left), shaft-box facades and box-window facades depending on how the cavity is divided over the height and the width of the building (see [Knaack et al., 2007] and [Pottgiesser, 2009]). The simplest of these typologies from a technical point of view is the second-skin facade which has neither horizontal nor vertical subdivisions. The other systems result from the objective to improve the quality of the incoming air in the different floors and to reduce the noise interference between neighbouring rooms through the cavity.

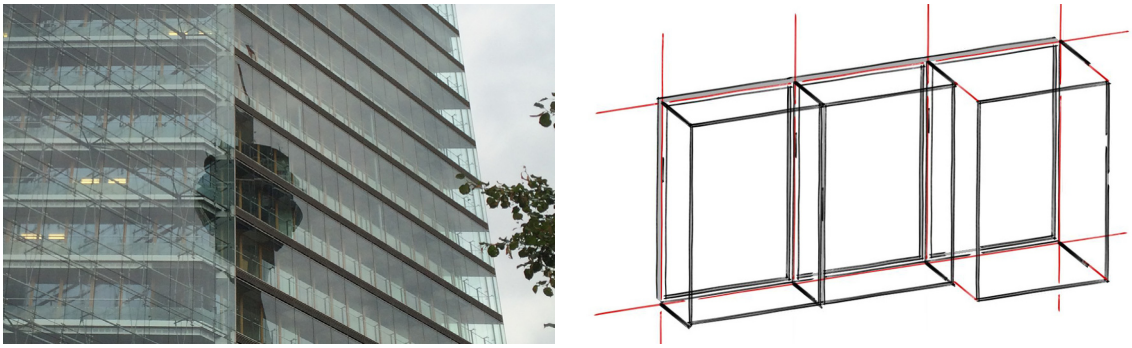

Fig. 2.3 *Example of a double-skin facade in Düsseldorf (left; © V.A. Silvestru) and schematic illustration of a double-skin facade (right)*

The connection of the outer skin to the main structure is generally realised by cantilever brackets. The design of these brackets is dependant on the type of double-skin facade and on the depth of the cavity. While for a second-skin facade rods with rather small cross sections and spider fixings can be used, in the case of deep corridor facades often an accessible flooring is desired, which results in larger brackets.

2.2 Properties of relevant facade materials

The facade design concepts of the last decades show a trend for higher transparency, especially in the case of public and office buildings. A noticeable consequence of these developments is the changing role of the material glass, which is used more and more in a structural way. Applications like facade glazing fixed on glass fins or pavilions with load-bearing glass walls are still challenging engineering tasks, but no longer exceptional in the building envelope industry.

Regarding the framing of transparent facade elements, the developments during the past years aim on the one hand at reducing the visible width for aesthetical reasons and on the other hand at improving the thermal performance of these linear elements by either using materials with a lower thermal conductivity or by dividing the metal profile sections in chamber systems with thin wall thicknesses and thermal separations.

Considering the aimed elements with composite structural behaviour between glass panes and metal framing and the fact that glass as a brittle material, which is not able to plastically redistribute occurring stress peaks, should not get in direct contact with harder materials, additional soft materials are required for the connections between glass and metal components. Several research projects focused in the last years on different connection types for structural glass applications covering mechanical and adhesive point fixings, setting blocks for transferring compressive loads at the glass edge and linear adhesive joints.

The state-of-the-art material related aspects, which are relevant to the topic of glass-metal elements with composite load-bearing behaviour are pointed out in the following subchapters.

2.2.1 Glass and glass products

Different from structural elements made of concrete, steel or timber, which are generally dimensioned and built according to existing standards, the design and the construction of structural glass components is often based on research results and experimental testing. The existing standardization on a national level for structural design of glass components covers only a limited part of todays applications. The elaboration process for a European standard in this field is initiated with [EUR 26439 EN, 2014], which aims at gathering the significant results and approaches from research.

In this subchapter only a brief overview of the key aspects regarding glass and glass products for the investigations in this thesis is given without going into details. Several books, which cover the properties of glass as a material, the production technologies of glass, the mechanical processing of glass, the thermal treatment as well as the further processing to laminated glass and insulating glass, were published during the past twenty years: [Knaack, 1998], [Schittich et al., 1998], [Knaack et al., 2000], [Wurm, 2007], [Haldimann et al., 2008], [Feldmann et al., 2012], [Siebert & Maniatis, 2012], [Schneider et al., 2016] and others. These publications also address topics like connections for glass elements, constructive detailing and structural design of glass components along with examples as well as additional aspects depending on the authors like

stability behaviour of glass components ([Haldimann et al., 2008] and [Feldmann et al., 2012]) or fracture mechanics of glass ([Haldimann et al., 2008] and [Siebert & Maniatis, 2012]).

Annealed glass

The glass material used in most building applications is soda lime silica glass. For special requirements like increased fire protection borosilicate glass can be chosen. The primary product in terms of glass used in more than *90%* of todays applications, whether it is in the building sector or in the automotive industry, is annealed glass (ANG) produced with the float glass technology. Hereby the glass melt having around *1100 °C* is floating over a tin bath before it reaches enough inherent rigidity at about *600 °C* and it is transferred to the cooling channel. The production size is limited in width by the size of the existing float lines with *3.21 m*, while the limits in length are generally given by logistics criteria. A standard maximum length of *6.0 m* can be found in most technical literature, but lengths up to *15.0 m* have already been produced by different companies. For the production thickness of float glass panes there are certain nominal values varying between *3 mm* and *19 mm* depending on the floating speed. Because float glass has a rather low characteristic value for the bending tensile strength of *45 MPa* according to [ÖNORM B 3716-1] and [DIN 18008-1] and it shows micro-cracks at the surface, it has to be further processed for structural applications. Design methods for glass elements based on fracture mechanics and crack growth models were investigated by [Overend, 2002] and [Haldimann, 2006].

Tempered glass

The tempering method helps to create a residual stress field with compressive stresses near the surfaces and tensile stresses in the core of the glass. As a result the micro-cracks can only grow if the tensile stresses due to exterior loading are larger than the residual compressive stresses. In general, thermal tempering and chemical tempering are differentiated. The thermal tempering process consists of heating the float glass up to around *650 °C* and afterwards cooling it rapidly down. Depending on the cooling speed, thermally toughened glass (TTG) or heat strengthened glass (HSG) can be obtained. TTG has the higher structural capacity with a characteristic value for the bending tensile strength of *120 MPa* according to standards, but due to its failure mode (breaks in tiny dice fragments) it also shows a poor post-failure performance. HSG shows a good post-failure performance due to larger fragmentation pieces, while having a characteristic bending tensile strength of *70 MPa*. A significant aspect related to thermal tempering of glass is the fact that all the mechanical processing, like cutting and drilling, has to be completed before the tempering process. Despite the strength values provided in standards for thermally tempered glass, [Laufs, 2000] shows that the distribution of the induced compressive stresses varies for the surface, the edges, the corners and the borehole areas of glass panes. He recommends different strength values for these four zones, both for TTG and HSG, and distinguishes as well between an out-of-plane and an in-plane loading of the glass pane, providing lower strength values for the latter one.

Chemical tempering is realised by exchanging the sodium ions in the glass surface with potassium ions by soaking the glass panes in an electrolytic bath. Due to the larger volume of the potassium ions a compression zone results at the glass surface, which is much thinner than in the case of thermal tempering. Chemically tempered glasses are used more in the display

industry until now due to their high scratch resistance, while in the building industry only exceptional applications can be noticed. Although, due to the new developments and trends towards thin glass and curved glass the interest for chemically toughened glass increases as shown by the movable canopy presented in [Neugebauer, 2015].

Laminated glass

Since glass is a brittle material even after tempering, for structural applications two or more glass panes are laminated together with transparent plastic interlayers in order to obtain an improved post-breakage behaviour. The lamination process generally takes place in an autoclave at a temperature of approximately *140 °C* and a pressure of around *14 bar*. The resulting product, called laminated glass (LG) or laminated safety glass (LSG), has a remaining structural capacity after breakage of the glass panes due to the interlayer which holds the glass splinters together. Additionally, it also provides a significantly lower risk for injuries since dangerous glass fragments do not fly through the air after failure. The level of remaining capacity after glass breakage depends on the type of glass fragmentation and on the used interlayer material. Laminated glass made of annealed glass or heat strengthened glass shows a high post-breakage structural capacity, while for laminated glass made of thermally toughened glass this capacity is rather poor.

For structural applications with laminated glass the most common interlayer materials are polyvinyl butyral (PVB) and the ionomer SentryGlass (SG). Both materials show visco-elastic properties, which means that their mechanical behaviour depends on temperature and load duration. While at low temperatures and short loading durations these materials show a high shear modulus and are therefore able to transfer high shear stresses between the glass panes, with higher temperatures and longer loading durations the shear modulus decreases significantly. The difference between standard PVB products and SG is that the first one reaches shear moduli up to *4 MPa*, while SG reaches values of around *200 MPa*, both at *20 °C*. Because of this complex material behaviour, design standards are rather conservative and generally allow to assume a composite action only for impact loads as in [DIN 18008-1] or only reduced values for short load durations like the shear modulus of *0.4 MPa* allowed by [ÖNORM B 3716-1].

Several research projects from the last ten years show results on the material behaviour and characterization of interlayers for laminated glass. In [Wellershoff, 2007] design values for the shear moduli of interlayers (PVB and SG) are determined based on size and duration of wind and snow loads correlated with the corresponding temperature of the interlayer material. [Ensslen, 2005] and [Sackmann, 2008] deal with the ageing behaviour of PVB under influence of moisture, UV-radiation and temperature, while [Kothe, 2013b] analyses the ageing behaviour for both PVB and SG along with other further polymeric interlayer materials. [Puller, 2012] and [Santarsiero, 2015] investigate embedded and laminated connections with SG ionomer and therefore derive material parameters based on uniaxial tensile tests at different temperatures and strain rates.

Insulating glass units

One of the main goals in the building sector is to reduce the energy consumption. This can be achieved by improving the thermal performance of the building envelope and implicitly of the

glazing, since up to *50%* of the heat losses occur through these elements. An insulating glass unit (IGU) is obtained by enclosing a hermetically sealed cavity between two glass panes. The cavity can be filled with dehydrated air or with an inert gas like argon or krypton. The distance between the glass panes is determined by a perimetrical spacer system, which has also the role to reduce the water vapour penetration. [Van den Bergh et al., 2013] gives an overview of different spacer systems, which are available on the market or which were developed by research facilities, and compares their dimensions and thermal properties. The most common spacer system consists of a metallic spacer, generally made of stainless steel, which contains a desiccant to absorb humidity. The spacer is connected to the glass panes by a primary seal made of polyisobutylene and a secondary edge seal made of polysulphide or silicone and provides the insulating glass unit with the required structural robustness. A further improvement of the thermal performance is achieved by adding a second cavity in order to obtain a triple IGU.

Investigations on insulated glass units from a structural point of view, focusing both on the global behaviour of double and triple units as well as on the mechanical properties of secondary silicone sealants, are presented in [Bao, 2014]. The proper functionality of IGUs depends on the water tightness of the spacer system to prevent damages by long-lasting condensate formation as well as on the minimised gas loss from the cavity over the lifetime. Results for the durability of double and triple IGUs from performed climatic tests are provided in [Oechsner et al., 2015].

Curved glass and thin glass

Although these glass products are not directly linked to the topic of this thesis, the increasing trend in todays architecture for curved shapes (see [Neugebauer, 2014]) makes them interesting to be considered for glass-metal elements with composite structural behaviour by adhesive bonding as an outlook. Both curved glass and thin glass are not covered by existing standards. Curved glass can be produced either by hot bending or cold bending. In the first case the glass is heated up above its softening point and it either sinks in the shaped mould by its own weight (generally used for single-curved glass) or it is formed with moulds from both sides (used for double-curved glass). This method is cost-intensive and shows difficulties with distorsions of the curved glass as well as with tolerances for producing laminated glass and insulating glass units in a further step. For smaller radii cold bending is a more attractive method. The glass units, whether monolithic, laminated or insulating glass, are produced in the regular way. Afterwards they are cold bend on site by pressing them on a curved substructure and then they are fixed mechanically. It is to consider that by cold bending permanent stresses are induced into the glass as well as into other components like the interlayer of laminated glass or the spacer and the sealing of insulating glass. A third method for producing curved glass is the bending by lamination, where the glass panes and the plastic foils are first layered, then fixed in the desired curved shape and afterwards they are laminated in an autoclave.

Several research projects from the last fifteen years deal with curved glass, focusing especially on cold bending and cold lamination bending. [Belis et al., 2007] presents the dependency of the cold bending process and the required forces for single-curved laminated glass panes on the interlayer material and thickness, the loading speed and the temperature during bending. [Datsiou & Overend, 2014] and [Galuppi et al., 2014a] deal both experimentally and numerically with the buckling behaviour of double-curved glass panes and the occurring snap-through

effect at larger curvatures. The cold lamination bending is investigated in [Fildhuth & al., 2014] and [Galuppi et al., 2014b] regarding spring back effects after lamination and release from fixing as well as relaxation effects over time due to the visco-elastic behaviour of the interlayers. Experimental results from a study on the durability of cold bend insulating glass units are presented in [Besserud et al., 2012], while some design recommendations for structural sealant glazing systems, where the glass units are adhesively bonded to adapter profiles and then cold bend all together, are given in [Beer, 2015].

Thin glass is a rather new product for applications in buildings and is referred to when the thickness of glass panes is lower than *2.0 mm*. The only existing market-ready application of thin glass is as an inner glass sheet for triple or quadruple IGUs (see [Jandl, 2015]). By using thin glass in curved shapes, the membrane load-bearing capacity is activated and lower deformations are obtained. Whether it is thermally tempered or chemically tempered, thin glass is not covered by existing glass standards. Therefore, current research is focusing on determining the bending tensile strength of this material (see [Maniatis et al., 2016] and [Neugebauer, 2016]).

The design strength of glass and insight into glass fracture aspects

Most available European standards for structural design of glass components (e.g. [DIN 18008-1], [ÖNORM B 3716-1]) are based on the semi-probabilistic safety concept in order to provide a good compatibility to other building materials. The verification in Ultimate Limit State (ULS) is generally conducted by ensuring that the determined design values of the maximum principal tensile stresses are lower than the design value of strength for the used glass type. In order to take the particularities of the material glass into consideration, additional factors are included in the equation for determining the design strength value, R_d. For example, the Austrian standard [ÖNORM B 3716-1] provides (Eq. 2.1) for the design value of strength of both annealed and tempered glass:

$$R_d = \frac{k_{mod} \cdot k_b \cdot f_k}{\gamma_M} \qquad \text{(Eq. 2.1)}$$

The notations used in (Eq. 2.1) have the following meanings:

f_k	characteristic value of the bending strength (f_k = *45 MPa* for annealed glass, f_k = *70 MPa* for heat strengthened glass and f_k = *120 MPa* for thermally toughened glass)
γ_M	material partial factor (γ_M = *1.5* for annealed glass, heat strengthened glass and thermally toughened glass)
k_b	coefficient to consider the type of loading (k_b = *1.0* for out-of-plane loading and k_b = *0.8* for in-plane loading)
k_{mod}	factor of load duration / corrosion (in the case of annealed glass different values of k_{mod} should be used depending on the load duration: $k_{mod,permanent}$ = *0.6*, $k_{mod,middle}$ = *0.6* and $k_{mod,short}$ = *1.0*; in the case of tempered glass k_{mod} = *1.0* without depending on the load duration)

A further reduction of the characteristic value of the bending strength by *20%* is requested in the case of annealed glass for glass edges under tensile stress according to [ÖNORM B 3716-1].

This approach as well as similar ones in other European standards are rather conservative and consider only to a limited extent the variety of factors which can influence the (bending) strength of a glass pane. This strength depends on the inherent strength of the annealed glass and on residual stresses resulting from an eventual tempering process. Furthermore, the inherent strength of annealed glass is influenced by size, shape, orientation and distribution of surface flaws as well as on load duration and environmental conditions. Details on how these factors can be considered as well as on related fracture mechanics aspects are provided by [Haldimann et al., 2008], [Feldmann et al., 2012], [Siebert & Maniatis, 2012], [Schneider et al., 2016] as well as briefly by [EUR 26439 EN, 2014]. In this section only the fundamental ideas and approaches, on which the design strength of glass and the design concepts for glass components are based, are pointed out. For advanced information the above references should be consulted.

The homogeneous and isotropic material glass exhibits a linear-elastic behaviour and fails brittle. To describe this type of failure, quasi-static linear elastic fracture mechanics can be applied in the form of models which characterise cracks (in the case of structural glass applications only surface cracks are of interest). A significant variable in this regard is the stress intensity factor *K* introduced by [Irwin, 1957] based on the energy balance concept by [Griffith, 1920]. This factor allows a characterization of a material with respect to its brittleness by relating the size of a crack to the stresses around the crack. For the crack loading mode I, which represents a normal separation of the crack surfaces under tensile loading, the stress intensity factor K_I can be determined by (Eq. 2.2):

$$K_I = \sigma_n \cdot Y \cdot \sqrt{\pi \cdot a} \qquad \text{(Eq. 2.2)}$$

The notations used in (Eq. 2.2) have the following meanings:

σ_n	nominal tensile stress normal to the crack‘s plane
Y	correction factor depending on the crack geometry and the crack depth
a	crack depth or half of the crack length

When the stress intensity factor K_I reaches a critical value (denoted as K_{Ic}) at the tip of a crack due to tensile stress, instantaneous failure occurs. For the critical stress intensity factor, also referred to as the fracture toughness, a value of $K_{Ic} = 0.75\ MPa{\cdot}m^{0.5}$ is recommended by [Haldimann et al., 2008] for soda lime silica glass. For $K_I = K_{Ic}$, (Eq. 2.2) can be used to determine a critical stress for a given crack depth or, conversely, a critical crack depth for a given stress value. However, this is only valid under inert conditions, since the approach by [Irwin, 1957] does not consider the influence of environmental exposure (e.g. humidity), which causes so called sub-critical crack growth. This means, that the surface cracks grow also under stresses below the critical value. The crack growth rate can be determined depending on the stress intensity factor by the relationship in (Eq. 2.3):

$$v = \frac{da}{dt} = S \cdot K_I^n = S \cdot (\sigma \cdot Y \cdot \sqrt{\pi \cdot a})^n \qquad \text{(Eq. 2.3)}$$

The parameters *S* and *n* depend on the material and the environment. A summary of values for these parameters determined by different authors under various conditions can be found in

[Schneider et al., 2016] (instead of S, the denotation A_K is used). The solution of the differential equation (Eq. 2.3) can be found in [Haldimann, 2006] and [Haldimann et al., 2008] and represents an expression of the uniform failure stress of a single surface crack depending on the stress duration and the crack geometry.

Since the size, shape and orientation of surface cracks is generally unknown, a probability distribution function is necessary to statistically characterise the variation of the glass strength. The probability of glass failure under inert conditions $P_{f,inert}$ can be determined with the two-parameter distribution function in (Eq. 2.4) according to [Weibull, 1951]:

$$P_{f,inert}(\sigma) = 1 - \exp\left\{-\frac{A}{A_0} \cdot \left(\frac{\sigma}{\theta_0}\right)^{m_0}\right\} \qquad \text{(Eq. 2.4)}$$

The notations used in (Eq. 2.4) have the following meanings:

σ	net crack-opening stress normal to the crack
A	surface area of the glass exposed to the crack-opening stress
A_0	reference surface area
θ_0	material parameter to be determined experimentally
m_0	material parameter to be determined experimentally

In [Haldimann et al., 2008] it is described how (Eq. 2.4) can be extended in order to account for non-uniform, biaxial stress fields, time-dependent loading and sub-critical crack growth. Furthermore, simplifications which are applicable for most structural design tasks are suggested.

In most structural glass applications, tempered glass panes are used. A common approach for these types of glass is to neglect the inherent strength and to ensure that under all potential loading scenarios no surface decompression is occurring. If this is the case, it means that surface cracks are not exposed to tensile stresses during the entire service life of the glass element and subsequently there is no influence of crack size, load duration or environmental exposure on its strength (see [Haldimann et al., 2008]). This is reflected by the approaches included in [DIN 18008-1] and [ÖNORM B 3716-1] for the determination of the design strength values R_d. These two standards specify a fix value of $k_{mod} = 1.0$ for the factor of load duration in the case of tempered glass types.

A more complex design methodology based on ensuring that an equivalent uniform equibiaxial stress $\sigma_{p,t0,A0}$ does not exceed a characteristic equibiaxial strength of glass $f_{gk,t0,A0}$ is investigated by [Overend & Zammit, 2012]. The characteristic tensile strength of glass under a specific stress state and stress history can be determined for a given probability with the distribution function according to [Weibull, 1951] based on experimental data. This strength can be then converted to the required characteristic equibiaxial tensile strength $f_{gk,t0,A0}$ which is valid for a reference stress duration t_0 and a reference area A_0 (see [Overend, 2010]). To determine the equivalent uniform equibiaxial stress $\sigma_{p,t0,A0}$ applied for a stress duration t_0-t_r on a reference area A_0, (Eq. 2.5) is proposed by [Overend & Zammit, 2012]. This equation allows to convert a

non-uniform transient stress state common for most glass applications into an equivalent uniform stress. Furthermore, it considers the location- and time-dependent principal surface stress resulting from a given loading scenario, $\sigma_1(x,y,t)$, as well as the surface pre-compression induced by an eventual tempering process, $f_{rk}(x,y)$, which is also a function of the location on the glass pane as shown by [Laufs, 2000].

$$\sigma_{p,t_0,A_0} = \left\{ \frac{1}{A_0} \cdot \int_{area} \left[\frac{1}{(t_0 - t_r)} \cdot \int_{t_0}^{t_d} [c_b \cdot \sigma_1(x,y,t) + f_{rk}(x,y)]^n dt \right]^{m/n} dA \right\}^{1/m} \quad \text{(Eq. 2.5)}$$

The rest of the notations used in (Eq. 2.5) have the following meanings:

c_b	biaxial stress correction factor; $c_b = 1$ when σ_1 is normal to the critical cracks
t_0-t_r	duration for which the applied surface stress $\sigma_1(x,y,t)$ exceeds the magnitude of the surface pre-stress $f_{rk}(x,y)$; for annealed glass, $f_{rk}(x,y) = 0$ and $t_r = 0$
t_d	duration of the design scenario
n	parameter for considering stress corrosion due to humidity as in (Eq. 2.3)
m	material parameter of the Weibull-distribution to be determined experimentally

This approach is rather unsuitable for hand calculations due to its complexity, but might be a good solution for implementation in structural design software.

For glass as a brittle material, a failure cannot be completely excluded. Monolithic glass panes, without depending whether annealed glass or tempered glass is used, exhibit no post-fracture strength. However, especially in the case of structurally used glass components a certain post-fracture strength is required to prevent an immediate collapse. Laminated glass is generally used to achieve this. The post-fracture performance of a laminated glass depends mainly on *(i)* the bulk material properties of the glass, *(ii)* the bulk material properties of the interlayer, *(iii)* the adhesion strength between glass and interlayer, *(iv)* the crack pattern and *(v)* the given support and loading conditions of the glass pane.

2.2.2 Frame materials for transparent facades

The metal framing for large highly glazed facades is made in most cases of aluminium or stainless steel and in rather few cases of carbon steel. Aluminium and most of its alloys show a high resistance to corrosion without further protective layers. For aggressive environments powder-coatings or anodic treatments can be used to better protect the aluminium surfaces. Facade profiles are generally produced by extrusion, method which allows for light, torsionally rigid constructions, which fulfil several functions by proper shaping of the cross section. For structural sealant glazing systems (SSGS - see details in subchapter 2.2.3), where the facade glazing is adhesively bonded to the framing with structural silicones, [ETAG 002, 2001] mentions as the commonly used aluminium alloys *EN AW-6060* and *EN AW-6063* (see [EN 755-2, 2016] and Tab. 2.1 for mechanical properties). For facade profiles the tempering grades *T6* and *T66* are used for these two alloys (for more details regarding aluminium properties and processing methods see [Ostermann, 2014]).

Tab. 2.1 *Aluminium alloys used for facade profiles and their main mechanical properties based on [EN 755-2, 2016]*

Material no.	**Chemical composition**	**Wall thickness** [mm]	**0.2% strength** [MPa]		**Tensile strength** [MPa]	
			T6	**T66**	**T6**	**T66**
EN AW-6060	AlMgSi	≤ 5	150	160	190	215
		10 < t ≤ 25	140	150	170	195
EN AW-6063	AlMg0.7Si	≤ 10	170	200	215	245
		10 < t ≤ 25	160	180	195	225

When carbon steel is used for the structural facade profiles, the corrosion protection has to be solved by constructive measures in the connection points to the glazing. This is usually achieved by aluminium elements for the screw channels. The advantage of stainless steel compared to carbon steel is its resistance to corrosion without any surface protection measures. Stainless steels usually have higher shear strengths than unalloyed steels and require therefore higher forces for tooling them. If only a small number of profiles is required, sheet plates are folded. For larger amount of the same profile forming machines are used, where the cold strips are shaped by a series of rollers. The most important stainless steels used in the building industry for facade profiles along with their mechanical properties are given in Tab. 2.2 based on [Merkblatt 875, 2004] and [EN 10088-4, 2009]. The materials *1.4401* and *1.4404* have a higher resistance to corrosion and are also stable in chloride containing or sulphuric atmosphere at ambient temperature. The materials *1.4307* and *1.4404* have a lower carbon content and can therefore also be welded in thicknesses higher than *6 mm*.

Tab. 2.2 *Stainless steels used for facade profiles and their main mechanical properties based on [Merkblatt 875, 2004] and [EN 10088-4, 2009]*

Material no.	**Short name**	**Density** [kg/m^3]	**Yielding stress** [MPa]	**Tensile strength** [MPa]
1.4301	X5CrNi18-10	7 900	230	540 - 750
1.4307	X2CrNi18-9	7 900	220	520 - 670
1.4401	X5CrNiMo17-12-2	8 000	240	530 - 680
1.4404	X2CrNiMo17-12-2	8 000	240	530 - 680

The shape of metal facade profiles is generally rectangular and their dimensions are determined by structural design. For the profile width the required size for fixing the glazing has also a significant influence, while for the depth only the occurring loads are essential. In the case of post-and-beam facades also T-shaped profiles are used in order to reduce the visible perception of the framing (see Fig. 2.4).

More recent projects show framing elements made of timber, a material which shows a significantly lower thermal conductivity compared to metals, but also reaches only lower values for stiffness and strength (see Tab. 2.3). Timber is a material which grows naturally and is characterized by its anisotropic material behaviour as well as by the dependency of its mechanical properties on the moisture content. Based on these characteristics, certain types of wood and

derived timber products prove to be more suitable for timber facade profiles than others. [Hochhauser, 2011] uses for the framing glue-laminated timber (*GL 24h*) and glue-laminated veneer made of Finnish spruce, while the adhesively bonded adapter elements are produced from veneer plywood made of birch. In [Nicklisch, 2016] adhesively bonded timber-glass elements for facades are investigated and for the framing veneer plywood made of birch and solid wood made of pine are used. One disadvantage of a timber framing are the large cross section dimensions needed for the profiles.

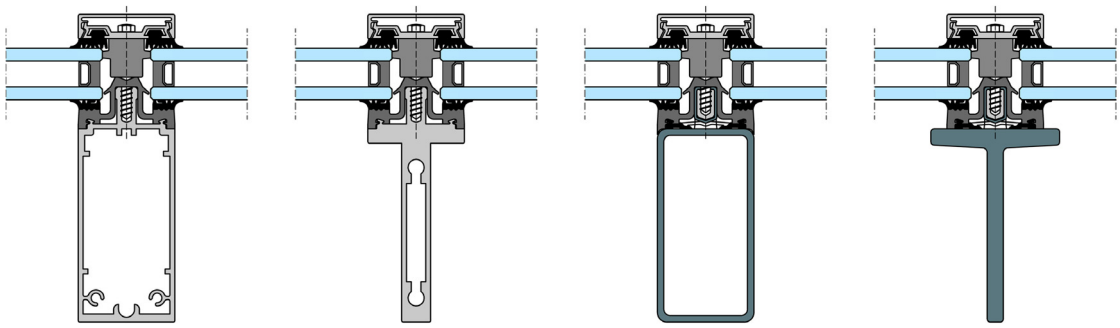

Fig. 2.4 *Framing elements made of aluminium and steel for post-and-beam facades based on [www.raico.de]*

Another material considered to have a high potential to be used for facade profiles is glass-fibre reinforced plastic (GFRP). This is mainly because of its low thermal conductivity while showing a very good load-bearing capacity as well as adequate modulus of elasticity and thermal expansion coefficient (see Tab. 2.3). In [Peters, 2006] results from an extensive experimental programme on adhesive connections between GFRP and glass are presented and application prototypes for this material combination are analysed. [Weller, 2007] presents developed constructive concepts for windows and facade elements with GFRP and glass as well as results from thermal analysis performed on these elements.

Tab. 2.3 *Properties of frame materials used for transparent facades compared to glass [Peters, 2006], [Weller, 2007], [Wetzell, 2009], [Merkblatt 821, 2012]*

Material	**Density** [kg/m^3]	**Young's modulus** [MPa]	**Tensile strength** [MPa]	**Thermal conductivity** [W/mK]	**Thermal expansion** [10^{-6}/K]
Glass	2 500	70 000	120 [a]	1.00	9.0
Steel S 235	7 850	210 000	360	50.00	12.0
Stainless steel	8 000	200 000	520 - 670	15.00	16.0
Aluminium	2 700	70 000	150 - 230	160.00	23.0
Wood C24	600	11 000 [b]	14 [b]	0.13	~ 4.5
GFRP	1 800	23 000 [b]	240 [b]	0.25	9.0

[a] this value is valid for thermally toughened glass

[b] these values are valid for the direction parallel to the grain

2.2.3 Structural adhesives for glass-metal connections

Connection types can be generally classified in force connections, mechanical interlock connections and adhesive connections according to [Wurm, 2007]. Examples from structural glass applications for the first category are friction grip connections realised by clamping plates for point fixings or by clamping rails for linear fixings. The disadvantage for this type of connections is the difficulty to ensure a constant prestressing force in the used bolts, especially due to creeping of the interlayer materials. An example for the second category are bearing bolt connections used especially for mechanical point fixings of glass elements. Due to the brittleness of the material glass, this type of connection results in high local stresses in the area of the borehole edge. Adhesive connections represent an attractive alternative for joining glass components since they allow for a more uniform load distribution.

Nowadays there is an extremely high number of industrial adhesives available on the market and new products are being developed constantly. The fundamentals for adhesive bonding, like chemistry of adhesives, classifications, required surface properties of the substrates, design of adhesive joints or testing of adhesive materials and joints can be found in [Adams, 2005], [Habenicht, 2009], [Dillard, 2010] and [Habenicht, 2012]. For the use in structural glass applications, certain adhesive types proved their suitability due to the chemical, physical and mechanical properties they provide. The most common ones are according to [Bucak & Hagl, 2006], [Weller et al., 2011] and [Belis et al., 2011a] silicones, MS-polymers, polyurethanes, acrylics and epoxies. All of these adhesive types cure by chemical reactions, whether they are one-component adhesives and cure for instance in contact with moisture from the surrounding air or they are two-component adhesives and cure when the base material is mixed with a catalyst. The choice of an adhesive depends on a series of factors including the surface condition of the substrate materials, the strength demands, the expected types of loading, the constructive design and the expected environmental influences. In the case of adhesives for applications in the building envelope the requirements are at a high level and the area of selection gets constrained. The following minimal requirements are generally set for linear adhesive joints within the building envelope according to [Weller et al., 2011]:

- sufficient strength for withstanding the occurring loading;
- durable resistance against UV-radiation, moisture and chemical cleaning agents;
- sufficient elasticity to compensate for different thermal elongations of the bonded materials;
- service temperature range between *-20 °C* and *+80 °C*;
- reduced tendency to creep under long-term loading.

A significant demand is the durable performance of the adhesive joints with respect to the listed requirements. To ensure a high quality, structural adhesive joints have to be manufactured under shop conditions. In practice, the only standard application of structurally efficient adhesives in facades are the structural sealant glazing systems (SSGS), which are regulated in standards and guidelines such as [ASTM C 1401-02, 2002], [EN 13022, 2014] and [ETAG 002, 2001]. The only adhesives which achieve the requirements of these documents and for which a technical approval is available are certain one-component and two-component structural silicones. The

reasons for which the other adhesive types generally fail are either the lack of sufficient elasticity or the sensitivity to moisture, UV-radiation and high temperatures.

According to [ETAG 002, 2001] four different types of SSGS are differentiated depending on the one hand on the existence of setting blocks for supporting the dead weight of the glazing elements and on the other hand on the use of additional retaining devices for holding the glazing elements back in case of adhesive failure (see Fig. 2.5).

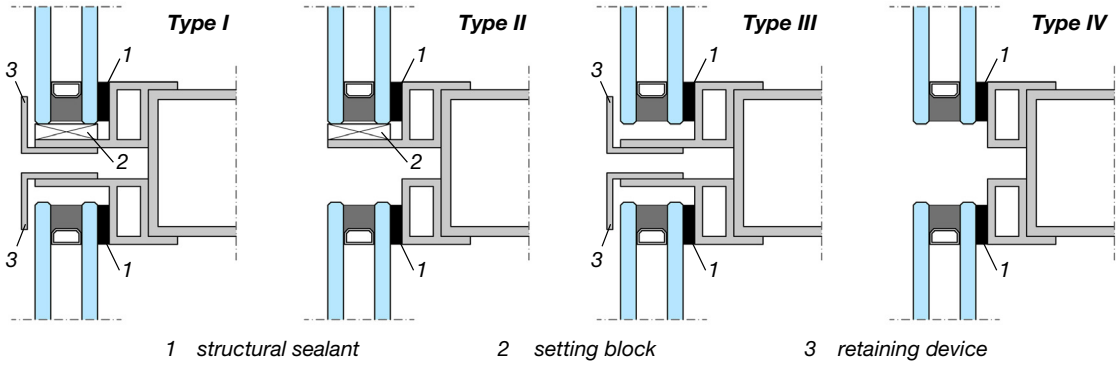

Fig. 2.5 *Structural sealant glazing types according to [ETAG 002, 2001]: with (I and II) and without setting blocks (III and IV) as well as with (I and III) and without additional retaining device (II and IV)*

Silicone adhesives prove to be a good solution for structural sealant glazing applications, among others because of existing documentation on their durable performance (see [Carbary, 2007]). However, as soon as higher loads, especially shear loads, are planned to be transferred by the adhesive in connections to structural glass elements, silicones reach their limits. This can be noticed from analysing recent research projects dealing with hybrid beams ([Weller et al., 2010], [Louter, 2011], [Netusil, 2011]) or activation of glass panes as shear panels by adhesive bonding ([Wellershoff, 2006], [Huveners, 2009]). In these projects adhesives with a higher stiffness, like acrylics or epoxies are used.

Structural silicones, especially *Dow Corning 993 (DC993)*, are well investigated both regarding their performance under different types of loading and under different environmental conditions as well as regarding suitable material laws. [Hagl, 2006] presents results from tensile, shear and compressive tests on *DC993* and the suitability of the hyperelastic material law *Mooney-Rivlin* for this adhesive. In [Hagl, 2007], [Hagl, 2008] and [Hagl, 2016] results on different joint geometries with the same structural silicone are presented and recommendations for the structural design of such joints are included. [Staudt, 2013] and [Staudt et al., 2014] deal as well with the material behaviour of adhesive joints with silicone *DC993*. Uniaxial tests are performed on dumbbells, considering different curing times, different loading speeds, cyclic loading, creep behaviour and relaxation. Based on the collected data, existing hyperelastic material models are compared to each other and to the experimental results in order to determine the best suitable ones. Finally, experimental testing and simulations are performed on H-specimens according to [ETAG 002, 2001] to validate the hyperelastic models on the material behaviour within an adhesive joint. Another extensive research programme with *DC993* which aims at the detailed char-

acterization of the material is documented in [Dias, 2013] and [Dias et al., 2014]. [Clift et al., 2014] presents investigations on a new design concept for structural sealant glazing joints with trapezoidal cross section of the adhesive, which leads to an improved stress distribution and allows therefore smaller SSG profile dimensions.

Due to the numerous results and the wide experience with *DC993*, this adhesive is generally included as a reference material in research investigations on adhesives for structural glass applications. In [Belis et al., 2011a] results from an extensive experimental programme on about 30 adhesives, including silicones, polyurethanes, acrylics and epoxies, are presented. For each adhesive single-lap shear tests are performed on specimens without conditioning as well as on specimens which are stored for *4 weeks* and for *12 weeks* at *90 °C* and *50% RH*. The bonding area is *25 mm* wide and *10 mm* long and the thickness of the adhesive varies depending on the recommendations of the producers. The results show for the silicones low shear strengths averaging around *1.0-1.5 MPa* (except *Dow Corning® TSSA*), but relatively constant values after the ageing exposure. For the acrylics and the epoxies significant higher shear strengths are reached, but a decrease of these values after ageing is observed. Selected results from this research project are summarized in Tab. 2.4.

Tab. 2.4 *Mean results of single-lap shear tests after zero, four and twelve weeks of exposure to 90 °C and 50% RH for selected adhesives from [Belis et al., 2011a]*

Adhesive	**Type** [a]	**Shear stress τ_{max} [MPa] depending on exposure time and difference after ageing in [%]**				
		0 weeks	**4 weeks**		**12 weeks**	
Dow Corning 993	S	1.36	1.37	+ 0.76%	1.45	+ 6.40%
Dow Corning TSSA	S	4.19	3.69	- 26.36%	- [b]	- [b]
Sikasil SG500	S	1.11	1.25	+ 12.61%	1.32	+ 19.54%
Sikaflex 521 UV	P	1.15	1.16	+ 0.43%	1.06	- 7.81%
Sikatack-Drive	P	6.15	5.54	- 10.00%	4.81	- 21.78%
3M Scotch Weld DP620_NS	P	8.70	7.03	- 19.22%	6.05	- 30.46%
DELO PB4468	A	9.39	9.40	+ 0.12%	4.64	- 50.57%
SikaFast 5211	A	7.68	5.16	- 32.86%	5.88	- 23.46%
Araldite 2047	A	16.26	12.56	- 22.75%	11.81	- 27.38%
Araldite 2015	E	5.91	6.84	+ 15.63%	7.72	+ 30.50%
3M Scotch Weld DP 190	E	6.79	5.19	- 23.60%	3.04	- 55.21%
3M Scotch Weld DP 490	E	28.75	18.18	- 36.76%	20.19	- 29.78%
SentryGlas (10 mm overlap)	I	14.64	12.13	- 17.11%	9.69	- 33.80%

[a] Notations for the adhesive type: Silicone - S, Polyurethane - P, Acrylic - A, Epoxy - E, Ionomer - I

[b] Conditioning was still in progress at the time [Belis et al., 2011a] was published

Another research project investigating the performance of adhesives for connections between glass and steel is documented in [Overend et al., 2010], [Overend et al., 2011] and [Nhamoinesu & Overend, 2012]. For five different adhesives (*Dow Corning 993* - silicone, *Sikaforce 7550 L15* - polyurethane, *3M 2216 B/A* - epoxy, *Holdtite 3295* - 2P-acrylic, *Bohle 682-T* - UV-acrylic) the

stress *vs.* strain behaviour is investigated by uniaxial tensile tests on dumbbell specimens in a first step to determine the visco-elastic and the elasto-plastic properties of the bulk material. In a second step, single-lap shear and T-peel tests are performed on connections between steel and glass with the five adhesives. The bonding area is *50.8 mm* wide and *26 mm* long and a symmetrical arrangement of the specimens is used - there are two bonding areas per specimen. Based on the performance under short duration loads in a laboratory environment, the silicone is recommended for joints with low strength and low stiffness requirements, while for stronger and stiffer joints the 2P-acrylic and the epoxy are considered to be suitable.

In [Peters, 2006] an experimental programme with 14 adhesives including silicones, polyurethanes, acrylics and epoxies is documented. The adhesives are used for joints between glass and glass fibre reinforced plastics (GFRP) and are tested in tension and compressive shear. The bonding area for the tensile tests is *50 mm* long and *10 mm* wide, while the one for the compressive shear tests is *30 mm* long and *10 mm* wide. All adhesives are tested at room temperature (*23 °C*) and selected adhesives are additionally tested after natural ageing (2 years storage under outdoor weathering), after storage at low and high temperatures (*-20 °C* and *+80 °C*) and after simulated ageing (conditioning in a climatic chamber with humidity and temperature changes). In the conclusion of [Peters, 2006] the following three adhesives are considered to be interesting for window and facade applications with glass and GFRP based on the obtained results: *Dow Corning 993* - silicone, *DELO PB VE 55075* - acrylic, *3M DP490* - epoxy.

The results of these investigations along with other research projects show that acrylic adhesives are an interesting alternative to silicones for specific applications. From the past research two types of acrylic adhesives can be differentiated. The first ones are two-component acrylics, which cure by mixing of the base substance with a catalyst and result in an opaque material. Such adhesives are used for instance by [Netusil, 2011] for hybrid glass-steel beams and by [Nhamoinesu, 2014] for hybrid glass-steel panels. The second category are one-component acrylics, which cure by irradiation with a certain wave length and generally result in a transparent material. The materials investigated in [Vogt, 2009] for instance need a wave length in the range of *320* to *450 nm* which is composed of both UVA-light and visible light. A recent innovative application of a UV-curing acrylic adhesive for a wall made of solid glass blocks is presented in [Oikonomopoulou et al., 2015] and [Oikonomopoulou et al., 2017]. A similar system was used in Madrid for the monument built in memory of the terrorist attacks from the 11th of March 2004 (see [Goeppert & Paech, 2008]).

Adhesive point fixings are an interesting alternative for mechanical ones since they do not require drilling of boreholes in the glass and therefore allow additionally to the more uniform stress distribution for a better thermal performance and a more aesthetic appearance. In [Belis et al., 2011a] certain adhesives are recommended to be used for point fixings based on the performed experimental investigations. A rather new adhesive which is interesting for point fixings is *Dow Corning® TSSA* (transparent structural silicone adhesive, see also [Dow Corning TSSA, 2013]). This one-component silicone is transparent and cures under heat exposure. The promising mechanical behaviour as well as the durability are documented in [Sitte et al., 2011]. [Santarsiero, 2015] shows results on the performance of *TSSA* and *SentryGlas* at different temperatures and under different strain rates from uniaxial tests on dumbbells as well as from

connections under shear loading. In this project suitable material models are derived (see also [Santarsiero et al., 2016a]) and laminated as well as embedded connections between glass and metal components with the two materials are investigated (see also [Santarsiero et al., 2016b]). The realisation of connections with both of these products requires the processing under heat and pressure in an autoclave. Another research project investigating the mechanical properties of *TSSA* and suitable material models is documented in [Drass et al., 2017a] and [Drass et al., 2017b]. Other research projects dealing with embedded glass-metal connections with SentryGlas are documented in [Puller, 2012] and [Carvalho, 2014].

Although adhesive connections and especially high strength adhesives show a high potential and several advantages compared to force connections and mechanical interlock connections, there are some aspects which slow their emergence in the building and facade sector.

- In practice generally simplified approaches are used to dimension adhesive joints by assuming a linear-elastic material behaviour and a uniform stress distribution. More exact design approaches allow for a better utilisation of the material, but require extensive testing for the implementation of plasticity, hyperelasticity or viscosity in finite element software applications (see [Menkenhagen & Koschecknick, 2012] or [Dias, 2013] and [Dias et al., 2014] as examples for silicones or [Dispersyn et al., 2017] as an example for a MS-polymer). More information on deriving suitable material models are given in subchapter 4.3 focusing on the adhesives investigated in this thesis.

- For the design of adhesive joints failure criteria are required. In this context it is important to differentiate between cohesive failure within the adhesive material, substrate failure within one of the bonded materials and adhesive failure at the interface between substrate and adhesive. The latter one should be avoided by appropriate finishing and pretreatment of the surfaces (see [Kothe, 2013a] and [Ebnesajjad, 2014]). This topic will be treated in depth in subchapter 4.4. For a substrate or a cohesive failure generally strength criteria are used. In the case of a cohesive failure the stress distribution in the joint is important in order to establish a reliable criterion (see investigations in [Callewaert et al., 2011] for elastic adhesives).

- Probably the biggest obstacles for a regular application of high strength adhesives are the uncertainties regarding their long-term performance. Considering the life period of facades averaging around 25 years, it is not possible to perform representative real-time testing. Therefore only accelerated ageing tests are performed under extreme conditions. High strength adhesives often fail in these tests or show a significant loss of strength due to low resistance against moisture, UV-radiation or other environmental influences. Durability aspects are not experimentally investigated within this thesis, but are considered in the selection process of the adhesives.

Analytical models for adhesive joints

Guidelines which define the requirements for adhesives to be used in structural sealant glazing systems request in general testing on specimens subjected separately to both tensile and shear loading (see for example the H-shaped specimens in [ETAG 002, 2001]). However, analytical studies on the mechanical behaviour of adhesive joints from the past decades focus mainly on

the stress distribution in single lap joints or double lap joints under shear loading. A clear overview of the different studies and developed models can be found in different books on the topic of adhesive bonding like [Adams, 2005], [da Silva & Öchsner, 2008] and [Habenicht, 2009]. In terms of tensile loading, some models include peel stresses resulting from bending and combine them along with the shear stresses in the lap joints. Analytical models for determining the stresses in adhesive joints under direct tension, as they occur in the tensile tests on H-specimens according to [ETAG 002, 2001], are rather rare.

In general, adhesive joints can be realised with thin and rigid adhesive layers or with thick and flexible adhesive layers. Most of the existing analytical models were developed for lap joints with thin and rigid adhesive layers, which are common in the automotive and the aeroplane industries. From the adhesive types used in structural glass applications only the epoxies and some acrylics can be considered thin and rigid. Polyurethanes and especially the silicones are flexible materials which in most cases are applied in thick layers. However, the stress distribution and the size of the stress peaks is of high importance regarding the structural design of such joints. [Callewaert et al., 2011] shows in a finite element study with linear calculations and pure elastic materials both for the adhesive and the substrate, that the shear stress in an adhesive joint is increasing with higher thickness of the adhesive layer.

According to [Nhamoinesu, 2014], three main challenges arise concerning the stress state in adhesive joints for glass-metal elements with composite structural behaviour: *(i)* a differential shear is occurring along the joints; *(ii)* the behaviour of the adhesive materials is generally non-linear; *(iii)* the joints are asymmetric because different substrate materials are bonded together. Only few of the existing models can meet all these requirements. In [da Silva et al., 2009a] a literature review of the existing analytical models is provided, including the early methods proposed by [Volkersen, 1938] and [Goland & Reissner, 1944] as well as more complex ones like [Bigwood & Crocombe, 1989] and [Wang et al., 2003]. [da Silva et al., 2009b] presents a comparative study between selected analytical models focusing on accuracy of the results and the cost of calculation in terms of time. One of the drawn conclusions is that by including non-linear material behaviour, the models become very complex, the analyses are time consuming and therefore the advantages compared to finite element simulations are questionable.

The investigations within this thesis focus mainly on experimental methods and finite element simulations and therefore the analytical models will not be discussed in more detail. However, as shown in [da Silva et al., 2009b] for specific conditions, certain models with limited complexity can achieve a good agreement with experimental results or at least lead to safe predictions. These possibilities should be considered in the respective cases before starting time consuming finite element simulations. Although complex analytical models are not the scope of this thesis, more exact design methods as those based on stresses determined by dividing the forces by the adhesion surfaces should be used. Two alternatives would be either to use true stresses from finite element simulations with solid elements or to develop design methods based on strain values instead of stresses. In the latter case, simplified finite element models with spring elements representing the adhesives could be used.

2.2.4 Materials for transferring compressive loads at the glass edge

In windows or transparent facade elements, generally setting blocks made of polyvinyl chloride (PVC) are used between the glass pane edge and the surrounding frame to fix the position of the first one. Supporting blocks, which transfer the dead weight of the glass pane to the frame, and distance blocks, which prevent a slip or a rotation of the glass pane, can be differentiated (see [Roto, 2015]). Based on this concept, by using materials which allow the transfer of higher compressive stresses and at the same time have a reduced surface hardness in order to minimize stress peaks in the glass, high compressive loads can be introduced into the edge of structural glass elements. [Ebert, 2014] gives a list of general requirements for materials to be used for controlled transferring of high compressive loads into the glass edge:

- high compressive strength and high stiffness;
- material properties as constant as possible between temperatures of *-20 °C* and *+80 °C*;
- significant lower surface hardness compared to glass;
- low tendency to creep under long-term loading;
- low friction coefficient in contact with glass;
- resistance to UV-radiation, cleaning agents and corrosion;
- compatibility to other materials used for structural glass applications (interlayer, sealants);
- good workability and processability for shaping.

In [Ebert, 2014] different thermoplastics, which show promising properties for this type of application, are investigated in uniaxial short-term tests at temperatures of *-20 °C*, *+23 °C* and *+50 °C* under tensile loads according to [EN ISO 527, 2012] and under compressive loads according to [EN ISO 604, 2003]. For some of the materials also alternatives with glass fibre reinforcement are tested. The product data sheets for these materials generally only provide mechanical properties under tensile loading for a range of operation temperatures. Selected mechanical properties from this research project at a temperature of *+23 °C* are summarized in Tab. 2.5. For further characteristics of the different materials [Ebert, 2014] or suppliers should be consulted.

[Ebert, 2014] also includes results on the behaviour of these materials under long-term static loading, parameters for representing this behaviour with the *Burgers*-model and extrapolated compressive creep strains after *50 years.* Results from dynamic-mechanical analysis and concepts for practical applications are provided as well. As a conclusion of this research project, the thermoplastic PEI is considered to be the most appropriate for applying compressive loads into glass edges due to its high short- and long-term compressive strength, the low tendency to creep, the low temperature dependency and the nearly linear-elastic stress-strain curve. Materials like POM and PA 6, which are already used for such applications, show a rather high tendency to creep.

Of significant importance for transferring loads at the glass edge is, beside the used transfer material, the finishing of the edge. At least a grinded edge should be used, when compressive loads are intended to be transferred into the glass edge by thermoplastic setting blocks. In the

case of laminated glass the possibility of an edge offset within the allowed production tolerances has to be considered as well. When dealing with such a case, a uniform transfer of the loads into all glass panes of the laminated unit with setting blocks made of thermoplastics is only possible through additional complex measures (see [Ebert, 2014] for examples).

Tab. 2.5 *Young's moduli, Poisson's ratios and yielding stresses determined in [Ebert, 2014] for different thermoplastics at 23 °C under uniaxial tensile and compressive loading*

Material	Density [kg/m³]	+23 °C					
		Young's modulus [MPa]		Poisson's ratio [-]		Yielding stress [MPa]	
		tension	compr.	tension	compr.	tension	compr. [b]
POM-C	1 410	3 084	4 356	0.35	0.49	58	96
POM-C GF25 [a]	1 580	5 008	6 450	0.38	0.49	69	123
PET	1 380	3 150	3 686	0.34	0.49	68	95
PEEK GF30 [a]	1 490	5 174	6 800	0.34	0.45	69	141
PEI	1 270	3 529	3 300	0.41	0.40	108	150
PA 6	1 140	2 773	3 000	0.38	0.45	52	86
PA 6 GF30 [a]	1 350	3 202	6 421	0.40	0.49	59	125
PA 66	1 150	2 895	4 190	0.39	0.49	59	95
PA 66 GF30 [a]	1 350	3 411	5 400	0.30	0.42	72	115

[a] the values for the glass fibre reinforced materials can vary depending on the orientation of the fibres; the values in this table are parallel to the fibres

[b] these values are determined based on the maximum reached stress; in [Ebert, 2014] also reduced values based on limiting the compressive strain or the change in stiffness are given

A more simple solution is the use of resin-based grouts, which are injected in a fluid state and therefore can counterbalance the offset. The most common products used for grouting in terms of structural glass components are *Hilti HIT-HY 70* or the more recent *Hilti HIT-HY 270*. These are hybrid systems consisting of an organic binder (reaction resin) and an inorganic binder (hydraulic curing cement) in a ratio of about three to one. In [Bucak, 2011] the Young's modulus and the compressive strength of *Hilti HIT-HY 70* are determined for short-term loading at temperatures of *-20 °C*, *+23 °C*, *+60 °C* and *+80 °C* (see Tab. 2.6). Additionally, the influence of the curing time on the development of the compressive strength is determined and a method to determine the long-term strength based on reduction factors is provided.

Tab. 2.6 *Young's modulus and compressive strength for Hilti HIT-HY 70 at different temperatures [Bucak, 2011]*

Hilti HIT-HY 70	-20 °C	+23 °C	+60 °C	+80 °C
Young's modulus [MPa]	2 301	1 525	1 214	854
Compressive strength [MPa]	76.5	58.7	60.2	37.1

The values in this table are 5%- fractiles

In [Kolany, 2018] experimental investigations on the material behaviour of the grout *Hilti HIT-HY 70* under short-term and long-term compressive loading are performed based on [EN ISO 604, 2003]. Furthermore, the performance of POM-C and *Hilti HIT-HY 70* under compressive loading in a laterally restrained system is investigated (see Fig. 2.6). The expectation to be able to transfer significantly higher loads by this type of constructive measures is confirmed by the obtained results.

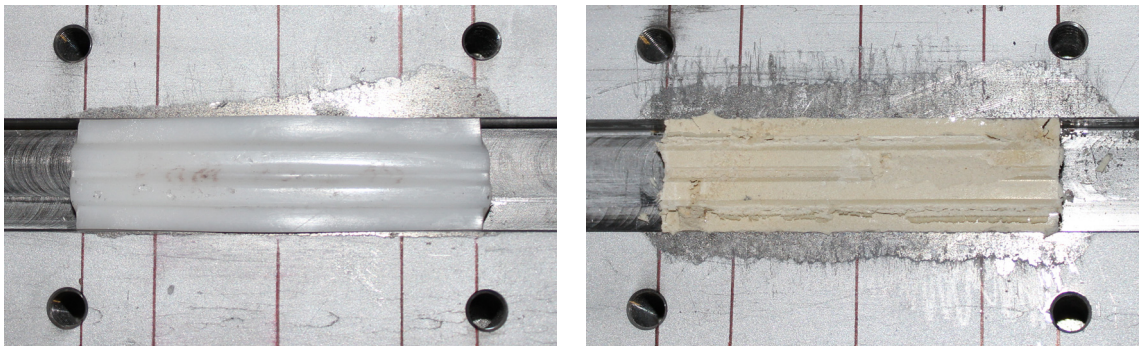

Fig. 2.6 *Laterally restrained specimens made of POM-C (left) and of Hilti HIT-HY 70 (right), tested under compressive loading with a laminated glass pane [Kolany, 2018]*

In [Silvestru, 2012] both the thermoplastic POM-C and the resin-based grout *Hilti HIT-HY 70* are used for the support of experimentally investigated cantilevered glass fins (see Fig. 2.7). As a conclusion it is stated that for such an application the grouting is easier to apply in the given gaps between laminated glass and steel bracket. Furthermore, also the structural behaviour of the system with grouting is better. Both the thermoplastics and the grouting can also be used for bushes in the case of bolted connections (see [Baitinger, 2009]).

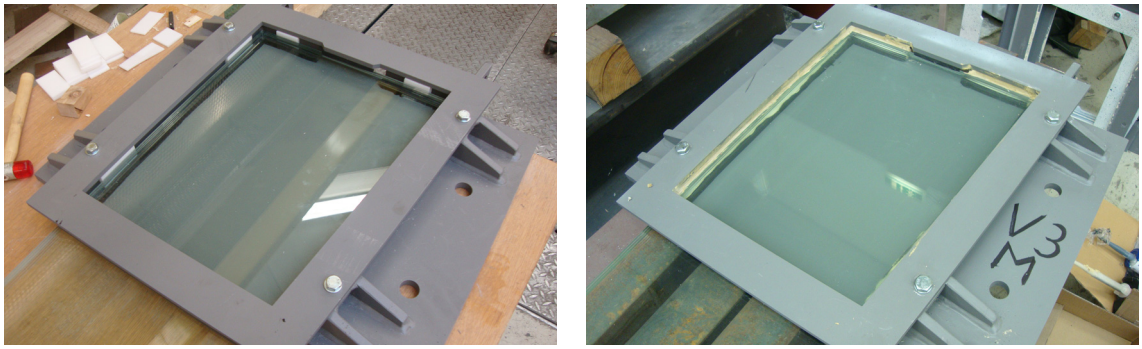

Fig. 2.7 *Clamped supports of cantilevered glass fins with compression loads transferred at the glass edge by setting blocks made of POM-C (left) and by grouting made of Hilti HIT-HY 70 (right) [Silvestru, 2012]*

More recent investigations on setting block materials for a timber-glass composite are presented in [Neumer & Siebert, 2016]. For POM, *Hilti HIT-HY 70*, beech and steel the maximum transferable loads are determined in dependency of the glass edge formation. Cut edges, raw edges, polished edges and rounded edges are investigated. For the tested monolithic glass panes and the boundary conditions without lateral restrain, POM shows the best results.

2.3 Glass panes in structural applications

Along with the trends in architecture towards transparency glass panes are considered more often as structural elements in facade design. Since the current standardization does not cover such applications, research results in this field are of significant value. Based on these results, new innovative applications are tested and implemented in impressive facade projects. Since these results are also important for the topic of this thesis, a summary of investigations conducted during the last fifteen years at different universities on structural applications of glass panes is provided in this subchapter, focusing especially on in-plane loaded elements, on the mechanisms and materials for transferring the loads into the glass panes as well as on the performed experimental tests.

Due to the high slenderness of structural glass elements, whether they are glass columns, glass beams or glass panes, the buckling behaviour has to be considered for design. One of the key parameter of influence for the buckling behaviour of an in-plane loaded structural glass element is its initial out-of-plane curvature, also referred to as its geometrical imperfection in literature. Results for these curvatures from measurements performed on linear glass elements (length significant larger than height) are presented in [Luible, 2004] and [Belis et al., 2011b]. The findings show that parabolic and sinusoidal functions approximate well the typical shape of these curvatures, with the mention that sinusoidal functions correspond to eigenmode shapes. A value of $w_0 = 1/400$ of the length is proposed as a characteristic value for the initial geometric imperfection. In the case of glass panes with a more uniform aspect ratio between length and height, results from measurements are provided in [Englhardt, 2007]. The shape of the initial curvature corresponds in most cases to the shape of the first eigenmode, which is generally used in finite element simulations of buckling problems. Curvature developments with L-shape, U-shape and the shape of a hyperbolic paraboloid are also observed. The sizes of these initial geometric imperfections are smaller than those measured for linear elements, reaching mean values of $w_0 = 1/1400$ of the length with a maximum measured value of around $1/800$.

2.3.1 In-plane loaded glass beams and hybrid glass beams

Glass beams are first used during the nineties as vertical structural elements (glass fins) for stiffening glass facades against out-of-plane loads. In this case the beams are subjected to bending around the strong axis due to variable wind loading. A susceptibility to lateral torsional buckling is generally given for the edge laying away from the facade, since the other edge can be laterally restrained through the facade glazing. More recent projects show glass beams as horizontal structural elements supporting glass roofs or interior glass bridges. In these cases also permanent loads act on the beams. Existing standards for glass structures do not cover such applications. Therefore, several research projects from the past fifteen years deal with aspects like lateral torsional buckling, post-breakage behaviour and possibilities to increase the load-bearing capacity and to achieve a ductile failure for glass beams.

Investigations on the lateral torsional buckling behaviour of single span glass beams made of monolithic glass as well as laminated safety glass are presented in [Luible, 2004] and [Kasper, 2005]. [Luible, 2004] proposes a design concept with buckling curves similar to the one used for steel structures, while [Kasper, 2005] determines resulting deformations and stresses by apply-

ing the second order theory and the linear-elastic bending theory. Although the two derived design concepts differ from each other, they have in common the consideration of the time- and temperature-dependent interlayer stiffness. Both projects focus only on single span beams with fork supports at both ends. The analysed loading scenarios are a centred point load, a constant line load and constant bending, but only for the first one physical testing is performed (see Fig. 2.8).

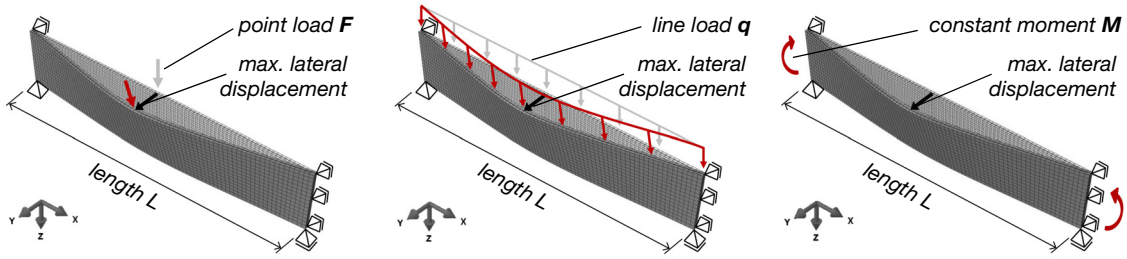

Fig. 2.8 *Loading scenarios for lateral torsional buckling of glass beams investigated in [Luible, 2004] and [Kasper, 2005]*

According to [Luible, 2004] the critical buckling moment of a single-span glass beam made of laminated safety glass with rectangular cross section can be determined with (Eq. 2.6).

$$M_{cr} = C_1 \cdot \frac{\pi^2 \cdot EI_{z,eff}}{(k_z \cdot L)^2} \cdot \left[\sqrt{\frac{(k_z \cdot L)^2 \cdot GI_{t,eff}}{\pi^2 \cdot EI_{z,eff}} + (C_2 \cdot z_g)^2} - (C_2 \cdot z_g) \right] \qquad \text{(Eq. 2.6)}$$

The parameters C_1 and C_2 consider the types of support and loading, while z_g is the distance between the shear centre of the cross section and the point of load application. For z_g a positive value has to be inserted if the point of load application is situated above the shear centre. The factor k_z considers the effective length by taking the rotation around the z-axis into account. The terms $EI_{z,eff}$ and $GI_{t,eff}$ are the effective bending stiffness and the effective torsional stiffness of a laminated safety glass cross section. The required equations to determine these values assume a linear elastic material behaviour of the interlayer and can be found in [Luible, 2004], [Amadio & Bedon, 2010] and [Bedon et al., 2014]. In [Bedon et al., 2014] critical loads determined with this analytical method are compared to results from experimental testing. The possibility to use (Eq. 2.6) also for cantilevered glass beams by choosing suitable values for k_z, C_1 and C_2 is shown in [Silvestru & Englhardt, 2015a] for a point load at the free end and in [Silvestru & Englhardt, 2015b] for a constant line load.

Efforts to increase the load-bearing capacity of glass beams and especially to improve their post-breakage behaviour resulted in the development of hybrid glass beams. These elements consist generally of a laminated glass and adhesively bonded linear elements made of other materials, which increase their structural safety. According to [Martens et al., 2015] hybrid glass beams can be classified in composite glass beams and reinforced glass beams depending on the shape of the resulting cross section and the percentage of the additional material to glass in the cross section. Composite glass beams generally have an I-shaped cross section with webs made of laminated glass and flanges made of another material. The material used for the flanges has generally a share higher than *25%* of the cross section area and is actively partici-

pating to the load-bearing from the start. In the case of reinforced glass beams, the share of the additional material to the cross section area is generally less than *10%* and the reinforcement is only activated after the glass breaks. The shape of the cross section of reinforced glass beams is not modified by the reinforcement material and is in most cases rectangular.

For composite glass beams combinations of monolithic and laminated glass with different materials can be found in research from the last fifteen years. Results on composite glass beams with steel flanges are presented in [Wellershoff & Sedlacek, 2003b], [Netusil, 2011] and [Abeln et al., 2013]. Beams of different sizes consisting of steel plates which are adhesively bonded one-sided on the glass edge (see example *(a)* in Fig. 2.9), two-sided near the glass edge (see example *(b)* in Fig. 2.9) or U-shaped around the glass edge are investigated. The used and suggested adhesives for these applications are high modulus polyurethanes and acrylics. An example for composite glass beams with adhesively bonded timber elements is investigated in [Cruz & Pequeno, 2008]. The cross section of these composite elements is generally composed of a laminated glass with rectangular solid wood beams adhesively bonded on both sides of the glass pane (see example *(c)* in Fig. 2.9). The used adhesives vary from project to project, including structural silicones, polyurethanes, acrylics and epoxies.

A unique system with flanges made of ultra-high-performance reinforced concrete (UHPC) is investigated in [Freytag, 2002]. The connection between the concrete and the glass panes is achieved by roughening the glass surface with a corundum containing enamelled coating and without using any adhesive. Results for two different systems are provided: the first one has only steel rebars in both the top and the bottom flange (see example *(d)* in Fig. 2.9), while for the second one two rebars in the bottom flange are replaced with prestressed tendons. Another concept for composite glass beams consists in adhesively bonding a layer of another material together with glass sheets. An example for this type of composite is investigated in [Härth-Großgebauer, 2013], where a sheet of polycarbonate is adhesively bonded with an UV-curing acrylic (Delo PB 4442) between two glass sheets (see example *(e)* in Fig. 2.9).

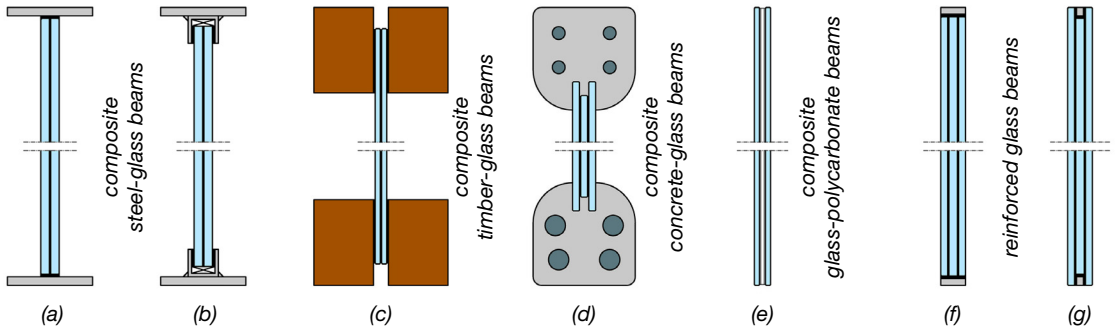

Fig. 2.9 *Schematic cross sections of investigated hybrid glass beams*

For reinforced glass beams, the reinforcement is generally made either of stainless steel or glass fibre reinforced polymers (GFRP). The reinforcement bars made of stainless steel are in most cases adhesively bonded at the glass edge or between the exterior glass sheets of a laminated glass made of three sheets (see examples *(f)* and *(g)* in Fig. 2.9). Two research projects investigating this type of systems are presented in [Weller & Weimar, 2011] and [Louter, 2011]. In both

cases UV-curing acrylic adhesives are used for the connection of the reinforcement bars to the glass. In [Louter, 2011] also a system, where the stainless steel reinforcement is bonded during the lamination process with SentryGlas between the two exterior glass sheets of a laminated glass consisting of three glass sheets, is analysed. The results from these experimental investigations show that after an initial crack in the glass pane coupled with a drop in the carried forces, the load can be further increased and additional cracks result at the tensile edge, which are then propagated horizontally. The obtained load-bearing behaviour is referred to as ductile and allows to avoid a brittle failure of the structural element. Glass beams with reinforcement rods made of GFRP, which are embedded in the SentryGlas interlayer, are investigated as well in [Louter, 2011]. A further development for hybrid glass beams, which is applied especially to reinforced systems, but in specific cases also to composite systems, are post-tensioned glass beams (see for example [Weller & Engelmann, 2014]).

2.3.2 Glass panes loaded in-plane by uniaxial compression

In-plane loaded glass panes under uniaxial compression can be either glass columns, case in which two opposite edges are loaded, while the other two are unsupported, or glass walls with all edges supported out-of-plane and two opposite edges loaded in-plane. The different boundary conditions of these two systems result in the case of glass columns in a susceptibility to column buckling and in the case of the four-sided supported glass walls in a susceptibility to plate buckling (see first eigenmode for the two systems illustrated in Fig. 2.10). The contents in this subchapter focus on investigations for the plate buckling behaviour of uniaxial loaded glass panes. The column buckling, for which investigations and design concepts based on buckling curves are presented in [Luible, 2004] and [Langosch, 2012], will be not further discussed.

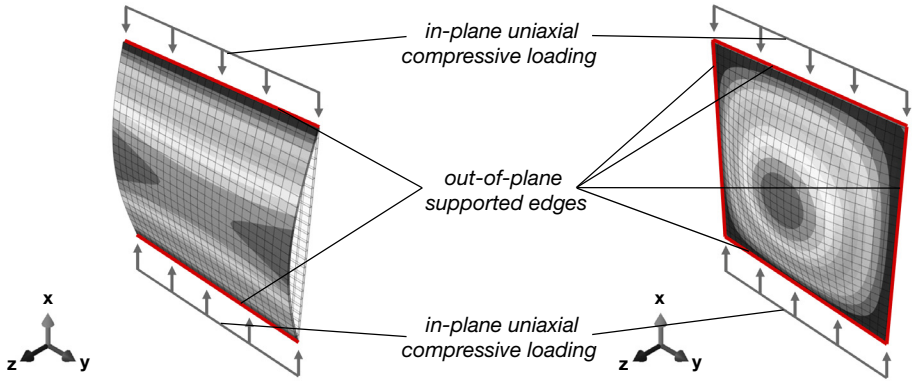

Fig. 2.10 *First eigenmode for a glass pane loaded in-plane by uniaxial compression with the unloaded edges unsupported (left) and with four-sided support out-of-plane (right)*

In [Luible, 2004] results for the plate buckling of squared monolithic and laminated glass panes with an edge length of *1.0 m* are presented. In the experimental investigations all the edges are supported out-of-plane by large steel profiles (*UNP 180* for the loaded edges and *IPE 160* for the edges without loading). The loading is applied in-plane on two opposite edges with especially designed aluminium supports (eight local supports on each edge), which allow the rotation of the glass panes (see system and detail sketches in Fig. 2.11, left). To avoid the contact between these supports and the glass edge a layer of soft aluminium is used.

[Englhardt, 2007] includes results from experimental testing on the plate buckling behaviour of squared (*1.0 m x 1.0 m*) and rectangular (up to *2.0 m x 1.0 m*) glass panes with monolithic and laminated composition under uniaxial loading on two opposite edges (the shorter edges for the rectangular panes). The loaded edges of the panes (in total over 120 test specimens) have linear hinged supports (see detail sketch in Fig. 2.11), while the edges without loading are free to move in the in-plane direction as well as to rotate around the loading axis during loading (Navier boundary conditions). An ideal supporting of the glass panes for the buckling investigations is aimed. The loading is applied both over the whole edge length and by setting blocks made of POM, which are positioned near the corners (see system sketch in Fig. 2.11, right).

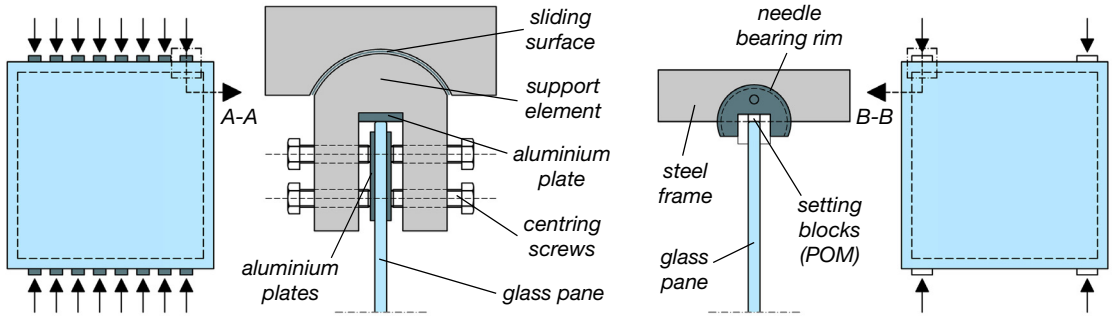

Fig. 2.11 *Different systems for glass panes loaded by uniaxial compressive loads investigated in [Luible, 2004] (left) and [Englhardt, 2007] (right)*

The investigations documented in [Luible, 2004] and [Englhardt, 2007] show that the glass panes subjected to plate buckling can carry loads which are higher than the ideal buckling load due to a post-critical load-bearing behaviour. This additional capacity, which is not occurring in the cases of column buckling and lateral torsional buckling, is the result of activated membrane forces for higher deflections. For a loading over the whole edge, the location of the maximal principal tensile stresses moves from the middle of the glass pane to the corners when entering the post-critical region. For a loading by setting blocks near the corners as in [Englhardt, 2007], the compressive load is transferred from the beginning near the unloaded edges. The initial cracks are noticed for both loading types not in the middle of the glass pane, but near the corners. After failure no post-breakage structural capacity is given in the case of the laminated glass panes, since all glass sheets fail at once and even in the case of heat strengthened glass, small fragments result because of the high released fracture energy.

[Luible, 2004] observes that the use of an effective thickness t_{eff} for a laminated glass pane in finite element simulations of plate buckling is not recommended, because the results regarding principal tensile stresses show high discrepancies for the post-critical behaviour. The most exact method for a buckling calculation is considered to be a finite element simulation, which takes into account the actual thickness and the initial geometric imperfection of the glass pane as well as the material properties of the interlayer. The resulting stresses and deformations can be than compared to resistance values and design limits. By finite element simulations, [Englhardt, 2007] notices that the ideal buckling load of glass panes loaded by setting blocks near the corners is higher (by about 60% for the investigated sizes) than for a loading over the whole edge length.

Both [Luible, 2004] and [Englhardt, 2007] determine the ideal buckling load for a loading over the whole edge length analytically with the calculation model proposed in [Zenkert, 1997] for sandwich constructions with thick surface layers based on the linear sandwich theory. By assuming Navier-type boundary conditions and a single half-wave perpendicular to the loading direction (y-direction), (Eq. 2.7) can be used to calculate the ideal buckling load $N_{x,cr,LG}$ for a laminated glass made of two glass sheets:

$$N_{x,cr,LG} = k_{LG} \cdot \frac{\pi^2 \cdot D}{b^2} \qquad \text{(Eq. 2.7)}$$

The buckling factor k_{LG} can be determined with (Eq. 2.8):

$$k_{LG} = \left(\frac{m \cdot b}{a} + \frac{a}{m \cdot b}\right)^2 \cdot \frac{\frac{(D_1 + D_2)}{D} \cdot \left(\left(\frac{m \cdot b}{a}\right)^2 + 1\right) + \frac{A \cdot b^2}{D_S \cdot \pi^2}}{\left(\left(\frac{m \cdot b}{a}\right)^2 + 1\right) + \frac{A \cdot b^2}{D_S \cdot \pi^2}} \qquad \text{(Eq. 2.8)}$$

While the lowest possible value for the buckling factor k of a monolithic glass pane is *4*, the buckling factor k_{LG} of a laminated glass pane can reach also values lower than *4*. This occurs because the buckling factor of a laminated glass depends not only on the geometry of the glass pane, but also on the shear stiffness of the interlayer. The unknowns D_1, D_2, D and A can be calculated with the following equations:

$$D = D_1 + D_2 + D_S \qquad \text{(Eq. 2.9)}$$

$$D_i = \frac{E \cdot t_i^3}{12 \cdot (1 - \nu^2)} \qquad \text{(Eq. 2.10)}$$

$$D_S = \frac{E \cdot t_1 \cdot z_1^2 + E \cdot t_2 \cdot z_2^2}{1 - \nu^2} \qquad \text{(Eq. 2.11)}$$

$$A = \frac{G_{IL} \cdot (z_1 + z_2)^2}{t_{IL}} \qquad \text{(Eq. 2.12)}$$

The notations used in (Eq. 2.7)-(Eq. 2.12) have the following meanings:

N_x	normal force per length unit ($N_x = \sigma_x \cdot t$)
m	number of half-waves in loading direction (x-direction)
a	glass pane dimension in loading direction
b	glass pane dimension perpendicular to the loading direction
D_i	plate stiffness for a unit width
t_i	thickness of the respective glass sheet
E	Young‘s modulus for glass

ν	Poisson‘s ratio for glass
z_i	distance between the centre of gravity for the whole section to the centre of gravity for the respective glass sheet
G_{IL}	shear modulus of the interlayer
t_{IL}	thickness of the interlayer

The structural behaviour of monolithic glass panes with U-shaped edge beams on two sides under uniaxial compression is documented in [Haese, 2013]. The objective of these investigations is to analyse the difference between a load application only into the glass pane, a load application only into the edge beams and a load application into both the glass pane and the edge beams (see sketches in Fig. 2.12) for a self-supporting facade construction (the dead weight of the glazing is not transferred to the main structure behind it). The used glass pane dimensions in the experimental tests are *1.0 m x 1.5 m*. Results for both situations of the glass pane as a portrait format and a landscape format are provided. The connection between the U-shaped edge beams and the glass pane is frictionless due to PTFE-layers. The load is applied at the element corners with hinged steel brackets (see Fig. 2.12, right). Between the steel brackets and the glass edge or the edge beam especially shaped setting blocks made of POM are used. To avoid a column buckling of the edge beams around the weak axis, guiding plates which do not restrain the torsion of the profiles are used.

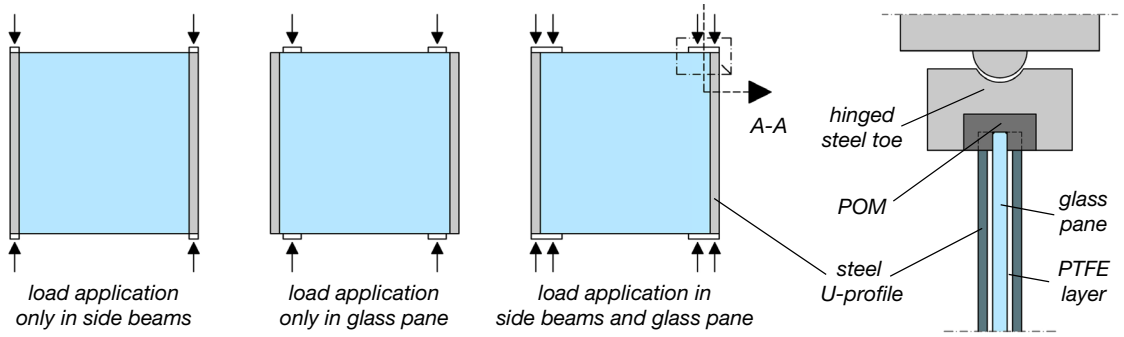

Fig. 2.12 *Different systems for glass panes loaded by uniaxial compressive loads investigated in [Haese, 2013] and detail of the load application*

The results of the performed experimental and numerical studies show that a load application only in the edge beam leads to the largest load-bearing capacity, which is beneficial since it allows at the same time to avoid stress peaks in the glass pane.

2.3.3 Glass panes activated as diagonal struts

In general, the lateral stability of a building has to be provided in two orthogonal directions by shear walls and stiff floor/roof diaphragms. In the case of frame constructions these elements can be realised by rigid frames and/or braced bays. The bracing of a rectangular frame with no or low corner stiffness can be achieved either by diagonal struts or by activation of an in-fill element as a shear panel. These two possibilities are followed as well when the activation of glass panes as in-plane load bearing elements is aimed (see Fig. 2.13). To activate the glass pane as a diagonal strut, setting blocks or grouting are used near the glass pane corners. Since glass can

transfer high compressive loads, but is rather sensible to tensile loads, only the compressive diagonal is activated by using materials which allow a separation in case of tensile loads. To obtain a shear panel, a perimetrical structural connection of the glass pane to the framing is required. In steel or timber framed buildings profiled metal sheeting or veneer panelling is fixed with mechanical connections to the linear structural members. For glass panes linear adhesive connections with sufficient shear stiffness are the preferred alternative, since bore holes and concentrated stress peaks can be avoided. In this subchapter research investigations on systems with glass panes activated as diagonal struts are presented. Projects with glass panes activated as shear panels are pointed out in subchapter 2.3.4.

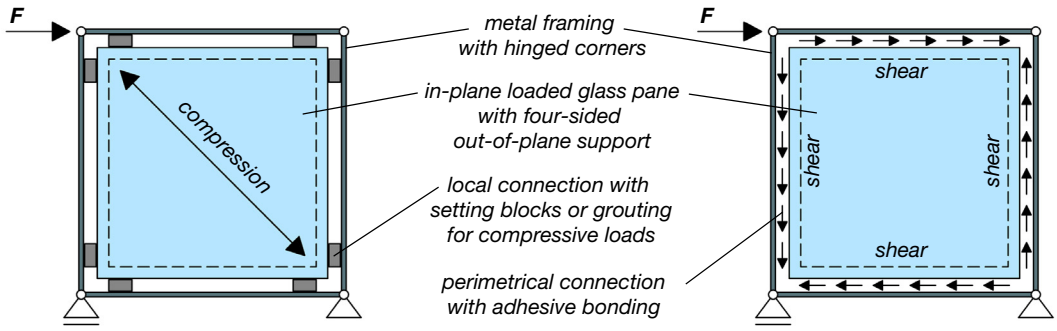

Fig. 2.13 *Activation of the glass pane as a bracing by setting blocks or grouting near the corners (left) and as a shear panel by perimetrical adhesive bonding (right)*

In [Wellershoff, 2006] the plate buckling behaviour of squared monolithic and laminated glass panes with an edge length of *1.2 m* and *1.6 m* is investigated under shear loading. For the support of the glass panes on a hinged squared steel framing, grouting at the corners (see also [Wellershoff, 2008b]) and perimetrical adhesive bonding (see also [Wellershoff, 2008a]) are analysed separately. For the grouted glass panes the material *Epple Glasmörtel* is used. The supports for the grout are connected with hinges to the steel framing to allow an optimal load application into the glass pane corners. The glass panes are supported out-of-plane only at the corners as illustrated in Fig. 2.14, left. In order to use only one grouting block in each corner, the glass pane is cut diagonally as shown in Fig. 2.14, right. The failure is generally noticed at the glass edge near one of the corners under compression after out-of-plane deformations due to buckling.

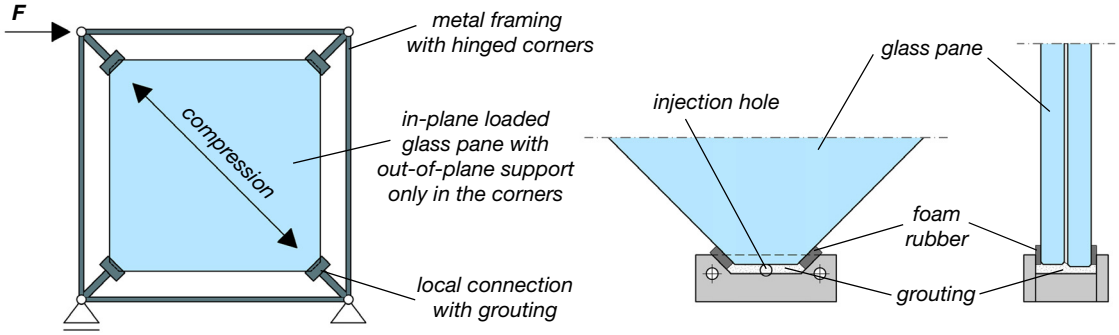

Fig. 2.14 *Conceptual sketch of the system investigated in [Wellershoff, 2006] for glass panes activated as bracing (left) and detail of the grouting in the corners (right)*

For determining the critical buckling load for glass panes in such a system, [Wellershoff, 2006] recommends to use either the energy method or finite element methods. Additionally, approaches for the structural design of glass panes in such systems under a diagonal compressive load as well as under combined diagonal compressive load and out-of-plane surface load are provided.

In [Freitag & Wörner, 2011] two concepts for mechanically prestressing the glass pane in order to introduce a compressive prestress state into the tension diagonal are presented. For the first one, a system with setting blocks near the corners (for instance made of POM) is used (see sketch in Fig. 2.15, left). Experimental tests are performed on squared monolithic panes made of annealed glass with an edge length of *1.0 m* and a thickness of *8 mm*. The glass panes fulfilled the function of a bracing for a framing with hinges in the corners made of profiles with large cross section and high bending and rotation stiffness. The observed failure mode shows a buckling behaviour along the compressive diagonal which leads to glass fracture after reaching the tensile strength. Despite the clear overview of forces acting on the glass pane, this concept is difficult to apply in reality because of the complex prestressing process in which each setting block receives forces from the prestressing of the other blocks. For the second concept the prestressing is applied over the whole perimeter of the glass pane by using an elastomer with a Poisson‘s ratio of about *0.5*, in which the glass pane is embedded (see Fig. 2.15, right). The results from tests performed on both monolithic (*8 mm* annealed glass) and laminated (*2 x 4 mm* annealed glass) squared panes show a failure pattern which is more common for glass panes activated as shear panels than as diagonal struts.

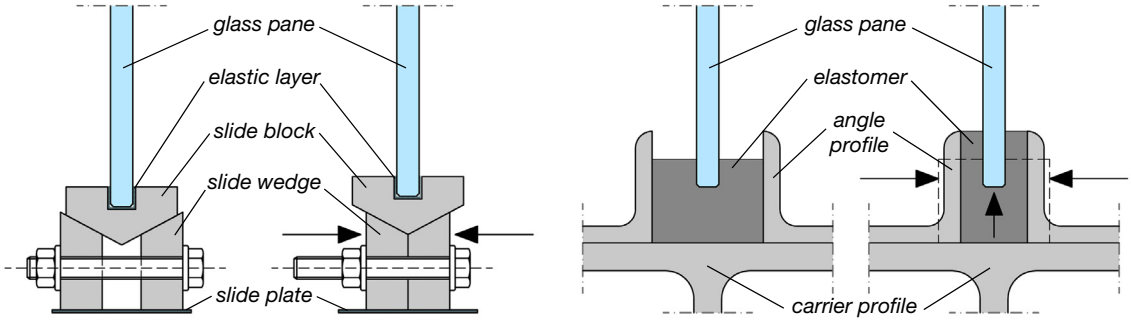

Fig. 2.15 *System details investigated in [Freitag & Wörner, 2011] for mechanically prestressed glass panes activated as bracing with local prestressing near the corners (left) and linear prestressing (right)*

A system which combines the concepts of diagonal struts and shear panels is investigated in [Mocibob, 2008]. Rectangular glass panes with the dimensions of *1.2 m x 3.5 m* made of laminated glass are tested under in-plane shear loading, combined in-plane shear loading and in-plane uniaxial compressive loading and combined in-plane loading and out-of-plane distributed pressure. Two support situations, the first one with bolted point fixings at the four corners (see Fig. 2.16, left) and the second one with a combination of blocked grouting with *Hilti HIT-HY 70* and linear adhesive bonding with *DC993* at the top and bottom edges (see Fig. 2.16, right), are compared to each other. For both alternatives a hinged frame made of *HEB 180* profiles is used around the glass panes. In the case of the point fixings, the glass pane is supported out-of-

plane only at the point fixings. In the second support case, the out-of-plane bearing is linear at the top and bottom edge. For both support situations an activation of the compressive and the tensile diagonal is observed. While in the first case both diagonals are activated by the bolted point fixings, in the second case the compressive diagonal is activated by two opposite grouting blocks and the tensile diagonal by the shear strength of the linear adhesive bonding.

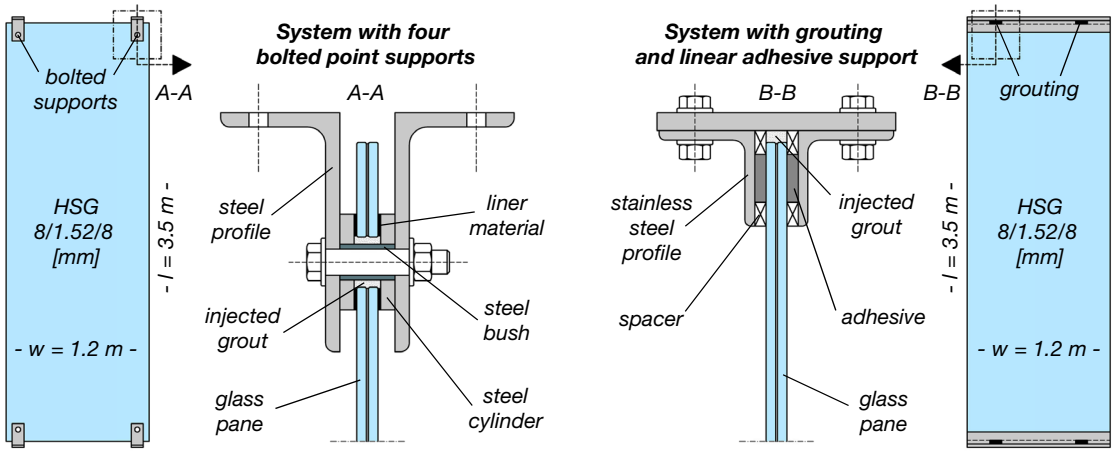

Fig. 2.16 *Load transfer systems for glass panes subjected to shear loads investigated in [Mocibob, 2008] for pavilion walls*

Based on the performed investigations [Mocibob, 2008] elaborates a design proposal for the resistance to shear buckling of the point supported and linear supported glass panels shown in Fig. 2.16. The characteristic shear buckling resistance $\tau_{b,Rk}$ of the glass pane can be determined by multiplying the characteristic shear resistance τ_{Rk} with a shear buckling reduction factor χ, which is a function of the non-dimensional shear plate slenderness $\bar{\lambda}$:

$$\bar{\lambda} = \sqrt{\frac{\tau_{Rk}}{\tau_{crit}}} \qquad \text{(Eq. 2.13)}$$

In (Eq. 2.13) the characteristic shear strength τ_{Rk} can be assumed to be the same as the characteristic bending strength σ_{Rk} for brittle materials like glass, while τ_{crit} is the critical shear stress. Furthermore, concepts for static proofs of the stress peaks near the bore hole for the point supported panel and of the stresses in the adhesive for the linear supported systems are included.

In [Amadio & Bedon, 2016] the influence of adhesively bonded vertical steel elements (mullions) on the buckling behaviour of glass panes supported by setting blocks and linear adhesive bonding at the top and bottom edges (system investigated in [Mocibob, 2008]) under shear loading is investigated by finite element methods. The horizontal steel elements (transoms) are considered to be fully rigid ($EI = \infty$), since glass panes spanning from floor to floor are assumed. For the mullions the bending stiffness is varied between the boundaries $EI = 0$ and $EI = \infty$. In the finite element model shell elements are used for the monolithic glass pane and beam elements for the mullions and transoms. The adhesive and the setting blocks are modelled with so-called slide-plane connectors, which behave as springs with certain stiffness. For different parameters like aspect ratio and stiffness of mullions, expected critical shear loads and ultimate buckling

resistances are determined. Since only linear-elastic material behaviour is assumed for all materials and no validation by experimental testing of the presented values and curves is given, these results have to be used carefully.

2.3.4 Glass panes activated as shear panels

As already described in the previous subchapter, glass panes can be activated as shear panels by a perimetrical connection to the framing. In [Wellershoff, 2006] and [Wellershoff, 2008a] squared monolithic and laminated glass panes, supported by two-sided perimetrical adhesive bonding to a hinged steel frame, are investigated under a shear load (see system sketch illustrated in Fig. 2.13, right). For an easier assembly of the specimens, angles are bonded on both sides of the glass panes and are screwed to the framing, which is built out of *HEB 200* profiles (see Fig. 2.17, left). The frame and the angles have a high stiffness in order to have no influence on the buckling behaviour. Polyurethane and acrylic adhesives with a width of *20 mm* are used. The thickness of the adhesive joint is *3.5 mm* for the polyurethane and *1.5 mm* in the case of the acrylic. Additional to the shearing load, an out-of-plane load is brought up by air pressure in the cavity of an insulated glass unit with soft spacer system.

It is observed, both from the out-of-plane deformations of the glass pane due to buckling as well as from the shear displacements within the adhesive, that the system shows a higher stiffness during the first load cycle compared to subsequent ones. According to [Wellershoff, 2006], this results due to the fact that the molecular chains within the adhesive polymer structure are straightened during the initial loading and do not go entirely back during the unloading. The reason for this can be either a time dependent resilience coupled with a too short recovery time or a plastic material behaviour. The observed failure modes are either a mixed failure of the adhesive or a failure of the glass pane due to exceeding the tensile strength along the tensioned diagonal or near the ends of this diagonal.

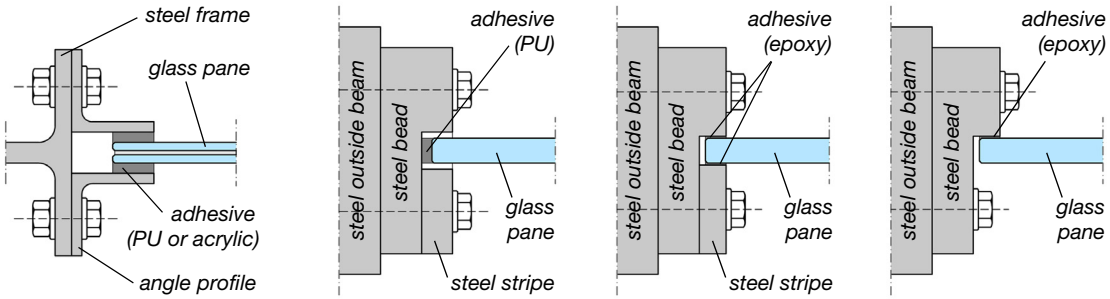

Fig. 2.17 *Load transfer systems for glass panes activated as shear panels investigated in [Wellershoff, 2006] (first from the left) and [Huveners, 2009] (first three from the right)*

[Huveners, 2009] investigates the plate buckling behaviour of squared monolithic glass panes (*12 mm* annealed float glass) with an edge length of *1.0 m* and perimetrical adhesive bonding to a steel frame, which consists of two transoms and two mullions with large cross sections. The mullions and transoms are joined with hinges to each other and are built out of an outside beam (rectangular full section with dimensions of *120 mm x 60 mm*) and a replaceable coupling ele-

ment, which are connected together by bolts and support the glass pane out-of-plane along its perimeter (similar system as the one used by [Wellershoff, 2006] and illustrated in Fig. 2.13, right). Different adhesive joint types are investigated, with a polyurethane at the glass edge across the thickness of the glass pane as well as with an epoxy one-sided and two-sided along the glass edge (see the first three sketches from the right in Fig. 2.17). While for the polyurethane a thickness of *6 mm* is used, the epoxy is applied in a layer of only *0.5 mm*.

In the case of the system with polyurethane two stages are observed during testing: *(i)* a first stage with a lower stiffness and large deformations of the glass pane relative to the steel profiles and *(ii)* a second stage after contact between glass and steel. This contact increases the stiffness but also quickly leads to cracks at the glass edge near the corners which are under compression. The system with two-sided epoxy adhesive bonding shows a significantly higher stiffness which gradually decreases with higher loading. After the first cracks, which occur near the corners of the tension diagonal, the system is able to redistribute the in-plane stresses and the load can be further increased, but the load transfer concentrates more and more within the compression diagonal. A similar behaviour and stiffness is observed for the system with one-sided epoxy adhesive bonding, but due to the excentric load transfer between glass pane and steel profiles, the final crack occurs at a significantly lower load. In the conclusion of his work [Huveners, 2009] attributes the highest potential to the system with a two-sided epoxy adhesive bonding due to its high in-plane stiffness and the good residual capacity which it shows.

For a rectangular glass pane under constant shear loading the critical shear stress can be determined according to [Wellershoff, 2006] by (Eq. 2.14):

$$\tau_{crit} = \frac{\pi^2 \cdot E}{12 \cdot (1 - \nu^2)} \cdot \left(\frac{t}{b}\right)^2 \cdot k_\tau \qquad \text{(Eq. 2.14)}$$

The buckling factor k_τ depends on the aspect ratio of the panel as well as on the out-of-plane support type. For hinged Navier-type boundary conditions the buckling factor can be determined with (Eq. 2.15):

$$\begin{aligned} k_\tau &= 4.00 + 5.34/\alpha^2 \qquad \text{for} \qquad \alpha < 1 \\ k_\tau &= 5.34 + 4.00/\alpha^2 \qquad \text{for} \qquad \alpha \geq 1 \end{aligned} \qquad \text{(Eq. 2.15)}$$

For fixed out-of-plane boundary conditions the buckling factor can be determined by (Eq. 2.16):

$$\begin{aligned} k_\tau &= 5.60 + 8.98/\alpha^2 \qquad \text{for} \qquad \alpha < 1 \\ k_\tau &= 8.98 + 5.60/\alpha^2 \qquad \text{for} \qquad \alpha \geq 1 \end{aligned} \qquad \text{(Eq. 2.16)}$$

In the case of panes made of several laminated glass sheets the critical shear stress depends as well on the shear stiffness of the interlayer material. For a laminated glass pane made of two glass sheets with the same thickness, [Wellershoff, 2006] recommends the use of an additional factor k_{LG}, extending (Eq. 2.14) to (Eq. 2.17), where t_{glass} is the thickness of a single glass sheet:

$$\tau_{crit} = \frac{\pi^2 \cdot E}{12 \cdot (1 - \nu^2)} \cdot \left(\frac{t_{glass}}{b}\right)^2 \cdot k_\tau \cdot k_{LG} \qquad \text{(Eq. 2.17)}$$

The notations used in (Eq. 2.14)-(Eq. 2.17) have the following meanings:

τ_{crit}	critical shear stress
a	length of the glass pane
b	width of the glass pane
t	thickness of the glass sheet
E	Young‘s modulus for glass
ν	Poisson‘s ratio for glass
k_τ	buckling factor
α	aspect ratio of the glass pane (α = *a/b*)

In [Wellershoff, 2006] values for the factor k_{LG} can be found depending on the boundary condition type as well as on the shear modulus of the interlayer for the investigated squared glass pane sizes. Based on finite element simulations it is shown that the two-sided perimetrical adhesive bonding of the glass panes behaves as a fixed support. Additionally, approaches for the structural design of glass panes in such systems under a shear load as well as under combined shear load and out-of-plane surface load are provided. The approach for the shear load is similar to the one in [Mocibob, 2008] based on a shear buckling reduction factor χ, determined in dependence of the non-dimensional shear plate slenderness $\overline{\lambda}$.

2.3.5 Timber-glass composite panels

The use of glass panes as bracing elements for timber frames is a research topic which has been investigated in several projects during the last 15 years (see [Niedermaier, 2005], [Edl, 2008], [Neubauer, 2011], [Hochhauser, 2011], [Nicklisch, 2016] and [Piculin et al., 2016]). The projects completed at the Technical University of Vienna in collaboration with Holzforschung Austria have a significant contribution to the developments for these systems. In the mentioned projects, a glass pane is generally adhesively bonded to a coupling frame made of solid wood or plywood, which is then screwed to the main timber frame.

The use of adhesively bonded glass panes as bracing elements in transparent walls with structural elements made of timber are investigated in [Neubauer, 2011]. After performing experimental investigations on three different adhesives (two silicones and one acrylic), the work focuses on the development of a functional facade system by using this structural concept. In addition to the mechanical performance, building physics aspects (permeability to air, resistance against wind-driven rain and behaviour under climate differences) are investigated and the manufacturing and assembling procedures are optimised. The dimensions of the used monolithic annealed glass panes (or of the used grid for several elements) are *1.25 m x 2.50 m*.

For the mechanical tests discussed in [Neubauer, 2011], *8 mm* thick glass panes are adhesively bonded to a coupling strip, which is then screwed to a mullion-transom structure with profile

section dimensions of *60 mm x 160 mm* (see sketch in Fig. 2.18, left). The timber-glass elements are loaded in shear by a horizontal force on one of the top corners. A single element in portrait and landscape format as well as two coupled elements are tested. In the case of the systems with silicone a cohesive failure within the adhesive is observed for all specimens. For the specimens with the acrylic adhesive, different failure scenarios are obtained due to the higher stiffness of the adhesive: ductile failure of the screws between coupling strip and main frame, failure of the screws in the corner support coupled with glass failure or failure of the plywood coupling strip coupled with glass failure.

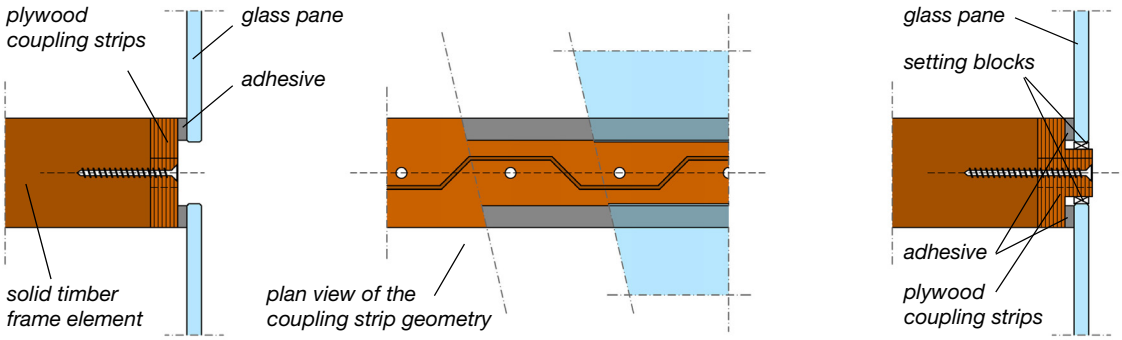

Fig. 2.18 *Load transfer systems investigated for timber-glass composite panels in [Neubauer, 2011] (left and middle) and in [Hochhauser, 2011] (right)*

In [Hochhauser, 2011] an extension of the system analysed in [Neubauer, 2011] to glass-timber composite panels with adhesive bonding and additional setting blocks in the corners (see sketch in Fig. 2.18, right) is investigated by theoretical, analytical and numerical methods. An approach for determining the buckling coefficients for glass panes activated for in-plane loads in this way is discussed in [Neumann et al., 2013] based on the Dunkerley straight line.

Another project focusing on adhesives with higher strength for timber-glass composite panels is presented in [Nicklisch, 2016]. After performing uniaxial tensile tests at different loading speeds (*1 mm/min*, *5 mm/min* and *50 mm/min*) and temperatures (*-20 °C*, *+25 °C* and *+80 °C*) as well as shear tests at different temperatures on several adhesives, a two-component silicone (*Otto-coll S660*), a modified two-component epoxy (*nolax C44.8505*) and a two-component epoxy-resin (*Skotch-Weld DP 490*) are chosen for detailed investigations. For these three adhesives, which are suitable for timber-glass connections, but show different strength values, the mechanical behaviour after ageing under UV-radiation, moisture and storage in cleaning agents as well as the creep behaviour are analysed in connections between glass and timber (plywood birch and solid wood pine) under tensile and shear loading. The best suitability for timber-glass composite panels, considering both high strength and stiffness as well as a certain flexibility, is shown by the modified two-component epoxy.

2.3.6 Out-of-plane loaded glass panes

Other than glass panes under in-plane loading discussed in the previous subchapters, out-of-plane loaded glass panes are covered by existing standards and can be designed according to these regulations (see [DIN 18008-1], [ÖNORM B 3716-1] and [EUR 26439 EN, 2014]). However,

the influence of the interlayer shear stiffness in the case of laminated glass and especially the value for the interlayer shear modulus, which can be used depending on the expected temperature conditions and loading durations, are still uncertainties which the standards define rather conservative. The state of the art for the design of out-of-plane loaded glass panes will not be further discussed in this subchapter; for details the mentioned standards are referred to.

By applying similar concepts to those followed in the case of hybrid glass beams, the structural behaviour of glass panes under out-of-plane loading can be improved as well. In [Nhamoinesu, 2014] the out-of-plane bending of glass panes with an adhesively bonded linear reinforcement at the edges is investigated. The used adhesive is the acrylic *Araldite A2047* and has a thickness of *3 mm*. The large-scale glass panes have dimensions of *3.5 m x 1.5 m* and consist of laminated glass made of *2 x 10 mm* heat strengthened glass. Different composite panel types are tested (see sketches in Fig. 2.19, right): double glazed with reinforcement in one direction (Type A), double glazed with reinforcement in both directions (Type B) and single glazed with reinforcement in one direction (Type C). The reinforcement is made of square hollow section profiles with the dimensions of *30 mm x 30 mm x 1.5 mm*. The panels are subjected to four-point-bending tests as illustrated in Fig. 2.19, left. Four rubber padded loading plates with dimensions of *150 mm x 130 mm x 13 mm* are used to apply the load. The support of the specimens during testing is realised at the four corners through pins welded to the reinforcement.

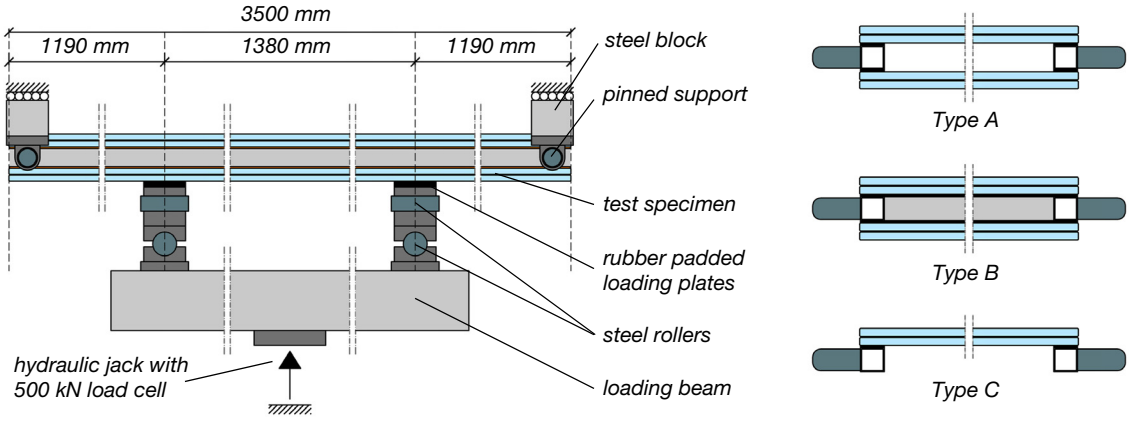

Fig. 2.19 *Side view of the test set-up (left) and sections of the composite panel types (right) investigated in [Nhamoinesu, 2014]*

The results of the large-scale tests show that the double glazed units lead to a more efficient composite behaviour in comparison with the single glazed units. Furthermore, it is noticed that the panels with reinforcement in both directions do not bring a significant improvement for the investigated aspect ratios compared to those with reinforcement in only one direction. The double glazed panels also show a substantial post-fracture strength of up to around *60%* of the strength before failure. Results from medium-scale tests (glass pane sizes of *0.7 m x 0.3 m*) on the same type of panels are also provided, but a scaling of these results to real-size elements is not recommended due to the concern of incorrect stiffness ratios. Monolithic glass panes made of totally tempered glass are used for these tests.

3 Transparent building envelopes with composite structural behaviour

Introduction to the concept
Fundamentals on composite action
Loads on transparent building envelopes
Functional requirements for transparent building envelopes
Challenges and preliminary concepts
Conclusions and delimitations for further investigations

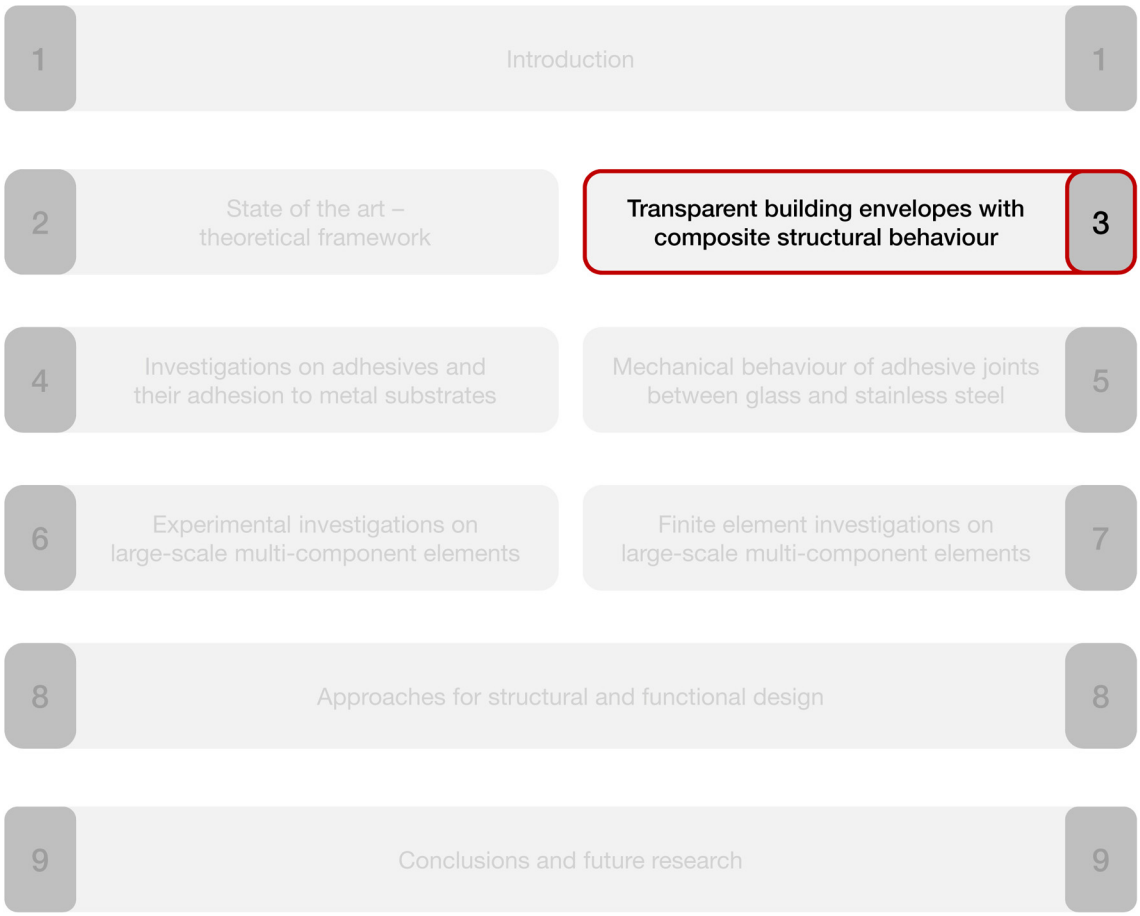

3.1 Introduction to the concept

The state-of-the-art aspects presented in the previous chapter and the research performed in the past years, in general, show a high potential for the material glass to be used in structural applications. Glass beams and glass fins can be more and more noticed in real applications like interior glass bridges and glass stairs or as supporting elements in glazed facades. Structurally used glass panes are on the other hand a rather exceptional application. Only isolated small projects like single-storey pavilions make use of the potential of glass panes to act as in-plane loaded walls (see [Wellershoff et al., 2011]).

However, by analysing the utilisation of the material glass in the construction field, the largest percentage are glass panes which have no structural function, but are used mainly for their transparency in large glazed building envelopes. When stepping from single-storey glazed buildings to larger ones, which require more than one glass pane over their height, facade systems with metal (or in some cases timber) structural elements are used. These are generally either post-and-beam facades or system facades with rather large framing profiles on which the glass panes are fixed as in-fill elements. Furthermore, in the case of double-skin facades the outer skin glazing is generally supported by large rigid metal brackets which are connected to the main structure. In these situations, the glass panes are not intentionally activated as shear panels and only transfer their own dead weight as an in-plane load.

Considering the structural capacity of glass, more efficient systems for transparent facades are thought to be possible in selected situations by aiming an optimised use of the installed materials (see also [Englhardt, 2013]). The concept of self-supporting transparent facades which show a high in-plane rigidity and only need an additional out-of-plane support depending on their size is introduced in this subchapter. Fig. 3.1 shows a virtual prismatic structure with the main loads acting on it as well as the resulting loads on one element if a self-supporting transparent facade is assumed.

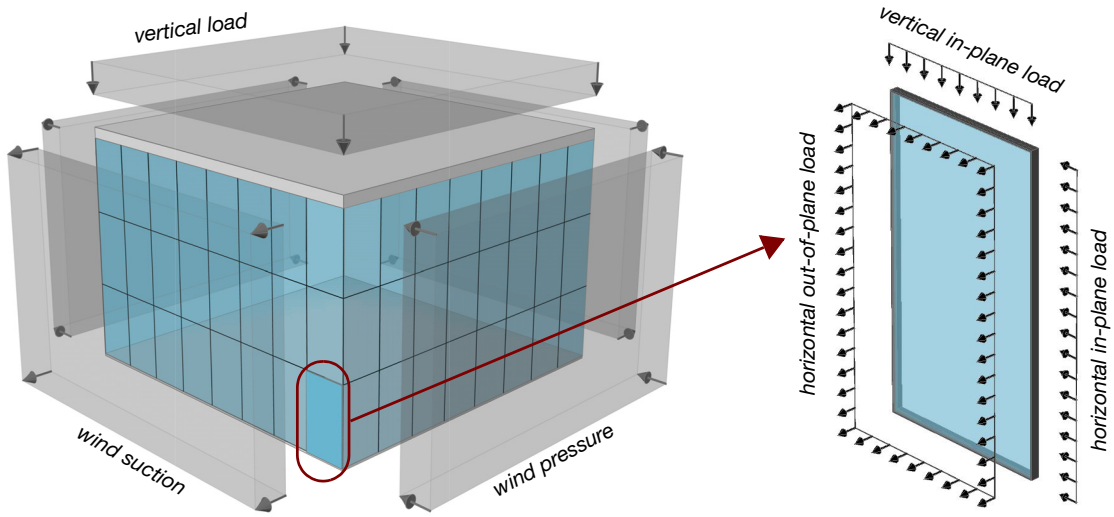

Fig. 3.1 *Loading on a virtual prismatic structure (left) and resulting loading on one element of the glazed facade (right)*

In the case of small structures, like the glass entryway shown in subchapter 1.1, Fig. 1.2, the self-supporting transparent facade could be assumed to ensure the lateral stability of the whole building. However, in the case of larger structures, further vertical walls would be required both for supporting the dead weight of the roof and eventual ceilings as well as for providing the lateral stability. Further considerations on loads acting on transparent building envelopes are provided in subchapter 3.3.

A complete avoidance of the framing materials is difficult because glass cannot be mechanically shaped as easily as metals or timber. Moreover, the connections between glass elements and other components either result in high stress peaks if executed mechanically or cannot be performed on site if executed adhesively. Therefore, the introduced concept is based on elements consisting of a filigree metal framing and a glass pane acting as a shear panel (see Fig. 3.2, left). The glass pane ensures the necessary in-plane rigidity of the element, while the metal framing provides a certain out-of-plane support to the glass pane and allows for mechanical connections between several elements as well as between elements and other structural components. The framing is divided into edge elements which determine the out-of-plane stiffness and corner elements which determine the rotational rigidity between the edge elements. In order to make the concept functional a load transfer mechanism between the metal framing and the glass pane, which enhances a composite structural behaviour of the two parts, is required. Preliminary concepts for these mechanisms based on adhesive bonding are introduced in subchapter 3.5.1.

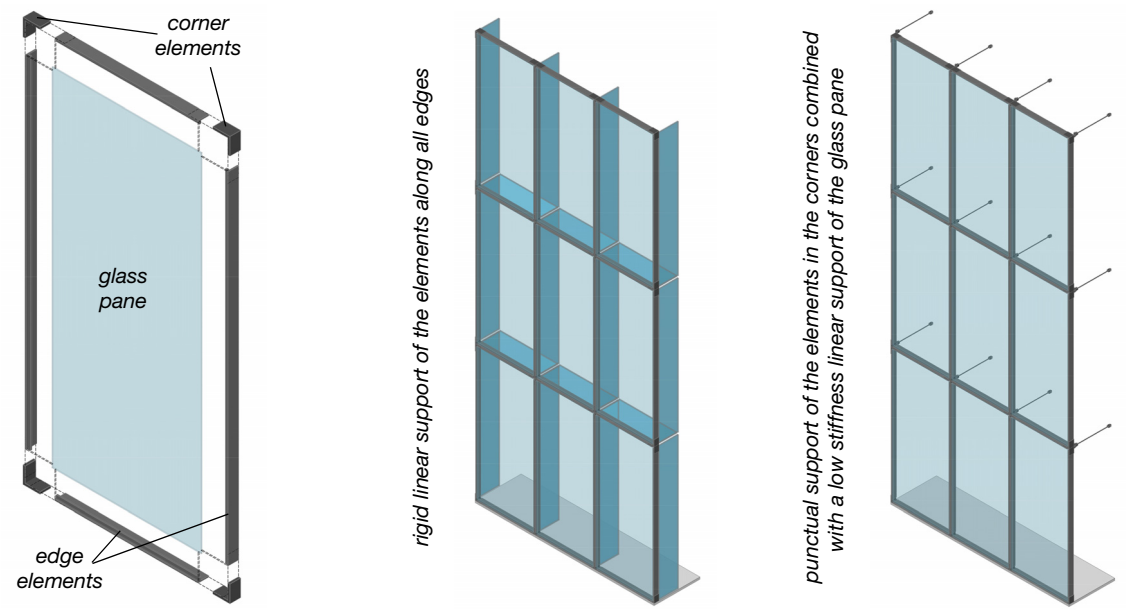

Fig. 3.2 *Element of a self-supporting transparent facade consisting of a glass pane and a filigree metal framing (left); possible out-of-plane support conditions for self-supporting transparent facades with composite structural behaviour (middle & right)*

Another factor which influences significantly the structural behaviour of such a system are the out-of-plane support conditions for the facade elements. Depending on the situation, either almost rigid linear supports realized by mullions and transoms (see example with glass fins in

Fig. 3.2, middle) or punctual supports with hinged rods (see example in Fig. 3.2, right), can or have to be used. Not only the bending of the element under out-of-plane loads, but also the buckling behaviour of the glass pane under in-plane loads depends on the out-of-plane support of the glass edges.

If the proposed element is supported out-of-plane along its perimeter by linear structural elements with high stiffness, a four-sided clamped or hinged support depending on the connection can be assumed for structural calculations of the glass pane. Both for out-of-plane bending and for plate buckling due to compressive or shear loading analytical calculations are possible in this case. However, the slenderness of the supporting linear elements, their susceptibility to lateral torsional buckling and the resulting consequences for the structurally activated glass pane have to be considered. For example in the case of the system illustrated in Fig. 3.2, middle, the glass fin edges situated away from the facade glazing could sidestep under a certain wind suction load. Due to this lateral torsional buckling of the glass fins, the glass pane may receive additional stresses and deformations.

In the case of elements supported out-of-plane punctually in their corners (system illustrated in Fig. 3.2, right), the structural behaviour of the glass pane gets more complicated. Since the metal framing is intended to be as filigree as possible, it cannot be assumed to be a linear rigid support for the glass pane along the edges. On the other hand, to assume that the glass pane is only supported at the corners would be wrong, because the influence of the framing stiffness would be neglected. These aspects lead to the impossibility to use existing analytical models for calculations of the glass pane as an in-plane activated structural element. The proposed element has to be treated as a composite system in which the framing has an influence on the structural behaviour of the glass pane, while at the same time the glass pane influences the structural behaviour of the framing.

The investigations performed in this thesis at material and connection level (chapters 4 and 5) are valid for both out-of-plane support types of the proposed elements with composite structural behaviour. However, the investigations at element level (chapters 6 and 7) focus mainly on the punctually supported elements, since these ones show a higher complexity.

3.2 Fundamentals on composite action

In the field of structures, composite action is generally referred to, when two (or more) layered components are interconnected and work together to reduce the deflections and stresses under bending loads. Composite action can be achieved *(i)* between components made of the same material as well as *(ii)* between components made of different materials. Examples for the first case are two wooden boards which are nailed together or laminated glass, discussed in subchapter 2.2.1. Probably two of the most common applications for the second case are steel-concrete composite systems, which are used both for slabs in buildings and for bridge decks, and facade sandwich panels, which usually consist of thin outer layers and a thicker soft core.

For a good understanding of the principle of composite action and of its potential, it is essential to explain the two boundary cases: the layered limit and the monolithic limit. This is done here based on [Nhamoinesu, 2014] by using a theoretical assembly of two components which are positioned on top of each other. The assembly is supported as a single-span beam and is loaded with a concentrated force at mid-span (three-point bending, see Fig. 3.3). These two components can represent *(i)* two panels, as it would occur for example in the case of a laminated glass pane, or *(ii)* a panel and a beam, as it would be the case of a glass pane connected to a metal beam.

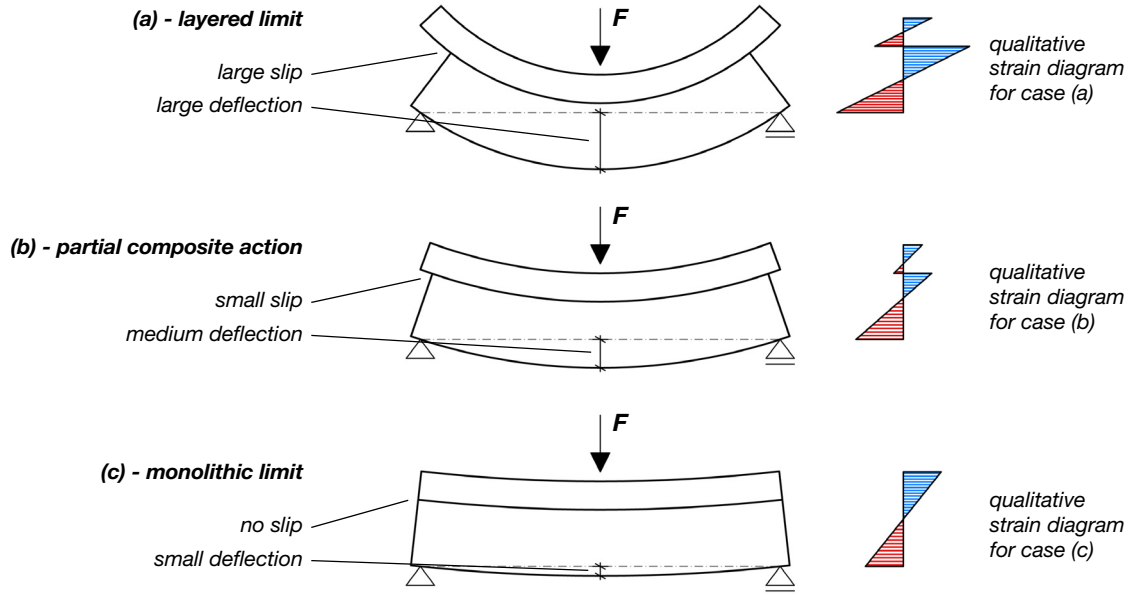

Fig. 3.3 *The concept of composite action illustrated schematically*

The layered limit is obtained by freely placing the top component above the bottom one and assuming there is no friction between the two (see case *(a)* Fig. 3.3). In this case, the two components act completely separately, a longitudinal slip is occurring between the two components and large vertical deflections are resulting. The bending stiffness of the assembly for the layered limit is equal to the sum of the bending stiffnesses of the single components. Composite action between the two components is achieved by connecting them to each other. The monolithic limit is obtained with a connection which exhibits the same stiffness as the two constituent

components (see case *(c)* in Fig. 3.3). In this case, full composite action is obtained, which leads to no longitudinal slip between the two components and to small vertical deflections. As illustrated by the examples discussed in subchapter 2.3, mainly adhesive joints are used to connect glass panes to components made of other materials in order to obtain composite or hybrid structural elements. Such connections can achieve partial composite action which translates into an intermediate case (see case *(b)* in Fig. 3.3) situated somewhere between the layered limit and the monolithic limit.

For the concept of self-supporting transparent facades with glass-metal elements introduced in subchapter 3.1, the degree of composite action between the glass pane and the filigree metal framing is of importance in the case of loading scenarios which generate out-of-plane deformations of the elements. This can be either direct out-of-plane loads (e.g. wind loads) or in-plane loads which lead to buckling of the glass pane. The degree of composite action is determined by the stiffness of the connection between glass pane and metal framing.

Published research results on composite structural elements with glass panes subjected to bending about their weak axis are rather limited. The recent investigations by [Nhamoinesu, 2014] on steel-glass panels subjected to four-point bending were already discussed in subchapter 2.3.6 with focus on the experimental part. For a simplified version of the panel of *Type A* illustrated in Fig. 2.19, [Nhamoinesu, 2014] also derives equations for analytical prediction of the maximum deflection as well as of the shear stress and bending stress profiles in the steel-glass composite unit (both for pre-fracture and post-fracture situations). The simplified panel consists of two monolithic glass panes with a single rectangular hollow-section profile adhesively bonded between them. The four-point bending loads are applied in the midplane of the steel reinforcement. Due to these simplifications the panel acts rather as a beam with glass flanges and a steel web. The equations derived by [Nhamoinesu, 2014] are based on the study by [Allen, 1969] on the bending of sandwich beams. [Allen, 1969] analyses, among other investigations, simply-supported composite beams with thick faces and anti-plane core under various loading scenarios (central point load, uniformly distributed load and four-point loading). The considered cross section of the composite beam and sketches of the beams with central point load and uniformly distributed load are shown in Fig. 3.4.

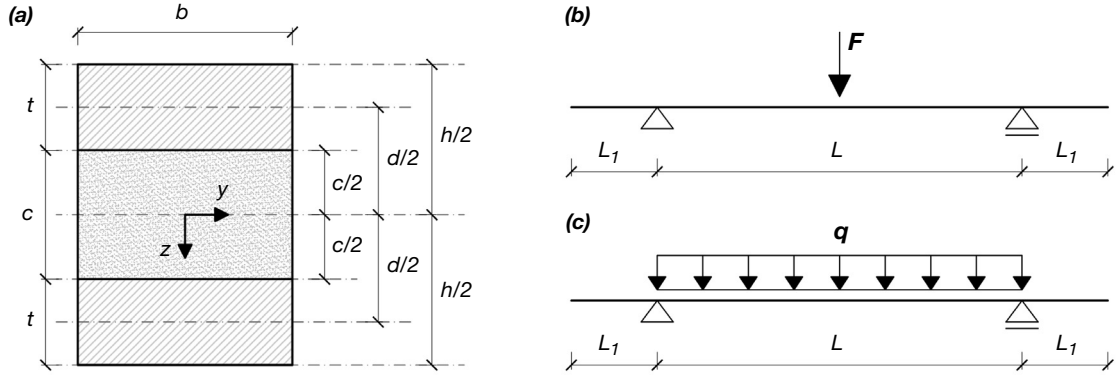

Fig. 3.4 *Geometry notations for the composite beam with thick faces and anti-plane core studied by [Allen, 1969]: (a) cross section, (b) beam with central point load F, and (c) beam with uniformly distributed load q*

The equations provided by [Allen, 1969] for calculation of the deflections (see (Eq. 3.1) for a central point load and (Eq. 3.2) for a uniformly distributed load) consist of two components, which represent *(i)* the deflection due to bending of the beam and *(ii)* the deflection due to shear of the core.

$$w_F = -\frac{FLx^2}{24EI}\cdot\left(3-\frac{2x}{L}\right)-\frac{FL}{4AG}\cdot\left(1-\frac{I_f}{I}\right)^2\cdot\left\{\frac{2x}{L}-\frac{2}{aL}\cdot[\sinh(ax)+\beta_1\cdot(1-\cosh(ax))]\right\} \quad \text{(Eq. 3.1)}$$

$$w_q = -\frac{qL^2x^2}{48EI}\cdot\left(3-\frac{2x^2}{L^2}\right)-\frac{q}{AG}\cdot\left(1-\frac{I_f}{I}\right)^2\cdot\left\{\frac{x^2}{2}+\frac{\beta_2 L^2}{4\theta}\cdot[1-\cosh(ax)]\right\} \quad \text{(Eq. 3.2)}$$

The following additional equations are necessary for solving (Eq. 3.1) and (Eq. 3.2), respectively:

$$\beta_1 = \frac{\sin\theta-(1-\cosh\theta)\cdot\tanh\phi}{\sinh\theta\cdot\tanh\phi+\cosh\theta} \;;\quad \beta_2 = \frac{1/\theta+\tanh\phi}{\sinh\theta\cdot\tanh\phi+\cosh\theta} \;;\quad \theta = \frac{aL}{2} \;;\quad \phi = aL_1 \;;$$

$$a = \sqrt{\frac{AG}{EI_f\cdot(1-I_f/I)}} \;;\quad A = \frac{bd^2}{c} \;;\quad I = \frac{bt^3}{6}+\frac{btd^2}{2} \;;\quad I_f = \frac{bt^3}{6} \;.$$

Except for the geometrical dimensions which are explained by the sketches in Fig. 3.4, the following notations are used:

a	ratio between the core's stiffness and the local bending stiffness of the faces
I	second moment of area of the faces about the centroid of the sandwich
I_f	sum of the second moments of area of the faces about their own centroids
G	modulus of rigidity of the core material
AG	shear stiffness of the composite

The form of the equations provided by [Allen, 1969] for calculating deflections substantiate that the out-of-plane deformations of a composite structural element strongly depend on the shear stiffness of the core material, which in the case of composite glass-metal elements is generally an adhesive. This is important to consider with respect to the concept introduced in subchapter 3.1 when materials for the load transfer mechanisms between glass pane and metal framing are selected. The sandwich theory by [Allen, 1969] could be extended to predict deflections of the glass-metal elements investigated in this thesis under out-of-plane loading, similar to the way this is done by [Nhamoinesu, 2014]. However, the scenarios of combined in-plane and out-of-plane loading which are examined in this thesis in chapters 6 and 7 are considered too complex for the derivation of manageable models which allow an analytical prediction of deflections and stresses. Since no such models are developed within this thesis, no further theoretical aspects on composite action (e.g. shear lag, which is generally taken into account by effective widths) are included in this subchapter. An extensive documentation of investigated composite structural elements with different geometries and materials is provided, however, by [Zenkert, 1997].

3.3 Loads on transparent building envelopes

In the previous subchapter the idea of glass-metal elements with composite structural behaviour, which are intended to carry both out-of-plane and in-plane loads, is introduced. The occurring loads can be generally classified as permanent, variable or exceptional. In terms of permanent loads, the dead weight has to be considered in the design of structural elements. In the case of the glass-metal elements with composite structural behaviour, the dead weight can act both in-plane and out-of-plane, depending on the inclination of the building envelope in which they are used. However, in this thesis only vertical facades are considered and therefore the dead weight is treated as an in-plane load. Since a self-supporting facade is aimed, one element should be able to carry its own dead weight plus the dead weight of the above lying elements. Additional loads, from roofs or ceilings for example, are not planned to be carried by this type of facade. However, this could be an option for small structures like pavilions or subway entry canopies.

The dead weight of one element is not only important for the structural design, but also for handling and assembling during the construction process. Facade companies aim at highly prefabricated systems, which are more cost-effective in the case of lighter units. This could be an achievement of the glass-metal elements with composite structural behaviour, since an optimised use of the materials may lead to reduced framing cross sections. The dead weight of one element can be approximated by summing up the dead weight of the glazing and the dead weight of the framing. As an example the dead weight of a *3.5 m x 1.5 m* large element is calculated. For the glazing a double IGU, consisting of an outer *8 mm* monolithic glass sheet and an inner *2 x 6 mm* laminated glass sheet, is assumed. The framing, which has a total length around the glass pane of about *10 m*, is made of L-profiles with the cross section dimensions of *80 mm x 40 mm x 8 mm* and a weight of *7.21 kg/m*. The approximate weight of the element is calculated by (Eq. 3.3):

$$G_{element} = G_{glazing} + G_{framing} = 262.5 + 72.1 = 334.6\ kg \approx 3.35\ kN \qquad \text{(Eq. 3.3)}$$

For determining variable loads acting on a structure, except for the life load, the first factor of influence which has to be defined is the location. Wind load, snow load and temperature load all depend on the climate zone as well as on micro-thermal climate conditions. Since the focus in this thesis lies on vertical facades, which are not planned to carry loads from roofs or ceilings, snow loads and life loads are not further discussed. Nevertheless, a line load in the height of a handrail might have to be considered as a life load for the bottom elements. For wind and temperature loads detailed aspects will be discussed in subchapters 3.3.1 and 3.3.2, respectively.

Another load belonging in the category of variable loads is the inner pressure occurring in insulating glass units. Due to the properties of the edge seal, changes of air pressure and temperature result in a pressure difference between the environment and the cavity space. Additional bending stresses in the glass panes as well as stresses in the edge seal have to be considered for structural design. However, for large flat insulating glass units, as those assumed for the investigations in this thesis, the stresses resulting from cavity pressure are very low compared to those resulting from wind loads. In the case of smaller glass formats as well as for curved geometries this load type can become more significant.

Exceptional loads are not within the scope of the performed investigations. Nevertheless, depending on the location and the use of the building, earthquake loads and explosion loads cannot be neglected and should be considered in further research. Especially bomb blast loading scenarios gained more importance during the last years and are critical especially in the case of glazed facades, because of sharp splinters which can be thrown through the air with high velocity. By using laminated glass with proper glass types and interlayers the risk for injuries can be reduced. Since in the case of the proposed glass-metal elements with composite structural behaviour the glass pane has a load-bearing role, exceptional scenarios with cracked glass panes or missing glass panes should be analysed during the design of such envelopes.

3.3.1 Considerations for wind loads

Wind loads can occur as pressure or suction on surfaces and are increasing with the height of a building. The size of the wind load depends on the geographic location of the building, the height of the building over ground, the terrain category (considers the density of building and the vegetation) and the shape of the building (determines the size of the pressure coefficients to be used).

For a transparent building envelope made of glass-metal elements with a height of *3.5 m* and a width of *1.5 m*, the resulting wind loads on the glazing are determined, as an example, for the location Vienna according to [ÖNORM EN 1991-1-4] and [ÖNORM B 1991-1-4]. First, the fundamental value of the basic wind velocity $v_{b,0}$ is required. This value represents the characteristic 10 minutes mean wind velocity which occurs once in 50 years, irrespective of wind direction and time of the year, at 10 metres above ground level in open country terrain with low vegetation. For Vienna this value is provided in the national annex with *27.0 m/s*. The basic wind velocity v_b, defined as a function of wind direction and time of the year at 10 metres above ground can be determined by (Eq. 3.4). For both the directional factor c_{dir} and the season factor c_{season} the value *1.0* is recommended for the location Vienna.

$$v_b = c_{dir} \cdot c_{season} \cdot v_{b,0} = 1.0 \cdot 1.0 \cdot 27.0 = 27.0 \text{ m/s} \qquad \text{(Eq. 3.4)}$$

The basic wind velocity pressure q_b can be determined with (Eq. 3.5) by using a value of *1.25 kg/m³* for the density of air ρ_{air} .

$$q_b = \frac{\rho}{2} \cdot v_{b,0}^2 = \frac{1.25}{2} \cdot 27.0^2 = 455.6 \ \frac{\text{kg}}{\text{m} \cdot \text{s}^2} \approx 0.46 \ \frac{\text{kN}}{\text{m}^2} = 0.46 \ \text{kPa} \qquad \text{(Eq. 3.5)}$$

In a next step, the peak velocity pressure q_p needs to be determined in dependence of the exposure factor $C_e(z)$ which considers the terrain category and the height above ground. For a terrain category with a high density of building and a minimum height of the building of *z = 15 m* (category IV), the peak velocity pressure is determined in (Eq. 3.6):

$$q_p = q_b \cdot C_e(z) = q_b \cdot 1.2 \cdot \left(\frac{z}{10}\right)^{0.38} = 0.46 \cdot 1.2 \cdot \left(\frac{15}{10}\right)^{0.38} = 0.64 \ \frac{\text{kN}}{\text{m}^2} = 0.64 \ \text{kPa} \qquad \text{(Eq. 3.6)}$$

The maximum values of wind pressure and wind suction on surfaces of a facade can be determined by multiplying the peak velocity pressure with external and internal pressure coefficients

(c_{pe} and c_{pi}) which take the shape of the building into account. For a closed prismatic structure as the one illustrated in Fig. 3.1 the maximum occurring wind pressure $w_{pressure}$ and wind suction $w_{suction}$ are determined in (Eq. 3.7) and (Eq. 3.8) by considering the unfavourable combination of external and internal pressure coefficients.

$$w_{pressure} = (c_{pe} + c_{pi}) \cdot q_p = (0.80 + 0.30) \cdot 0.64 = 0.70 \ \ kN/m^2 = 0.70 \ \ kPa \qquad \text{(Eq. 3.7)}$$

$$w_{suction} = (c_{pe} + c_{pi}) \cdot q_p = (-1.45 - 0.20) \cdot 0.64 = 1.06 \ \ kN/m^2 = 1.06 \ \ kPa \qquad \text{(Eq. 3.8)}$$

The proposed facade elements are loaded by wind both out-of-plane and in-plane. Similar to facades in general, wind pressure or wind suction is acting out-of-plane on the glazed envelope. Due to the bracing function of the glass-metal elements with composite structural behaviour, they are also loaded in-plane by lateral wind as illustrated in Fig. 3.1, right.

Fig. 3.5 *Maximum wind speed and wind gust during the year 2015 for six different locations based on weather data from [www.wunderground.com]*

To allow a comparison between the wind loads occurring in Vienna and those in other large cities with significant building activity, the wind speed and wind gust distribution during the year 2015 is plotted in Fig. 3.5 for Vienna, London, Moscow, New York, Abu-Dhabi and Hong Kong based on data from [www.wunderground.com]. However, these diagrams only provide a

qualitative comparison. For structural design purposes, the standards valid for each location along with the recommended values for wind velocities and annual probabilities of exceedance have to be used. The different amount of values for the wind gust in the diagrams is due to the available measurement data for the different locations. From the diagrams it can be generally observed that the highest wind speeds during the considered year occurred in Vienna and London, while the lowest values were measured in New York. In general, the wind speeds are measured in areas with low vegetations like airports. For New York, the values plotted in the diagram were measured in Central Park, where a certain shielding is provided by the high surrounding buildings.

3.3.2 Considerations for temperature loads

Depending on the material used for the framing of transparent building envelopes, a different elongation of the profiles and the glass pane due to temperature changes can occur. The resulting movements have either to be allowed by properly designed mechanical connections (for example by slotted holes) or by the flexibility of the chosen load transfer materials. The temperature load is directly influenced by the occurring maximum and minimum temperatures on the exterior surfaces. While the minimum temperature depends mainly on the geographic location, the maximum temperature is additionally influenced by the orientation and the colour of the surfaces.

For example, the elongation difference between the framing made of stainless steel and the glass pane is determined for the previous assumed facade element with a height of *3.5 m* and a width of *1.5 m* for the location Vienna based on [ÖNORM EN 1991-1-5] and [ÖNORM B 1991-1-5]. It is further assumed that both materials are in direct contact with the external environment and are not protected by any insulating layers or sun shading systems. The maximum temperature T_{max} of the external air for a location in Austria (occurs once in 50 years) is determined by (Eq. 3.9) depending on the sea level *h*:

$$T_{max} = 39 - 0.006 \cdot h = 39 - 0.006 \cdot 171 = 38\ °C \qquad \text{(Eq. 3.9)}$$

The minimum temperature of the external air T_{min} which occurs once in 50 years averages for Vienna a value of *-26 °C*. Depending on the properties of the surface a radiation related temperature part has to be added to the maximum temperature of the external air T_{max}. The values to be used for a location in Austria are summarized in Tab. 3.1.

Tab. 3.1 *Radiation related temperature part according to [ÖNORM B 1991-1-5]*

Application field	**Radiation related temperature part [°C]**		
	brightly shining surfaces - T_3	**light-coloured surfaces - T_4**	**dark-coloured surfaces - T_5**
building components facing north-east and nearly horizontal bottom side surfaces of building components	0	2	4
building components facing south-west and nearly horizontal surfaces of building components, which are shined from above	18	30	42

Considering the values determined for T_{max} and T_{min} and the values from Tab. 3.1 the following maximum temperature differences result for surfaces made of glass and stainless steel showing a south-west orientation:

$$\Delta T_{total,\,glass} = 38 - (-26) = 64\ °C \quad \text{(Eq. 3.10)}$$

$$\Delta T_{total,\,frame} = 38 - (-26) + 42 = 106\ °C \quad \text{(Eq. 3.11)}$$

The stainless steel framing is assumed to be a dark-coloured surface, while for the glass surface no radiation related part is considered. This results in the largest elongation difference. However, the resulting maximum elongations and shortenings are not obtained based on the temperature difference between T_{max} and T_{min}, but on the differences between T_{max} and the temperature during assembling for the elongation and between T_{min} and the temperature during assembling for the shortening, respectively. A temperature of *20 °C* is assumed during assembling of the elements for this example. The elongation and shortening caused by changes in temperature are determined with (Eq. 3.12) and depend on the thermal expansion coefficient, the original length and the temperature difference.

$$\Delta l = \alpha_T \cdot l_0 \cdot \Delta T \quad \text{(Eq. 3.12)}$$

In this example the elongation difference between the glass pane and the stainless steel framing along the height of the element is determined. The respective temperature differences for the two materials are given by (Eq. 3.13) and (Eq. 3.14):

$$\Delta T_{e,\,glass} = \Delta T_{max,\,glass} - \Delta T_{assembly} = 38 - 20 = 18\ °C \quad \text{(Eq. 3.13)}$$

$$\Delta T_{e,\,frame} = \Delta T_{max,\,frame} - \Delta T_{assembly} = (38 + 42) - 20 = 60\ °C \quad \text{(Eq. 3.14)}$$

For determining the elongation of the glass pane and the framing along the height of the element it is assumed that the fix point is located in the middle of the height dimension. Therefore, the elongations in the height direction of the elements result to:

$$\Delta l_{e,\,l,\,glass} = \alpha_{T,\,glass} \cdot \frac{l_0}{2} \cdot \Delta T_{e,\,glass} = 9 \cdot 10^{-6} \cdot \frac{3500}{2} \cdot 18 = 0.28\ mm \quad \text{(Eq. 3.15)}$$

$$\Delta l_{e,\,l,\,frame} = \alpha_{T,\,frame} \cdot \frac{l_0}{2} \cdot \Delta T_{e,\,frame} = 16 \cdot 10^{-6} \cdot \frac{3500}{2} \cdot 60 = 1.68\ mm \quad \text{(Eq. 3.16)}$$

The difference in elongation between the glass pane and the stainless steel framing along the height of the element results to:

$$\Delta l = \Delta l_{e,\,l,\,frame} - \Delta l_{e,\,l,\,glass} = 1.68 - 0.28 = 1.40\ mm \quad \text{(Eq. 3.17)}$$

This relative movement between the framing and the glass pane has to be considered when selecting the mechanisms and the materials for load transfer in order to avoid undesired restraint stresses. Nevertheless, the connection between glass panes and framing is often located on the interior side of the facade. Due to the use of insulating glass units or opaque sun shading elements the occurring temperature difference and implicitly the difference in elongation might be significantly lower.

As in the case of the wind loads, a qualitative comparison between the temperatures occurring in Vienna and temperatures in other large cities with significant building activity is provided. For the same cities as in subchapter 3.3.1, the distributions of the highest and the lowest temperatures during the year 2015 are plotted in the diagrams from Fig. 3.6 based on measurement data from [www.wunderground.com]. Also in this case the standards valid for the different locations have to be used for determining design temperatures with a required annual probability of exceedance. For the considered year it can be noted that the highest temperature differences over the whole year were measured in Moscow and New York, while the smallest differences occurred in Hong Kong. The highest overall temperatures were measured in Abu-Dhabi, located in a hot desert climate. As shown in the calculation example, not only the occurring air temperatures are important for structural design on temperature loads, but also the temperature during manufacturing, for instance during application of a structural adhesive.

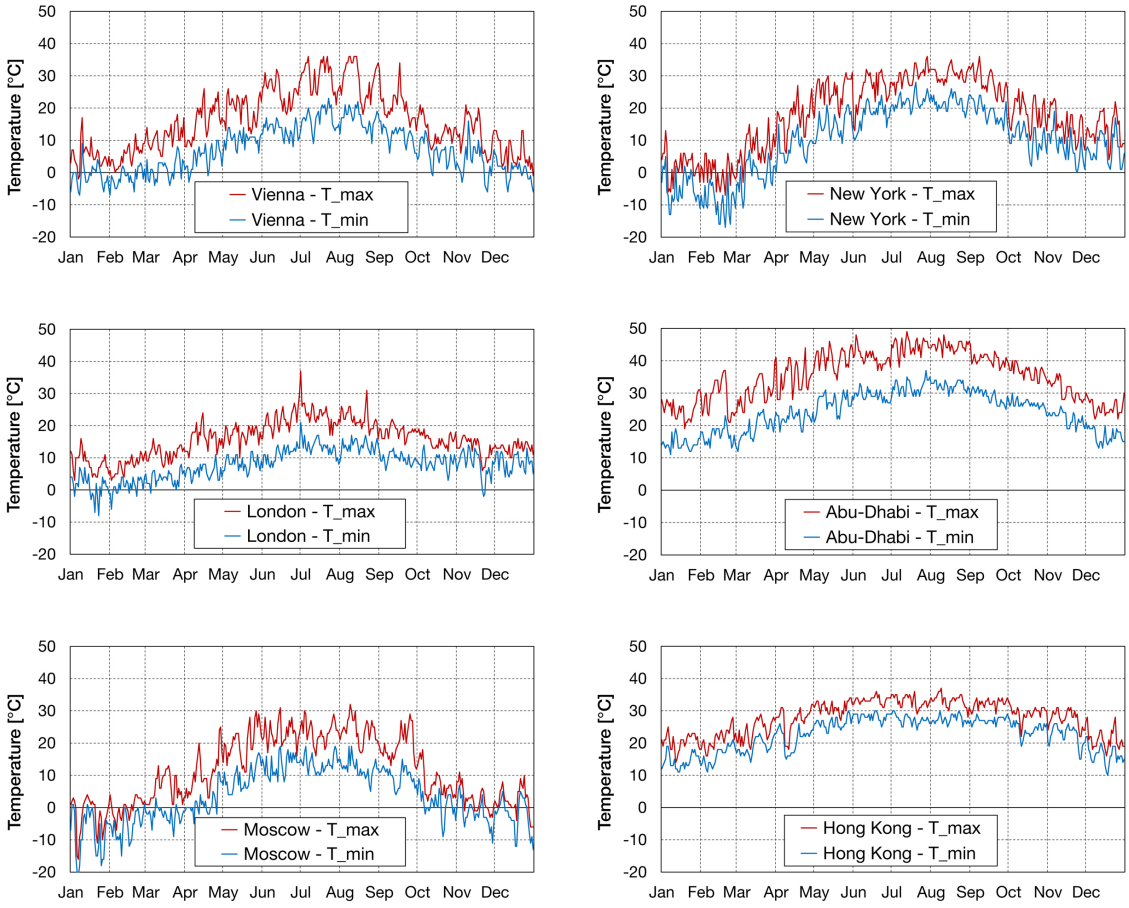

Fig. 3.6 *Maximum and minimum air temperature during the year 2015 for six different locations based on weather data from [www.wunderground.com]*

3.4 Functional requirements for transparent building envelopes

Due to its position between the outside and the inside of a building, a facade has to achieve several functional requirements to ensure comfort standards. There is no difference concerning this aspect when discussing about transparent building envelopes with composite structural behaviour. However, this thesis focuses on glass-metal elements with composite structural behaviour for transparent building envelopes from a mechanical point of view. The scope of the thesis is to investigate the mechanical performance of a structural concept and not to deliver a finished unitised facade product. Nevertheless, some considerations on selected building physics requirements are provided in this subchapter. These aspects will be taken into account in subchapter 8.4, which is intended to be an outlook for further developments towards an application of the structural concept in real facades.

Resistance to weathering

The first requirement a facade, roof or building envelope has to achieve is the resistance to weathering. For both wind and rain protection the weak points, which have to be solved appropriately, are the seals. These elements have to ensure a durable and reliable water and air proof. Important factors for the classification of a building regarding weather tightness are the resistance against wind loads, the water tightness and the air permeability.

The occurring positive or negative wind loads on a building envelope are discussed in subchapter 3.3.1. A facade has to offer a certain protection to the inside of the building for defined wind loads, quantities and durations of rain. Experimental tests can be performed to verify the water tightness of a facade system. Leaks at the joints between frame and glass in glazed facades result in an air permeability of the building envelope. The negative consequences of a high air permeability can be considerable heat losses.

Regarding moisture protection, the building envelope has on the one hand to prevent water from the outside to enter the inside of the building. On the other hand condensation occurring on interior surfaces or inside of envelope components has to be directed to the outside by decreasing the tightness from the inside to the outside. Temporary condensation is allowed on glazed elements, but the contact of the moisture with adjacent sensitive materials has to be avoided.

In the case of a unitised facade system the aspects regarding resistance to weathering have to be considered at two different levels. Firstly, the weather tightness has to be analysed and ensured within a single element. For this, the joint between the framing and the glass pane has to be designed properly. Secondly, the connection between several elements has to achieve an appropriate weather tightness as well. These challenges become more complex when dealing with transparent building envelopes with composite structural behaviour, where the glass panes are activated as in-plane load-bearing elements. Between the components of one element as well as between several elements displacements can occur, to which the sealing materials have to withstand. If the proposed structural system is applied as an exterior second skin, the requirements regarding water and air tightness can be reduced.

Thermal insulation and energetic performance

The thermal comfort in a room depends on the air temperature, the temperature of the surfaces enclosing the room, the humidity and the air quality in the room. On the first two factors the amount of solar radiation into the room has the highest influence and can be regulated by suitable solar shading concepts. Another method to influence the temperature in the room as well as an indispensable aspect to control the humidity and the air quality inside a room is an appropriate ventilation concept.

In terms of thermal insulation winter conditions and summer conditions have to be differentiated, especially for locations with temperate climate. During winter the aims are to reduce the heat loss from the building, to prevent surface condensation by reaching high enough surface temperatures and to reduce the energy consumption used for heating. To achieve these requirements the selected glass, framing and seals are of high importance. During summer the aims are to maintain a comfortable indoor climate by avoiding an overheating through solar radiation and to reduce the energy consumption for cooling. Suitable glass coatings and solar shading systems are methods to achieve these requirements.

The thermal insulation properties of a building envelope component are given by the heat transfer coefficient (*U-value*). For curtain wall facades the U_{cw}*-value* is used, which considers the heat transfer coefficients of the glass (U_g) and of the framing (U_f) as well as length-related heat transfer coefficients ψ_s for the sealing between glazing and framing. The surface proportions of the glazing and framing, the length of the glazing edge perimeter and the heat transfer coefficients of the components are required to determine the U_{cw}*-value* according to (Eq. 3.18):

$$U_{cw} = \frac{\sum(A_g \cdot U_g) + \sum(A_f \cdot U_f) + \sum(\Psi_s \cdot l_s)}{\sum(A_g + A_f)} \qquad \text{(Eq. 3.18)}$$

Since generally there are different requirements regarding the solar energy input through the transparent building envelope during summer and during winter, systems with adjustable permeability of solar energy are recommended. Operable sun protection systems can help to avoid an overheating during the summer season and allow the solar energy to penetrate the facade during the colder winter time. However, when considering the proposed facade system consisting of elements with a filigree framing and a structurally in-plane activated glass pane, there is only little available space for sun protection systems like fixed or movable louvres, roller blinds or interior screens made of foils and textiles. Such systems are only an option when the proposed structural facade system is a second skin or one layer of a closed cavity facade and the sun protection elements are positioned in the resulting cavity or inside the inner layer. When the structural facade system is the only building envelope layer, smart glasses like electronically tintable glass could be an option. With this type of products the solar energy transmittance of the transparent facade (*g-value*) can be adjusted to solar conditions during different seasons as well as for different day times.

The energetic performance of buildings is significantly influenced by the used facade types and is awarded increasing attention in the last years, since the European Parliament released the *Directive 2010/31 EU, Article 9.1*, which requires that starting with 2018 all new public buildings

and by 2020 all new buildings in general will have to supply themselves with the energy required for their operation. In other words, the energy consumption in buildings has to be more efficient and the energy should be provided less by primary sources and more by renewable sources. The renewable energy source which is collectable through the building envelope and can be used passively or actively is the solar energy.

For a passive use the solar energy is stored in the thermal mass of the building elements during solar radiation periods and is then released to heat the room when no radiation is available anymore. Large transparent facades as in the case of the proposed structural building envelope system are advantageous from this point of view. However, during summer the possibility of an overheating of the spaces behind the facade has to be considered. For an active use the solar energy is extracted, transported and stored with the help of additional technical components like photovoltaic modules. In the case of the transparent envelopes consisting of glass-metal-elements with composite structural behaviour the use of building-integrated photovoltaics (BIPV) in some of the elements could be an option. The compatibility of BIPV, as well as of the before mentioned smart glasses, with the structural function of the proposed building envelope system would need to undergo extensive research before implementation.

Ventilation

The replacement of the exhausted air with fresh air is one of the main requirements to ensure a high level of comfort and helps regulating the temperature and the relative humidity of a room. Natural ventilation and mechanical ventilation systems can be generally differentiated (see [Knaack et al., 2007] and [Wurm, 2007]).

The first category is the result of pressure differences caused by wind and temperature between the exterior and the interior of a building or between the top and the bottom of a building. Natural ventilation can be achieved by gap ventilation, window ventilation or shaft ventilation. Due to the advanced development in the field of windows and facades, undesired gap ventilation is no longer problematic. The most common natural ventilation type in residential buildings and also appreciated by office building users is the window ventilation. The performance of this ventilation type depends on the used hardware and fittings as well as on the number of directions from which the ventilation is provided for a room. When larger room depths are required and higher volumes of air need to be exhausted faster, shaft ventilation is a suitable natural option. The location of the shafts is usually in the interior of the buildings, but some double-skin facades also make use of this effect. For a continuous ventilation mechanical systems are incorporated. Centrally controlled ventilation and air-conditioning systems which need large space volumes for supply ducts and exhaust ducts and decentralized systems which are individually adjustable can be differentiated.

Improvements of the building envelopes regarding energy performance as well as different ventilation approaches of the users due to the time spent and the activities done in buildings lead to problems with moisture and mould. Reasons for these problems are continuous emission of humidity, chemical and biological pollution by people and their surrounding inside buildings and the undersized rate of ambient air exchange. This rate should be determined in order to avoid damaging condensation and to minimise the growth of mould. Due to the increasing tightness

of building envelopes and the often missing possibility of an appropriate natural ventilation by the users an increase of mechanical ventilation can be observed especially in the cases of office and public buildings.

For transparent building envelopes using the proposed glass-metal elements with composite structural behaviour a natural ventilation will be difficult to achieve. Since the glass panes have a load-bearing role, the integration of openable elements would need to be considered in the structural design by defining load paths. On the one hand special elements with ventilation flaps could be a possible solution. On the other hand the application range of such structural facade systems is mainly in the field of office and public buildings where mechanical ventilation is a common option.

Noise insulation and acoustic comfort

Glass products for noise control are gaining more and more importance. On the one hand the increasing noises of exterior sources like high traffic roads, rail traffic, airports, construction sites, shopping centres or factories are faced inside buildings. On the other hand noises from inside the building, like discussions in neighbouring rooms, footfall sounds and operating machines affect the acoustic comfort (see also [Knaack et al., 2007]). In addition, recent studies show that due to the raising population density in urban areas, the noise exposure will increase in the next years.

The real acoustic performance of a transparent building envelope firstly depends on the dimensions of the glazing, the used glass assemblies and the gas filling the air cavity. Asymmetrical assemblies and deep cavities of insulating glass units, flexible interlayers for laminated glass or a second skin improve the sound insulation. Secondly, the air-tightness of the elements and especially of the joints between the elements as well as the connection of the glazed elements to the main structure of the building have a significant influence. Sound-decoupling materials should be used in the connections. Finally, a significant factor is the origin of the noises. For instance a second skin reduces the noise from the outside, but it may increase the noise from neighbouring rooms if windows of the inner skin are open.

3.5 Challenges and preliminary concepts

The discussed aspects concerning loads on transparent facades and building physics requirements which these facades have to meet highlight the complexity of the innovative structural concept for building envelopes made of glass-metal elements with composite structural behaviour. This complexity can be illustrated by a list of challenges which have to be solved in order to provide a basis for implementing this concept in real projects. These challenges address different types of aspects, among which the most important ones are concerning the material selection, the structural performance, the functional performance, the production process and the assembling on site. As suggested by the theoretical framework covered in chapter 2, the investigations in this thesis will focus on some of the challenges regarding material selection and structural performance. However, in this subchapter also other challenges will be indicated, which will be considered in the further investigations if possible.

Material selection

- *Glass panes:* since a structural activation for transferring in-plane loads is aimed, laminated glass should be used. The strength and stiffness values of the materials but also the post-breakage structural capacity of the laminated glass should be considered when selecting the glass type and the interlayer.
- *Framing:* on the one hand the mechanical properties are important for the metal selection. On the other hand the material and the surface finishing have to be chosen with regard to corrosion protection and suitability for adhesive bonding if required.
- *Load transfer materials:* for enhancing a composite structural behaviour between the glass pane and the framing, load transfer materials (in this thesis mainly adhesives) with adequate and durable mechanical properties are required.

Structural performance

- *At material level:* the challenges at this level concern mainly new selected load transfer materials for which mechanical values have to be determined and material models have to be derived and for which no experience is available regarding ageing and durability. The material properties for the glass panes as well as for the metal framing are expected to be known.
- *At connection level:* the load transfer materials generally behave different in connections, where they are restrained in certain directions, compared to how they behave as bulk specimens. Especially for adhesives a failure at the interface to unsuitable substrates can be only noticed in connections.
- *At element level:* since the proposed elements have a composite structural behaviour, the interaction between the different components and materials as well as the overall stiffness of the element and the failure modes have to be investigated on an element which includes all components and is subjected to the combined occurring loads. These aspects cannot be simply derived from the properties of the single components.
- *At system level:* after the structural performance and the failure modes of one element are known in detail, the behaviour of several elements together along with their connections to each other has to be investigated.

Functional performance

- *Weather tightness:* the connection between framing and glass panes as well as the connections between several elements have to be sealed with suitable materials in order to obtain a weather resistant facade. The functionality of the sealing has also to be provided during the loading of the structurally active elements.
- *Thermal insulation:* the elements investigated to determine the structural performance, which only require a laminated glass pane, need to be further developed to insulating glass units in order to fulfil thermal requirements. Thermal bridges need to be avoided or at least kept to a reduced level within one element and especially at the connections between elements. Furthermore, the functionality of the spacer and of the secondary sealing has also to be provided during the loading of the structurally active elements.
- *Other requirements:* an assessment of aspects like ventilation, energetic performance, fire protection, sun protection and others in further investigations might be required.

Production process

- *Components:* it should be aimed to use already existing products for all components or at least existing production processes.
- *Elements:* the production of the elements needs a high degree of planning in the prototype phase, since no existing line production is able to combine the different components as required. Inaccuracies need to be minimized and working times of certain materials like adhesives have to be considered. In a further step an automation of the production process or at least part of it should be possible.

Assembling on site

- *Tolerances:* the glass-metal elements with composite structural behaviour show certain production tolerances which have to be considered for the connections between elements. At the same time these connections have to be able to transfer the occurring loads between the elements.
- *Construction sequence:* since the proposed building envelope system has a load-bearing role, its structural performance during construction has to be considered for assembly. Eventually, additional supports during construction are required in order to provide stability to the unfinished facade.

By analysing the different challenges, it can be noticed that two main tasks have to be solved for the transparent building envelopes composed of glass-metal elements with composite structural behaviour. The first one, addressed at a conceptual level in subchapter 3.5.1, concerns the connection between framing and glass pane in order to achieve a composite structural behaviour. The second one concerns the connection between several elements and is approached with preliminary concepts in subchapter 3.5.2. Most of the investigations discussed in the further chapters of this thesis deal with the first task and focus on the structural performance. However, the other challenging aspects are accounted for in the adopted decisions. Furthermore, a basic concept for the connection between elements is required for the constructive detailing of one element and the definition of the load application on this element.

3.5.1 Load transfer within one element

To achieve a composite structural behaviour between the framing and the glass pane of the elements solutions with adhesive bonding are looked for in this thesis. The concepts introduced in this subchapter define the possible geometry of the adhesive joint and the loads which the adhesive has to transfer. A selection of material types and material products will be conducted in chapter 4. The cross section geometries of the framing are represented schematically and need to be defined with respect to structural calculations and constructive detailing of the connections between elements in further steps.

The first idea is to use only a perimetrical adhesive bonding between the framing and the glass pane as already investigated by [Wellershoff, 2006] and [Huveners, 2009]. However, in their cases the framing is designed to be a rigid out-of-plane support for the glass pane, while in this case the filigree framing shows a certain flexibility out-of-plane. The first three concepts illustrated in Fig. 3.7 show possible cross section geometries of the adhesive joint. In the case of the rectangular and the L-shaped cross sections, the adhesive joint has to transfer both in-plane and out-of-plane loads between the glass pane and the framing. For the U-shaped joint, a clamping can be assumed for out-of-plane loads and only in-plane loads need to be transferred by the adhesive. In all three cases the glass pane is activated as a shear panel and the size of the shear load which can be transferred by the adhesive depends on the bonding surface. The largest surface is provided by the U-shaped joint, but the concept with this cross section is difficult to be further developed to insulating glass units.

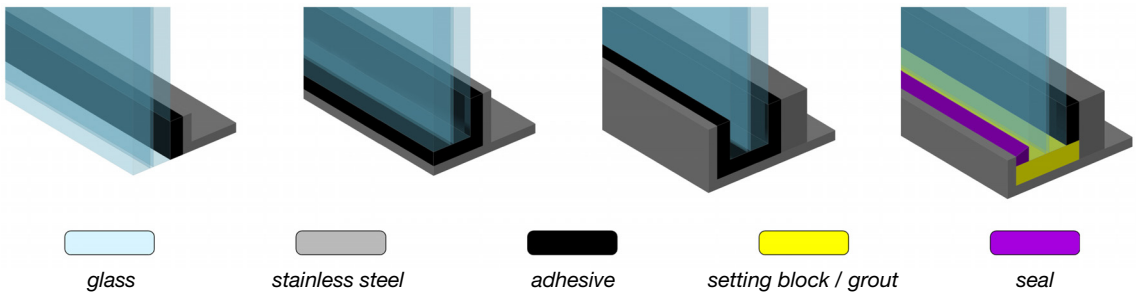

Fig. 3.7 *Simplified models for the load transfer between framing and a laminated glass pane by perimetrical adhesive bonding with different cross section geometry (first three from left) as well as by combined perimetrical adhesive bonding and setting blocks at the glass edge near the corners (right)*

For transferring in-plane loads between the framing and the glass pane by perimetrical adhesive bonding, adhesives with high shear strength and stiffness like acrylics or epoxies are required. These materials are not approved for structural applications in facades due to their sensitivity to moisture or high temperatures and generally require reduced joint thicknesses which are critical for the adjustment of different temperature elongations. Therefore, a concept with a perimetrical adhesive joint which only has to transfer the out-of-plane loads between framing and glass pane is also introduced (see Fig. 3.7, right). For the transfer of the in-plane loads additional setting blocks or grouting blocks are positioned between framing and glass pane near the corners of the glass pane (eight blocks per element as illustrated in Fig. 2.13, left). In this way the glass pane is activated as a bracing under compression by the setting blocks and for the adhesive

joint, which only has to connect the glass pane to the framing out-of-plane, structural silicones can be used.

The concepts illustrated in Fig. 3.7 include only a laminated assembly for the glass pane. For the experimental investigations discussed in the next chapters this type of glass pane, or even a monolithic one to avoid non-measurable influences from the interlayer material, will be used. However, the further development to insulating glass units of these concepts is taken into account and is illustrated in Fig. 3.8. The concepts using only a perimetrical adhesive bonding with rectangular or L-shaped cross section as well as the concept with rectangular adhesive bonding and additional setting blocks can also be used for insulating glass units. Only the inner glass layer of the IGU is activated structurally for in-plane loads.

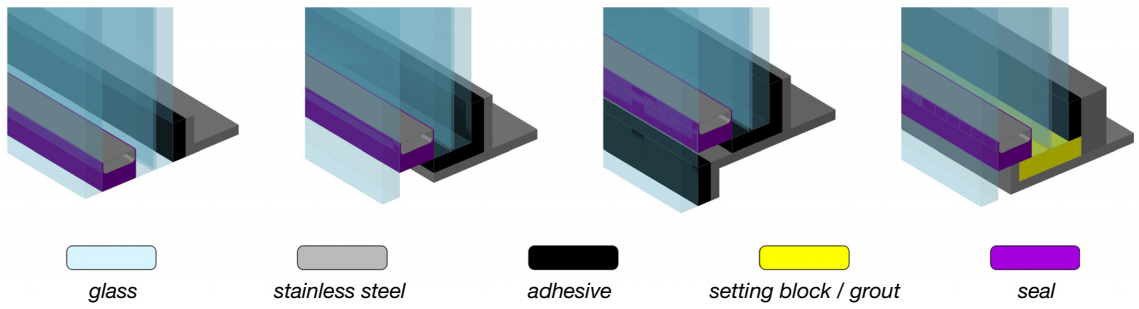

Fig. 3.8 *Simplified models for the load transfer between framing and an insulating glazing by perimetrical adhesive bonding with different cross section geometry (first three from left) as well as by combined perimetrical adhesive bonding and setting blocks at the glass edge near the corners (right)*

The concept with U-shaped perimetrical adhesive bonding can only be used in a modified way for insulating glass units. The U-shaped joint is divided into an L-shaped joint between the inner glass pane and the framing and a shifted rectangular joint between the outer glass pane and the framing. In this way both glass panes would be structurally activated in-plane, but thermal bridges and larger profile widths are difficult to avoid.

3.5.2 Load transfer between several elements

In the case of unitised facade systems the primary challenges for the connections between the elements are the weather tightness and the avoidance of thermal bridges. For the glass-metal elements with composite structural behaviour, additionally, the occurring loads have to be transferred by the connections from one element to the next one without neglecting the before mentioned requirements. Considering the introduced load transfer concepts within one element, two different concepts for the transfer between elements are proposed from a structural point of view.

For the elements with a connection between framing and glass pane only by perimetrical adhesive bonding, the glass pane is activated as a shear panel with a load transfer along the whole perimeter. Therefore, a connection between the elements along the whole perimeter of the framing would be conclusive. The sketch in Fig. 3.9, left, illustrates a concept with bearing-type shear connections between the framing of neighbouring elements. One disadvantage of this

concept is the excentricity of the screws related to the position of the adhesive joints between framing and glass panes. The weather tightness of the connections could be solved similar to standard unitised elements by shaping the framing profiles accordingly. In the case of insulating glass units the exterior glass layer would slightly overlap the structural connection and the remaining gap would be filled with a silicone sealant.

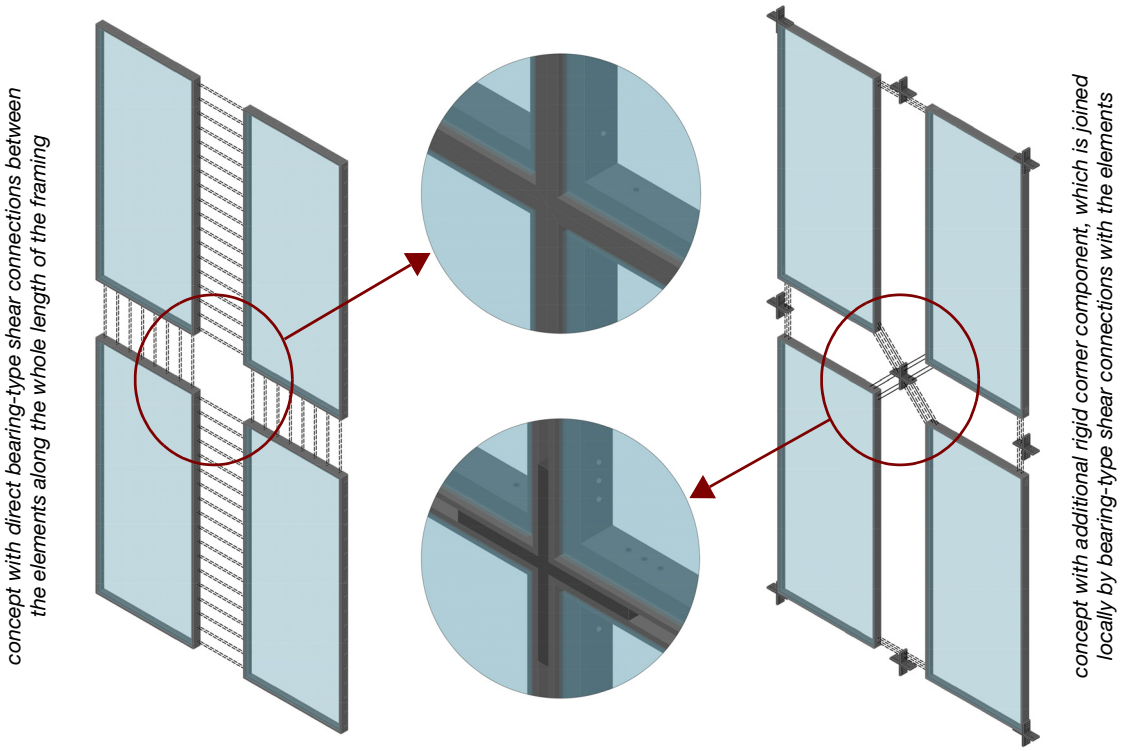

Fig. 3.9 *Concepts for the connection and the load transfer between several glass-metal elements with composite structural behaviour*

In the case of the concept with additional setting blocks for a more concentrated transfer of the in-plane loads between framing and glass pane the same idea is followed for the connection between the elements. An additional component in the form of a metal cross is introduced between the corners of neighbouring elements. This component is connected with bolts to the framing profiles and determines the rotation stiffness in the corners. Also in the case of this concept there is an excentricity between the screws and the setting blocks. The weather tightness on the inside could be solved with sealing clamping strips between the framing profiles; the depth of the cross elements would need to be slightly smaller than the depth of the framing profiles.

Both concepts need to be further improved in order to fulfil the functional requirements to a transparent building envelope. Another important aspect valid for both concepts are the low tolerances they allow for. Resulting gaps and solutions with filler plates lead to a suboptimal transfer of the occurring loads.

3.6 Conclusions and delimitations for further investigations

Glass-metal elements with composite structural behaviour show a promising potential for transparent building envelopes with regard to efficient material use and optimised structural performance. However, the aspects covered in the previous subchapters highlight the complexity of such systems. On the one hand the load transfer in-plane and out-of-plane has to be solved both at element level and at system level. On the other hand functional requirements typical for facades, especially the weather tightness and in most cases thermal insulation, have to be fulfilled. All these challenges cannot be solved at once, but their interdependencies need to be considered when addressing them isolated.

The investigations in this thesis focus mainly on the load-transfer of in-plane and out-of-plane loads at element level. In order to achieve a composite structural behaviour between the framing and the glass pane of one element, adhesive bonding is considered to be the most suitable load transfer mechanism. Therefore, the investigations at material and connection level performed within this thesis (chapters 4 and 5) deal with the performance of different adhesives. However, the present work and the obtained results are limited to room ambient boundary conditions and short-term loading. The performance of the adhesives under extreme conditions as well as the ageing behaviour under the influence of parameters like moisture or UV-radiation is left for future research.

The structural performance of one glass-metal element with composite structural behaviour cannot be optimally determined by just summing up the knowledge on the performance of the single components. Therefore, the structural behaviour of one element including all relevant components is analysed experimentally and numerically considering the previous findings at material and connection level as well as available related state-of-the-art knowledge. For the properties of materials used for setting blocks and grouting blocks in the experimental and finite element investigations at element level, results published in [Ebert, 2014] and [Kolany, 2018] are referred to.

The load-transfer of in-plane and out-of-plane loads at system level as well as extensions with regard to building physics requirements are addressed in chapter 8. However, only basic studies are carried out and general concepts are elaborated, since a more exact examination is beyond the scope of this thesis and is only considered productive for precise boundary conditions as in the case of a real project.

4 Investigations on adhesives and their adhesion to metal substrates

Properties of the selected adhesives
Uniaxial tensile tests on dumbbell specimens
Material models for finite element simulations
Adhesion to metal substrates with different surface finishing

1 Introduction 1

2 State of the art – theoretical framework

3 Transparent building envelopes with composite structural behaviour

4 Investigations on adhesives and their adhesion to metal substrates

5 Mechanical behaviour of adhesive joints between glass and stainless steel

6 Experimental investigations on large-scale multi-component elements

7 Finite element investigations on large-scale multi-component elements

8 Approaches for structural and functional design 8

9 Conclusions and future research 9

4.1 Properties of the selected adhesives

Within this research work adhesive bonding is aimed to be used for achieving a composite structural behaviour between the glass pane and the metal framing of a facade element. Since it is a structural application of linear adhesive joints within the building envelope, the requirements valid for structural sealant glazing systems and already listed in subchapter 2.2.3 are important criteria for the adhesive selection. On the one hand a sufficient strength for transferring the occurring loads as well as a sufficient elasticity to avoid indirect stresses in the glass from temperature loads have to be provided. On the other hand the durable performance, including reduced tendency to creep, resistance against moisture, cleaning agents and UV-radiation as well as a service temperature range between *-20 °C* and *+80 °C*, has to be ensured. From the adhesives available on the market only a few structural silicones fulfil these requirements. However, for achieving a composite structural behaviour adhesives with a higher shear strength are required.

After narrowing the spectrum of adhesives to be taken into consideration based on these criteria as well as based on results from past research projects on adhesive connections between glass and metal substrates (see subchapter 2.2.3), discussions with adhesive producers as well as with facade designers are conducted. The objectives of this consulting is on the one hand to see which adhesives the producers would recommend for the aimed application. On the other hand the opinion of the facade designers is of interest in order to determine if they are open to consider adhesives without a current approval for novel structural applications in facades.

An investigation procedure with several steps for the selected adhesives is established with the objectives to gather relevant material data on their mechanical properties, to derive suitable material models with limited complexity for finite element simulations and to validate these models for different joint geometries and loading types. The investigation procedure includes the following steps:

- selection of adhesives based on the before mentioned criteria;
- gathering of material properties from technical data sheets, producers and publications;
- experimental testing on bulk material specimens to add required data;
- selection of suitable existing material models and determination of the required parameters;
- experimental testing to determine the adhesion behaviour to relevant substrates;
- experimental testing on adhesive connections with different joint geometries.

The listed criteria show some contradictions which make the selection process a difficult task. None of the adhesives available on the market can satisfy all requirements. Therefore, priorities are defined and recommendations from leading producers in this field are considered. Three adhesives are selected to be investigated for the use in glass-metal elements with composite structural behaviour. Two of them are two-component silicones (*Dow Corning 993* and *Sikasil SG-550*), which show the advantage to be approved for the use in structural sealant glazing systems. They are suitable for transferring loads out-of-plane, but, because of their low strength and stiffness, they are not appropriate for transferring in-plane loads to the required extent. In

the case of these adhesives a combination with setting blocks or resin-based injection grout for transferring the in-plane loads is aimed in the element design.

The third adhesive is a two-component acrylic (*SikaFast-5221 NT*). This material is not approved for the use in structural applications with glass according to [ETAG 002, 2001]. Existing research results as well as its higher strength and stiffness recommend the adhesive as appropriate for transferring in-plane loads by shear. The possibility to design glass-metal elements with composite structural behaviour with only adhesive joints for both out-of-plane and in-plane loads is investigated for this material.

The main properties mentioned in the technical data sheets of the three materials are summed up in Tab. 4.1. Further information on the adhesives as well as existing findings from past research projects are summarized in the next paragraphs.

Tab. 4.1 *Significant properties and information on the adhesives planned to be used for experimental investigations [Dow Corning 993, 2014], [Sikasil SG-550, 2016], [SikaFast-5221 NT, 2013]*

Property	**Dow Corning 993**	**Sikasil SG-550**	**SikaFast-5221 NT**
type	2-component silicone	2-component silicone	2-component acrylic
colour	black/white/grey	black	grey
curing mechanism	polycondensation	polycondensation	radical polymerisation
density	1.30 kg/l	1.30 kg/l	1.19 kg/l
consistency	non-slump paste	paste	thixotropic paste
application temperature	10-35 °C	5-40 °C	5-40 °C
working / snap / open time	~ 10 to 30 min	~ 30 min	~ 10 min
tack-free time / fixture time	~ 80 to 100 min	~ 150 min	~ 25 min
tensile strength	~ 0.95 MPa [a]	~ 3.4 MPa [c]	~ 10.0 MPa [c]
elongation at break	~ 130% [a]	~ 300% [c]	~ 200% [c]
Young's modulus	~ 2.4 MPa [b]	~ 2.6 MPa [d]	~ 250 MPa [c]
service temperature	-50 °C to +150 °C	-40 °C to +150 °C	-40 °C to +80 °C
availability	drum/pail and cartridge	drum/pail	cartridge and pail
shelf life	14 months	12 months	9 months

[a] Values are determined according to [ISO 8339, 2005]

[b] Value used in [Mocibob, 2008]; no value is provided in the product data sheet

[c] Values are determined according to [ISO 37, 2011]

[d] Value is recommended by the adhesive manufacturer based on internal investigations

Dow Corning 993

This two-component structural silicone rubber meets the requirements from [ETAG 002, 2001] and is one of the most often used sealants for structural glazing systems. According to [Dow Corning 993, 2014] it provides a good adhesion to anodised or polyester paint coated aluminium and stainless steel as well as to coated, enamelled and reflective glass substrates. Further-

more, it shows a high resistance to weathering, UV-radiation and humidity as well as a good compatibility to the most commonly used glazing components, like weatherproofing sealants, insulating glass sealants and interlayer materials. However, testing to ensure the adhesion and the compatibility are recommended when selecting components for a project.

For a proper mixing and dispensing the use of a two-component silicone dispensing machine with an airless mixing system is advised. In the case when only small material quantities are required, special two-part hand mixed cartridge systems are available. However, these systems should be used with caution, since the risk of an air incorporation into the material and a resulting reduction of the properties is given. The curing takes place at room temperature by releasing a small amount of alcohol. Basic recommendations for cleaning, priming and tooling are provided in the product data sheet.

In subchapter 2.2.3 some references to research projects focusing on this adhesive are provided. The mechanical behaviour of the material shows several typical characteristics of elastomers, which can be generally described by hyperelastic models. Linear-elastic models, as they are currently used in practice, lead either to underestimating the stresses for the initial strain range or to overestimating the stresses after this range. However, [Dias, 2013] shows that also the simpler hyperelastic models like *Neo-Hooke* and *Mooney-Rivlin* are not able to represent the material behaviour well over the whole strain range for different loading types (tension, shear). He proposes a new isochoric strain energy formulation based on five material constants, which then is implemented as a user subroutine in the finite element software *Abaqus*. While this approach is of significant value from a scientific point of view, it is in most cases not feasible for practical applications.

Sikasil SG-550

This structural silicone adhesive is a similar product to *Dow Corning 993*, meeting as well the requirements from [ETAG 002, 2001], and is recommended for applications where silicones with higher strength are required. Since it is a rather new product, there is less experience available on adhesion to different substrates and compatibility issues to other glazing components. According to [Sikasil SG-550, 2016] the technical department of the producer should be consulted regarding these aspects before using this adhesive. The recommended mixing procedure and the curing mechanism are the same as in the case of *Dow Corning 993*. However, for this product there is no possibility of hand mixed cartridge systems available due to the higher viscosity of the material.

Unlike for *Dow Corning 993*, only few published research results are available for this silicone [Nardini & Doebbel, 2015]. The reason for this is that *Sikasil SG-550* is a rather new product, which has only been used in isolated projects until now (see for example [Doebbel et al., 2014]). However, the silicone adhesive from which it is developed, *Sikasil SG-500*, is often included in research projects dealing with the selection of suitable adhesives for certain applications (see for example [Belis et al., 2011a] and [Nicklisch et al., 2014]). Furthermore, the material properties of *Sikasil SG-500* are investigated in [Van Lancker et al., 2016] with regard to linear glass-metal connections.

SikaFast-5221 NT

This two-component structural acrylic is a fast curing, flexibilised adhesive system based on the Acrylic Double Performance (ADP) polymer technology developed by Sika. This technology allows to obtain acrylic adhesives with rapid strength development, high flexibility and good adhesion properties to different substrates. According to [SikaFast-5221 NT, 2013], a cohesive failure is obtained in joints between substrates made of stainless steel or aluminium under shear loading, while for glass substrates also adhesive failure can occur. Also a lower shear strength is indicated for joints with glass substrates compared to joints with metal substrates. In order to obtain the best adhesion performance a pretreatment of the substrate surfaces with an activating agent (see [Sika ADPrep, 2013]) is recommended. The open and fixture time can be increased by lower temperatures and can be also influenced by variation of the mixing ratio. Furthermore, there are different *SikaFast* products available (*SikaFast-5211 NT*, *SikaFast-5215 NT* and *SikaFast-5221 NT*), which differ only in open (from 3 minutes to 10 minutes) and fixture time (from 9 minutes to 25 minutes), while showing the same structural properties.

For application, the two components are mixed with a static mixer and can be applied both manually with a cartridge gun from dual cartridges or by pump and robot in production lines. The thickness of the joints should measure at least *0.5 mm* and should not exceed *3.0 mm*, to avoid an excessive temperature increase due to the exothermic reaction during curing. Even though a service temperature range between *-40 °C* and *+80 °C* is indicated in the product data sheet, a decrease of the strength and stiffness properties occurs with increased temperatures according to the producer. Typical applications of this product are in the automotive industry, for advertising signs and traffic guidance systems, household appliances, electronics, furniture or windows.

SikaFast products have been already used in past research projects on structural glass applications. In [Wellershoff, 2006] a predecessor of the product (*SikasFast-5211*) is investigated for activating glass panes as shear panels. Results from double-lap-shear tests with glass and steel substrates performed at different temperatures show in the case of the acrylic a significant decrease in strength and stiffness between *20 °C* and *40 °C*. Furthermore, partially adhesive failure is noticed both on glass and steel surfaces with the observation that this could be avoided by controlled laboratory conditions. Even though this adhesive is considered as not suitable for structural applications in facades, it is included in the large-scale testing programme from [Wellershoff, 2006] (see description in subchapter 2.3.4). For finite element simulations with this adhesive, a multi-linear model is used based on an initial Young‘s modulus and further pairs of true stress and true plastic strain. The same product (*SikaFast-5211*) is used by [Netusil, 2011] for connecting steel flanges to glass panes in order to obtain hybrid beams. A decrease of strength and stiffness with increasing thickness of the joint is noticed for the acrylic in steel-glass connections tested under shear loading. For finite element simulations a similar multi-linear model as proposed in [Wellershoff, 2006] is used.

4.2 Uniaxial tensile tests on dumbbell specimens

To represent the behaviour of adhesive materials in specific joints or in more complex systems, like the glass-metal facade elements with composite structural behaviour, suitable material models are necessary. Usually such models require large data sets resulting from extensive experimental tests. First, mechanical tests under different loadings (tension, compression and shear) have to be performed at standardized ambient conditions (*23 °C* and *50%* relative humidity) to determine the strength and the stiffness of the material for these load scenarios. Afterwards, the influence on these properties due to several factors like loading speed, test specimen geometry, load cycles, temperature as well as the long-term behaviour in form of creeping and relaxation should be investigated.

Since this research work aims to study the potential of glass-metal facade elements with composite structural behaviour and not to deliver a complete material model of the selected adhesives, only uniaxial tensile tests at room ambient conditions are performed at material level. The reason for these tests is to provide an own data set to verify existing material models as well as to determine the required parameters for selected material models implemented in finite element software. Additional necessary investigations on the adhesives are specified as an outlook for future research.

4.2.1 Specimens and procedure for the uniaxial tensile tests

The most common experimental test to determine material properties of adhesives is the uniaxial tensile test performed on dumbbell specimens. Two series of tests are completed for the selected adhesives. All the tests are performed at *~23 °C* and *~50%* relative humidity. The used materials, the number of specimens and the investigated loading speeds as well as the facilities where the specimens are manufactured and the tests are performed are given in Tab. 4.2.

Tab. 4.2 *Performed test series for the selected adhesives under uniaxial tension*

Series	Adhesive	Loading speed	Number of specimens	Manufacturing facility	Testing facility
1	Dow Corning 993	5 mm/min	4	Dow Corning	Graz University of Technology
	Sikasil SG-550	5 mm/min	4	Sika Services AG	
	SikaFast-5211 NT	5 mm/min	4	Sika Services AG	
2	Sikasil SG-550	5 mm/min	5	Sika Services AG	Sika Technology AG polymer testing lab
		200 mm/min	5		
	SikaFast-5221 NT	5 mm/min	5		
		1 mm/min	5		
		10 mm/min	5		
		100 mm/min	5		

In the second series only the silicone and the acrylic from *Sika* are further investigated, since for the silicone *Dow Corning 993* the results form the first series along with data obtained from literature are sufficient. Furthermore it can be observed, that the acrylic *SikaFast-5211 NT* is replaced with *SikaFast-5221 NT* due to the longer required open time. Different standards which

propose different specimen geometries are available for uniaxial tensile tests. For the two-component silicone *Dow Corning 993* the uniaxial tests are performed on test specimens of type C according to [ASTM D412, 2013]. The geometry of the tested dumbbells is shown in Fig. 4.1. For the two-component silicone *Sikasil SG-550* and for the two-component acrylics *SikaFast-5211 NT* and *SikaFast-5221 NT* dumbbells of type 2 according to [ISO 37, 2011], respectively [DIN 53504, 2009], are used. The geometry of these dumbbells is shown in Fig. 4.2.

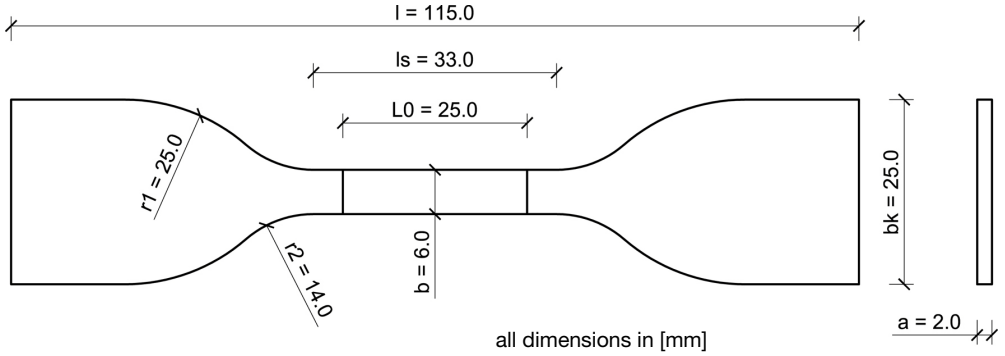

Fig. 4.1 *Geometry for dumbbells of type C according to [ASTM D412, 2013] used for the adhesive Dow Corning 993*

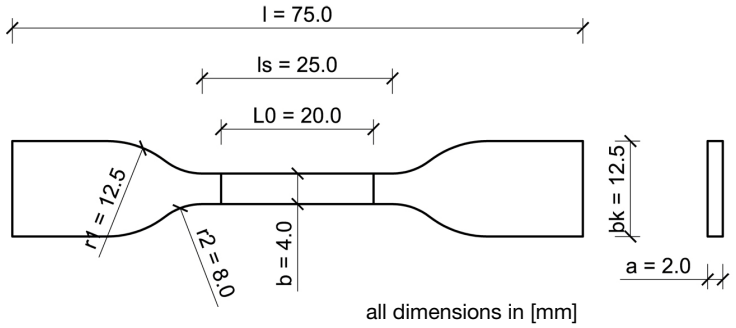

Fig. 4.2 *Geometry for dumbbells of type 2 according to [ISO 37, 2011], respectively [DIN 53504, 2009], used for the adhesives Sikasil SG-550 and SikaFast-5221 NT*

Before testing, the thickness and the width of the specimens in the narrow area are determined. The measured values can be found in [Appendix A]. The measurement of the dimensions is performed with a dial gauge. The tolerances according to the specified standards for the specimens are *±0.2 mm* for the thickness and *±0.1 mm* for the width. Some of the measured values are situated outside these ranges.

All the uniaxial tests of the first series are performed displacement controlled with a loading speed of *5 mm/min*. A *Shimadzu* testing machine with a *100 kN* load cell is used. The deformation is measured with a video-extensometer in the narrow section of the dumbbells where a constant stress state is expected to occur. The limits of the defined measurement length L_0 are marked with a coloured line to obtain a strong contrast. The load and the distance between the two marks are measured during the test. For the second series the tests are performed displacement controlled on a *Zwick/Roell* testing machine for loads up to *2.5 kN*. Beside a speed

of *5 mm/min* also the influence of higher loading speeds is investigated, especially for the acrylic. The deformations are measured with a touching extensometer with soft callipers for the silicone and sharp callipers for the acrylic.

4.2.2 Uniaxial tensile test results for Dow Corning 993

Four test specimens of type C according to [ASTM D412, 2013] are tested for the adhesive *Dow Corning 993* in the first series at material level under uniaxial tensile load with a speed of *5 mm/min*. The elastic material behaviour is indicated by the complete return of the specimen to the initial length after failure (compare the left and the right picture in Fig. 4.3).

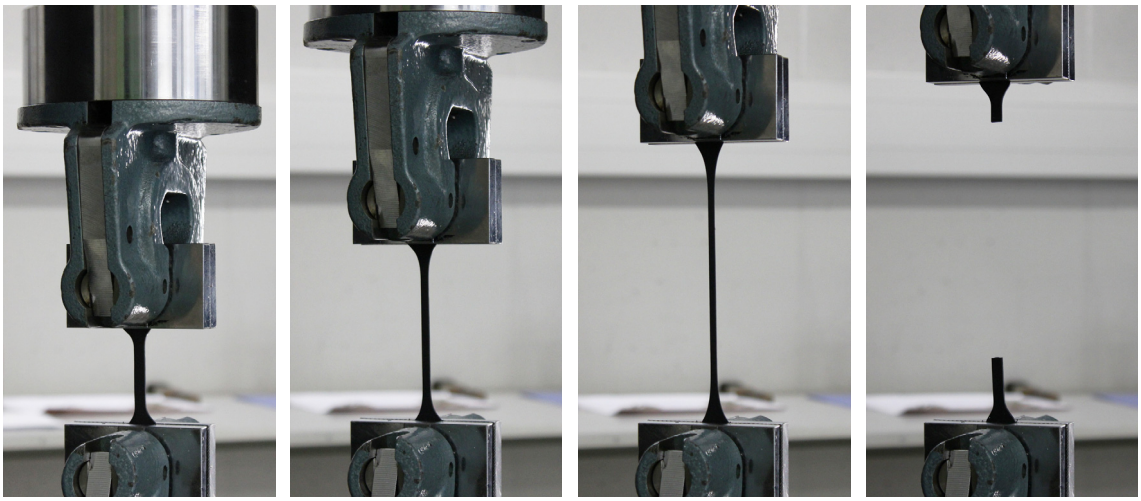

Fig. 4.3 *Test specimen of the adhesive Dow Corning 993 in different stages during the uniaxial tensile test*

The relationships between the engineering stresses and the engineering strains for the four specimens of *Dow Corning 993 (DC 993)* are illustrated in Fig. 4.4, left. The maximum engineering stress varies between *2.03 MPa* and *2.43 MPa*, while the maximum engineering strain reaches values between *198%* and *246%*. Further results in table form can be found in [Appendix A]. Fig. 4.4, right, shows the relationships between true stresses and true strains for the four specimens. While the engineering stresses are calculated in relation to the initial cross section of the specimen, the calculation of true stresses considers the reduction of the cross section during the lengthening of the specimen. The true stresses σ_{tru} and the true strains ε_{tru} can be calculated with (Eq. 4.1) and (Eq. 4.2), respectively, assuming that the material behaves similar in both directions perpendicular to the direction of the tensile load and that no local necking effects are occurring:

$$\sigma_{tru} = \sigma_{eng} \cdot (1 + \varepsilon_{eng})^{2 \cdot \nu} \qquad \text{(Eq. 4.1)}$$

$$\varepsilon_{tru} = \ln(1 + \varepsilon_{eng}) \qquad \text{(Eq. 4.2)}$$

The Poisson‘s ratio ν is assumed to be *0.50* for the silicone *Dow Corning 993*, since it is an elastomer, materials which are almost incompressible. Furthermore, since no measurement of the transverse strain was possible during the performed uniaxial tensile tests, the value of the Pois-

son's ratio is assumed to remain constant over the whole strain range for all adhesives investigated in this thesis. The engineering stress σ_{eng} is calculated by dividing the force F by the initial cross section A_0. The engineering strain ε_{eng} is the difference in length of the defined measurement span.

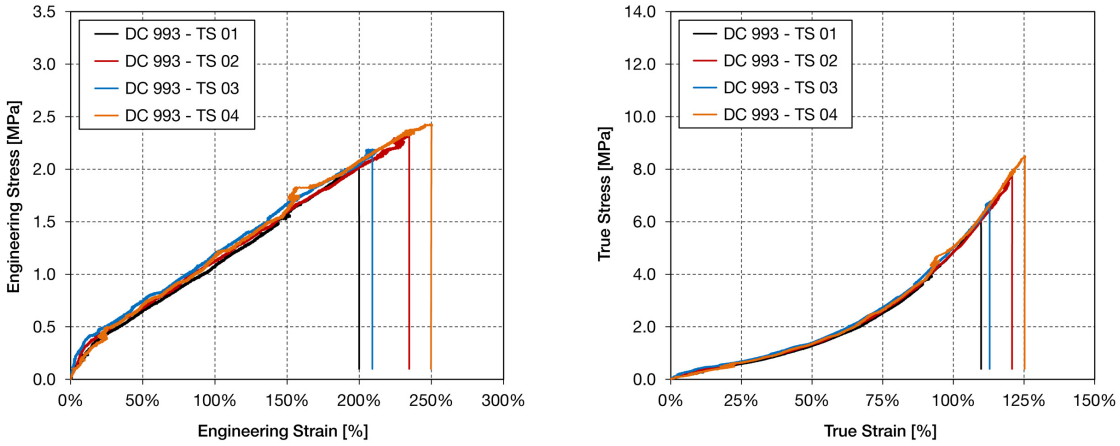

Fig. 4.4 *Relationship between engineering stresses and engineering strains (left) and between true stresses and true strains (right) for the four specimens of Dow Corning 993*

By comparing the curves for the four test specimens a good agreement can be observed for the stiffness of the material, while the maximum stresses and strains vary. The noise which is present in the plotted curves results from the elongation of the specimens during loading in the area of the measurement marks as well as from the rather large measurement range of the used load cell for the occurring load magnitude.

4.2.3 Uniaxial tensile test results for Sikasil SG-550

For the adhesive *Sikasil SG-550 (SS SG-550)* four test specimens of type 2 according to [ISO 37, 2011] are tested in the first series at material level under uniaxial tensile load with a speed of *5 mm/min*. In the second series ten additional test specimens of the same type are tested, five with *5 mm/min* and the other five with *200 mm/min*. Similar to the specimens of *Dow Corning 993*, the elastic material behaviour can be observed by the complete return of the specimen to the initial length after failure (see specimen from the second series in Fig. 4.5).

The relationships between the engineering stresses and the engineering strains for the specimens of *Sikasil SG-550* tested with a loading speed of *5 mm/min* are illustrated in Fig. 4.6, left. The curves from the first series are all plotted in grey, those from the second series in colour. The maximum engineering stress varies between *2.75 MPa* and *2.96 MPa* for series one and between *2.67 MPa* and *2.91 MPa* for series two. The maximum engineering strain reaches values between *228%* and *270%* for tests in the first series and between *261%* and *282%* for the tests in the second series. Results in tabular form for each test specimen as well as mean values, including Young's moduli for strains up to *5%* and *50%*, can be found in [Appendix A].

Fig. 4.6, right, shows the relationships between true stresses and true strains for the same specimens. The true stresses and the true strains are calculated in the same way as explained for the

adhesive *Dow Corning 993*. A Poisson's ratio of *0.50*, which is assumed to remain constant over the whole strain range, is considered.

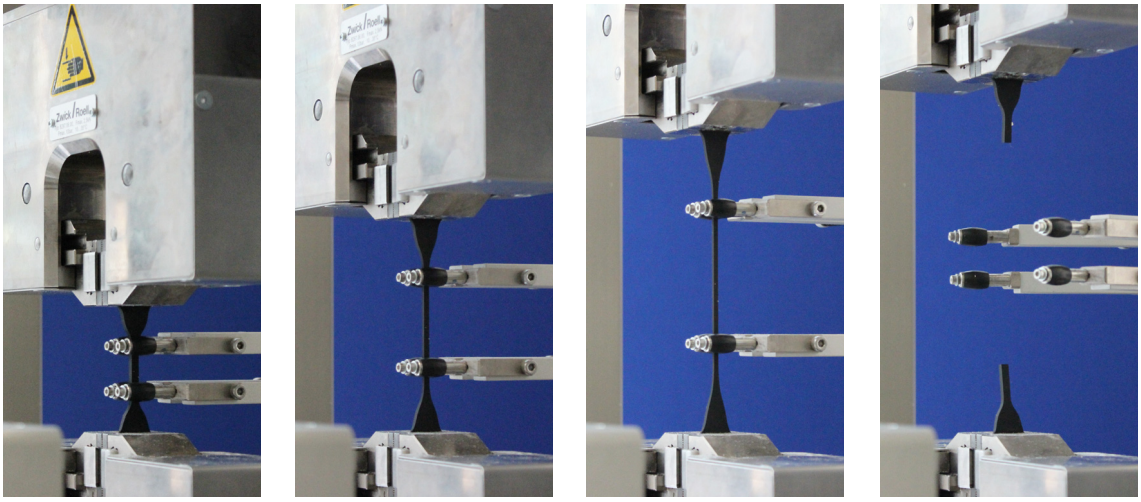

Fig. 4.5 *Test specimen of the adhesive Sikasil SG-550 in different stages during the uniaxial tensile test*

By comparing the curves it can be concluded that the material shows a similar variation as the silicone *Dow Corning 993*, but it reaches higher stresses and strains. The results for the specimens of the first test series show a stronger noise due to the rather unsuitable used load cell for the applied forces. For one test specimen from the first series lower stresses between *0%* and *50%* strain can be observed. An explanation for this could be an unwanted preload of the specimen, indicating the presence of a Mullins effect, which is typical for elastomers.

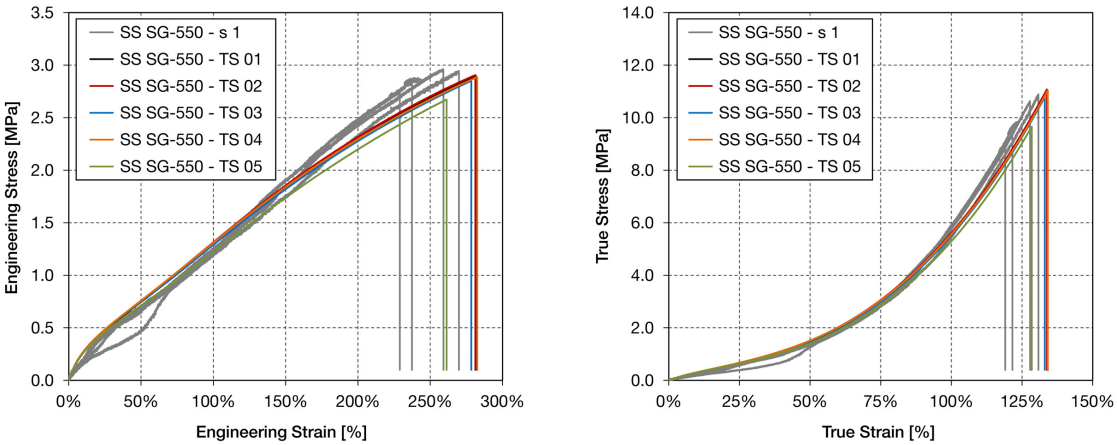

Fig. 4.6 *Relationship between engineering stresses and engineering strains (left) and between true stresses and true strains (right) for the specimens of Sikasil SG-550 tested with a loading speed of 5 mm/min*

In Fig. 4.7 the relationships between engineering stresses and engineering strains (left) as well as between true stresses and true strains (right) are plotted for the specimens tested in the second series with loading speeds of *5 mm/min* and *200 mm/min*. A small dependency of the

material stiffness as well as of the strength on the loading speed or on the strain rate can be observed. Considering the high difference of the used loading speeds compared to the small variation of the curves, this effect can be neglected for this material in most applications.

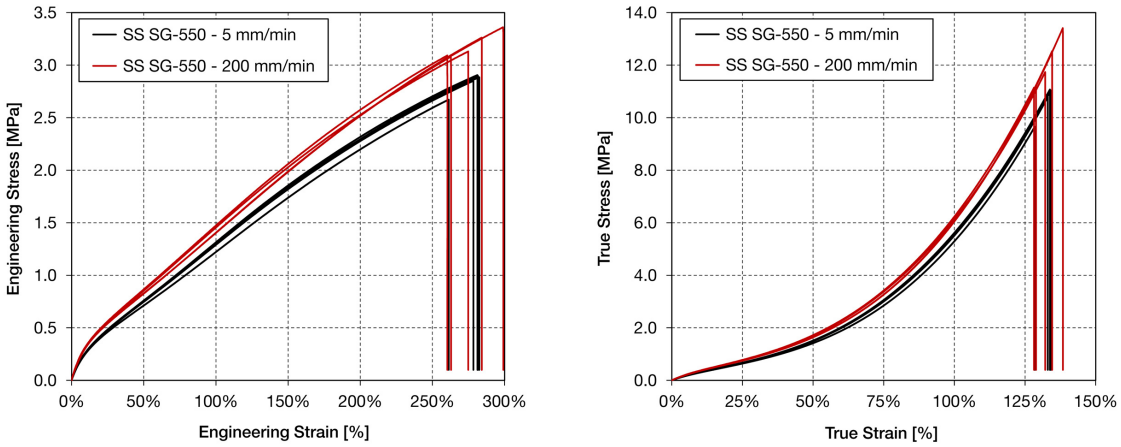

Fig. 4.7 *Influence of the loading speed on the stress-strain relationships for specimens of Sikasil SG-550*

4.2.4 Uniaxial tensile test results for SikaFast-5221 NT

For the selected acrylic, four test specimens of type 2 according to [ISO 37, 2011], made of *SikaFast-5211 NT,* are tested in the first series at material level under uniaxial tensile load with a loading speed of *5 mm/min*. Due to the required longer open time the second test series is carried out with *SikaFast-5221 NT (SF-5221 NT)*. Four different loading speeds are used in the second series, since a strong dependency of the material behaviour on this parameter is indicated by the producer. For each loading speed of *5 mm/min*, *1 mm/min*, *10 mm/min* and *100 mm/min* five specimens are tested. Different than in the case of the silicone, a yielding of the material can be observed for the acrylic. This is indicated by a whitening of the specimens while increasing the load. Furthermore, the plastic material behaviour can be observed by the remaining deformation in the specimens after failure (compare the first and the last picture in Fig. 4.8).

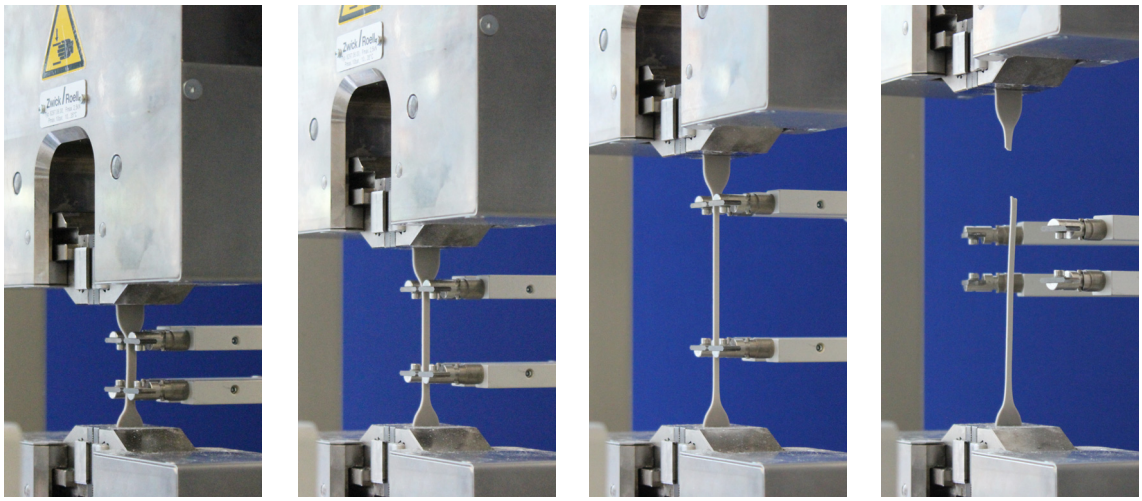

Fig. 4.8 *Test specimen of the adhesive SikaFast-5221 NT in different stages during the uniaxial tensile test*

The relationships between the engineering stresses and the engineering strains for the four specimens of *SikaFast-5211 NT* and the five specimens of *SikaFast-5221 NT* loaded with a speed of *5 mm/min* are illustrated in Fig. 4.9, left. The maximum engineering stress varies between *9.58 MPa* and *10.38 MPa* for specimens of series one and between *9.37 MPa* and *10.10 MPa* for specimens of series two. The maximum engineering strain reaches values between *216%* and *243%* for the first series and between *242%* and *256%* for the second series. Although these strain values are in a good agreement, the stress values at which the yielding occurs show a significant difference, averaging around *8 MPa* for specimens of the first series and only *6.5 MPa* for specimens of the second series. Additionally to the different type of *SikaFast* products, also the storage time between manufacturing and testing of the specimens, which has been longer for the dumbbells tested in series one, could be a reason for this discrepancy. As in the case of the silicones, further results for the acrylic specimens are provided in [Appendix A] in tabular form, including Young's modulus values for the elastic part.

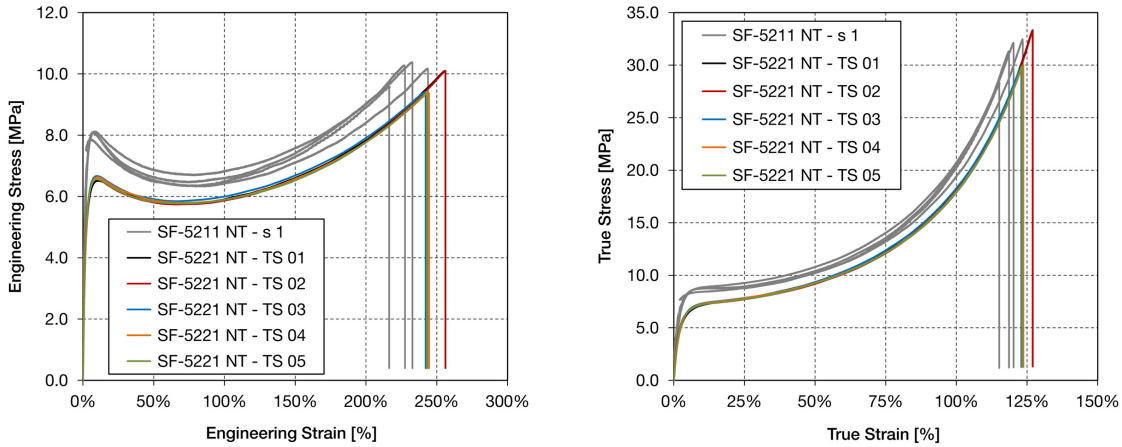

Fig. 4.9 *Relationships between engineering stresses and engineering strains (left) and between true stresses and true strains (right) for the specimens of SikaFast-5211 NT (grey) and SikaFast-5221 NT (coloured) tested with a loading speed of 5 mm/min*

Fig. 4.9, right, shows the relationships between true stresses and true strains for the same specimens. A Poisson's ratio of *0.47*, as recommended by the producers, is used for the acrylic. Similar to the two silicones, a constant Poisson's ratio is assumed over the whole strain range, since values for the transverse strain could not be measured. This assumption is supported by the absence of local necking effects. Regarding the agreement between the results for specimens with *SikaFast-5211 NT* and for specimens with *SikaFast-5221 NT*, a similar behaviour as for the engineering stresses is noticed. By comparing the two diagrams it can be observed that the decrease in stresses occurring after yielding in case of engineering stresses is not present when plotting the true stresses.

By comparing the curves for the two series independently, it can be concluded that the material shows a good agreement in the case of stiffness and small variations for stresses and strains. The reached stresses are around three times higher than in the case of the silicones, but the material shows less flexibility, especially when considering only the strain range where it behaves elastically.

The relationships between engineering stresses and engineering strains as well as between true stresses and true strains are plotted in Fig. 4.10 for the specimens of *SikaFast-5221 NT* tested in the second series with different loading speeds. A strong dependency of the material behaviour on the loading speed can be observed regarding stresses and strains. For structural applications, the variation of the yielding stress is of high importance. While for higher loading speeds (see curves for *100 mm/min*) the acrylic starts yielding at stresses of almost *10 MPa*, the lower the loading speed the more the yielding stress decreases. For a loading speed of *1 mm/min* the acrylic starts yielding already at around *5 MPa*. An interesting observation which can be made from Fig. 4.10 is that the engineering stresses and the true stresses are almost equal up to the yielding point. After passing this point, the true stresses increase exponentially, while for the engineering stresses, first, a decrease depending on the loading speed is noticed. This observation indicates, that a narrowing of the dumbbell‘s initial cross section starts after yielding.

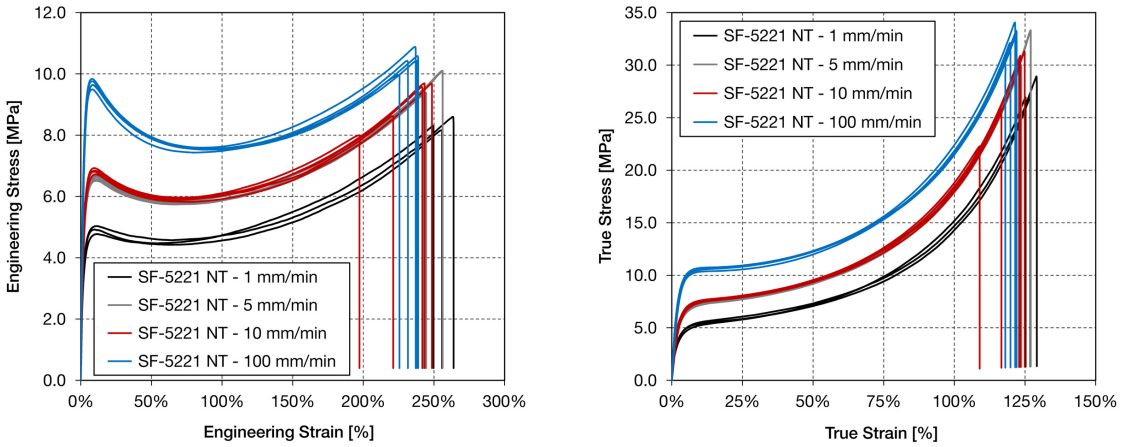

Fig. 4.10 *Influence of the loading speed on the stress-strain-relationships for specimens of SikaFast-5221 NT*

4.3 Material models for finite element simulations

Material models have the purpose to predict the qualitative and quantitative reaction of a material to external influences, like forces or addition of heat. Generally, they are based on experimental investigations and they use mathematical equations to reproduce physical characteristics of the materials. In practice, assumptions are made which have the aim to simplify the models or, respectively, to reduce the number of required parameters and equations. The disadvantages of this procedure are limitations to the area of validity. Examples for such assumptions are the following:

- certain environmental conditions like temperature and relative humidity;
- short-term or long-term material behaviour under given conditions;
- static or dynamic load application;
- size effects if a material model established for small samples is used for larger ones.

Material models are mainly differentiated by linearity (linear and non-linear), by loading speed and time dependency (viscous and non-viscous) and by the capability of the material body to return to the original shape after unloading (elastic and plastic). The schematic examples in Fig. 4.11 illustrate some of the possible combinations and explain the different terms.

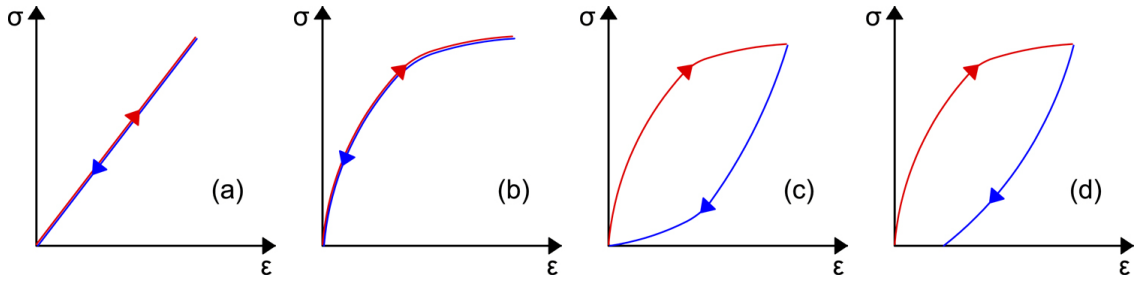

Fig. 4.11 *Different material model types: (a) linear elastic, (b) non-linear elastic, (c) non-linear visco-elastic (t -> ∞), (d) non-linear visco-plastic*

Two important effects related to viscosity are creeping and relaxation. The first one describes an increase of strain over time under a constant stress. The deformation as a consequence of creeping is composed of an elastic part (immediately reversible), a visco-elastic part (time-dependent reversible) and a visco-plastic part (time-dependent irreversible). Relaxation describes the decrease of stresses in the material over time under a constant applied strain. Creeping and relaxation behaviour of materials can be generally represented by spring and dashpot models (see [Schwarzl, 1990] for details).

Another factor of influence on the material behaviour of plastics and implicitly adhesives is temperature. An important term in this context is the glass transition temperature at which a polymer goes from the solid state to a viscous rubber-like state. Below the glass transition temperature polymers show a brittle energy-elastic behaviour, while above it their behaviour gets softer and entropy-elastic. Elastomers, which also include silicone adhesives, have generally their application range at temperatures above the glass transition temperature. Thermoplastics, which include most of the acrylic adhesives, can be used both below and above the glass

transition temperature. However, their properties suffer modifications after passing the glass transition temperature.

The glass transition temperature as well as the visco-elastic properties of a material can be determined with a dynamic-mechanical analysis (DMA) (see [Staudt, 2013]). Investigations on both the time and the temperature dependency of the material behaviour for the selected adhesives are not within the scope of this thesis. Nevertheless, these aspects are considered in the selection process and are discussed with the adhesive producers.

An effect occurring in the case of most elastomers is the Mullins effect (see [Diani et al., 2009]), which describes a softening of the material after the first loading. This means that in the case of two consecutive loading cycles up to a certain strain the reached stress amplitudes are lower for the second cycle. In the case of an idealised Mullins effect, the reloading curve corresponds to the unloading curve of the first cycle and no irreversible deformations remain in the unstressed state. Additionally, no more softening is occurring in further loading cycles up to the same strain value. No load cycles are investigated in the uniaxial tensile tests for the selected adhesives. However, in a part of the connection tests with silicone adhesives load cycles are run and this effect can be noticed (see results in chapter 5).

In order to be able to analyse diverse connections with the chosen adhesives without performing each time experimental tests in the laboratory, suitable material models are required. For the selected silicones, which are categorized as elastomers, hyperelastic material models (see [Abaqus, 2013a], [Ali et al., 2010] and [Staudt, 2013]) are recommended both in literature and by the producers. Several hyperelastic models are available in technical literature and are implemented in finite element software applications. Furthermore, different producers recommend different material models for their products. Therefore, some of the available models, which are considered more adequate than a linear elastic law, but not too complex to be used in practice, are derived for the two silicones and are compared to the experimental results.

In the case of the selected acrylic a plastic material behaviour as well as a dependency on the loading speed is observed in the tensile tests on dumbbells. The best way to represent such a behaviour is a visco-plastic material law. However, these type of models show a high complexity and are generally not implemented in finite element software like *Abaqus*. Users can write their own subroutines if required. Since the aim is to select material models which are applicable in practice, a strain rate dependent elastic-plastic material model is investigated for the acrylic. Furthermore, an additional model which takes initial voids in the adhesive material into consideration is analysed in chapter 5 to reproduce the load-displacement relationships from the adhesive joints at the glass surface tested under tensile and under shear loading.

4.3.1 Hyperelastic material models

When performing numerical simulations on silicone adhesives, non-linearities for both material and geometry have to be considered. The non-linearity on the material side can be described by hyperelastic material models. These models are based on strain energy potentials $U(\varepsilon)$. These potentials describe the strain energy which is stored in the material per unit of the initial volume as a function of the strain in the material at a certain time (see [Abaqus, 2013a], [Staudt, 2013]).

In general, several assumptions are made for the hyperelastic models. The first one is the isotropic behaviour of the materials, which allows formulations of the strain energy potential in dependency of the strain invariants (I_1, I_2 and I_3) instead of the principal strains (λ_1, λ_2, λ_3):

$$I_1 = \lambda_1^2 + \lambda_2^2 + \lambda_3^2 \qquad \text{(Eq. 4.3)}$$

$$I_2 = \lambda_1^2 \cdot \lambda_2^2 + \lambda_1^2 \cdot \lambda_3^2 + \lambda_2^2 \cdot \lambda_3^2 \qquad \text{(Eq. 4.4)}$$

$$I_3 = \lambda_1^2 \cdot \lambda_2^2 \cdot \lambda_3^2 \qquad \text{(Eq. 4.5)}$$

The second assumption made for silicones is related to the compressibility of the materials. Since silicones and elastomers in general show a small compressibility compared to their shear flexibility, they are often assumed to be incompressible, except for thermal expansions. This simplifies the strain energy formulations and usually deliver good results in numerical simulations. In the case of compressible materials the deformation can be divided in a deviatoric component and a volumetric component. The deviatoric component describes an isochoric deformation, where only the shape of the body changes, while the volume remains constant. On the other hand, the volumetric component describes the change in volume of the body. These two components can be recognised in all the strain energy formulations presented below. As mentioned before, generally, an incompressible material behaviour is assumed for silicones, which results in considering only the deviatoric part of the strain energy formulations.

In the next sections the deviatoric strain invariants ($\bar{I}_i$) and the deviatoric principal strains ($\bar{\lambda}_i$) are represented with a bar above, while in the case of incompressible material behaviour the strain invariants (I_i) and the principal strains (λ_i) are represented without the bar.

Neo-Hooke

The *Neo-Hooke* model represents the easiest way to describe the hyperelastic behaviour of a material. It uses a linear relationship between the strain energy potential U and the first deviatoric strain invaraint $\bar{I}_1$ as shown in (Eq. 4.6) (see also [Abaqus, 2013a] and [Staudt, 2013]).

$$U = C_{10}(\bar{I}_1 - 3) + \frac{1}{D_1}(J_{el} - 1)^2 \qquad \text{(Eq. 4.6)}$$

The parameters C_{10} and D_1 describe temperature-dependent material properties. J_{el} is the elastic volume ratio and relates the total volume ratio J to the thermal volume ratio J_{th} as follows:

$$J_{el} = \frac{J}{J_{th}} \qquad \text{with} \qquad J_{th} = (1 + \varepsilon_{th})^3 \qquad \text{(Eq. 4.7)}$$

The linear thermal expansion strain ε_{th} can be determined by considering the temperature and the isotropic thermal expansion coefficient. The initial shear modulus μ_0 and bulk modulus K_0 can be determined with the following equations:

$$\mu_0 = 2C_{10} \qquad \text{and} \qquad K_0 = \frac{2}{D_1} \tag{Eq. 4.8}$$

If incompressible material behaviour is assumed, (Eq. 4.6) can be simplified to (Eq. 4.9).

$$U = C_{10}(\bar{I}_1 - 3) \tag{Eq. 4.9}$$

The Neo-Hooke model results from the reduced polynomial form for the strain energy potential showed in (Eq. 4.10) in the case of n = 1.

$$U = \sum_{i=1}^{n} C_{i0}(\bar{I}_1 - 3)^i + \sum_{i=1}^{n} \frac{1}{D_i}(J_{el} - 1)^{2i} \tag{Eq. 4.10}$$

Mooney-Rivlin

The *Mooney-Rivlin* model considers, additionally to the linear approach of the *Neo-Hooke* model, a second linear part including the second deviatoric strain invariant $\bar{I}_2$. The *Mooney-Rivlin* model results from the general polynomial form for the strain energy potential shown in (Eq. 4.11) (see also [Abaqus, 2013a] and [Staudt, 2013]).

$$U = \sum_{i,j=0}^{n} C_{ij}(\bar{I}_1 - 3)^i(\bar{I}_2 - 3)^j + \sum_{i=1}^{n} \frac{1}{D_i}(J_{el} - 1)^{2i} \tag{Eq. 4.11}$$

For the generally used version with $i = j = 1$, (Eq. 4.11) can be simplified to the *Mooney-Rivlin* form as shown by (Eq. 4.12).

$$U = C_{10}(\bar{I}_1 - 3) + C_{01}(\bar{I}_2 - 3) + \frac{1}{D_1}(J_{el} - 1)^2 \tag{Eq. 4.12}$$

The parameter D_1 is the same as in the case of the *Neo-Hooke* model and considers the incompressible material behaviour, while the temperature-dependent constants C_{10} and C_{01} have a physical meaning and can be related to the initial shear modulus μ_0 as follows:

$$\mu_0 = 2(C_{10} + C_{01}) \tag{Eq. 4.13}$$

If incompressible material behaviour is assumed, (Eq. 4.12) can be further simplified to:

$$U = C_{10}(I_1 - 3) + C_{01}(I_2 - 3) \tag{Eq. 4.14}$$

Arruda-Boyce

Other than the previous models, the *Arruda-Boyce* model uses the deviatoric principal stretches instead of the invariants of the strain tensor. The model is based on the behaviour of molecular chains within a cube. The strain energy potential *U* is therefore the sum of the strain energy

potentials of the single molecular chains within the considered region as shown by (Eq. 4.15) (see also [Abaqus, 2013a] and [Staudt, 2013]).

$$U = \mu \cdot \sum_{i=1}^{5} \frac{C_i}{\lambda_m^{2i-2}} (\bar{I}_1^{\,i} - 3^i) + \frac{1}{D_1}\left(\frac{J_{el}^2 - 1}{2} - \ln(J_{el})\right) \qquad \text{(Eq. 4.15)}$$

For the coefficients C_i the following values are resulting:

$$C_1 = \frac{1}{2} \qquad C_2 = \frac{1}{20} \qquad C_3 = \frac{11}{1050} \qquad C_4 = \frac{19}{7000} \qquad C_5 = \frac{519}{673750}$$

If incompressible material behaviour is assumed, (Eq. 4.15) can be simplified to:

$$U = \mu \cdot \sum_{i=1}^{5} \frac{C_i}{\lambda_m^{2i-2}} (I_1^i - 3^i) \qquad \text{(Eq. 4.16)}$$

The parameters μ, λ_m and D_1 describe temperature-dependent material properties. The initial shear modulus μ_0 can be determined with the help of μ and λ_m by (Eq. 4.17).

$$\mu_0 = \mu\left(1 + \frac{3}{5\lambda_m^2} + \frac{99}{175\lambda_m^4} + \frac{513}{875\lambda_m^6} + \frac{42039}{67375\lambda_m^8}\right) \qquad \text{(Eq. 4.17)}$$

The parameter λ_m represents the strain at which the inclination of the stress-strain-curve increases considerable. A typical value given in [Abaqus, 2013a] is $\lambda_m = 7$.

Ogden

The *Ogden* model represents the strain energy potential *U* in dependency of the deviatoric principal stretches as shown by (Eq. 4.18) (see also [Abaqus, 2013a] and [Staudt, 2013]).

$$U = \sum_{i=1}^{n} \frac{2\mu_i}{\alpha_i^2}\left(\bar{\lambda}_1^{\alpha_i} + \bar{\lambda}_2^{\alpha_i} + \bar{\lambda}_3^{\alpha_i} - 3\right) + \sum_{i=1}^{n} \frac{1}{D_i}(J_{el} - 1)^{2i} \qquad \text{(Eq. 4.18)}$$

The parameters μ_i, α_i and D_i describe temperature-dependent material properties, while λ_i are the deviatoric principal stretches. The initial shear modulus μ_0 can be calculated by (Eq. 4.19).

$$\mu_0 = \sum_{i=1}^{n} \mu_i \qquad \text{(Eq. 4.19)}$$

If incompressible material behaviour is assumed, (Eq. 4.18) can be simplified to:

$$U = \sum_{i=1}^{n} \frac{2\mu_i}{\alpha_i^2}(\lambda_1^{\alpha_i} + \lambda_2^{\alpha_i} + \lambda_3^{\alpha_i} - 3) \qquad \text{(Eq. 4.20)}$$

Other hyperelastic material models, like, for example, *Neo-Hooke* or *Mooney-Rivlin*, can be derived from the *Ogden* model by choosing appropriate values for *n* and α_i.

4.3.2 Suitable material models for Dow Corning 993

As mentioned before, hyperelastic material models are recommended to be used in numerical simulations for silicone adhesives. Nevertheless, linear elastic material models should be considered as well, because they can show a good agreement for certain strain ranges.

Different hyperelastic models are implemented in the engineering software package *Abaqus*. The required parameters for these models can be determined with a curve fitting tool provided in *Abaqus* based on input data from experimental tests. Generally, test data from multiple test configurations including uniaxial tests, biaxial tests, planar shear tests and volumetric tests is recommended for obtaining a material model which can be used for several loading situations. In this research work only data from uniaxial tensile tests are available for determining the parameters and therefore material models with a small number of parameters are examined.

A second curve fitting is carried out with the *Matlab* software for solving mathematical problems to compare the parameters delivered by *Abaqus*. For this operation stress-strain relations are required for the different energy potentials. These relations can be determined according to [Abaqus, 2013c]. First the principal strains for the uniaxial loading can be determined to:

$$\lambda_1 = \lambda_U \qquad \lambda_2 = \lambda_3 = \lambda_U^{-\frac{1}{2}} \qquad \lambda_U = 1 + \varepsilon_U \tag{Eq. 4.21}$$

ε_U is the given strain value and at the same time the x-value in the searched function *y=f(x)*. Based on the uniaxial strain λ_U, the first and the second deviatoric strain invariants can be determined to:

$$\bar{I}_1 = \lambda_U^2 + 2\lambda_U^{-1} \qquad \bar{I}_2 = \lambda_U^{-2} + 2\lambda_U \tag{Eq. 4.22}$$

Finally the stress-strain relationships can be determined for the different strain energy potential forms to the following equations:

Neo-Hooke: $$\sigma_U = 2(\lambda_U - \lambda_U^{-2})C_{10} \tag{Eq. 4.23}$$

Mooney-Rivlin: $$\sigma_U = 2(1 - \lambda_U^{-3})(C_{10}\lambda_U + C_{01}) \tag{Eq. 4.24}$$

Arruda-Boyce: $$\sigma_U = 2\mu(\lambda_U - \lambda_U^{-2})\sum_{i=1}^{5} \frac{iC_i}{\lambda_m^{2i-2}} \bar{I}_1^{i-1} \tag{Eq. 4.25}$$

Ogden: $$\sigma_U = \sum_{i=1}^{n} \frac{2\mu_i}{\alpha_i}\left(\lambda_U^{\alpha_i - 1} - \lambda_U^{-\frac{1}{2}\alpha_i - 1}\right) \tag{Eq. 4.26}$$

The parameter results of both curve fittings are shown in Tab. 4.3. For both cases the stresses used as input data have the unit *[MPa]*. This is important to consider when using the parameters in other simulations with different input units.

For the curve fitting operations test data from the uniaxial tensile tests on test specimens *TS 1*, *TS 2* and *TS 3* are used. The data pairs of engineering stresses and engineering strains up to

200% strain are considered. Some discrepancies can be observed between the values determined for the parameters with the two methods. The difference between the curve fitting with *Abaqus* and the one with *Matlab* is that the second one allows for modifying some starting parameters. *Matlab* uses a nonlinear least squares method for the curve fitting and allows to set the lower and upper limits for the searched parameters. By modifying these limits the parameters delivered by *Abaqus* could be further approached. For the values in Tab. 4.3 the limits are set to minus and plus infinite, which in particular cases can lead to negative values for certain parameters. According to [Bonet et al., 2016], strain energy functions used to describe hyperelastic materials at large strains should satisfy the mathematical requirement of polyconvexity. This implies however positive material parameters (see also [Hartmann & Neff, 2003]). Therefore, the use of negative material parameters should be avoided in finite element simulations, since they can lead to an unstable material behaviour and implicitly to convergence issues.

Tab. 4.3 *Parameters for different hyperelastic material models implemented in Abaqus for the silicone adhesive Dow Corning 993, determined with Abaqus and with Matlab*

Strain energy function	**Parameters**		
	Labelling	**Abaqus**	**Matlab**
Neo-Hooke	C_{10} [MPa]	0.342307	0.339700
Mooney-Rivlin	C_{10} [MPa]	0.333349	0.365000
	C_{01} [MPa]	0.010943	-0.059030
Arruda-Boyce	μ [MPa]	0.684613	0.618800
	λ_m [-]	2058.136550	4.054000
Ogden (1st order)	μ_1 [MPa]	0.730986	0.627800
	α_1 [-]	1.811519	2.162000

In Fig. 4.12 and Fig. 4.13 the experimental data from the performed uniaxial tensile tests on dumbbells made of *Dow Corning 993* is compared to results obtained by using the different material models.

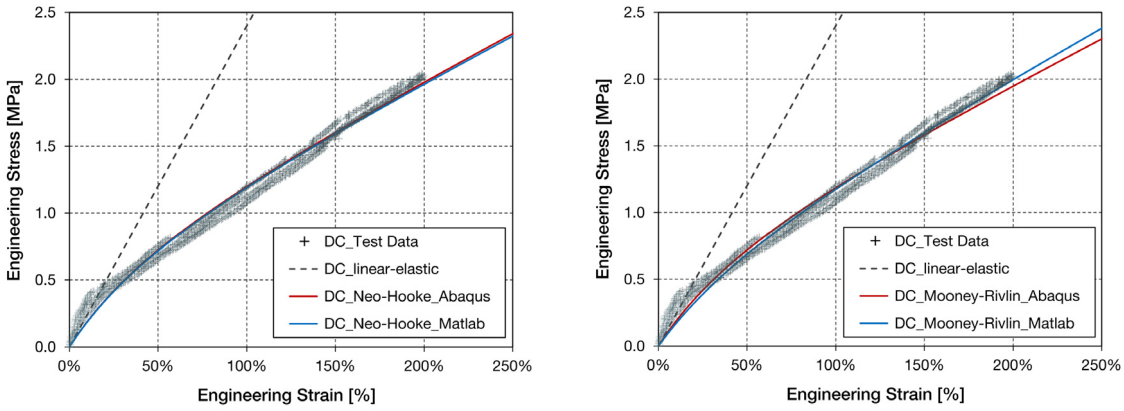

Fig. 4.12 *Uniaxial tensile test data for Dow Corning 993 compared to results obtained with the parameters determined by curve fitting for the Neo-Hooke model (left) and the Mooney-Rivlin model (right)*

In a first step, a linear elastic material model is analysed. A Young's modulus of $E = 2.40\ MPa$ and a Poisson's ratio of $\nu = 0.49$ are chosen according to information provided in literature (see [Mocibob, 2008]). The results from this model are plotted in all diagrams. It can be observed that the linear elastic model slightly underestimates the experimental results up to around *20%* strain and increasingly overestimates them above this value.

In Fig. 4.12 the results for the *Neo-Hooke* model (left) and the *Mooney-Rivlin* model (right) with the parameters from Tab. 4.3 are plotted. In the case of the *Neo-Hooke* model there is almost no difference between the two curves. For the *Mooney-Rivlin* model the parameters determined with *Abaqus* lead to a better fit for strains up to around *40%*, while for higher strains the parameters determined with *Matlab* lead to a better agreement. However, it should be considered that the strain energy function with the parameters determined by *Matlab* for the *Mooney-Rivlin* model does not satisfy the requirement of polyconvexity.

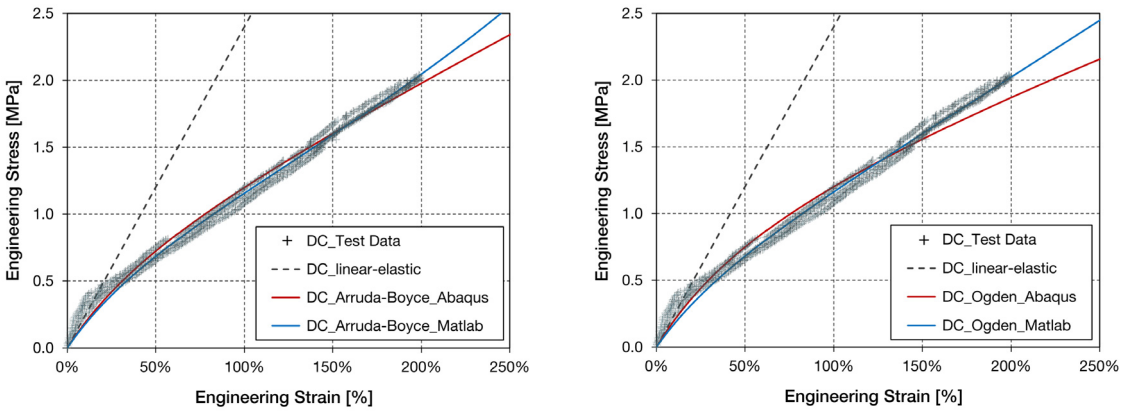

Fig. 4.13 *Uniaxial tensile test data for Dow Corning 993 compared to results obtained with the parameters determined by curve fitting for the Arruda-Boyce model (left) and the Ogden model (right)*

Fig. 4.13 shows the results for the *Arruda-Boyce* (left) and the *Ogden* models (right) with the parameters from Tab. 4.3. Similar differences between the curves obtained with the *Abaqus* parameters and the *Matlab* parameters as in the case of the *Mooney-Rivlin* model can be observed. For small strains up to around *30-40%* the *Abaqus* parameters provide a better fit. Furthermore, for strains up to around *150%* the *Matlab* parameters lead to smaller stress values than the *Abaqus* parameters, while for higher strains the curves obtained with the *Abaqus* parameters increasingly underestimate the test results.

All the analysed hyperelastic material models are stable over the considered strain range. They behave similar and underestimate the test results for strains below *30%*. Due to the small number of parameters used in the simulations (maximum 2 parameters) the models are not able to simulate the S-shaped development of the experimental curves. A strain energy function of a higher order, like for example a higher order *Ogden* model, is required. In general, the parameters determined with *Matlab* lead to a slightly better fitting of the test results over the whole considered strain range. Although, if only strains up to *30%* are considered, the stress values obtained with the *Abaqus* parameters are closer to the test results.

4.3.3 Suitable material models for Sikasil SG-550

For the silicone *Sikasil SG-550* the same procedure as for the adhesive *Dow Corning 993* is carried out to investigate material models for numerical simulations. The parameters for the different hyperelastic models are determined by curve fitting operations both with *Abaqus* and with *Matlab*. The same models are used and the same assumptions are made as in the case of *Dow Corning 993*. Only the results from the uniaxial tensile tests on test specimens *TS 01*, *TS 02*, *TS 03* and *TS 04* from the second test series up to *250%* strain are used for the curve fitting. The parameter results of both curve fittings are shown in Tab. 4.4.

Tab. 4.4 *Parameters for different hyperelastic material models implemented in Abaqus for the silicone adhesive Sikasil SG-550, determined with Abaqus and with Matlab*

Strain energy function	**Parameters**		
	Labelling	**Abaqus**	**Matlab**
Neo-Hooke	C_{10} [MPa]	0.386578	0.389500
Mooney-Rivlin	C_{10} [MPa]	0.412161	0.426400
	C_{01} [MPa]	-0.060069	-0.095050
Arruda-Boyce	μ [MPa]	0.754770	0.731500
	λ_m [-]	7.332971	5.349000
Ogden (1st order)	μ_1 [MPa]	0.771461	0.719600
	α_1 [-]	2.005514	2.138000

In Fig. 4.14 and Fig. 4.15 the experimental data from the uniaxial tensile tests on dumbbells of *Sikasil SG-550* is compared to results obtained by using the different material models.

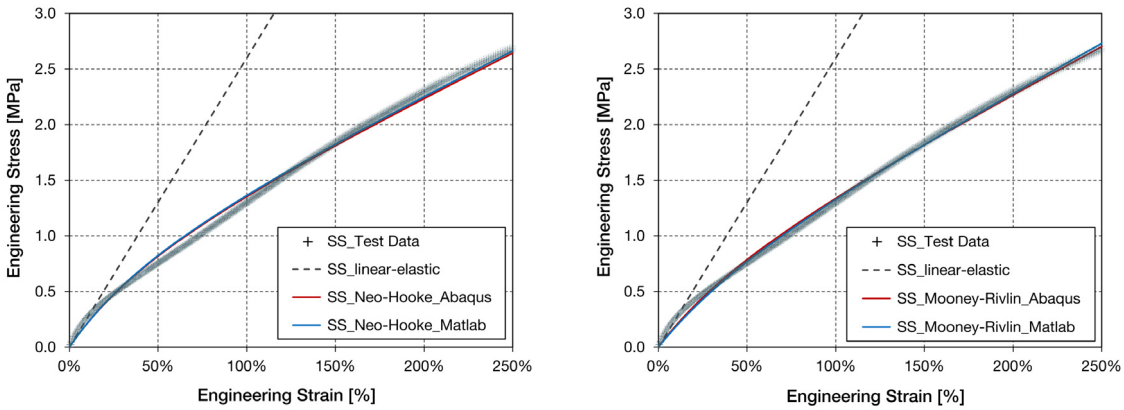

Fig. 4.14 *Uniaxial tensile test data for Sikasil SG-550 compared to results obtained with the parameters determined by curve fitting for the Neo-Hooke model (left) and the Mooney-Rivlin model (right)*

First, a linear elastic material model with a Young‘s modulus of $E = 2.6\ MPa$ and a Poisson‘s ratio of $\nu = 0.49$ is analysed. It can be observed that the linear elastic model underestimates the experimental results slightly for small strains up to around *20%*, while for larger strains it

increasingly overestimates the stiffness and the tensile stresses. The results obtained with the linear-elastic model are plotted in all diagrams.

In Fig. 4.14 the results for the *Neo-Hooke* model (left) and the *Mooney-Rivlin* model (right) with the parameters from Tab. 4.4 are plotted. In the case of both models a good agreement between the curves obtained with differently determined coefficients is given. Nevertheless, it should be considered that, in the case of the *Mooney-Rivlin* model, both applied curve fitting procedures lead to negative values for the material parameter C_{01}. Therefore the strain energy function resulting with these parameters does not satisfy the mathematical requirement of poly-convexity, which is necessary according to [Bonet et al., 2016] and [Hartmann & Neff, 2003].

The curves obtained with the *Arruda-Boyce* model and with the *Ogden* model, which are plotted in Fig. 4.15, show as well a similar behaviour for the parameters determined with *Abaqus* and those determined with *Matlab*.

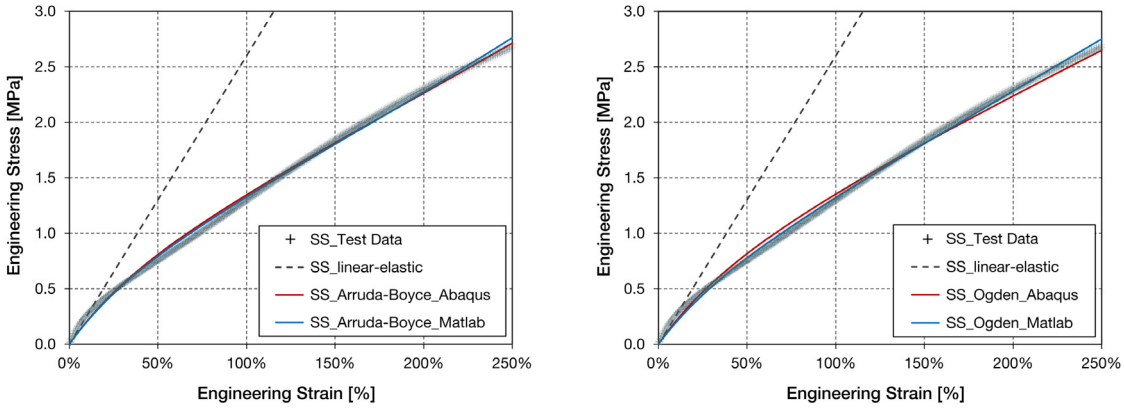

Fig. 4.15 *Uniaxial tensile test data for Sikasil SG-550 compared to results obtained with the parameters determined by curve fitting for the Arruda-Boyce model (left) and the Ogden model (right)*

Generally, it can be concluded that both the parameters determined with *Abaqus* and those determined with *Matlab* lead to a good curve fitting. However, all the examined hyperelastic models slightly underestimate the stresses for low strains up to around *30%*.

4.3.4 Suitable material models for SikaFast-5221 NT

The acrylic adhesive *SikaFast-5221 NT* shows a different material behaviour than the two selected and evaluated silicones. Therefore, other material models need to be investigated. These models should cover both for the plasticity and the displacement rate dependency identified in the performed uniaxial tensile tests. Visco-plastic material models generally have a high complexity and request extensive knowledge from the user. For practice simpler models are required. Therefore a plastic strain-rate dependent model is analysed in this thesis.

To consider strain rate dependency, the stress-strain relationships at different strain rate values are required. However, generally, results at constant displacement rates are available from experimental tests. These results can be plotted in a three-dimensional diagram showing stress *vs.* strain *vs.* strain rate (σ *vs.* ε *vs.* $\bar{\varepsilon}$). True values are generally required as input data for finite element software. The true stress and the true strain can be determined according to (Eq. 4.1) and (Eq. 4.2), respectively, while the strain rate is defined as the first derivative of the applied strain over time and the true values can be obtained with (Eq. 4.27).

$$\bar{\varepsilon}_{tru} = \frac{\Delta\varepsilon_{tru}}{\Delta t} \qquad \text{(Eq. 4.27)}$$

The stress-strain data at constant displacement rates need then to be fitted with a surface described by a function $\sigma(\varepsilon,\bar{\varepsilon})$. The curve fitting tool from *Matlab*, where either the *Trust-Region-Method* or the *Levenberg-Marquard-Algorithm* can be selected to determine optimised parameters, can be used to perform the fitting. Stress-strain curves at constant strain rates are finally obtained by cutting the determined surface with stress-strain planes. The main challenge is to find a suitable surface which is able to fit the experimental data well. The easiest approaches are polynomial equations, but generally this type of function leads to an unsatisfying approximation of the experimental results for small strains at which the yielding starts. Other functions used in past research for this kind of task are approaches based on the model by [Johnson & Cook, 1985], like the one described by (Eq. 4.28) and applied in [Becker, 2009] and in [Rühl, 2016], or based on the model by [G'Sell & Jonas, 1979], described by (Eq. 4.29) and applied in [Becker, 2009] and in [Kuntsche, 2015]. These two equations are written here according to [Becker, 2009].

$$\sigma(\varepsilon,\bar{\varepsilon}) = (A + B\cdot\varepsilon_{pl}^{n})\cdot\left(1 + C\cdot\ln\frac{\bar{\varepsilon}}{\varepsilon_0}\right) = \sigma_0(\varepsilon)\cdot\left(1 + C\cdot\ln\frac{\bar{\varepsilon}}{\varepsilon_0}\right) \qquad \text{(Eq. 4.28)}$$

$$\sigma(\varepsilon,\bar{\varepsilon}) = K\cdot\left(1 - \exp\left(-\frac{\varepsilon}{\varepsilon_v}\right)\right)\cdot\exp(h\cdot\varepsilon^2)\cdot\left(\frac{\bar{\varepsilon}}{\bar{\varepsilon}_0}\right)^m = \sigma_0(\varepsilon)\cdot\left(\frac{\bar{\varepsilon}}{\bar{\varepsilon}_0}\right)^m \qquad \text{(Eq. 4.29)}$$

The parameters *A*, *B*, *n* and *C* from (Eq. 4.28) and the parameters *K*, ε_v, *h* and *m* from (Eq. 4.29) need to be determined from the experimental data by the before mentioned surface fitting. For (Eq. 4.28), *A* is the yielding stress, *B* and *n* are strain hardening coefficients and *C* is a strain rate constant. For (Eq. 4.29), the parameters *K* and ε_v describe the material behaviour until yielding occurs, *h* is a strain hardening coefficient and *m* considers the strain rate sensitivity. With the first approach only the plastic strain range can be fitted well, while the second approach allows

for a satisfying fit of the range of elastic strains as well. However, the parameter *m* in (Eq. 4.29) should be determined according to [Becker, 2009] as a function of the strain, $m(\varepsilon)$, which results in a complex task.

A novel approach to represent the strain rate dependent stress-strain behaviour over the whole strain range, including both the elastic strain range and plastic strain range, is introduced in this thesis by using the inverse polynomial after [Nelder, 1966]. This inverse polynomial is successfully transferred into the context of incompressible hyperelasticity in [Drass et al., 2017a] and [Drass et al., 2017b], compressible hyperelasticity accounting for the cavitation effect in [Drass et al., 2018] and a continuum damage formulation at finite strains in [Drass et al., 2017c]. Originally, the inverse polynomial has been proposed by Nelder for a yield-fertilizer model in agriculture and had the form given in (Eq. 4.30).

$$\frac{x}{y} = \beta_0 + \beta_1 \cdot x + \beta_2 \cdot x^2 \qquad \text{(Eq. 4.30)}$$

For fitting functions, which first rise and then start to fall with an increasing x, the inverse polynomial exhibits useful properties. For small *x*-values, the function can be approximated by $y \sim \beta_0^{-1} \cdot x$, while for large *x*-values, the function can be approximated by $y \sim (\beta_2 \cdot x)^{-1}$. The peak of the function occurs at $x = (\beta_0 / \beta_2)^{-0.5}$ with a value of $y_{max} = 2 \cdot (\beta_0 / \beta_2)^{-0.5} + \beta_1$. As a consequence, β_1 only influences the value of *y*, but does not affect the position of the maximum. A further advantage of the Nelder-function compared to usual quadratic polynomial functions is that it has no built-in symmetry and its two extremes are described by two separate parameters. In order to bring (Eq. 4.30) into the context of plasticity it is reformulated to:

$$\sigma(\varepsilon, \bar{\varepsilon}) = \frac{\varepsilon \cdot \bar{\varepsilon}^{m}}{\beta_0 + \beta_1 \cdot \varepsilon + \beta_2 \cdot \varepsilon^2} \qquad \text{(Eq. 4.31)}$$

Although (Eq. 4.31) is adequate to represent the plastic behaviour, this simple function requires further modification in order to better fit the stresses in the yielding zone. By extending (Eq. 4.31) to a fourth order inverse polynomial, the novel surface fitting function given in (Eq. 4.32) is obtained.

$$\sigma(\varepsilon, \bar{\varepsilon}) = \frac{\varepsilon \cdot \bar{\varepsilon}^{m}}{\beta_0 + \dfrac{\beta_1 \cdot \varepsilon}{\bar{\varepsilon}^{n}} + \beta_2 \cdot \varepsilon^2 + \beta_3 \cdot \varepsilon^3 + \beta_4 \cdot \varepsilon^4} \qquad \text{(Eq. 4.32)}$$

By second order Taylor-series expansion of (Eq. 4.32) with respect to the strain, ε, around the point $\varepsilon = 0$, the linearised form of the novel fitting function shown by (Eq. 4.33) is obtained.

$$\sigma(\varepsilon, \bar{\varepsilon}) = \frac{\varepsilon \cdot \bar{\varepsilon}^{m}}{\beta_0} + O(\varepsilon^2) \qquad \text{(Eq. 4.33)}$$

The Landau-symbol $O(\varepsilon^2)$ represents a small error term, which describes the less significant terms of (Eq. 4.32) for small strains. From (Eq. 4.33) it can be noticed that the initial Young‘s

modulus reads to $E = 1/\beta_0$, without depending on the strain rate. However, the initial Young's modulus should be a function of the strain rate $\bar{\varepsilon}$ and therefore is characterized by $E = \bar{\varepsilon}^m/\beta_0$.

The parameter β_1 controls the yield point. It is significant, that this parameter is equipped in (Eq. 4.32) with an additional parameter which considers the strain rate. Due to this fact, the yield point, characterized by β_1 and $\bar{\varepsilon}^n$, increases with increasing strain rate. To substantiate this, the first order derivative of (Eq. 4.32) is determined to:

$$\sigma'(\varepsilon, \bar{\varepsilon}) = \frac{(-3\beta_4 \cdot \varepsilon^4 - 2\beta_3 \cdot \varepsilon^3 - \beta_2 \cdot \varepsilon^2 + \beta_0) \cdot \bar{\varepsilon}^{m+2n}}{(\beta_0 \cdot \bar{\varepsilon}^n + \beta_1 \cdot \varepsilon + \beta_2 \cdot \varepsilon^2 \cdot \bar{\varepsilon}^n + \beta_3 \cdot \varepsilon^3 \cdot \bar{\varepsilon}^n + \beta_4 \cdot \varepsilon^4 \cdot \bar{\varepsilon}^n)^2} \qquad \text{(Eq. 4.34)}$$

A second order Taylor-series expansion of (Eq. 4.34) with respect to the strain ε leads to (Eq. 4.35).

$$\sigma'(\varepsilon, \bar{\varepsilon}) = \frac{\bar{\varepsilon}^m}{\beta_0} - 2 \cdot \frac{\beta_1 \cdot \varepsilon \cdot \bar{\varepsilon}^m}{\beta_0^2 \cdot \bar{\varepsilon}^n} + O(\varepsilon^2) \qquad \text{(Eq. 4.35)}$$

An approximate solution for the critical yielding strain can be determined with (Eq. 4.36) by setting (Eq. 4.35) equal to zero.

$$\varepsilon_{yield} \cong \frac{1}{2} \cdot \frac{\beta_0 \cdot \bar{\varepsilon}^n}{\beta_1} \qquad \text{(Eq. 4.36)}$$

By inserting (Eq. 4.36) into (Eq. 4.33), an approximate solution for the critical yield stress can be determined. As shown in (Eq. 4.37), the critical yield stress is a function of the strain rate and depends on $\bar{\varepsilon}^m$, $\bar{\varepsilon}^n$ and β_1.

$$\sigma_{yield} \cong \frac{1}{2} \cdot \frac{\bar{\varepsilon}^{m+n}}{\beta_1} \qquad \text{(Eq. 4.37)}$$

The novel Nelder-based surface fitting function introduced in this chapter in the form of (Eq. 4.32) is applied to fit a surface to the experimental data from the uniaxial tensile tests performed on dumbbells made of the acrylic adhesive *SikaFast-5221 NT*. The Trust-Region-Method is used in the curve fitting tool from Matlab to optimise the required parameters. The determined values for the different parameters are provided in Tab. 4.5.

The fitting results are illustrated by the 3D-diagram in Fig. 4.16, left, in which the experimental data is plotted with dot markers as true stress *vs.* true strain *vs.* true strain rate. The surface fit is represented as a surface mesh. For better illustration, a logarithmic scale is used for the true strain rate. The surface fit obtained with the novel Nelder-based surface fitting function leads to a good agreement with the experimental data. Based on this surface, the stress-strain behaviour at constant true strain rates can be determined. True stress *vs.* true strain curves for selected true strain rate values are depicted in Fig. 4.16, right. Based on these curves, input data for plasticity in finite element simulations can be derived.

Tab. 4.5 *Material parameters used for fitting the strain rate dependent stress-strain data obtained from uniaxial tensile tests on dumbbell specimens made of SikaFast-5221 NT with the novel Nelder-based surface fitting function*

β_0	β_1	β_2	β_3	β_4	m	n
0.0008334	0.0605	0.03669	-0.1115	0.04568	0.1305	-0.02228

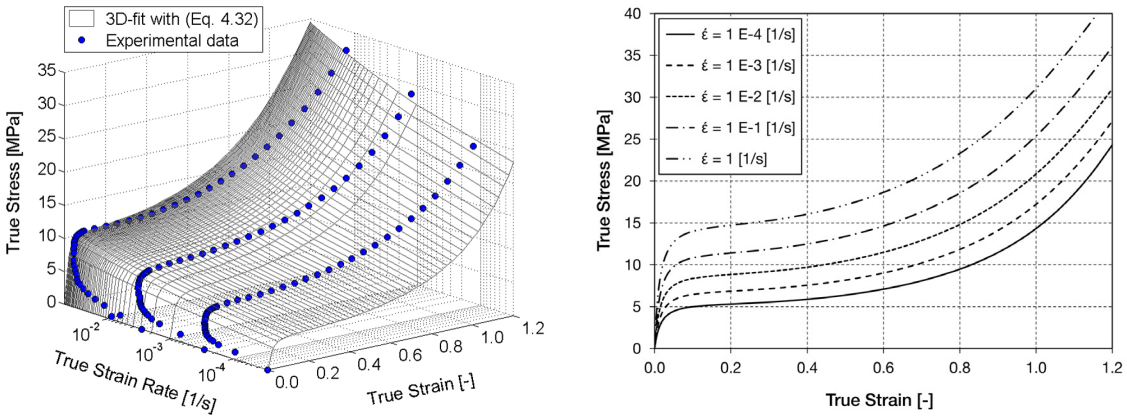

Fig. 4.16 *Determination of stress-strain curves at constant true strain rates: surface fitting results of the experimentally determined stress-strain curves under different displacement rates with the novel Nelder-based surface fitting function (left); true stress vs. true strain curves at constant true strain rate values (right)*

For using plasticity in *Abaqus*, first, elastic properties have to be defined. A Young's modulus of $E = 250\ MPa$ and a Poisson's ratio of $\nu = 0.47$ are chosen according to the technical data provided by the adhesive producer. Further, data pairs consisting of true yield stress $\sigma_{tru,y}$ and true plastic strain $\varepsilon_{tru,pl}$ are required. The more data pairs are provided, the more accurate the fitting is. The true plastic strain $\varepsilon_{tru,pl}$ can be determined with (Eq. 4.38) by subtracting the true elastic strain $\varepsilon_{tru,el}$ from the total true strain ε_{tru}:

$$\varepsilon_{tru,pl} = \varepsilon_{tru} - \varepsilon_{tru,el} = \varepsilon_{tru} - \sigma_{tru} / E \qquad \text{(Eq. 4.38)}$$

For an implementation of plasticity in *Abaqus* it is recommended to calculate the yield stresses and the plastic strains as true values (see [Abaqus, 2013d]). For simulating the uniaxial tensile tests on the dumbbell specimens, this approach leads to good results, as shown in this subchapter. However, the performed simulations on linear adhesive joints with the investigated acrylic, which are discussed in subchapter 5.2.4 of this thesis, show that by using true stresses and engineering strains better results are obtained in the case of connections with this material. The use of true strains instead of engineering strains leads in the case of the connections to an overestimation of the stiffness after yielding.

In Tab. 4.6 the input data for a plastic strain rate dependent model of the acrylic *SikaFast-5221 NT* based on the stress-strain curves at constant strain rates depicted in Fig. 4.16, right, are provided with both true plastic strains and corresponding engineering plastic strains. The yield stresses for true strain rates of $1E^{-3}\ s^{-1}$, $1E^{-2}\ s^{-1}$, $1E^{-1}\ s^{-1}$ and $1\ s^{-1}$ are determined based on the

performed uniaxial tensile tests. The yield stresses for a strain rate of $0\ s^{-1}$ are required by *Abaqus* and are actually the values determined for a strain rate of $1E^{-4}\ s^{-1}$. Therefore, this should be considered before using this model for lower strain rates. For strain rates different than those for which input values are provided, the software interpolates the yield stresses. Since the relationship between stresses and strains of the adhesive is non-linear in the plastic part, less data pairs lead to a non-satisfying fit.

Tab. 4.6 *Yield stress at certain plastic strains depending on the strain rate for implementation of a plastic strain rate dependent material model for the acrylic adhesive SikaFast-5221 NT in Abaqus*

True plastic strain [-]	**Corr. engineering plastic strain** [-]	**Yield stress** [MPa]				
		Strain rate: 0 [s^{-1}]	**Strain rate:** $1E^{-3}$ [s^{-1}]	**Strain rate:** $1E^{-2}$ [s^{-1}]	**Strain rate:** $1E^{-1}$ [s^{-1}]	**Strain rate:** 1 [s^{-1}]
0.00	0.00	2.2607	3.6283	5.6547	8.9823	12.7017
0.01	0.01	3.2805	4.6444	6.5755	9.5637	13.1234
0.02	0.02	3.8511	5.2383	7.1458	9.9637	13.4330
0.05	0.05	4.6265	6.0779	7.9989	10.6356	13.9990
0.10	0.11	5.0438	6.5499	8.5108	11.1044	14.4498
0.30	0.35	5.5685	7.1898	9.2889	12.0482	15.6195
0.50	0.65	6.4397	8.2691	10.6348	13.7779	17.8361
0.70	1.01	8.2039	10.4046	13.2360	17.0305	21.8908
0.90	1.46	11.7106	14.4739	18.0012	22.7597	28.7613
1.10	2.00	18.9694	22.2199	26.4246	32.1865	39.3190
1.30	2.67	32.2412	34.3009	37.9498	43.4364	50.4286

The diagrams in Fig. 4.17 show results for the relationship between engineering stresses and engineering strains (left) as well as between true stresses and true strains (right) obtained with a linear-elastic material model ($E = 250\ MPa$) and with the proposed strain rate dependent plastic model compared to the data from the uniaxial tensile tests.

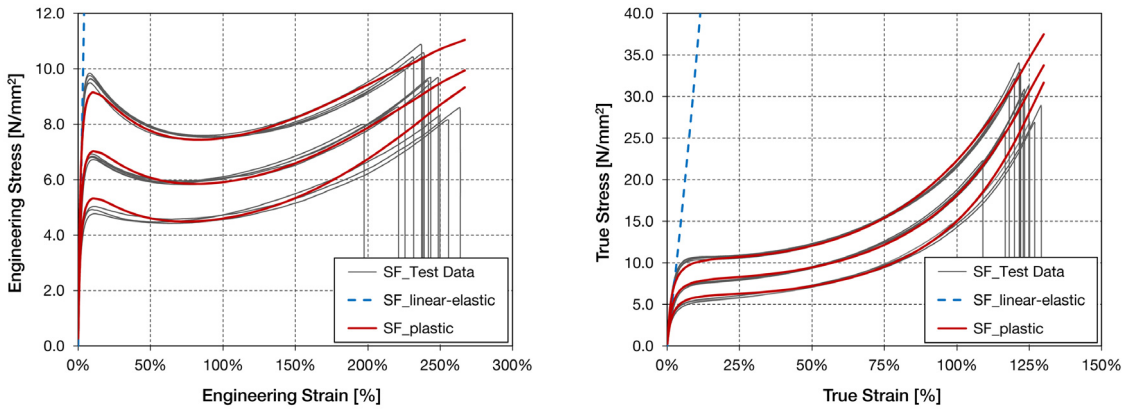

Fig. 4.17 *Uniaxial tensile test data for SikaFast-5221 NT compared to results obtained with a linear-elastic model and the proposed strain rate dependent plastic model*

Firstly, it can be observed that the linear-elastic model predicts the stresses well for low strains in the elastic part. For certain calculations this model might be sufficient. However, for exact predictions of the elastic behaviour, the strain rate dependency of the Young‘s modulus should be investigated. The evaluations provided in [Appendix A] show that the Young‘s modulus increases with higher strain rate. If the decrease in stiffness due to yielding of the adhesive is important for the performed calculations, the linear-elastic model is not suitable anymore. The proposed plastic model shows a good agreement with the test results in both diagrams. It reproduces well especially the hardening of the material. Regarding the size of the yield stress, small discrepancies can be noticed in the diagram with engineering values between the experimental results and the data determined with the proposed model. For a displacement rate of *1 mm/min*, the experimental data are slightly overestimated, while in the case of a displacement rate of *100 mm/min* the opposite is the case. The investigations on a suitable material model for the acrylic adhesive *SikaFast-5221 NT* are included in the journal paper entitled *„Performance of a structural acrylic adhesive for linear glass-metal connections under shear and tensile loading“* (see *[Publication List]* at the end of the thesis).

It can be concluded that for exact calculations with the acrylic adhesive *SikaFast-5221 NT* a model which considers plasticity should be used. With a linear-elastic model it has to be ensured that only load levels which generate elastic stresses are examined. Otherwise an overestimation of stresses and especially a significant underestimation of the strains in the adhesive will be the result. Furthermore, global displacements in the investigated system can be significantly overestimated, if the yielding of the adhesive is not covered by the model applied in the simulation. Since the plasticity properties are based on true stress values, the assumption of a constant Poisson‘s ratio over the whole strain range should be verified for the investigated acrylic in order to exclude the influence of an eventual slight decrease at higher strains.

4.4 Adhesion to metal substrates with different surface finishing

In the case of adhesive joints between two surfaces, three different failure types can occur. Depending on the type and the strength of the used adhesive as well as on the substrate materials and the surface finishing the following cases can be differentiated (see also Fig. 4.18):

- adhesive failure: a peeling of the adhesive from one of the substrate surfaces occurs;
- cohesive failure: the strength of the adhesive is reached and a fracture occurs within the adhesive material;
- substrate failure: the strength of one of the substrate materials is reached and a fracture occurs within one of the substrate materials.

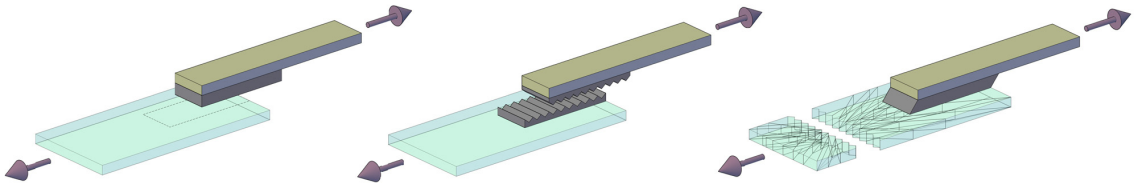

Fig. 4.18 *Failure types of adhesive joints between two surfaces: adhesive failure (left), cohesive failure (middle) and substrate failure (right)*

For structural design purposes an adhesive failure should be avoided due to the difficulty of defining a failure criterium in such a case. Therefore, advanced knowledge and suitable testing procedures are required for the selection of the substrate materials and the processing treatments of their surfaces during the planning of adhesive connections.

In the laboratories of adhesive producers a common test for the qualitative evaluation of surfaces regarding adhesion is a peel test (used especially for silicones as described in [Dow Corning, 2011]). An approximately *200 mm* long, *15 mm* wide and *6 mm* thick strip is applied on the analysed surface in such a way that at least *50 mm* lay over a bond breaking tape. After curing, (usually *24 hours*) the adhesive strip is pulled perpendicular to the substrate surface until failure. To facilitate the pulling a fine mesh can be bonded within the adhesive strip. The procedure is illustrated in Fig. 4.19.

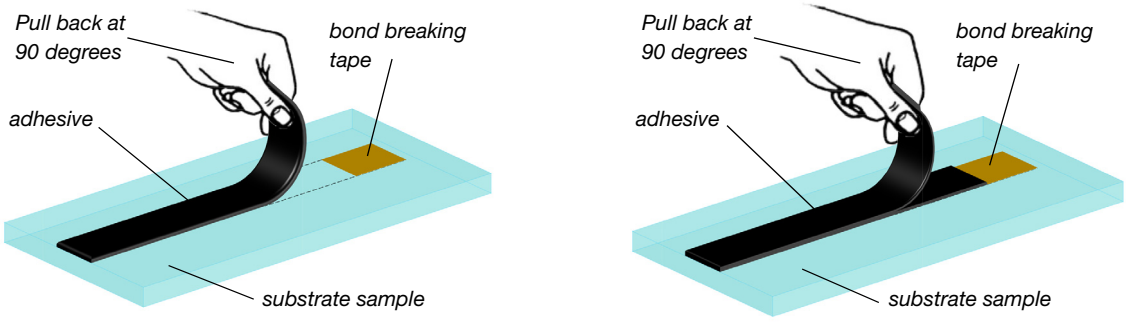

Fig. 4.19 *Sketch of the procedure during a peel test used for the qualitative evaluation of adhesion on given substrates - adhesive failure (left) and cohesive failure (right)*

For the investigated glass-metal facade elements with composite structural behaviour both the surface treatments of the metal framing and of the glass panes can vary and are of importance for the adhesion properties. In the case of the glass pane, coatings for improving the solar energy transmittance or the luminous transmittance can have an influence on the adhesion. For the metal components, steel with corrosion protection, stainless steel or aluminium can be used. Additional to possible coatings, a high influence on the adhesion is provided by the roughness of the surface, which can be controlled by using different mechanical treatments. The investigations discussed within this subchapter focus on the influence of different surface finishings of stainless steel and aluminium on the adhesion of the three selected adhesives to these substrates. The chosen testing procedure is a double-lap shear test. The specimen geometry, the support conditions and the load application are illustrated in Fig. 4.20. A detailed description of the test procedure is provided in subchapter 4.4.3.

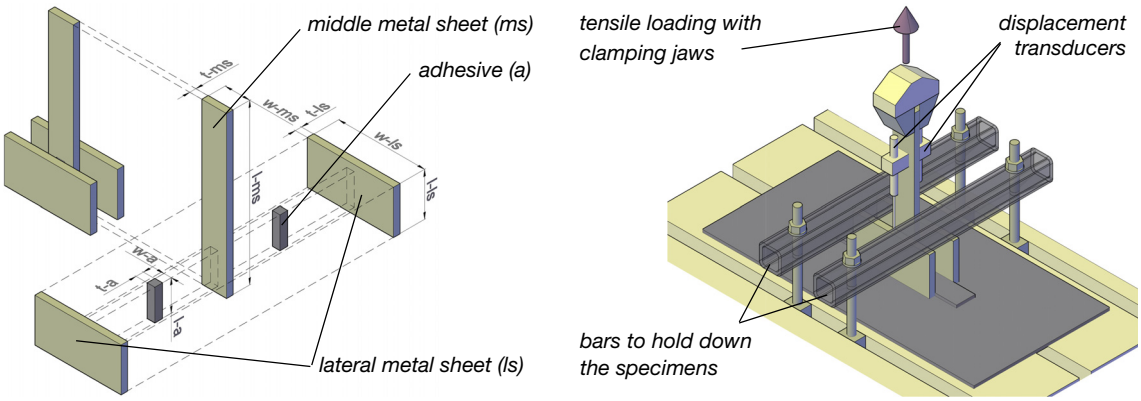

Fig. 4.20 *Explosion sketch of the test specimen (left) and planned test setup (right)*

4.4.1 Substrate materials and surface finishings

The main consideration during the material selection process is to choose metals which are generally used in facade constructions. These are mainly stainless steels and aluminiums with varying composition depending on the given requirements. Another interesting materials category, especially considering the forming possibilities and the lower thermal conductivity, are fibre reinforced plastics. Since the focus of this research is on glass-metal facade elements, the investigations are limited to stainless steel and aluminium.

In the case of the stainless steel the material no. *1.4404* with the short name *X2CrNiMo 17-12-2* is chosen. Additional to the untreated finish, grinded surfaces with different corn sizes are investigated. The chosen aluminium is the material no. *3.3206* with the short name *EN AW 6060 T66 (AlMgSi 0.5)*. Additional to the untreated finish, anodised surfaces and powder-coated surfaces are investigated. A highly weather-proof powder-coating on polyester basis is used (see [Tiger Drylac, 2016]). An overview of all experimentally tested surfaces is provided in Tab. 4.7. All the metal substrate sheets are made of cold-rolled flat bars.

Two different geometries of the adhesive joints are tested. The first one with a cross section of *12 mm x 12 mm* and a length of *50 mm* is chosen based on the H-sample proposed in [ETAG 002, 2001] for linear joints. For the second geometry the thickness of *12 mm* and the length of

50 mm are kept constant, while the width is increased to *60 mm* to obtain an adhesion surface five times larger than in the case of the first geometry. The objective is to observe if a complete curing and a good adhesion are obtained as well for a more laminar joint. For the second configuration only one surface finishing is investigated for each material. In the case of the acrylic the thickness of the adhesive is reduced to *3 mm*.

Tab. 4.7 *Investigated surface finishings and number of test specimens for adhesive joints on stainless steel and aluminium*

Material and surface finishing		**Number of test specimens and denomination**		
		Dow Corning 993	**Sikasil SG-550**	**SikaFast-5221 NT**
stainless steel no. 1.4404				
untreated		3 (mss_015-017)	3 (mss_079-081)	3 (mss_111-113)
grinded P50		3 (mss_012-014)	3 (mss_076-078)	3 (mss_108-110)
grinded P80		3 (mss_009-011)	3 (mss_073-075)	3 (mss_105-107)
grinded P150		3 (mss_006-008)	3 (mss_070-072)	3 (mss_102-104)
grinded P300	geometry 1	5 (mss_001-005)	5 (mss_065-069)	5 (mss_097-101)
	geometry 2	3 (mss_018-020)	3 (mss_082-084)	3 (mss_114-116)
aluminium no. 3.3206				
untreated		3 (mss_027-029)	3 (mss_091-093)	3 (mss_123-125)
powder-coated		3 (mss_024-026)	3 (mss_088-090)	3 (mss_120-122)
anodised	geometry 1	3 (mss_021-023)	3 (mss_085-087)	3 (mss_117-119)
	geometry 2	3 (mss_030-032)	3 (mss_094-096)	3 (mss_126-128)
Total number		32 specimens per adhesive --> 96 test specimens		

Before manufacturing the test specimens, the roughness of the differently treated surfaces is measured with a stylus instrument (*Mitutoyo SJ-201*). This device has a diamond stylus and scans the surface by contact over a predefined profile length with a predefined speed. The length of the measured distance and the speed are determined depending on the expected roughness. For the investigated surfaces a speed of *0.5 mm/sec* and a measuring length of *5 x 2.5 mm* are used.

To describe the roughness of a surface, profile roughness parameters, which provide a linear characterization, and surface roughness parameters, which allow more significant values, can be used. Two of the more important and most widely used roughness parameters are the arithmetic average of the absolute values R_a and the average distance between the highest peak and the lowest valley in each sampling length R_z (see also [Whitehouse, 2004]). These two values are measured and evaluated for the investigated metal surfaces.

The value R_a is the arithmetic average of the absolute values for the distance between the actual profile and the mean profile and can be calculated with (Eq. 4.39). The sketch in Fig. 4.21, left, explains the determination of the values y_i.

$$R_a = \frac{1}{L} \cdot \int_0^1 |y_i| \cdot dx \qquad \text{(Eq. 4.39)}$$

The value R_z is the arithmetic average between the roughness depths Z_i of five equidistant consecutive measured distances L_i. The roughness depth Z_i is the distance between two parallels to the mean line, which touch the actual profile within the measured distance L_i at the highest and, respectively, at the lowest point. The value R_z can be calculated with (Eq. 4.40). The values Z_i should be determined according to Fig. 4.21, right.

$$R_z = \frac{1}{5} \cdot (Z_1 + Z_2 + Z_3 + Z_4 + Z_5) \qquad \text{(Eq. 4.40)}$$

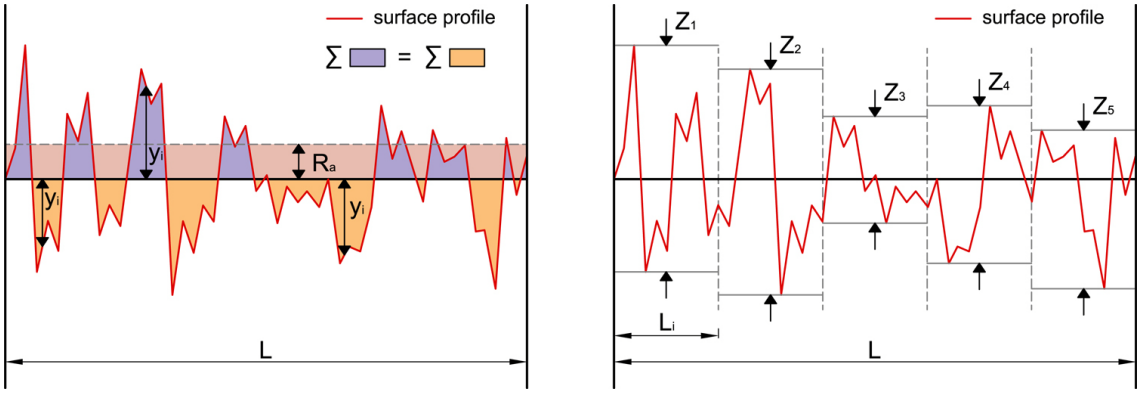

Fig. 4.21 *Determination of the roughness parameters R_a (left) and R_z (right) within the measured distance L*

For each metal sheet the roughness over one significant profile is measured. The position of this profile is chosen to be located in the area of adhesion. The direction of the measurement is perpendicular to the grinding grooves. Fig. 4.22 shows the mean values and the deviation range of the measured roughness parameters R_a and R_z, respectively, for the different types of stainless steel and aluminium surfaces. The mean values are in a good agreement with the expected tendency; for the stainless steel surfaces the roughness parameters are decreasing with smaller corn size used for grinding.

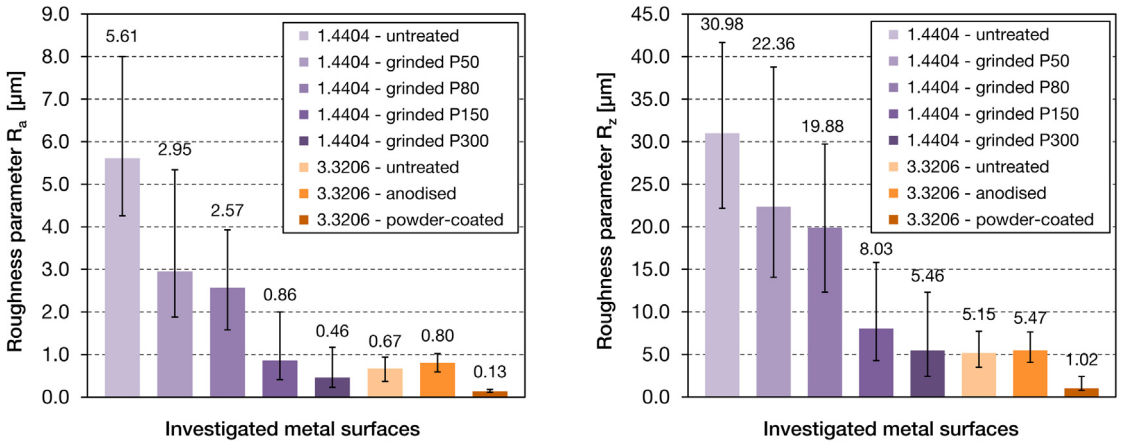

Fig. 4.22 *Mean values and deviation range of the profile roughness parameters R_a [µm] (left) and R_z [µm] (right) for the different investigated stainless steel and aluminium surfaces*

Despite this appropriate tendency, a certain variation of the measured values can be observed. Roughness parameters of different type of surfaces reach similar values in particular cases. To illustrate this, the normal distributions of the measured roughness parameters R_a and R_z for the different stainless steel surfaces are plotted in Fig. 4.23. Beside the measured values represented by diamond symbols, the *5%-fractile* and the *95%-fractile* are illustrated with red vertical lines. The higher and the narrower the Gauss-curve is, the smaller is the variation of the measured roughness parameters for the specific surface type.

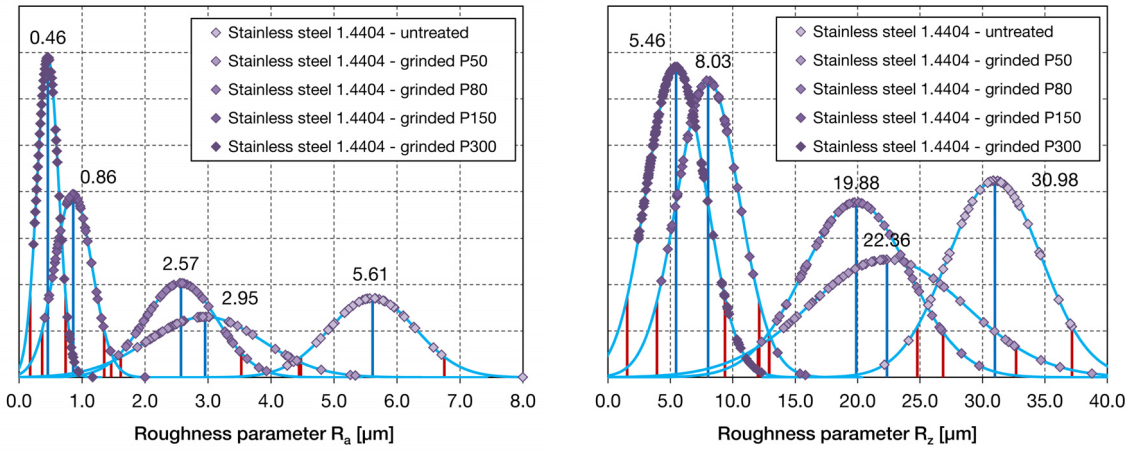

Fig. 4.23 *Normal distribution of the measured values for the profile roughness parameters R_a [µm] (left) and R_z [µm] (right) for the investigated stainless steel surfaces*

For stainless steel surfaces, producers of structural silicone adhesives generally recommend a roughness parameter R_a of maximum *3 µm*. The measured and evaluated roughness parameters of the investigated stainless steel surfaces show values higher than *3 µm* for the untreated as well as for the grinded surfaces with corn size *P50* and *P80* (see Fig. 4.22, left). In the case of the aluminium surfaces, roughness parameter values R_a lower than *1 µm* are measured for all three treatments. The smoothest surfaces are achieved by powder-coating.

4.4.2 Manufacturing of the test specimens

The manufacturing process of the specimens is performed in the laboratories of the adhesive producers in Seneffe, Belgium (*Dow Corning Europe S.A.*), and in Widen, Switzerland (*Sika Services AG*), with the support of the laboratory staff and based on their advices.

The decision to design specimens to be tested in double-lap shear resulted from the intention to avoid a rotation of the substrates and implicitly of the adhesive joint during the pulling. By using a test specimen which is symmetric to the plane of the loading, an occurring rotation can be reduced considerably. Small rotations can still occur due to manufacturing tolerances. The size of the lateral metal sheets is chosen in order to allow an appropriate bearing of the specimens. The length of the middle metal sheet is necessary due to the required clamping distance and the span needed for fixing displacement transducers. The dimensions of the middle and the lateral metal sheets for both investigated joint geometries are summarized in Tab. 4.8. The notations of the different dimensions are made according to Fig. 4.20.

The manufacturing concept for the two tested geometries is shown by the sketches in Fig. 4.24 and Fig. 4.25. The test specimens with adhesive joints with geometry 1 (*50 mm x 12 mm x 12 mm*) are manufactured in a lying position (rotated by *90°*) to achieve a smaller depth of the gap during the adhesive application. The test specimens with geometry 2 are manufactured in a standing position, the same position as the one during the testing.

Tab. 4.8 *Dimensions of the metal sheets for the two investigated joint geometries*

Dimension [mm]	Middle metal sheet			Lateral metal sheet		
	Notation	Geometry 1	Geometry 2	Notation	Geometry 1	Geometry 2
length	l-ms	260	260	l-ls	140	180
width	w-ms	40	80	w-ls	70	70
thickness	t-ms	10	10	t-ls	10	10

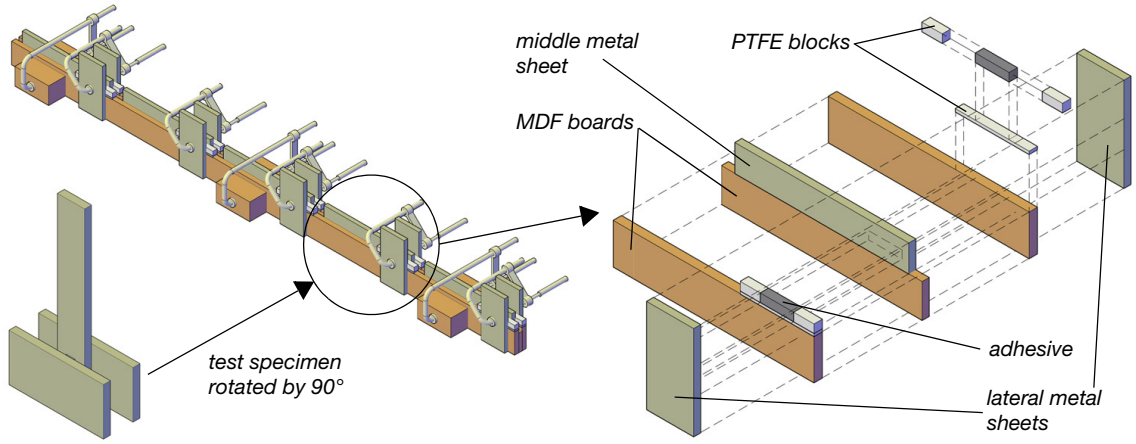

Fig. 4.24 *Manufacturing concept for the adhesion test specimens with geometry 1*

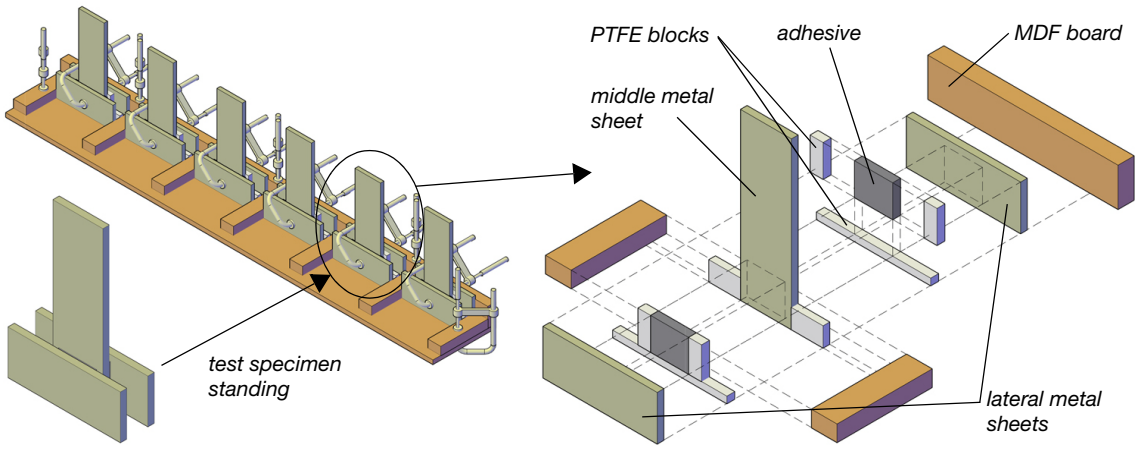

Fig. 4.25 *Manufacturing concept for the adhesion test specimens with geometry 2*

For both geometries the following steps are performed during manufacturing:

- taping of the metal sheets: a PTFE tape is applied on the metal sheets to delimit the adhesion area in order to have a clean edge of the adhesive joint after removing the tape;
- cleaning the adhesion area of the metal surfaces: to remove the dust and especially the residual grease remained from production and finishing on the surfaces, special cleaners are wiped over with a clean industrial paper; for the Dow Corning silicone the universal cleaner *Dow Corning® R-40* [Dow Corning R40, 2012] is used, while for the silicone and the acrylic from Sika the product *Sika® Cleaner P* [Sika Cleaner P, 2015] is applied;
- application of primer: to increase the adhesive strength a primer is wiped over the surfaces with a clean industrial paper before applying the adhesive; for the Dow Corning silicone the product *Dow Corning® 1200 OS* [Dow Corning 1200 OS, 2012] is used, while for the Sika silicone the product *Sika® Aktivator-205* [Sika Aktivator-205, 2010] and for the Sika acrylic the product *Sika® ADPrep* [Sika ADPrep, 2013] are applied;
- assembling of the metal sheets: the metal sheets are fixed between medium density fibreboards (MDF boards) together with polytetrafluorethylene (PTFE) blocks to ensure a predefined joint thickness; screw clamps are used to hold all the components together;
- application of the adhesive: different mixers and application guns are used for the different adhesives and are explained later in this subchapter;
- tooling and removing of the tapes: the surface of the adhesive joints is straightened with a spatula to achieve a smooth finish and the tapes are torn off before curing;
- removing of the PTFE blocks: if possible, the PTFE blocks are removed before curing to allow an eventual small shrinkage of the adhesive joint during the curing process (this may occur especially in the case of the acrylic).

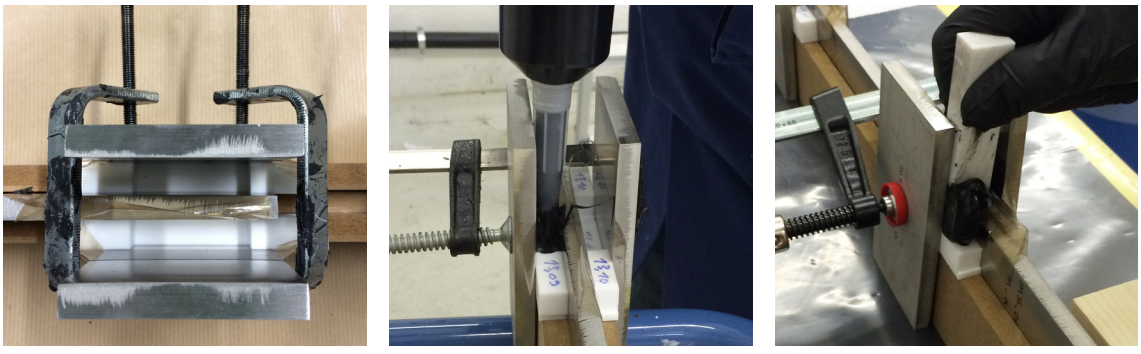

Fig. 4.26 *Application of the silicone adhesives into the defined gap for the double-lap metal-metal test specimens tested under shear loading*

As mentioned in the enumeration of the performed steps, the application of the adhesives shows some differences between the three investigated products. In the case of the two silicones the metal sheets are first fixed together and the adhesive is applied afterwards in the

resulting gap as shown in Fig. 4.26. For both silicones a dynamic mixer is used to mix and to apply the adhesive into the formed gaps.

The application procedure for the adhesive *SikaFast-5221-NT* is different from the one for the silicones. Because of the smaller thickness of just *3 mm* compared to the *12 mm* thick gap in the case of the silicones, it is not possible to fill the gap after the metal sheets are fixed together. Therefore, after cleaning and priming of the metal surfaces, the PTFE blocks which determine the thickness are fixed with tape to one of the metal sheets (in the case of geometry 1 to the middle sheet) as shown in Fig. 4.27, left. Then, an adhesive stripe is applied with a static mixer on the metal sheet as illustrated in Fig. 4.27, right. Afterwards, the second metal sheet (in the case of geometry 1 both lateral sheets) are pressed on the stripe and fixed with screw clamps. Finally, the adhesive joint is tooled with a spatula, the tapes are torn off and, after the fixture time, the PTFE blocks are removed.

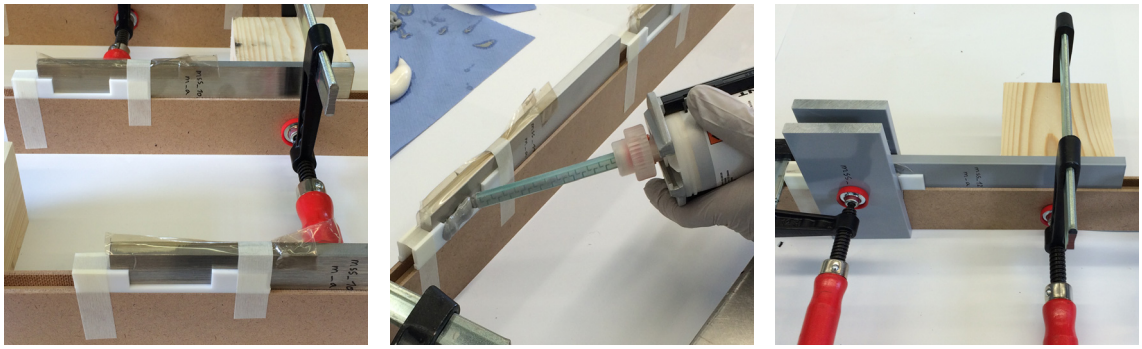

Fig. 4.27 *Application of the acrylic adhesive on the defined surface and fixing of the double-lap metal-metal test specimens tested under shear loading*

Since the dimensions of the adhesive bite have an influence on the mechanical behaviour of the joint, the real values are measured for all specimens before testing. Deviations up to *~2 mm* can be observed. The measured values for each specimen as well as mean values are provided in [Appendix B].

4.4.3 Test setup and test procedure

In previous experimental research on shear properties of adhesives a single-lap test setup is often used. It could be observed that it is difficult to measure the rotation occurring due to the different axes of the load and of the reaction force as well as due to the non-symmetrical setup. Therefore, the chosen test procedure for investigating the adhesion on different metal surfaces within this thesis is a double-lap-shear test. The symmetrical arrangement allows to avoid peel stresses and undesired bending moments. Before testing, all the specimens are stored in a climatic chamber at *23 °C* and *50%* relative humidity for *28 days*. Furthermore, all the tests are performed at the same temperature and relative humidity conditions.

The test setups for both geometries are identical and are illustrated in Fig. 4.28, left, for a specimen with silicone adhesive and geometry 1 and in Fig. 4.28, right, for a specimen with acrylic adhesive and geometry 2. In a first step, two displacement transducers are fixed on the cured specimens to measure the deformation of the two adhesive joints in order to capture an eventual asymmetric movement. The used displacement transducers are able to measure a deformation up to around *12 mm*. Afterwards, the specimens are firstly centred and fixed with the clamping jaws and secondly hold down with two hollow-section steel profiles. In this way an unwanted deformation of the adhesive before testing is avoided. The two steel profiles are dimensioned in order to have only small deformations due to bending (in the case of the acrylic, square bars are used). Moreover, the transducers measure the displacements between the middle metal sheet and the lateral metal sheet, without including the deformation of the steel bars.

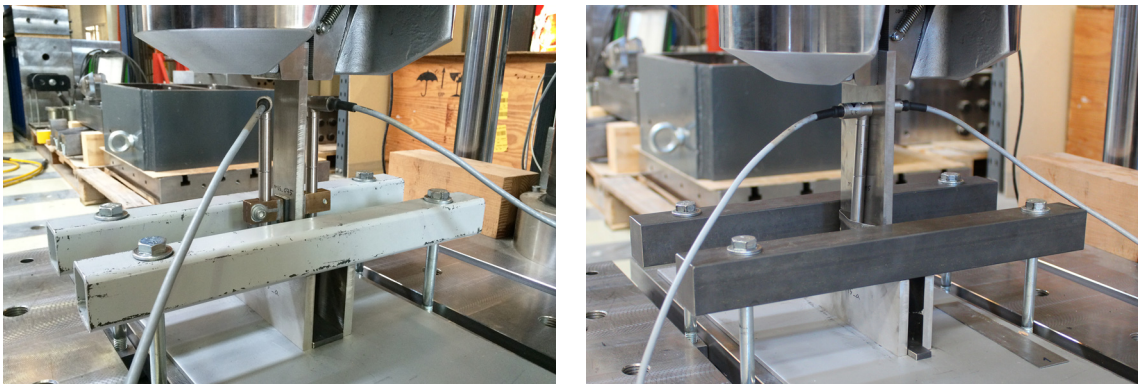

Fig. 4.28 *Double-lap shear test setup to investigate the adhesion on different metal substrates for a specimen with silicone adhesive and geometry 1 (left) and for a specimen with acrylic adhesive and geometry 2 (right)*

After fixing the specimens, the tests are performed displacement controlled on a universal testing machine *Messphysik BETA1000* with a loading speed of *5 mm/min* for *Dow Corning 993* and *Sikasil SG-550* and *2 mm/min* for *SikaFast-5221 NT*. The speed for the silicones is chosen according to the recommendations in [ETAG 002, 2001] for H-shaped specimens tested in tension or shear. For the acrylic a smaller value is chosen for the loading speed because of the thinner adhesive bite. In addition to the two displacements measured with the transducers, the applied force is measured with the load cell and the displacement of the machine including all the deformations of the test setup is recorded.

4.4.4 Failure pattern evaluation for the adhesives

Two types of test results obtained from the performed double-lap shear tests are discussed. First, the failure patterns of the adhesive joints in relation to the measured roughness parameters are evaluated in this subchapter. In a second step, the mechanical properties of the adhesives are analysed in subchapter 4.4.5 based on the relation between stresses and strains derived from the measured test data.

All the tested specimens with silicone adhesives show a cohesive failure, independent on the different substrate surface treatment. However, the crack propagation through the joint differs between specimens with *Dow Corning 993* and specimens with *Sikasil SG-550*. In both cases the crack is initiated in the adhesive near one of the substrate surfaces, but for the joints with *Dow Corning 993* the crack propagates more or less diagonally through their whole thickness (see Fig. 4.29), while for the joints with *Sikasil SG-550* the crack propagation is parallel to the surface where it is initiated (see Fig. 4.30).

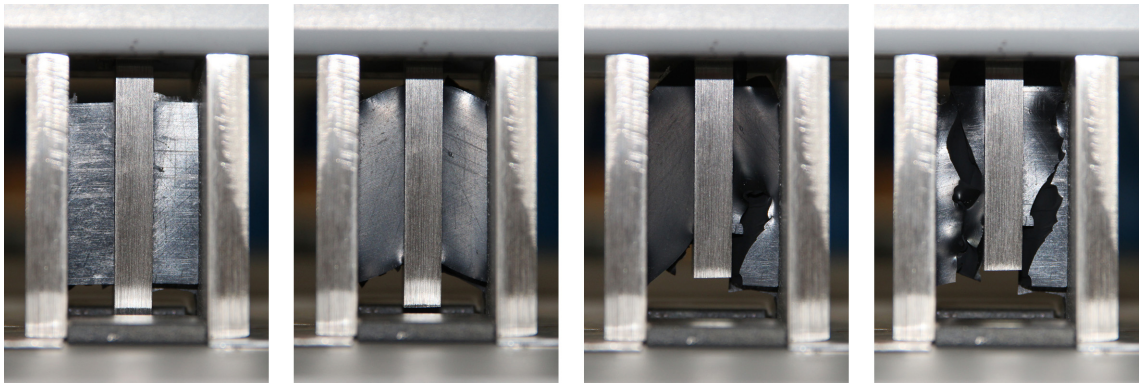

Fig. 4.29 *Test specimen with the adhesive Dow Corning 993 in different stages during the double-lap-shear test*

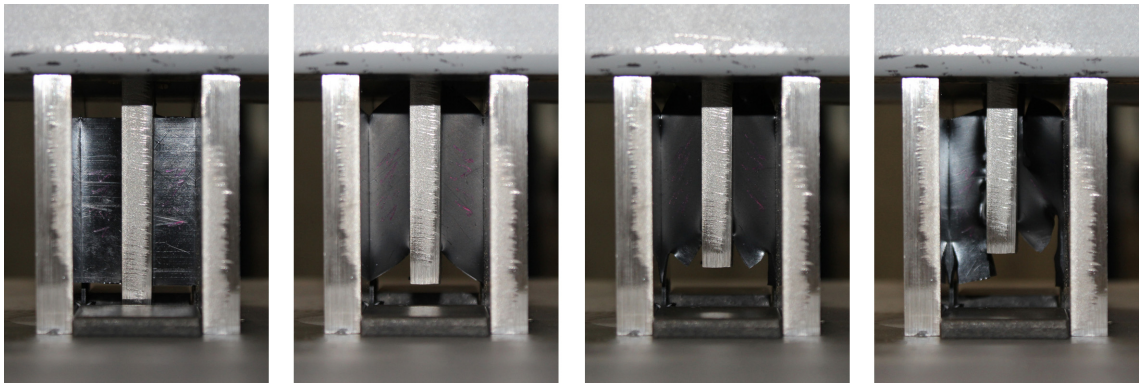

Fig. 4.30 *Test specimen with the adhesive Sikasil SG-550 in different stages during the double-lap-shear test*

Fig. 4.31 shows typical failure patterns for selected specimens with *Dow Corning 993* and geometry 1. Both the untreated stainless steel and aluminium surfaces as well as the grinded stainless steel surface with P300 and the anodised aluminium surface are selected. It can be

observed that the crack runs diagonal over the cross section and a wave-like pattern can be noticed perpendicular to the loading direction. The crack initiation is observed to be located in the adhesive near one of the substrate surfaces. These are the zones where peak stresses occur because of the connection to the stiff substrate components. The crack propagates for most specimens towards the opposite substrate surface and approximately equal amounts of adhesive remain on both substrate surfaces after total rupture. Pictures of the failure patterns for all the specimens can be found in [Appendix B].

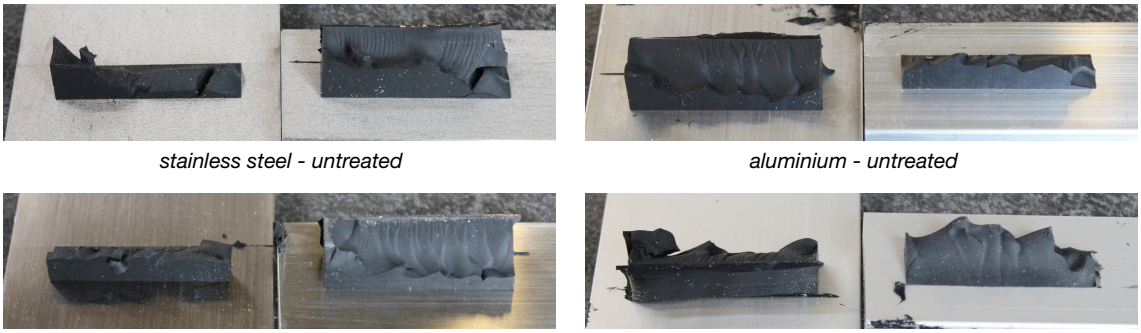

stainless steel - untreated *aluminium - untreated*

stainless steel - grinded P300 *aluminium - anodised*

Fig. 4.31 *Typical failure patterns for selected Dow Corning 993 specimens with geometry 1*

Fig. 4.32 illustrates typical failure patterns for the specimens with *Dow Corning 993* and geometry 2. The crack progress is more irregular than in the case of the specimens with geometry 1, but similar wave-like patterns can be noticed.

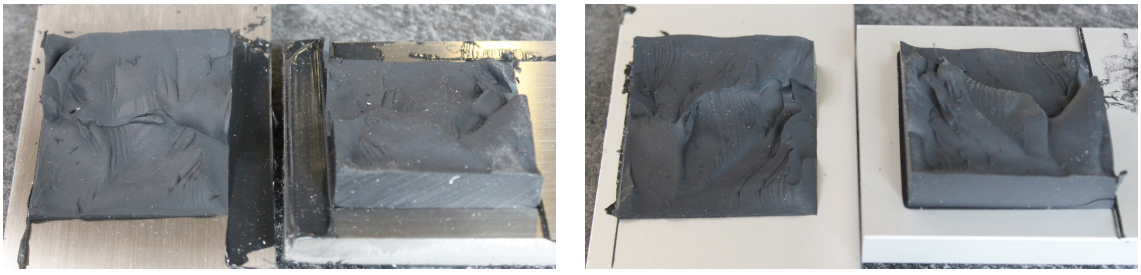

stainless steel - grinded P300 *aluminium - anodised*

Fig. 4.32 *Typical failure patterns for the Dow Corning 993 specimens with geometry 2*

In the case of the stiffer material *Sikasil SG-550* the position of the crack initiation is located as well in the adhesive near one of the substrate surfaces, but the cracks propagate parallel to these surfaces. As a result, only a thin layer of adhesive remains on one of the substrates, as it can be noticed from the examples in Fig. 4.33. A wave-like pattern perpendicular to the loading direction can be observed for some specimens, but not as explicit as for the specimens with *Dow Corning 993*. Failure patterns for all the specimens can be found in [Appendix B].

Fig. 4.34 illustrates typical failure patterns for the specimens with *Sikasil SG-550* and geometry 2. For some of the specimens crack propagations parallel to the substrate surfaces can be noticed over parts of the failure patterns.

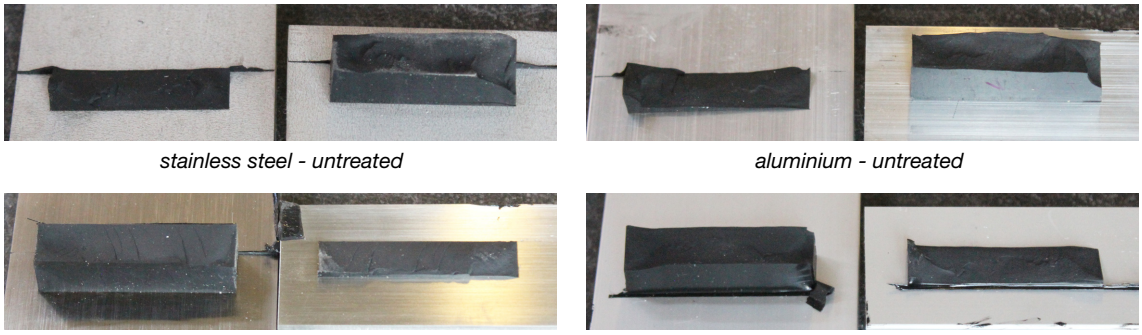

stainless steel - untreated *aluminium - untreated*

stainless steel - grinded P300 *aluminium - anodised*

Fig. 4.33 *Typical failure patterns for selected Sikasil SG-550 specimens with geometry 1*

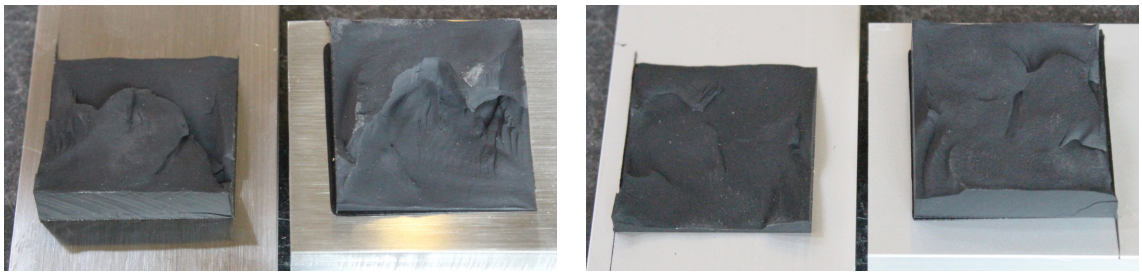

stainless steel - grinded P300 *aluminium - anodised*

Fig. 4.34 *Typical failure patterns for the Sikasil SG-550 specimens with geometry 2*

The specimens with *SikaFast-5221 NT* show different failure modes including adhesive failure, cohesive failure and mixed failure. Independent on the final failure mode, the initial cracks occur within the adhesive joint as illustrated in Fig. 4.35.

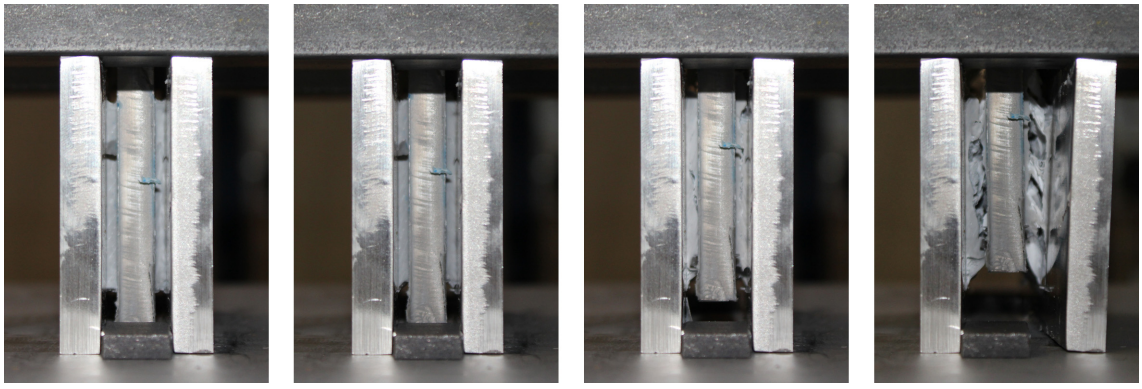

Fig. 4.35 *Test specimen with the adhesive SikaFast-5221 NT in different stages during the double-lap-shear test*

Typical failure patterns for the specimens with geometry 1 and selected surfaces are illustrated in Fig. 4.36. It can be observed that for the stainless steel substrates with untreated surfaces an adhesive failure occurrs, while for the grinded surfaces with corn size P300 cohesive or mixed failure is obtained. For the aluminium substrates only for part of the anodised surfaces a mixed failure is obtained, while for the untreated and the powder-coated surfaces adhesive failure is

noticed. The failure patterns of all specimens can be found in [Appendix B]. Fig. 4.37 illustrates typical failure patterns for the specimens with *SikaFast-5221 NT* and geometry 2. While for all specimens with stainless steel surfaces cohesive failure is obtained, for the specimens with anodised aluminium surfaces cohesive and mixed failure are noticed.

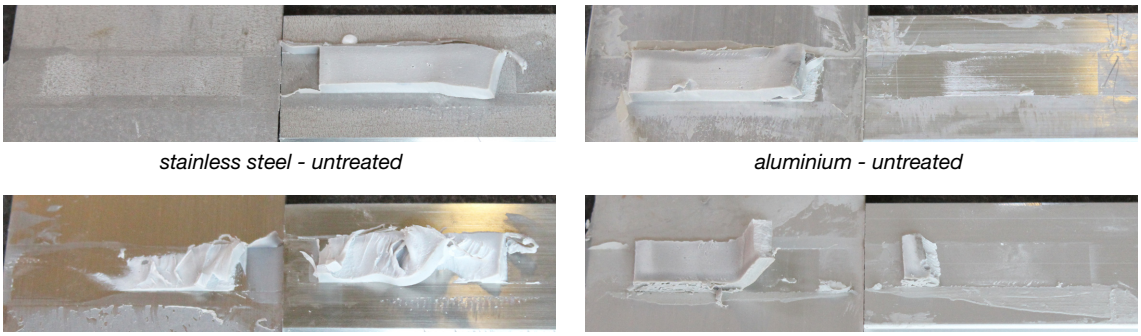

stainless steel - untreated *aluminium - untreated*

stainless steel - grinded P300 *aluminium - anodised*

Fig. 4.36 *Typical failure patterns for selected SikaFast-5221 NT specimens with geometry 1*

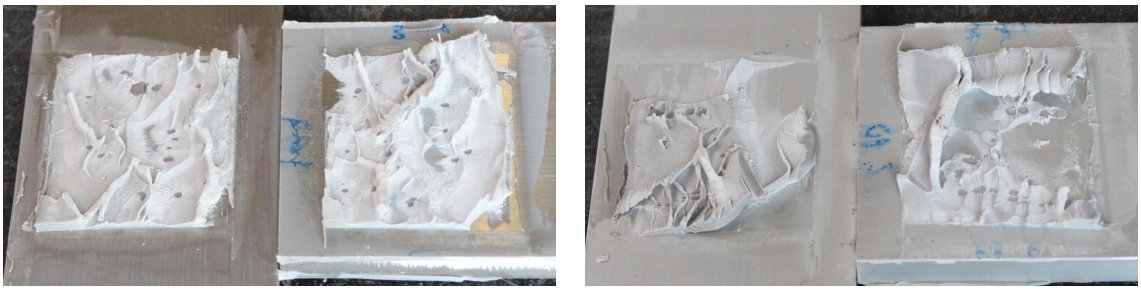

stainless steel - grinded P300 *aluminium - anodised*

Fig. 4.37 *Typical failure patterns for the SikaFast-5221 NT specimens with geometry 2*

4.4.5 Evaluation of the mechanical properties

To evaluate the mechanical properties the recorded forces and displacements are transformed to stresses and elongations by considering the original dimensions of the adhesive joint. The occurring shear stresses τ are calculated by (Eq. 4.41) according to [ETAG 002, 2001], where F is the recorded force and $w_{a,i}$ and $l_{a,i}$ are the width and the length of the adhesive joints for the two sides of the double-lap shear test specimens.

$$\tau = \frac{F}{w_{a,1} \cdot l_{a,1} + w_{a,2} \cdot l_{a,2}} \qquad \text{(Eq. 4.41)}$$

The elongations are determined as shear displacements d by (Eq. 4.42) according to [ETAG 002, 2001], where Δl is the extension and $t_{a,i}$ are the thicknesses of the adhesive for the two sides.

$$d = \tan^{-1}\gamma = \frac{\Delta l}{(t_{a,1} + t_{a,2})/2} \qquad \text{(Eq. 4.42)}$$

The relationships between engineering stresses and shear displacements are illustrated for representative test specimens in Fig. 4.38. The left diagram includes for each of the two investigated silicones one curve from a specimen with joint geometry 1 and one curve from a specimen with joint geometry 2. For the acrylic a different range is chosen for both the x-axis and the y-axis because of the higher reached values. For the x-axis a ten times higher range is chosen, while for the y-axis the range is only two times higher. One stress versus shear displacement curve from specimens with the acrylic adhesive is plotted for each of the two investigated joint geometries in the right diagram. Additionally, the curves for the silicones are plotted in grey for comparison. Diagrams with the relationship between engineering stresses and shear displacements from each specimen can be found grouped by test series in [Appendix B].

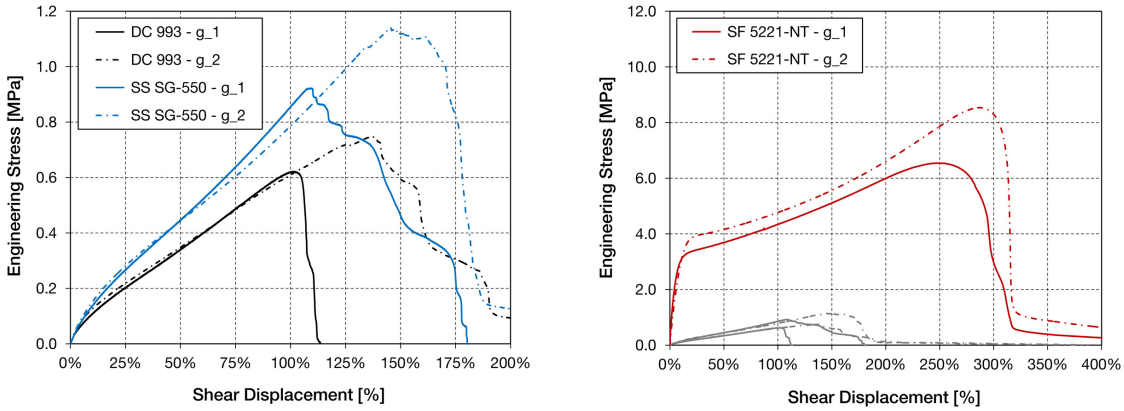

Fig. 4.38 *Representative test results obtained for the double-lap shear test specimens with the silicone adhesives (left) and with the acrylic adhesive (right)*

The stress vs. shear displacement relationships show a good consistency for the mechanical behaviour of each of the three adhesives for both geometries. Especially the stiffness shows only small variations among the specimens with the same adhesive and geometry. This is also the reason why only representative curves are plotted in Fig. 4.38. In the case of failure stresses higher deviations to the mean values are occurring, especially for the specimens with geometry 1 (see [Appendix B]).

In Tab. 4.9 the mean shear stresses at *5%*, *15%* and *25%* shear displacement as well as the failure stresses are specified, categorized by adhesive and size of the joint. Additionally, the mean maximum reached loads and the elongations for these loads are listed. Detailed values for the different specimens and series can be found in [Appendix B]. The values summarized in Tab. 4.9 together with the diagrams in Fig. 4.38 allow a good comparison of the three investigated adhesives. By comparing the stresses at the different elongations for the two silicones, it can be noticed that *Sikasil SG-550* shows the higher stiffness and failure stresses. The acrylic *Sikafast-5221 NT* shows significantly higher stiffness and stresses compared to the silicones.

By comparing the failure stresses of the specimens with geometry 1 with those of the specimens with geometry 2 for each adhesive separately, it can be noticed that for geometry 2 higher stresses are reached. This is due to the larger adhesion surface which results in a smaller influence of the resulting stress peaks at the substrate interfaces. Although *Sikasil SG-550* shows

the higher stiffness and failure stress from the two silicones, before selecting an adhesive for a task, the manufacturing and the application of the adhesives should be considered as well. During the assembly of the specimens for the investigations presented in subchapter 4.4 the silicone *Dow Corning 993* showed a more convenient handling than *Sikasil SG-550* mainly because of its lower viscosity.

Tab. 4.9 *Mean values of the shear stress at different shear displacements (strains), maximum load and corresponding elongation depending on the adhesive and the size of the joint*

Adhesive	**Size**	**Stress at 5% strain** [MPa]	**Stress at 15% strain** [MPa]	**Stress at 25% strain** [MPa]	**Failure stress** [MPa]	**Max. load** [kN]	**Elongation at max. load** [mm]
Dow Corning 993	small	0.07	0.14	0.20	0.55	0.72	11.8
	large	0.08	0.16	0.22	0.74	4.48	16.7
Sikasil SG-550	small	0.08	0.19	0.28	0.90	1.13	14.9
	large	0.09	0.20	0.28	1.10	6.50	18.7
Sikafast-5221 NT	small	2.12	3.18	3.33	6.64	8.60	7.1
	large	1.67	3.38	3.83	8.47	50.13	7.9

4.4.6 General conclusions on the adhesion tests and outlook

The main objective of the adhesion tests has been to investigate the influence of stainless steel and aluminium surfaces with different finishing on the failure type of the selected adhesives. A significant aspect for the general evaluation are the temperature and humidity conditions used during testing (*23 °C* and *50%* relative humidity) as well as the curing procedure. The obtained results are only valid for these boundary conditions.

For the specimens with both silicones, no dependency on the roughness of the stainless steel surfaces grinded with different corn sizes is observed. All the specimens fail cohesively within the adhesive joint. Furthermore, also the specimens with differently finished aluminium surfaces show only cohesive failures. However, an extension of the experimental programme with the same type of specimens tested at high temperatures as well as a series with specimens cured under higher moisture conditions would be important in order to provide a more complete evaluation.

In the case of the specimens with acrylic adhesive, different failure modes are observed. For all the small specimens with aluminium surfaces and rougher grinded stainless steel surfaces an adhesive failure occurs. For the small specimens with finer grinded stainless steel surfaces (P150 and P300) combined and cohesive failure modes are noticed. In the case of the larger specimens, cohesive failure occurs for the stainless steel surfaces, while a combined failure is observed for the aluminium surfaces. For practice it is important to specify that all the failures, independent of the type, occur far after the acrylic started to yield. Also in the case of the acrylic adhesive, an extension of the experimental programme for higher temperatures during testing as well as for specimens cured in moisture conditions is recommended.

5 Mechanical behaviour of adhesive joints between glass and stainless steel

Investigation procedure and experimental programme
Linear adhesive joints at the glass surface
Linear adhesive joints at the edge of laminated glass panes
Evaluation of the results on adhesive joints

1 Introduction 1

2 State of the art – theoretical framework

3 Transparent building envelopes with composite structural behaviour

4 Investigations on adhesives and their adhesion to metal substrates

5 Mechanical behaviour of adhesive joints between glass and stainless steel

6 Experimental investigations on large-scale multi-component elements

7 Finite element investigations on large-scale multi-component elements

8 Approaches for structural and functional design

9 Conclusions and future research

5.1 Investigation procedure and experimental programme

In this subchapter investigations on linear adhesive joints with different geometry between glass and stainless steel are presented. The position of the joints at the glass surface or at the edge of laminated glass as well as the selected cross section geometries of the joints are chosen based on the load transfer concepts within one element with composite structural behaviour which are introduced in subchapter 3.5.1. The investigation procedure consists of an extensive experimental programme and concomitant finite element simulations of the performed tests.

The experimental programme includes joints between stainless steel and glass with the three selected adhesives at the glass surface and at edge of laminated glass under different loading types. A summarized overview of the whole programme, showing the tested geometries, the selected adhesives, the different loading types, the number of tested specimens for each series and the denomination of the test specimens, is given in Tab. 5.1. For the joints at the glass surface the performance of the joints under tensile and under shear loading is investigated, while the joints at the edge of laminated glass are loaded by tensile, compressive and shear loads.

Tab. 5.1 *Overview of the experimental programme for different linear adhesive joints between glass and stainless steel*

Test setup / adhesive geometry	**Loading type**	**Number of test specimens and denomination**		
		Dow Corning 993	**Sikasil SG-550**	**SikaFast-5221 NT**
rectangular linear joint between stainless steel and glass surface	tension	24 (rst_46-69)	24 (rst_22-45)	21 (rst_01-21)
	shear	12 (rss_22-33)	12 (rss_10-21)	9 (rss_01-09)
rectangular linear joint between stainless steel and laminated glass edge	tension	3 (ret_07-09)	3 (ret_04-06)	3 (ret_01-03)
	compression	3 (rec_07-09)	3 (rec_04-06)	3 (rec_01-03)
	shear	3 (res_07-09)	3 (res_04-06)	3 (res_01-03)
L-shaped linear joint between stainless steel and laminated glass edge	tension	3 (let_07-09)	3 let_04-06)	3 (let_01-03)
	compression	3 (lec_07-09)	3 (lec_04-06)	3 (lec_01-03)
	shear	3 les_07-09)	3 (les_04-06)	3 (les_01-03)
U-shaped linear joint between stainless steel and laminated glass edge	tension	3 (uet_07-09)	3 (uet_04-06)	3 (uet_01-03)
	compression	3 (uec_07-09)	3 (uec_04-06)	3 (uec_01-03)
	shear	3 (ues_07-09)	3 (ues_04-06)	3 (ues_01-03)

An overview of the different test specimens is illustrated by sketches in Fig. 5.1. Additionally, the dimensions of the specimens are given and the abbreviations used to name the test series are explained (e.g. ***rst*** stands for **r**ectangular **s**urface **t**ension and specifies the cross section geometry of the adhesive joint, the position of the joint on the glass pane and the type of applied loading).

All the tests are performed displacement-controlled on the same universal testing machine *BETA 1000* used for the double-lap shear adhesion tests. The relative displacements between the stainless steel components and the glass panes are measured with inductive displacement transducers up to *~20 mm*.

Linear adhesive joints at the glass surface

Rectangular joints tested under tensile loading

length: 50 / 100 / 200 mm

width: 10 / 20 / 30 mm

thickness:
- silicones: 6 / 12 / 18 mm
- acrylic: 3 / 6 mm

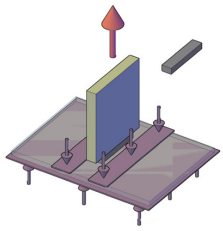

rst - *rectangular surface tension*

Rectangular joints tested under shear loading

length: 100 mm

width: 20 mm

thickness:
- silicones: 6 / 12 / 18 mm
- acrylic: 3 / 6 mm

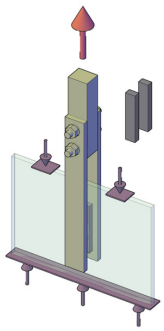

rss - *rectangular surface shear*

Linear adhesive joints at the edge of laminated glass

Rectangular joints tested under tensile, compressive and shear loading

length: 100 mm

width: 21.5 mm

thickness:
- silicones: 6 mm
- acrylic: 3 mm

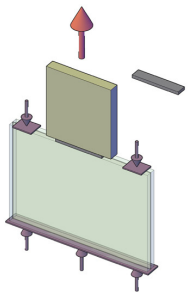

ret - *rectangular edge tension*

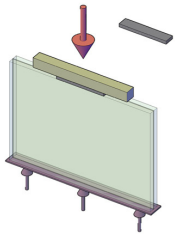

rec - *rectangular edge compression*

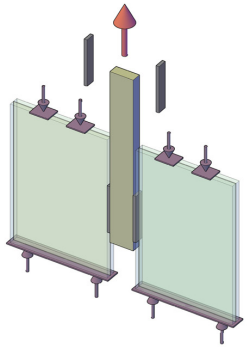

res - *rectangular edge shear*

L-shaped joints tested under tensile, compressive and shear loading

length: 100 mm

width: 21.5 + 20 mm

thickness:
- silicones: 6 mm
- acrylic: 3 mm

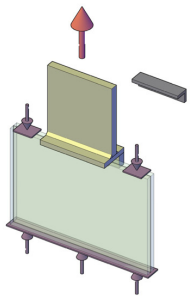

let - *L-shaped edge tension*

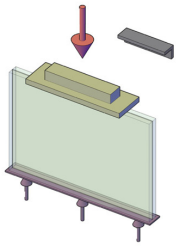

lec - *L-shaped edge compression*

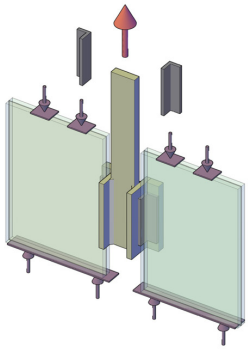

les - *L-shaped edge shear*

U-shaped joints tested under tensile, compressive and shear loading

length: 100 mm

width: 21.5 + 2 x 20 mm

thickness:
- silicones: 6 mm
- acrylic: 3 mm

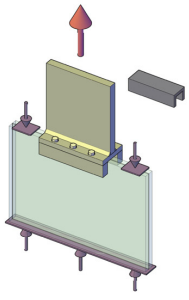

uet - *U-shaped edge tension*

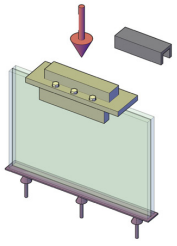

uec - *U-shaped edge compression*

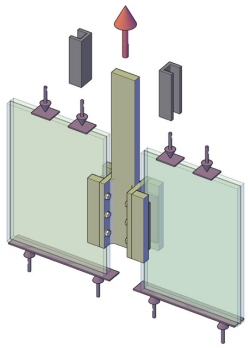

ues - *U-shaped edge shear*

Fig. 5.1 *Overview of the different test specimens investigated in the experimental programme on linear adhesive joints between glass and stainless steel*

For all the specimens a stainless steel *no. 1.4404* is used and the bonded surfaces of the stainless steel components show a grinded finish with corn size *P300*. This type of finish is chosen based on the results of the adhesion tests in order to ensure that no adhesion failure occurs on the stainless steel surfaces. In the case of the glass different types are used for the joints at the glass surface and the joints at the edge of laminatd glass. For the first ones monolithic thermally toughened glass panes (TTG) with a thickness of *10 mm* are used. For the joints at the glass edge laminated glass consisting of two heat strengthened glass panes (HSG) with a thickness of *10 mm* each and a polyvinyl butyral interlayer (PVB) with a thickness of *1.52 mm* is used.

In subchapters 5.2 and 5.3 the different test series are discussed separately for the joints at the glass surface and those at the edge of laminated glass as well as partially separately for the different types of loading. In each of the two subchapters, firstly, a general description of the test specimens, the test setups and the particularities of the testing procedures is provided. Secondly, the manufacturing process of the test specimens is described. This process has several similarities for all the series, but also significant differences between the types of specimens as well as depending on the used adhesive. For experimental tests on adhesive joints, a detailed documentation of the manufacturing process is important, since small details in preparing the specimens can have a large impact on the obtained results. Finally, test results focusing on load-displacement and stress-strain relationships, but including also selected failure patterns, are presented and discussed separately for the different loading types.

In the case of the adhesive joints at the glass surface different dimensions of the joints with rectangular cross section are investigated in the experimental tests. One aim of this variation is to examine the mechanical performance of the joints depending on their thickness, width and length. The more important objective is to analyse the sensitivity of selected material models, which have been derived in subchapter 4.3 for the three investigated adhesives, to geometrical parameters. For this task finite element simulations of the performed tensile and shear tests are carried out and their results are compared to the test results in subchapter 5.2.4.

The preliminary load transfer concepts between glass pane and metal framing with adhesive joints presented in subchapter 3.5.1 also include alternatives with joints at the glass edge. The experimental tests on this type of joints aim to compare the mechanical performance of rectangular, L-shaped and U-shaped joint geometries. The applied loading types are chosen based on the loads occurring in the connections if the glass pane is activated as a shear panel in the investigated glass-metal elements with composite structural behaviour.

5.2 Linear adhesive joints at the glass surface

Applications of linear adhesive joints at the glass surface with rectangular cross section are for example facades with structural sealant glazing. In these systems silicone adhesives are used to transfer both out-of-plane wind loads from the glass panes to the metal frame profiles as well as in-plane loads resulting from temperature differences or from the dead weight of the glass panes. Although compressive loading can also result locally, the significant loading types occurring in such adhesive joints are tension and shear.

For the three selected adhesives the thickness, the length and the width of a linear rectangular adhesive joint at the glass surface are varied in order to determine their influence on the mechanical behaviour of the joint under tensile loading. The used test specimen and the planned test setup are illustrated with sketches in Fig. 5.2. Glass panes made of thermally toughened glass (TTG) with the dimensions of *210 mm x 300 mm* and a thickness of *10 mm* are used. The stainless steel component is made of the material *no. 1.4404* and has a length of *150 mm* in order to allow a proper clamping in the testing machine and enough space for connecting the displacement transducers. The width and the thickness of the stainless steel component varies depending on the length and the width of the adhesive joint dimensions.

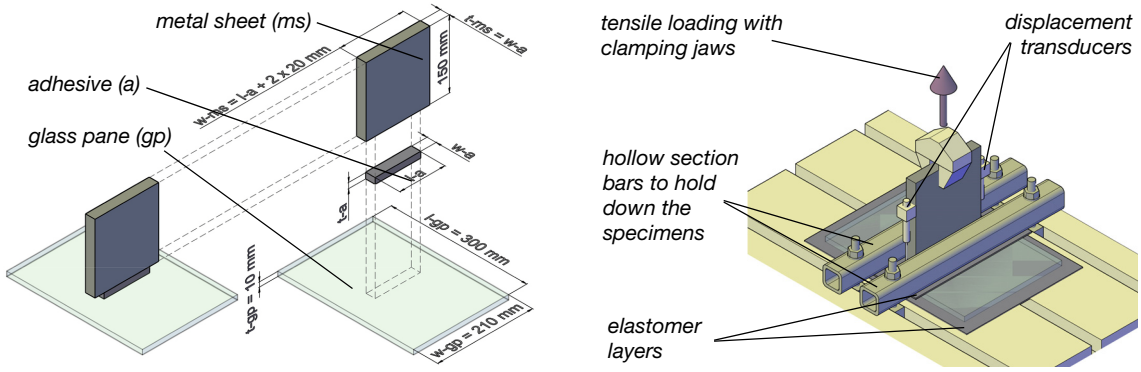

Fig. 5.2 *Exploded view of the test specimen (left) and sketch of the planned test setup (right) for adhesive joints at the glass surface under tensile loading*

For testing, the specimens are positioned on the machine table as shown in Fig. 5.2, right. The glass pane is held down with two square hollow section bars (*40 mm x 40 mm x 5 mm*) which are fastened with tension rods and T-shaped sliding blocks to the machine table. Between the glass pane and the machine table as well as between the glass pane and the hollow section bars *3 mm* thick elastomer layers are positioned in order to avoid a glass failure due to stress peaks. The tensile load is applied with a clamping device which pulls the stainless steel component away from the glass pane.

The tests on the specimens with *Dow Corning 993* and with *Sikasil SG-550* are all run displacement-controlled with a loading speed of *5 mm/min*. For these specimens also load cycles are run to capture signs of the *Mullins* effect. Three cycles are performed for each test specimen as follows: loading up to *10%* strain, unloading, loading up to *20%* strain, unloading, loading up to *30%* strain, unloading, loading until failure. The strain values are provided to the loading soft-

ware as displacements of the machine. Therefore also the compression of the intermediate elastomer layers is included and the reached values are a little lower. The tests on the specimens with *SikaFast-5221 NT* are performed displacement-controlled with a loading speed of *1 mm/min*. No load cycles are run for this adhesive.

For shear loading only the thickness of the adhesive joints is varied, since the other two dimensions are expected to have an insignificant influence on the mechanical behaviour of the joint. The designed test specimen and the used test setup are illustrated in Fig. 5.3. The same type of glass panes as for the adhesive joints under tensile loading are used. A double-lap shear test setup is chosen instead of a single-lap shear test setup for the same reasons explained in subchapter 4.4.3 for the experimental investigations on the adhesion to metal substrates. Two stainless steel straps are adhesively bonded on the surfaces of the glass pane, one on each side. The straps are made of the material *no. 1.4404* and have a length of *320 mm*, a width of *40 mm* and a thickness of *10 mm*. The length of the straps is needed to allow enough space for connecting the displacement transducers as well as for attaching a steel adapter between them, which is then clamped with the clamping jaws and pulled by the testing machine.

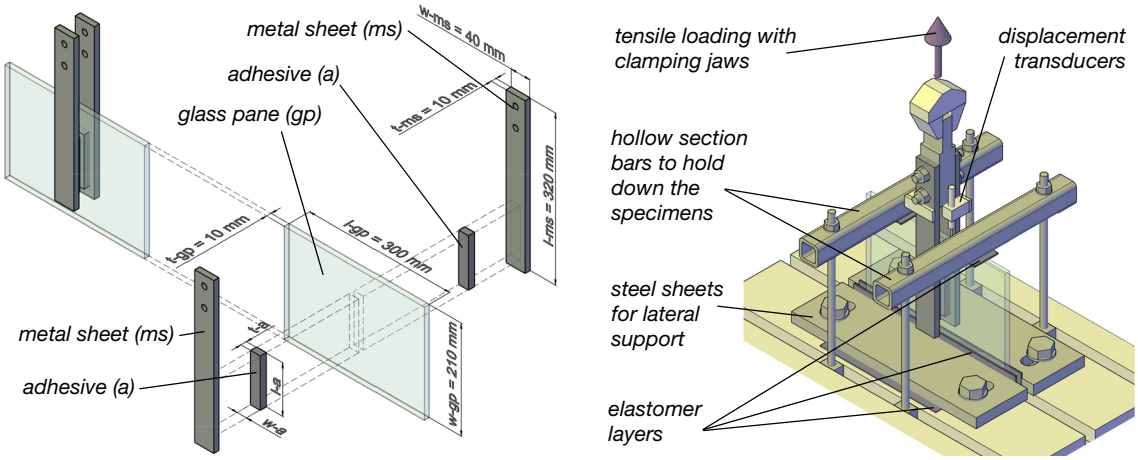

Fig. 5.3 *Exploded view of the test specimen (left) and sketch of the planned test setup (right) for adhesive joints at the glass surface under shear loading*

The position of the test specimens on the machine table is shown in Fig. 5.3, right. The glass pane is held down in a standing position with the same square hollow section bars as in the case of the specimens tested under tensile loading. At the bottom of the glass pane, perpendicular to it, two metal sheets are used to restrain the specimens laterally. These sheets are fixed with bolts through slotted holes to the machine table. Between the glass pane and the machine table as well as between the glass pane and the hollow section bars *3 mm* thick elastomer layers are positioned in order to avoid a glass failure due to stress peaks. The load is applied with a clamping device which pulls the steel adapter and implicitly the two stainless steel straps parallel to the glass pane.

The tests on the specimens with *Dow Corning 993* and with *Sikasil SG-550* are all run displacement-controlled with a loading speed of *5 mm/min*. As in the case of the specimens tested under tensile loading, load cycles are run as follows: loading up to *25%* shear displacement,

unloading, loading up to *50%* shear displacement, unloading, loading up to *75%* shear displacement, unloading, loading until failure. The shear displacement values are provided to the loading software as displacements of the machine. The tests on the specimens with *SikaFast-5221 NT* are performed displacement-controlled with a loading speed of *2 mm/min*, without running load cycles.

Tab. 5.2 *Test series denomination and varied parameters for the adhesive joints at the glass surface tested under tensile and shear loading*

	Tensile loading		**Shear loading**	
Varied parameter	**Test series**	**Number of specimens**	**Test series**	**Number of specimens**
		Dow Corning 993		
	DC_rst_100x20x12	6 (rst_46-51)	**DC_rss_100x20x12**	6 (rss_22-27)
thickness	DC_rst_100x20x6	3 (rst_52-54)	DC_rss_100x20x6	3 (rss_28-30)
	DC_rst_100x20x18	3 (rst_55-57)	DC_rss_100x20x18	3 (rss_31-33)
length	DC_rst_50x20x12	3 (rst_58-60)	-	-
	DC_rst_200x20x12	3 (rst_61-63)	-	-
width	DC_rst_100x10x12	3 (rst_64-66)	-	-
	DC_rst_100x30x12	3 (rst_67-69)	-	-
		Sikasil SG-550		
	SS_rst_100x20x12	6 (rst_22-27)	**SS_rss_100x20x12**	6 (rss_10-15)
thickness	SS_rst_100x20x6	3 (rst_28-30)	SS_rss_100x20x6	3 (rss_16-18)
	SS_rst_100x20x18	3 (rst_31-33)	SS_rss_100x20x18	3 (rss_19-21)
length	SS_rst_50x20x12	3 (rst_34-36)	-	-
	SS_rst_200x20x12	3 (rst_37-39)	-	-
width	SS_rst_100x10x12	3 (rst_40-42)	-	-
	SS_rst_100x30x12	3 (rst_43-45)	-	-
		SikaFast-5221 NT		
	SF_rst_100x20x3	6 (rst_01-06)	**SF_rss_100x20x3**	6 (rss_01-06)
thickness	SF_rst_100x20x6	3 (rst_07-09)	SF_rss_100x20x6	3 (rss_07-09)
length	SF_rst_50x20x3	3 (rst_10-12)	-	-
	SF_rst_200x20x3	3 (rst_13-15)	-	-
width	SF_rst_100x10x3	3 (rst_16-18)	-	-
	SF_rst_100x30x3	3 (rst_19-21)	-	-

Tab. 5.2 shows for all the test series on linear rectangular adhesive joints at the glass surface under tensile and shear loading the denomination of the series, the number of tested specimens and the denomination of these specimens. The first series for each adhesive is considered as reference series. Therefore *6* specimens are manufactured and tested for these series. All other series include *3* test specimens each. The same parameter values are used for all three adhesives, except in the case of the thickness. For this parameter values of *6 mm*, *12 mm* (reference)

and *18 mm* are chosen for the silicones, while for the acrylic only *3 mm* (reference) and *6 mm* thick joints are tested. The reason for this is the recommendation of the adhesive producer to not use thicker joints for *SikaFast-5221 NT* than *3 mm*. The value of *6 mm* for the acrylic is chosen to allow a direct comparison of the results between the different adhesives. The real dimensions of the manufactured adhesive joints are measured before testing and are provided in [Appendix C].

5.2.1 Manufacturing of the test specimens

The manufacturing of all test specimens with adhesive joints at the glass surface is carried out in the laboratory facilities at Graz University of Technology by following advices and recommendations of the adhesive producers. The used mixing procedures are different for each of the three adhesives.

In the case of *Dow Corning 993* cartridges with the base component (*300 g*) and tubes with the catalyst component (*30 g*) as well as a special mixing toolkit are used (see Fig. 5.4, left). The content of one tube is added into one cartridge in order to obtain a mixing ratio of *10:1* (see Fig. 5.4, middle). The cartridge is fixed on a clamping device and afterwards the two components are mixed with a special device which is fixed into a drilling machine with adjustable number of revolutions (see Fig. 5.4, right). A number of *150-200* revolutions per minute is used. The duration of the mixing is around *90 seconds* until the mass is uniformly black. An up-and-down movement of the mixing tool of around *2-3 cm* is applied during the mixing. Afterwards the top of the cartridge is reattached and fixed with an adhesive tape. The application of the adhesive is performed within *10-15 minutes* after mixing with a hand application gun. This mixing procedure is used for all adhesive joints with *Dow Corning 993*, both those at the glass surface and those at the edge of laminated glass.

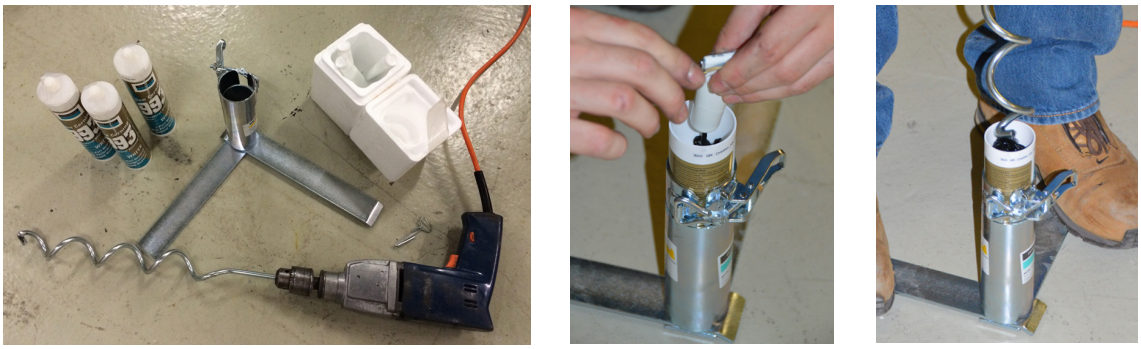

Fig. 5.4 *Mixing procedure used for manufacturing the adhesive joints at the glass surface and at the glass edge with Dow Corning 993*

In the case of the silicone *Sikasil SG-550* a different mixing procedure is used because of the higher viscosity of the material. The base component and the catalyst are provided by the producer in *300 g* cartridges. A dissolver (high speed mixer) *Dispermat CN10* along with a vacuum disperser system *CDS 1000* and a vacuum pump *MZ2C* from the company [www.vma-getzmann.de] (see Fig. 5.5, left) are used for the mixing. With this system a proper mixing of the two components without undesired entrapped air is possible. The two components are filled into the

recipient in a volume ratio of *10:1*. The recipient is fixed in the special double-walled support of the vacuum disperser system (see Fig. 5.5, middle), which is then sealed with a glass cap. The components are first premixed and then the vacuum pump is switched on and the dispersion process is conducted until a uniform black mixture can be observed through the glass cap.

The application of the adhesive is performed with a hand application gun as in the case of *Dow Corning 993*. In order to fill the mixed adhesive from the recipient in empty cartridges a special stainless steel tool is manufactured (see Fig. 5.5, right). It consists of a hollow section circular profile with a wider attached ring at one end. The hollow section profile has an inner radius equal to the outer radius of the cartridge, while the outer radius of the attached ring is equal to the inner radius of the recipient. The cartridge is fixed into the tool and then the tool is pushed into the full recipient. In this way the mixed adhesive is filled into the cartridge.

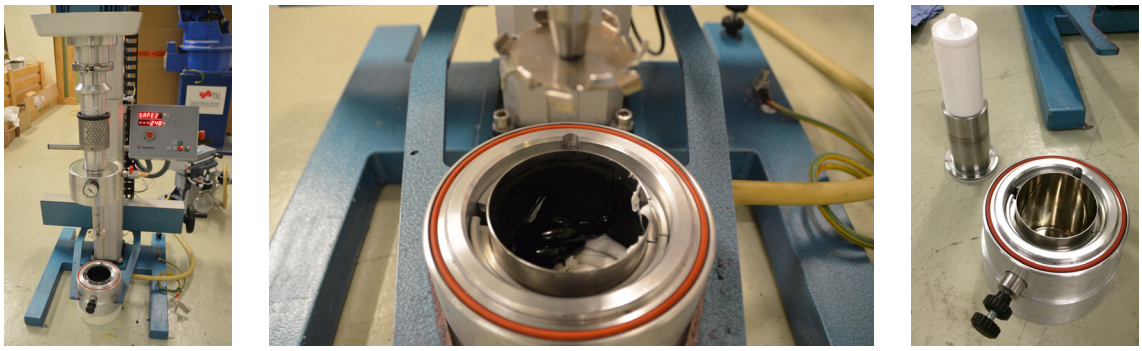

Fig. 5.5 *Mixing procedure used for manufacturing the adhesive joints at the glass surface with Sikasil SG-550*

This mixing and application procedure is thought to be the best suitable for the required adhesive quantity and with the available equipment, but it proves to show several disadvantages. Firstly, it is quite time consuming since only small quantities are mixed at one time and the recipient, the mixing tools and the stainless steel filling tool have to be cleaned after each mixing. Secondly, a high amount of material remaines in the recipient and on the mixing tool and has to be thrown away. And finally, the failure patterns show that a uniform mixture is not obtained after each mixing. Therefore, this procedure is only used for the manufacturing of the test specimens for adhesive joints at the glass surface.

For manufacturing the specimens with the adhesive *SikaFast-5221 NT* the mixing procedure is the user-friendliest. Dual cartridges (*250 ml*) are used with a compressed-air handgun which allows the application with a constant pressure (same procedure as in the case of the specimens for investigations on the adhesion to metal substrates).

Independent of the used adhesives the following steps, similarly to the adhesion tests described in subchapter 4.4.2, are performed:

- taping of the metal sheets and of the glass panes: a PTFE tape is applied on the metal sheets and on the glass panes to delimit the adhesion area in order to have a clean edge of the adhesive joint after removing the tape;

- cleaning the adhesion area on the metal and the glass surfaces: to remove the dust and especially the residual grease from production and finishing from the surfaces, special cleaners are wiped over with a clean industrial paper; for the Dow Corning silicone the universal cleaner *Dow Corning® R-40* is used, while for the silicone and the acrylic from Sika the product *Sika® Cleaner P* is applied;

- application of primer: to increase the adhesive strength, a primer is wiped over the adhesion area of the stainless steel surfaces with a clean industrial paper before applying the adhesive; for the Dow Corning silicone the product *Dow Corning® 1200 OS* is used, for the Sika silicone the product *Sika® Aktivator-205* is applied; in the case of the Sika acrylic the product *Sika® ADPrep* is applied both on the stainless steel and the glass surfaces;

- assembling of the test specimens: the glass panes and the metal sheets are fixed together with polytetrafluorethylene (PTFE) blocks to ensure a predefined joint thickness; different procedures are used for the silicones and for the acrylic;

- application of the adhesive: different mixers and application guns are used for the different adhesives as explained earlier in this chapter;

- tooling and removing of the tapes: the surface of the adhesive joints is straightened with a spatula to achieve a smooth finish and the tapes are torn off before curing;

- removing of the PTFE blocks: the PTFE blocks are loosened before curing to allow the contact with the surrounding air for a larger surface.

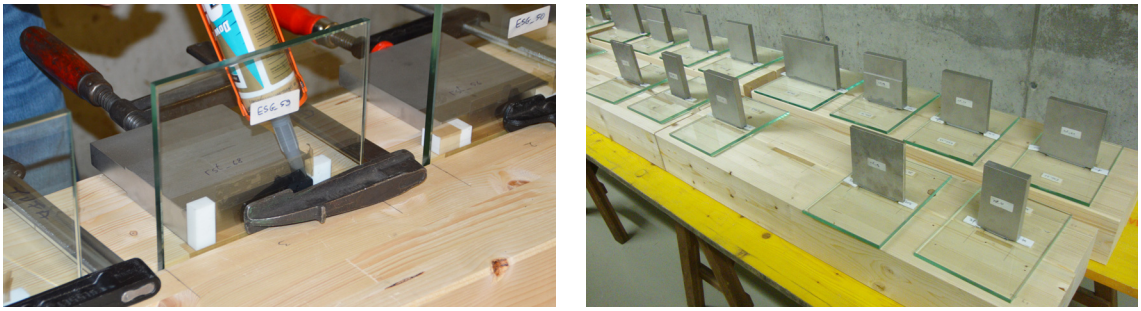

Fig. 5.6 *Application procedure of the adhesive for the silicones (left) and for the acrylic (right) during the manufacturing of the adhesive joints at the glass surface*

For the assembling of the test specimens glued-laminated timber elements are used for fixing the glass panes. The assembling of the test specimens for tensile loading is performed for the silicone adhesives in a lying position (rotated by 90°) as shown in Fig. 5.6, left while for the acrylic a standing position is chosen (see Fig. 5.6, right). The reason for this difference is the thickness of the adhesive joints: for the thicker silicone stripes it is possible to fill the adhesive in a formed gap, but in the case of the acrylic, the injection needle is to thick to allow a proper filling of the thin gap. Therefore, an enough thick adhesive caterpillar is applied on the glass pane and then the metal sheet is pressed on it and on the PTFE blocks in order to achieve the desired joint thickness.

The assembling of the specimens and the application of the adhesives for the silicones and for the acrylic differes also in the case of the specimens tested under shear loading. For all the specimens the glass pane is fixed between glued-laminated timber elements. In the case of the silicones, the lateral stainless steel straps and the PTFE blocks for determining the adhesive joint thickness are fixed to the glass pane with screw clamps (see Fig. 5.7, left). Then the adhesive is filled with a handgun from cartridges into the resulting gaps (see Fig. 5.7, right).

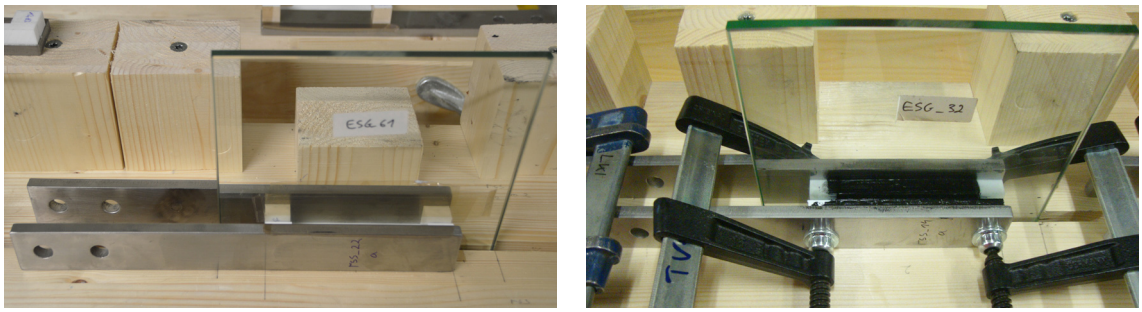

Fig. 5.7 *Assembling of the test specimens before and after application of the adhesive for the adhesive joints with silicone at the glass surface tested under shear loading*

In the case of the acrylic, the PTFE blocks are brought in place on one side of the glass pane (see Fig. 5.8, left) and an adhesive caterpillar is applied with the compressed-air handgun on the adhesion area of the glass pane. Afterwards one of the lateral stainless steel straps is pressed on the PTFE blocks and on the adhesive caterpillar and is then fixed with screw clamps to the glass pane (see Fig. 5.8, right). After curing of the first adhesive joint, the second one is completed in the same way on the other side of the glass pane.

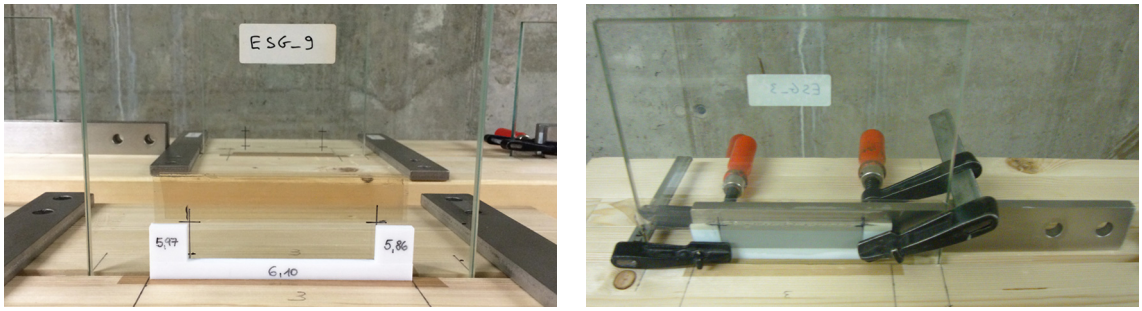

Fig. 5.8 *Assembling of the test specimens before and after application of the adhesive for the adhesive joints with acrylic at the glass surface tested under shear loading*

5.2.2 Test results for adhesive joints at the glass surface under tensile loading

Two types of results from the tensile tests on adhesive joints at the glass surface are discussed in this subchapter. Firstly, the failure patterns for the three different adhesives are evaluated, focusing only on noteworthy observations. Secondly, the mechanical behaviour is analysed for the three adhesives by comparing stress-strain relationships as well as stress values for the different joint dimensions.

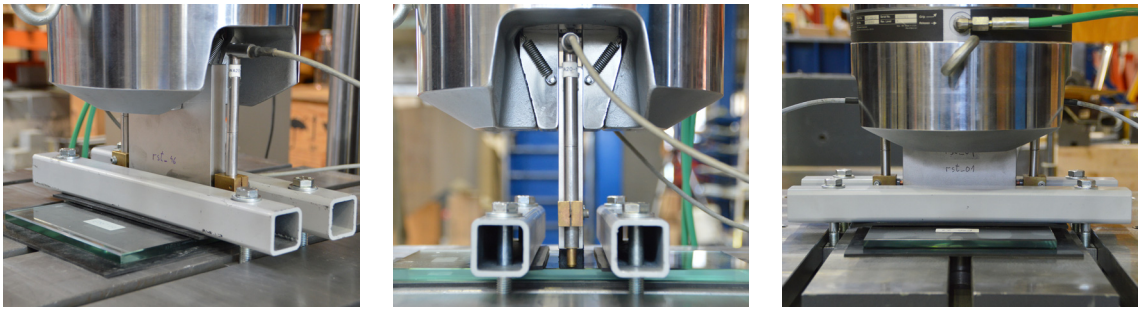

Fig. 5.9 *Specimens with adhesive joints at the glass surface tested under tensile loading*

The real test setup with installed specimens is illustrated in Fig. 5.9 from different perspectives. The evaluated displacements and strains are calculated based on the measurements of the two transducers in order to exclude the deformations within the elastomer layers as well as an eventually occurring rotation in the adhesive joint during pulling of the stainless steel part. In this subchapter only selected failure patterns and mean values from the performed tests are provided. The failure patterns for all specimens as well as tables with mechanical values for each specimen can be found in [Appendix C].

Evaluation of the failure patterns

For all adhesive joints at the glass surface with silicones tested under tensile loading only cohesive failure is observed. The failure patterns are illustrated exemplary in Fig. 5.10 for the specimens with *Dow Corning 993* and different joint thicknesses. Tiny air inclusions can be noticed along the rupture surfaces which are the result of the used mixing procedure.

DC_rst_100x20x12 *DC_rst_100x20x6* *DC_rst_100x20x18*

Fig. 5.10 *Typical failure patterns for the adhesive joints at the glass surface with Dow Corning 993 and different thicknesses tested under tensile loading*

Fig. 5.11 shows exemplary failure patterns of the adhesive joints with *Sikasil SG-550* and different joint thicknesses. Especially in the case of the first specimen from the left, some white tracks can be noticed in the rupture surface. This pattern occurs only for part of the specimens

and is probably the result of a too little mixing time in the case of particular charges. However, the obtained mechanical results show an insignificant influence of this aspect.

SS_rst_100x20x12 *SS_rst_100x20x6* *SS_rst_100x20x18*

Fig. 5.11 *Typical failure patterns for the adhesive joints at the glass surface with Sikasil SG-550 and different thicknesses tested under tensile loading*

In the case of the adhesive joints at the glass surface tested under tensile loading with *SikaFast-5221 NT* several aspects are noteworthy. By comparing the patterns of the specimens with a thickness of *3 mm* (see Fig. 5.12, left) and of those with a thickness of *6 mm* (see Fig. 5.12, middle) it can be observed, that in the second case larger air inclusions are present. On the one hand this can be a result of an improper application of the adhesive, but on the other hand it is also a result of the exothermic reaction of the material after mixing the two components. In the case of the specimens with small width (see Fig. 5.12, right) as well as for some specimens with small length, partially adhesive failure on the glass surface is noticed. A complete overview of the occurred failure patterns is given in [Appendix C].

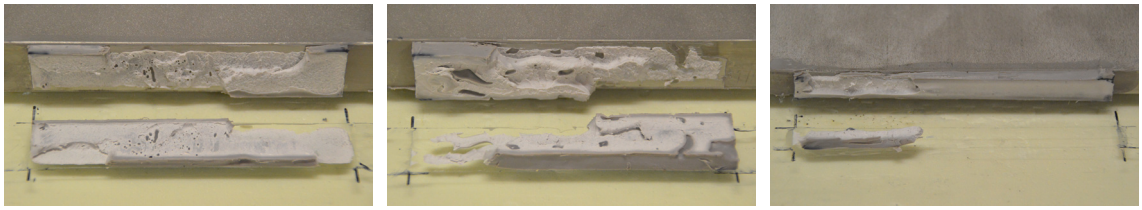

SF_rst_100x20x3 *SF_rst_100x20x6* *SF_rst_100x10x3*

Fig. 5.12 *Typical failure patterns for the adhesive joints at the glass surface with SikaFast-5221 NT and different thicknesses (left and middle) as well as with small width (right) tested under tensile loading*

Analysis of the mechanical behaviour

In order to evaluate the mechanical behaviour of linear adhesive joints at the glass surface with rectangular cross section and different dimensions, diagrams with the stress-strain relationships for the different series are plotted in Fig. 5.13 to Fig. 5.19. The diagrams on the left show the curves for the specimens with silicone adhesives (*Dow Corning 993* in black and *Sikasil SG-550* in blue). For these diagrams the same range is chosen for the two axes to allow a better comparison. The results for the specimens with acrylic adhesive are plotted separately in the diagrams on the right (*SikaFast-5221 NT* in red), using a different range on the y-axis for the stresses. For the reference series (Fig. 5.13) only four of the six specimens are considered in the diagrams, since the first two are used as pilot tests. In the case of the other series the results for all three specimens are plotted, except for cases in which the measurement instrumentation delivered broken or no data. In [Appendix C] explanatory statements are provided for the speci-

mens which are not considered in the diagrams and the results evaluation as well as for those where no usable measurement data are available.

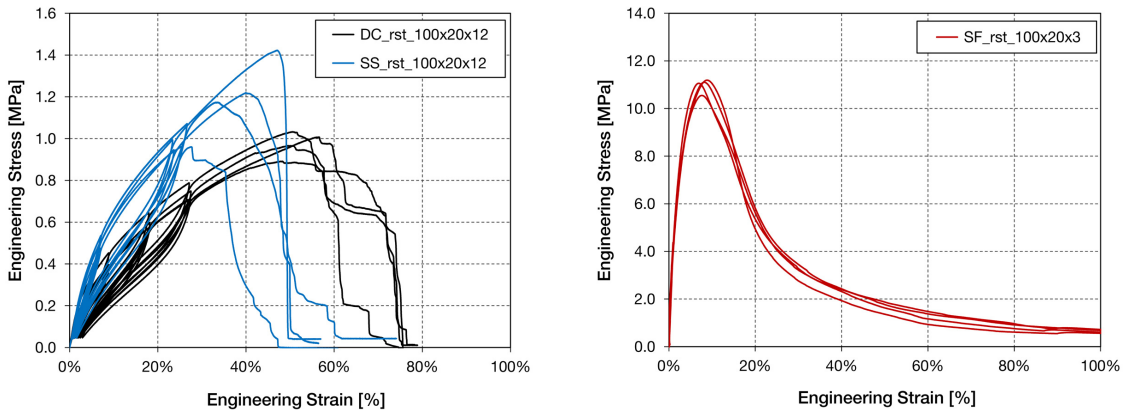

Fig. 5.13 *Stress-strain curves from the tensile tests on adhesive joints at the glass surface: 100 mm x 20 mm x 12 mm for the silicones (left) and 100 mm x 20 mm x 3 mm for the acrylic (right)*

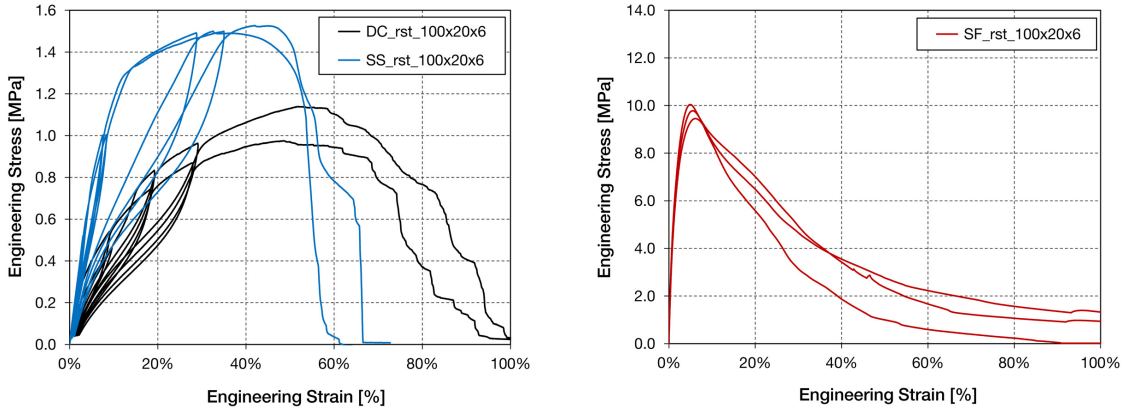

Fig. 5.14 *Stress-strain curves from the tensile tests on adhesive joints at the glass surface: 100 mm x 20 mm x 6 mm for the silicones (left) and 100 mm x 20 mm x 6 mm for the acrylic (right)*

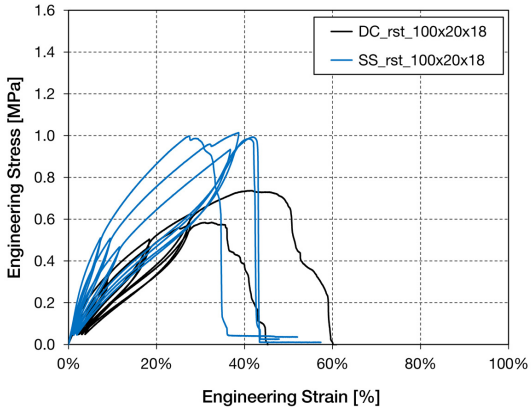

Fig. 5.15 *Stress-strain curves from the tensile tests on adhesive joints at the glass surface: 100 mm x 20 mm x 18 mm for the silicones*

A general comparison of the results for all test series on adhesive joints at the glass surface under tensile loading shows that around *20%* higher engineering stresses are reached by the specimens with *Sikasil SG-550* compared to those with *Dow Corning 993*. Furthermore, the specimens with *SikaFast-5221 NT* reach around *10 times* higher engineering stress values compared to the specimens with silicones. A good agreement regarding the stiffness of the joints can be noticed for specimens of the same series, especially for the acrylic and for the silicone *Dow Corning 993*. A qualitative evaluation of the joint stiffness by comparing the inclination of the curves from specimens with different adhesives points out that, between the silicones, the joints with *Sikasil SG-550* behave stiffer than those with *Dow Corning 993*, while the joints with the acrylic *SikaFast-5221 NT* show a significantly higher stiffness.

Regarding the influence of different joint thicknesses on the mechanical behaviour of the linear adhesive joints under tensile loading it can be noticed from the diagrams in Fig. 5.13, Fig. 5.14 and Fig. 5.15 for all three investigated adhesives, that, by reducing the joint thickness, higher stresses and implicitly higher loads can be transferred and the joint behaves stiffer. However, it has to be considered as well that the thinner the joints are, the less displacement they allow.

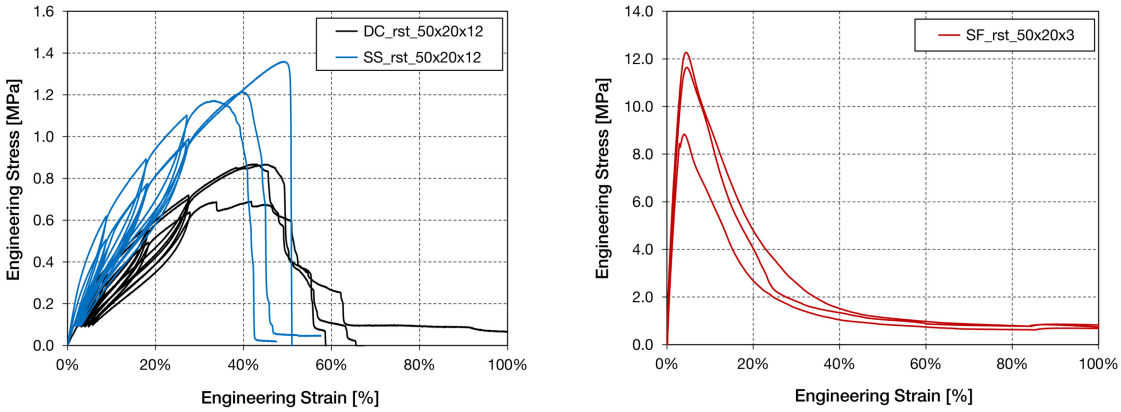

Fig. 5.16 *Stress-strain curves from the tensile tests on adhesive joints at the glass surface: 50 mm x 20 mm x 12 mm for the silicones (left) and 50 mm x 20 mm x 3 mm for the acrylic (right)*

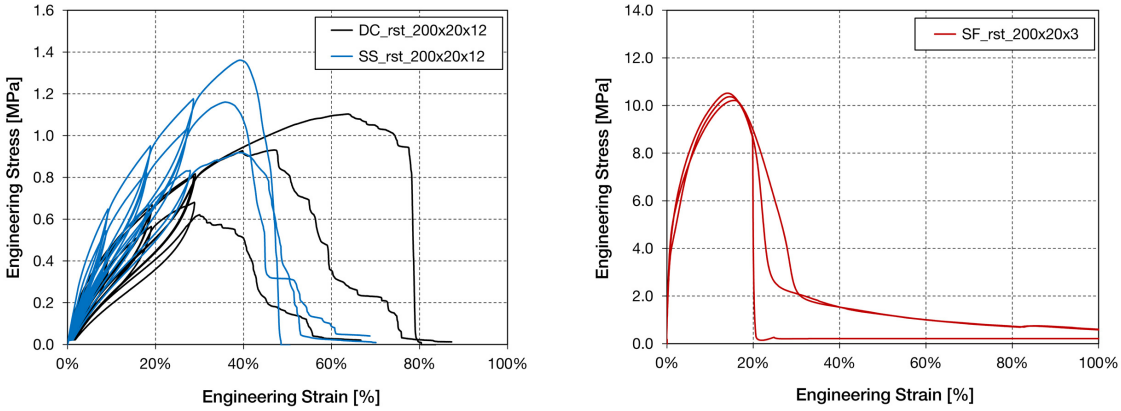

Fig. 5.17 *Stress-strain curves from the tensile tests on adhesive joints at the glass surface: 200 mm x 20 mm x 12 mm for the silicones (left) and 200 mm x 20 mm x 3 mm for the acrylic (right)*

Different joint lengths have a rather small influence both on the reached maximum engineering stresses and on the inclination of the stress-strain curves in the case of the two silicones (see left diagrams in Fig. 5.13, Fig. 5.16 and Fig. 5.17). In the case of the acrylic it can be observed, by comparing the right diagrams in the same figures that, with increasing the joint length, the yielding of the adhesive material gets more pronounced.

The variation of the joint width shows no significant influence on the reached maximum engineering stresses (see Fig. 5.13, Fig. 5.18 and Fig. 5.19). However, it can be noticed in the case of the two silicones, that wider joints lead to a steeper gradient of the stress-strain curves. In the case of the acrylic however, a similar influence as in the case of the length variation can be observed: with increasing width of the joint the yielding is more pronounced.

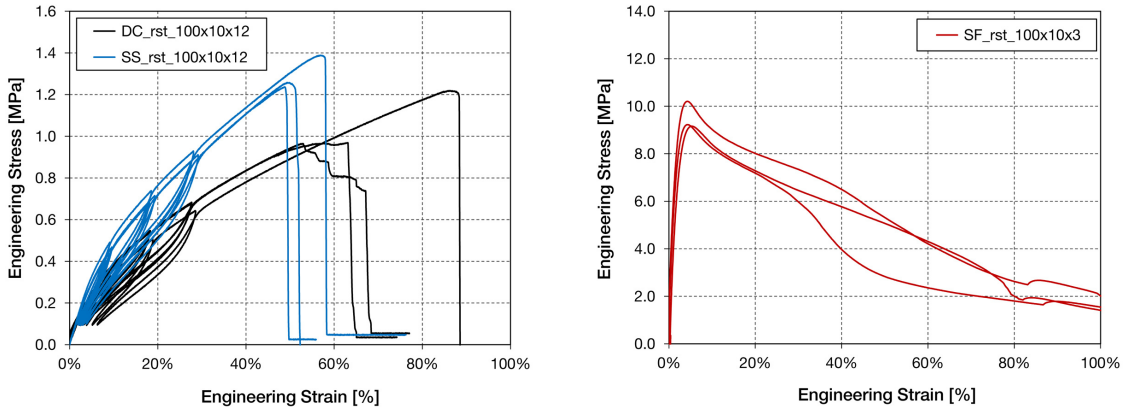

Fig. 5.18 *Stress-strain curves from the tensile tests on adhesive joints at the glass surface: 100 mm x 10 mm x 12 mm for the silicones (left) and 100 mm x 10 mm x 3 mm for the acrylic (right)*

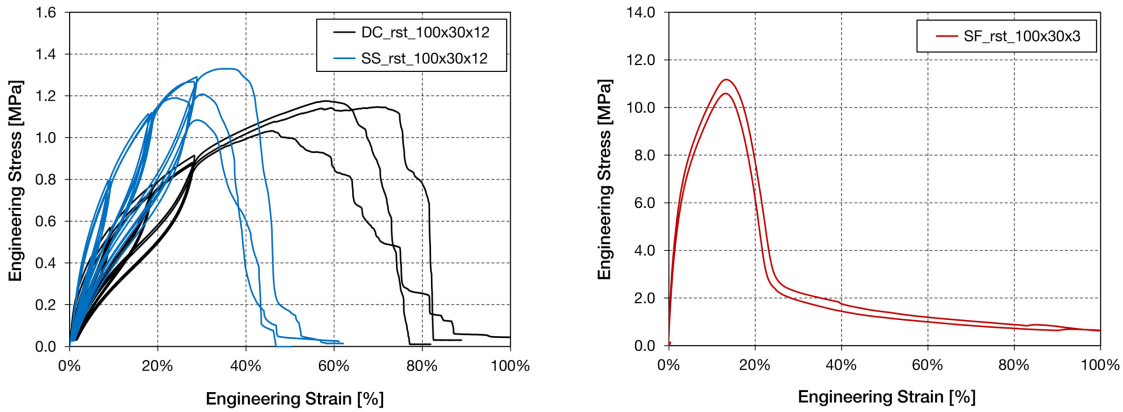

Fig. 5.19 *Stress-strain curves from the tensile tests on adhesive joints at the glass surface: 100 mm x 30 mm x 12 mm for the silicones (left) and 100 mm x 30 mm x 3 mm for the acrylic (right)*

The findings from the tensile tests on linear adhesive joints at the glass surface discussed on a qualitative level based on the stress-strain diagrams are fostered by quantitative data in Tab. 5.3, Tab. 5.4 and Tab. 5.5. Mean values for the maximum reached load and the corresponding displacement as well as for the maximum engineering stress and the corresponding strain are

provided for each test series. In [Appendix C] the values determined for each test specimen along with the determined standard deviation can be found.

Tab. 5.3 *Mean values for results from the tensile tests on linear adhesive joints between glass and stainless steel substrates at the glass surface with Dow Corning 993*

Test series	**Max. load** [N]	**Corr. displ.** [mm]	**Max. eng. stress** [MPa]	**Corr. eng. strain** [-]
DC_rst_100x20x12	1 954	6.6	0.98	0.51
DC_rst_100x20x6	2 234	3.1	1.06	0.50
DC_rst_100x20x18	1 336	7.2	0.67	0.37
DC_rst_50x20x12	850	5.5	0.81	0.43
DC_rst_200x20x12	3 718	5.7	0.90	0.47
DC_rst_100x10x12	1 081	8.4	1.05	0.67
DC_rst_100x30x12	3 372	7.2	1.12	0.58

Tab. 5.4 *Mean values for results from the tensile tests on linear adhesive joints between glass and stainless steel substrates at the glass surface with Sikasil SG-550*

Test series	**Max. load** [N]	**Corr. displ.** [mm]	**Max. eng. stress** [MPa]	**Corr. eng. strain** [-]
SS_rst_100x20x12	2 409	4.6	1.19	0.36
SS_rst_100x20x6	3 139	2.2	1.53	0.37
SS_rst_100x20x18	2 029	6.9	1.00	0.36
SS_rst_50x20x12	1 257	5.3	1.25	0.41
SS_rst_200x20x12	4 675	4.8	1.15	0.38
SS_rst_100x10x12	1 299	6.4	1.30	0.52
SS_rst_100x30x12	3 875	3.6	1.26	0.29

Tab. 5.5 *Mean values for results from the tensile tests on linear adhesive joints between glass and stainless steel substrates at the glass surface with SikaFast-5221 NT*

Test series	**Max. load** [N]	**Corr. displ.** [mm]	**Max. eng. stress** [MPa]	**Corr. eng. strain** [-]
SF_rst_100x20x3	20 595	0.24	10.98	0.08
SF_rst_100x20x6	17 449	0.34	9.76	0.05
SF_rst_50x20x3	10 252	0.13	10.91	0.04
SF_rst_200x20x3	38 205	0.45	10.37	0.15
SF_rst_100x10x3	7 858	0.14	9.53	0.04
SF_rst_100x30x3	30 382	0.41	10.88	0.13

For the specimens with silicone adhesive joints three cycles up to *10%*, *20%* and *30%* strain are run before loading to failure. The evaluation of these load cycles is illustrated in Tab. 5.6 for the specimens with *Dow Corning 993* and in Tab. 5.7 for those with *Sikasil SG-550* by providing for each test series the mean values of the reached engineering stresses at *5%*, *15%* and *25%* strain during the first and the second load cycle in which these strains are reached. Additionally, the decrease of these stresses during the second cycle compared to the first one is given in percent. It is important to consider that in case of load cycles the silicones get softer after the first

loading which results in lower transferable stresses during the second cycle for a given strain. The quantitative values provided in Tab. 5.6 and Tab. 5.7 have to be considered in combination with the performed cycles, since a loading up to other strain values could result in slightly different decreasing percentages. However, as a rough qualitative statement it can be mentioned that the decrease of the stresses between the first and the second load cycle for a given strain averages for both silicones around *15-25%*.

Tab. 5.6 *Engineering stresses at different strain values for the first and the second load cycle from the tensile tests on linear adhesive joints with Dow Corning 993*

Test series	**Eng. stress at 5% strain** [MPa]			**Eng. stress at 15% strain** [MPa]			**Eng. stress at 25% strain** [MPa]		
	1st cycle	**2nd cycle**	**Diff.** [%]	**1st cycle**	**2nd cycle**	**Diff.** [%]	**1st cycle**	**2nd cycle**	**Diff.** [%]
DC_rst_100x20x12	0.30	0.22	- 27%	0.54	0.45	- 17%	0.71	0.62	- 13%
DC_rst_100x20x6	0.36	0.29	- 19%	0.71	0.56	- 21%	0.88	0.72	- 18%
DC_rst_100x20x18	0.22	0.16	- 27%	0.43	0.36	- 16%	0.58	0.49	- 16%
DC_rst_50x20x12	0.23	0.17	- 26%	0.48	0.40	- 17%	0.65	0.56	- 14%
DC_rst_200x20x12	0.29	0.22	- 24%	0.55	0.45	- 18%	0.72	0.59	- 18%
DC_rst_100x10x12	0.24	0.19	- 21%	0.47	0.39	- 17%	0.63	0.54	- 14%
DC_rst_100x30x12	0.40	0.30	- 25%	0.68	0.56	- 18%	0.85	0.72	- 15%

Tab. 5.7 *Engineering stresses at different strain values for the first and the second load cycle from the tensile tests on linear adhesive joints with Sikasil SG-550*

Test series	**Eng. stress at 5% strain** [MPa]			**Eng. stress at 15% strain** [MPa]			**Eng. stress at 25% strain** [MPa]		
	1st cycle	**2nd cycle**	**Diff.** [%]	**1st cycle**	**2nd cycle**	**Diff.** [%]	**1st cycle**	**2nd cycle**	**Diff.** [%]
SS_rst_100x20x12	0.41	0.35	- 15%	0.78	0.56	- 28%	1.00	0.92	- 8%
SS_rst_100x20x6	0.78	0.61	- 22%	1.35	0.73	- 46%	1.47	1.06	- 28%
SS_rst_100x20x18	0.34	0.27	- 21%	0.65	0.39	- 40%	0.85	0.57	- 33%
SS_rst_50x20x12	0.36	0.29	- 19%	0.73	0.62	- 15%	0.97	0.86	- 11%
SS_rst_200x20x12	0.38	0.29	- 24%	0.73	0.61	- 16%	0.96	0.82	- 15%
SS_rst_100x10x12	0.31	0.24	- 23%	0.63	0.53	- 16%	0.84	0.73	- 13%
SS_rst_100x30x12	0.56	0.42	- 25%	1.02	0.82	- 20%	1.23	1.01	- 18%

5.2.3 Test results for adhesive joints at the glass surface under shear loading

The same types of results as for the tensile tests on adhesive joints at the glass surface are discussed in this subchapter for the shear tests. Firstly, the noteworthy findings regarding failure patterns are evaluated. Secondly, the mechanical behaviour is analysed for the three adhesives by comparing shear stress *vs.* shear displacement relationships as well as stress values for the different joint thicknesses.

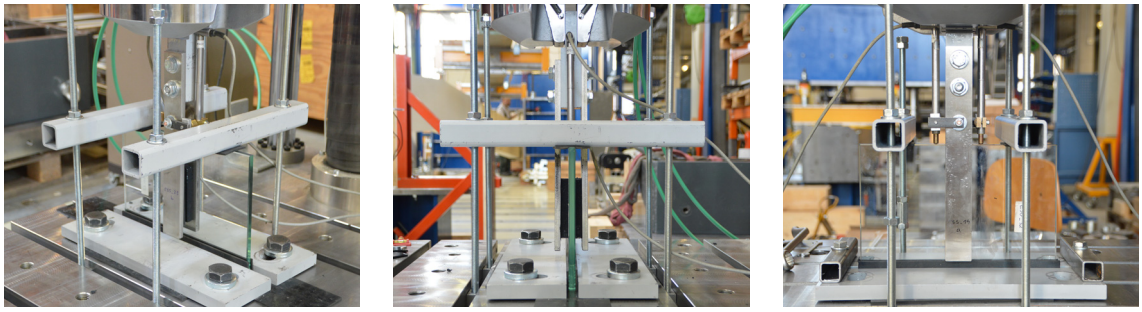

Fig. 5.20 *Specimens with adhesive joints at the glass surface tested under shear loading*

The real setup for the double-lap shear tests with the installed specimens is illustrated in Fig. 5.20 from different perspectives. The evaluated displacements are calculated as mean values from the measurements of the two transducers, each of them recording the relative deformation between one of the two metal sheets and the glass pane. The deformations within the elastomer layers are not included in these measurements. Similar to the tensile tests, in this subchapter only selected failure patterns and mean values from the performed tests are provided. The failure patterns for all specimens as well as tables with mechanical values for each specimen can be found in [Appendix C].

Evaluation of the failure patterns

In the case of the adhesive joints with silicones only cohesive failure occurs and no additional noteworthy aspects are noticed. Therefore, these failure patterns are provided in [Appendix C] and are not further discussed in this subchapter.

In the case of the adhesive joints with *SikaFast-5221 NT* tested under shear loading cohesive, mixed and adhesive failure patterns are observed. The adhesive failure occurs always only on one side of the double-lap shear test specimens (see examples in Fig. 5.21, left and middle). In order to explain this occurrence a possible dependency of the adhesion on glass surfaces on the production process for float glass is investigated. During this process the glass melt is floating over a tin bath and therefore the two surfaces of a float glass pane have different surface properties. The surface facing the tin bath has a stannic oxide (SnO_2) layer with an inhomogeneous SnO_2-concentration and an uneven thickness. The side facing the air shows a silica rich surface because alkalis and earth alkalis evaporate in the reduced gaseous atmosphere of the float chamber. The roughness of the tin bath side reaches values of *1-2 nm*, while the air side is a little rougher with values of *4-10 nm*. These differences in structure and composition cause different adhesion and ageing behaviour of certain adhesives to the two float glass surfaces [Kothe, 2013a].

The tin side of a float glass pane can be determined with a lamp with ultraviolet light. When illuminating the tin surface with a wavelength of *~254 nm* in a dark room the tin is stimulated to fluorescence and the surface reflects in a milky colour (see Fig. 5.21, right top). This does not occur when illuminating the air surface, because the ultraviolet light passes through (see Fig. 5.21, right bottom). Noteworthy, the same procedure applied with a wavelength of *~365 nm* leads to no differences between the reflections of the two float glass surfaces.

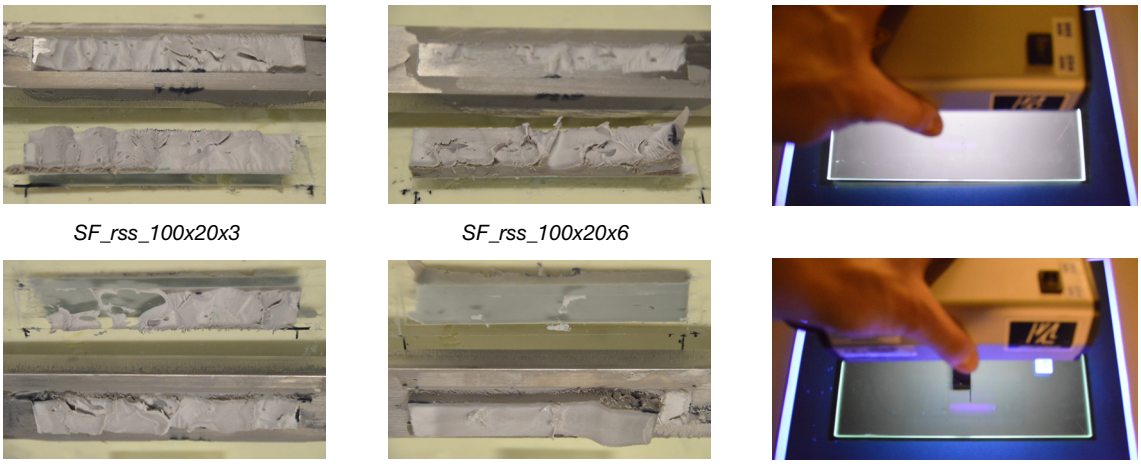

Fig. 5.21 *Typical failure patterns for the adhesive joints at the glass surface with SikaFast-5221 NT tested under shear loading (left and middle) and determining of the tin (right top) and the air surface (right bottom) of thermally toughened glass panes made of float glass with a lamp with ultraviolet light*

After investigating all nine glass panes used for the adhesive joints at the glass surface with *SikaFast-5221 NT* tested under shear loading it can be concluded that the adhesive (or mixed) failure always occurs on the air surface of the glass panes. This observation should be followed up with experimental investigations on a larger number of test specimens in order to verify it and avoid future adhesive failures by choosing the suitable float glass side for adhesive joints with *SikaFast-5221 NT* on glass surfaces.

For the glass panes used for the adhesive joints at the glass surface with *SikaFast-5221 NT* tested under tensile loading it is subsequently determined whether the joint is located on the tin or on the air side of the glass panes. For the two series *SF_rst_50x20x3* and *SF_rst_100x10x3*, where partial adhesive failure has occurred, no dependency on the tin or air side is given.

Analysis of the mechanical behaviour

The influence of different joint thicknesses on the mechanical behaviour of linear adhesive joints under shear loading is illustrated by shear stress *vs.* shear displacement diagrams in Fig. 5.22, Fig. 5.23 and Fig. 5.24. The same representation modality as in the case of the tensile tests is chosen, by plotting the results for the two silicones together in the diagrams on the left side and the results for the acrylic separately in the diagrams on the right side. Since the acrylic reaches significantly higher stresses and also exhibits larger shear displacements both for the x-axis and the y-axis a different range than in the case of the silicones is chosen. A comparison of the performance of the different adhesives leads to similar conclusions as in the case of the tensile

tests. The specimens with *Sikasil SG-550* generally reach around *20%* higher engineering stresses than those with *Dow Corning 993* and also show a higher stiffness.

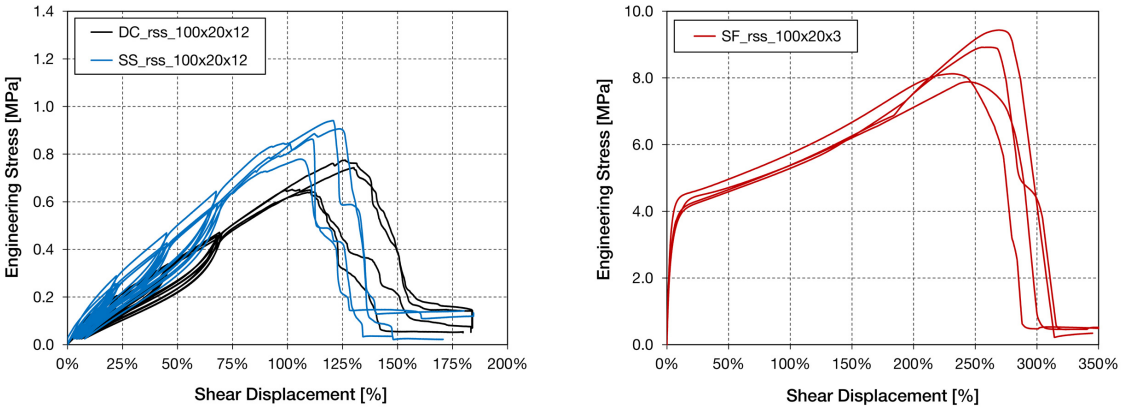

Fig. 5.22 *Stress-shear displacement curves from the shear tests on adhesive joints at the glass surface: 100 mm x 20 mm x 12 mm for the silicones (left) and 100 mm x 20 mm x 3 mm for the acrylic (right)*

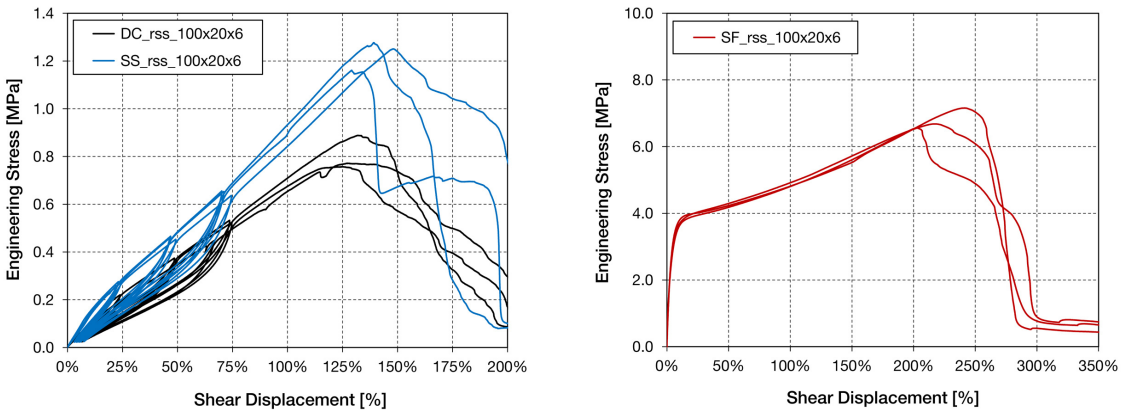

Fig. 5.23 *Stress-shear displacement curves from the shear tests on adhesive joints at the glass surface: 100 mm x 20 mm x 6 mm for the silicones (left) and 100 mm x 20 mm x 6 mm for the acrylic (right)*

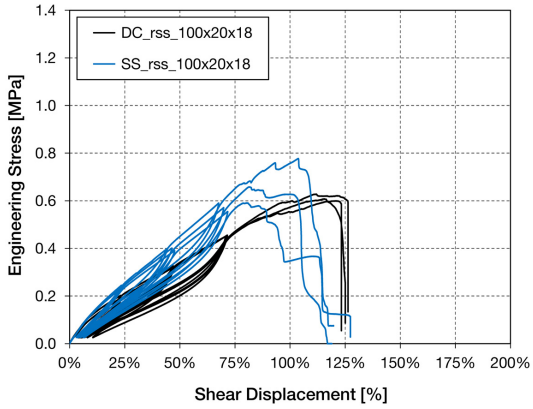

Fig. 5.24 *Stress-shear displacement curves from the shear tests on adhesive joints at the glass surface: 100 mm x 20 mm x 18 mm for the silicones*

The specimens with *SikaFast-5221 NT* show a significantly higher stiffness before yielding and exhibit afterwards pronounced plastic deformations. The reached maximum engineering shear stresses in the acrylic adhesive are *8-10* times higher than in the case of the silicones. However, the engineering stresses at which the yielding starts average only around *50%* of the engineering failure stresses. The agreement between the results for specimens of the same series is even better than in the case of the tensile tests both regarding gradient of the curves as well as engineering failure stress.

The thickness variation of the adhesive joint has as similar influence on the occurring engineering shear stresses as in the case of the tensile tests. The thinner the joint is, the higher loads and implicitly failure stresses can be transferred. In the case of the acrylic also the yielding stress is a little higher in the case of the thinner joint. Regarding the gradient of the shear stress *vs.* shear displacement curves, there is almost no influence of the joint thickness in the case of the silicones and only a small influence in the case of the acrylic after yielding. Also in the case of this loading type it has to be considered, that smaller thickness values lead to less possible relative displacement between the substrates. In terms of shear loading this is for instance important when dealing with temperature loads.

Tab. 5.8 *Mean values for results from the shear tests on linear adhesive joints between glass and stainless steel substrates at the glass surface with Dow Corning 993*

Test series	**Max. load** [N]	**Corr. displ.** [mm]	**Max. shear stress** [MPa]	**Corr. shear displ.** [-]
DC_rss_100x20x12	2 752	15.2	0.70	1.18
DC_rss_100x20x6	3 203	7.7	0.81	1.28
DC_rss_100x20x18	2 370	22.1	0.61	1.16

Tab. 5.9 *Mean values for results from the shear tests on linear adhesive joints between glass and stainless steel substrates at the glass surface with Sikasil SG-550*

Test series	**Max. load** [N]	**Corr. displ.** [mm]	**Max. shear stress** [MPa]	**Corr. shear displ.** [-]
SS_rss_100x20x12	3 352	15.0	0.87	1.15
SS_rss_100x20x6	4 910	8.4	1.23	1.39
SS_rss_100x30x18	2 549	16.8	0.68	0.88

Tab. 5.10 *Mean values for results from the shear tests on linear adhesive joints between glass and stainless steel substrates at the glass surface with SikaFast-5221 NT*

Test series	**Max. load** [N]	**Corr. displ.** [mm]	**Max. shear stress** [MPa]	**Corr. shear displ. (max)** [-]	**Approx. yield. stress** [MPa]	**Corr. shear displ. (yield.)** [-]
SF_rss_100x20x3	34 771	7.7	8.59	2.50	4.2	0.13
SF_rss_100x20x6	26 000	13.4	6.80	2.20	3.8	0.13

Tab. 5.8, Tab. 5.9 and Tab. 5.10 show mean values of the maximum load and the corresponding displacement as well as the maximum reached engineering shear stress and the corresponding shear displacement for the different test series performed with the three investigated adhesives. For the acrylic, approximate mean values of the yielding stress and the corresponding shear

displacement are provided additionally in Tab. 5.10, since these values are considered of high importance for a practical application. The values for each specimen along with the calculated standard deviation can be found in [Appendix C].

Similar as in the case of the tensile tests on linear adhesive joints at the glass surface, three load cycles up to *25%*, *50%* and *75%* shear displacement are run for the silicones before loading until failure. In Tab. 5.11 and Tab. 5.12 the mean values of the reached engineering shear stresses at *5%*, *15%* and *25%* shear displacement during the first and the second load cycle in which these values are reached are provided for the specimens with *Dow Corning 993* and *Sikasil SG-550* along with the relative decrease of the stresses in percent. Qualitatively, it can be stated that there is a decrease in the recorded stresses between the first and the second load cycle for a given shear displacement.

Tab. 5.11 *Engineering shear stresses at different shear displacement values for the first and the second load cycle from the shear tests on linear adhesive joints with Dow Corning 993*

Test series	**Shear stress at 5% shear displacement** [MPa]			**Shear stress at 15% shear displacement** [MPa]			**Shear stress at 25% shear displacement** [MPa]		
	1st cycle	**2nd cycle**	**Diff.** [%]	**1st cycle**	**2nd cycle**	**Diff.** [%]	**1st cycle**	**2nd cycle**	**Diff.** [%]
DC_rss_100x20x12	0.058	0.034	- 41%	0.141	0.116	- 18%	0.207	0.152	- 27%
DC_rss_100x20x6	0.048	0.033	- 31%	0.130	0.112	- 14%	0.197	0.153	- 22%
DC_rss_100x20x18	0.066	0.033	- 50%	0.146	0.113	- 23%	0.203	0.145	- 29%

Tab. 5.12 *Engineering shear stresses at different shear displacement values for the first and the second load cycle from the shear tests on linear adhesive joints with Sikasil SG-550*

Test series	**Shear stress at 5% shear displacement** [MPa]			**Shear stress at 15% shear displacement** [MPa]			**Shear stress at 25% shear displacement** [MPa]		
	1st cycle	**2nd cycle**	**Diff.** [%]	**1st cycle**	**2nd cycle**	**Diff.** [%]	**1st cycle**	**2nd cycle**	**Diff.** [%]
SS_rss_100x20x12	0.085	0.053	- 38%	0.196	0.159	- 19%	0.279	0.203	- 27%
SS_rss_100x20x6	0.070	0.043	- 39%	0.195	0.152	- 22%	0.281	0.196	- 30%
SS_rss_100x20x18	0.070	0.045	- 36%	0.171	0.139	- 19%	0.246	0.186	- 24%

5.2.4 Finite element simulations of the experimental tests

For the linear adhesive joints at the glass surface tested under tensile and under shear loading finite element simulations are performed. The main objectives of these simulations are to examine the suitability of the material models derived in subchapter 4.3 for linear adhesive joints with rectangular cross section and to investigate their sensitivity to varying dimensions of the joints. Furthermore, based on the finite element simulations a more exact distribution of the stresses in the adhesive joints and the position of the stress peaks which lead to crack initiation within the adhesive can be determined.

Characteristics of the used finite element models

Firstly, the general assumptions made for generating the finite element models for tensile loading and for shear loading as well as their significant characteristics are described in this section. Afterwards, the results of the simulations are discussed separately for the three investigated adhesives.

For both loading setups a double symmetry is given and therefore only one quarter of the systems is modelled in order to reduce the computation time (see Fig. 5.25). Second order solid elements are used for all materials, for glass, stainless steel and the acrylic adhesive element type *C3D20* and for the silicone adhesives element type *C3D20H* according to [Abaqus, 2013b]. The hybrid formulation (*C3D20H*) is recommended for nearly incompressible materials like the two silicones.

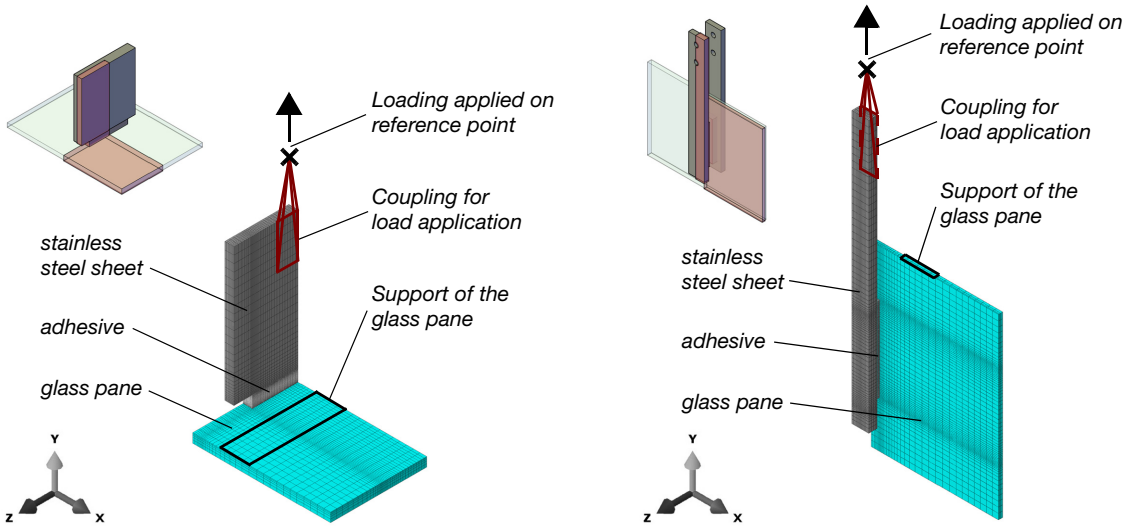

Fig. 5.25 *Models used for the finite element simulations of adhesive joints between glass and stainless steel at the glass surface subjected to tensile loading (left) and to shear loading (right)*

The contact between the adhesives and the substrate materials is modelled with tie constraints, without considering an eventual adhesive failure. Furthermore, since the stiffness of the joints is primarily of interest, no failure criteria is defined for the adhesive material. The glass and the stainless steel are modelled linear-elastic. For the glass a Young‘s modulus of *70 GPa* and a Poisson‘s ratio of *0.23* are used, while the assumed values for the stainless steel are *200 GPa*

for the Young‘s modulus and *0.30* for the Poisson‘s ratio. The adhesives are modelled as well linear-elastic in a first step. Afterwards, a suitable hyperelastic model is used for each silicone and the proposed strain rate dependent plastic model for the acrylic. The simulations in the second step are performed geometrically non-linear, since for all three adhesives large deformations are expected.

For the thickness of the adhesive joints, the mean value of the real measured thicknesses is used in the simulations. For the length and the width of the joints, the target values are used, since the real measured dimensions diverged significantly less compared to the thickness. The mesh size for the adhesive is chosen based on a convergence study. Additionally, a mesh refinement is applied towards all edges of the prismatic adhesive joint in order to obtain a more exact distribution of the true stresses. For the mesh on the glass and on the stainless steel parts the same size as for the adhesive is chosen in the contact areas. Further away from the contact area to the adhesive the mesh on the other materials gets coarser. The load is applied displacement-controlled with the same rates as used during the testing on a reference point, which is connected to the stainless steel part as shown in Fig. 5.25. The support of the glass panes through the hollow section bars is modelled by suppressing the translational degree of freedom in loading direction for the assumed contact surfaces (see Fig. 5.25).

Finite element results for specimens with Dow Corning 993

For the silicone *Dow Corning 993* the hyperelastic material model *Mooney-Rivlin* is used in the simulations based on the results obtained in subchapter 4.3.2 as well as on its repeated use in literature. The parameters provided in Tab. 4.3, which are determined by the curve fitting tool from *Abaqus*, are used. The diagrams plotted in Fig. 5.26 show a comparison between load-displacement curves obtained from the experimental tests and from the FE-simulations on linear adhesive joints at the glass surface with different lengths (left) and with different widths (right), subjected to tensile loading.

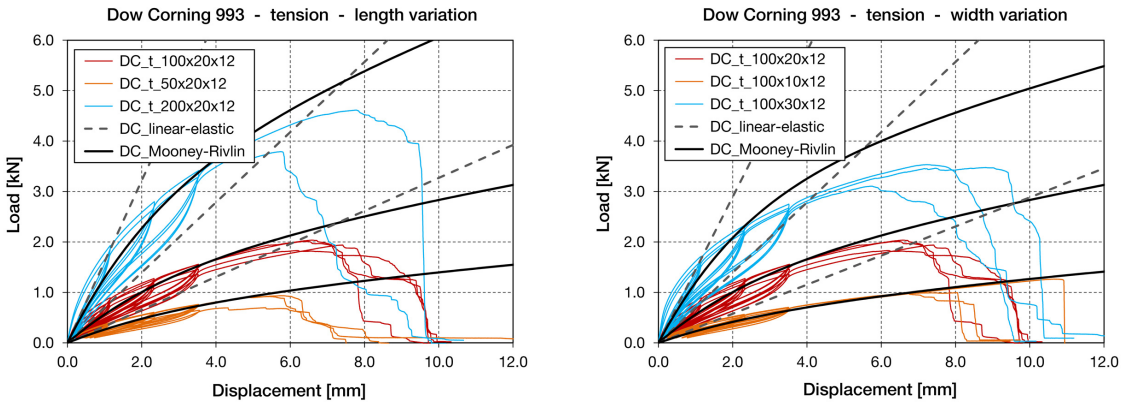

Fig. 5.26 *Comparison between experimental results and FE-simulation results for linear adhesive joints at the glass surface with different lengths (left) and different widths (right), subjected to tensile loading - Dow Corning 993*

Firstly, it can be noticed, that in the case of all investigated joint dimensions, the models with a linear-elastic material law for the silicone adhesive (dashed grey lines in the diagrams) underes-

timate the connection stiffness during the first loading cycle for displacements of up to around *1.2 mm*, which correspond to strains of approx. *10%*. Above these values, the linear-elastic models increasingly overestimate the connection stiffness and deliver unrealistic results. A Young's modulus of $E = 2.40$ *MPa* is used for the adhesive in these simulations. The models with the hyperelastic material law for the silicone adhesive show a better overall agreement with the experimental curves. However, they tend to slightly underestimate the connection stiffness during the first loading cycle up to higher displacement (and strain) values than the linear-elastic models. An approximate boundary displacement cannot be given, since these values vary with the joint size. For the larger joint lengths and widths an overestimation of the real connection stiffness can be observed above these values.

Similar comparisons between load-displacement curves obtained experimentally and by FE-simulations are illustrated in Fig. 5.27 for linear adhesive joints at the glass surface with different thicknesses subjected to tensile loading (left) and to shear loading (right). For tensile loading similar observations as in the case of the length and width variations can be made in general. Only for the smallest joint thickness of *6 mm*, the hyperelastic model leads as well to a pronounced overestimation of the connection stiffness for larger displacements.

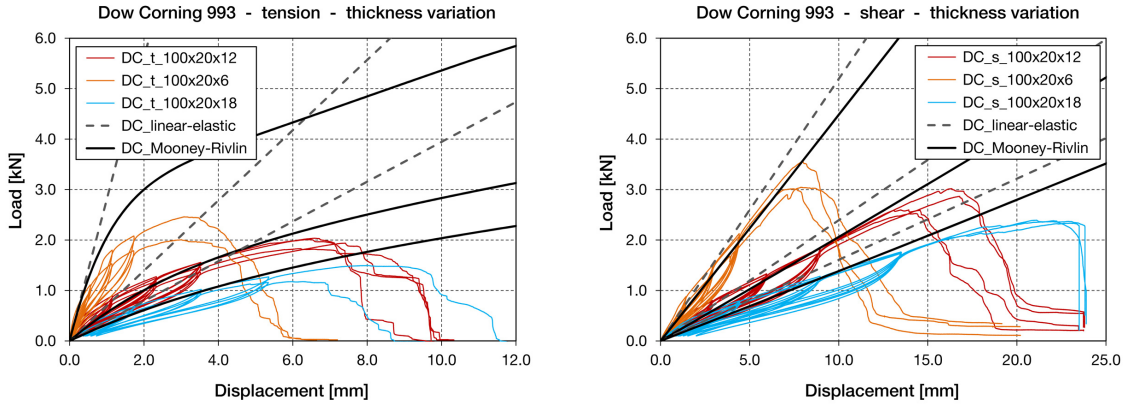

Fig. 5.27 *Comparison between experimental results and FE-simulation results for linear adhesive joints at the glass surface with different thicknesses, subjected to tensile loading (left) and to shear loading (right) - Dow Corning 993*

In the case of shear loading, an almost linear development of the experimental curves (excluding the loading cycles) can be observed. The comparison with the two analysed material models for the silicone adhesive shows a better overall fit of the hyperelastic model. However, for small displacements a slightly better agreement can be achieved with the linear-elastic model. Since in reality, generally a combined loading by tension or compression and shear is given, a non-linear material model as the hyperelastic *Mooney-Rivlin* model should be used, especially when the deformation behaviour of the connection as well as of the system including the connection is of primary interest.

In a next step, the distribution of the maximum principal stresses in the adhesive joints is analysed for the two different applied load types based on the results obtained with the hyperelastic model. Fig. 5.28 shows the coloured plot of the maximum principal stresses in the adhesive

(*Dow Corning 993*) from the joint with the dimensions of *100 mm x 20 mm x 12 mm* subjected to tensile loading at a strain of *50%*, which is the approximate average failure strain for the series with these dimensions. It can be noticed that stress peaks result at the edges of the adhesion areas to the two substrates (top and bottom surfaces of the prismatic adhesive body). These stress peaks are not to be treated as singularities from the finite element simulation, but result due to the resistance provided by the adhesion areas against deformations perpendicular to the loading direction. A good agreement is given between the location of these stress peaks and the positions of initial cracks observed during the experimental testing.

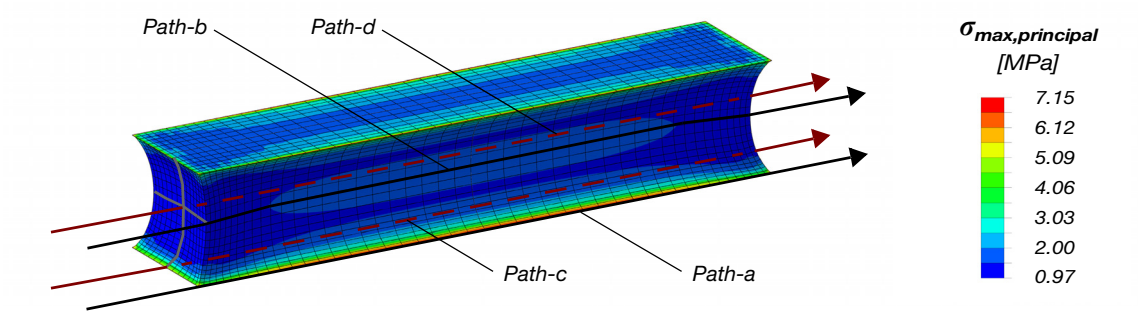

Fig. 5.28 *Distribution of maximum principal stresses in the adhesive from linear joints subjected to tensile loading and illustration of analysed paths*

Four paths are marked in Fig. 5.28 in length direction. Two paths extend along the adhesion surface adjacent to the glass substrate, *Path-a* along the edge of this surface and *Path-c* along its centre line. The other two paths are located in the midplane of the joint in thickness direction, *Path-b* at the lateral extremity of this plane and *Path-d* along its centre line. The diagrams in Fig. 5.29 show the maximum principal stresses along these paths for the adhesive joints with different thicknesses at a strain value of *25%*. This value is chosen on the one hand because the hyperelastic models for *Dow Corning 993* show a good agreement to the experimental results in this range and on the other hand because this strain value is also reached by the specimens with *Sikasil SG-550*, which allows a better comparison.

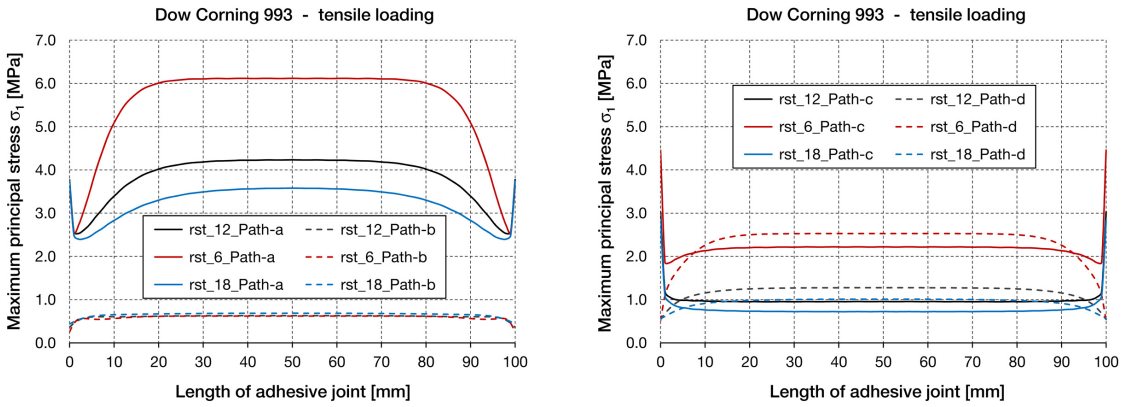

Fig. 5.29 *Distribution of maximum principal stresses along the length of the adhesive joints with different thicknesses, subjected to tensile loading at the border (left - paths a & b) and in the centre (right - paths c & d) of the joint at a strain of 25% for specimens with Dow Corning 993*

The distributions along the different paths plotted in the two diagrams show that the stresses occurring in the prismatic adhesive joint are more complex than the assumed constant engineering stresses determined as the force divided by the adhesion area, which are often used in design calculations. The maximum stress values occur either in the corners of the adhesion surface or towards the midpoint of the edges of these surfaces depending on the thickness of the joint. These are also the locations of crack initiation during the testing. The cohesive failure starts in direct vicinity of one of the two adhesion surfaces. Furthermore, it can be observed that on the lateral surface of the joint, the stresses along *Path-a* are significantly higher than along *Path-b* (percentaged, for lower strains this difference is larger than for higher strains). In the midplane of the joint however, the stresses along *Path-d* in the centre of the joint are slightly higher than the stresses along *Path-c* on the adhesion surface.

Fig. 5.30 shows the coloured plot of the maximum principal stresses in the adhesive (*Dow Corning 993*) from the joint with the dimensions of *100 mm x 20 mm x 12 mm* subjected to shear loading at a shear displacement of *120%*, which is the approximate average shear displacement at failure for the series with these dimensions. Stress peaks can be observed for this loading type at the edges of the adhesion surfaces which belong to the two front faces of the joint. On each of the front faces one edge shows tensile stresses and the other compressive stresses. The tensile stresses are significantly higher and correspond also to the locations of crack initiation which are observed for the cohesive failures during the experimental testing.

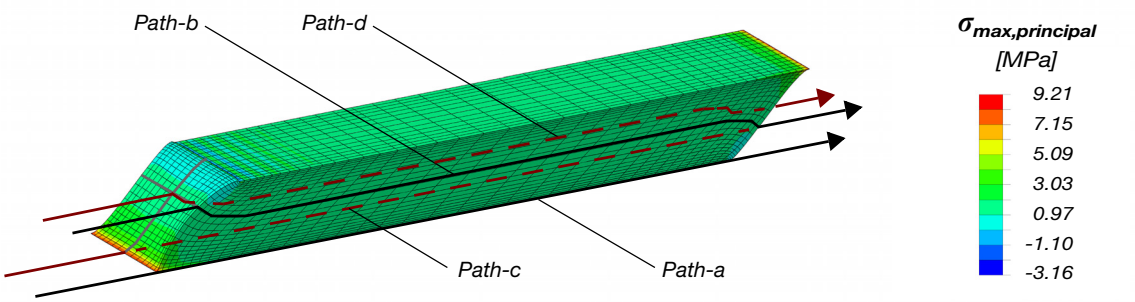

Fig. 5.30 *Distribution of maximum principal stresses in the adhesive from linear joints subjected to shear loading and illustration of analysed paths*

The same four paths as those used for the evaluation of the stress distribution in the case of tensile loading are marked in Fig. 5.30. The distribution of the maximum principal stresses along these paths for shear loading are plotted in the two diagrams from Fig. 5.31 at a shear displacement of *100%*. This value is chosen since almost all specimens with *Dow Corning 993* and with *Sikasil SG-550* tested under shear loading reach this value. By comparing the curves for the different paths and one joint thickness as well as the curves for the different joint thicknesses, it can be noticed that, apart from the areas in vicinity of the front faces, the stress values are almost constant averaging a value of approx. *1.2 MPa*. At the extremity where compressive stresses result along *Path-a* and *Path-c* a tremble can be observed in the curves, which is most pronounced for the *18 mm* thick joint at the end of *Path-c*. This is due to large distortions of the elements in this area. However, as also noted by [Staudt, 2013], these are not the locations of crack initiation.

For the tensile stress peaks occurring at the other extremity of *Path-a* and *Path-c* two explanations can be found: either *(i)* they are the result of peel stresses from an undesired rotation of the bonded parts, or *(ii)* they result because of the adhesion between the substrate and the adhesive, which have different stiffnesses. Although a double-lap specimen is used in the experimental tests, due to the pulling of the lateral metal sheets instead of the middle glass pane, the lower ends of the metal sheets are attempting to slightly move away from the glass pane with increasing loading. However, finite element simulations with and without a lateral restraint of the metal sheets show similar stress distributions.

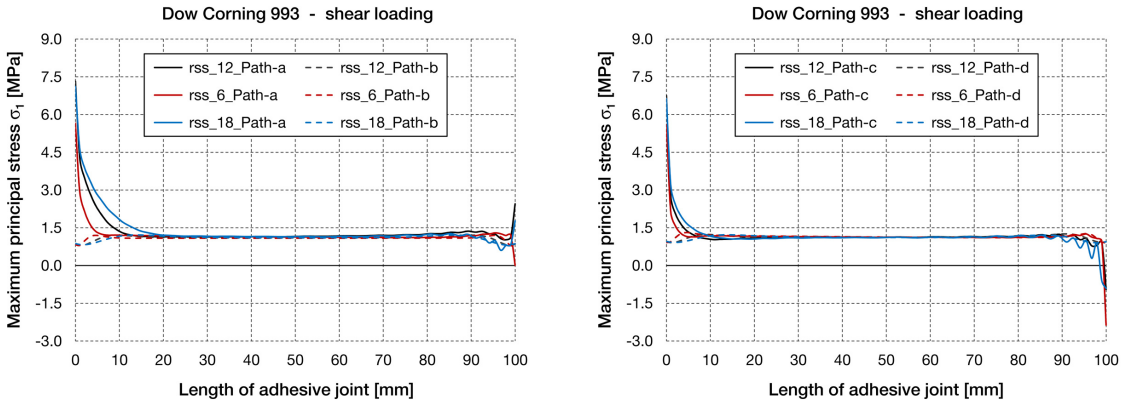

Fig. 5.31 *Distribution of maximum principal stresses along the length of the adhesive joints with different thicknesses, subjected to shear loading at the border (left - paths a & b) and in the centre (right - paths c & d) of the joint at a strain of 100% for specimens with Dow Corning 993*

A comparison to existing analytical models for adhesive joints loaded by shear as discussed in [Adams, 2005], [Habenicht, 2009] or [da Silva et al., 2009a] is not provided in this thesis, because of the following reasons: *(i)* the less complex models do not cover the boundary conditions given in these investigations, like different substrate materials and non-linear behaviour of the adhesive; *(ii)* the more complex models are time consuming and therefore do not provide advantages compared to finite element simulations as concluded in [da Silva et al., 2009b].

A possible design approach for adhesive joints with cohesive failure types based on finite element simulations, which would allow for a much more precise dimensioning of the joints, would be to compare the peak values of the maximum principal stresses obtained from the simulations to the true stress values determined in bulk material tests. For the silicone adhesive *Dow Corning 993* an average characteristic true stress of approx. *7.2 MPa* has been reached in the uniaxial tensile tests on dumbbell specimens, which are discussed in subchapter 4.2.2 (the value is determined based on the mean engineering stress provided in [Appendix A]). The maximum values reached with the hyperelastic material model for the principal stresses in the linear adhesive joint with the dimensions of *100 mm x 20 mm x 12 mm* at the approximate failure strains from the corresponding experimental tests show a good agreement for tensile loading (*7.15 MPa* in Fig. 5.28) and a relatively good agreement for shear loading (*9.21 MPa* in Fig. 5.30). If the development of such an approach is followed, safety factors in compliance with the semi-probabilistic safety concept, which consider a possible variation of the measured stresses as well as ageing influences, need to be included.

Finite element results for specimens with Sikasil SG-550

The hyperelastic material model used for the silicone *Sikasil SG-550* in the simulations is *Arruda-Boyce*. This choice is made based on the results obtained in subchapter 4.3.3 as well as on recommendations from the producer. Also in this case the parameters determined by the curve fitting tool from *Abaqus* are used (see Tab. 4.4 in subchapter 4.3.3). Load-displacement curves from the experimental tests and from the FE-simulations on linear adhesive joints subjected to tensile loading are compared in Fig. 5.32 for different joint lengths (left) and for different joint widths (right).

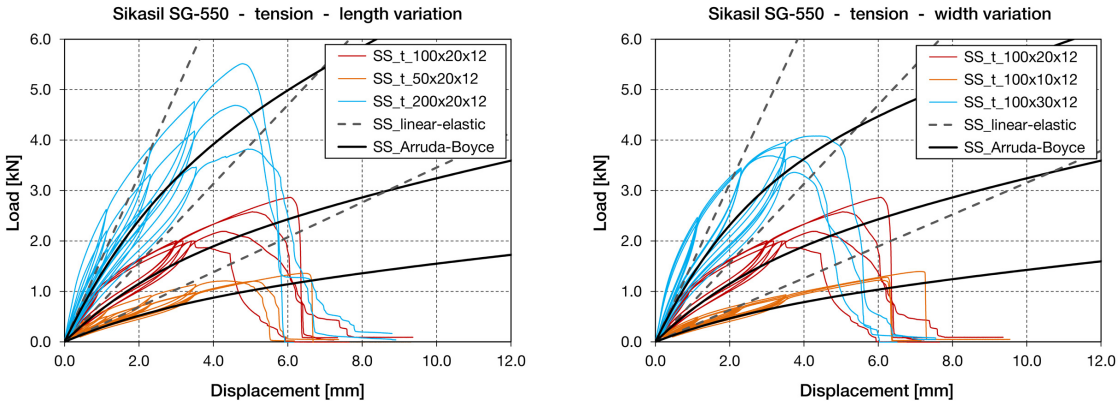

Fig. 5.32 *Comparison between experimental results and FE-simulation results for linear adhesive joints at the glass surface with different lengths (left) and different widths (right), subjected to tensile loading - Sikasil SG-550*

Similar comparisons for the linear adhesive joints with different thicknesses are plotted in Fig. 5.33 for tensile loading (left) and for shear loading (right). For both loading types and for all investigated dimensions it can be noticed from the four diagrams that neither the curves obtained with the linear-elastic adhesive model nor the curves determined with the hyperelastic adhesive model lead to a good fit of the experimental results. This is especially the case for tensile loading.

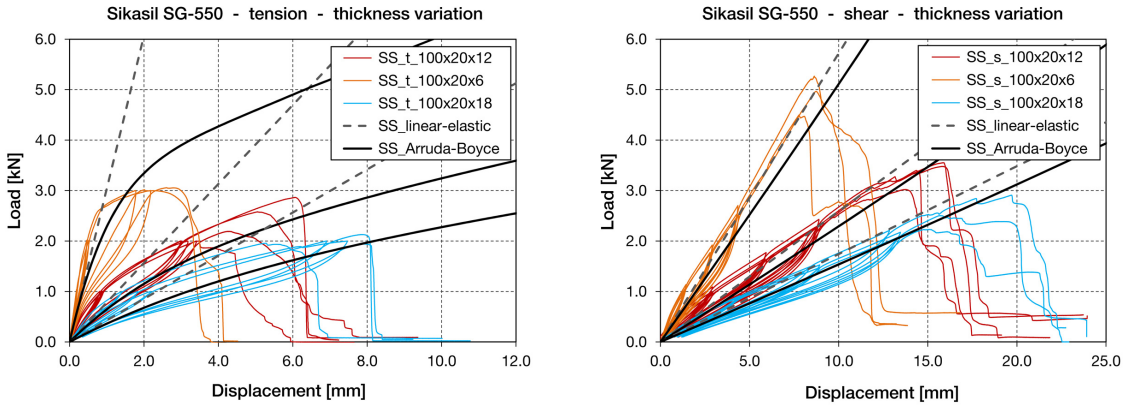

Fig. 5.33 *Comparison between experimental results and FE-simulation results for linear adhesive joints at the glass surface with different thicknesses, subjected to tensile loading (left) and to shear loading (right) - Sikasil SG-550*

For the linear-elastic material model of the adhesive a Young's modulus of $E = 2.60$ *MPa* is used. In the case of the joints with a thickness of *12 mm* under tensile loading (diagrams in Fig. 5.32) these models underestimate the loads (and the stiffness) from the experimental testing up to displacements of around *2.0-2.5 mm*, which correspond to strains of approx. *20%*. Above these values, the linear-elastic models increasingly overestimate the experimental results. A similar behaviour of these models can also be noticed for joints with different thicknesses under tensile loading. In the case of shear loading, the linear-elastic models slightly underestimate the experimental curves up to around *50%* shear displacement, but above this value they show a good fit.

The hyperelastic model (*Arruda-Boyce*) derived from the uniaxial tensile tests discussed in subchapter 4.2.3 leads to a good qualitative approximation of the experimental curves, but from a quantitative point of view, the experimental results are underestimated for all investigated joint dimensions and for both loading types. Also the other hyperelastic models analysed in subchapter 4.3.3 show a similar behaviour. Since the stresses reached in the uniaxial tests in both performed series are lower than the values specified in the technical data sheet of the material, further investigations are required for deriving a suitable material model.

Although the used hyperelastic model did not show a satisfying agreement with the experimental results, the stress distribution in the joints is analysed along the same paths as in the case of the specimens with the silicone *Dow Corning 993*. The location of the paths is illustrated in Fig. 5.28 for the specimens under tensile loading and Fig. 5.30 for the specimens under shear loading). Since the distribution and the location of the stress peaks is similar to the specimens with the silicone *Dow Corning 993*, only the diagrams for *Path-a* and *Path-b* are plotted in Fig. 5.34 for both load types. The same strain (25%) and shear displacement (100%) values are chosen. The resulting maximum principal stresses are slightly higher for the specimens with *Sikasil SG-550* than for those with *Dow Corning 993*. Additionally, it should be considered that qualitatively the stresses are correct, but quantitatively they are slightly lower than in reality because of the suboptimal material model.

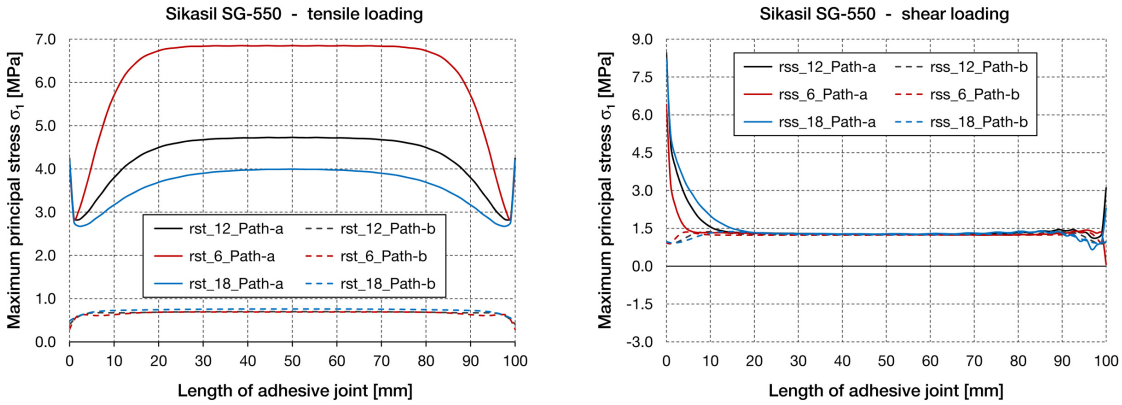

Fig. 5.34 *Distribution of maximum principal stresses along the length (paths a & b) of the adhesive joints with different thicknesses at a strain of 25% for tensile loading (left) and at a shear displacement of 100% for shear loading (right) for specimens with Sikasil SG-550*

Finite element results for specimens with SikaFast-5221 NT

In the finite element simulations of the experimental tests on linear adhesive joints with the acrylic *SikaFast-5221 NT* a linear-elastic model and the strain rate dependent plastic model proposed in subchapter 4.3.4 are investigated. For the plastic model, true yield stresses and both engineering and true plastic strains are used as input data. Furthermore, an extension of the proposed plastic model, which additionally takes a dilute concentration of voids in the adhesive material into account, is analysed as well. This additional model is included because the strain rate dependent plastic model alone leads to a significant overestimation of the maximum loads in the case of tensile loading. An explanation for this behaviour can be the air inclusions (voids) in the adhesive joints (see pictures in Fig. 5.35 and in [Appendix C]), which definitely have an influence on the maximum loads, but are not included in the plastic material model proposed in subchapter 4.3.4.

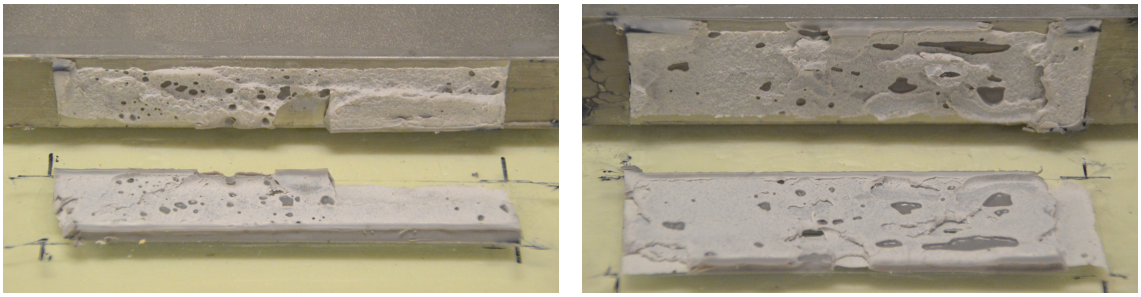

Fig. 5.35 *Voids noticed in the failure patterns of the adhesive joints at the glass surface with SikaFast-5221 NT tested under tensile loading*

In [Abaqus, 2013a] a model for porous (metal) plasticity is described which is implemented in the software and which is based on the yield condition in (Eq. 5.1) as a function of the void volume fraction *f*. This yield condition has been derived by [Tvergaard, 1981] from the initially proposed model by [Gurson, 1977].

$$\Phi = \left(\frac{q}{\sigma_y}\right)^2 + 2q_1 \cdot f \cdot \cosh\left(-q_2 \cdot \frac{3p}{2\sigma_y}\right) - (1 + q_3 \cdot f^2) = 0 \qquad \text{(Eq. 5.1)}$$

In (Eq. 5.1), q is the effective Mises stress, p is the hydrostatic pressure and σ_y is the yield stress of the fully dense matrix material and depends on the equivalent plastic strain $\bar{\varepsilon}_m^{pl}$ in the matrix. For using this model in *Abaqus*, only the relative density $r = 1 - f$, expressing the volume ratio of solid material to the entire volume of the material (f is the void volume fraction), and the material parameters q_1, q_2 and q_3 are required as input data. According to [Abaqus, 2013a], the ranges for these parameters found in literature are $q_1 = 1.0$ to 1.5, $q_2 = 1.0$ and $q_3 = q_1^2 = 1.0$ to 2.25.

This porous plasticity model is a simplified fracture mechanics method which allows to cover the damage development after yielding due to existing voids in the material. The advantage of the model is that it depends only on the relative density as a variable. However, it is sensitive to the adopted discretisation of the finite element mesh and it often shows convergence issues. The development of new voids as well as coalescence during loading can be additionally considered in Abaqus, but are not included for the simulations discussed in this subchapter, since no values for the required parameters are available (see [Abaqus, 2013a]). An extended discus-

sion on further material models which cover damage due to porosity can be found in [Kintzel, 2007].

For the performed finite element investigations it is assumed that $q_1 = q_2 = q_3 = 1.0$ (as proposed in the original *Gurson* model). For the relative density a value of *0.92* is used as a result of an iterative approach. The size of this value, which could be categorized as unrealistic, is on the one hand the result of large pores illustrated by the failure patterns in Fig. 5.35 and in [Appendix C] and can be on the other hand explained by the fact that the model does not account for the formation of new voids and for coalescence of growing voids.

The results from the simulations of the joints with different lengths and with different widths under tensile loading are compared in the diagrams from Fig. 5.36 with the load-displacement curves from the corresponding experimental tests. By using the linear-elastic model for the acrylic a good agreement with the experimental results is reached for small displacements (see dashed grey curves). However, once the adhesive starts to yield, this model leads to an overestimation of the transferable loads and implicitly of the occurring stresses.

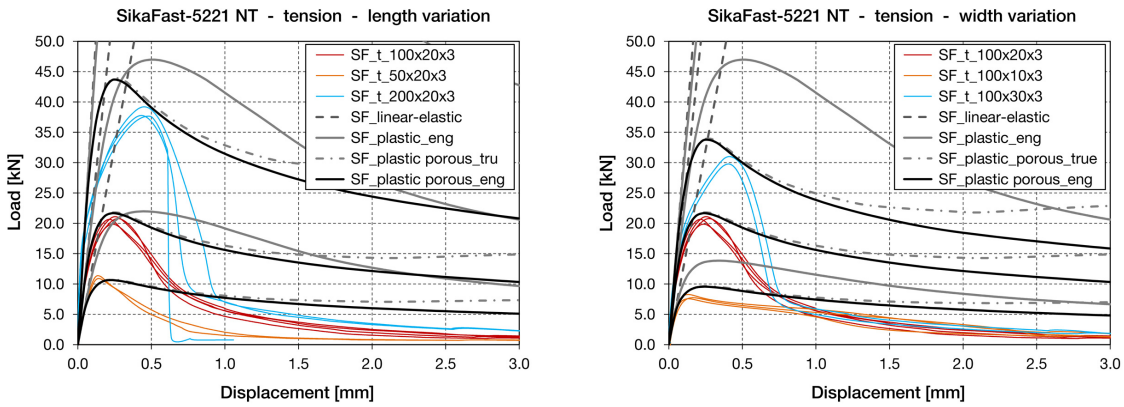

Fig. 5.36 *Comparison between experimental results and FE-simulation results for linear adhesive joints at the glass surface with different lengths (left) and different widths (right), subjected to tensile loading - SikaFast-5221 NT*

For the strain rate dependent plastic model only the results obtained with true yield stresses and engineering plastic strains as input data are shown in Fig. 5.36 as continuous grey curves. This model shows a slightly better agreement for small displacements, but is not capable to reproduce the yielding as it occurs in the experimental tests with tensile loading. Although, qualitatively, the curves from the simulations look similar to the experimental ones, the yielding seems to start at significantly higher loads. Therefore, the maximum loads from the tests are substantially overestimated in these simulations (for most joint geometries by over *100%*). The alternative with true plastic strains as input data leads to similar results in the case of tensile loading. The explanation for this behaviour is assumed to be the presence of voids in the adhesive joints.

The addition of porous plasticity to the strain rate dependent plastic model with engineering plastic strains as input data leads for tensile loading to significant improvements concerning the agreement between the maximum loads reached in the simulations and those from the experi-

mental tests (see results plotted as black continuous curves in Fig. 5.36). The inclination of the curves until reaching the maximum load is predicted better by this model, but there are still discrepancies compared to the exeprimental data. For the *50 mm* long joint, the simulation leads to a smaller inclination than in the experiments, while for the *200 mm* long joint and the *30 mm* wide joint the opposite is the case. Furthermore, the simulation leads to around *10%* higher maximum loads for the *200 mm* long joint as well as for the *10 mm* and the *30 mm* wide joints compared to the experimentally obtained loads. The existing variations can be explained by the inhomogeneous distribution of the pores as well as by their different sizes observed in the failure patterns (see [Appendix C]). For all investigated dimensions of the joints tested under tensile loading, the simulation results show higher load values in the part where the load starts to drop. The use of true plastic strains instead of engineering plastic strains as input data in the case of this model (see grey curves alternating one dash and one dot in Fig. 5.36) has no influence on the part where the transferable load is rising, but leads to a slightly worse fit (higher loads) in the part where the load starts to drop. The mesh sensitivity mentioned in literature for this model can be confirmed, since a large number of elements along the joint thickness or a high aspect ratio of the elements leads to convergence issues. A number of ten elements are used in thickness direction.

For the joints with different thicknesses loaded by tension a similar behaviour of the different models can be noticed in the left diagram from Fig. 5.37. For the thicker joint (*6 mm*), the difference between the maximum load from the experimental tests and the maximum load from the simulation with the plastic model without porosity gets smaller. It can be therefore concluded that for thick joints the influence of voids on the damage after yielding is smaller than for thin ones.

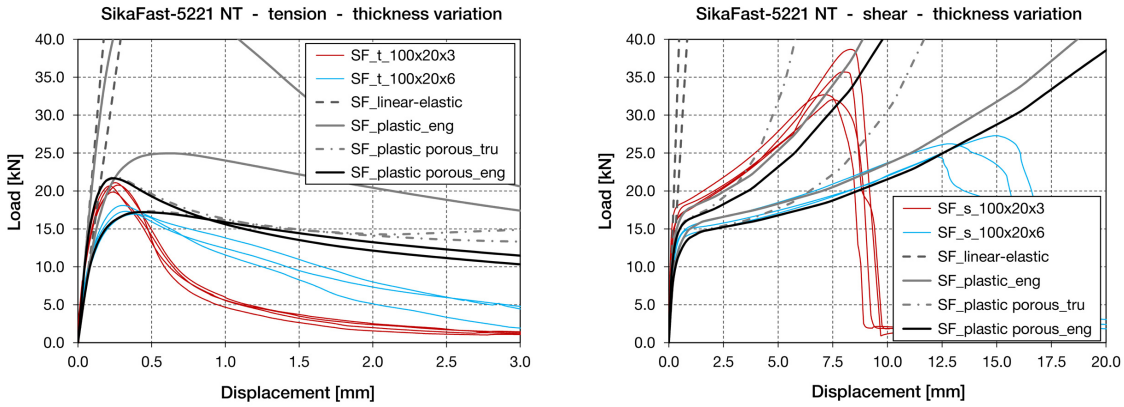

Fig. 5.37 *Comparison between experimental results and FE-simulation results for linear adhesive joints at the glass surface with different thicknesses, subjected to tensile loading (left) and to shear loading (right) - SikaFast-5221 NT*

The comparison of load-displacement curves obtained from finite element simulations and experimental testing on joints subjected to shear loading is shown in the right diagram from Fig. 5.37. The results obtained in the simulations with the linear elastic model show a good agreement with the experimental results only until the yielding starts. Interestingly, the strain rate dependent plastic model with engineering plastic strains as input data (continuous grey curves)

shows a good agreement both before and after yielding. For both investigated thicknesses the development and the inclination of the simulation curves are similar to the experimental ones.

Different to tensile loading, in the case of shear loading the addition of porous plasticity leads to a slightly worse agreement between simulation and experimental results (compare black continuous curves to grey continuous curves in Fig. 5.37, right). However, the difference between the load values obtained with the plastic model alone and those from the model which takes the voids into account is small compared to the case of tensile loading. The effect of using engineering plastic strains as input data for plasticity instead of true values on the load-displacement curves in case of shear loading is illustrated by the grey curves alternating one dash and one dot in Fig. 5.37, right. Until yielding the results are similar, but shortly afterwards, the models with true plastic strains as input data lead to increasingly higher loads compared to the experimental results.

The stress distributions along the length of the joints with a thickness of *3 mm* are provided for shear loading in Fig. 5.38 (obtained with the strain rate dependent plastic model) and in Fig. 5.39 (obtained with the model including porous plasticity). In the case of both models, engineering plastic strains are used as input data. The principal stresses are plotted for different shear displacements along *Path-a* in the left diagram and along *Path-b* in the right one.

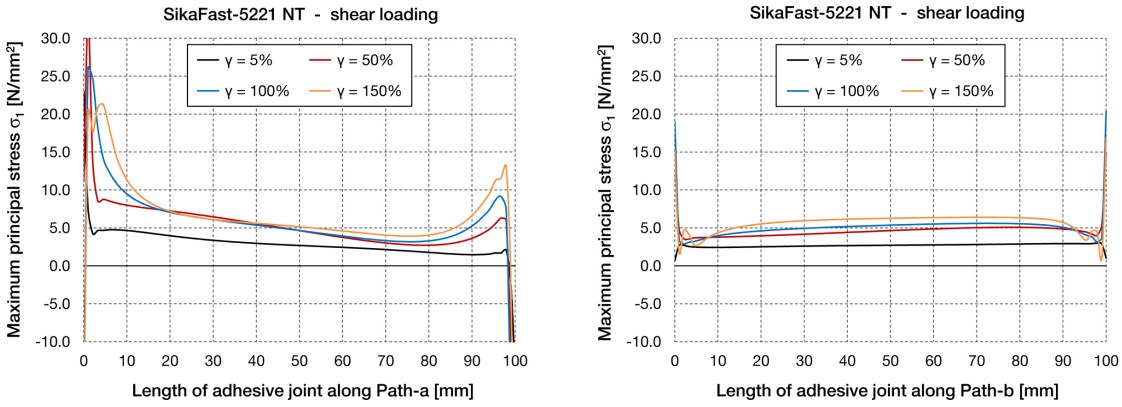

Fig. 5.38 *Distribution of maximum principal stresses along the length of the adhesive joints under shear loading for specimens with SikaFast-5221 NT and a joint thickness of 3 mm at different shear displacements (path a - left and path b - right) obtained with the strain rate dependent plastic model alone*

It can be noticed for both models, that once the yielding starts, the maximum stress value at the left end of *Path-a* is not increasing anymore, but is moving slightly towards the middle of the path, while the stresses along *Path-b* are slowly getting higher. The addition of porous plasticity leads to a more uniform stress distribution along both *Path-a* and *Path-b* coupled with a reduction of the maximum stress values at the ends of *Path-a* (excepting the singularities at the right end). A similar redistribution of stresses is noticed for a joint thickness of *6 mm* as well.

The stress distributions along the length of the joints with the same dimensions (*100 mm x 20 mm x 3 mm*) subjected to tensile loading are plotted in Fig. 5.40 at different strain values. Only the results from the simulations with the model including porous plasticity are pro-

vided, since the values obtained with the model without these properties are considered unrealistic due to the high overestimation of occurring loads. It can be noticed, that with increasing strain, the stresses near the lateral surfaces are redistributed from the substrate interfaces towards the centre of the joints. While the maximum principal stresses along *Path-a* are decreasing with increasing strain (see Fig. 5.40, left), they are increasing along *Path-b* (see Fig. 5.40, right).

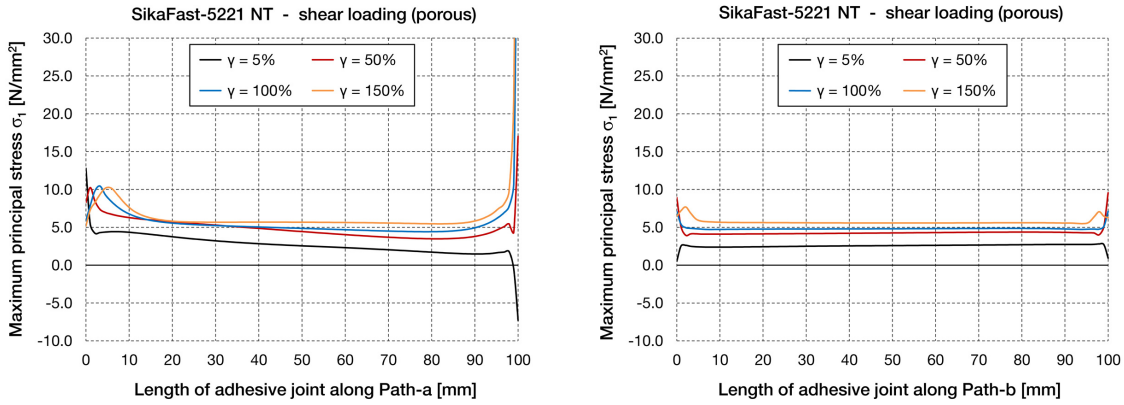

Fig. 5.39 *Distribution of maximum principal stresses along the length of the adhesive joints under shear loading for specimens with SikaFast-5221 NT and a joint thickness of 3 mm at different shear displacements (path a - left and path b - right) obtained with the strain rate dependent plastic model with additional porous plasticity*

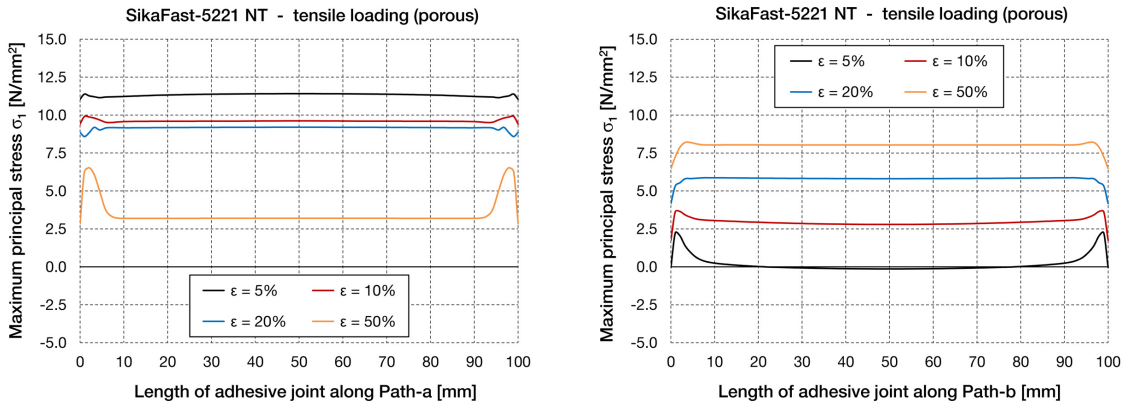

Fig. 5.40 *Distribution of maximum principal stresses along the length of the adhesive joints under tensile loading for specimens with SikaFast-5221 NT and a joint thickness of 3 mm at different strain values (path a - left and path b - right) obtained with the strain rate dependent plastic model with additional porous plasticity*

Since in the intended application for the acrylic adhesive in glass-metal elements with composite structural behaviour the main loading type is shear and because the porous plasticity model shows convergence issues depending on joint geometry, FE-mesh and loading type, the strain rate dependent plastic model which doesn‘t take existing voids into account is used in the finite element studies to follow within this thesis. However, for certain scenarios, additional simulations with the porous plasticity model are carried out in order to show possible improvements in

terms of agreement with the experimental results.

Nevertheless, for an exact reproduction of the material behaviour, further investigations at material and at connection level should be conducted in order to improve this model for all potential loading types. The limitations of the porous plasticity model investigated in this subchapter result from the fact that it is based on the Mises criterion, which, generally, is considered to show poor suitability for polymer materials. Other porous plasticity models, also addressed to as cavitation models in litertaure (see [Duncan & Dean, 2003] and [NPL Manual, 2007]), which need to be implemented by user subroutines in Abaqus, should be analysed for their suitability. The yield function for a modified Drucker-Prager model proposed in this literature, which considers the influence of cavitation, is given in (Eq. 5.2):

$$\Phi = \frac{\sigma_e^2}{\sigma_M^2} - (q_1 \cdot f)^2 + 2q_1 \cdot f \cdot \cosh\left(\frac{3\sigma_k}{2\sigma_M}\right) - \left(1 - \frac{\mu \cdot \sigma_k}{\sigma_M}\right) = 0 \qquad \text{(Eq. 5.2)}$$

The variables in this equation are the effective shear stress, σ_e, the hydrostatic stress, σ_k, and the shear yield stress of the matrix material, σ_M. The parameter μ accounts for the sensitivity of yielding to hydrostatic stress, while q_1 considers the influence of void interactions on the stress distribution in the matrix. f is the void volume fraction as in the case of the yield criterion in (Eq. 5.1). However, for this model stress-strain properties determined from experimental tests on bulk material under three different stress states are required (tension, shear and compression). Such investigations are beyond the scope of this thesis

5.3 Linear adhesive joints at the edge of laminated glass panes

Adhesive joints at the glass edge with different cross section geometries are interesting on the one hand for some of the load transfer concepts introduced in subchapter 3.5.1 for glass-metal elements with composite structural behaviour and on the other hand for the connection of a facade glazing to glass fins. In both application cases the joints can be subjected to tensile, compressive and shear loading in the in-plane direction of the glass pane.

Linear adhesive joints at the glass edge with rectangular, L-shaped and U-shaped joint geometries of the three selected adhesives are investigated separately under tensile, compressive and shear loading. The designed test specimen for the rectangular joints tested under tensile loading and the used test setup are illustrated in Fig. 5.41. The glass panes are *300 mm* long and *210 mm* wide and are made of laminated glass consisting of two *10 mm* thick sheets of heat strengthened glass (HSG) and a *1.52 mm* thick PVB interlayer. The stainless steel component made of the material *no. 1.4404* has a width of *140 mm*, a thickness of *20 mm* and a length of *150 mm* in order to allow a proper clamping in the testing machine and enough space for connecting the displacement transducers.

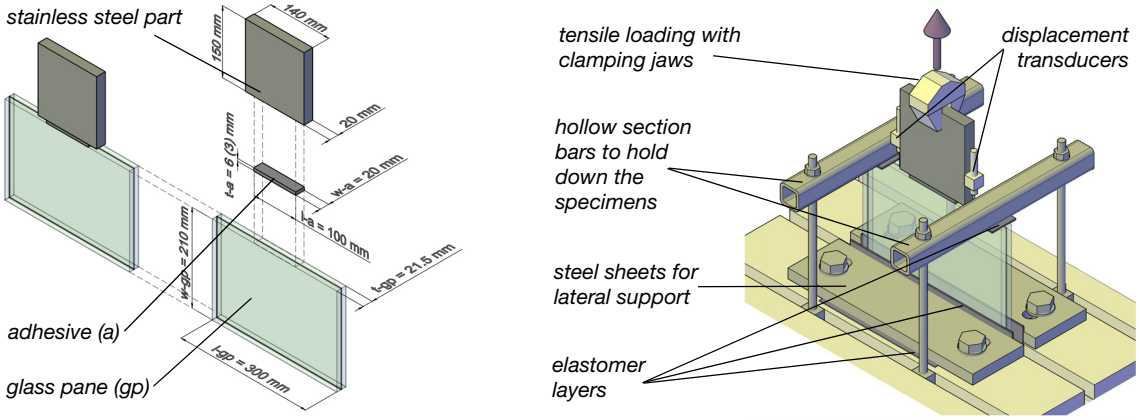

Fig. 5.41 *Exploded view of the test specimen (left) and sketch of the planned test setup (right) for adhesive joints with rectangular cross section at the glass edge under tensile loading*

For testing, the glass pane is held down in a standing position with two square hollow section bars (*40 mm x 40 mm x 5 mm*) as in the case of the test specimens with adhesive joints at the glass surface tested under shear loading. To restrain the specimens laterally, two steel sheets are fixed on the machine table at the bottom of the glass panes. Elastomer layers are positioned between the glass pane and all tangent steel elements to avoid a glass failure due to stress peaks. The load is applied similar to the test series discussed in subchapter 5.2 with a clamping device which pulls the stainless steel sheet away form the glass pane.

The test specimens with L-shaped and U-shaped cross sections of the adhesive joints tested under tensile loading are illustrated in Fig. 5.42. In order to facilitate the realisation of the desired joint geometries the stainless steel parts are designed as follows: *10 mm* thick stainless steel sheets with varying width depending on the used adhesive thickness are welded perpendicularly to sheets of the type used for the rectangular joints; then, *15 mm* thick stainless steel

sheets with gashed threads are screwed to the welded parts. The screwed parts are connected only on one side of the glass pane for the L-shaped and on both sides for the U-shaped joints. Three *M6* bolts of quality *8.8* are used for each connection.

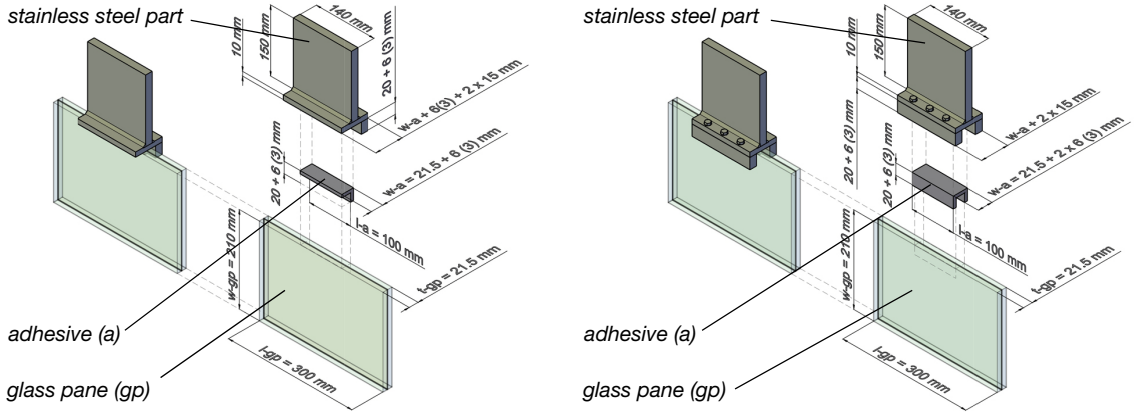

Fig. 5.42 *Exploded view of the test specimens for adhesive joints with L-shaped (left) and U-shaped (right) cross section at the glass edge under tensile loading*

The designed test specimens for the adhesive joints at the edge of laminated glass tested under compressive loading are similar to those tested under tensile loading. Only the stainless steel parts are adapted for applying a compressive load, since no clamping is required. The test specimen for the rectangular joint and the used test setup are illustrated in Fig. 5.43. The same type and size of laminated glass panes as for the specimens tested under tensile loading are used. The stainless steel component made of the material *no. 1.4404* has a length of *200 mm* in order to allow enough space for connecting the displacement transducers. The height and the thickness are both *20 mm*.

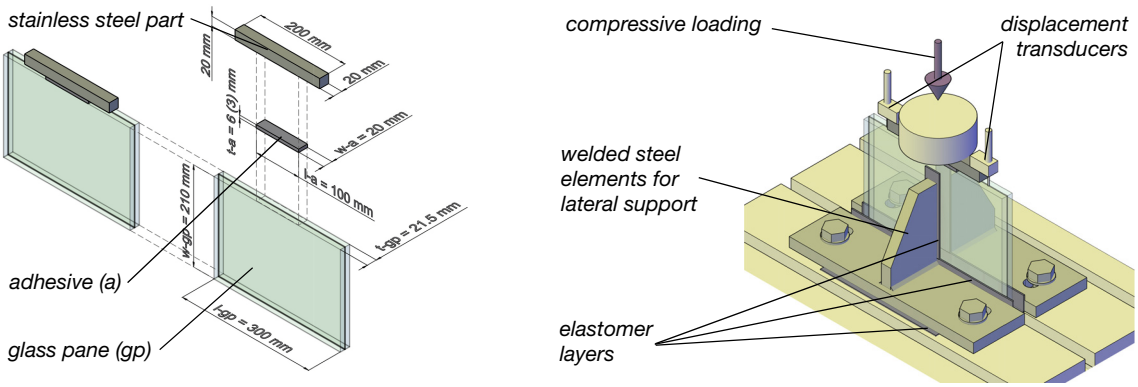

Fig. 5.43 *Exploded view of the test specimen (left) and sketch of the planned test setup (right) for adhesive joints with rectangular cross section at the glass edge under compressive loading*

During testing, the specimens are placed in a standing position on the machine table and restrained laterally with steel elements. Other than in the case of the specimens loaded by tension, a vertical steel sheet is welded to the horizontal sheet in order to prevent an eventual buckling of the glass pane. The load is applied directly with the universal testing machine by pressing the stainless steel part towards the glass pane. The stainless steel parts of the test

specimens with L-shaped and U-shaped cross sections of the adhesive joint tested under compressive loading consist of a *200 mm* long and *10 mm* thick stainless steel sheet to which *15 mm* thick stainless steel elements with gashed threads are screwed (similar to the welded parts in the case of the specimens tested under tensile loading). Sketches of these specimens can be found in [Appendix D].

For the adhesive joints at the edge of laminated glass tested under shear loading a double-lap shear test specimen is chosen, similar to the other performed shear tests described in subchapters 4.4 and 5.2. Fig. 5.44 shows the specimen for the rectangular joint and the used test setup. Two laminated glass panes of the same size and composition as those used for the tensile and the compressive tests on adhesive joints at the edge of laminated glass are used for each test specimen. A stainless steel component made of the material *no. 1.4404* is adhesively bonded between the two glass panes at their edge. In the case of the rectangular joints a *370 mm* long, *50 mm* wide and *20 mm* thick sheet is used. The length is chosen in order to have enough space for connecting the displacement transducers. The width is needed to provide a large enough clamping surface.

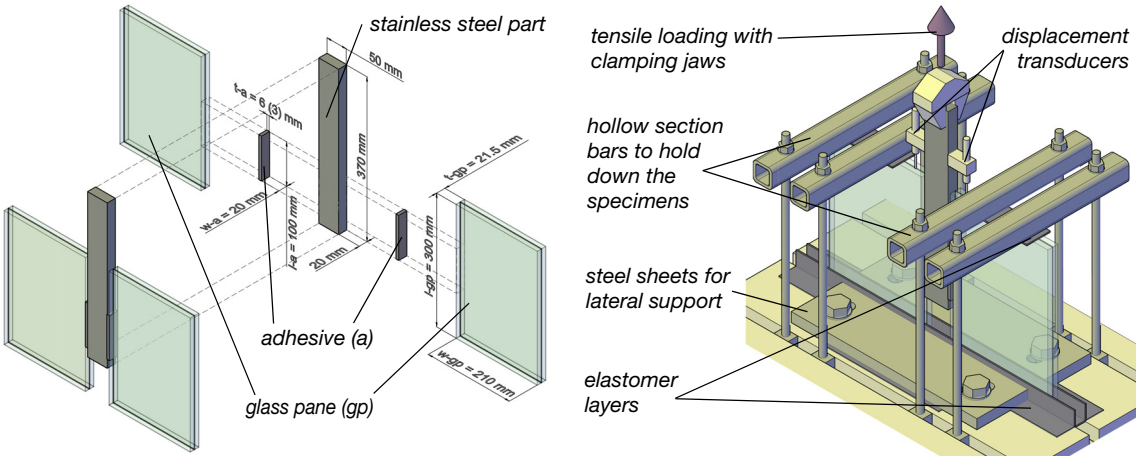

Fig. 5.44 *Exploded view of the test specimen (left) and sketch of the planned test setup (right) for adhesive joints with rectangular cross section at the glass edge under shear loading*

The specimens are tested in a standing position. Each of the two glass panes is held down with two square hollow section bars (*40 mm x 40 mm x 5 mm*) in order to avoid a rotation during loading. A lateral restraint at the bottom of the glass panes is realized with steel sheets as in the case of the test specimens with adhesive joints at the glass edge tested under tension. The direct contact between the metal parts and the glass pane is avoided by placing *3 mm* thick elastomer layers between the two materials. The load is applied with clamping jaws which pull the stainless steel part upwards parallel to the glass edges.

For the test specimens with L-shaped and U-shaped cross sections of the adhesive joints, the stainless steel part consists of the same stainless steel sheet as in the case of the rectangular cross sections to which *140 mm* long and *10 mm* thick stainless steel sheets with screwed elements are welded perpendicular on each length edge. These welded elements are similar to those used for the specimens tested under tensile loading. Sketches of the specimens with L-

shaped and U-shaped cross section of the adhesive joint tested under shear loading can be found in [Appendix D].

All tests on adhesive joints at the edge of laminated glass are run displacement-controlled. For the specimens with *Dow Corning 993* and with *Sikasil SG-550* tested under tensile loading and under shear loading a speed of *5 mm/min* is used. For the specimens with *SikaFast-5221 NT* tested under the same types of loading a smaller loading speed of *1 mm/min* is chosen because of the thinner joint and the related smaller expected displacements. No load cycles are run for these series for none of the three adhesive. The compressive tests on adhesive joints at the glass edge are run with a loading speed of *1 mm/min* for the two silicones and a loading speed of *0.5 mm/min* for the acrylic. In the case of the silicones also load cycles are run as follows: loading up to *25%* compression (*1.5 mm*), unloading, loading up to *50%* compression (*3 mm*), unloading, loading until a load of *400 kN*, unloading. The load is not increased further since a glass failure is not the scope of these test and is aimed to be avoided.

Tab. 5.13 *Number of test specimens and denominations for the adhesive joints at the edge of laminated glass tested under tensile, compressive and shear loading*

Joint dimensions [mm] length x width x thickness	**Cross section**	**Number of test specimens and denomination**		
		Dow Corning 993 (DC)	**Sikasil SG-550 (SS)**	**SikaFast-5221 NT (SF)**
			Tensile loading	
ret_100 x 20 x 6	rectangular	3 (ret_07-09)	3 (ret_04-06)	3 (ret_01-03)
let_100 x (21.5+20) x 6	L-shaped	3 (let_07-09)	3 (let_04-06)	3 (let_01-03)
uet_100 x (21.5+2x20) x 6	U-shaped	3 (uet_07-09)	3 (uet_04-06)	3 (uet_01-03)
			Compressive loading	
rec_100 x 20 x 6	rectangular	3 (rec_07-09)	3 (rec_04-06)	3 (rec_01-03)
lec_100 x (21.5+20) x 6	L-shaped	3 (lec_07-09)	3 (lec_04-06)	3 (lec_01-03)
uec_100 x (21.5+2x20) x 6	U-shaped	3 (uec_07-09)	3 (uec_04-06)	3 (uec_01-03)
			Shear loading	
res_100 x 20 x 3	rectangular	3 (res_07-09)	3 (res_04-06)	3 (res_01-03)
les_100 x (21.5+20) x 3	L-shaped	3 (les_07-09)	3 (les_04-06)	3 (les_01-03)
ues_100 x (21.5+2x20) x 3	U-shaped	3 (ues_07-09)	3 (ues_04-06)	3 (ues_01-03)

Tab. 5.13 shows the target dimensions of the adhesive joints, the number of tested specimens and the denomination of these specimens for the test series on linear adhesive joints at the edge of laminated glass with different cross section geometries and different loading types. The real dimensions of the adhesive joints are measured in thickness direction based on the thickness of the used PTFE blocks and in length directions directly on the adhesive after curing where possible. These dimensions are provided in [Appendix D]. In width direction a good measurement of the real dimensions is only possible for the specimens with rectangular cross section, since for the other geometries no good access with a sliding calliper is available.

5.3.1 Manufacturing of the test specimens

The specimens for the test series with the silicone *Dow Corning 993* and with the acrylic *Sika-Fast-5221 NT* are assembled and adhesively bonded in the laboratory facilities of *Graz University of Technology*. For the specimens with the silicone *Sikasil SG-550* the laboratory facilities of *Sika Services AG* in Widen (CH) are used in order to ensure a proper mixing. The preparation of all the surfaces to be adhesively bonded is carried out in the same way as done for the adhesive joints at the glass surface, including taping, cleaning and application of primer. For the silicone *Dow Corning 993* and the acrylic *SikaFast-5221 NT* also the same mixing procedures are used. In the case of the silicone *Sikasil SG-550* a dynamic mixer is used to mix and to apply the adhesive in the same way as described in subchapter 4.4.2 for the investigations on the adhesion of this material.

The assembling of the test specimens differs depending on the cross section geometry. The ones with a rectangular cross section are assembled in a lying position. Firstly, the glass pane is fixed against a timber plank and the PTFE blocks which determine the joint thickness are brought in position. Secondly, an adhesive caterpillar is applied on the glass edge, between the PTFE blocks and the stainless steel sheet is pressed on the adhesive towards the PTFE blocks. Finally, the joint is tooled with a spatula, the tapes are removed and the specimen is fixed with a screw clamp. The manufacturing procedure is illustrated in Fig. 5.45.

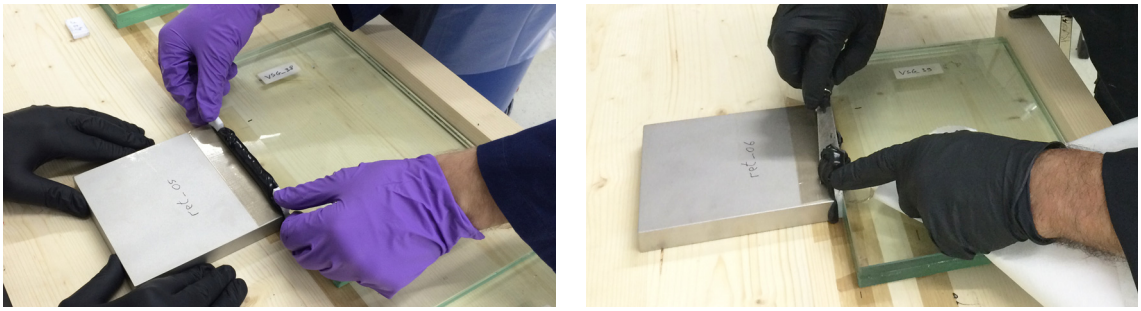

Fig. 5.45 *Assembling of the test specimens for adhesive joints at the glass edge with rectangular cross section (example of a specimen with Sikasil SG-550 tested under tensile loading)*

The specimens with an L-shaped cross section are assembled in a standing position. Firstly, the stainless steel parts are fixed between glued-laminated timber beams and the PTFE blocks are positioned in such a way that they can be easily removed at a later time. Secondly, the adhesive is applied on the stainless steel part (see Fig. 5.46, left) and the glass pane is pressed both downwards and laterally on the adhesive towards the PTFE blocks. Finally, the glass pane is fixed with timber blocks and screw clamps, the joint is tooled and the tapes are removed (see Fig. 5.46, right).

The amount and the distribution of applied adhesive together with the way the glass pane is pressed on it are decisive for the final quality of the joint. This assembling procedure is chosen instead of a procedure where the glass pane is first fixed and the resulting gaps are then filled with adhesive because of the small thickness of the joints (*6 mm* for the silicones and *3 mm* for the acrylic) and the occurring difficulty to inject and uniformly distribute the adhesive into the gaps.

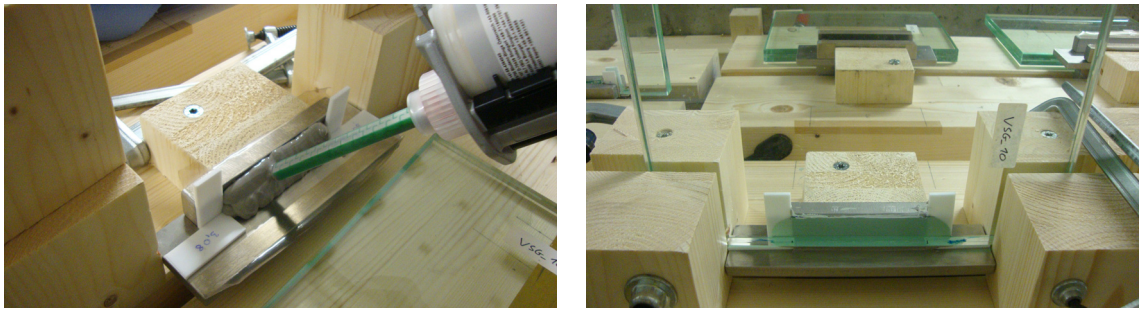

Fig. 5.46 *Assembling of the test specimens for adhesive joints at the glass edge with L-shaped cross section (example of a specimen with SikaFast-5221 NT tested under tensile loading)*

The specimens with a U-shaped cross section are assembled in a similar way to those with the L-shaped cross section (see Fig. 5.47). After fixing of the stainless steel part and preparing of the adhesion surfaces, the adhesive is applied inside the U-part between the PTFE blocks. In a next step, the glass pane is pressed downwards into the U-part, while the adhesive is distributed and the superfluous material is pressed outside laterally. A gap filling procedure is not used for the same reasons as in the case of the L-shaped joints.

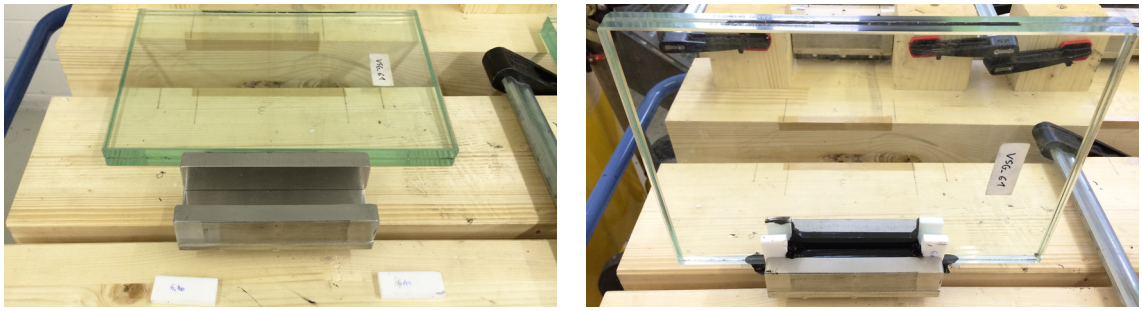

Fig. 5.47 *Assembling of the test specimens for adhesive joints at the glass edge with U-shaped cross section (example of a specimen with Sikasil SG-550 tested under tensile loading)*

The test specimens for adhesive joints at the edge of laminated glass tested under compressive loading are manufactured in the exact same way as those tested under tensile loading. The manufacturing of the test specimens for the adhesive joints at the edge of laminated glass tested under shear loading is carried out in a similar way to those tested under tensile and compressive loading. The only difference is resulting from the fact that two joints have to be produced, which is done in two steps. Firstly, the joint between one glass pane and the stainless steel part is made and the half-way finished specimen is left over night to cure. Secondly, the next day, the joint between the stainless steel part and the second glass pane is produced.

All specimens for adhesive joints at the edge of laminated glass are stored in a climatic chamber at *23 °C* and *50% RH* for *28 days* before testing.

5.3.2 Adhesive joints at the glass edge under tensile loading

The results of the investigations on adhesive joints between glass and stainless steel substrates at the edge of laminated glass are presented separately for tensile loading, compressive loading and shear loading in subchapters 5.3.2, 5.3.3 and 5.3.4. In each of these subchapters, firstly, noteworthy findings concerning the failure modes and patterns are discussed. Secondly, the mechanical behaviour of the joints with different cross section geometries and different adhesives is analysed based on load-displacement relationships as well as stress values in the case of the shear tests.

Fig. 5.48 *Specimens with adhesive joints at the glass edge tested under tensile loading*

Fig. 5.48 illustrates the real test setups used for the tensile tests on linear adhesive joints at the edge of laminated glass, showing a specimen with rectangular (left), one with L-shaped (middle) and one with U-shaped (right) cross section of the joint geometry. The test setups are basically identical, only the positioning on the testing machine is rotated by *90°* in the case of the specimens with *Sikasil SG-550* (see Fig. 5.48, middle). This results in a slightly different fixing of the two steel plates, which restrain the glass pane laterally at the bottom, to the testing machine table. The displacements used in the evaluation of the results are determined based on the measurements of the two transducers, since the displacement of the testing machine includes also compressions within the elastomer intermediate layers used to avoid stress peaks in the glass.

Evaluation of the failure patterns

Typical failure patterns are described in this subchapter for the adhesive joints at the edge of laminated glass with different adhesives as well as with different cross sections of the joint geometry. Figures with the failure pattern for each specimen are provided in [Appendix D]. In the case of the specimens with *Dow Corning 993* only cohesive failure is noticed independently on the cross section of the joint geometry (see Fig. 5.49). Some tiny air inclusions similar to those in the case of the joints at the glass surface can be noticed along the rupture surfaces.

The specimens with joints made of *Sikasil SG-550* at the edge of laminated glass, tested under tensile loading, show as well mainly cohesive failure (see Fig. 5.50). However, some specimens exhibit also areas where a debonding from the glass surfaces occurs. On the glass edge itself, small areas with adhesion failure are noticed for almost all specimens and can be observed in the examples from Fig. 5.50. For some specimens a complete adhesive debonding from the edge of one of the two laminated glass panes occurs (see examples in [Appendix D]). In the

case of some specimens with L-shaped and U-shaped cross sections also a partial adhesive failure on the glass pane surfaces is noticed (see [Appendix D]). The reason for this can be either the rotation to which the adhesive joint is subjected during loading (especially in the case of the L-shaped cross sections) or the fact that the manufacturing concept did not allow to press the lateral stainless steel parts and the glass panes together after filling the adhesive in the gaps.

DC_ret_100x20x6 *DC_let_100x(21.5+20)x6* *DC_uet_100x(21.5+2x20)x6*

Fig. 5.49 *Typical failure patterns for the adhesive joints at the glass edge with Dow Corning 993 and different cross sections tested under tensile loading*

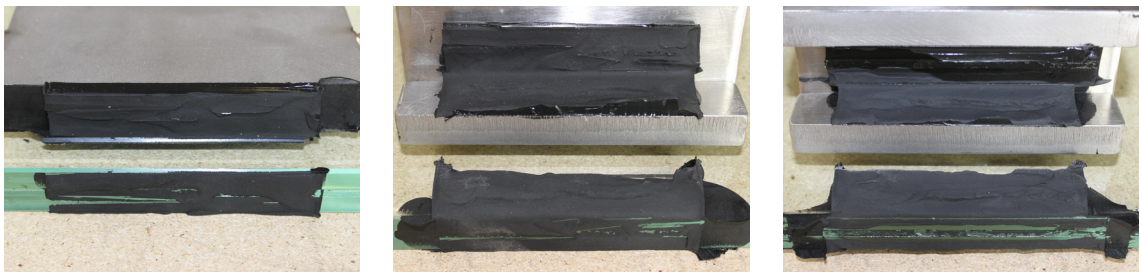

SS_ret_100x20x6 *SS_let_100x(21.5+20)x6* *SS_uet_100x(21.5+2x20)x6*

Fig. 5.50 *Typical failure patterns for the adhesive joints at the glass edge with Sikasil SG-550 and different cross sections tested under tensile loading*

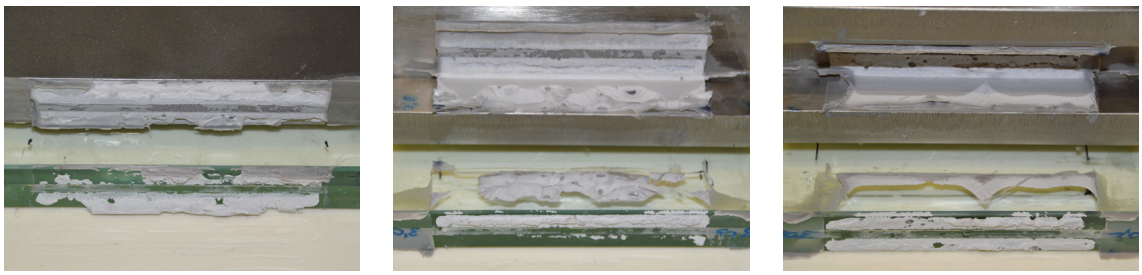

SF_ret_100x20x3 *SF_let_100x(21.5+20)x3* *SF_uet_100x(21.5+2x20)x3*

Fig. 5.51 *Typical failure patterns for the adhesive joints at the glass edge with SikaFast-5221 NT and different cross sections tested under tensile loading*

The specimens with adhesive joints at the edge of laminated glass made of *SikaFast-5221 NT* exhibit generally mixed cohesive and adhesive failure for all investigated cross section geometries. On the glass pane edges either only small areas fail adhesively, as shown in Fig. 5.51, left, for a rectangular joint cross section, or a complete debonding from one of the two

laminated glass pane edges occurs, as in the case of the specimen with an L-shaped joint cross section illustrated in Fig. 5.51, middle. Furthermore, it is noticed that the bonding of the acrylic to the interlayer material is poor. The failure modes on the glass pane surfaces in the case of the specimens with L-shaped and U-shaped cross sections of the joints are rather adhesive. Only on small parts of the bonding area a cohesive failure occurs.

Analysis of the mechanical behaviour

The mechanical behaviour of the adhesive joints at the edge of laminated glass with different cross section geometries tested under tensile loading is analysed based on load-displacement relationships. An evaluation based on stresses is difficult to conduct, since in the case of the L-shaped and the U-shaped cross sections parts of the joints are under tensile stresses while the other parts are under shear stresses. The results of the tensile tests are plotted separately for the three investigated adhesives. The two diagrams in Fig. 5.52 show the load-displacement curves for the specimens with rectangular, L-shaped and U-shaped joint cross section made of *Dow Corning 993* (left) and of *Sikasil SG-550* (right), while the curves for the specimens with *SikaFast-5221* are plotted in Fig. 5.53 with different ranges of the two axes.

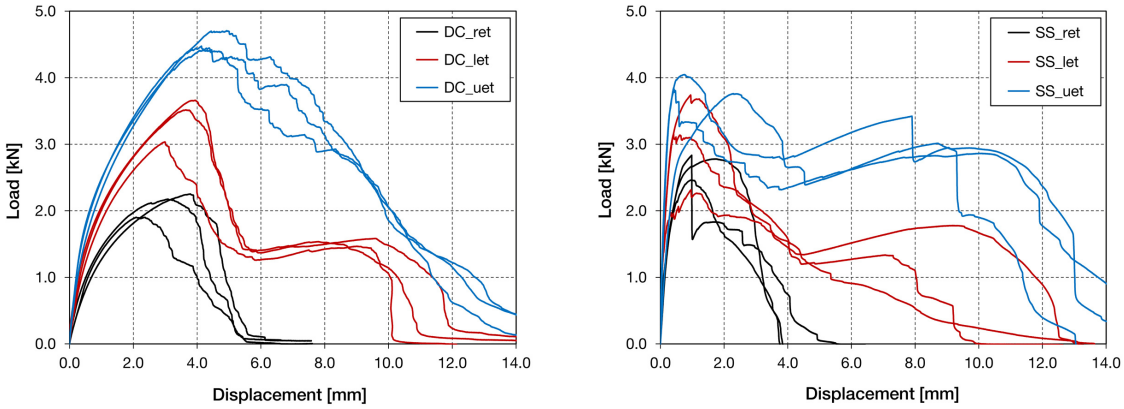

Fig. 5.52 *Load-displacement curves obtained from the tensile tests on adhesive joints with different cross sections at the glass edge with Dow Corning 993 (left) and with Sikasil SG-550 (right)*

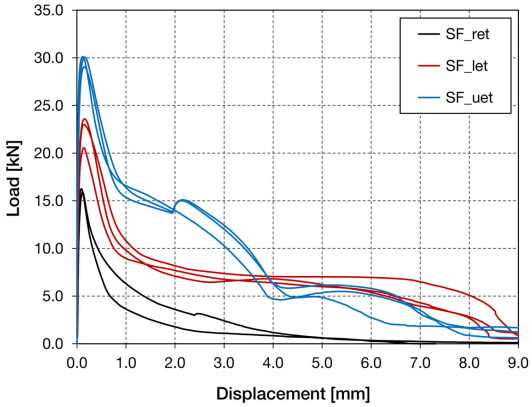

Fig. 5.53 *Load-displacement curves obtained from the tensile tests on adhesive joints with different cross sections at the glass edge with SikaFast-5221 NT*

For the specimens with *Dow Corning 993* and those with *SikaFast-5221 NT* a good agreement of the curves for specimens from the same series can be noticed. In the case of the specimens with *Sikasil SG-550* the results vary a little more, especially for the L-shaped joint cross sections. Considering the size of the bonding surface in the case of the different cross sections, a clear increase of the maximum reached loads between the rectangular, the L-shaped and the U-shaped was expected. This dependency is confirmed by the results for the silicone *Dow Corning 993* and the acrylic *SikaFast-5221 NT*, but is a little ambiguous in the case of the silicone *Sikasil SG-550*, according to the obtained load-displacement curves.

By analysing the mean values of the reached maximum loads provided in Tab. 5.14 for the different test series, the expected dependency on the cross section of the joint geometry is confirmed for all three adhesives. Interestingly, for the specimens with *Dow Corning 993* and those with *SikaFast-5221 NT* the displacements at which the maximum loads are reached are also increasing with the size of the bonding area. This is not the case for the specimens with *Sikasil SG-550*.

Tab. 5.14 *Mean values for results from the tensile tests on linear adhesive joints at the glass edge with different joint cross section geometries for the three investigated adhesives*

Test series	Dow Corning 993		Sikasil SG-550		SikaFast-5221 NT	
	Max. load [N]	**Corr. displ.** [mm]	**Max. load** [N]	**Corr. displ.** [mm]	**Max. load** [N]	**Corr. displ.** [mm]
ret_100 x 20 x 6 (3)	2 110	2.98	2 691	1.22	16 069	0.11
let_100 x (21.5+20) x 6 (3)	3 404	3.52	3 071	0.77	22 385	0.14
uet_100 x (21.5+2x20) x 6 (3)	4 542	4.47	3 878	1.16	29 753	0.14

The curves for the specimens with an L-shaped cross section show for all three adhesives a certain remaining load-bearing capacity after the decrease in load due to the first cracks. By analysing the displacements measured during the tensile tests and the shear tests on linear adhesive joints at the glass surface (see subchapters 5.2.2 and 5.2.3), it can be concluded that the part of the joint on the edge surface, which is subjected to tensile stresses, fails first, while the part of the joint on the glass pane surface, which is subjected to shear stresses, is further able to transfer loads and to deform.

A similar behaviour can be observed for the specimens with U-shaped cross section, especially for the joints with *Sikasil SG-550*. In the case of the joints with *Dow Corning 993* the load does not drop immediately after the first cracks in the adhesive, but decreases almost with a constant gradient while the deformation increases. The curves of the joints with U-shaped cross section and *SikaFast-5221 NT* show after the first cracks an abrupt drop in load to a certain value and afterwards, a decrease with an almost constant gradient while the deformation increases.

5.3.3 Adhesive joints at the glass edge under compressive loading

Similar as in the case of the tensile tests on linear adhesive joints at the edge of laminated glass, the real test setups for specimens with rectangular (left), L-shaped (middle) and U-shaped (right) cross section of the joint geometry are illustrated in Fig. 5.54, before discussing the different results. Also in this case the displacements measured by the transducers are used for evaluation in order to avoid any influence of strains within the elastomer layers or within the glass.

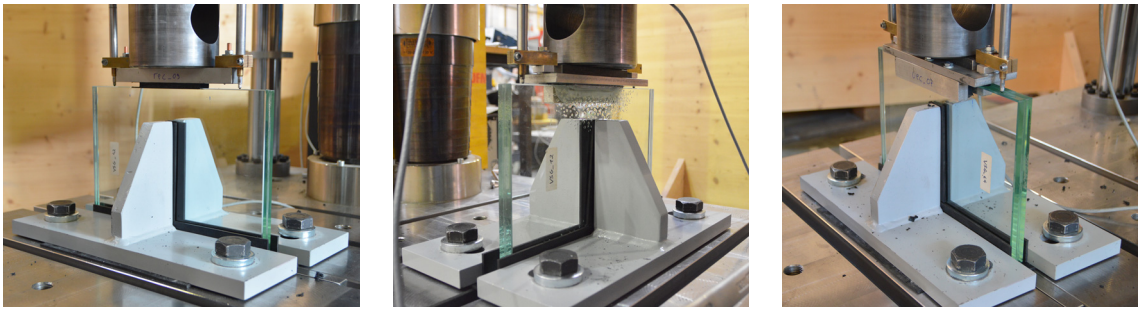

Fig. 5.54 *Specimens with adhesive joints at the glass edge tested under compressive loading*

Evaluation of the failure patterns

In the case of the linear adhesive joints at the edge of laminated glass tested under compressive loading the question regarding the failure patterns is not whether there is an adhesive or a cohesive failure of the material, but mainly how the interlayer reacts to the applied load and where the adhesive is redistributed, since all investigated adhesives are almost incompressible. With increasing load, a part of the adhesive is pressed into the interlayer between the two laminated glass panes, while the rest is pressed laterally between the glass pane and the stainless steel components. At a certain load level, depending on the used adhesive as well as on the cross section of the joint, a delamination of the interlayer from the glass panes starts. This is preceded by the formation of small visible bubbles within the interlayer indicating cavitation effects.

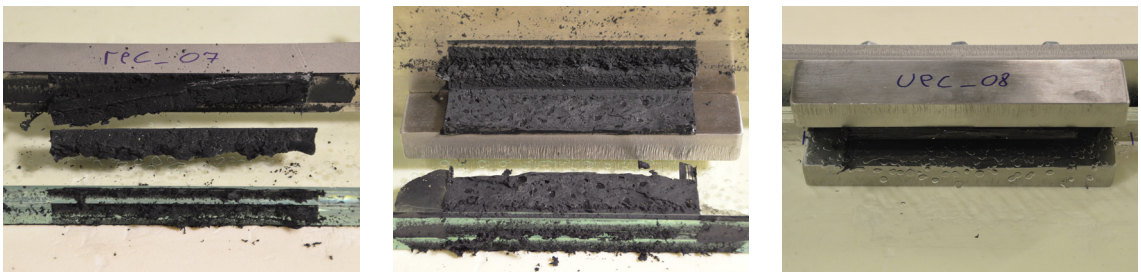

DC_rec_100x20x6 *DC_lec_100x(21.5+20)x6* *DC_uec_100x(21.5+2x20)x6*

Fig. 5.55 *Typical failure patterns for the adhesive joints at the glass edge with Dow Corning 993 and different cross sections tested under compressive loading*

Examples of specimens with *Dow Corning 993* after failure are illustrated in Fig. 5.55 for the different cross sections. At the end of the tests the stainless steel components are in contact with the edges of the glass panes, which means that all the adhesive is pressed away. In the case of the rectangular and the L-shaped cross sections the adhesive becomes brittle under high loads and a rupture in the joint occurs. In the case of the U-shaped cross section there is no full rup-

ture of the joint, since the lateral parts loaded by shear allow more deformation than the *6 mm* of the joint part on the edge loaded by compression. Due to the symmetric format also no rotation of the joint, as in the case of the L-shaped cross section, is possible. However, it is observed that adhesive is pressed out on the two frontal sides.

The specimens with *Sikasil SG-550* behave similar to those with *Dow Corning 993* and therefore no detailed descriptions are given here. Failure patterns of selected specimens with the three different cross sections are shown in Fig. 5.56. A complete overview with the failure patterns of all specimens is provided in [Appendix D]. In the case of the specimens with *Sikasil SG-550*, the bubble formation in the interlayer near the adhesive joint starts at loads of around *20-25 kN* for the joints with rectangular cross section and at loads of around *40-45 kN* for those with L-shaped cross section. For the joints with U-shaped cross section, the first bubbles are observed at around *100 kN*. However, the formation of bubbles at lower loads in the are behind the stainless steel flanges cannot be excluded. In the case of the specimens with *Dow Corning 993*, the start of bubble formation is not documented, but since it has similar material properties as well as similar failure patterns, values in the same range can be assumed.

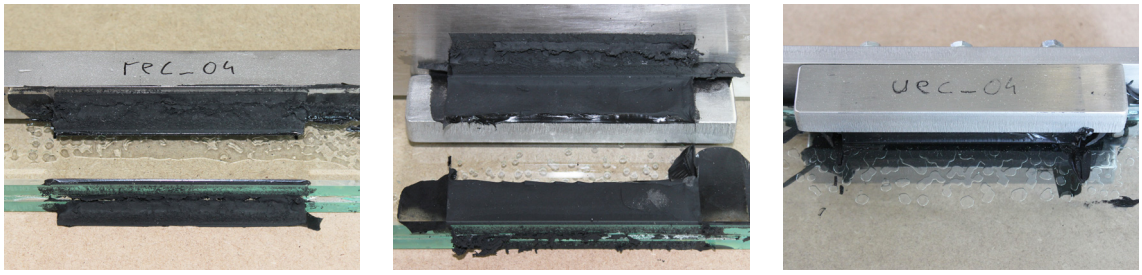

SS_rec_100x20x6 *SS_lec_100x(21.5+20)x6* *SS_uec_100x(21.5+2x20)x6*

Fig. 5.56 *Typical failure patterns for the adhesive joints at the glass edge with Sikasil SG-550 and different cross sections tested under compressive loading*

The specimens with *SikaFast-5221 NT* show a slightly different behaviour than those with silicones, on the one hand due to the higher stiffness of the adhesive and on the other hand because the acrylic is a little compressible (Poisson‘s ratio of around *0.47*). Up to the maximum applied load of *400 kN* no contact between the stainless steel parts and the glass pane edges occurs. Also, it is not noticed that the acrylic would get brittle under higher compressive loads.

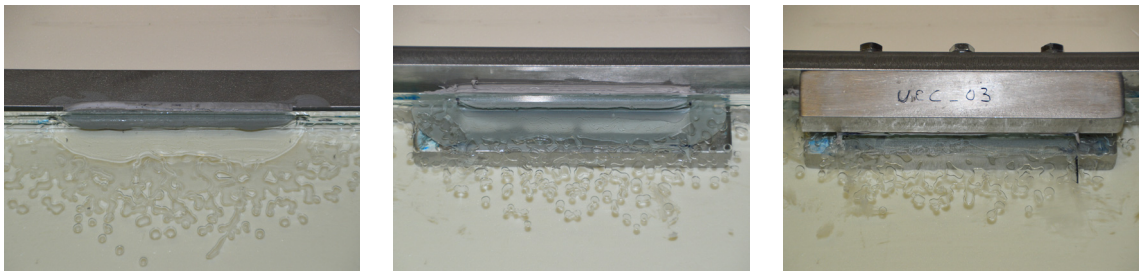

SF_rec_100x20x3 *SF_lec_100x(21.5+20)x3* *SF_uec_100x(21.5+2x20)x3*

Fig. 5.57 *Typical failure patterns for the adhesive joints at the glass edge with SikaFast-5221 NT and different cross sections tested under compressive loading*

The delamination in the case of the specimens with acrylic adhesive is more pronounced and for the rectangular and the L-shaped cross sections it is observed that adhesive material is pressed into the interlayer (see Fig. 5.57). The first bubbles in the interlayer preceding delamination occur at around *40 kN* in the case of the specimens with rectangular joint cross section and at around *70-80 kN* for those with L-shaped joint cross section. In the case of the joints with U-shaped cross section, the first bubbles are visible at loads of around *110-120 kN*. However, as in the case of the specimens with silicone adhesive, the formation of bubbles at lower loads for the specimens with U-shaped joint cross section cannot be excluded, since the visibility is restricted by the flanges of the stainless steel part.

A delamination is also observed near the laminated glass edges on which the test specimens are positioned on the machine table and which press on the used intermediate elastomer layers. A selected test specimen with each of the three adhesives is shown for the joints with rectangular cross section in Fig. 5.58 to illustrate this behaviour. This observation was not an objective of the performed investigations but could be of interest when planning to introduce compressive loads into the edges of laminated glass.

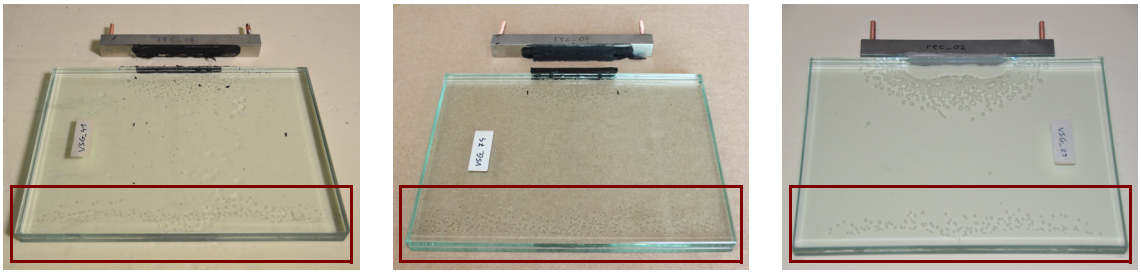

Dow Corning 993 *Sikasil SG-550* *SikaFast-5221 NT*

Fig. 5.58 *Bubble formation in the interlayer at the bottom edge of the laminated glass pane for specimens with adhesive joints under compressive loading*

Analysis of the mechanical behaviour

All the specimens with adhesive joints at the glass edge tested under compression are loaded up to *400 kN*. The results for the specimens with silicone adhesives are shown in Fig. 5.59 in the form of load-displacement relationships. The curves for all three investigated joint cross sections are plotted left for specimens with *Dow Corning 993* and right for specimens with *Sikasil SG-550*. It can be generally noticed that the specimens with *Sikasil SG-550* behave slightly stiffer than those with *Dow Corning 993*.

There is a good agreement between the specimens with the same joint cross section of each adhesive, especially up to *4 mm* displacement. After passing this value a kind of tremble is present in the curves because the adhesives get brittle. At around *6 mm* displacement the load starts to increase significantly without further noticeable deformation, since there is a direct contact between the stainless steel part and the glass edges.

The load-displacement curves for the specimens with *SikaFast-5221 NT* are illustrated in Fig. 5.60. Firstly, a significantly higher stiffness compared to the joints with silicones can be noticed.

Secondly, the S-shape of the curves is an indication of yielding. The facts, that a displacement of *3 mm*, which would be equal to the thickness of the joint, is not reached and also no significant increase of load without an increase of displacement occurs, confirm that there is no direct contact between the stainless steel parts and the glass edges. The curve of one specimen with rectangular cross section ends at *300 kN*, since the displacement transducers are removed at this load for the first tested specimen.

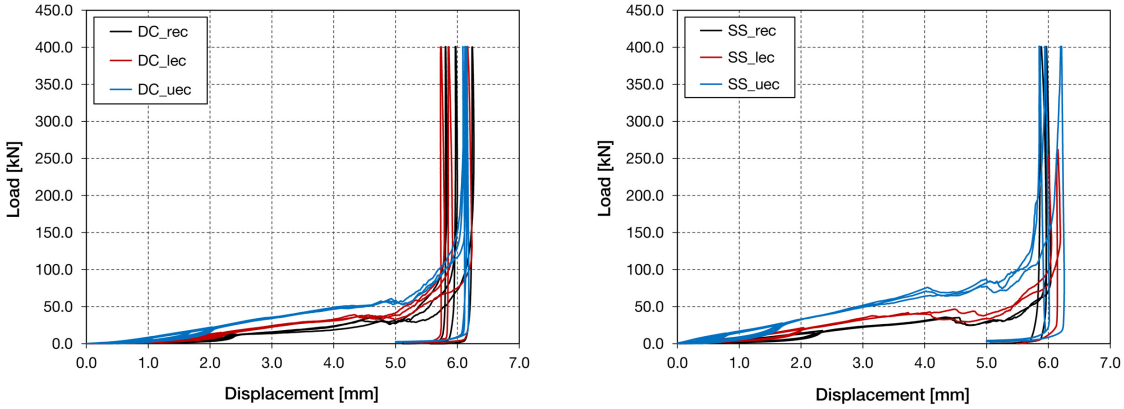

Fig. 5.59 *Load-displacement curves obtained from the compressive tests on adhesive joints with different cross sections at the glass edge with Dow Corning 993 (left) and with Sikasil SG-550 (right)*

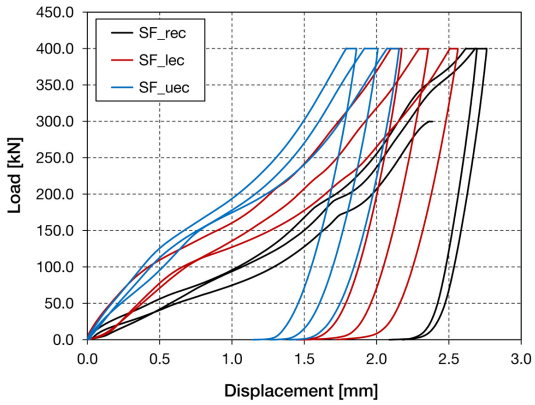

Fig. 5.60 *Load-displacement curves obtained from the compressive tests on adhesive joints with different cross sections at the glass edge with SikaFast-5221 NT*

For the specimens with the two silicone adhesives the parts with the load cycles at the beginning of the compressive tests are illustrated in Fig. 5.61. The fact that during a second loading only lower loads can be transferred, which is noticed in the tensile and shear tests on adhesive joints at the glass surface, is confirmed also for compressive loading. The size of the difference in reached loads between the first and a following cycle is indicated by mean values for loads at *15%* and *25%* strain in Tab. 5.15 for *Dow Corning 993* and in Tab. 5.16 for *Sikasil SG-550*. Moreover, the mean values for loads reached during the first cycle at *5%*, *15%*, *25%* and *50%* strain provided in Tab. 5.15, Tab. 5.16 and Tab. 5.17 allow a quantitative comparison of the stiffness for joints with different cross sections as well as with different adhesives.

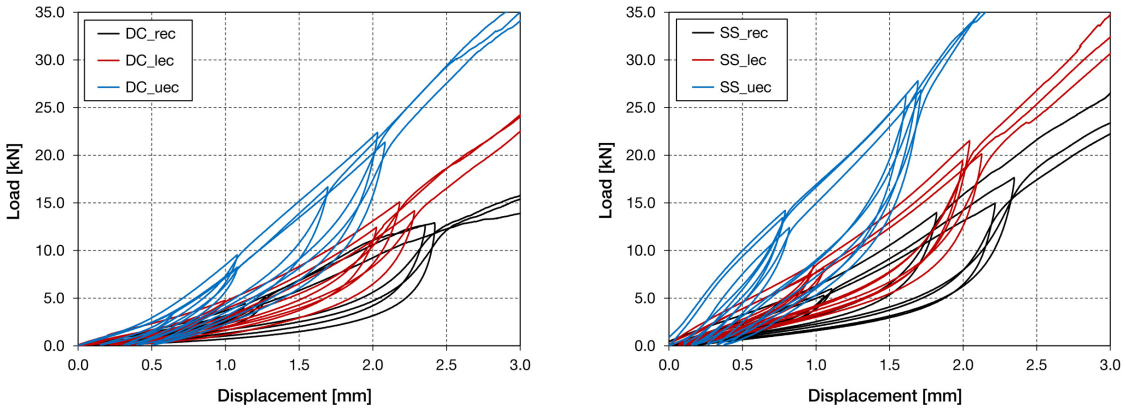

Fig. 5.61 *Load-displacement curves for the cycles performed at the beginning of the compressive tests on adhesive joints at the glass edge with Dow Corning 993 (left) and with Sikasil SG-550 (right)*

Tab. 5.15 *Mean values for results from the compressive tests on linear adhesive joints at the glass edge with different joint cross section geometries and Dow Corning 993*

Test series Dow Corning 993	**Load at 5% strain** [kN]	**Load at 15% strain** [kN]			**Load at 25% strain** [kN]			**Load at 50% strain** [kN]
		1st cycle	**last cycle**	**Diff.** [%]	**1st cycle**	**last cycle**	**Diff.** [%]	
rec_100 x 20 x 6	0.82	2.71	1.28	- 53%	6.57	2.71	- 59%	15.11
lec_100 x (21.5+20) x 6	1.07	3.54	2.15	- 39%	7.85	5.19	- 34%	24.78
uec_100 x (21.5+2x20) x 6	1.52	6.89	3.47	- 50%	15.03	10.43	- 31%	36.37

Tab. 5.16 *Mean values for results from the compressive tests on linear adhesive joints at the glass edge with different joint cross section geometries and Sikasil SG-550*

Test series Sikasil SG-550	**Load at 5% strain** [kN]	**Load at 15% strain** [kN]			**Load at 25% strain** [kN]			**Load at 50% strain** [kN]
		1st cycle	**last cycle**	**Diff.** [%]	**1st cycle**	**last cycle**	**Diff.** [%]	
rec_100 x 20 x 6	1.76	4.94	2.22	- 55%	9.59	4.90	- 49%	24.49
lec_100 x (21.5+20) x 6	2.70	7.65	3.75	- 51%	14.06	8.22	- 42%	35.03
uec_100 x (21.5+2x20) x 6	5.59	15.19	7.51	- 51%	24.88	19.89	- 20%	52.36

Tab. 5.17 *Mean values for results from the compressive tests on linear adhesive joints at the glass edge with different joint cross section geometries and SikaFast-5221 NT*

Test series SikaFast-5221 NT	**Load at 5% strain** [kN]	**Load at 15% strain** [kN]	**Load at 25% strain** [kN]	**Load at 50% strain** [kN]
rec_100 x 20 x 3	16.15	41.60	67.62	148.81
lec_100 x (21.5+20) x 3	23.86	79.99	119.49	216.28
uec_100 x (21.5+2x20) x 3	39.43	103.79	154.25	280.41

5.3.4 Adhesive joints at the glass edge under shear loading

In the case of the linear adhesive joints at the edge of laminated glass tested under shear loading double-lap specimens consisting of two glass panes and a stainless steel component are used. The installed specimens with rectangular (left), L-shaped (middle) and U-shaped (right) cross section of the joint geometry are illustrated in Fig. 5.62. For the L-shaped specimen a more detailed perspective of the adhesive joint during testing is chosen, in order to indicate also the failure development which includes a tearing of the interlayer. For the same reasons as in the case of the tensile and the compressive tests, the displacement measurements of the two transducers are used for the results evaluation.

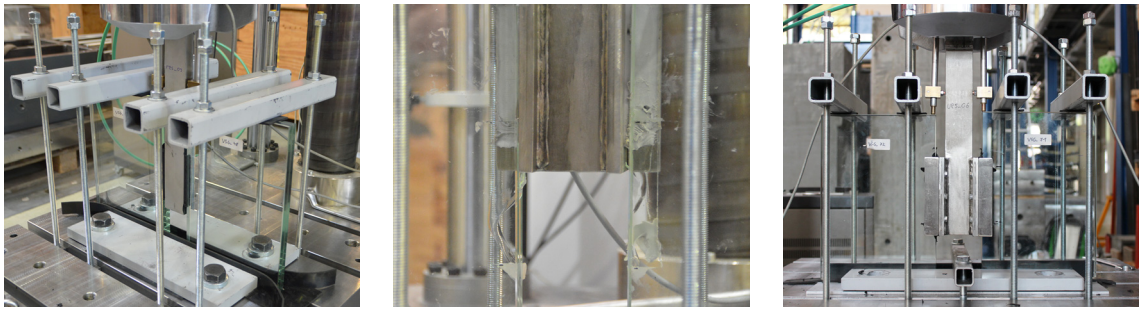

Fig. 5.62 *Specimens with adhesive joints at the glass edge tested under shear loading*

Evaluation of the failure patterns

The failure patterns for the adhesive joints at the edge of laminated glass with silicones tested under shear loading show cohesive failure with only small local areas of adhesive failure for some specimens with *Sikasil SG-550*, as in the case of the tensile tests. A complete overview of these patterns can be found in [Appendix D], without providing a further discussion here.

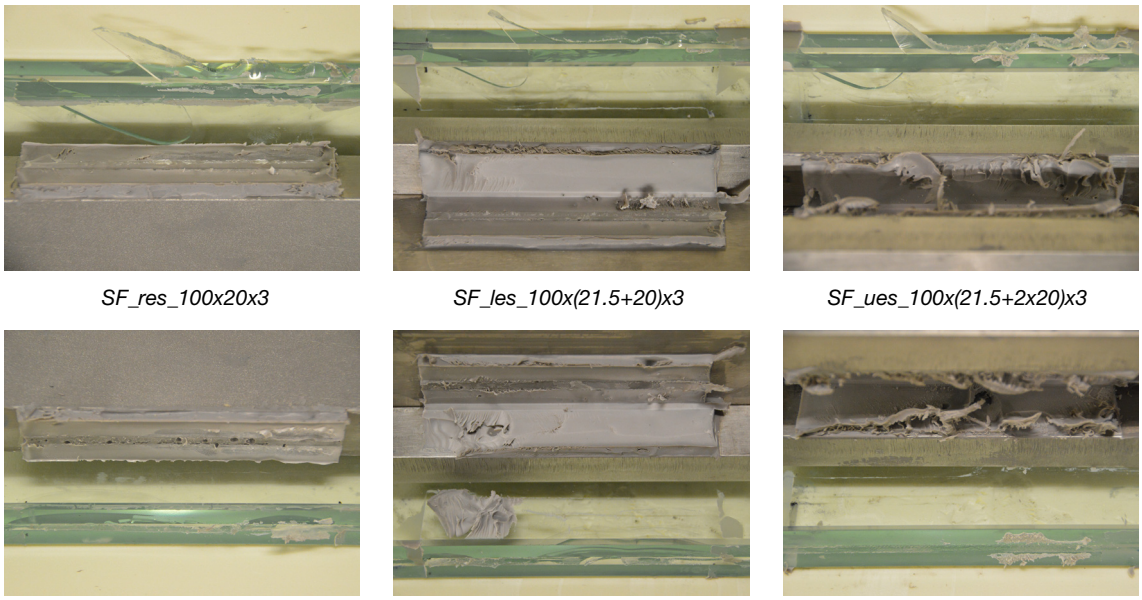

SF_res_100x20x3 *SF_les_100x(21.5+20)x3* *SF_ues_100x(21.5+2x20)x3*

Fig. 5.63 *Typical failure patterns for the adhesive joints at the glass edge with SikaFast-5221 NT and different cross sections tested under shear loading*

The specimens with *SikaFast-5221 NT* on the other hand show mainly adhesive failure independently on the geometry of the joint cross section. Examples for each type of cross section are illustrated in Fig. 5.63. Beside the almost complete debonding from both the glass edge and the glass surface areas, it can be observed that the interlayer is teared away during loading, which is a sign of good adhesion between the two materials.

Analysis of the mechanical behaviour

In the case of the shear tests on adhesive joints at the edge of laminated glass an evaluation in the form of stress-strain relationships would be possible, since all the parts of the L-shaped and U-shaped joints are subjected only to shear stresses. However, in order to be consistent with the procedure used for the tensile and the compressive tests, load-displacement relationships are plotted in Fig. 5.64 for the two silicones and in Fig. 5.65 for the acrylic, while the occurring engineering stresses are compared based on mean values in Tab. 5.19.

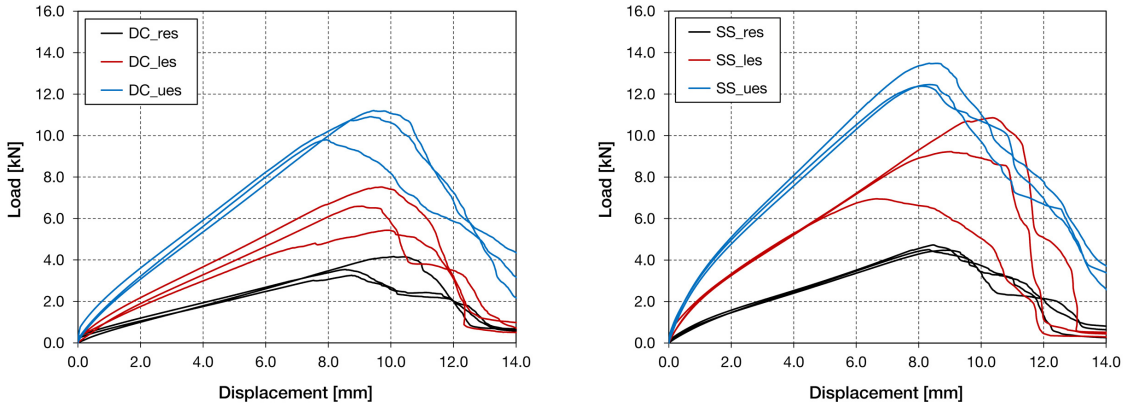

Fig. 5.64 *Load-displacement curves obtained from the shear tests on adhesive joints with different cross sections at the glass edge with Dow Corning 993 (left) and with Sikasil SG-550 (right)*

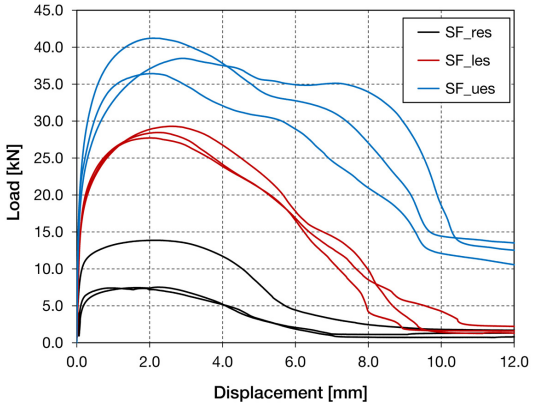

Fig. 5.65 *Load-displacement curves obtained from the shear tests on adhesive joints with different cross sections at the glass edge with SikaFast-5221 NT*

By comparing the curves for specimens with different cross sections for each adhesive, the expected higher load-bearing capacity with larger adhesion surface is confirmed. It can be also

observed that the failure in the two joints of one specimen can occur either at once or slightly time-shifted. Between the two silicones, the specimens with *Sikasil SG-550* reach a little higher maximum loads and behave a little stiffer, as also noticed in the previously performed shear tests at the glass surface. A good agreement between the curves with the same joint geometry is given for the specimens with silicones, especially for those with rectangular and U-shaped cross sections. The agreement of the curves for the joints with acrylic adhesive is good until yielding, but shows larger discrepancies afterwards. In the case of the specimens with U-shaped cross sections a certain load can be transferred also after failure, by friction.

Tab. 5.18 and Tab. 5.19 summarise mean values of the maximum reached loads and the corresponding displacements and, respectively, the maximum engineering shear stresses and the corresponding shear displacements. For the two silicones, both the tendency of the increase in load between the different cross section types and the range of the stress values are consistent with the expectations. In the case of the acrylic, the results for the specimens with rectangular cross section are not in a good agreement with the others, which is also indicated by the load-displacement curves. This inconsistency is probably due to the unpredictability of adhesive failure modes.

Tab. 5.18 *Mean values for results from the shear tests on linear adhesive joints at the glass edge with different joint cross section geometries for the three investigated adhesives (maximum loads and corresponding displacements)*

Test series	Dow Corning 993		Sikasil SG-550		SikaFast-5221 NT	
	Max. load [N]	**Corr. displ.** [mm]	**Max. load** [N]	**Corr. displ.** [mm]	**Max. load** [N]	**Corr. displ.** [mm]
res_100 x 20 x 6 (3)	3 653	9.12	4 567	8.56	9 593	1.77
les_100 x (21.5+20) x 6 (3)	6 515	9.54	9 013	8.69	28 484	2.26
ues_100 x (21.5+2x20) x 6 (3)	10 640	8.92	12 775	8.27	38 710	2.35

Tab. 5.19 *Mean values for results from the shear tests on linear adhesive joints at the glass edge with different joint cross section geometries for the three investigated adhesives (maximum engineering shear stresses and corresponding shear displacements)*

Test series	Dow Corning 993		Sikasil SG-550		SikaFast-5221 NT	
	Max. shear stress [MPa]	**Corr. shear displ.** [-]	**Max. shear stress** [MPa]	**Corr. shear displ.** [-]	**Max. shear stress** [MPa]	**Corr. shear displ.** [-]
res_100 x 20 x 6 (3)	0.87	1.50	1.12	1.42	2.31	0.58
les_100 x (21.5+20) x 6 (3)	0.78	1.55	1.05	1.40	3.35	0.74
ues_100 x (21.5+2x20) x 6 (3)	0.86	1.44	1.03	1.33	3.18	0.77

The investigations on linear adhesive joints at the edge of laminated glass panes are included in the journal paper entitled *„Linear adhesive connections at the edge of laminated glass panes: an experimental study under tensile, compressive and shear loading“* (see *[Publication List]* at the end of the thesis).

5.4 Evaluation of the results on linear adhesive joints

The investigations on adhesive joints discussed in chapter 5, comprising experimental tests on a total of 183 specimens as well as finite element simulations, focus on the performance of two flexible silicone adhesives and one stiffer acrylic adhesive. The substrate materials are a grinded stainless steel selected based on discussions with structural facade engineers as well as on the results from subchapter 4.4 and an uncoated glass surface. The environmental conditions for manufacturing, curing and testing of the joints are close to room ambient conditions. The main aspect, whose influence on the performance of the joints under different loadings is analysed, is the geometry of the joint.

For linear adhesive joints at the glass surface, the dimensions of a joint with rectangular cross section are varied under tensile loading and under shear loading. The variation of the joint thickness has the biggest influence on the mechanical behaviour. In the case of tensile loading thinner joints lead to steeper stress-strain curves and allow for transferring higher stresses. Under shear loading, the inclination of the shear stress *vs.* shear displacement curves is similar for all thicknesses, but higher shear stresses can be transferred as well over thinner adhesive layers. These observations are valid for all three investigated adhesives. In the case of tensile loading, also the length and the width of the joints are varied. While the length has a rather small influence on the occurring stresses, the different widths show a similar influence as the different thicknesses due to the fact that the ratio between width and thickness is modified.

The specimens with silicone adhesive joints at the glass surface show for both tensile and shear loading only cohesive failure within the adhesive layer. The specimens with acrylic adhesive exhibit mainly cohesive failure under tensile loading. However, for the specimens with the smaller width (*100 mm x 10 mm x 3 mm*) and length (*50 mm x 20 mm x 3 mm*) partial adhesive failure from the glass surface is noticed. Under shear loading both cohesive failure within the adhesive layer and adhesive failure on the glass surface are observed. The adhesive failures always occur on the air surface (from the float glass production process) of the glass pane.

The finite element simulations of the tests on linear adhesive joints at the glass surface show for both silicones the same suitability and limits of linear elastic material models. For tensile loading these models are only suitable for small strains of around up to *10-20%* with the remark that they slightly underestimate the real loads and stresses. For larger strains non-linear material models which can reproduce hyperelasticity deliver suitable results. The investigated *Mooney-Rivlin* model for *Dow Corning 993*, with the coefficients determined in subchapter 4.3.2 based on uniaxial tensile test results, show a good agreement considering its complexity. For *Sikasil SG-550* the analysed *Arruda-Boyce* model, with the coefficients determined in subchapter 4.3.3 in a similar way, behaves more flexible than the test results. Under shear loading, the load-displacement curves from the experimental tests are almost linear (without considering the performed load cycles). Therefore, the deviation in terms of stresses between the values obtained with the linear elastic models, the values obtained with the hyperelastic models and the values from the experimental tests is rather small. However, since in reality, generally, a combined loading is occurring, including tension and shear or compression and shear, the use of non-linear models is more appropriate.

For the adhesive joints with the acrylic *SikaFast-5221 NT*, the finite element simulations with a linear elastic model for the adhesive deliver suitable results only until the adhesive starts to yield for both tensile and shear loading. Afterwards, the real loads and stresses are significantly overestimated. The strain rate dependent plastic model proposed in subchapter 4.3.4 allows a good agreement in the case of shear loading in terms of load-displacement curves both before and after yielding. The only remark is a small underestimations of the loads after yielding. For tensile loading however, the proposed model is not capable to reproduce the yielding in good agreement with the experimental results. Although the load-displacement curves show a similar qualitative curve progression, quantitatively the values from the experiments are substantially overestimated.

The addition of porosity to the material properties of the acrylic adhesive in the simulations, based on the model implemented in *Abaqus* which relies on [Gurson, 1977] and [Tvergaard, 1981], leads to a significant improvement regarding the prediction of the yielding loads under tensile loading. Only in the area after yielding, where the loads are decreasing, the experimental values are still overestimated. Under shear loading, the addition of porosity has a rather small influence on the finite element simulation results. However, convergence issues are exhibited with this model depending on the joint geometry and the used mesh refinement. Investigations on more complex cavitation models along with additional experimental tests on bulk material specimens under compressive and shear loading, necessary for determining the required parameters for these models, are recommended for the acrylic in a next step.

In order to investigate the different methods introduced in subchapter 3.5.1 for transferring loads between the glass pane and the metal framing by adhesive bonding, experimental tests are carried out for linear joints at the edge of laminated glass with the three selected adhesives. Joints with rectangular, L-shaped and U-shaped cross sections of the adhesive are loaded by tension, compression and shear. For the rectangular cross section, joint dimensions of *100 mm x 20 mm x 6 mm* are used for the silicones and of *100 mm x 20 mm x 3 mm* for the acrylic to allow a comparison with the results for joints at the glass surface.

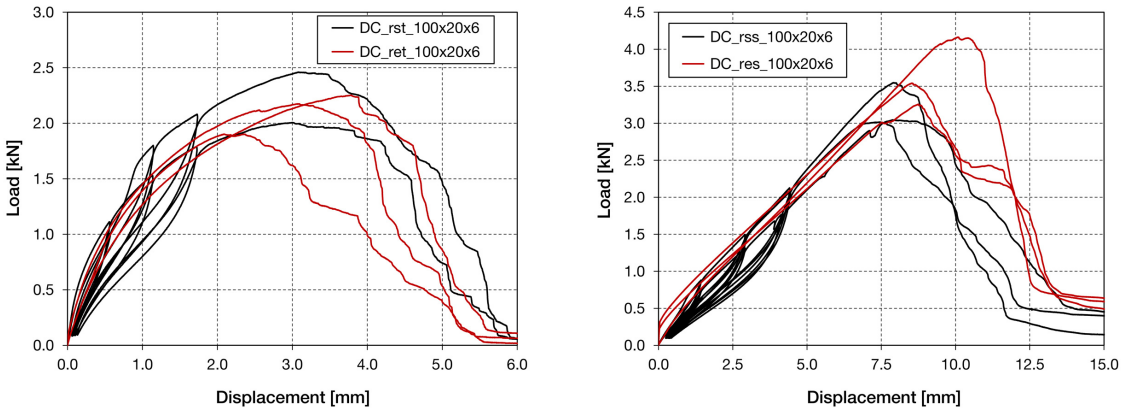

Fig. 5.66 *Load-displacement curves obtained for the linear adhesive joints at the glass surface (black) and at the glass edge (red) with Dow Corning 993 and rectangular cross section tested under tensile loading (left) and under shear loading (right)*

Despite the similar joint geometry, differences in the structural behaviour are expected between the joints at the glass surface and those at the edge of laminated glass due to the fact that in the first case the whole adhesion area is a flat glass surface, while in the second case the adhesion area is composed of the chamfered glass edges and the interlayer edge of the laminated glass panes. However, for the two silicones the results for the joints at the glass surface and for those at the edge of laminated glass are in good agreement both for tensile and for shear loading (see the load-displacement curves for *Dow Corning 993* in Fig. 5.66 as example). For all these specimens a cohesive failure of the adhesive occurs.

In the case of the acrylic adhesive, the joints at the edge of laminated glass with rectangular cross section perform worse than the similar ones at the glass surface, both under tensile and under shear loading (see curves in Fig. 5.67). This is mainly due to adhesive failures on the glass edge surfaces. Furthermore, a good adhesion of the acrylic to the interlayer material is noticed, which explains the smoother decay of the load in the case of shear loading. The specimens with L-shaped and U-shaped cross sections, exhibiting adhesion areas two times and three times larger than the rectangular ones, show for all three investigated adhesives an increased structural capacity both for tensile and for shear loading. However, such joints are difficult to manufacture for large-scale elements with perimetrical adhesive bonding.

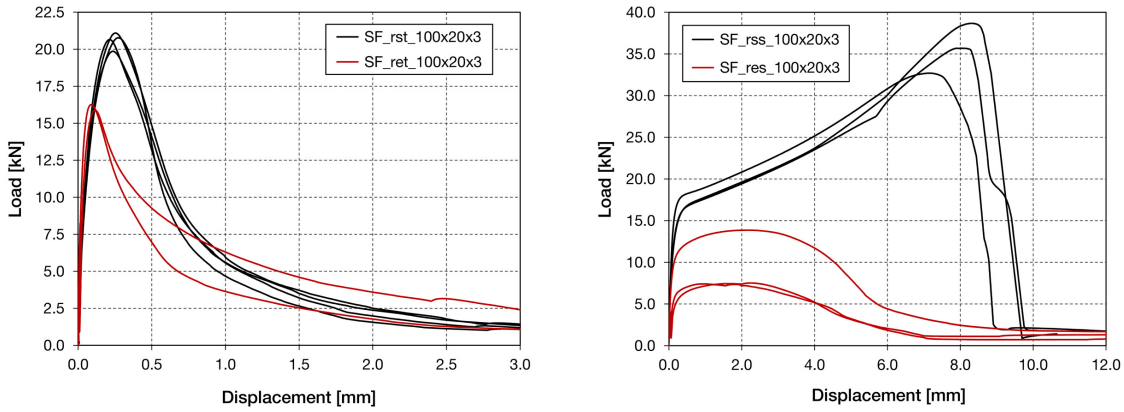

Fig. 5.67 *Load-displacement curves obtained for the linear adhesive joints at the glass surface (black) and at the glass edge (red) with SikaFast-5221 NT and rectangular cross section tested under tensile loading (left) and under shear loading (right)*

In the case of adhesive joints at the glass edge used for activating the glass pane as a shear panel, the joints can also be subjected to compressive loading. The tests performed to cover this aspect show a certain capacity of the adhesives for transferring compressive forces into the glass edges. However, a limiting factor are cavitation effects by bubble formation in the interlayer and delamination of the interlayer, which can be observed in the case of all three investigated adhesives during loading.

Since no previous tests on adhesive joints at the edge of laminated glass under compressive loading are documented in literature, a comparison of the phenomenon of bubble formation in the interlayer to similar results is not possible. Such effects are known from tensile tests on rubber-like materials and are referred to as cavitation. Investigation results on materials for lami-

nated connections on glass substrates subjected to tensile loading and proposed material models with regard to this topic are discussed by [Drass et al., 2017c], by [Drass et al., 2018] and by [Santarsiero et al., 2017b]. Generally, such connections have a small thickness compared to their surface. The same is valid in the case of the interlayer in the laminated glass panes from the specimens investigated for adhesive joints at the edge of laminated glass under compressive loading. Under tensile loading in thickness direction, the nearly incompressible materials are subjected to large hydrostatic stresses. Since the materials used for laminated connections or for interlayers cannot expand due to their high Poisson‘s ratio (nearly *0.5*), bubbles are resulting. Considering these aspects, a possible explanation for the bubble formation observed in the case of the specimens tested under compressive loading is the following. By pressing the stainless steel components towards the laminated glass panes, some of the adhesive material is pressed into the interlayer and the two glass sheets are pushed away from each other. Therefore, a similar hydrostatic stress state as in the case of the pancake tests is applied to the interlayer, which responds by bubble formation. This is not the case for tensile loading, because by pulling the stainless steel away from the laminated glass pane, the interlayer is stretched and the distance between the two glass sheets slightly reduces. In further research steps, the observed cavitation effects should be investigated in detail in order to assess to what extent the bubbles are generated within the interlayer material or at the interface between interlayer and glass sheets. In either of the two cases, for application of such joints, these effects need to be avoided because of their negative impact both from a structural and an aesthetical point of view.

Linear adhesive joints are a possible load transfer method for achieving a composite structural behaviour between the glass pane and the metal framing of a facade element. For the investigations on real-size elements in the chapters 6 and 7, the silicone *Dow Corning 993* and the acrylic *SikaFast-5221 NT* are considered. In the case of the silicones, *Dow Corning 993* is preferred instead of *Sikasil SG-550*, because the latter one is more difficult to apply and to handle, while showing only a small improvement in terms of mechanical properties. Furthermore, the hyperelastic model for finite element simulations derived for *Dow Corning 993* shows a better fit. However, due to its low stiffness, an activation of the glass panes as shear panels only with silicone adhesive bonding is not realisable. Therefore, a combination with setting blocks is aimed. The acrylic *SikaFast-5221 NT* does not exhibit fully satisfying properties at connection level, especially because of the partial adhesive failure modes. Nevertheless, its higher stiffness recommends it for achieving a composite structural behaviour and thereby activating the glass panes as shear panels. In terms of joint geometry, adhesive layers at the glass surface with rectangular cross sections are used for the investigations at element level, discussed in the next chapters. Although showing a high structural potential, joints with L-shaped and U-shaped cross sections are difficult to manufacture all around the glass pane perimeter. Furthermore, their performance under compressive loading requires further investigations regarding loading limits and interaction with other interlayer materials.

6 Experimental investigations on large-scale multi-component elements

Test concept and objectives
Development of test specimens and test setup
Experimental procedure and test results
Conclusions on the large-scale testing

1 Introduction 1

2 State of the art – theoretical framework

3 Transparent building envelopes with composite structural behaviour

4 Investigations on adhesives and their adhesion to metal substrates

5 Mechanical behaviour of adhesive joints between glass and stainless steel

6 Experimental investigations on large-scale multi-component elements

7 Finite element investigations on large-scale multi-component elements

8 Approaches for structural and functional design 8

9 Conclusions and future research 9

6.1 Testing concept and objectives

Glass-metal elements with composite structural behaviour by adhesive bonding for the use in building envelopes cannot be fully evaluated and efficiently designed only by summing up the available knowledge on their single components. The interaction between these components as well as the influence of one component on the behaviour of the others unfold a high potential of this concept and at the same time require to deal with its high complexity. In order to evaluate the structural performance of such elements as well as their failure modes large-scale experimental testing is performed on real size multi-component elements.

Based on the concept introduced in chapter 3 and by considering the findings on adhesives and adhesive joints from chapters 4 and 5, test specimens consisting of a glass pane adhesively bonded to a filigree metal framing are designed and tested under horizontal in-plane loads, vertical in-plane loads, horizontal out-of-plane loads as well as load combinations. The chosen glass pane dimensions of *3.5 m x 1.5 m* are common values for storey-high facade grids in office buildings. Furthermore the value of *1.5 m* is half of the production width for float glass and allows for less wasted material. Due to the boundary conditions provided in the laboratory a testing of the specimens in a standing position as they would probably be used in building envelopes is not possible. Therefore the specimens are tested in landscape format as illustrated by the setup sketch in Fig. 6.1. Also the applied load directions and the supports are pointed out in this figure. A detailed description of these aspects can be found in subchapter 6.2.3.

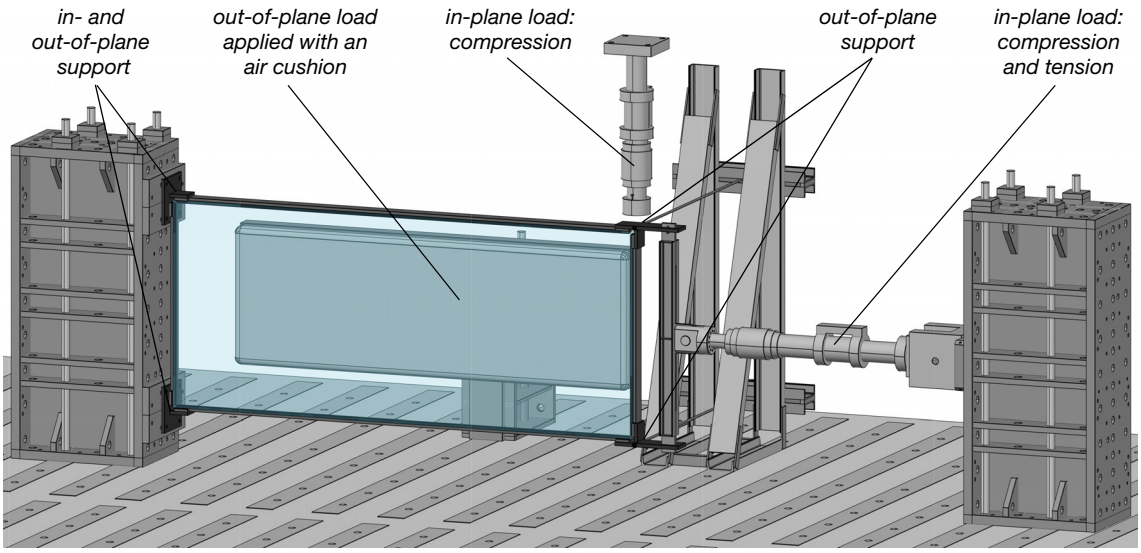

Fig. 6.1 *Test setup used for the experimental investigations on large-scale multi-component elements under combined in-plane and out-of-plane loading*

The achievement of several objectives is aimed with the findings from the large-scale multi-component tests on glass-metal elements with composite structural behaviour by adhesive bonding:

- to prove that the concept of glass-metal elements with composite structural behaviour by using adhesive bonding alone or in combination with grouting blocks for transferring the

loads between the framing and the glass pane can be applied from a manufacturing point of view and to evaluate the structural performance of elements using this concept;

- to determine the structural behaviour of the filigree metal framing, the glass pane and especially the adhesive during different loading scenarios and loading levels derived from real situations (dead weight, wind load in-plane, wind load out-of-plane);
- to compare the measurements recorded during the testing to values determined by finite element simulations (displacements, strains, etc.) and hereby validate the numerical models (both complex models and simplified models);
- to determine the load-bearing capacity and the stiffness of such elements and to evaluate their possible failure modes;
- to engineer and structurally evaluate a glass-metal element with composite structural behaviour by adhesive bonding which allows for further development to a facade product in subsequent steps.

The uniqueness of the used test specimens and of the followed testing concept is primarily given by the filigree metal framing bonded to the glass pane along its perimeter. Large-scale test setups used in past research projects for glass panels exhibit either no out-of-plane support along the edges (for example the system with corner grouting from [Wellershoff, 2006] discussed in subchapter 2.3.3) or a rigid out-of-plane support by large steel profiles (for example the systems with perimetrical adhesive bonding from [Wellershoff, 2006] and [Huveners, 2009] discussed in subchapter 2.3.4). In past investigations, basically the structural behaviour of the glass pane under in-plane loads is investigated in dependence of different mechanisms of load application. Other than in these cases, the filigree metal framing used for the test specimens discussed in this chapter shows a certain flexibility and therefore provides only a limited out-of-plane support to the glass pane.

Furthermore, a combined support of the glass panes by grouting blocks and adhesive bonding, as used for half of the tested large-scale specimens, has only been investigated similarly in past research by [Mocibob, 2008] for load application on two opposite edges of one-storey high elements without out-of-plane support of the free edges (see description in subchapter 2.3.3). The loading concept used for the large-scale tests discussed in this chapter is as well rather exceptional. Each test specimen is subjected to several loading series on serviceability level. In-plane loads in two directions as well as an out-of-plane load are applied both alone and combined up to previously defined values. The test specimens with laminated glass panes are finally loaded until failure with the shearing in-plane load (vertical in-plane load in Fig. 6.1). A detailed description of the loading scenarios is given in subchapter 6.3.1.

6.2 Development of test specimens and test setup

Both for the large-scale test specimens and the test setup several boundary conditions have to be considered during their development. This results in a thorough planning for the test specimens design and their assembly as well as for the test setup and the required measurement instrumentation for obtaining the desired data. The made assumptions and the significant steps towards the final results are discussed in subchapters 6.2.1 to 6.2.4.

6.2.1 Design of the test specimens

Based on the results for the investigated adhesives in chapters 4 and 5 two different concepts are followed in the design of specimens for large-scale tests on glass-metal elements with composite structural behaviour by adhesive bonding:

- *Type 1* - perimetrical adhesive bonding with a silicone adhesive (*Dow Corning 993*) between the glass pane and the metal framing to transfer out-of-plane loads and additional grouting blocks near the glass pane corners to transfer in-plane loads (see Fig. 6.2, left);
- *Type 2* - perimetrical adhesive bonding between the glass pane and the metal framing with an acrylic adhesive (*SikaFast-5221 NT*), which has to transfer both the out-of-plane and the in-plane loads (see Fig. 6.2, right).

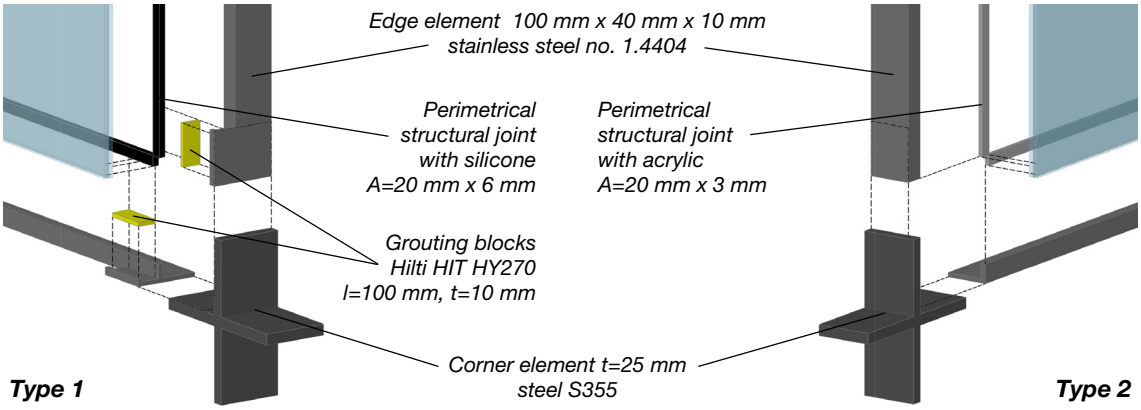

Fig. 6.2 *Test specimen types for investigations on large-scale multi-component elements under combined in-plane and out-of-plane loading*

For *Type 1* two specimens with a monolithic *10 mm* thick thermally toughened glass pane (*Type 1A* in Tab. 6.1) and one with a laminated glass made of two sheets of *6 mm* thermally toughened glass and a *1.52 mm* thick PVB interlayer (*Type 1B* in Tab. 6.1) are manufactured and tested. For *Type 2* only one specimen with a monolithic glass pane and one with a laminated glass with the same thicknesses as for *Type 1* are tested (*Type 2A* and *Type 2B* in Tab. 6.1). Although five test specimens are manufactured and tested in total, only four are evaluated in subchapter 6.3, since the first tested specimen of *Type 1A* is considered a pilot test.

Thermally toughened glass (TTG) is chosen for all the test specimens in order to reduce the risk of injuries by large sharp glass pieces which could fly away in case of glass failure during test-

ing. However, in real applications laminated glass panes made of heat strengthened glass (HSG) would be more appropriate because of their higher post-breakage structural capacity.

Tab. 6.1 *Characteristics of test specimen types for large-scale multi-component elements*

Specimen type	Glass pane	Adhesive	Grouting
Type 1A	10 mm TTG	Dow Corning 993 A = 20 mm x 6 mm	Hilti HIT HY270 l = 100 mm, t = 10 mm
Type 1B	2 x 6 mm TTG with 1.52 mm PVB	Dow Corning 993 A = 20 mm x 6 mm	Hilti HIT HY270 l = 100 mm, t = 10 mm
Type 2A	10 mm TTG	SikaFast-5221 NT A = 20 mm x 3 mm	-
Type 2B	2 x 6 mm TTG with 1.52 mm PVB	SikaFast-5221 NT A = 20 mm x 3 mm	-

Apart from the size of the glass panes, which is defined based on common values for facade grids, the other dimensions of the different components are determined by simplified calculations and under consideration of recommendations from guidelines and literature. An exact dimensioning is not possible since no references are available for taking the composite interaction into consideration. Therefore, the chosen dimensions are rather conservative to reduce the risk for undesired failure occurrence during testing.

The thickness of the glass panes is determined based on calculations of stresses and deformations under out-of-plane loads of up to *3.0 kPa* as well as based on separately determined critical buckling loads for the glass pane alone under the two different in-plane loads to be investigated during the large-scale tests.

For the specimens with silicone adhesive the product *Dow Corning 993* is chosen over *Sikasil SG-550*, since the results from the tests at connection level show a better consistency and because it is a more standard product. A smaller thickness allows the transfer of higher loads both in shear and in tension. Therefore, the minimal thickness of *6 mm* recommended by [ETAG 002, 2001] is used. The width is determined according to the same guideline in order to be able to transfer out-of-plane suction loads of up to *3.0 kPa*. A value of *20 mm* is chosen. For the specimens with acrylic adhesive, the same width is used, while the thickness is reduced to *3 mm* according to the recommendations of the adhesive producer. For the grouting blocks a length of *100 mm*, a thickness of *10 mm* and a width equal to the glass pane thickness plus *6 mm* on each side to avoid a direct contact between glass and metal are used. These assumptions are made based on the results at connection level obtained in [Kolany, 2018] as well as on previous findings related to setting blocks from [Englhardt, 2007] and [Ebert, 2014].

The used metal framing consists of corner elements made of structural steel *1.0045* (*S355JR*) and of edge elements made of stainless steel *1.4404*. The surfaces of the stainless steel on which the adhesive is applied are grinded with corn size *P300*. The main dimensions of the frame elements are provided in Fig. 6.3. The top half of the figure shows sections for the specimens of *Type 1*, while the bottom half of the figure presents the same sections in a mirrored arrangement around the symmetry axis for the specimens of *Type 2*.

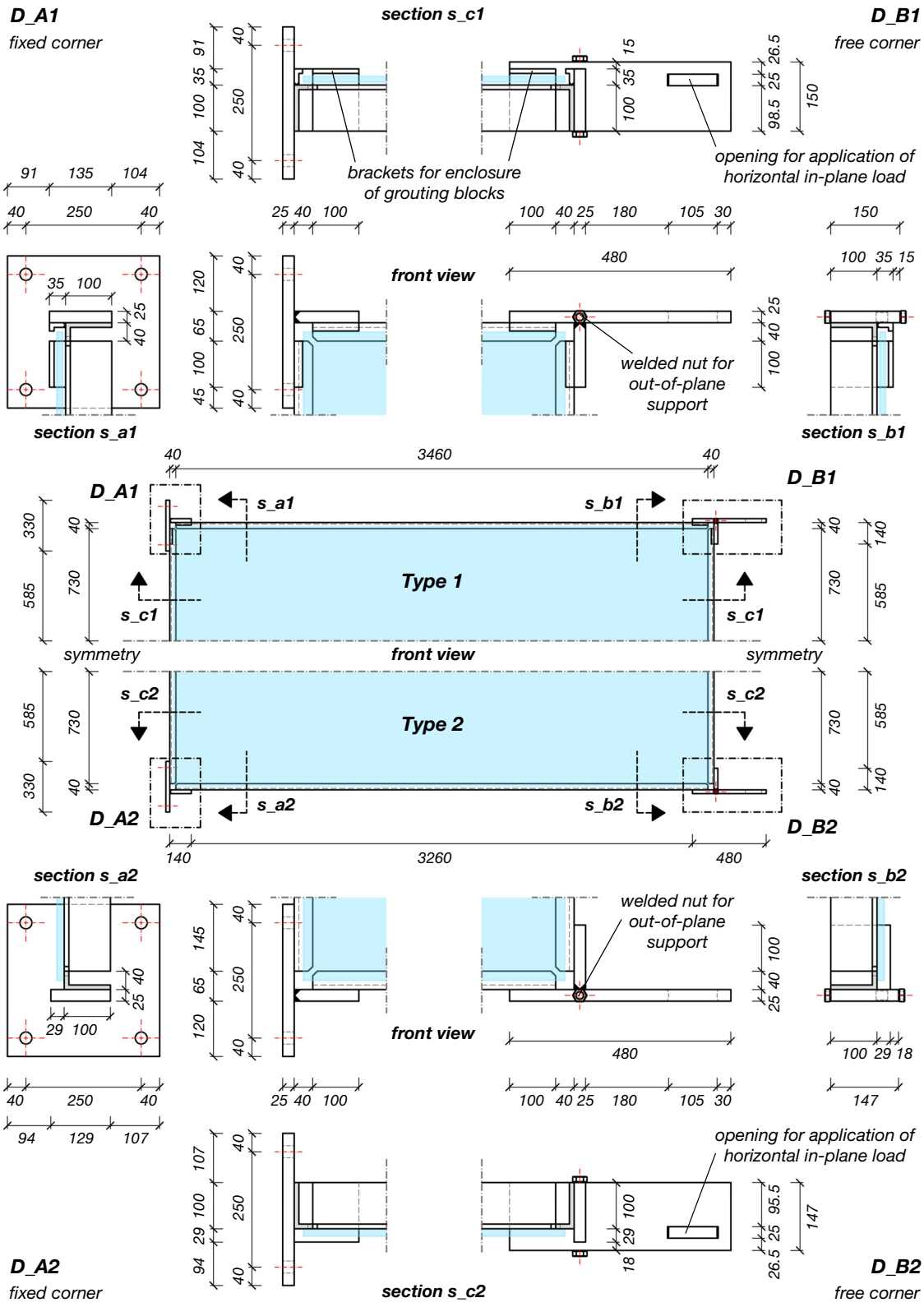

Fig. 6.3 *Main dimensions of the metal framing in [mm] for the large-scale test specimens in front view and sections for Type 1 (top) and Type 2 (bottom)*

The metal frames are first designed for the specimens of *Type 1* and then adopted with minimum changes for the specimens of *Type 2* in order to allow a better comparison. The edge elements have the same dimensions in the case of all different specimen types and are made of standard unequal angles with the dimensions of *100 mm x 50 mm 10 mm* by reducing the shorter leg to *40 mm*. The depth of *100 mm* and the thickness of *10 mm* are determined based on bending around the strong axis due to the same out-of-plane load as in the case of the glass pane and the adhesive as well as based on normal forces which result between the grouting blocks in the case of specimens of *Type 1*. The width of *40 mm* is the result of summing up the width of the adhesive (*20 mm*), the thickness of the grouting blocks (*10 mm*) and the thickness of the framing edge elements (*10 mm*). In the case of the edge elements for the specimens of *Type 1* brackets made of the same stainless steel are welded in the region where the grouting blocks are applied in order to laterally restrain these components. These brackets are left out for the specimens of *Type 2*.

Compared to the sketches in Fig. 6.2, the geometry of the corner elements needs to be modified in order to allow at one end of the glass-metal elements the fixing to the abutment block and at the other one the application of the two in-plane loads. Therefore, the cross-shaped corner elements are adapted to two types of T-shaped elements with the dimensions shown by the drawings in Fig. 6.3. The few differences between these dimensions for the specimens of *Type 1* and the specimens of *Type 2* result from the different used adhesive thicknesses and from the intention to apply the in-plane loads central to the glass pane thickness.

For joining the edge elements and the corner elements welded connections are used for the test specimens in order to exclude the influence of an eventual slip in the case of bolted connections. However, for practical applications where a modular assembly is desired, these connections can be replaced by bolted connections, but the high required accuracy needs to be considered.

6.2.2 Assembly of the test specimens

The different components of the glass-metal elements with composite structural behaviour are ordered separately and assembled together in the laboratory at Graz University of Technology. Only in the case of the metal framing the corner elements and the edge elements are welded together by the metal processing company. Since the metal and the glass components have weights which require a crane and because of the limited working time of the adhesives, a precise step by step planning of the whole assembling process is of high importance.

Because of the size of the elements and the need of a crane for handling, it is not possible to perform the assembly and to let the specimens cure at fully controlled climatic conditions. However, the temperature and the relative humidity in the laboratory during assembly, curing and testing is monitored and the measurements are provided in Fig. 6.4. The temperature is around *20 °C* during assembling and curing and increases slightly towards *25 °C* in the testing period. The relative humidity varies between 30% and *50%* during assembly and the first two weeks of curing and between *40%* and 60% during the last two weeks of curing and the three weeks of testing.

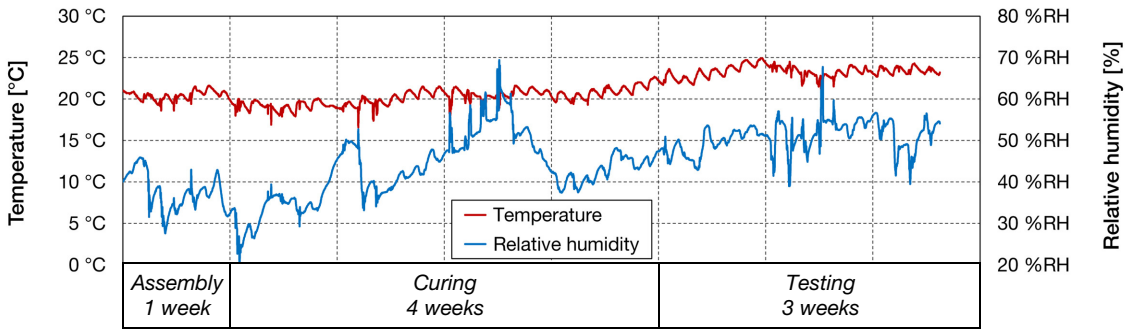

Fig. 6.4 *Temperature and relative humidity in the laboratory during assembly, curing and testing of the large-scale multi-component specimens*

Application of the perimetrical adhesive bonding

The application of the two different adhesives is completed based on the following main steps:

- (a) positioning of the metal frames on timber blocks in order to have access for tooling of the adhesive joints both from above and from below the elements (see top pictures on the left in Fig. 6.5 and Fig. 6.6);
- (b) taping of the metal frames and of the glass panes to delimit the adhesion area in order to obtain a clean edge of the joints (blue tape in Fig. 6.5 and Fig. 6.6);
- (c) cleaning of the adhesion areas and application of primers (the same products are used as in the case of the specimens for adhesive joints discussed in subchapter 5.2.1);
- (d) positioning of PTFE blocks on the metal frames for determining the desired thickness of the adhesive joints (white blocks in Fig. 6.5 and Fig. 6.6);
- (e) bringing the glass panes in position with a crane between guiding elements made of POM which are fixed in the corners of the frames;
- (f) application of the adhesive (see bottom pictures on the left in Fig. 6.5 and Fig. 6.6);

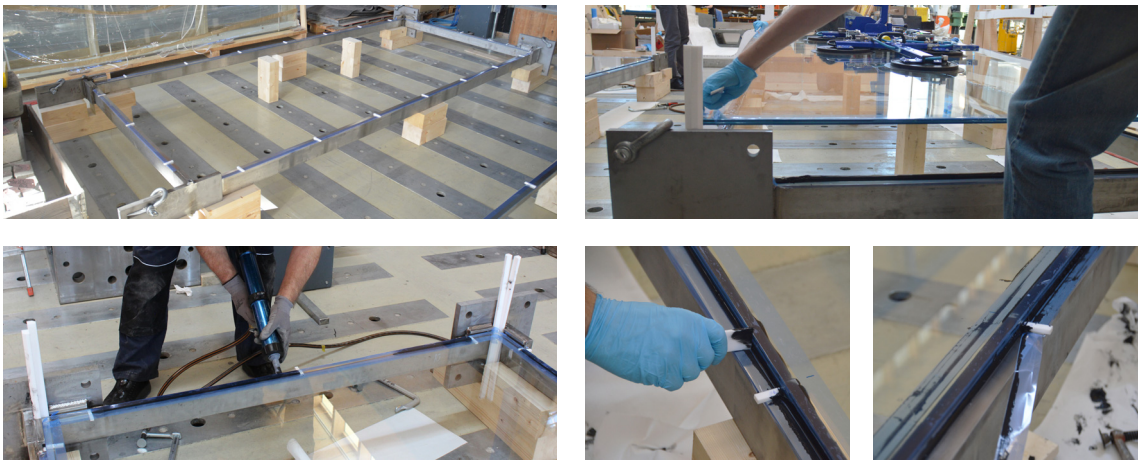

Fig. 6.5 *Application of the perimetrical adhesive bonding with silicone Dow Corning 993*

- (g) fixing of the glass panes to the metal frames with screw clamps, tooling of the lateral joint surfaces with a spatula and removing of the tapes;
- (h) removing of the screw clamps and the PTFE blocks after the adhesive is hard enough.

Fig. 6.6 *Application of the perimetrical adhesive bonding with acrylic SikaFast-5221 NT*

The different joint thicknesses used for the two adhesives as well as their different working time requires small differences in the steps (e) and (f) for specimens of *Type 1* and specimens of *Type 2*. The thicker joint of *6 mm* in the case of the silicone allows to lower completely the glass pane on the PTFE blocks which determines the joint thickness and to fill the resulting gaps with the adhesive afterwards. Furthermore, because of the longer working time of up to 30 minutes a single handgun is enough in the case of the silicone. In the case of the acrylic, the thickness of *3 mm* and the working time of maximum 10 minutes makes the application process more difficult. In step (e) the glass pane is positioned with the crane between the guiding POM rods in a height of around *30 cm* above the PTFE blocks which determines the joint thickness. In step (f) the adhesive is applied on the metal frame with two handguns simultaneously from dual cartridges of *250 ml* each. Five cartridges are required in total for the perimeter length of *10 m*. Afterwards, the glass pane is lowered in position and the procedure is continued with step (g) as described.

Application of the grouting blocks

For the specimens of *Type 1*, the adhesive joints are left to cure for three days and afterwards the grouting is applied in the corners. The areas of the stainless steel brackets are left without silicone adhesive in order to avoid complications in tooling and cleaning these surfaces before injecting the grout (see Fig. 6.7, right). The gaps for the grouting blocks are partially delimited by the welded stainless steel brackets and by the glass pane edges. In order to have a completely closed gap in which the grout can be injected from a dual cartridge, POM blocks are fixed with screw clamps to delimit the grouting block size in all other directions (see Fig. 6.7, left and middle). One of the POM blocks has two holes, one for injecting the grout and the other one to allow the air to come out. More details on the application of the grouting blocks can be found in [Kolany, 2018], where also the structural performance of this component is evaluated.

Fig. 6.7 *Application of the grouting blocks with Hilti HIT HY270*

6.2.3 Design of the test setup

The final test setup for testing the large-scale specimens is designed in a landscape format as illustrated in Fig. 6.8, since an application of the in-plane shear load ($F_{s,i}$ in Fig. 6.9) horizontally in a height of around *3.5 m* is not possible with the desired size of up to around *200 kN*. The setup is build on a *1.0 m* thick prestressed concrete slab with steel mounting rails every *0.5 m*. The slab has an anchoring grid of *50 x 50 cm* which allows for anchors loaded by a maximum of *500 kN* each. The four-column test rig for the in-plane shear load ($F_{s,i}$), the abutment blocks for the in-plane compression and tension load ($F_{n,i}$) and the out-of-plane pressure load ($F_{p,o}$) as well as the abutment wall and the triangular structures for the specimen supports are all fixed to this slab.

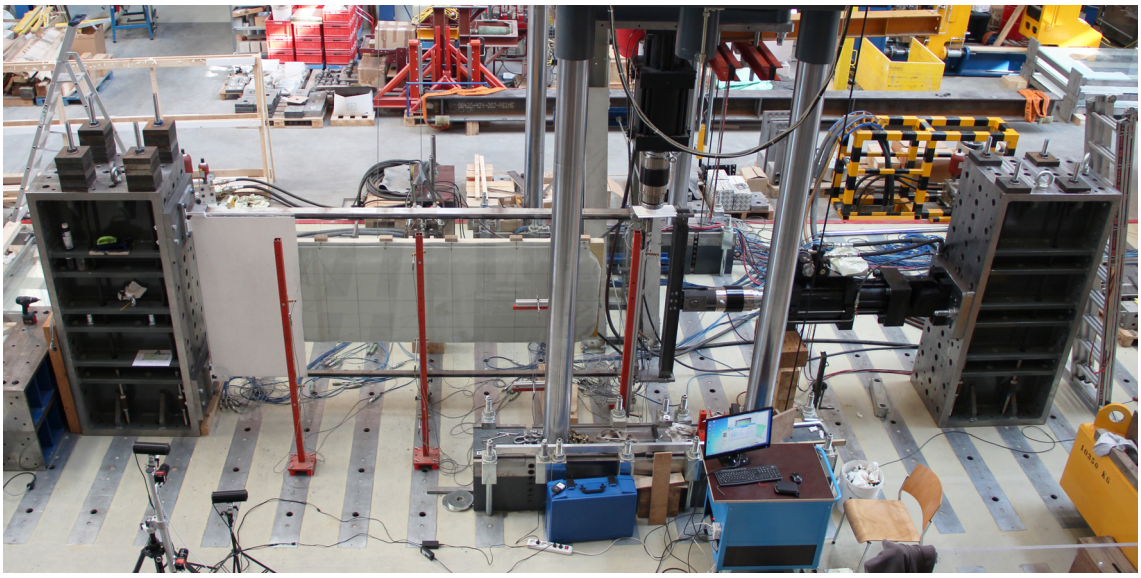

Fig. 6.8 *Overview of the setup for testing the large-scale multi-component specimens*

The main dimensions of the test setup components and the distances between axes of fixing and loading as well as a labelling of the main elements is provided in the drawings from Fig. 6.9. The sizes of the hydraulic jacks as well as given constrains by fix axes have to be considered during planing and request some additional adapter plates in order to fix the specimens in the desired position and to load them in the appropriate axes.

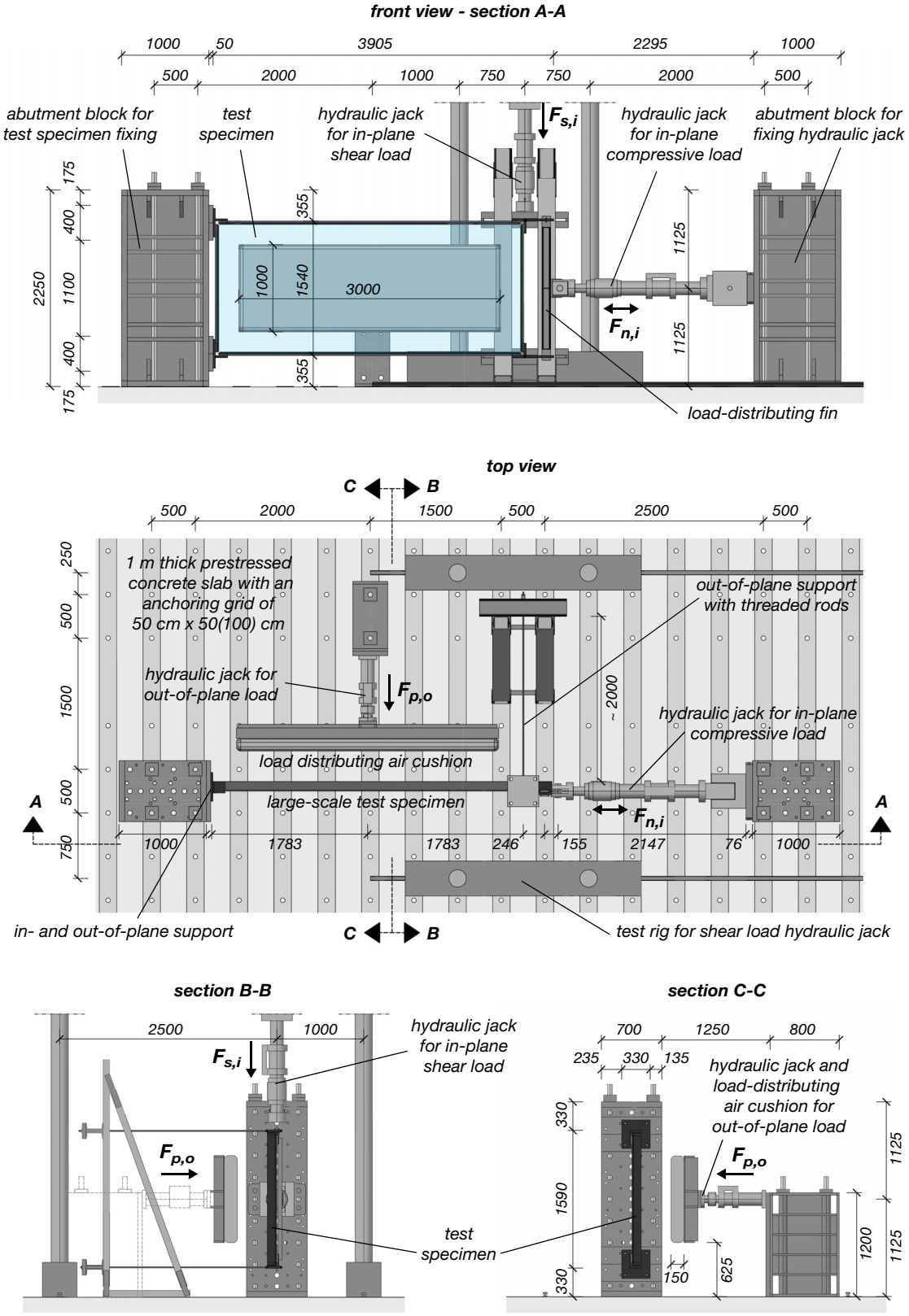

Fig. 6.9 *Main dimensions of the setup in [mm] for testing the large-scale multi-component specimens in top view and different sections*

In-plane and out-of-plane supports

At one end of the test specimens (the left shorter side in Fig. 6.8) all six degrees of freedom are locked by connecting the two corner elements of the metal framing with four *M24 8.8* bolts each to the abutment wall (see Fig. 6.10 left). The in-plane shear load at the opposite end of the test specimens is planed to act in the intersection point between the middle plane of the glass panes and the middle plane of the corner element leg attached to the shorter edge element. This objective coupled with the fact that the hydraulic jack for the shear load can only be moved in a grid of *25 cm* requires the use of *50 mm* thick adapter plates between the abutment block and the test specimens which have threaded holes, allowing for an excentric fixing.

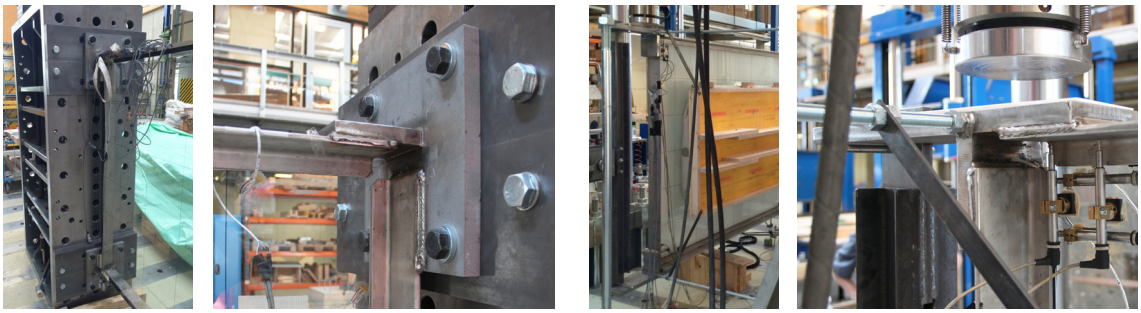

Fig. 6.10 *In- and out-of-plane support at the fixed end (left) and out-of-plane support with threaded rods at the free end (right)*

At the opposite end of the test specimens (the right shorter side in Fig. 6.8) only the translational out-of-plane degree of freedom is locked by connecting threaded rods to the nuts which are welded on the corner elements of the metal framing (see Fig. 6.10, right). The rods have a diameter of *16 mm* and a length of around *2000 mm* to provide only negligible resistance in the other degrees of freedom. At the other end the threaded rods are connected to a bearing construction built of two connected triangles made of U-shaped profiles (see Fig. 6.9).

In-plane load application

For the two applied in-plane loads, which act at the cantilevering end of the test specimens as shown in Fig. 6.11, left, hydraulic jacks for up to *1000 kN* and allowing maximum strokes of *250 mm* are used. The jack for the in-plane shear load ($F_{s,i}$) is fixed to the four-column test rig and acts vertically in the test setup at the intersection point between the middle plane of the glass pane and the middle plane of the corner element legs. In order to avoid a rotational restraint of the specimen deformation by the load applying surface, a spherical pressure plate is used for the load introduction. Furthermore, a translational restraint is reduced by adding two thin PTFE sheets between the bottom pressure plate surface and the top surface of the corner element (see Fig. 6.11, middle).

The jack for the in-plane compression and tension load ($F_{n,i}$) is connected to an abutment block similar to the one used for supporting the test specimens. The load is applied with a distributing fin into the longer legs of the two corner elements at the cantilevering end of the test specimens (see Fig. 6.11, right). The fin is dimensioned to withstand loads up to *50 kN*. The surfaces of the openings in the corner elements on which the fin transfers the load are rounded to allow small

rotations occurring due to the movement of the specimens downwards. The hydraulic jack is connected with hinges both to the abutment block and to the load-distributing fin. To avoid a loading of the test specimens with the dead weight of the jack, a cable is connected to the cylinder and diverted with a pulley to the basement through an anchoring whole, where a counterbalancing weight is holding the jack in equilibrium.

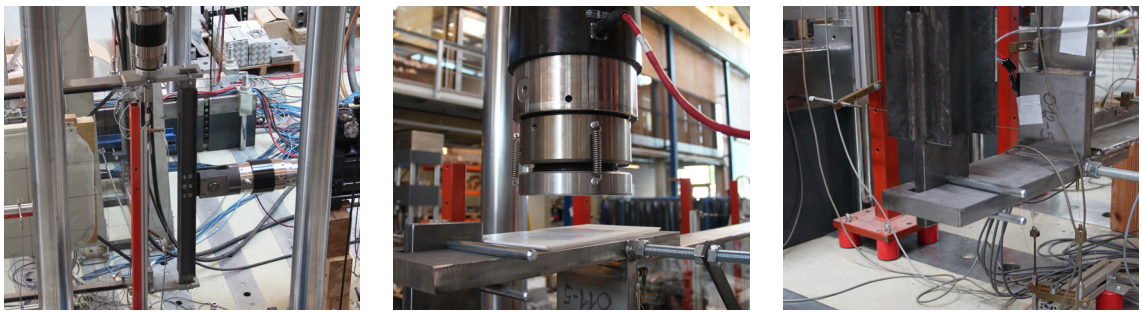

Fig. 6.11 *Application of the in-plane loads: overview (left), shear load (middle) and compression-tension load (right)*

Out-of-plane load application

For the out-of-plane load acting on the glass pane a hydraulic jack for up to *100 kN* and allowing a maximum stroke of *250 mm* is used. At the end towards the test specimen the jack is connected to a structure made of formwork panels on which an air cushion is hanging. The air cushion has a length of *3000 mm, a height of 1000 mm and a thicknes of 150 mm* and is used to distribute the load from the hydraulic jack on the glass surface simulating wind suction. The connection to the hydraulic jack as well as the links to the test specimen allow the air cushion to rotate with the specimen loaded simultaneously by the in-plane shear load. At the other end the jack is fixed with a hinge to a smaller abutment block as shown in Fig. 6.9 and Fig. 6.12. Since the axis of loading in the centre of the glass pane and the axis of the abutment block are misaligned, an adapter plate is used. Similar to the jack for the in-plane compression and tension load, also the dead weight of this one is counterbalanced with a weight hanging in the basement.

Fig. 6.12 *Application of the out-of-plane load with a distributing air cushion mounted on a construction made of formwork panels*

6.2.4 Measurement instrumentation

One of the stated objectives for the large-scale tests is to determine and evaluate the structural behaviour of the glass-metal multi-component elements as a whole as well as of their single components. This objective can only be achieved by using appropriate measurement instrumentation to record the applied forces as well as occurring displacements and strains. For comparison between results from experimental testing and results from finite element simulations, the real initial dimensions are significant. Furthermore, for geometrically nonlinear analysis the initial imperfections are of high importance. Therefore several measurements are completed during assembly of the specimens and before starting the testing.

Most of the performed measurements during testing are done with linear variable differential transformers (LVDT), which will be further addressed as displacement transducers (DT) in this thesis. Additionally, strain gauge rosettes are used on the glass panes near the compressed grouting blocks for specimens of *Type 1* and in the opposite two corners for specimens of *Type 2*. These are the areas where the maximum principal tensile stresses are expected based on preliminary finite element simulations. On a predefined area at the fixed end of the test specimens a digital image correlation (DIC) system (*Mercury*) is used for deformation measurements. The area can be recognised by the white colour with an irregular black dot pattern in Fig. 6.8. These measurements are made from the front for specimens of *Type 1* and from the back for specimens of *Type 2*. The measurements performed during testing can be divided in such used to characterise the global behaviour of the elements and such used to evaluate the local behaviour of the load transfer materials.

Measurements before testing

During assembly of the test specimens the dimensions of the different components are measured. Especially the thicknesses of the glass panes and of the stainless steel edge elements are important, since generally manufacturers aim to produce at the lower limits allowed by tolerances. Furthermore, the real thickness of the PTFE blocks used to determine the adhesive thickness is measured as well. The mean values of the significant measurements are provided in Tab. 6.2.

Tab. 6.2 *Mean values of the component dimensions measured during assembling*

Specimen type	**Glass pane thickness** [mm]	**L-shaped stainless steel edge element**				**Adhesive thickness** [mm]
		Thickness short leg [mm]	**Thickness long leg** [mm]	**Length short leg** [mm]	**Length short leg** [mm]	
Nominal value	10.0 / 13.52 [a]	10.0	10.0	40.0	100.0	6.0 / 3.0 [b]
Type 1A	9.9	9.0	9.8	40.3	100.6	6.2
Type 1B	13.0	8.8	9.9	39.7	101.1	5.8
Type 2A	9.9	9.0	9.8	39.8	100.4	3.1
Type 2B	13.1	9.2	9.8	40.7	100.5	3.1

[a] Different thicknesses for specimens with monolithic glass panes and specimens with laminated glass panes
[b] Different thicknesses for specimens with silicone adhesive and specimens with acrylic adhesive

From the measured values it can be observed that the glass pane thickness is always smaller than the nominal value. Therefore, especially in literature dealing with buckling analysis the use of glass pane thicknesses at the lower limit of the allowed production tolerances is recommended. Furthermore, it can be noticed that the thickness of the short leg is lower than the one of the long leg for all specimens. This is because of the applied grinding with corn size P300 on the surfaces to be adhesively bonded, which has a reduction of the thickness as a result.

After installing the test specimens, the planarity (or the initial geometrical imperfection) of the glass panes is examined by measuring the position in space of a total of 105 points for each glass pane. The measurement is performed tactile with a *Romer* absolute arm. For the evaluation of the planarity two possibilities are given. The first one is to determine a plane with three corner points and then to calculate the distance of the other points to this plane. The second possibility is to determine a centred plane for all the points and then calculate their distance to this plane. In the first case only positive values are obtained, while in the second case both positive and negative values result. For the evaluation in this thesis the second method is used, since it provides a better overview on the shape of the initial geometrical imperfections. The results of this evaluation are shown in Fig. 6.13 for the two monolithic glass panes and in Fig. 6.14 for the two laminated glass panes both in the form of front views and elevations.

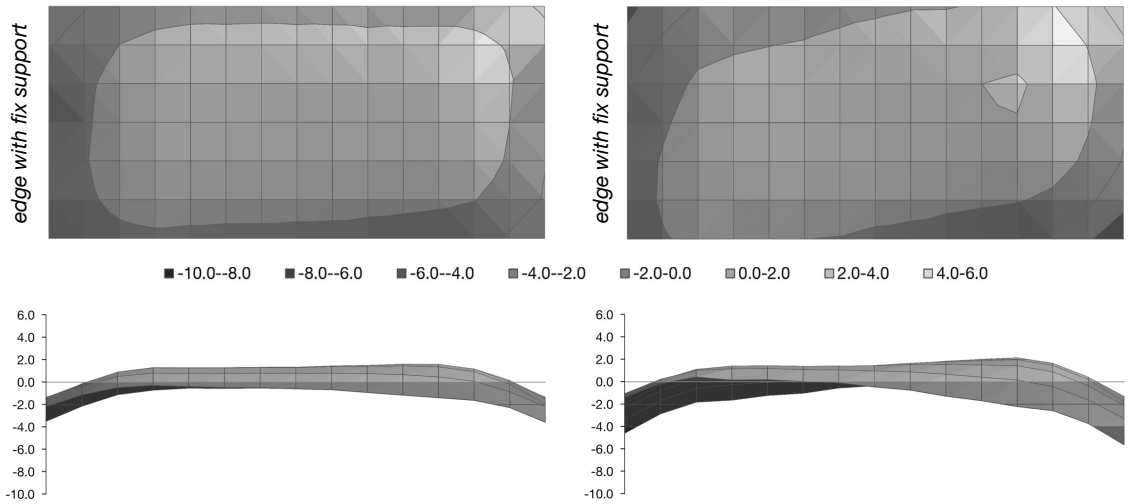

Fig. 6.13 *Planarity measurements of the monolithic glass panes used for the test specimens Type 1A and Type 2A*

In the case of both monolithic glass panes a single bulge spanning over the whole surface can be observed. The bulge has a shape similar to a deformation resulting from an out-of-plane loading. In the case of the laminated glass panes a shape similar to a hyperbolic paraboloid results. It can also be noticed that the size of the initial geometric imperfections is higher for the laminated glass panes compared to the monolithic ones.

The size of the measured imperfections is around *L/500* for the monolithic glass panes and increase up to around *L/250* for the laminated glass panes. These values need to be considered with care, firstly, because only a small number of specimens are measured and secondly, because the measurements are performed after assembling the specimens and fixing them to

the abutment wall. A certain imperfection could have been also induced by these steps. However, the measured imperfections are larger than the values provided in [Englhardt, 2007] for slightly smaller glass panes, but in the range of the values suggested by [Luible, 2004] and [Belis et al., 2011b] for linear glass elements.

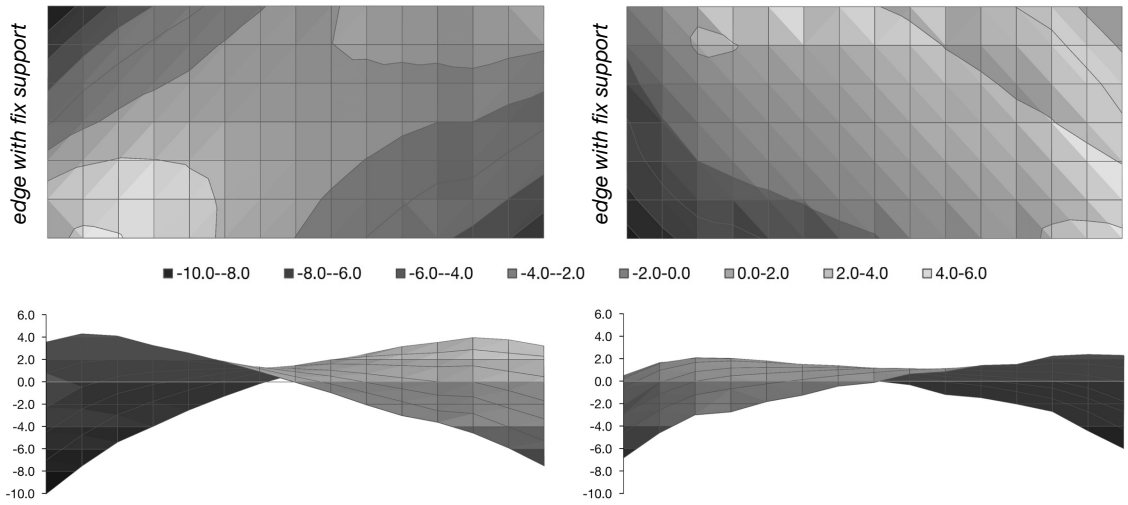

Fig. 6.14 *Planarity measurements of the laminated glass panes used for the test specimens Type 1B and Type 2B*

Measurement instrumentation during testing

A high number of measurement instruments is used to obtain detailed results on the structural behaviour of the glass-metal elements as a whole on the one hand and on the deformations occurring in the load transfer materials on the other hand. An overview of the used displacement transducers with those measuring absolute global deformations labelled with upper case letters (e.g. $DT_{z,1}$) and those recording relative deformations between metal framing and glass pane labelled with lower case letters (e.g. $dt_{z,1}$) is provided in Fig. 6.15. All transducers are plotted in a front view (left), while those measuring absolute deformations, which are positioned identically for the four specimen types, are also represented in a side view (right).

Beside the recorded displacements corresponding to the three applied loads ($D_{s,i}$, $D_{n,i}$ and $D_{p,o}$), the out-of-plane deformation of the glass pane (z-direction in Fig. 6.15) and the out-of-plane deformation of the longer leg belonging to the bottom L-shaped edge element (y-direction in Fig. 6.15) are measured. For the glass pane a total of ten displacement transducers ($DT_{z,1}$ to $DT_{z,10}$) are positioned in order to capture the shape of out-of-plane deformations resulting either direct from the out-of-plane load ($F_{p,o}$) or from plate buckling due to the two in-plane loads ($F_{s,i}$ or $F_{n,i}$). The bottom edge element is subjected to compressive stresses under each of the three applied loads and therefore is susceptible either to lateral torsional buckling in the case of the out-of-plane load ($F_{p,o}$) and of the in-plane shear load ($F_{s,i}$) or to column buckling in the case of the in-plane compressive load ($F_{n,i}$). To capture the occurring deformations in y-direction as well as an eventual twisting around the x-axis two displacement transducers ($DT_{y,1}$ and $DT_{y,2}$) are positioned at the free end of the edge element and another two ($DT_{y,3}$ and $DT_{y,4}$) in the middle of the edge element. $DT_{y,1}$ and $DT_{y,3}$ measure the displacement in y-direction near the edge of the

longer leg towards the glass pane, while $DT_{y,2}$ and $DT_{y,4}$ measure the displacement in the same direction near the opposite edge.

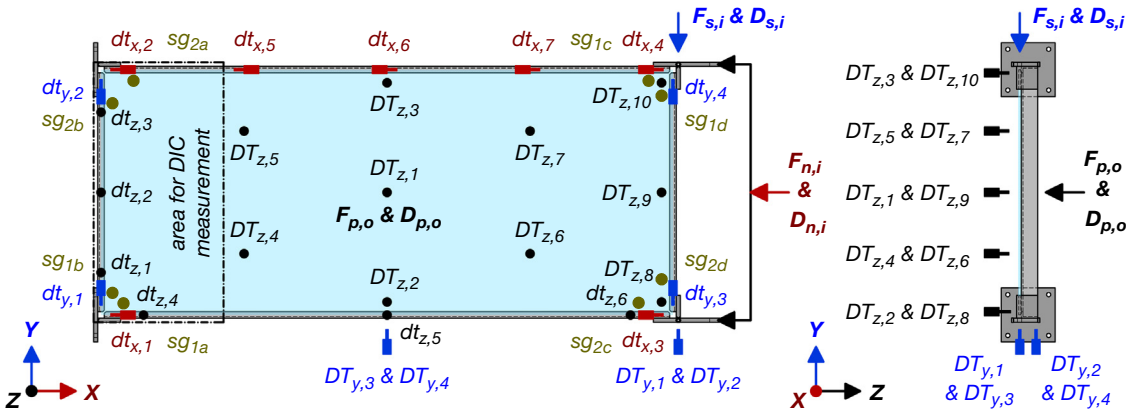

Fig. 6.15 *Measurement instrumentation for recording the global deformations of the glass-metal elements (labelled with upper case letters) as well as the local relative displacements between metal framing and glass pane (labelled with lower case letters)*

Other than in the case of the displacement transducers for the global behaviour, the position of the transducers for measuring relative displacements as well as the area for *DIC* measurement and the position of the strain gauges show differences between the specimens of *Type 1* and the specimens of *Type 2*. The relative displacements between the metal framing and the glass pane in z-direction are measured for both specimen types on the back side of the glass pane with a total of six transducers ($dt_{z,1}$ to $dt_{z,6}$), three along the fixed short edge element and three along the bottom long edge element.

The *DIC* measurement is performed on the front side of the glass pane for specimens of *Type 1*, since the air cushion is not interfering and a larger area can be covered. In the case of specimens of *Type 2* a direct view on the adhesive joint is desired for observing when the adhesive starts to yield by a whitening effect. For this reason the *DIC* measurement is performed on the back side of the glass pane, where only a strip of around *25 cm* is recorded. The displacement transducers for relative measurements in x-direction and y-direction are mounted for all specimen types on the other glass pane side, than the one on which the *DIC* measurement is performed in order to not interfere.

In the case of the specimens of *Type 2*, in each corner one transducer is used to measure the relative displacement in x-direction between the long edge elements and the glass pane ($dt_{x,1}$ to $dt_{x,4}$) and one to measure the relative displacement in y-direction between the short edge elements and the glass pane ($dt_{y,1}$ to $dt_{y,4}$). Furthermore, three additional transducers are used to measure the relative displacement in x-direction between the top edge element and the glass pane in the middle and in the quarter-points of the edge element ($dt_{x,5}$ to $dt_{x,7}$). In Fig. 6.15 the position of the transducers for specimens of *Type 2* and their measuring direction are illustrated. The position of the mounted transducers in the four corners and the fixing solutions are shown for the specimens of *Type 2B* in Fig. 6.16. In this way the relative displacements between metal framing and glass pane parallel to the perimetrical adhesive joints are measured in direct proximity of the glass edge.

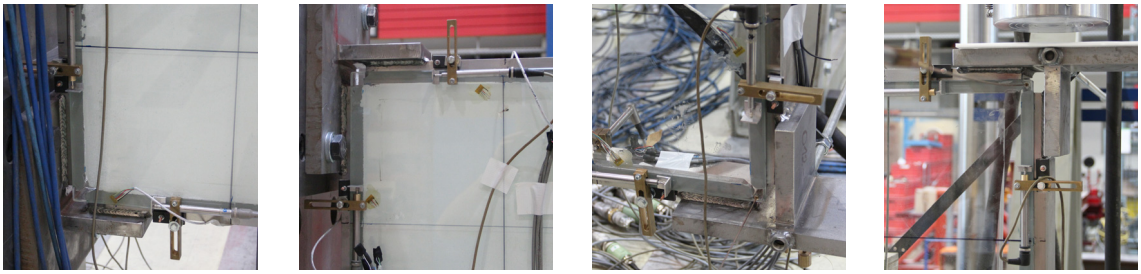

Fig. 6.16 *Measurement instrumentation for recording the relative displacements between metal framing and glass panes in the corners for specimens of Type 2*

In the case of the specimens of *Type 1* the transducers for relative displacements in x-direction and y-direction are mounted in the corners rotated by *90°* compared to the specimens of *Type 2*. This means, that the relative displacements in x-direction are measured between the glass pane and the short edge elements and the relative displacements in y-direction between the glass pane and the long edge elements. The reason for this is the primary objective to measure the occurring compression in the grouting blocks or the resulting gaps between the grouting blocks and the glass pane edges. The position and the orientation of the displacement transducers in the four corners for the specimen of *Type 1B* are shown in Fig. 6.17. It can be observed that in the two corners in which the grouting blocks are under compression due to the in-plane shear load (bottom left corner and top right corner in Fig. 6.15), two displacement transducers are used for each direction in order to determine a non-uniform compression of the grouting block. Due to this fact and because of the measurement amplifier limits, the three additional transducers along the top edge have to be left out for specimens of *Type 1*.

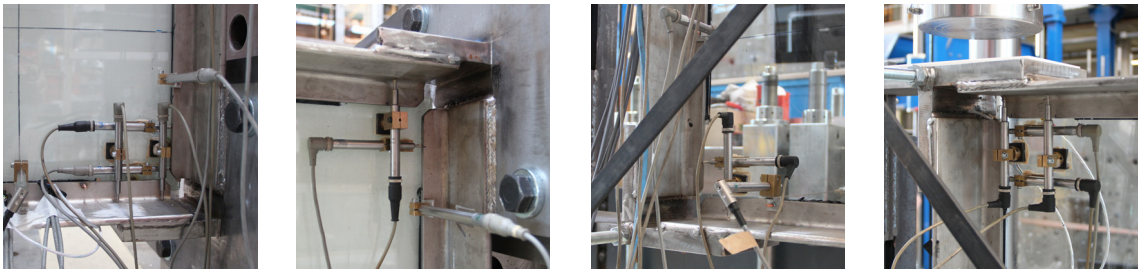

Fig. 6.17 *Measurement instrumentation for recording the relative displacements between metal framing and glass panes in the corners for specimens of Type 1*

Four strain gauge rosettes for measurements in *0°/45°/90°* are used for each test specimen on the same glass pane side on which the *DIC* measurement is performed. For the specimens of *Type 1* the rosettes are positioned centred to the four grouting blocks in the compressed corners (sg_{1a} and sg_{1b} in the bottom left corner and sg_{1c} and sg_{1d} in the top right corner from Fig. 6.15). For the specimens of *Type 2* the four rosettes are positioned near the two other corners (sg_{2a} and sg_{2b} in the top left corner and sg_{2c} and sg_{2d} in the bottom right corner from Fig. 6.15) around *20 cm* towards the middle of the edge elements.

6.3 Experimental procedure and test results

For all specimens several load scenarios with single loads increased up to a certain value or load combinations with one or two loads kept constant and the shear load increased up to a specific value are run. Only the two specimens with laminated glass panes (*Type 1B* and *Type 2B*) are tested to failure under shear loading. In the next subchapters first the experimental procedure with the different loading series is explained and afterwards, selected significant results are discussed for the different series.

6.3.1 Loading scenarios and cycles

The loading programme is worked out with the aim to obtain from the reduced number of test specimens as much information and data as possible. An overview of the performed load scenarios showing the order of the series, the level of loading, the used loading speeds and the number of driven cycles is provided in Tab. 6.3. The primary focus in this experimental programme is set on the behaviour of the large-scale multi-component elements under in-plane shear loading as well as on the influence which additional loadings (in-plane axial compressive or tensile loading and out-of-plane surface loading) have on this behaviour.

In a first step, cycles with only one load direction at a time are performed in order to analyse the effects of each load separately. For defining the driven load levels two main criteria are used. The first one is to keep the loads at a level at which no plastic deformations occur in the metal framing and no or only very low plastic deformations result in the used load transfer materials between glass pane and framing. The second criteria is to use realistic load levels which might occur in transparent building envelopes made of glass-metal elements with composite structural behaviour. These assumptions are made based on the considerations discussed in subchapter 3.3 as well as on preliminary hand calculations and finite element simulations.

For the in-plane compressive axial load ($F_{n,i}$) forces up to *40 kN* in steps of *10 kN* are applied. This load levels can result from the dead weight of further elements as well as partially from the weight of a (glass) roof supported by the elements. The dead weight of one glass-metal element is estimated with around *4-5 kN* depending on the used glazing and the actual size of the metal framing profiles. For the out-of-plane surface loading ($F_{p,o}$) forces up to *15 kN* in steps of *5 kN* are applied with the hydraulic jack. Considering the dimensions of the glass panes of *3.5 mm x 1.5 m*, a force of *5 kN* corresponds approximately to a surface load of *1.0 kPa*. The in-plane shear load is increased up to *30 kN* in steps of *10 kN*. This value is estimated based on a prismatic body as the one illustrated in Fig. 3.1 by additionally considering to not get close to the critical buckling load of a glass pane with the same dimensions and with Navier boundary conditions.

The load levels are increased stepwise in order to be able to capture eventual plastic deformations. This is also the reason for performing series with combined loading intercalated between the series with single in-plane shear loading up to *10 kN* (series no. 03), up to *20 kN* (series no. 09) and up to *30 kN* (series no. 14). For the series with single loads, displacement-controlled cycles with different loading speeds (chosen based on the expected deformations) are performed to observe the influence of this parameter on the mechanical behaviour of the system.

Tab. 6.3 *Concept for loading control and order of performed loading series*

Series no. & loading description		$F_{n,i}$		$F_{p,o}$		$F_{s,i}$		No. of cycles
		Load level	**Loading speed**	**Load level**	**Loading speed**	**Load level**	**Loading speed**	
		[kN]	[mm/min] (* *[kN/sec]*)	[kN]	[mm/min] (* *[kN/sec]*)	[kN]	[mm/min]	
01	$F_{n,i}$(10-c)	10	2 20	-	-	-	-	3 3
	$F_{n,i}$(20-c)	20	2 20	-	-	-	-	1 3
	$F_{n,i}$(30-c)	30	2 20	-	-	-	-	1 3
	$F_{n,i}$(40-c)	40	2 20	-	-	-	-	1 3
02	$F_{p,o}$(5-c)	-	-	5	10 50	-	-	3 3
	$F_{p,o}$(10-c)	-	-	10	10 50	-	-	1 3
	$F_{p,o}$(15-c)	-	-	15	10 50	-	-	1 3
03	$F_{s,i}$(10-c)	-	-	-	-	10	2 10 50	1 3 10
04	$F_{n,i}$(40) + $F_{s,i}$(10-c)	40	** 2*	-	-	10	10	3
05	$F_{n,i}$(-40) + $F_{s,i}$(10-c)	-40	** 2*	-	-	10	10	3
06	$F_{p,o}$(10) + $F_{s,i}$(20-c)	-	-	10	** 1*	10	10	3
07	$F_{n,i}$(40) + $F_{p,o}$(10-c)	40	** 2*	10	** 1*	-	-	3
08	$F_{n,i}$(40) + $F_{p,o}$(10) + $F_{s,i}$(10-c)	40	** 2*	10	** 1*	10		3
09	$F_{s,i}$(20-c)	-	-	-	-	20	2 10 50	1 3 10
10	$F_{n,i}$(40) + $F_{s,i}$(20-c)	40	** 2*	-	-	20	10	3
11	$F_{n,i}$(-40) + $F_{s,i}$(20-c)	-40	** 2*	-	-	20	10	3
12	$F_{p,o}$(10) + $F_{s,i}$(20-c)	-	-	10	** 1*	20	10	3
13	$F_{n,i}$(40) + $F_{p,o}$(10) + $F_{s,i}$(20-c)	40	** 2*	10	** 1*	20	10	3
14	$F_{s,i}$(30-c)	-	-	-	-	30	2 10 50	1 3 10
15	$F_{n,i}$(40) + $F_{s,i}$(30-c)	40	** 2*	-	-	30	10	3
16	$F_{n,i}$(-40) + $F_{s,i}$(30-c)	-40	** 2*	-	-	30	10	3
17	$F_{p,o}$(10) + $F_{s,i}$(30-c)	-	-	10	** 1*	30	10	3
18	$F_{n,i}$(40) + $F_{p,o}$(10) + $F_{s,i}$(30-c)	40	** 2*	10	** 1*	30	10	3
19	$F_{s,i}$(30) dynamic cycles	-	-	-	-	30	-	1000
20	$F_{s,i}$ increased until failure	-	-	-	-	-	-	-

In a second step, series with two of the three loads acting on the test specimens are performed. The loads are applied successively in order to be able to distinguish the deformations resulting from each load. Since the shear load is considered the primary load of interest, this is the last load to be applied and three displacement-controlled cycles are run with this load. The other loads are applied load-controlled in order to allow to hold them constant on the desired level.

For the in-plane axial load ($F_{n,i}$) values of *+40 kN* (series no. 04, no. 10 and no. 15) and *-40 kN* (series no. 06, no. 11 and no. 16) are used. The negative value is considered as well since this combination is unfavourable for certain displacements and for the stress values in certain components (for instance for the long frame profile which is then tensioned under shear load). This situation can occur in the front elements of a shear wall consisting of several glass-metal elements with composite structural behaviour which rotates as a whole rigid body. For the out-of-plane surface load ($F_{p,o}$) a value of *10 kN* is used (series no. 06, no. 12 and no. 17). Series no. 07, in which the in-plane axial compressive load and the out-of-plane surface load are combined deliveres rather uninteresting results and is therefore not discussed in the next subchapters.

In a third step, all three loads are combined (series no. 08, no. 13 and no. 18). First, the in-plane axial compressive load is applied load controlled with *40 kN*, then the out-of-plane surface load is applied load-controlled with *10 kN* and finally three load cycles are run displacement-controlled with the in-plane shear load up to *10 kN* (series no. 08), up to *20 kN* (series no. 13) and up to *30 kN* (series no. 18). The first shear loading is applied simultaneously with the out-of-plane load due to a mistake in the programming. However, this has only an influence on the path of the load-displacement curves during the first loading cycle, but not on the maximum reached displacements.

For series no. 19 one thousand cycles are run with the in-plane shear load up to *30 kN*, applied as a sinusoidal oscillation with a frequency of *1 Hz*. The scope of this dynamic loading is mainly to allow a better visual analysis of the resulting local deformations and gaps. Additionally, these series give a hint on the behaviour of the elements under cyclic loading. However, for meaningful statements on this aspect, which is not within the objectives of these experimental investigations, a significantly higher number of cycles is required. The series no. 20 is only performed for the two specimens with laminated glass panes (*Type 1B* and *Type 2B*) and consists of a displacement-controlled in-plane shear loading until failure of the glass-metal elements with composite structural behaviour.

6.3.2 Test results from series with a single load direction

The evaluation of the test results from the series with a single load direction is done based on diagrams showing selected absolute out-of-plane and in-plane displacements of the elements as well as relative out-of-plane and in-plane displacements between the glass pane and the metal framing. For each of the three loading directions only the diagrams with meaningful results are plotted. Furthermore, since almost no plastic deformations are noticed during the cycles with different load levels, only the results from the cycles with the highest load level are plotted in the diagrams for better readability. The provided results are given for each of the four specimens in order to allow a comparison both between the two tested concepts (*Type 1* and *Type 2*) as well as between the specimens with monolithic glass panes and the ones with laminated glass panes using the same concept (*Type 1A* and *Type 1B*, respectively *Type 2A* and *Type 2B*).

In-plane compressive axial loading

The cycles performed under in-plane axial loading in compression are illustrated in Fig. 6.18 along the time axis for the specimen *Type 1A*, as an example. Additional to the different loading speeds indicated by the inclination, almost flat parts of the curve can be observed between the cycles as well as between loading and unloading of each cycle. At these load values the displacement is kept constant for a period of ten seconds. A holding of a constant load is difficult because of the displacement-controlled loading procedure.

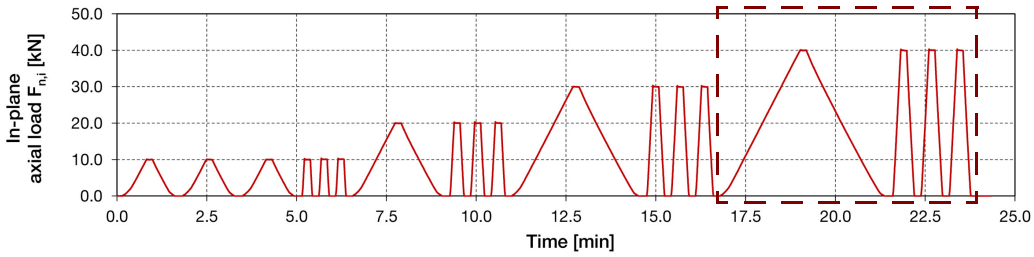

Fig. 6.18 *Load-time diagram of the performed cycles for in-plane compressive loading (Type 1A)*

Only the cycles performed up to a load of *40 kN* are evaluated in the following diagrams (the cycles which are framed with the dashed rectangle in Fig. 6.18). However, also this load size resulted only in small absolute displacements and insignificantly low relative displacements. Therefore only the absolute out-of-plane displacements of the glass panes along the compressed diagonal are plotted in diagrams (for specimens *Type 1A* and *Type 2A* in Fig. 6.19 and for specimens *Type 1B* and *Type 2B* in Fig. 6.20). The notations *compressed diagonal* and *tensioned diagonal* which will be used throughout the next subchapters refer to the in-plane shear loading ($F_{s,i}$) under which the diagonal going from the bottom left corner to the top right corner of the element (as it is fixed during testing) is compressed, while the other diagonal is tensioned.

For all the results discussed in this subchapter as well as in subchapters 6.3.3 and 6.3.4 based on load-displacement diagrams, the results for the specimens of *Type 1* are plotted left, while those for specimens of *Type 2* are plotted right. The range of the horizontal axes is the same throughout these three subchapters for the diagrams showing similar results in order to allow an

easier comparison. Furthermore the diagrams on the right include sketches of the test specimens which show the evaluated measurement instrumentation by circles coloured according to the colours used for the plotted curves.

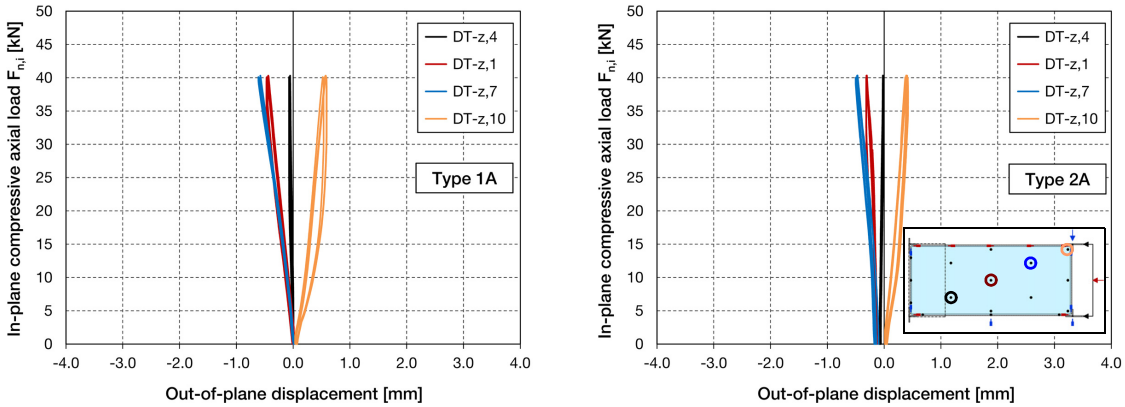

Fig. 6.19 *Out-of-plane displacements of the monolithic glass pane along the compressed diagonal for specimens Type 1A (left) and Type 2A (right) under in-plane compressive axial loading*

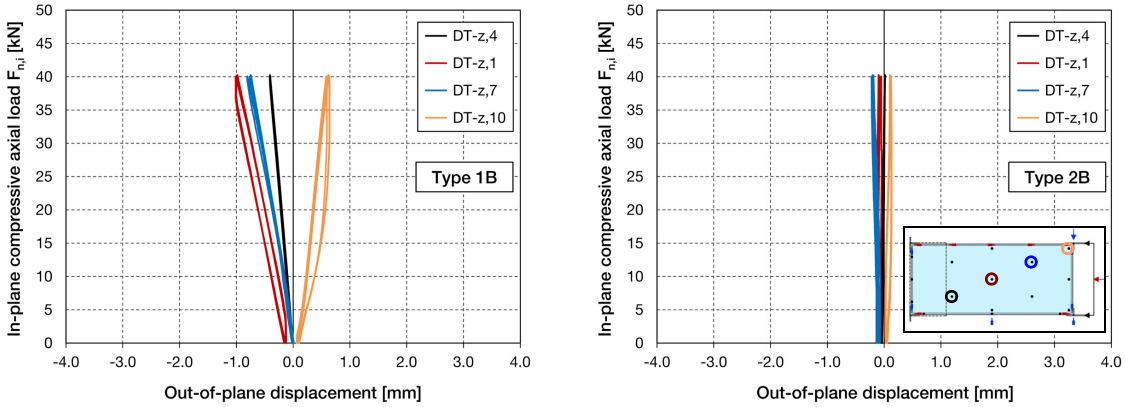

Fig. 6.20 *Out-of-plane displacements of the laminated glass pane along the compressed diagonal for specimens Type 1B (left) and Type 2B (right) under in-plane compressive axial loading*

The out-of-plane displacements along the compressed diagonal of the glass pane reach values less than *1.0 mm* for all four tested specimens under in-plane axial compressive loads of *40 kN*. The out-of-plane displacements along the tensioned diagonal are in a similar range as those along the compressed diagonal. Furthermore, for all investigated loads and load combinations the out-of-plane displacements along the glass pane diagonals are either in a similar range for both paths or are higher along the compressed diagonal. Therefore, only the displacements along this diagonal are evaluated in the thesis. Because of the small size of the displacements, it is difficult to draw meaningful conclusions by comparing the curves for the different specimens under in-plane axial compressive loads, especially considering the results from the performed planarity measurements. However, it seems in all four cases that a buckle is starting to grow towards the loaded side of the element since the displacements measured by the transducer $DT_{z,7}$ (*DT-z,7* in the diagram legends) are higher than those measured by $DT_{z,4}$.

The relative in-plane displacements between glass-pane and metal framing in the direction of loading in the four corners ($dt_{x,1}$ to $dt_{x,4}$ according to Fig. 6.15) reach values of up to *0.3 mm* for the specimens of *Type 1* and up to *0.1 mm* for the specimens of *Type 2*.

Out-of-plane surface loading

The cycles performed under out-of-plane surface loading are illustrated in Fig. 6.21 with a load-time diagram for specimen *Type 1A*, as an example. For the same reasons as in the case of the series with in-plane axial compressive loading, only the cycles run up to the maximum load of *15 kN*, marked with the dashed rectangle, are evaluated. However, for comparison with the results from series with combined loading (see subchapters 6.3.3 and 6.3.4) the displacement values reached at *10 kN*, which can be read from the diagrams, should be considered.

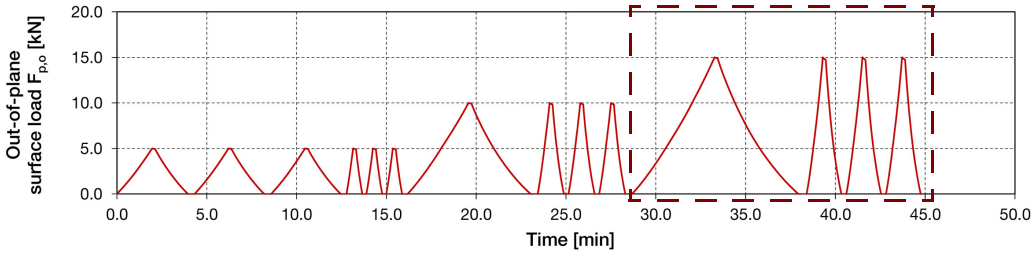

Fig. 6.21 *Load-time diagram of the performed cycles for out-of-plane surface loading (Type 1A)*

Under this type of loading significant higher out-of-plane displacements of the glass panes occur (see Fig. 6.22 and Fig. 6.23). Values of up to *37 mm* are reached in the case of specimens of *Type 1* and of up to *30 mm* for specimens of *Type 2* in the centre of the glass panes ($DT_{z,1}$). The deformation shape is not completely symmetric (compare $DT_{z,4}$ and $DT_{z,7}$), since the out-of-plane support at the free end is softer than the one at the fixed end. This can be also observed in the small occurring displacements measured by $DT_{z,10}$.

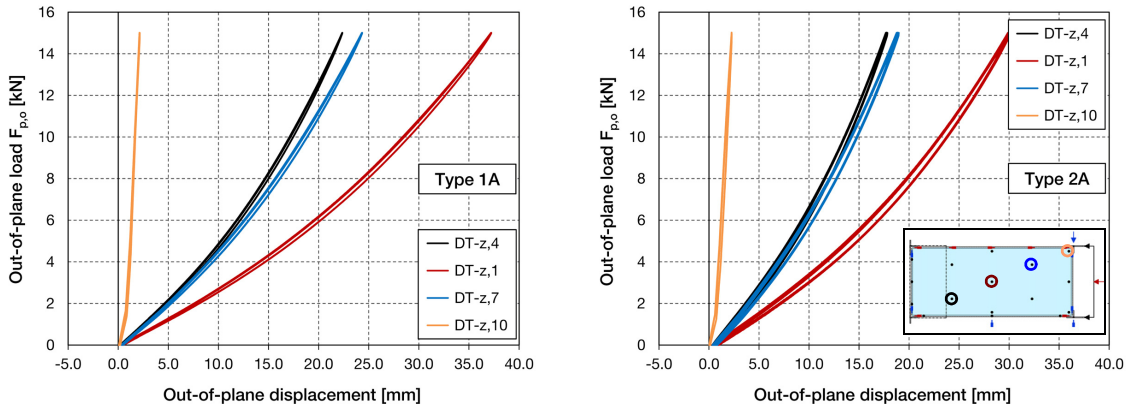

Fig. 6.22 *Out-of-plane displacements of the monolithic glass pane along the compressed diagonal for specimens Type 1A (left) and Type 2A (right) under out-of-plane surface loading*

By comparing the specimens with different design concepts to each other, it can be observed that those with acrylic adhesive joints behave, as expected, slightly stiffer than those with silicone adhesive joints. For this loading direction the setting blocks used for specimens of *Type 1*

in the element corners have no significant influence on the system behaviour. A comparison between specimens based on the same design concept shows that the maximum displacements are almost the same, independently if *10 mm* thick monolithic glass panes or *2 x 6 mm* thick laminated glass panes are used. However, there are some differences in the development of the curves. In the case of monolithic glass panes (*Type 1A* and *Type 2A*), the loading and the unloading paths are almost the same for all cycles. For the two specimens with laminated glass panes (*Type 1B* and *Type 2B*), firstly, discrepancies between the loading and the unloading path can be noticed and, secondly, the displacements reached during the cycle with lower loading speed are slightly higher than during the faster cycles. Both of these aspects result due to the viscous material behaviour of the *1.52 mm* thick interlayer used to laminate the glass panes together. Furthermore, the behaviour of the interlayer is also the reason for the incomplete recovery during the *10 sec* between the loading cycles.

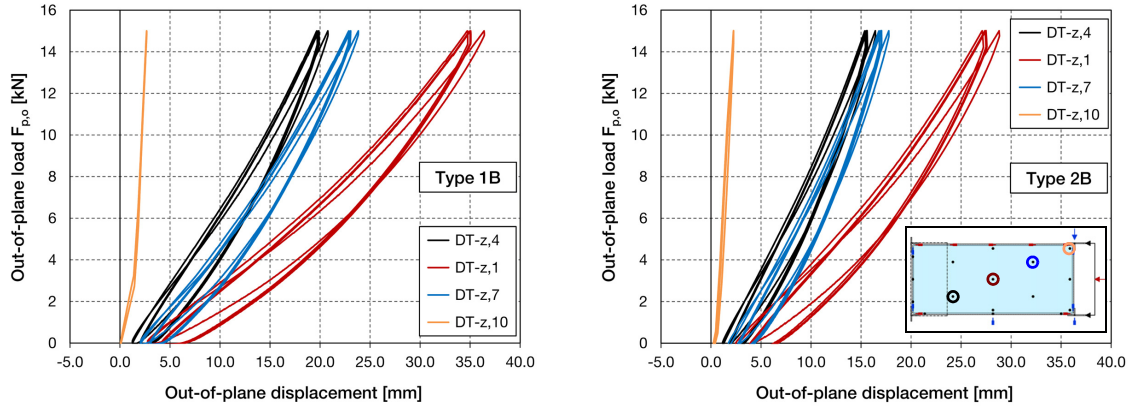

Fig. 6.23 *Out-of-plane displacements of the laminated glass pane along the compressed diagonal for specimens Type 1B (left) and Type 2B (right) under out-of-plane surface loading*

The occurring out-of-plane displacements are easily visible with the naked eye and can be noticed by comparing the two pictures shown in Fig. 6.24. While in the unloaded state on the left hand side a clear reflection is given, heavy distortions can be observed in the right image.

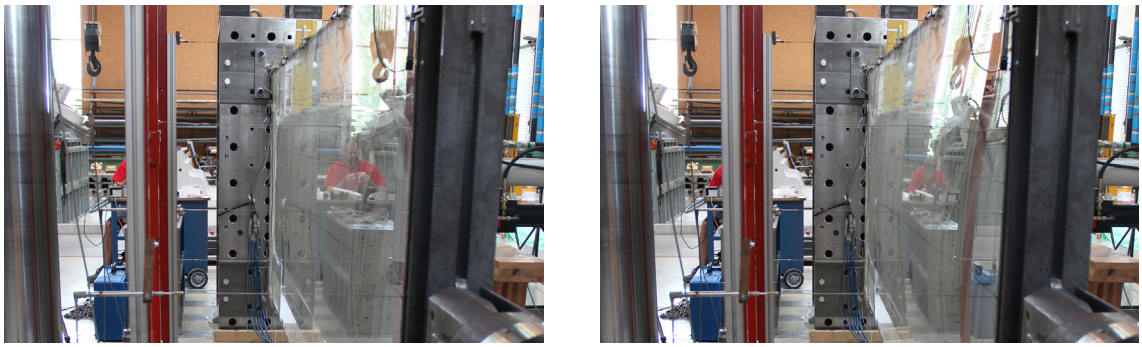

Fig. 6.24 *Selected test specimen unloaded (left) and under 15 kN out-of-plane surface loading (right)*

For the series in which the specimens are tested under out-of-plane surface loading, the absolute in-plane displacements measured in the middle ($DT_{y,3}$ and $DT_{y,4}$) and at the free end ($DT_{y,1}$

and $DT_{y,2}$) of the elements are evaluated. The curves plotted in Fig. 6.25 for the specimens with monolithic glass panes and in Fig. 6.26 for the specimens with laminated glass panes show that almost no displacement occurs at the free end. However, in the middle of the elements both measurement points on the frame profile move upwards (towards the centre of the glass pane). The displacements of the point near the glass pane ($DT_{y,3}$) are in the case of all four specimens smaller than those of the other point ($DT_{y,4}$), which means that the out-of-plane loading causes a rotation of the edge elements around their longitudinal axis. The fact that this rotation is more pronounced in the case of the specimens with acrylic adhesive is a confirmation of the expected stronger composite behaviour for this type of loading.

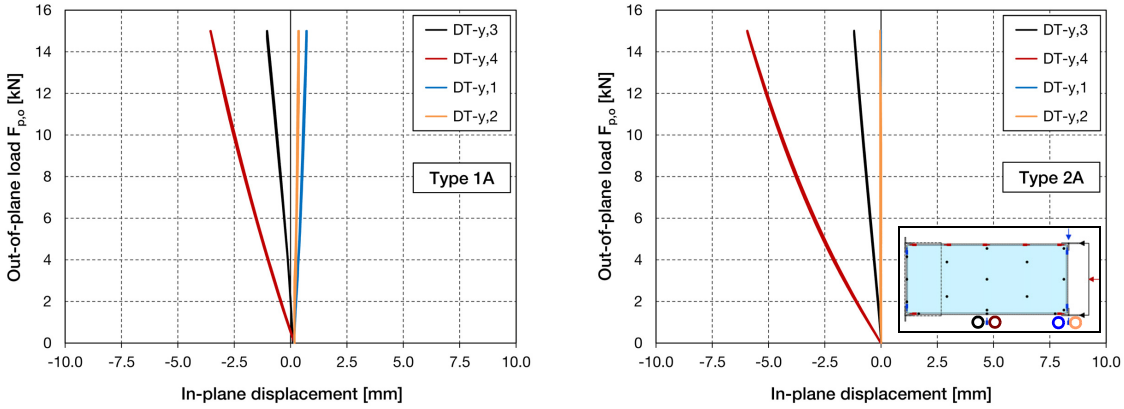

Fig. 6.25 *In-plane displacements of the bottom frame profile in the middle and at the end of the element for specimens Type 1A (left) and Type 2A (right) under out-of-plane surface loading*

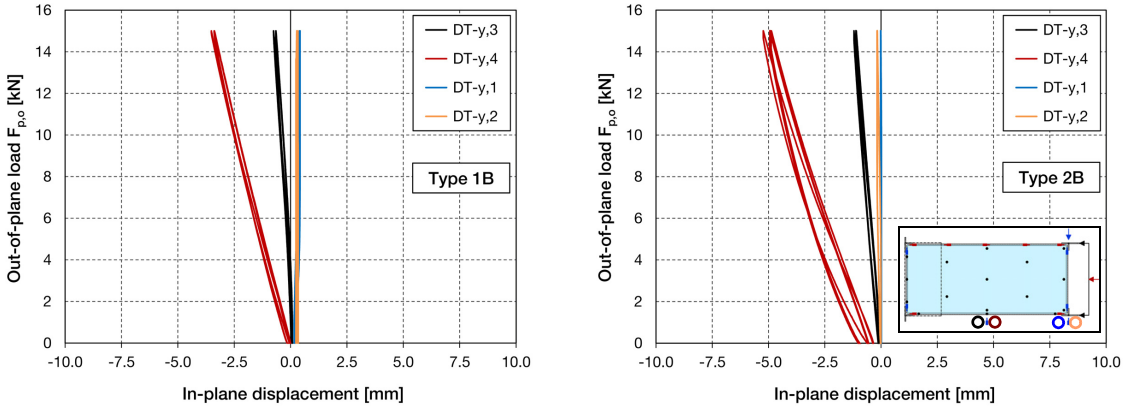

Fig. 6.26 *In-plane displacements of the bottom frame profile in the middle and at the end of the element for specimens Type 1B (left) and Type 2B (right) under out-of-plane surface loading*

Other aspects which have already been discussed for the absolute out-of-plane displacements, like the discrepancies between the loading paths and the unloading paths in the case of the specimens with laminated glass panes, can also be observed in the curves for the absolute in-plane displacements. Furthermore, the same aspects can also be noticed in the diagrams from Fig. 6.27 and Fig. 6.28 showing the relative out-of-plane displacements between glass pane and metal framing along the bottom edge of the elements. These displacements are signifi-

cantly higher for the specimens with silicone adhesive joints, reaching values of around *1.0 mm* for *Type 1A* and of around *1.2 mm* for *Type 1B*. Considering the used joint thickness of *6 mm* the occurring displacements represent strains of around *20%*. For the specimens with acrylic adhesive joints the measured displacements lead to strains of only up to *5%* for the used joint thickness of *3 mm*.

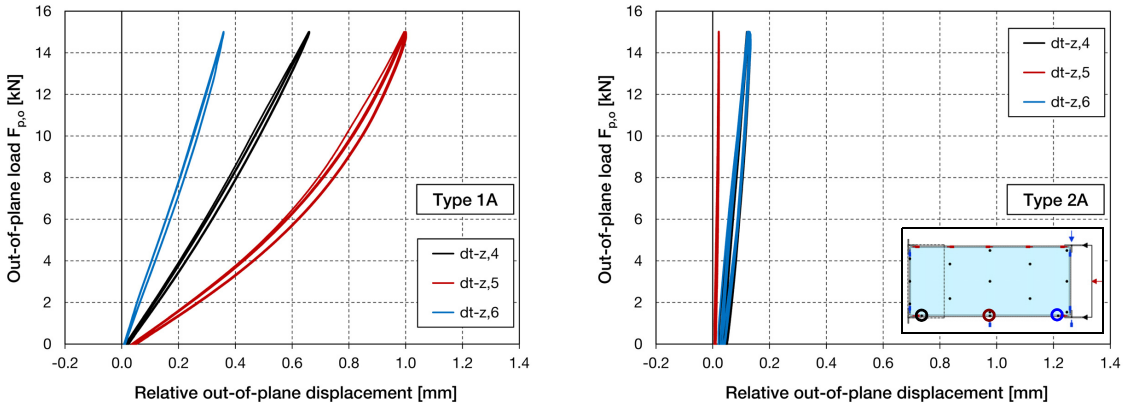

Fig. 6.27 *Relative out-of-plane displacements between glass pane and framing along the bottom edge for specimens Type 1A (left) and Type 2A (right) under out-of-plane surface loading*

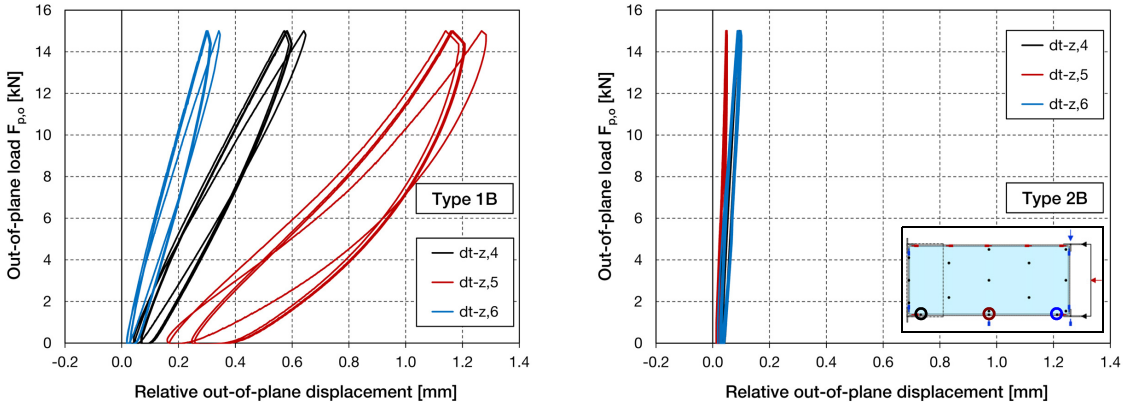

Fig. 6.28 *Relative out-of-plane displacements between glass pane and framing along the bottom edge for specimens Type 1B (left) and Type 2B (right) under out-of-plane surface loading*

In-plane shear loading

Under in-plane shear loading, cycles with three different loading speeds are performed: one cycle with a low loading speed of *2 mm/min*, three cycles with *10 mm/min* and ten cycles with a high loading speed of *50 mm/min*. These cycles are illustrated in Fig. 6.29 for specimen *Type 1A* as load-time diagrams for loading up to *10 kN* (series no. 03), up to *20 kN* (series no. 09) and up to *30 kN* (series no. 14). The cycles with high loading speed are added to observe if an eventual plastic deformation in the load transfer materials is increasing with additional loading cycles. However, since no plastic deformations are noticed for the used load levels, these cycles are not included in the further diagrams of this section.

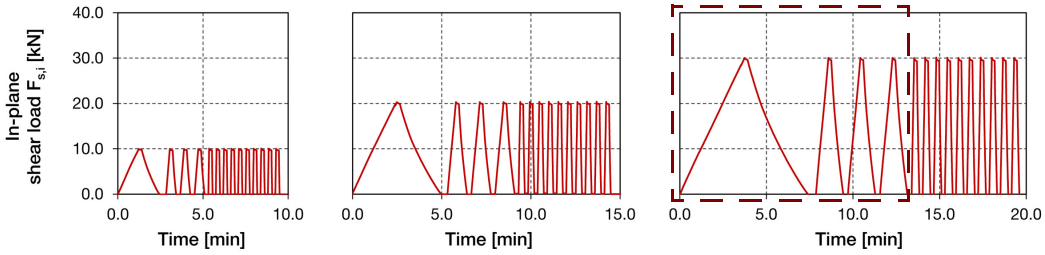

Fig. 6.29 *Load-time diagrams of the performed cycles for in-plane shear loading (Type 1A)*

The out-of-plane displacements along the compressed diagonal of the glass pane (see Fig. 6.30 and Fig. 6.31) show different characteristics for the specimens of *Type 1* and those of Type 2. For the specimens with silicone adhesive and grouting blocks, the displacements measured in the quarter points ($DT_{z,7}$ for both *Type 1A* and *Type 1B* and $DT_{z,4}$ for *Type 1A*) indicate the start of plate buckling. In the case of the specimens with acrylic adhesive only small displacements occur in the range of the values obtained under in-plane axial compressive loading.

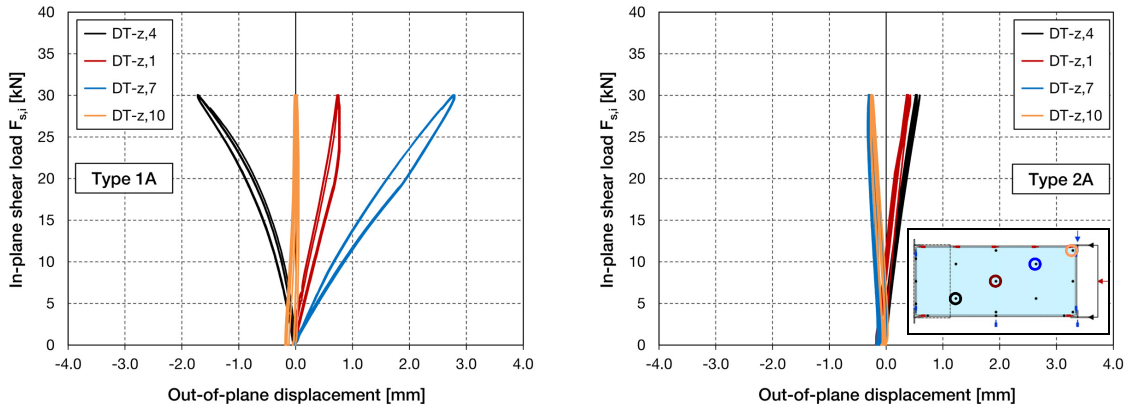

Fig. 6.30 *Out-of-plane displacements of the monolithic glass pane along the compressed diagonal for specimens Type 1A (left) and Type 2A (right) under in-plane shear loading*

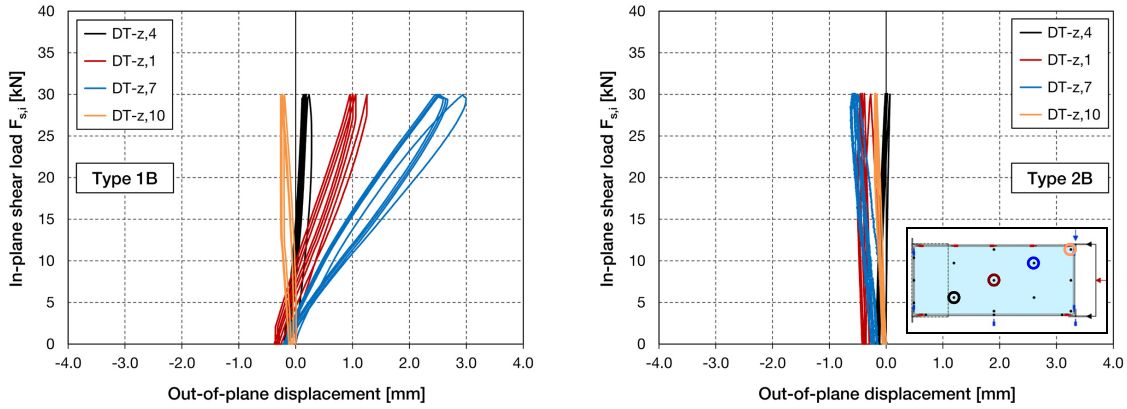

Fig. 6.31 *Out-of-plane displacements of the laminated glass pane along the compressed diagonal for specimens Type 1B (left) and Type 2B (right) under in-plane shear loading*

The global in-plane displacements measured on the bottom edge element, which are plotted in Fig. 6.32 for specimens *Type 1A* and *Type 2A* and in Fig. 6.33 for specimens *Type 1B* and *Type 2B*, show a good agreement between the values measured near the glass pane ($DT_{y,1}$ and $DT_{y,3}$) and those measured near the other edge of the L-shaped profiles ($DT_{y,2}$ and $DT_{y,4}$). This consistency indicates that, in contrast to the case of an out-of-plane surface loading, no rotation results in the edge elements for in-plane shear loads up to *30 kN*.

By comparing the specimens with silicone adhesive and grouting blocks to those with acrylic adhesive, it can be observed that for the same load size significantly lower in-plane displacements are obtained with specimens of *Type 2*. This higher system stiffness is also an evidence of better composite structural behaviour of the specimens with acrylic adhesive for this load level.

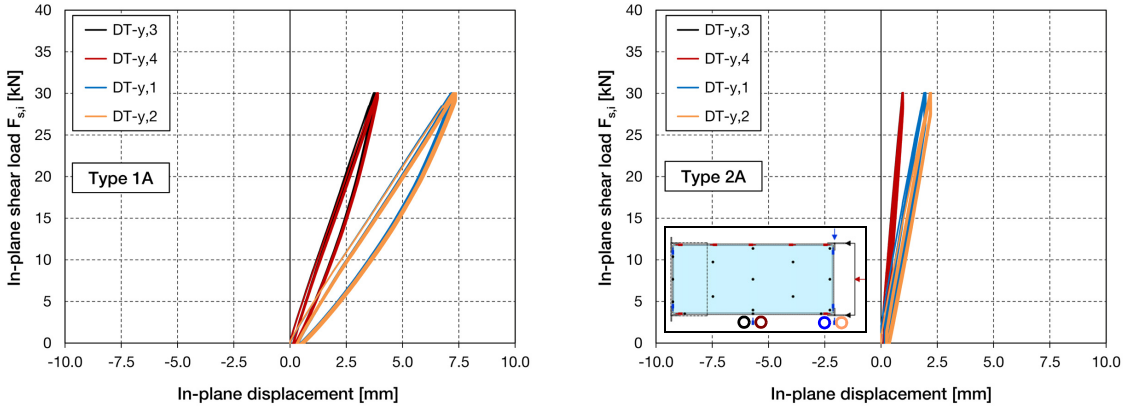

Fig. 6.32 *In-plane displacements of the bottom frame profile in the middle and at the end of the element for specimens Type 1A (left) and Type 2A (right) under in-plane shear loading*

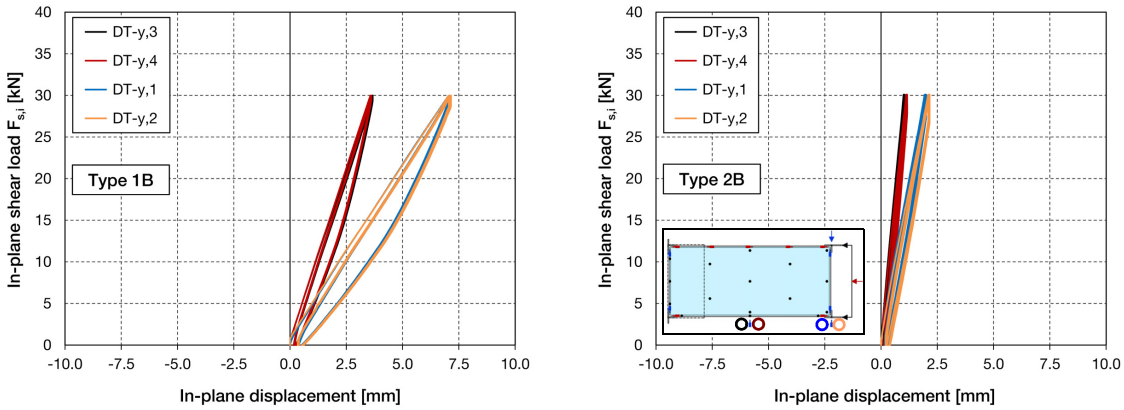

Fig. 6.33 *In-plane displacements of the bottom frame profile in the middle and at the end of the element for specimens Type 1B (left) and Type 2B (right) under in-plane shear loading*

The different system stiffness obtained with the two investigated concepts is reflected as well in the relative in-plane displacements between the glass pane and the metal framing. The diagrams in Fig. 6.34 and Fig. 6.35 show the relative displacements in longitudinal direction (x-

direction according to Fig. 6.15) measured in the four corners of the different specimens. For the relative displacements in y-direction lower values are measured in all testing series and therefore only the displacements in x-direction are discussed.

In the case of the specimens of *Type 1* the grouting blocks can only transfer compressive loads, while under tensile loading gaps result between glass pane and framing. This can be observed in the left diagrams from Fig. 6.34 and Fig. 6.35, where the transducers in the compressed corners ($dt_{x,1}$ and $dt_{x,4}$) measure lower displacements than the transducers in the corners under tension ($dt_{x,2}$ and $dt_{x,3}$). The shear loads which can be transferred by the silicone are rather low. This is different in the case of the specimens with acrylic adhesive, which has a higher shear strength. The relative in-plane displacements are in the same size range in all four corners and reach lower values than in the case of the specimens with silicone adhesive and grouting blocks.

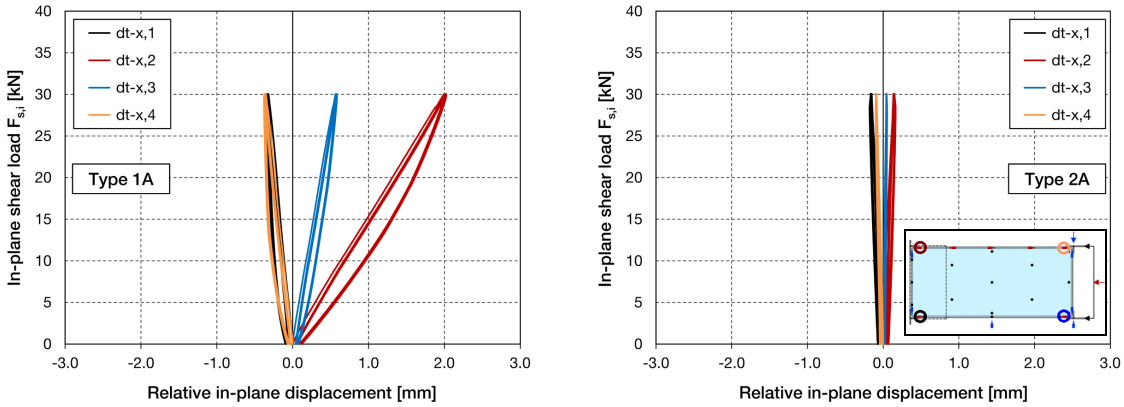

Fig. 6.34 *Relative in-plane displacements between glass pane and framing in the four corners in x-direction for specimens Type 1A (left) and Type 2A (right) under in-plane shear loading*

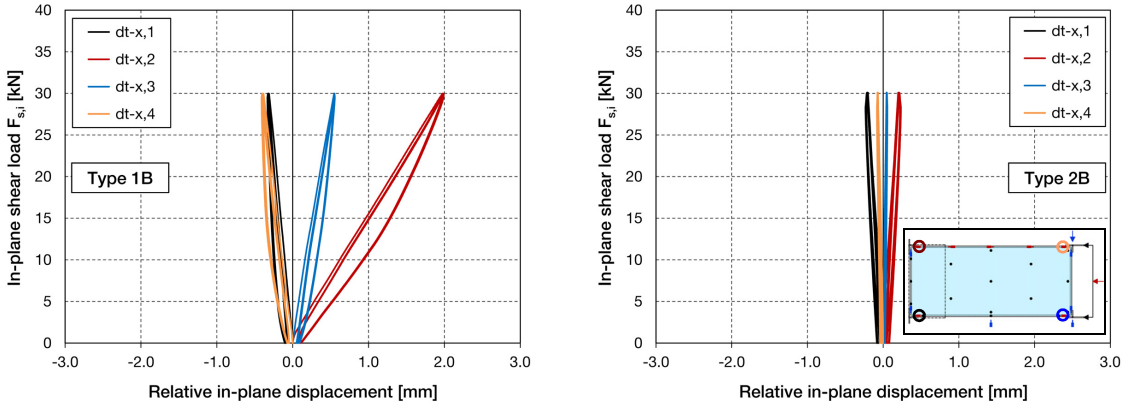

Fig. 6.35 *Relative in-plane displacements between glass pane and framing in the four corners in x-direction for specimens Type 1B (left) and Type 2B (right) under in-plane shear loading*

6.3.3 Test results from series with two combined load directions

For the series in which the in-plane shear load is combined either with an in-plane axial loading or with the out-of-plane surface loading the same type of diagrams showing absolute or relative displacements are used for the evaluation. The displacement values are plotted versus the in-plane shear load, since this is considered the load of primary interest. However, since the series with a single applied load show that there is no other significant difference between the results for specimens with monolithic glass panes and those with laminated glass panes than the influence coming from the viscous interlayer material, only the results for the second category (*Type 1B* and *Type 2B*) are plotted in the diagrams from this subchapter. The corresponding diagrams for the specimens *Type 1A* and *Type 2A* are provided in [Appendix E]. Furthermore only the results from the cycles with in-plane shear loads increased up to *30 kN*, which are marked with a dashed rectangle in Fig. 6.36, Fig. 6.40 and Fig. 6.44, are plotted in the diagrams.

Combined in-plane compressive axial loading and in-plane shear loading

The loading procedure for the series with combined in-plane compressive axial loading and in-plane shear loading is shown in Fig. 6.36. The compressive axial load is applied and then kept constant while three cycles are performed with the in-plane shear load. It can be noticed that the increase of the in-plane compressive axial load already leads to a small shear load measured by the hydraulic jack which is in contact with the specimen from the start of the series.

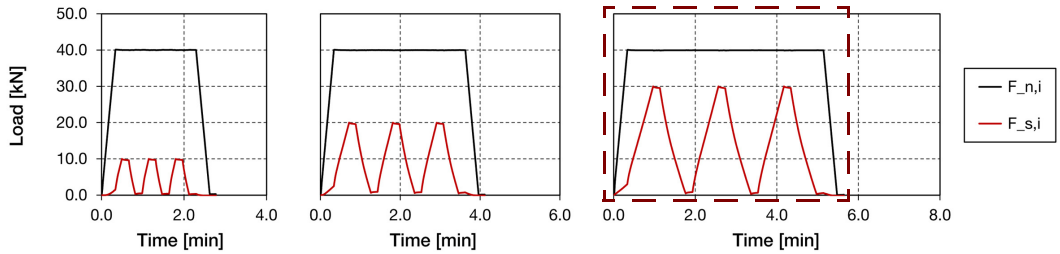

Fig. 6.36 *Load-time diagram of the performed cycles for series with combined in-plane compressive axial loading and in-plane shear loading (Type 1B)*

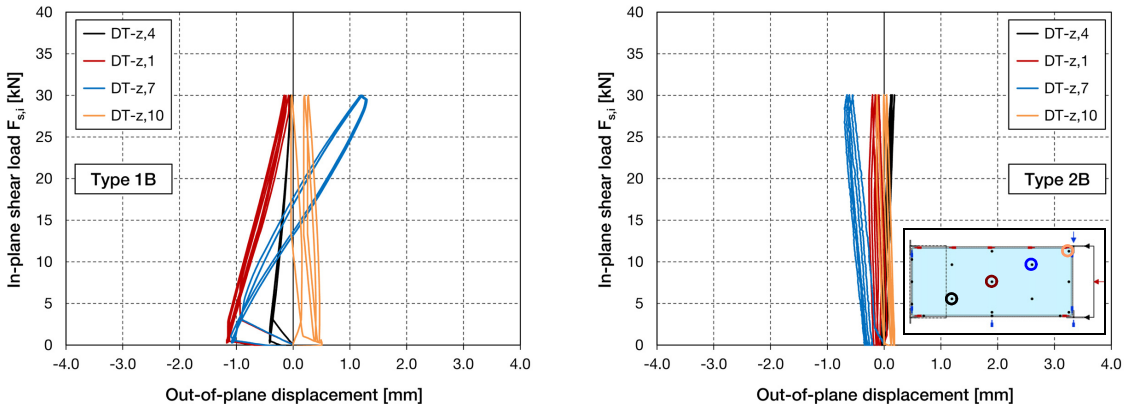

Fig. 6.37 *Out-of-plane displacements of the laminated glass pane along the compressed diagonal for specimens Type 1B (left) and Type 2B (right) under combined in-plane compressive axial loading and in-plane shear loading*

The resulting out-of-plane displacements along the compressed diagonal of the glass pane, which are plotted in Fig. 6.37 for specimens *Type 1B* and *Type 2B*, can be interpreted as a combination of the results from the single load series with in-plane compressive axial loading and with in-plane shear loading. This can be best recognized in the displacements measured by $DT_{z,1}$ and $DT_{z,7}$ for specimen *Type 1B* where first the glass pane slightly deforms to the interior due to the compressive axial load and then starts to deform to the exterior whilst the shear load is increased.

For specimens of *Type 1* and the used load application concept it can be generally concluded that an additional in-plane compressive axial load slightly reduces the occurring displacements. This is valid for the absolute out-of-plane displacements in Fig. 6.37 and the absolute in-plane displacements in Fig. 6.38 as well as for the relative in-plane displacements in Fig. 6.39. The same conclusion can be drawn for the specimens of *Type 2*, although this is not as easily to notice from the diagrams because of the generally lower resulting displacements.

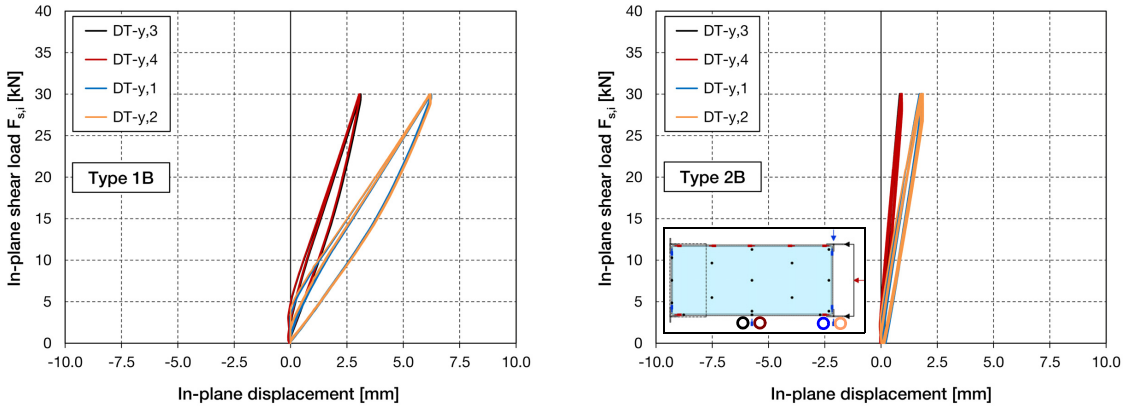

Fig. 6.38 *In-plane displacements of the bottom frame profile in the middle and at the end of the element for specimens Type 1B (left) and Type 2B (right) under combined in-plane compressive axial loading and in-plane shear loading*

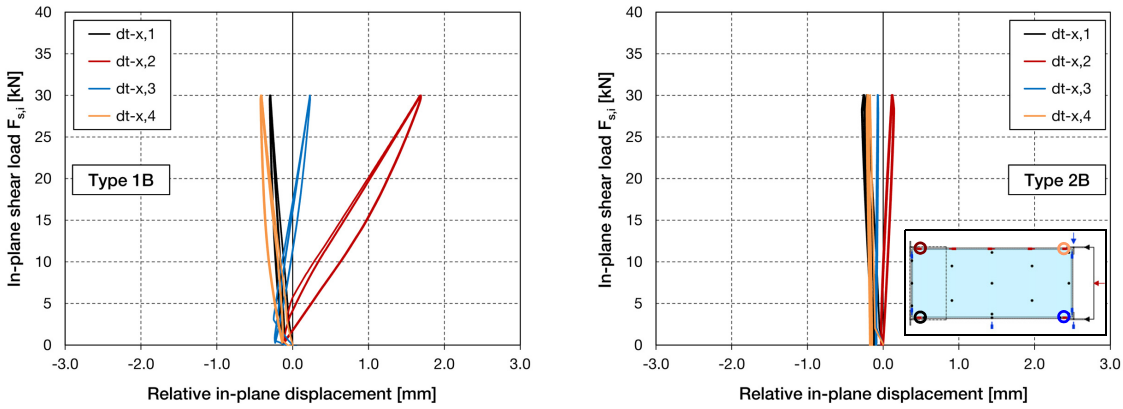

Fig. 6.39 *Relative in-plane displacements between glass pane and framing in the four corners in x-direction for specimens Type 1B (left) and Type 2B (right) under combined in-plane compressive axial loading and in-plane shear loading*

Combined in-plane tensile axial loading and in-plane shear loading

The same loading procedure is used for the series with combined in-plane tensile axial loading ($F_{n,i}$) and in-plane shear loading ($F_{s,i}$). As illustrated in Fig. 6.40, the tensile axial load (plotted in negative y-direction) is applied first and then kept constant while three cycles are performed with the in-plane shear load.

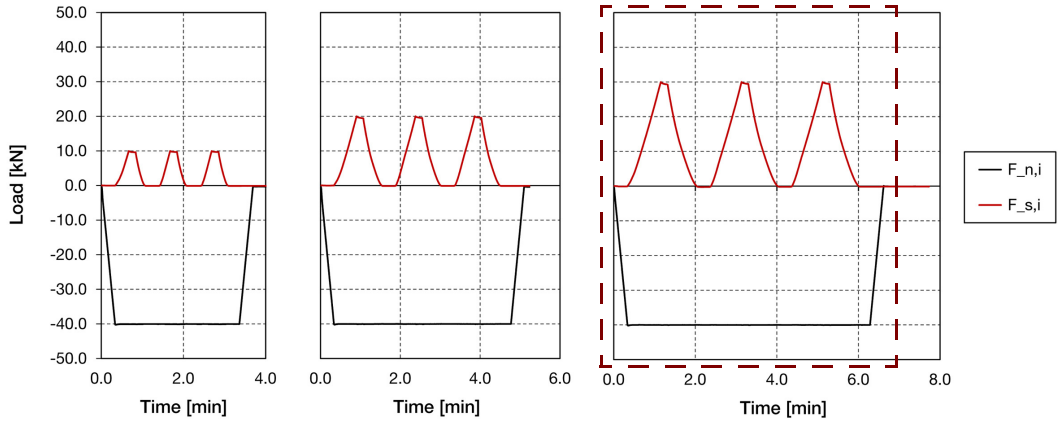

Fig. 6.40 *Load-time diagram of the performed cycles for series with combined in-plane tensile axial loading and in-plane shear loading (Type 1B)*

Opposite to the case of a combination with an in-plane compressive axial load, it can be observed from the diagrams in Fig. 6.41, Fig. 6.42 and Fig. 6.43 (especially for specimen *Type 1B* in the left diagrams) that an additional in-plane tensile axial load generally slightly increases the occurring displacements resulting from an in-plane shear loading alone. For the out-of-plane displacements measured in the middle ($DT_{z,1}$) and in the quarter points ($DT_{z,4}$ and $DT_{z,7}$) of the compressed diagonal (see Fig. 6.41 left for specimen *Type 1B*) it can be noticed that the glass pane deforms to the exterior both due to the in-plane tensile axial load and due to the in-plane shear load (a positive displacement value means that the needle of the transducer is pressed in).

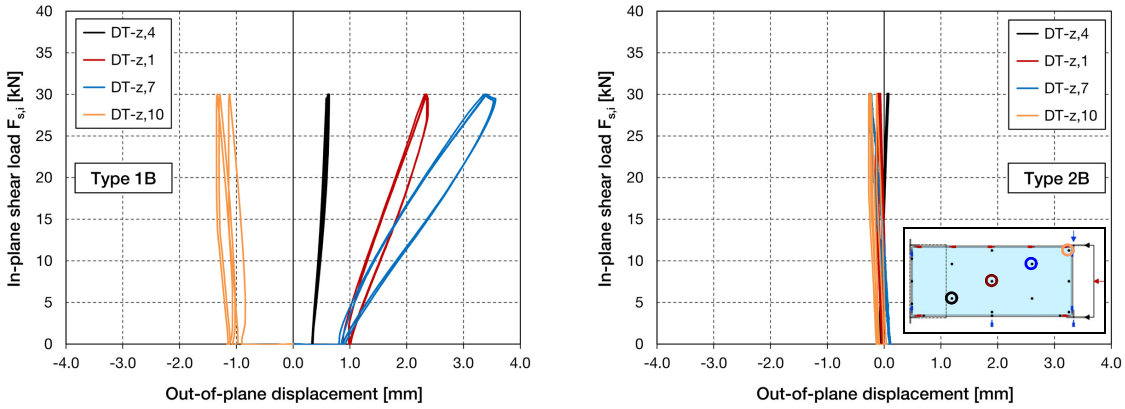

Fig. 6.41 *Out-of-plane displacements of the laminated glass pane along the compressed diagonal for specimens Type 1B (left) and Type 2B (right) under combined in-plane tensile axial loading and in-plane shear loading*

All the displacements in the case of specimen *Type 2B* are again significantly smaller in comparison to specimen *Type 1B*. The equal range chosen for the displacement axis in the diagrams makes it difficult to recognize the influence of the additional in-plane tensile axial load. However, this also shows that the applied axial loads of *40 kN*, both in tension and compression, have a small influence on the deformation behaviour of the glass-metal elements with acrylic adhesive.

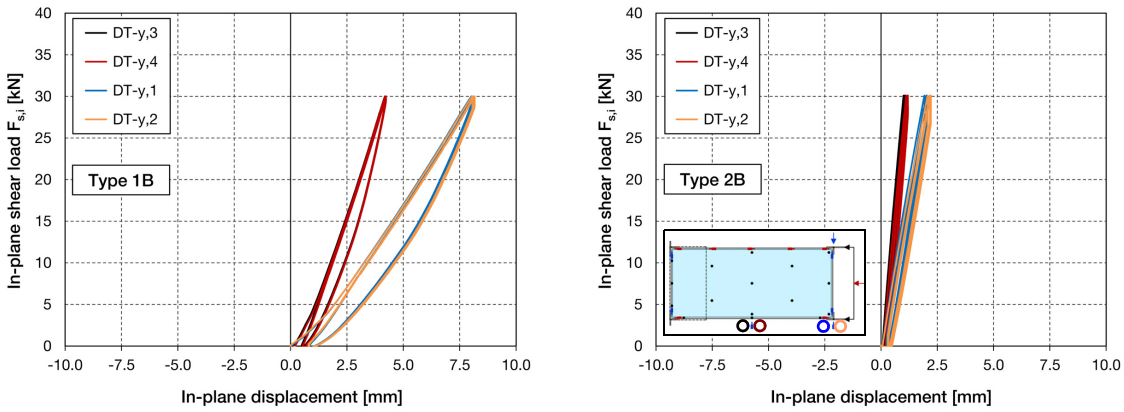

Fig. 6.42 *In-plane displacements of the bottom frame profile in the middle and at the end of the element for specimens Type 1B (left) and Type 2B (right) under combined in-plane tensile axial loading and in-plane shear loading*

In the case of the relative in-plane displacements for specimens of *Type 1* measured in x-direction (see Fig. 6.43, left) the in-plane tensile axial loading causes a gap opening between the glass panes and the grouting blocks in all four corners. These gaps are then increased by the in-plane shear load in the top left corner ($dt_{x,2}$) and in the bottom right corner ($dt_{x,3}$). In the case of specimens of *Type 2* the in-plane relative displacements due to the tensile axial load are smaller because of the higher shear strength of the acrylic compared to the silicone.

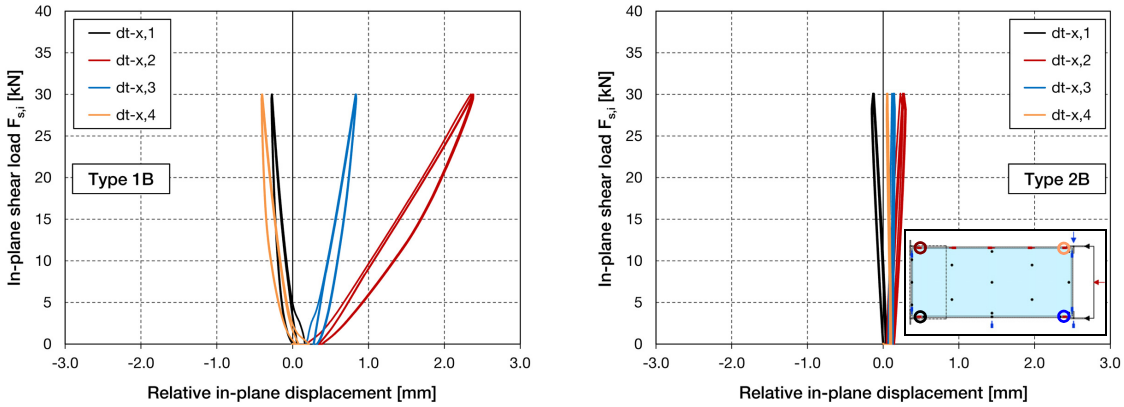

Fig. 6.43 *Relative in-plane displacements between glass pane and framing in the four corners in x-direction for specimens Type 1B (left) and Type 2B (right) under combined in-plane tensile axial loading and in-plane shear loading*

Combined out-of-plane surface loading and in-plane shear loading

For the series with combined out-of-plane surface loading ($F_{p,o}$) and in-plane shear loading ($F_{s,i}$), an out-of-plane load of *10 kN* is first applied and then three cycles are performed with the shear load (see diagrams in Fig. 6.44) up to *10 kN* (series no. 06), up to *20 kN* (series no. 12) and up to *30 kN* (series no. 17). The maximum value of *15 kN* applied in the series with out-of-plane loading alone is considered a rather extreme case and therefore the lower value of *10 kN* is used for these series. This should be considered for comparison with the results from the series with out-of-plane loading alone.

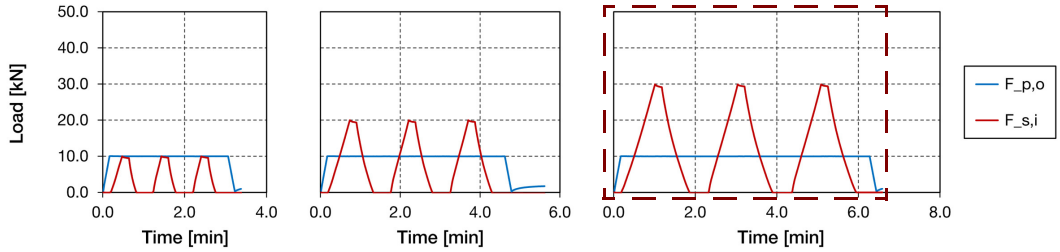

Fig. 6.44 *Load-time diagrams of the performed cycles for series with combined out-of-plane surface loading and in-plane shear loading (Type 1B)*

The absolute out-of-plane displacements along the compressed diagonal of the glass pane, which are plotted in Fig. 6.45, show for both specimen types that the larger share results from the out-of-plane loading. Even though for the applied shear load levels in these series this cannot be observed, it is expected that an additional out-of-plane load leads to an earlier plate buckling due to in-plane shear loading. This is investigated in subchapter 7.4 by finite element simulations.

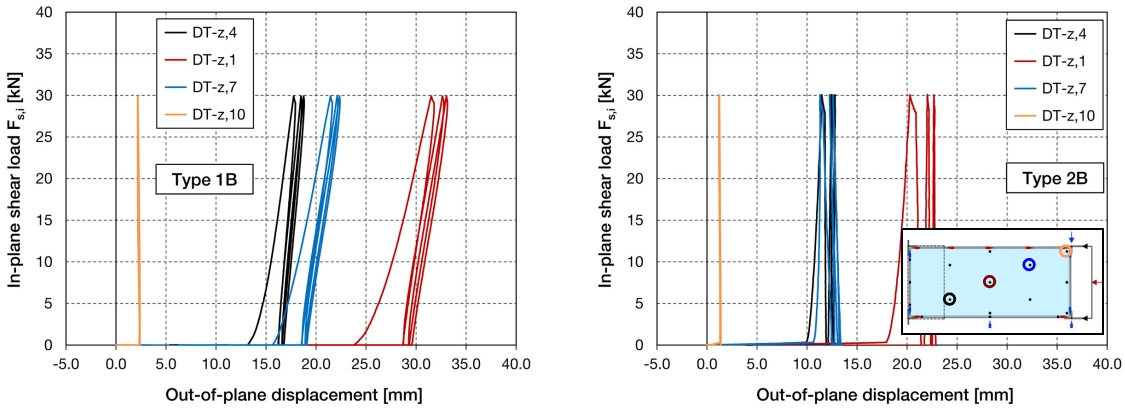

Fig. 6.45 *Out-of-plane displacements of the laminated glass pane along the compressed diagonal for specimens Type 1B (left) and Type 2B (right) under combined out-of-plane surface loading and in-plane shear loading*

The absolute in-plane displacements in the middle of the elements are smaller in the case of the additional out-of-plane surface loading compared to the case of shear loading alone (compare Fig. 6.46 to Fig. 6.33). In the case of the values measured with the transducer positioned away from the glass pane ($DT_{y,4}$) for specimen *Type 2B*, the displacement induced by the out-of-plane

loading towards the centre of the glass pane is even larger than the displacement resulting from the in-plane shear loading in the opposite direction. The in-plane displacements at the free end of the elements ($DT_{y,1}$ and $DT_{y,2}$) are slightly higher due to the additional out-of-plane loading in the case of specimen *Type 1B*, while for specimen *Type 2B* no significant difference can be noticed.

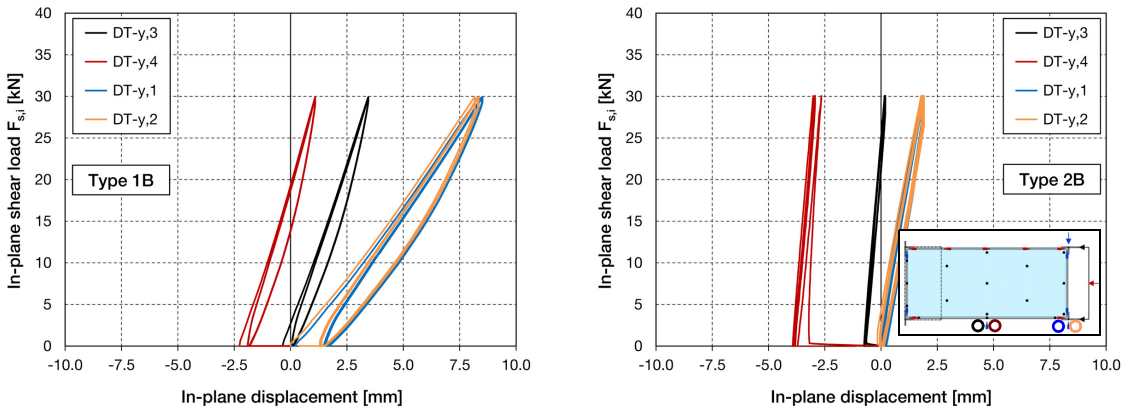

Fig. 6.46 *In-plane displacements of the bottom frame profile in the middle and at the end of the element for specimens Type 1B (left) and Type 2B (right) under combined out-of-plane surface loading and in-plane shear loading*

The relative out-of-plane displacements between the glass pane and the framing plotted in Fig. 6.47 are mainly the result of the out-of-plane loading, especially in the case of specimens of *Type 2* where the stiffer acrylic only allows a small deformation. The difference in relative out-of-plane deformations in the middle of the elements ($dt_{z,5}$) between the two specimen types correlates with the difference in rotation of the bottom edge elements indicated by the absolute in-plane displacements measured with the transducers $DT_{y,3}$ and $DT_{y,4}$.

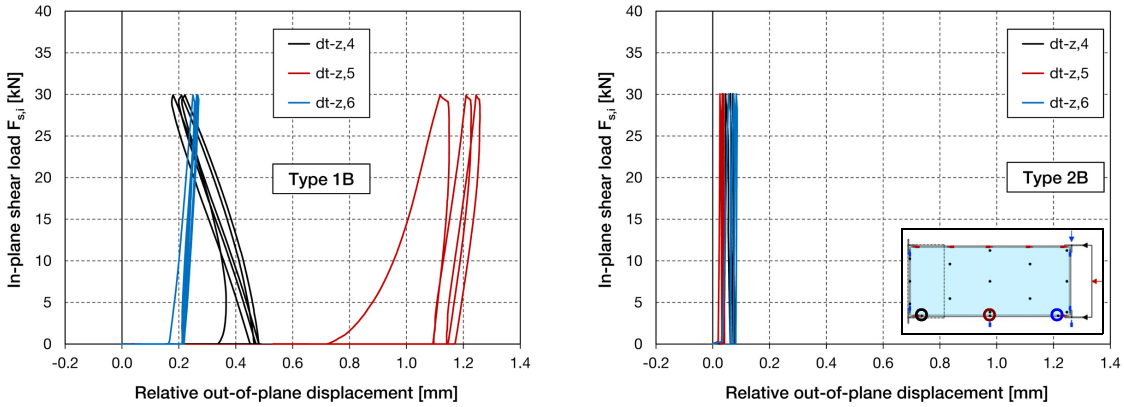

Fig. 6.47 *Relative out-of-plane displacements between glass pane and framing along the bottom edge for specimens Type 1B (left) and Type 2B (right) under combined out-of-plane surface loading and in-plane shear loading*

On the relative in-plane displacements between the glass pane and the metal framing measured in the four corners in x-direction there is almost no influence of the additional out-of-plane loading for the specimens of *Type 2* (compare right diagrams in Fig. 6.48 and Fig. 6.35). For the

specimens of *Type 1*, the relative displacements measured in the top left corner and in the bottom right corner are larger than in the case of shear loading alone. These are the two corners in which gaps result between glass pane and grouting blocks due to shear loading.

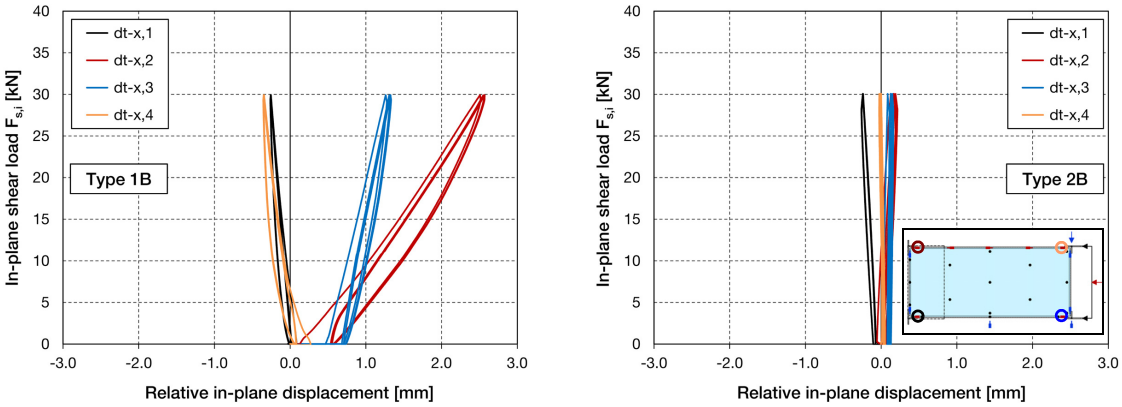

Fig. 6.48 *Relative in-plane displacements between glass pane and framing in the four corners in x-direction for specimens Type 1B (left) and Type 2B (right) under combined out-of-plane surface loading and in-plane shear loading*

6.3.4 Test results from series with three combined load directions

After discussing the mechanical results for the glass-metal elements with composite structural behaviour under a single loading direction at a time and under in-plane shear loading combined with a second loading direction in the previous two subchapters, in this subchapter the results for the series with all three loads acting on the specimens are analysed. The loading procedure with the in-plane compressive axial load applied first, followed by a simultaneous loading with the out-of-plane surface load and the in-plane shear load as well as the three cycles carried out with the shear load is illustrated in Fig. 6.49. As in the case of the series with two combined load directions only the displacements for specimens *Type 1B* and *Type 2B* are discussed in this chapter. The corresponding diagrams for specimens *Type 1A* and *Type 2A* can be found in [Appendix E].

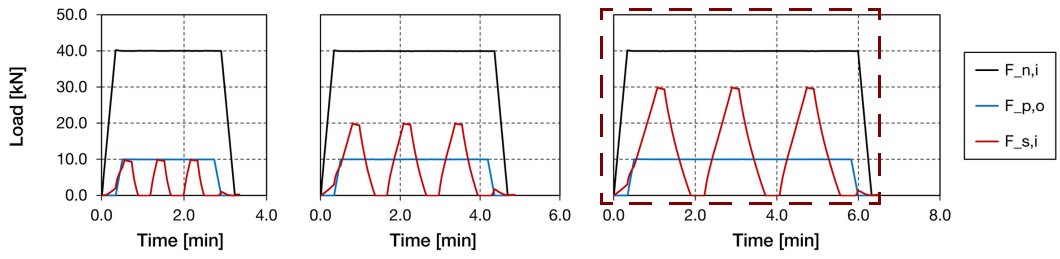

Fig. 6.49 *Load-time diagram of the performed cycles for series with combined in-plane compressive axial loading, out-of-plane surface loading and in-plane shear loading (Type 1B)*

The absolute out-of-plane displacements which are measured along the compressed diagonal of the glass pane under the three combined loads are illustrated by the diagrams in Fig. 6.50. The maximum reached values diverge only little from the values obtained under combined in-

plane shear loading and out-of-plane surface loading. This emphasises once again the small influence of the applied in-plane compressive axial load of *40 kN* on the deformation behaviour of the glass panes for the investigated test specimens. However, the loading path during the first cycle with the in-plane shear load for this series differs. Firstly, a load is measured with the load cell for the in-plane shear load already during the application of the in-plane compressive axial load, since the hydraulic jack for the shear load is in contact with the specimen from the start of the series. Secondly, the in-plane shear load increases simultaneously with the out-of-plane surface load and the displacements generated by this one.

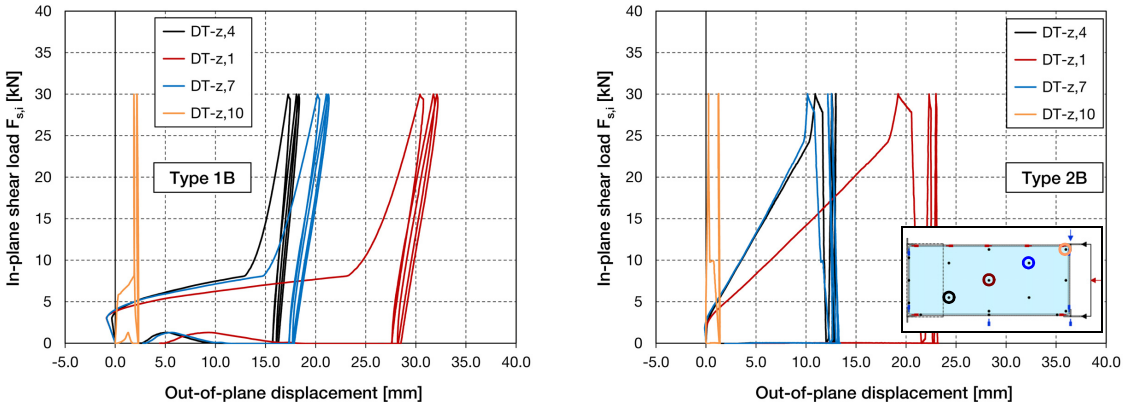

Fig. 6.50 *Out-of-plane displacements of the laminated glass pane along the compressed diagonal for specimens Type 1B (left) and Type 2B (right) under combined in-plane compressive axial loading, out-of-plane surface loading and in-plane shear loading*

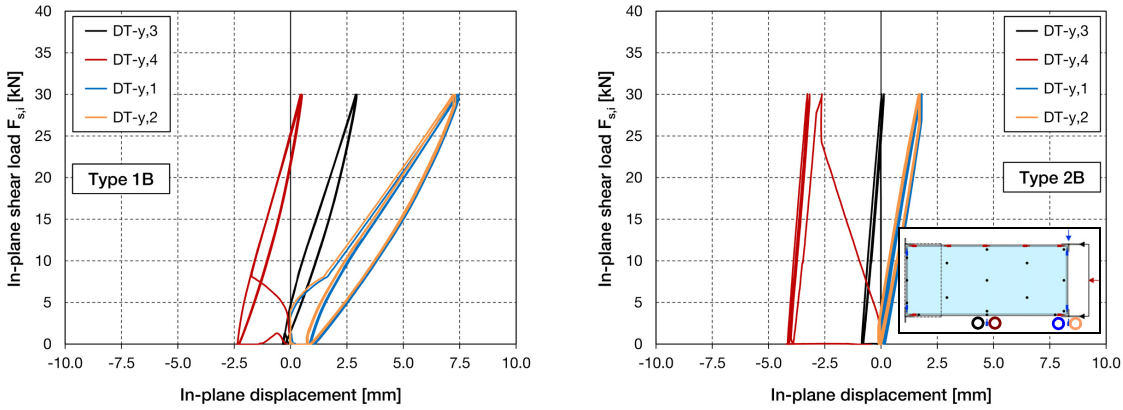

Fig. 6.51 *In-plane displacements of the bottom frame profile in the middle and at the end of the element for specimens Type 1B (left) and Type 2B (right) under combined in-plane compressive axial loading, out-of-plane surface loading and in-plane shear loading*

Similar observations can be made also for the measured absolute in-plane displacements plotted in Fig. 6.51. However, in the case of the specimen *Type 1B* the maximum displacement values are slightly lower than those measured in the series without in-plane compressive axial loading. This additional load increases the resistance of the glass-metal elements against in-plane deformations due to shear loading. A small reduction of the measured values under loading by all three hydraulic jacks compared to the series with loading only with the out-of-plane

surface load and the in-plane shear load can also be observed for specimen *Type 1B*, both in the case of the relative out-of-plane displacements plotted in Fig. 6.52, left, and in the case of the relative in-plane displacements plotted in Fig. 6.53, left. Also the characteristics concerning the development of the loading path are in good agreement with the description made for the absolute out-of-plane displacements.

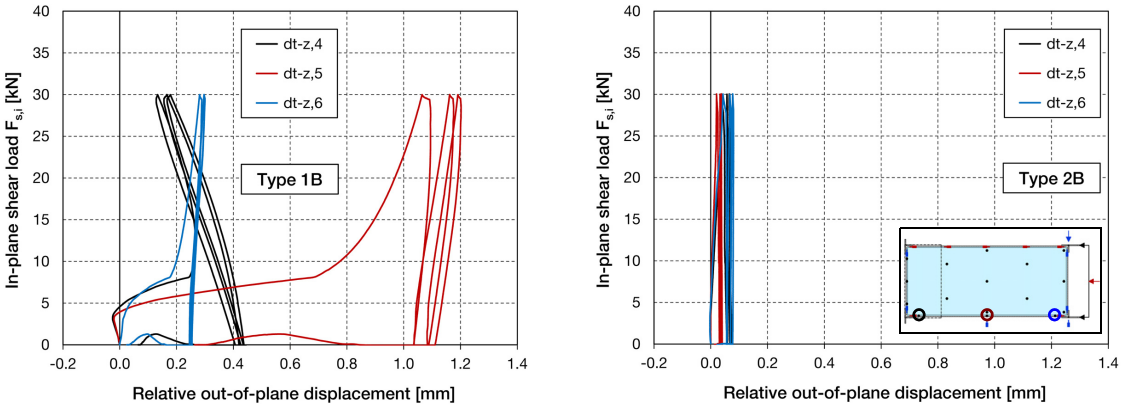

Fig. 6.52 *Relative out-of-plane displacements between glass pane and framing along the bottom edge for specimens Type 1B (left) and Type 2B (right) under combined in-plane compressive axial loading, out-of-plane surface loading and in-plane shear loading*

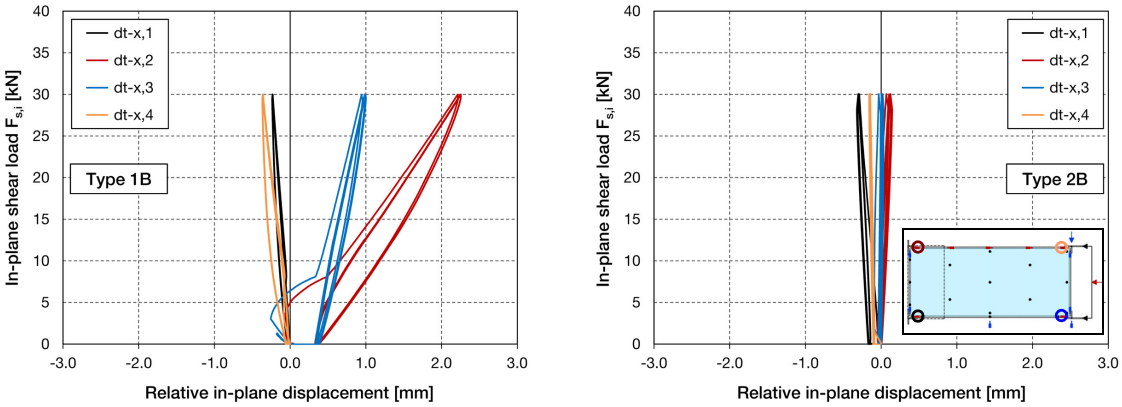

Fig. 6.53 *Relative in-plane displacements between glass pane and framing in the four corners in x-direction for specimens Type 1B (left) and Type 2B (right) under combined in-plane compressive axial loading, out-of-plane surface loading and in-plane shear loading*

The smaller absolute displacements measured for specimens of *Type 2* compared to specimens of *Type 1*, especially the in-plane displacements, are advantageous for the use of the glass-metal elements with composite structural behaviour as bracing elements. However, the higher flexibility suggested by the larger relative out-of-plane and especially in-plane displacements in the case of the specimens of *Type 1* is to rate positively concerning the temperature loads acting on facades.

6.3.5 Failure test results for the specimen with silicone adhesive bonding

After completing the series with combinations of the three loads increased up to predefined values, the specimens with laminated glass panes are tested until failure by increasing displacement-controlled the in-plane shear load. The results for the specimen with silicone adhesive bonding and grouting blocks in the corners (*Type 1B*) are discussed in this subchapter, while the findings from the series on the specimen with acrylic adhesive (*Type 2B*) are evaluated in subchapter 6.3.6. For specimen *Type 1B* a loading speed of *2 mm/min* is used. The test specimen is shown in Fig. 6.54 unloaded (left), loaded shortly before failure (middle) and immediately after failure (right). By comparing the reflection in the first two pictures, distortions can be observed in the loaded state which indicate the occurring plate buckling.

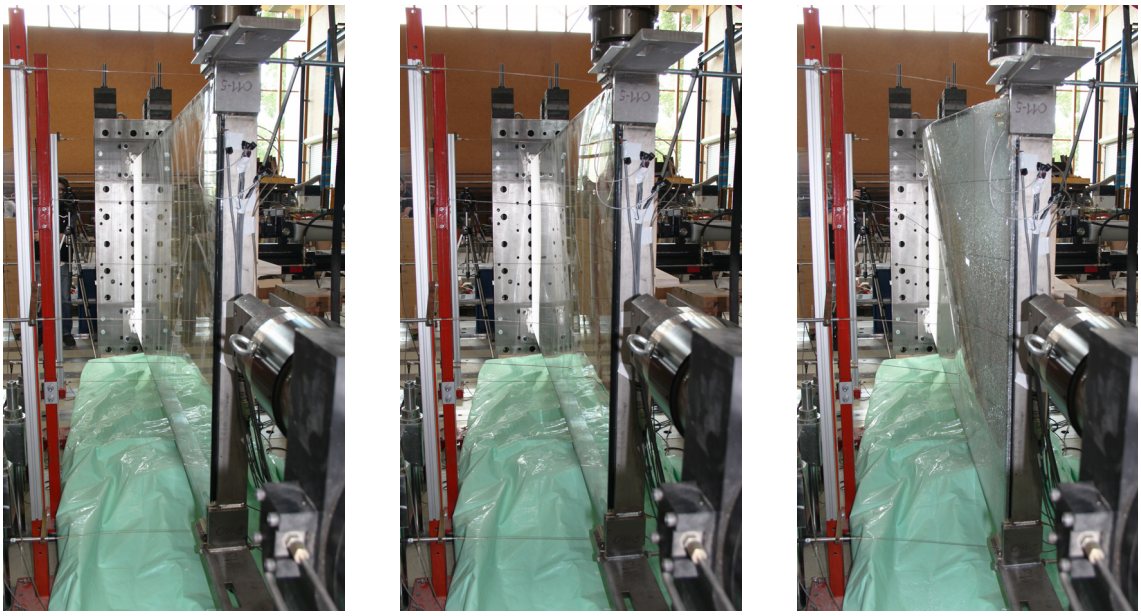

Fig. 6.54 *Test specimen Type 1B unloaded, loaded shortly before failure and after failure (from left to right)*

The failure is recorded at a load of approximately *93 kN* and results first by cracks in the silicone adhesive along the top edge followed immediately by a glass failure near the corner on which the load is applied. By watching the video recording of the test it is noticed that the crack in the adhesive initiates approximately in the centre of the top edge and then propagates towards the loaded corner. In the moment the crack reaches the corner, the glass receives a shock, probably hits the bracket for grouting block enclosure and glass breakage results. After failure the system gets significantly softer, which can be recognized by the way it is hanging under its dead weight in the pictures from Fig. 6.55. Without the intact glass pane activated as a shear panel the filigree metal framing has a low in-plane stiffness despite its rigid corners and is subjected to bending around the weak axis of the used L-shaped edge elements.

The relative in-plane displacements between the glass pane and the metal framing are visible with the naked eye in the top left corner. Due to the occurring tensile stresses and the incapability of the used grouting blocks to transfer them, gaps are resulting between the glass pane edge and the grouting. The gap in x-direction reaches values of several millimetres and is illustrated in

Fig. 6.56, left. At the moment of glass failure the adhesive joint along the top edge element is cracked over almost its entire length (see Fig. 6.56, middle). The failure pattern is entirely cohesive, showing a good agreement with the results from the experimental investigations on metal-metal and glass-metal connections discussed in subchapters 4.4 and 5.2.

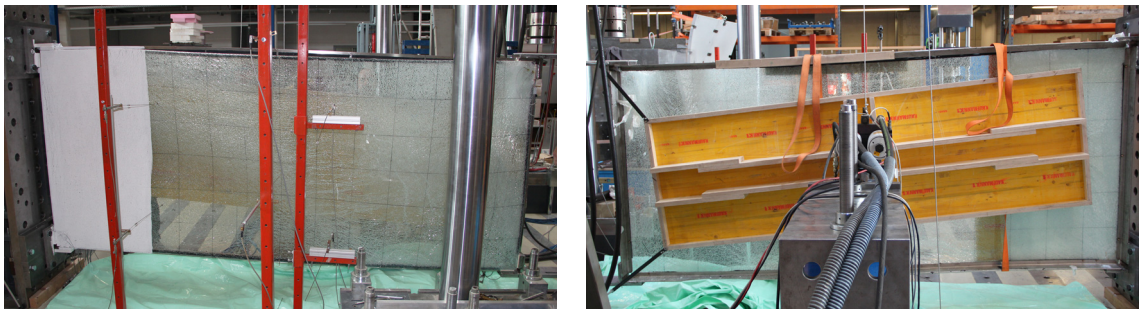

Fig. 6.55 *Front view (left) and rear view (right) of the test specimen Type 1B after failure*

The crack in the glass pane is initiated near the top right corner in which the in-plane shear load is applied. The crack pattern on the glass pane indicates the stress development across the surface by noticeable trajectories. Compressive stress trajectories spread slightly non-linear from the glass edge areas where loads are introduced by the grouting blocks towards the diagonally opposite corner (indicated with blue coloured curves in Fig. 6.56, right). Approximately perpendicular to the compressive trajectories, tensile trajectories can be noticed (indicated with red coloured curves in Fig. 6.56, right).

Fig. 6.56 *Detailed views of gap between glass pane and framing in the top left corner (left), crack pattern in the adhesive (middle) and crack initiation point of the glass pane (right)*

Similar diagrams as in the case of the series with single and combined loading up to predefined load values are used for evaluating the performance of the specimens loaded to failure. In Fig. 6.57 the out-of-plane displacements of the glass pane are shown for specimen *Type 1B* along the compressed diagonal (left) and along the tensioned diagonal (right). The displacements measured in the midpoint ($DT_{z,1}$) and in the left quarter points ($DT_{z,4}$ and $DT_{z,5}$) of the diagonals increase to the exterior up to a load of around *30* to *40 kN* and then change direction and start to increase faster in the opposite direction. Also at around *30 kN* the displacements measured in the right quarter points ($DT_{z,7}$ and $DT_{z,8}$) start to increase faster towards the exterior. By „exterior“ the direction away from the metal framing is meant, which in the case of using this structural concept in transparent facades would be the exterior of the building and implicitly of the elements. This behaviour indicates the start of plate buckling. At a load of approximately *70 kN*

the displacement curves in both quarter points on the compressed diagonal as well as the displacement curve in the right quarter point on the tensioned diagonal change again their direction indicating a stability problem. The maximum measured displacement in the centre of the glass pane of around *14 mm* is approximately half of the displacement resulting from a surface load of around *2 kPa* (corresponds to the applied out-of-plane load of *10 kN*).

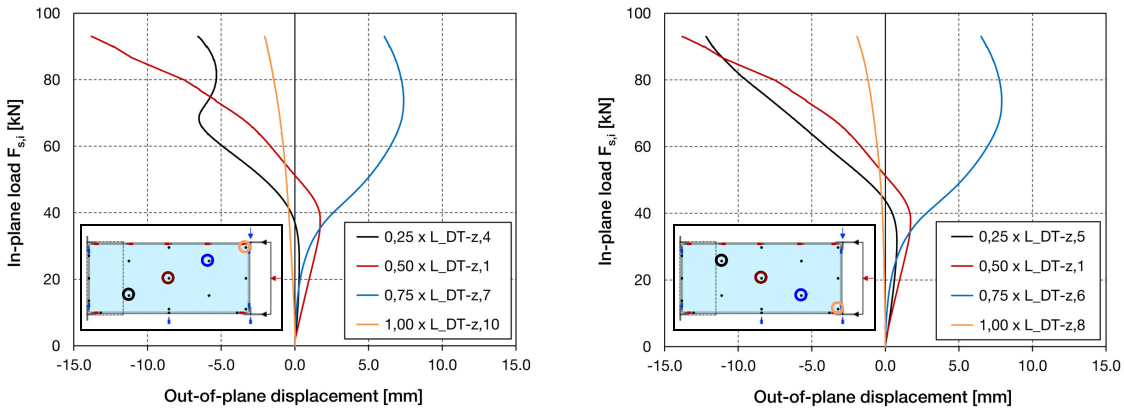

Fig. 6.57 *Out-of-plane displacements of the glass pane for specimen Type 1B along the compressed diagonal (left) and along the tensioned diagonal (right)*

The shape development of the glass pane while increasing the in-plane shear load is illustrated by the plots in Fig. 6.58. These show the out-of-plane deformation of the glass pane along the compressed diagonal (left) and the tensioned diagonal (right) as interpolated curves based on the displacements measured with the transducers at different load levels. These curves are only an approximation. For an exact representation more measurement points are required.

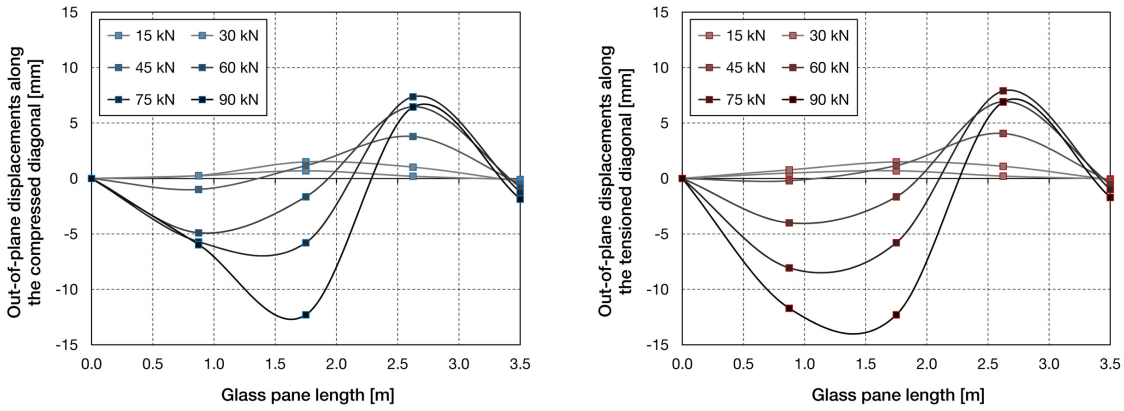

Fig. 6.58 *Out-of-plane displacements of the glass pane along the compressed diagonal (left) and along the tensioned diagonal (right) for specimen Type 1B at different load levels*

The area for DIC measurement is chosen at the fixed end of the specimen extending over a width of only around *75 cm*. The scope of this measurement is to obtain surface information about the occurring displacements. The pilot test shows that a recording of the whole glass surface is not efficient due to the resolution of the used DIC measurement system as well as due to the challenge of uniform light exposure. For the chosen area, the measured out-of-plane dis-

placements of the glass pane shown in Fig. 6.59 reveal that by just interpolating the values obtained with the displacement transducers in the midpoint and in the quarter points of the diagonals, local effects can be overlooked. An example is the bulge occurring between the bottom left corner and the left quarter point on the compressed diagonal which is not visible in the diagrams from Fig. 6.58. As an assumption, positive values are displacements towards the exterior and negative values displacements towards the interior of the elements (of the facade).

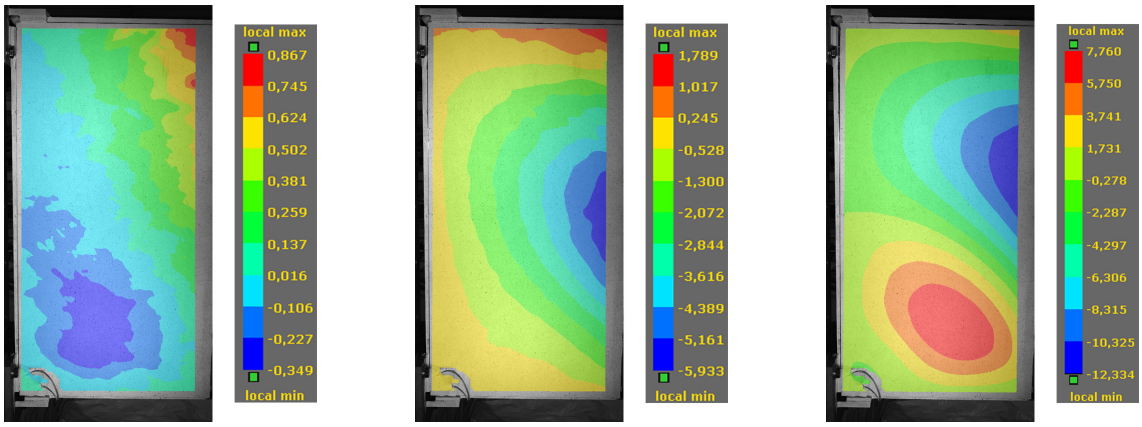

Fig. 6.59 *Absolute out-of-plane displacements [mm] of the glass pane at 30 kN, 60 kN and 90 kN (from left to right) obtained with the DIC measurement system for specimen Type 1B*

For the large area chosen to be recorded with the DIC measurement system and with the given dot pattern and exposure, it is not possible to obtain from the measurement data feasible surface results in the areas near the glass edges. Such results would be interesting for illustrating the relative in-plane displacements between the glass pane and the metal framing. However, these displacements can be evaluated in selected single points offering similar results to standard displacement transducers. The in-plane relative displacements in the two corners included in the DIC measurement area are plotted in the diagram from Fig. 6.60. The position of the evaluated points, which corresponds approximately to the position of the displacement transducers fixed in the corners on the opposite glass side ($dt_{x,1}$, $dt_{y,1}$, $dt_{x,2}$ and $dt_{y,2}$), is illustrated in the picture from the same figure.

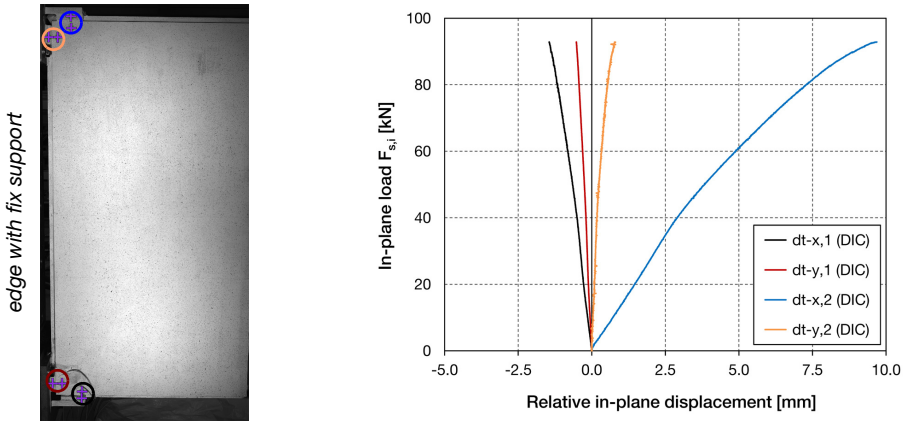

Fig. 6.60 *Relative in-plane displacements between glass pane and metal framing in the two corners of the fixed edge obtained with the DIC measurement system for specimen Type 1B*

The relative in-plane displacements measured with the transducers are plotted in Fig. 6.61, for the two corners of the fixed edge in the left diagram and for the two corners of the free edge in the right one. A good agreement can be noticed between the values obtained from the DIC measurement and those delivered by the displacement transducers (compare diagram in Fig. 6.60 with the left diagram in Fig. 6.61 by considering the different x-axis).

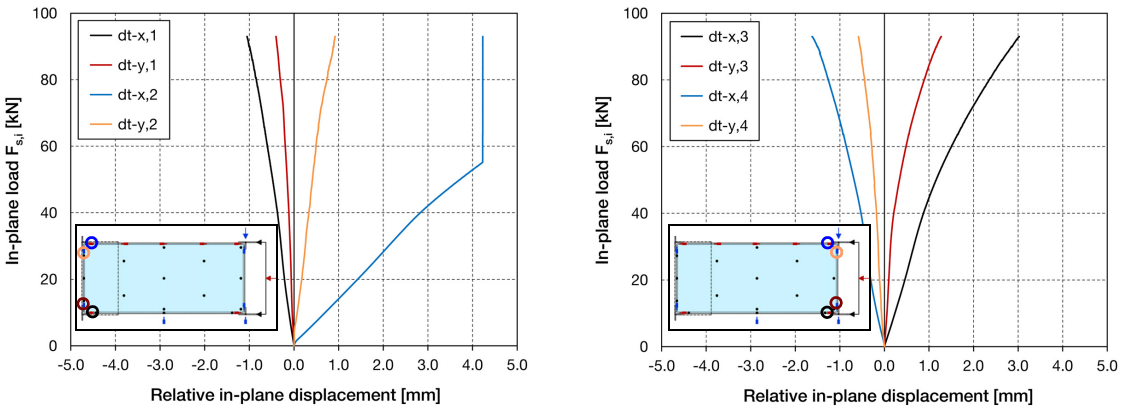

Fig. 6.61 *Relative in-plane displacements between glass pane and metal framing for specimen Type 1B in the two corners of the fixed edge (left) and in the two corners of the free edge (right)*

The advantage of using a DIC measurement system is the possibility to select the points for displacement and strain evaluation also after completing the tests, which allows for higher flexibility. For example, the transducer $dt_{x,2}$ measures useful data up to a load of around *55 kN* and then stops measuring either because it reaches its maximum range or because of an error. In the case of the DIC measurement a neighbouring point can be evaluated additionally later, if the target point shows unusable data.

The measured relative in-plane displacements in the corners under compression reach maximum values of up to *1.0 mm* in the bottom left corner and of up to *1.5 mm* in the top right corner, both in x-direction. By comparing these values with the used thickness for the grouting blocks a compression of *10-15%* of these components can be expected. For the silicone adhesive the in-plane relative displacements in the corners under tension are more significant. The maximum value is reached in the top left corner in x-direction with almost *10 mm*. By considering the thickness used for the silicone adhesive joint of *6 mm*, a shear displacement of around *160%* at the left extremity of the top adhesive stripe can be calculated. This value is slightly higher than the failure shear displacements reached in the experimental tests at connection level under shear loading discussed in subchapter 5.2.3 (averaging around *130%* for a joint thickness of *6 mm*).

The measurement data obtained from the strain gauge rosettes is evaluated in Fig. 6.62 for the test specimen *Type 1B* loaded until failure. From the strains measured in *0°/45°/90°* the principal strains are first determined by (Eq. 6.1):

$$\varepsilon_{1,2} = \frac{\varepsilon_{0°} + \varepsilon_{90°}}{2} \pm \frac{1}{2} \cdot \sqrt{2} \cdot \sqrt{(\varepsilon_{0°} - \varepsilon_{45°})^2 + (\varepsilon_{90°} - \varepsilon_{45°})^2} \qquad \text{(Eq. 6.1)}$$

Then the principal stresses are calculated with (Eq. 6.2) and (Eq. 6.3):

$$\sigma_1 = \frac{E}{1-\nu^2} \cdot (\varepsilon_1 + \nu \cdot \varepsilon_2) \qquad \text{(Eq. 6.2)}$$

$$\sigma_2 = \frac{E}{1-\nu^2} \cdot (\varepsilon_2 + \nu \cdot \varepsilon_1) \qquad \text{(Eq. 6.3)}$$

In Fig. 6.62 the maximum principal stresses σ_2 are plotted. The reached compressive stress values of up to *190 MPa* are not critical for the glass pane.

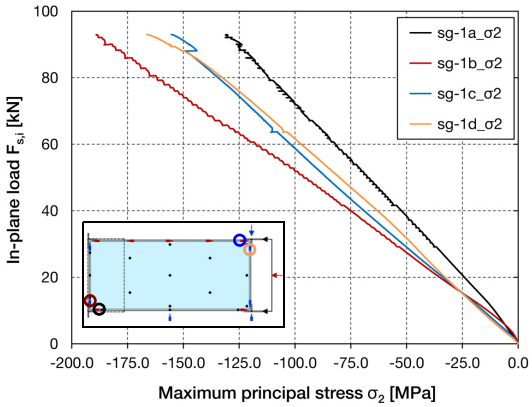

Fig. 6.62 *Maximum principal stresses in the glass pane in the two compressed corners for specimen Type 1B*

6.3.6 Failure test results for the specimen with acrylic adhesive bonding

For the test series on specimen *Type 2B* loaded until failure by increasing the in-plane shear load a displacement-controlled procedure with an initial loading speed of *0.5 mm/min* is chosen. Due to the rather unexpected large in-plane displacements and the resulting long duration of the testing, the speed is increased to *1 mm/min* after reaching a load of *100 kN*. This change of loading speed is noticeable in all load-displacement diagrams provided in this subchapter by a tooth in the curves at approximately *100 kN* and a small change in stiffness of the system above this value (indicated by the inclination of the curves). The test specimen *Type 2B* is shown in Fig. 6.63 unloaded (left), loaded shortly before failure (middle) and immediately after failure (right). In contrast to the case of the specimen with silicone adhesive joint and grouting blocks in the corners (*Type 1B*), no glass breakage occurs in the case of the specimen with acrylic adhesive joint. Also the distortions observable in the loaded state are significantly smaller for specimen *Type 2B* and barely visible with the naked eye.

The maximum recorded force before the ultimate failure of the test specimen is approximately *133 kN*, which is almost one and a half times larger than in the case of specimen *Type 1B*. The failure of the test specimen is caused by mixed cohesive and adhesive failure within the acrylic adhesive joint. However, the adhesive already starts to yield locally at around *60 kN* with the consequence of a significant stiffness reduction for the whole system, since the glass pane can-

not be activated anymore as a bracing to the same extent. At the end of testing, the failure of the adhesive can be observed near all four corners as well as on significant parts along the edges. However, there are still parts with an effective adhesive bonding which prevents the glass pane from falling to the ground. Although the glass pane receives an acoustically perceptible shock at the moment of ultimate failure, no glass breakage occurs, probably because, compared to the specimen *Type 1B*, there are no stainless steel brackets in the corners to block the movement of the glass pane after the shock.

Fig. 6.63 *Test specimen Type 2B unloaded, loaded shortly before failure and after failure (from left to right)*

The pictures in Fig. 6.64 illustrate different failure types of the adhesive observed in the two top corners and along the top edge. While in the top left corner, which is located at the end of the tensioned diagonal, adhesive failure on the glass surface can be noticed (see Fig. 6.64, left), in the top right corner, which is located at the end of the compressed diagonal and is also the corner in which the in-plane shear load is applied, cohesive failure occurs (see Fig. 6.64, right). Along the top edge of the glass pane combined adhesive and cohesive failure results as illustrated in the middle picture from Fig. 6.64.

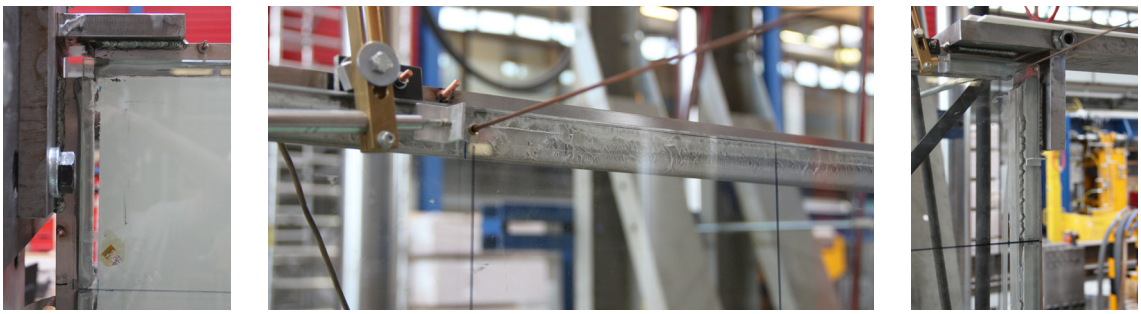

Fig. 6.64 *Detailed views of failure pattern in the adhesive in the top left corner (left), along the top edge (middle) and in the top right corner (right)*

The video recording of the test reveals that the initial failure in the adhesive starts in the top left corner and propagates along the top edge towards the top right corner. The ultimate failure after which the load drops comes together with the cohesive failure starting in the top right corner and extending along the right glass edge.

Although the glass pane remaines intact and is partially still bonded to the metal framing, the in-plane stiffness of the specimen is significantly reduced after failure. From Fig. 6.65, left and middle, it can be observed how the broken specimen is bending under its dead weight around the weak axis of the L-shaped edge elements. In some areas, in which the glass pane is still bonded to the metal framing, a certain degree of whitening can be noticed in the adhesive through the glass. This effect is a sign of yielding and is illustrated in the right picture from Fig. 6.65.

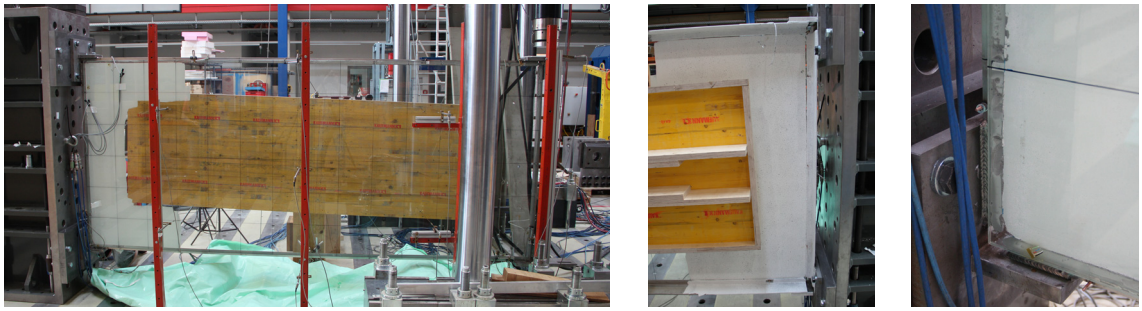

Fig. 6.65 *Front view (left) and rear view (middle) of the test specimen Type 2B after failure; whitening effect in the adhesive due to yielding (right)*

The discussion of results obtained with the used measurement instrumentation is carried out in the same order as for specimen *Type 1B* in subchapter 6.3.5. The out-of-plane displacements of the glass pane along the two diagonals are shown in the diagrams from Fig. 6.66.

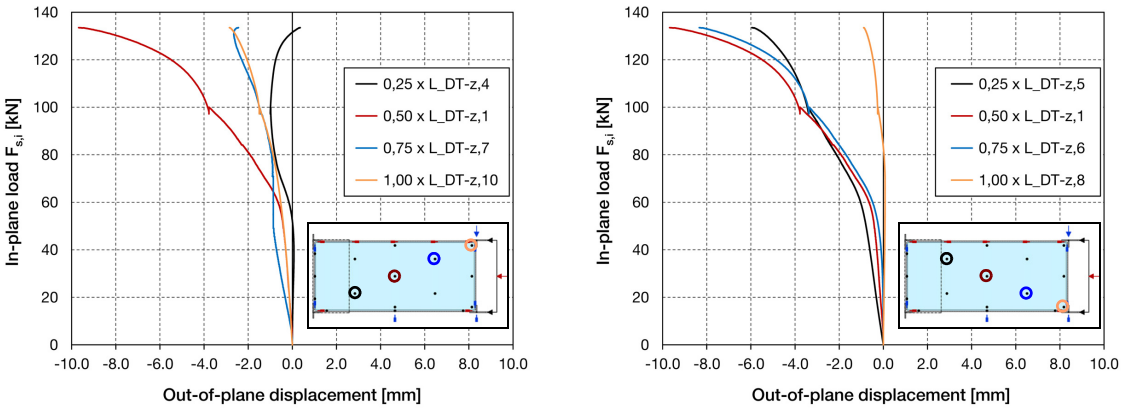

Fig. 6.66 *Out-of-plane displacements of the glass pane for specimen Type 2B along the compressed diagonal (left) and along the tensioned diagonal (right)*

In contrast to the case of the specimen with silicone adhesive, for specimen *Type 2B* only the displacements measured by the transducer $DT_{z,4}$ in the left quarter point of the compressed diagonal show a change in direction with increasing load. In this point, almost no displacement is occurring up to a load of around *60 kN*, then the point starts to move slightly to the interior up

to a load of *100 kN* and after passing this value it deforms in the opposite direction.

The displacements measured by the transducers in the midpoint and in the other three quarter points of the diagonals increase from the beginning until failure towards the interior of the elements (negative values in the diagrams). The change in inclination of the load-displacement curves, which are becoming more and more flat, indicates the start of buckling. However, the maximum measured displacement in the centre of the glass pane of almost *10 mm* is less than the maximum displacement measured for the specimen *Type 1B*, which is in agreement with the higher critical buckling load for the system concept with acrylic adhesive.

Fig. 6.67 shows the shape of the glass pane along the compressed diagonal (left) and along the tensioned diagonal (right) at different load levels. These curves are obtained by interpolating the displacement values measured with the transducers and are therefore only an approximation, which allows for overlooking local effects. The development of these curves with increasing load indicates the formation of a large bulge towards the interior of the element.

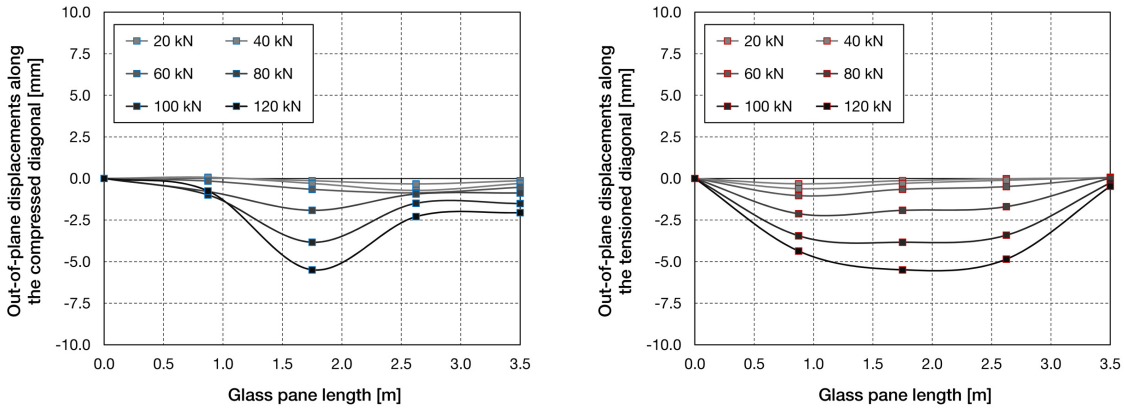

Fig. 6.67 *Out-of-plane displacements of the glass pane along the compressed diagonal (left) and along the tensioned diagonal (right) for specimen Type 2B at different load levels*

For specimen *Type 2B* the area for DIC measurement is chosen as well at the fixed end over a width of *75 cm*, but on the opposite glass pane side compared to specimen *Type 1B*. This decision is made in order to leave the adhesive visible on the front side, but has the disadvantage to allow the recording of only an approximately *25 cm* wide strip around the construction for the air cushion (see plots in Fig. 6.68). Furthermore, the displacement transducers used to measure the relative out-of-plane displacements between the glass pane and the metal framing reduce as well the measurement area.

Although measuring on the opposite side, the coordinate system is modified in such way, that positive measured values (maximum coloured red in Fig. 6.68) are displacements to the exterior, while negative values (maximum coloured blue in Fig. 6.68) are displacements to the interior. The recorded displacements indicate a good agreement along the tensioned diagonal (top corner), but show, similar to the results for specimen *Type 1B*, the formation of a small bulge towards the exterior between the bottom corner at the fixed edge and the nearest quarter point. This bulge is overlooked by just interpolating the displacement values measured in the midpoint

and in the quarter points of the diagonals with the transducers as represented in Fig. 6.67.

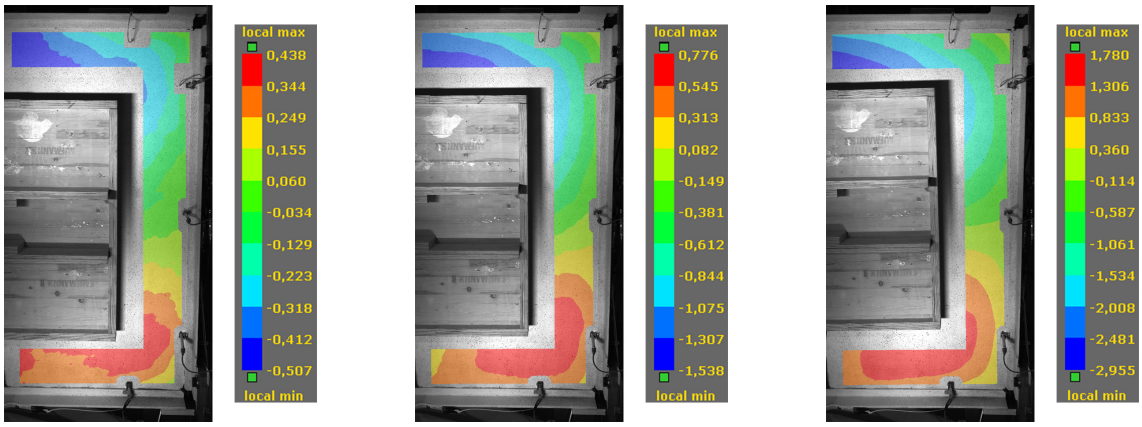

Fig. 6.68 *Absolute out-of-plane displacements [mm] of the glass pane at 40 kN, 80 kN and 120 kN (from left to right) obtained with the DIC measurement system for specimen Type 2B*

Fig. 6.69 shows relative in-plane displacements determined from the DIC measurement results in points corresponding to the position of the transducers $dt_{x,1}$, $dt_{y,1}$, $dt_{x,2}$ and $dt_{y,2}$.

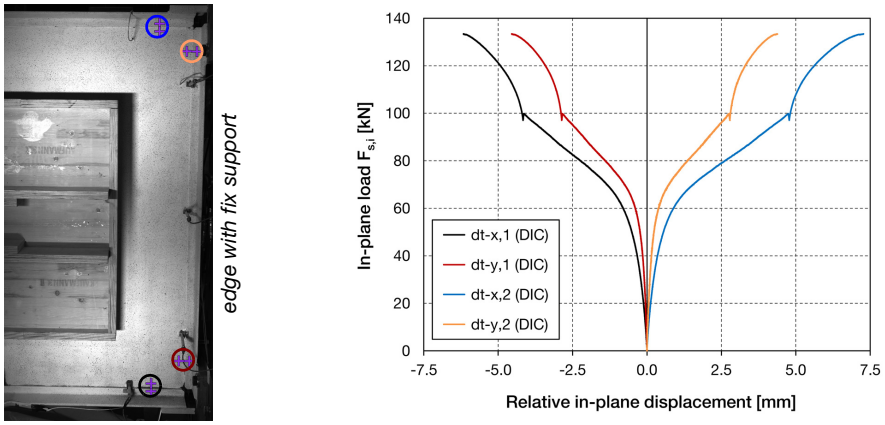

Fig. 6.69 *Relative in-plane displacements between glass pane and metal framing in the two corners of the fixed edge obtained with the DIC measurement system for specimen Type 2B*

The relative in-plane displacements between glass pane and metal framing recorded approximately in the same location with the displacement transducers (on the opposite glass pane side) are plotted in the left diagram from Fig. 6.70. Positive displacement values represent a movement of the glass pane towards the corner elements, while negative values mean that the glass pane moves away from the corner elements. The results from the DIC measurement and from the displacement transducers are in good agreement. Only the transducer $dt_{x,2}$ stops to record useful data after the change of loading speed. In the corners of the fixed edge, the relative displacements in x-direction are larger than those in y-direction, while in the corners of the free edge they are almost equal (see right diagram in Fig. 6.70). This is due to the fact that the corner elements at the fixed edge are rigidly attached to the abutment block, while the corner elements at the free edge are free to rotate. The maximum measured value of approximately *7.0 mm* in the bottom left corner means a shear displacement of around *230%* which is in a

good agreement with the values reached in the experimental tests at connection level under shear loading with the same acrylic adhesive (see subchapter 5.2.3).

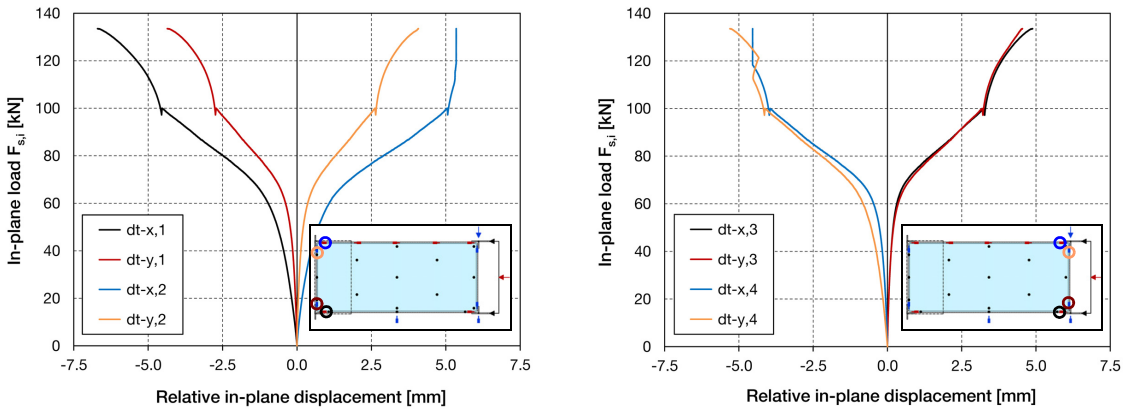

Fig. 6.70 *Relative in-plane displacements between glass pane and metal framing for specimen Type 2B in the two corners of the fixed edge (left) and in the two corners of the free edge (right)*

For the test specimen *Type 2B* three additional displacement transducer are used to measure the relative in-plane displacements in x-direction along the top edge of the glass pane. The results plotted in the left diagram from Fig. 6.71 show that the relative displacement is not constant along the length of the edge element, but is increasing from the top right corner to the top left corner. This is due to the rigid connection of the left corner element to the abutment block.

The results from the strain gauge rosettes are evaluated as described in subchapter 6.3.5 for specimen *Type 1B*. The maximum principal stresses σ_1 are plotted in Fig. 6.71, right, and reach values of around *32 MPa*, which are not critical for the used thermally toughened glass. The stress decrease in the top left corner (sg_{2a} and sg_{2b}) shortly before system failure is due to the failure initiation in the acrylic adhesive.

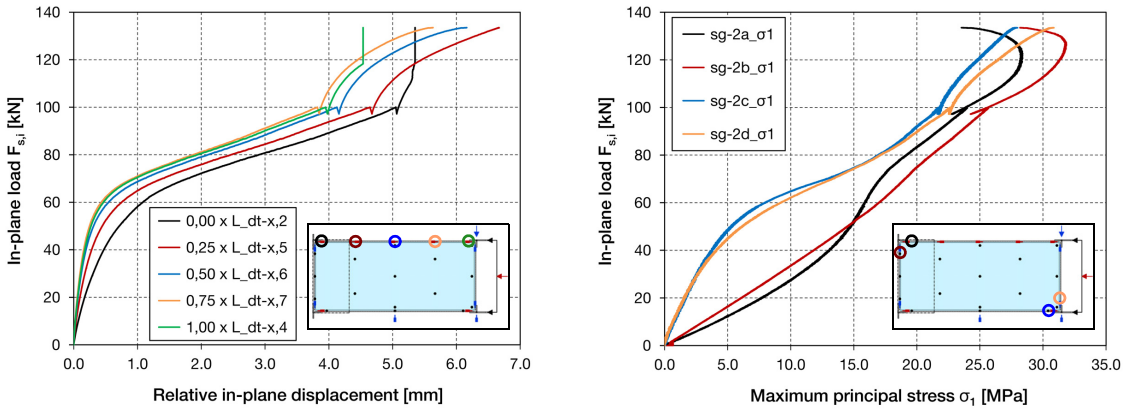

Fig. 6.71 *Relative in-plane displacements between glass pane and metal framing along the tensioned long edge (left) and maximum principal stresses in the glass pane near the two corners under tension (right) for specimen Type 2B*

6.4 Conclusions on the large-scale testing

Several objectives to be achieved with investigations on large-scale glass-metal elements with composite structural behaviour by adhesive bonding are stated at the beginning of this thesis in subchapter 1.2 and are pointed out more precise for the experimental tests in subchapter 6.1. Most of these objectives address issues concerning the structural performance of the elements as a whole as well as of their single components separately under different loading configurations.

In a first step, concluding statements on the assembly of the elements are provided in this subchapter. Both for the concept with combined perimetrical silicone adhesive bonding and grouting blocks (*Type 1*) and for the concept with perimetrical acrylic adhesive bonding alone (*Type 2*) a precise step by step planning of the assembly procedure proves to be essential for a smooth and trouble-free workflow. Especially when working with adhesives, which require an appropriate preparation of the substrate surfaces before application and access to the joints for tooling after application, a thorough planning of the steps order as well as the duration and the setup for each step is recommended.

Three different load directions are investigated in the experimental tests: *(i)* an in-plane axial load, *(ii)* an out-of-plane surface load, and *(iii)* an in-plane shear load. Firstly, loading cycles with one load acting at a time, two loads acting combined and all three loads acting combined on the specimens are performed in order to see the influence of the different loading directions on absolute and relative in-plane and out-of-plane displacements. The sizes of the loads for these cycles are assumed based on values expected in real facades without risking an early failure of the specimens. In general, the specimens with silicone adhesive bonding and grouting blocks (*Type 1*) exhibit larger displacements than the specimens with acrylic adhesive bonding (*Type 2*) during these loading series.

The in-plane axial load with a size of *40 kN* causes almost no displacements, both relative between the glass pane and the framing and absolute of the whole element. Furthermore, this load has also only a reduced influence on the displacements resulting in the cycles with combined load directions. The out-of-plane load with values up to *15 kN* when applied alone and of *10 kN* in combination with other loads causes the largest out-of-plane displacements of the glass panes. Under this load also a twisting of the longer edge elements is observed. This twisting is more pronounced in the case of the specimens with acrylic adhesive because of its higher stiffness compared to the silicone. The shear load with a size of *30 kN* leads as well to out-of-plane displacements of the glass pane, but their size is significantly smaller than those resulting from the out-of-plane surface load of *10 kN*. Also no twisting is noticed in the edge elements under in-plane shear load alone. However, the failure tests show that at higher load values the out-of-plane displacements of the glass pane increase due to plate buckling and also a twisting of the edge elements is occurring.

For the applied loads in these series, the specimens with acrylic adhesive behave significantly stiffer, exhibiting similar displacement values to the specimens with silicone adhesive and grouting blocks only under out-of-plane loading. The specimens with a monolithic *10 mm* thick glass

pane and those with a laminated glass pane made of *2 x 6 mm* glass sheets show similar results in terms of the reached displacements. However, from the repeated loading and unloading, the viscous material behaviour of the interlayer can be noticed in the case of the latter ones. The series with combined loads show the influence of additional loads on the behaviour of the element under shear loading for the given test configuration. An in-plane compressive axial load leads to a reduction of the measured absolute in-plane and out-of-plane displacements as well as of the maximum relative in-plane displacements between glass pane and metal framing. A tensile axial load on the other hand has the opposite effect. The combination with an out-of-plane surface load (suction) leads to significantly higher out-of-plane displacements of the glass pane as well as to slightly increased relative in-plane displacements.

For the two specimens with laminated glass panes failure tests under in-plane shear load alone are performed in order to investigate an eventual buckling behaviour and the failure modes. Significantly higher out-of-plane displacements of the glass panes occur, but they start to increase faster only after passing a load of around *40 kN* for the specimen with silicone adhesive and grouting blocks (~*14 mm*) and of around *60 kN* for the specimen with acrylic adhesive (~*10 mm*). The plate buckling phenomenon is better noticeable for specimen *Type 1B*. In the case of specimen *Type 2B*, the acrylic adhesive starts to yield before reaching critical load values for buckling and the element becomes softer in loading direction.

The weakest component is for both specimens the adhesive. In the case of specimen *Type 1B*, the silicone fails cohesively mainly due to tensile stresses caused by the out-of-plane deformation of the glass pane. In the case of specimen *Type 2B*, the acrylic exhibits mixed cohesive and adhesive failure caused by combined shear and tensile stresses. Up to a load of around *60 kN* the specimen with acrylic adhesive behaves significantly stiffer showing displacements in loading direction approximately half as large as the specimen with silicone adhesive and grouting blocks. Above this load value the acrylic starts to yield and the in-plane stiffness of the specimen *Type 2B* decreases significantly. At a load of *90 kN* both specimens show almost the same in-plane displacement in loading direction.

Both investigated concepts prove to have potential for further development to structural facade products. Although the specimen with acrylic adhesive shows a higher stiffness until the adhesive exceeds its yielding stress as well as a higher failure load, the concept with silicone adhesive and grouting blocks is considered to be more suitable for facade applications. The reasons herefore are on the one hand the existing approvals for structural silicones and on the other hand the need for a certain flexibility of the system under temperature loads. The used acrylic does not exhibit the required strength and stiffness for causing a plate buckling failure of the glass pane and shows partially adhesive failure on the glass surface. Moreover, internal investigations from the adhesive producer indicate a significant reduction of strength and stiffness for the acrylic already at temperatures of *50°C*. Therefore, further investigations should be conducted in order to find an alternative adhesive suitable for an implementation of the concept with adhesive bonding for transferring both in-plane and out-of-plane loads between the glass pane and the framing.

7 Finite element investigations on large-scale multi-component elements

Introduction and finite element model characteristics
Comparison between finite element results and test results
Parametric study on large-scale multi-component elements
Investigation of different loading scenarios and levels
Conclusions on the large-scale finite element simulations

1 Introduction 1

2 State of the art – theoretical framework

3 Transparent building envelopes with composite structural behaviour

4 Investigations on adhesives and their adhesion to metal substrates

5 Mechanical behaviour of adhesive joints between glass and stainless steel

6 Experimental investigations on large-scale multi-component elements

Finite element investigations on large-scale multi-component elements 7

8 Approaches for structural and functional design 8

9 Conclusions and future research 9

7.1 Introduction and finite element model characteristics

The experimental investigations on large-scale multi-component elements with composite structural behaviour between the glass pane and the metal framing by adhesive bonding, which were discussed in the previous chapter, delivered first findings on the performance of such elements under different load scenarios as well as on their failure modes under in-plane shear loading. However, the reduced number of available test specimens leaves several questions unanswered concerning the influence of different parameters on the mechanical behaviour of these innovative structural elements. Due to their composite structural behaviour, modified properties of the different components have an influence on the behaviour of the elements as a whole as well as on the behaviour of other single components. Both geometrical parameters of the components as well as alternative more suitable materials with varying stiffness and strength values for the load transfer components are important to be investigated in this regard. Furthermore, additional load combinations with different load sizes need to be analysed, especially at a level at which materials start to yield and stability issues begin to occur.

To perform these investigations and gather findings about the influence of these parameters on the mechanical behaviour of the glass-metal elements with composite structural behaviour, models developed in the software for finite element analysis and computer aided engineering *Abaqus 6.14* are introduced in this subchapter. After presenting the characteristics of the models for the two specimen types investigated experimentally in chapter 6 and introduced in subchapter 6.2.1 and after explaining the assumptions made for these models, they are validated in subchapter 7.2 by comparing absolute and relative displacement values with the results obtained from the experiments. In the rest of chapter 7 as well as in chapter 8 the models for specimens with silicone adhesive and grouting blocks will be referred to as models of *Type 1* and the models for specimens with acrylic adhesive as models of *Type 2*. These notations are in agreement with the test specimen names used in chapter 6.

Mainly due to the in-plane shear load, which is not symmetrical, no simplifications could be made for the models to reduce the computation time from this point of view. The whole glass-metal elements with all of their components are included in the models. The glass, the interlayer and the grouting are modelled linear-elastic. The value for the Young‘s modulus of the interlayer is assumed according to the value proposed in [Wellershoff, 2006] for wind loading as well as according to the value recommended in [ÖNORM B 3716-1] for PVB. For the grouting, more detailed material models including plasticity and creep effects are investigated in [Kolany, 2018] based on short-term and long-term experimental testing at material and at connection level. However, for the aspects studied in this thesis and the laterally restrained situation of the grouting blocks, the linear-elastic model is considered sufficiently exact. An additional consideration of plasticity and non-linear material behaviour would eventually result in lower stresses at the glass edge near the grouting blocks, but would have only a negligible influence on the occurring in-plane and out-of-plane displacements.

For the stainless steel used for the edge elements and the structural steel used for the corner elements, plastic properties are implemented by providing additional to the Young‘s modulus and the Poisson‘s ratio yielding stress values at given plastic strains (values assumed based on

[EN 10025-2, 2011] and [EN 10088-4, 2009]). For the adhesives, linear-elastic material models are used in a first step. In a second step, the non-linear models investigated in subchapter 5.2.4 are analysed: *(i)* the hyperelastic *Mooney-Rivlin* model for the silicone *Dow Corning 993* and *(ii)* the strain rate dependent plastic model without porosity as well as with porosity for the acrylic *SikaFast-5221 NT*. The parameter studies are carried out with the *Mooney-Rivlin* model for the silicone, while for the acrylic, a strain rate dependent plastic model without porosity, obtained by an additional fitting step, is used. This model is explained in subchapter 7.2.2. The input values for the material properties used in the finite element simulations are summarised in Tab. 7.1.

Tab. 7.1 *Material properties used in the finite element simulations*

Material	**Model type**	**Elastic properties**		**Plastic properties**			
		Young's modulus [MPa]	**Poisson's ratio** [-]	**Yield stress** [MPa]	**Plastic strain** [%]	**Tensile strength** [MPa]	**Plastic strain** [%]
Glass	linear-elastic	70 000	0.23		-		
Interlayer	linear-elastic	1.2	0.49		-		
Stainless steel	plastic	200 000	0.30	240	0%	600	40%
Structural steel	plastic	210 000	0.30	345	0%	550	20%
Grout	linear-elastic	2 500	0.40		-		
Silicone adhesive	linear-elastic	2.4	0.49		-		
	hyperelastic	Mooney-Rivlin (see subchapters 4.3.2 and 5.2.4)					
Acrylic adhesive	linear-elastic	250	0.47		-		
	plastic	250	0.47	(see subchapters 4.3.4, 5.2.4 and 7.2.2)			

For the mesh discretisation several aspects are considered: *(i)* a fine enough mesh size is required for the load transfer materials (adhesives and grouting blocks) in order to allow the occurring deformations and to obtain meaningful stress results; *(ii)* the mesh size for the other materials should be as coarse as possible in order to reduce computation time, but simultaneously too high aspect ratios of the elements need to be avoided; *(iii)* points for which results are planned to be read should correspond to a node in the mesh. By considering these requirements and as a result of a convergence study, a finer mesh is defined in the corners of the elements. Towards the middle of the edge elements as well as towards the centre of the glass pane the mesh gets coarser, as illustrated in Fig. 7.1. For the two adhesives and for the grouting blocks a minimum of four elements across their thickness as well as across their width was defined.

Second order solid elements are used for all components, similar as in the case of the finite element models used for the simulation of the tests on adhesive joints. In models of *Type 1* elements of type *C3D20* are used for the glass pane, the interlayer, the metal framing and the grouting blocks, while the silicone adhesive is modelled with elements of type *C3D20H*. In the models of *Type 2* all components including the acrylic adhesive are modelled with elements of type *C3D20*. The second order elements are used to avoid eventual shear locking problems in the components subjected to bending and due to the fact that they allow a higher accuracy for capturing stress concentrations. The hybrid formulation for the silicone adhesive is chosen to

avoid volumetric locking, which can be problematic for nearly incompressible materials (see [Abaqus, 2013b]). Although the interlayer is also such a material (nearly incompressible), for the given finite element problem the use of hybrid elements for this component led to a worse convergence and an earlier abortion of the simulations.

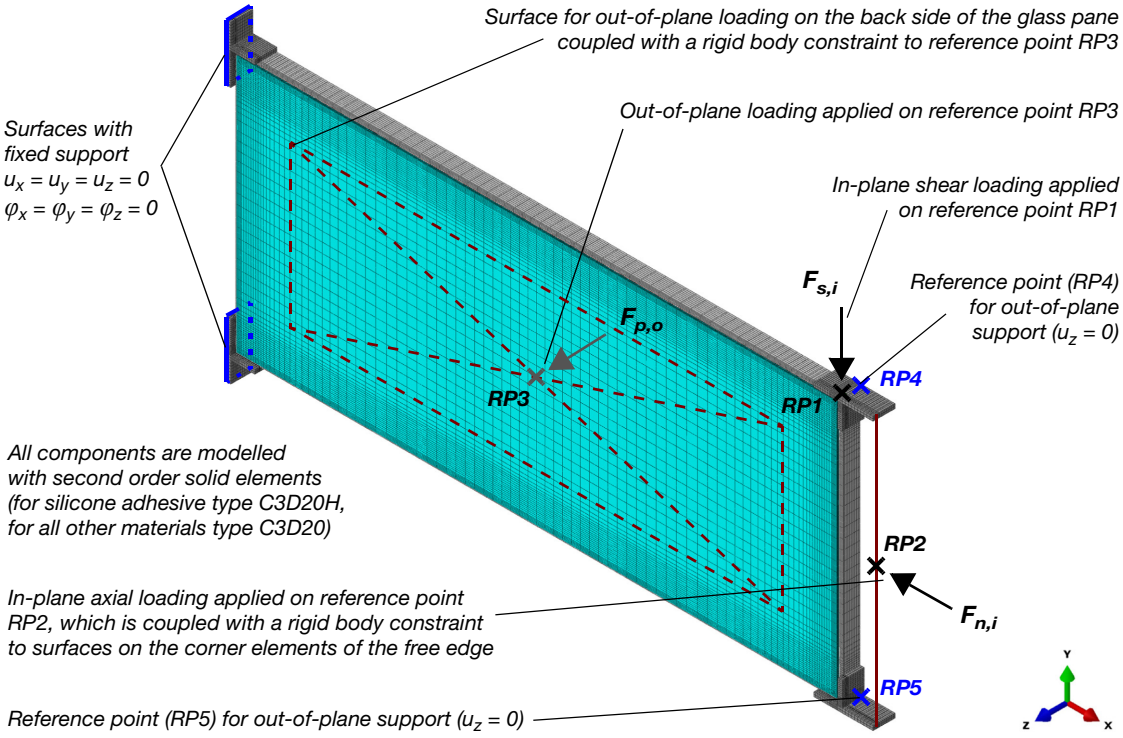

Fig. 7.1 *Finite element model with global mesh discretisation, boundary conditions and reference points for applied loads and displacements*

The contact between the two adhesives and the substrates is modelled with tie constraints, in which the adhesives provide always the slave surfaces, while the stiffer substrates include the master surfaces. The same type of constraint is used in the model between the corner elements and the edge elements, which in reality were welded together. In the case of the models with laminated glass the connection between the glass panes and the interlayer is modelled as well with tie constraints. For the contact of the grouting blocks to the framing and to the glass pane different assumptions are made. It is assumed that there is a certain bonding between the grout and the stainless steel edge elements, which was noticed in the tests at connection level from [Kolany, 2018]. Therefore, a tie constraint is applied between these two surface types. Between the glass and the grouting on the other hand, there is no adhesion. For this contact, interaction properties are defined: *(i)* in normal direction contact occurs when the two components are pushed together (hard contact), while in the case of a movement away from each other, separation is allowed; *(ii)* in tangential direction a friction coefficient of $\mu = 0.2$ is assumed.

For the boundary conditions and the load application simplifications are made in terms of the geometry of the corner elements. Fig. 7.2 and Fig. 7.3 show in the left sketches detailed views of the bottom left corner belonging to the fixed edge for the models of *Type 1* and of *Type 2*,

respectively. In both cases the dimensions of the fixed corner elements in z-direction are reduced, since their size used for the test specimens was only required for the connection to the abutment block. For the blue framed surface all translational and rotational degrees of freedom are suppressed.

The investigated loads are applied as concentrated forces on defined reference points, which are then connected with rigid body constraints to surfaces of the glass-metal elements in accordance with the experimental test setup (see Fig. 7.1). Fig. 7.2 and Fig. 7.3 show in the right sketches detailed views of the top right corner belonging to the free edge for the models of *Type 1* and of *Type 2*, respectively. This is the corner on which the in-plane shear load is applied and on which also half of the in-plane axial load is acting. For the corner elements belonging to the free edge, the length in x-direction of the leg with the opening for application of the in-plane axial load is reduced in the models.

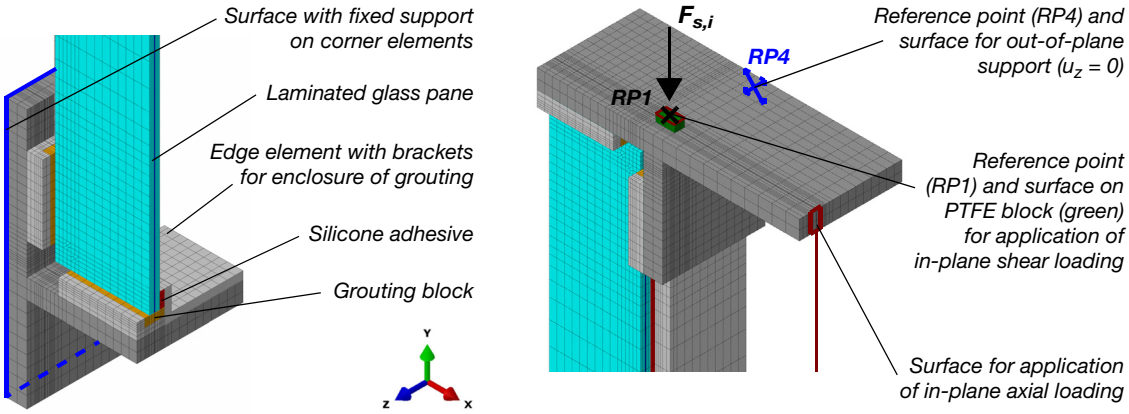

Fig. 7.2 *Detailed model view of one corner from the fixed edge (left) and of the corner loaded by the in-plane shear load (right) for the model with silicone adhesive and grouting blocks*

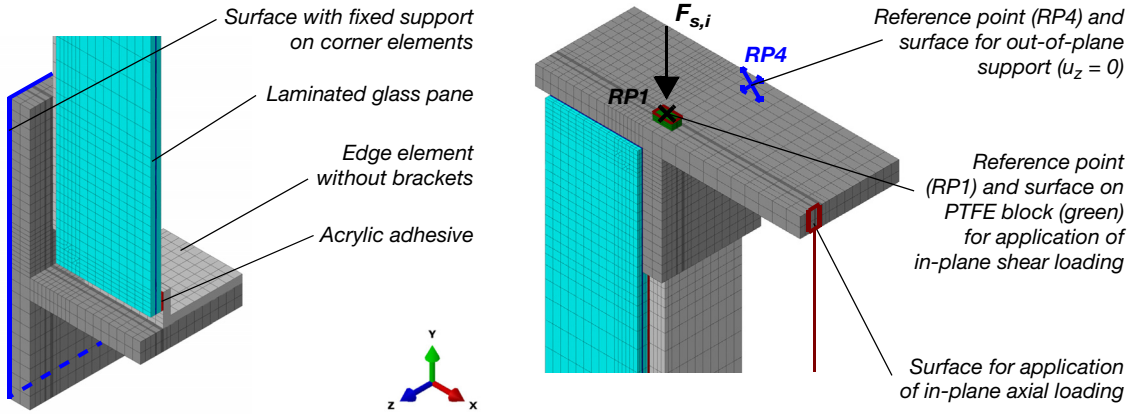

Fig. 7.3 *Detailed model view of one corner from the fixed edge (left) and of the corner loaded by the in-plane shear load (right) for the model with acrylic adhesive*

The surfaces to which the reference points are connected are highlighted in Fig. 7.2 and Fig. 7.3. For the in-plane shear load an additional block made of PTFE (Young‘s modulus of

420 MPa and Poisson's ratio of *0.46*) is modelled to allow a direct comparison between the experimental results and the simulation results. This *10 mm* thick block represents the two *~5 mm* thick PTFE sheets used in the experiments between the pressure plate connected to the hydraulic jack and the corner element. The block is required in the model for comparison of the global displacements in y-direction, since the displacement transducers positioned below the element ($DT_{y,1}$ and $DT_{y,2}$ from Fig. 6.15) were removed during the failure tests and only the displacements of the hydraulic jack are available.

For stability simulations with finite element software certain steps need to be followed as described for example in [Luible, 2004] and [Englhardt, 2007]. Leaning on these literature, the general procedure, which is also considered for the finite element investigations on large-scale multi-component elements, which are examined in this thesis and deal with stability issues, includes the following steps:

- *(a)* generation of the FE-model with appropriate element types and material properties;
- *(b)* definition of contact interactions, boundary conditions and acting loads;
- *(c)* determination of the eigenvalues of the system and their corresponding eigenmodes;
- *(d)* definition of an initial geometric imperfection by scaling an eigenmode (generally the first);
- *(e)* execution of a geometrically non-linear analysis on the imperfect and deformed system;
- *(f)* examination and evaluation of resulting displacements and stress values.

The steps *(c)* and *(d)* are required for stability investigations of structural elements with both symmetrical geometry and symmetrical loading. In such cases, without an initial geometric imperfection, the structural elements would not sidestep under loading during the simulations. However, in the case of the investigated glass-metal elements with composite structural behaviour, the loading is applied centric to the glass pane, but the framing is positioned on one side of the glass pane, towards the inside of the facade. Due to these circumstances, a non-linear analysis without initial imperfections can be enough for most loading scenarios. This aspect is analysed in subchapter 7.2.2 for the failure tests as well as in subchapter 7.3 for different parameters.

A finite element simulation generally is composed of pre-processing, analysis and post-processing. For the pre-processing in this thesis, scripts written with the programming language *Python* are used together with the software application *Abaqus/CAE*. The finite element analysis are carried out with *Abaqus/Standard*, while the post-processing is completed in *Abaqus/CAE*. For the determination of eigenvalues and eigenmodes, a linear perturbation step of type *Buckle* is performed under a unit force. For the determination of displacements and stresses, general steps of type *Static, General* are performed either load-controlled, if the results under a certain load are desired, or displacement-controlled, if a comparison to the experimental results is aimed.

7.2 Comparison between finite element results and test results

Before the influence of different parameters on the mechanical behaviour of the glass-metal elements with composite structural behaviour is investigated by finite element simulations, the models are validated by comparing selected experimental results discussed in chapter 6 to values obtained from the numerical analysis. The geometry of the glass-metal elements and of their components for these validation studies is modelled based on the dimensions provided in Fig. 6.3 for the large-scale test specimens as well as on the real dimensions measured for specimens *Type 1B* and *Type 2B*, which can be found in Tab. 6.2.

7.2.1 Evaluation of eigenvalues and eigenmodes

In simulations of buckling problems, especially in the case of linear structural elements, the initial geometric imperfections are generally assumed based on the shape of the first eigenmode, by scaling the normalised displacements with an empirically determined factor. For glass panes with a more uniform aspect ratio between length and height, [Englhardt, 2007] observed additional to curvatures corresponding to the first eigenmode also such corresponding to the second eigenmode as well as such with L-shape, U-shape or the shape of a hyperbolic paraboloid. The latter one was also noticed in the case of the laminated glass panes used for specimens *Type 1B* and *Type 2B* (see Fig. 6.14). In this subchapter the first and the second eigenmodes and the corresponding eigenvalues are analysed for the models of these two specimens under in-plane shear loading as well as under in-plane axial loading.

Beside the fact that the eigenmodes can be used to apply initial geometric imperfections, they provide an overview on how the system will deform under a certain load. Furthermore, the ideal buckling load F_{crit} of a system can be determined by multiplying the first eigenvalue with the applied load F. In the case of a unit load, as in the performed simulations, the ideal buckling load and the first eigenvalue are equal. Fig. 7.4 shows the first eigenmodes and the first eigenvalues for the model with silicone adhesive and grouting blocks (left) and for the model with acrylic adhesive (right) under in-plane shear loading. Displacement values in z-direction (perpendicular to the glass pane) are positive (red colour) for deformations towards the outside and negative (blue colour) for deformations towards the inside of the glass-metal element.

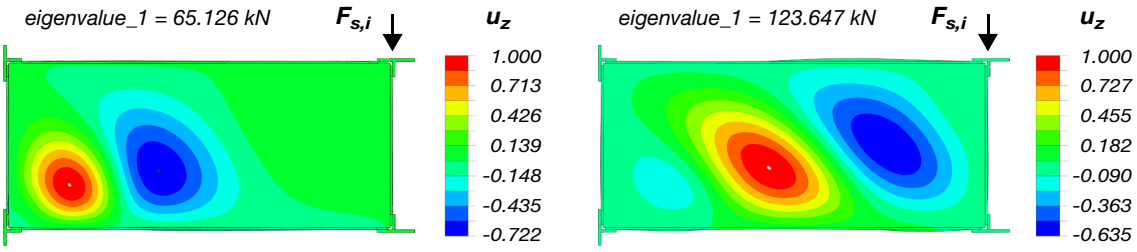

Fig. 7.4 *First eigenmode under in-plane shear loading for the model with silicone adhesive and grouting blocks (left) and for the model with acrylic adhesive (right)*

It can be noticed, that in the model of *Type 1* (left) the largest bulge is located nearest to the fixed corner of the compressed diagonal. In the model of *Type 2* (right) the largest bulge occurs nearer to the centre of the glass pane. This is mainly due to the different way of load transfer

from the framing to the glass pane: *(i)* in the first case the load is transferred primarily by the grouting blocks by compression in the top right and in the bottom left corners; *(ii)* in the second case the load transfer occurs by shear along the whole perimeter of the element. The more uniform load transfer is reflected also by the larger deformations of the longitudinal framing profiles in y-direction (see Fig. 7.5). This is also a sign, that with stronger composite action also the risk for lateral torsional buckling of the edge element profiles is increasing. The load transfer concept with the stiffer acrylic adhesive leads also to an *~1.9* times higher first eigenvalue.

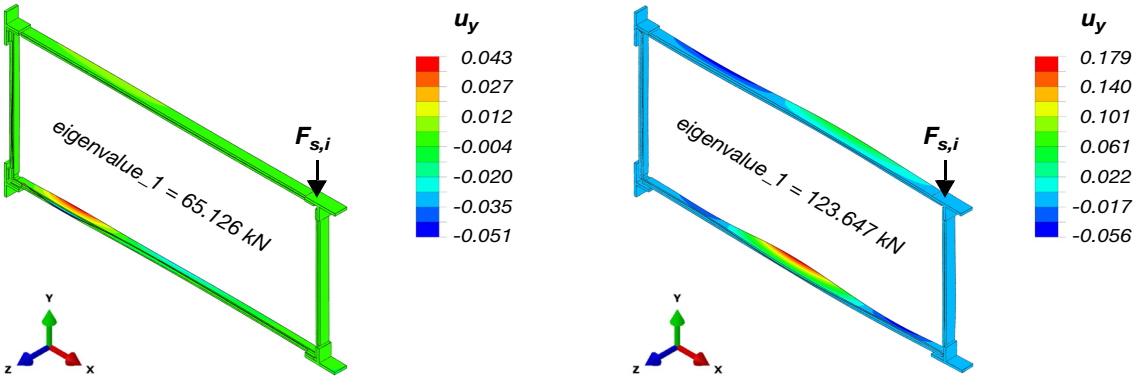

Fig. 7.5 *First eigenmode under in-plane shear loading without glass pane for the model with silicone adhesive and grouting blocks (left) and for the model with acrylic adhesive (right)*

Since the first and the second eigenvalues are quite close to each other for both model types, the second eigenmodes with the corresponding eigenvalues are plotted in Fig. 7.6 for the two models under shear loading. The shape of these eigenmodes differ only little compared to the first eigenmodes.

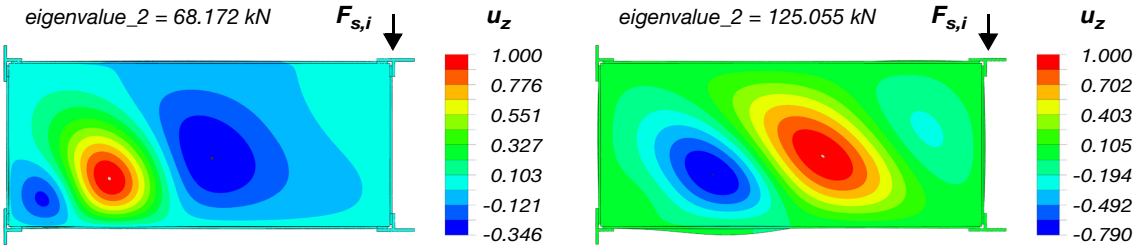

Fig. 7.6 *Second eigenmode under in-plane shear loading for the model with silicone adhesive and grouting blocks (left) and for the model with acrylic adhesive (right)*

Under in-plane compressive axial loading higher eigenvalues are reached for both model types. However, different than in the case of shear loading, almost equal eigenvalues can be observed for both investigated model types. The first eigenmodes and the corresponding eigenvalues are illustrated in Fig. 7.7. The shapes of the eigenmodes for the two model types look similar at first sight. They both show two bulges of the glass pane pointing in opposite directions. However, in the case of the model with silicone adhesive and grouting blocks, the bulge towards the outside is located near the free edge, while in the case of the model with acrylic adhesive its position is near the fixed edge. Furthermore, the deformations of the edge elements in y-direction are *3.4* times larger for the model with acrylic adhesive due to the higher composite action along the

longitudinal adhesive joints (see Fig. 7.8). A bulge of the glass pane oriented to the outside results in a sidestepping inwards of the laterally unrestrained edges belonging to the frame profiles, while in the case of a glass pane bulge oriented to the inside the opposite is the case.

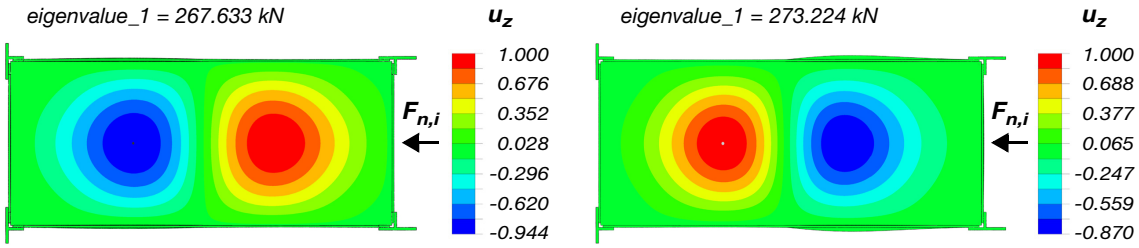

Fig. 7.7 *First eigenmode under in-plane axial compressive loading for the model with silicone adhesive and grouting blocks (left) and for the model with acrylic adhesive (right)*

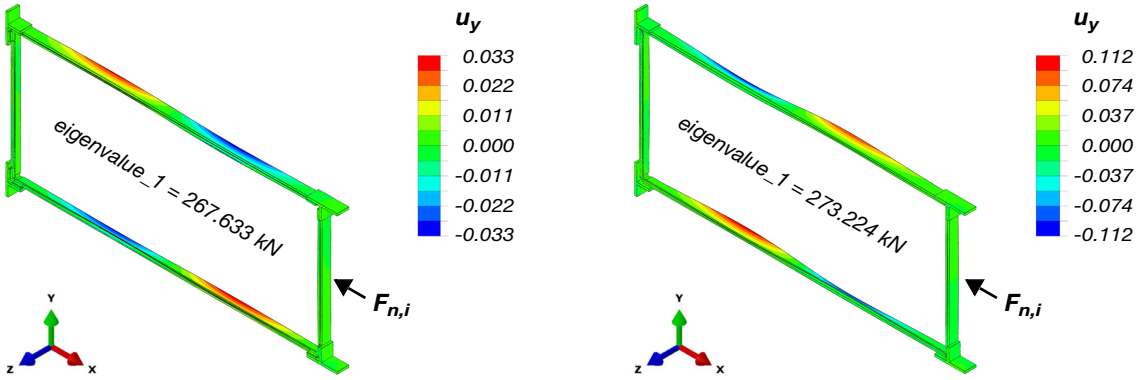

Fig. 7.8 *First eigenmode under in-plane axial compressive loading without glass pane for the model with silicone adhesive and grouting blocks (left) and for the model with acrylic adhesive (right)*

Similar as in the case of in-plane shear loading, also the second eigenmodes and their corresponding eigenvalues are provided for in-plane compressive axial loading in Fig. 7.9. The formation of an additional bulge can be noticed for both model types. In both cases the bulge in the middle is orientated outwards and the other two inwards.

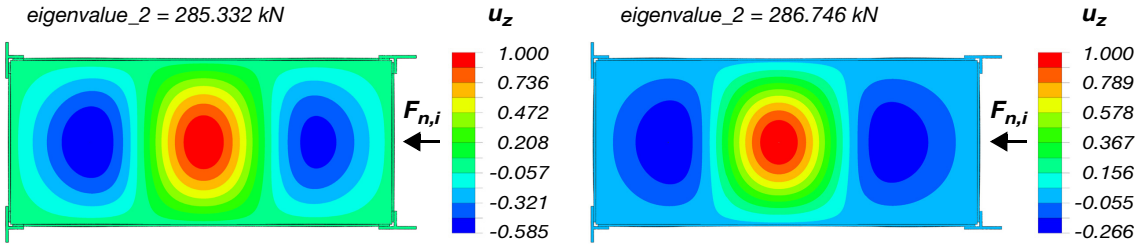

Fig. 7.9 *Second eigenmode under in-plane axial compressive loading for the model with silicone adhesive and grouting blocks (left) and for the model with acrylic adhesive (right)*

7.2.2 Simulation results for the failure tests

For validation of the finite element models, a comparison to the results from the experimental failure tests under in-plane shear loading is considered the most conclusive, since under the higher load level more non-linearities, both material-related as well as geometrical ones, are relevant. Therefore, the simulation results for these test series on specimens *Type 1B* and *Type 2B* are evaluated first. The diagrams in Fig. 7.10 show the relationships between the applied in-plane shear load and the in-plane displacement in load direction recorded by the hydraulic jack for the two different test specimens (see continuous coloured curves). Additionally, curves obtained from finite element simulations with different model and analysis approaches are plotted for the two different glass-metal elements with composite structural behaviour.

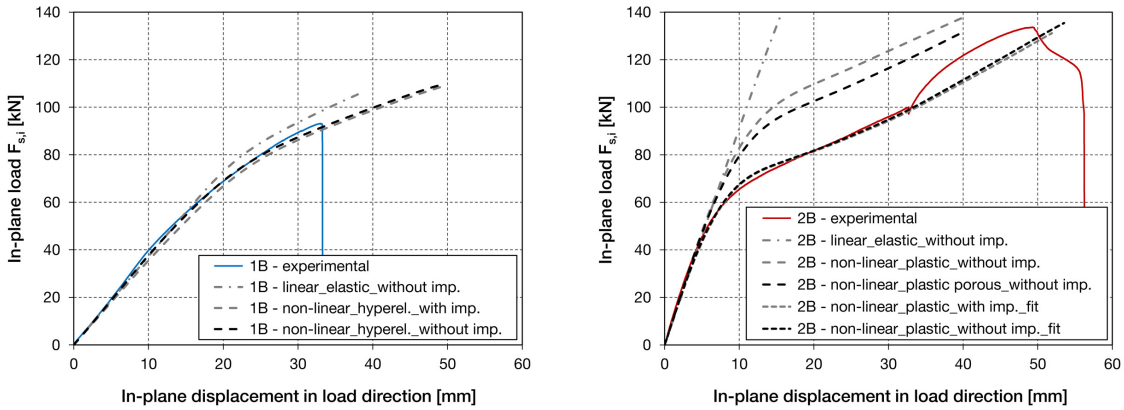

Fig. 7.10 *In-plane shear load vs. in-plane displacements of the hydraulic jack during the failure tests for specimens Type 1B (left) and Type 2B (right) compared to the in-plane displacements of reference point RP1 from the finite element simulations of these tests*

In a first step, geometrically linear analysis were performed with elastic material properties of the adhesives for both systems. The results of these simulations are plotted with dashed and dotted grey curves in Fig. 7.10. The properties of all other materials were used according to Tab. 7.1. Moreover, no initial geometric imperfections were implemented in these simulations. The results show an acceptable agreement with the experimental curves in the case of the model for specimen *Type 1B*. This agreement indicates that the non-linearity of the curves results to a high extent due to yielding in the metal framing. The non-linear behaviour of the silicone adhesive has a rather small influence on the development of the curve. In the case of the model for specimen *Type 2B*, a good agreement is provided only up to a load of around *50 kN*. Above this value, the acrylic adhesive starts to yield and the in-plane stiffness of the glass-metal elements begins to decrease.

In a second step, geometrically non-linear analysis with the investigated non-linear material models for the two adhesives are performed for the two systems. In the case of the silicone, the hyperelastic *Mooney-Rivlin* model is used. The results of these simulations are plotted with dashed curves in Fig. 7.10, left. A grey dashed curve is used for the simulation with initial geometric imperfections based on the first eigenmode scaled by a factor of *L/500*, which results in a maximum initial out-of-plane deflection of the glass pane of *7 mm*. For the simulation without initial geometric imperfections, a black dashed curve is used. In terms of in-plane load *vs.* in-

plane displacement there is almost no difference between the results with initial imperfections and those without one for the specimen of *Type 1B*. Compared to the linear analysis with elastic properties of the adhesive, a slightly better agreement between the simulation results and the experimental ones can be noticed for the system with silicone adhesive and grouting blocks.

For the system with acrylic adhesive, the strain rate dependent plastic model without porosity (see subchapter 4.3.4) is analysed as a first alternative for a non-linear material model. The results of this simulation (without initial imperfections) are plotted with a grey dashed curve (long dashes) in Fig. 7.10, right. The differences to the linear analysis with elastic properties of the adhesive are obvious, since the yielding behaviour of the adhesive is reproduced by the non-linear material model. Both the in-plane stiffness of the system before yielding and after yielding are in good agreement between simulation and test results. However, the yielding starts in the model a little delayed and therefore the loads from the experimental test are overestimated after yielding (by *~30%*). An improvement of this discrepancy can be achieved by adding porosity to the properties of the acrylic adhesive, as described in subchapter 5.2.4. The results obtained with this model are illustrated by the black dashed curve (long dashes) in Fig. 7.10, right. By comparing the results obtained with the strain rate dependent plastic model including porosity with the experimental ones, the agreement in terms of load size after yielding is still non-satisfying. The following findings and hypothesis are derived:

- Before yielding of the adhesive both the inclination of the load *vs.* displacement curve (equivalent to system stiffness) and the size of the loads are reproduced well; in this range, due to the high stiffness of the adhesive, the glass pane is activated as a shear panel and consequently deforms out-of-plane due to buckling (this was observed during testing); the activation as shear panel generates shear stresses in the adhesive, while the buckling generates tensile stresses (peel stresses) in the adhesive;

- In the experiment, the yielding of the adhesive starts slightly above a load of *50 kN* due to a combination of shear and tensile stresses; the applied strain rate dependent plastic model including porosity showed a limited suitability for reproducing the material behaviour of the adhesive under tensile loading, overestimating the yielding point for joints with larger lengths (see subchapter 5.2.4); therefore the yielding in the simulations starts delayed;

- After yielding there is a good agreement between simulation results and experimental results regarding the inclination of the curves, but the loads are significantly overestimated by the simulation; due to the reduced stiffness of the adhesive after yielding, the glass pane cannot be activated optimally anymore and therefore mainly shear stresses are generated in the adhesive; this is sustained by the similar curve development to those from the double-lap shear tests discussed in subchapter 5.2.3 and explains the agreement regarding inclination.

Based on this hypothesis and in order to obtain with the available material data a model which reproduces also the occurring loads well, an additional fitting procedure is performed in this thesis. The result of the fitting consists in a reduction of the strain rate dependent yield stresses provided in Tab. 4.6 for selected plastic strains by *30%*. Porosity is not considered for the fitted material model. This approach allows to obtain a model which leads to reasonable results and can be used for the parameter studies in subchapters 7.3 and 7.4. Nevertheless, thorough

investigations aiming at developing a generally suitable strain and temperature dependent plastic model taking existing voids, void nucleation and coalescence into account is recommended for the acrylic adhesive in future research.

The simulation results obtained with the fitted strain rate dependent plastic model for the acrylic adhesive are plotted in Fig. 7.10 with dashed curves (short dashes). As in the case of the results for the specimen of *Type 1B*, a grey dashed curve is used for the simulation without initial geometric imperfections (same assumptions are made as for system with silicone adhesive and grouting blocks) and a black dashed curve for the simulation without initial geometric imperfections. A good overall agreement can be observed, both in the case of the inclination of the curves and the size of the load before and after yielding. Similar to the simulation results for the specimen of *Type 1B*, no significant influence of the initial geometric imperfections is noticed.

All the simulations of the failure tests were performed displacement-controlled with the same loading speeds as in the tests. For the model with silicone adhesive and grouting blocks a loading speed of *2 mm/min* was used, while for the model with acrylic adhesive the speed was only *0.5 mm/min*. The change of displacement-controlled loading speed at *100 kN* for specimen *Type 2B* was not included in the model. The non-linear analysis converges for the system with silicone adhesive and grouting blocks up to in-plane loads of around *~110 kN* and for the system with acrylic adhesive up to values of *~135 kN*.

The simulation results for the in-plane load *vs.* in-plane displacement relationships show that especially for the system with acrylic adhesive non-linear analysis are required. Furthermore, the plastic behaviour of the acrylic adhesive needs to be included in the models of *Type 2* in order to obtain useful results under higher loads. In the case of the models of *Type 1*, hyperelastic properties of the silicone adhesive lead to better results and therefore their consideration is recommended. In terms of initial geometric imperfections, further results regarding out-of-plane displacements of the glass pane as well as regarding stresses in the different components need to be evaluated in order to decide if they can be neglected for the investigated glass-metal elements or not. Tab. 7.2 provides for the two systems without and with initial geometric imperfections a summary of different selected values recorded in the simulations at loads which correspond approximately to the failure loads in the tests.

By comparing the values in Tab. 7.2 obtained for model *Type 1* without an initial geometric imperfection with those obtained for the same model with an initial geometric imperfection of *L/500* (*L* being the length of the glass pane with *3.5 m*), it can be noticed that there is almost no difference regarding the maximum stresses in the framing and in the adhesive. Similar observations can be made for these two components also in the case of the model *Type 2*. When it comes to the glass pane, slightly higher maximum principal stresses (*~7%*) occur in the models with initial geometric imperfections. Moreover, there are also some discrepancies regarding the size of the out-of-plane displacements of the glass panes. While in the case of model *Type 2* both the positive and the negative maximum displacements are higher when considering initial geometric imperfections, in the case of model *Type 1* the opposite is occurring. In order to evaluate the influence of initial geometric imperfections on the simulation results, the out-of-plane displacements of the glass pane are illustrated as contour plots for the system with silicone

adhesive and grouting blocks at an in-plane shear load of *90 kN* and for the system with acrylic adhesive at a load of *130 kN*. The results obtained from the models without initial imperfections are plotted in Fig. 7.11, those from the models with initial imperfections in Fig. 7.12.

Tab. 7.2 *Comparison of selected values obtained from the finite element simulations for the models of Type 1 and Type 2 without and with initial geometric imperfections*

Selected displacement and stress values	**Unit**	**Model Type 1 ($F_{s,i}$ = 90 kN)**		**Model Type 2 ($F_{s,i}$ = 130 kN)**	
		without initial geom. imp.	**initial geom. imp. L/500**	**without initial geom. imp.**	**initial geom. imp. L/500**
max. out-of-plane displ. of glass pane (+)	[mm]	29.5	29.1	7.2	12.8
max. out-of-plane displ. of glass pane (-)	[mm]	-25.2	-21.2	-9.9	-11.9
max. principal stress in the glass pane	[MPa]	124.6	133.7	71.4	76.0
max. principal stress in the adhesive	[MPa]	4.6	4.5	147.8	146.8
max. Mises stress in the adhesive	[MPa]	4.0	4.0	33.2	33.3
max. Mises stress in the edge elements	[MPa]	336.0	335.5	401.0	400.7
max. Mises stress in the corner elements	[MPa]	449.1	449.6	624.9	624.5

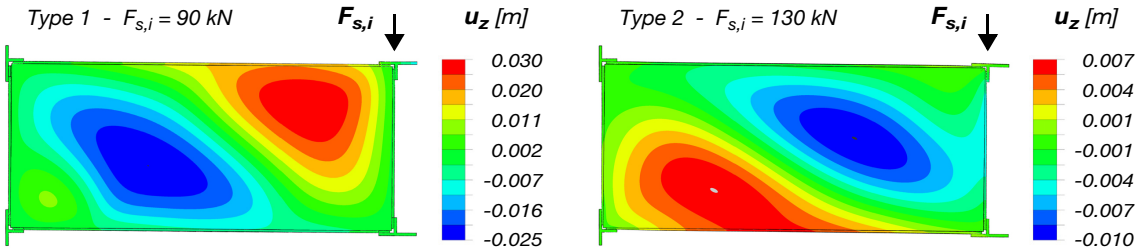

Fig. 7.11 *Out-of-plane displacements of the glass pane for specimen Type 1B (left) at 90 kN and for specimen Type 2B (right) at 130 kN from the models without initial geometric imperfections*

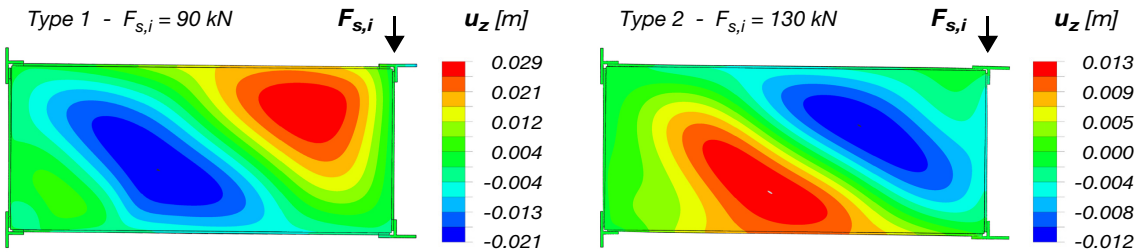

Fig. 7.12 *Out-of-plane displacements of the glass pane for specimen Type 1B (left) at 90 kN and for specimen Type 2B (right) at 130 kN from the models with initial geometric imperfections*

It can be observed, that although different displacement values are reached, qualitatively the deformation shape is similar for the models without and those with initial geometric imperfections. Since in the case of model *Type 1*, neglecting initial imperfections lead to unfavourable displacement results and in case of model *Type 2* a glass failure is rather not expected (see test results for specimen *Type 2B*), the results for the models without initial geometric imperfections will be further evaluated in this subchapter.

The maximum principal stresses in the glass panes before failure of the elements are significantly higher in the case of the system with silicone adhesive and grouting blocks (*Type 1*), although lower in-plane shear loads were reached with this system in the experimental tests. This is due to the concentrated load transfer from the metal framing to the glass pane by the grouting blocks. The maximum stress of *125 MPa*, occurs in the loaded corner, directly near the location of the grouting blocks as shown in Fig. 7.13, left, and is slightly higher than the characteristic strength value for thermally toughened glass given in standards with *120 MPa*.

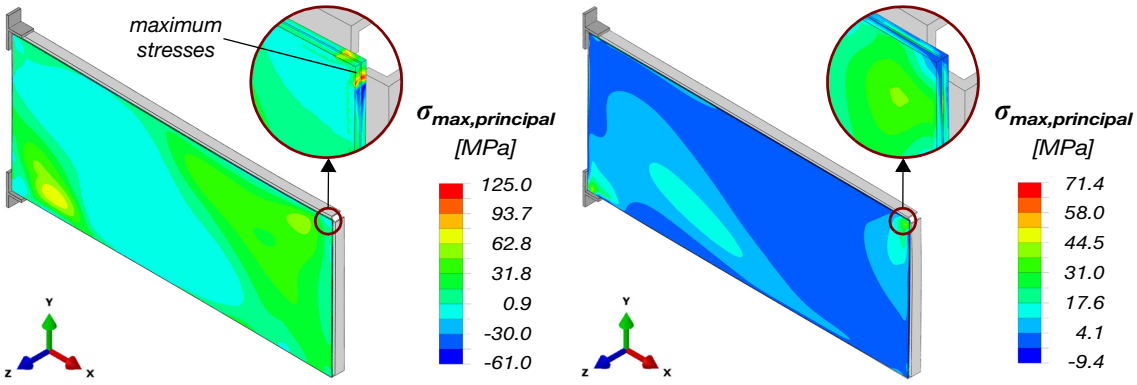

Fig. 7.13 *Maximum principal stresses in the glass panes from the models for specimen Type 1B (left) at a load of 90 kN and for specimen Type 2B (right) at a load of 130 kN*

The position of the maximum stress in the glass pane for model *Type 1* is in good agreement with the location of the crack initiation noticed in the failure test on specimen *Type 1B*. However, if a more exact material model would be added for the grouting blocks, covering plasticity and non-linearity, the peak stress values in these area are expected to be slightly reduced. Over the surface of the glass pane, where the bulges are located, significantly lower stresses are reached (see Fig. 7.13, left, and Fig. 7.14, left).

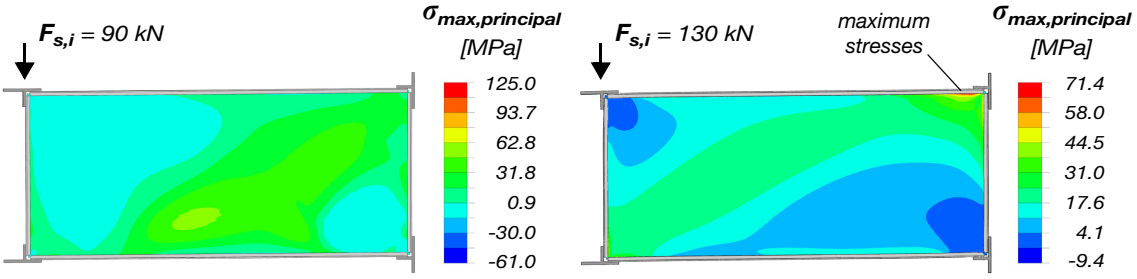

Fig. 7.14 *Maximum principal stresses on the back side of the glass panes from the models for specimen Type 1B (left) at a load of 90 kN and for specimen Type 2B (right) at a load of 130 kN*

In the case of the system with acrylic adhesive, the principal stresses over the glass pane surface are even lower and there are no peaks in the area of the loaded corner of the elements (see Fig. 7.13, right). The maximum principal stress of *71.4 MPa* occurs on the back side of the glass pane near the fixed corner belonging to the tensioned diagonal in the vicinity of the adhesive joint (see Fig. 7.14, right).

In order to evaluate the results from the simulations for the load transfer materials and especially for the two adhesives, in a first step, the relative in-plane displacements between metal framing and glass pane are compared to the values measured during testing. This comparison shows a good agreement in the case of the system with silicone adhesive and grouting blocks as illustrated by the diagrams in Fig. 7.15. Only in the fixed corner belonging to the compressed diagonal the relative displacements obtained from the simulation are lower than those measured during testing (see curves for $dt_{x,1}$ and $dt_{y,1}$ in Fig. 7.15, left).

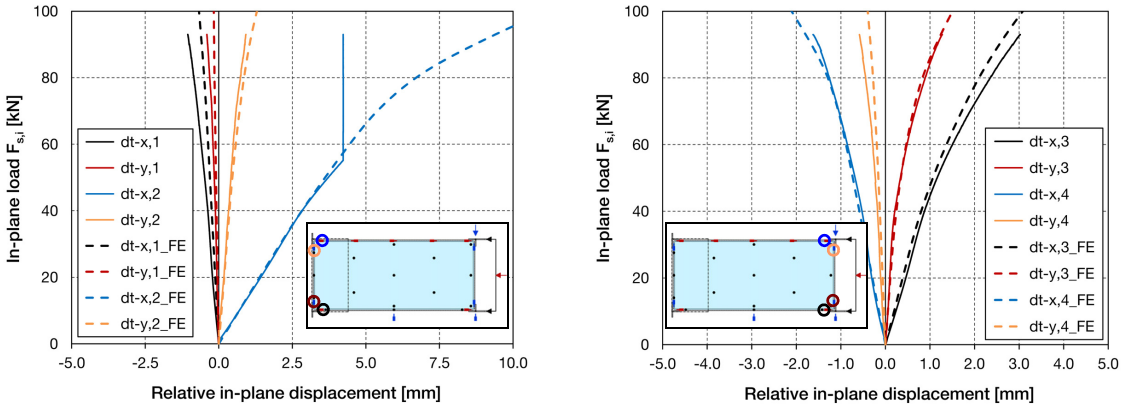

Fig. 7.15 *Relative in-plane displacements between glass pane and metal framing in the four corners from the experimental test and from the FE simulation for specimen Type 1B*

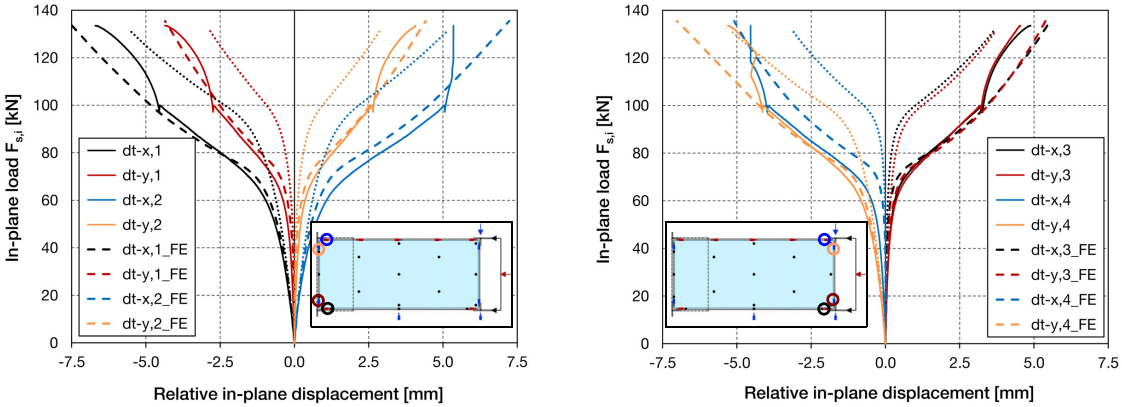

Fig. 7.16 *Relative in-plane displacements between glass pane and metal framing in the four corners from the experimental test and from the FE simulation for specimen Type 2B*

In the case of the system with acrylic adhesive the agreement between the simulation results obtained with the fitted strain rate dependent plastic model and the experimental ones regard-

ing relative in-plane displacements is generally good (see dashed curves in Fig. 7.16). For comparison, results obtained with the strain rate dependent plastic model including porosity are additionally plotted in Fig. 7.16 as dotted curves. Although qualitatively good, the same delayed yielding of the acrylic adhesive can be noticed from these curves in all four corners as in the case of the in-plane load *vs.* in-plane displacement curves plotted in Fig. 7.10.

In a second step, stresses in the load transfer materials are evaluated. The Mises stresses reached in the simulation for the grouting blocks with the linear elastic material model are significantly higher than the strength provided in [Bucak, 2011] for the same material (*~60 MPa* for short term loading at *23°C*). However, it should be considered that the values provided in [Bucak, 2011] are valid for uniaxial loading and in the case of the investigated elements a certain lateral restraint is given. The mechanical performance of the grouting blocks in these tests is analysed in detail in [Kolany, 2018].

In the case of the silicone adhesive the maximum principal stresses are evaluated. The location and the size of the maximum values are pointed out in Fig. 7.17. The maximum values occur near the fixed corner of the tensioned diagonal since here no loads can be transferred by the grouting blocks and the relative displacements between framing and glass pane are larger than in the free corner of the same diagonal.

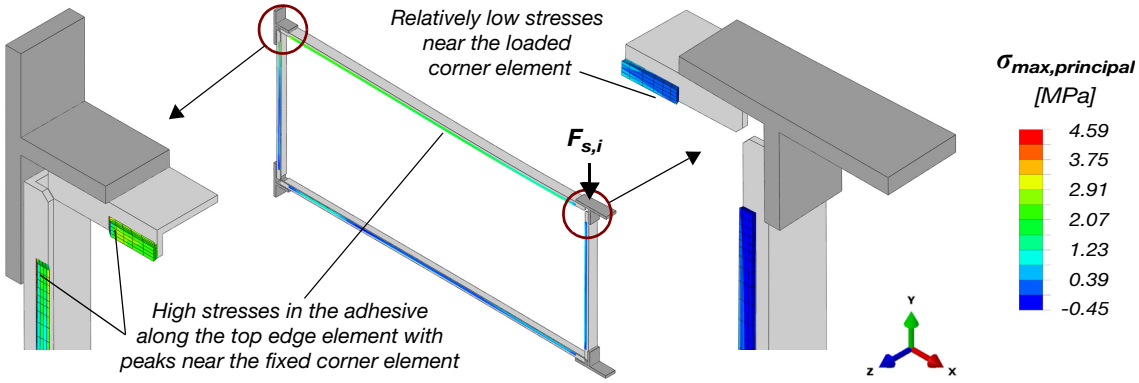

Fig. 7.17 *Maximum principal stresses in the silicone adhesive joints from the model for specimen Type 1B at an in-plane shear load of 90 kN*

The size of the maximum principal stresses of up to *4.59 MPa* at an in-plane shear load of *90 kN* is in good agreement with the stress peaks reached in the simulations of the tests at connection level discussed in subchapter 5.2.4. High stress values in the adhesive occur as well along the top edge element, where additional to shear stresses, tensile stresses result due to the out-of-plane deformation of the glass pane. Near the two corners belonging to the compressed diagonal the stresses are rather low since the loads are transferred mainly by the grouting blocks.

In the case of the acrylic adhesive used in the system of *Type 2*, Mises stresses are evaluated instead of maximum principal stresses, since the first ones are considered more significant for a plastic material. The location and the size of the maximum values are pointed out in Fig. 7.18. High stresses result in all four corners at the exterior edges of the contact surfaces to the substrate materials. However, the peak values shown in the legend of Fig. 7.18 occur only in local

FE-nodes near the corners belonging to the compressed diagonal at the contact surfaces to the framing and can be considered as singularities. Maximum stress values extending over several mesh elements are in the range of up to *20 MPa* and confirm a yielding of the adhesive in these areas. The exactness of this evaluation of stresses in the adhesive, especially regarding their size, should be treated under consideration of using a material model with certain limitations for the acrylic. Furthermore, local stress peaks at the weak singularities resulting from geometry and material change can generally not be properly estimated in finite element modelling.

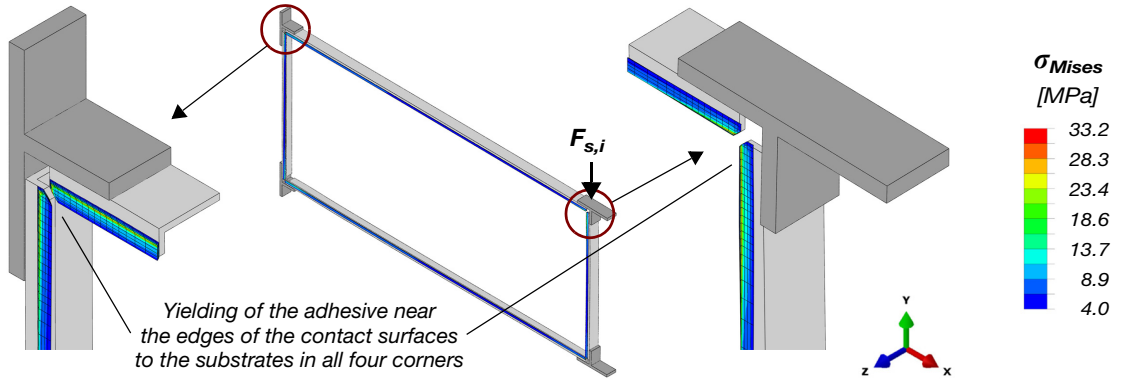

Fig. 7.18 *Mises stresses in the acrylic adhesive joints from the model for specimen Type 2B at an in-plane shear load of 130 kN*

For the metal framing consisting of the corner elements made of structural steel (*1.0045*) and of the edge elements made of stainless steel (*1.4404*), contour plots of the Mises stress distribution are shown for the two systems in Fig. 7.19 and Fig. 7.20, respectively. The different load transfer methods between metal framing and glass pane have a clear influence on the stresses in the framing. In the case of the system with silicone adhesive and grouting blocks, the load is mainly transferred by compression over the grouting in the two corners belonging to the compressed diagonal. Therefore, in these two corner elements high stresses of up to *449 MPa* result at an in-plane shear load of *90 kN* and lead to yielding of the used structural steel type. In the case of the system with acrylic adhesive, the load is transferred by shear, which leads to local stress peaks in the corner elements near to their contact surface to the edge elements. However, at the intersection of the corner element brackets no yielding is occurring.

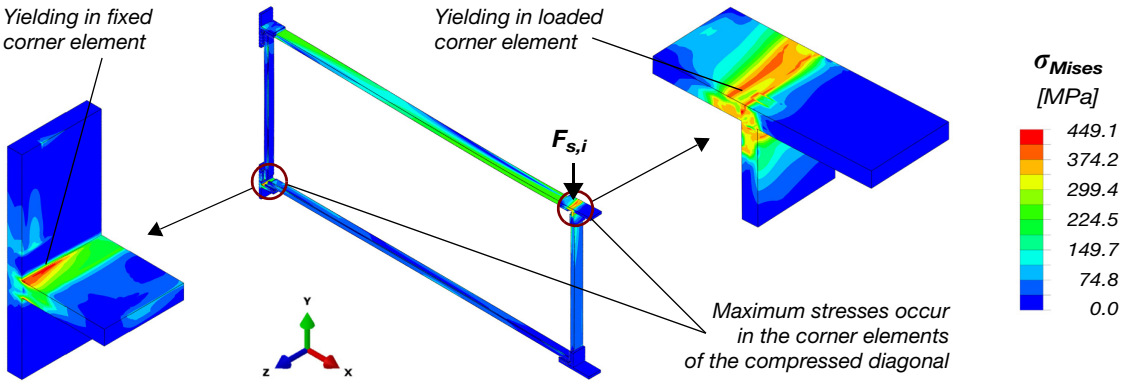

Fig. 7.19 *Mises stresses in the metal framing from the model for specimen Type 1B at an in-plane shear load of 90 kN*

The edge elements show as well different stress distributions for the two system types. In the model of *Type 1* higher stresses can be observed in Fig. 7.19 only in the longer top edge element, which functions as a tie member. In the model of *Type 2* a more uniform distribution can be noticed from Fig. 7.20 with increased stresses in both longer edge elements towards the fixed end. The stresses in the edge elements are generally slightly below the assumed yielding strength of *240 MPa*, except for local peaks in the vicinity of the connection to the corner elements.

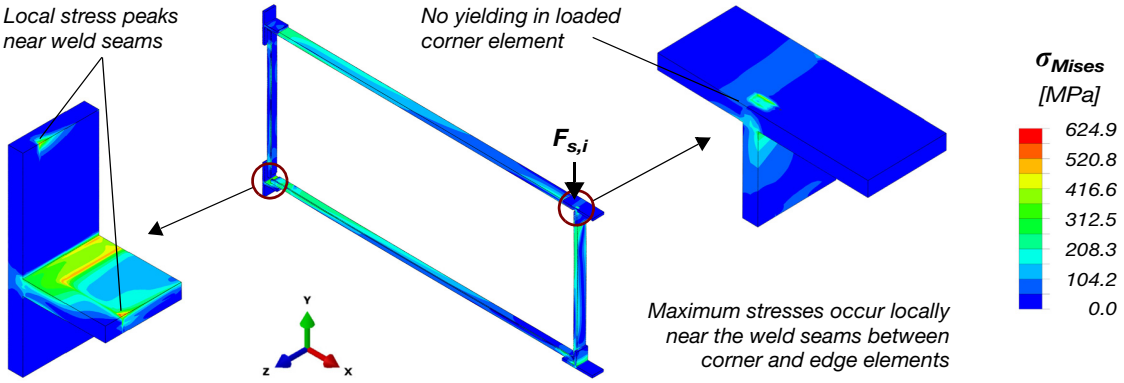

Fig. 7.20 *Mises stresses in the metal framing from the model for specimen Type 2B at an in-plane shear load of 130 kN*

7.2.3 Simulation results for other selected test series

In order to analyse the quality of the finite element models also for other loads and load combinations, simulations of the test series with out-of-plane loading alone up to *15 kN* and of the test series with out-of-plane loading of *10 kN* combined with an in-plane shear loading of *30 kN* (series no. 17 from Tab. 6.3) are performed. A simulation of the series with three combined loads (series no. 18) was avoided, since an exact reproduction is difficult due to the uncorrelated simultaneous application of the out-of-plane load and the in-plane shear load in the tests.

For an out-of-plane surface load equivalent to *15 kN*, a good agreement between experimental and simulation results can be noticed from Fig. 7.21 and Fig. 7.22 both for the out-of-plane displacements in the quarter points and in the midpoint of the compressed glass pane diagonal as well as for the in-plane displacements occurring at the free end and in the middle of the bottom edge element. For the experimental results plotted by continuous curves, only the first loading cycle is illustrated in the figures for better clarity.

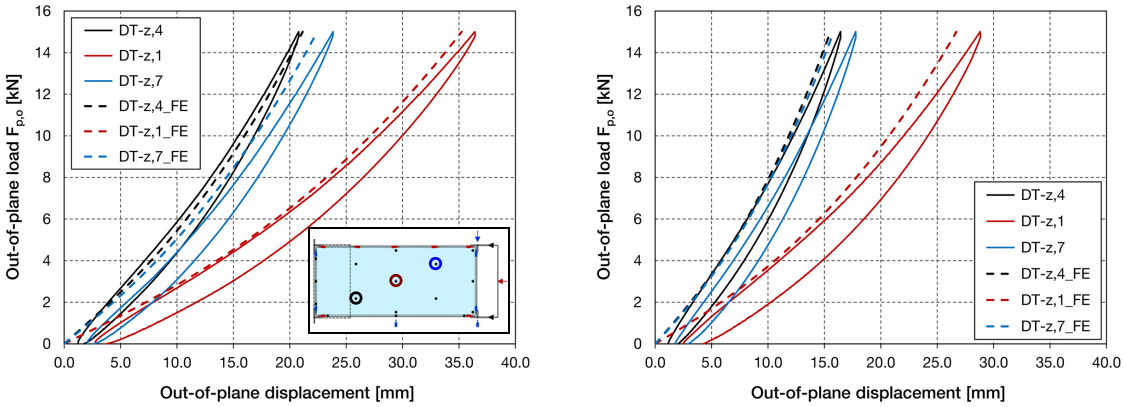

Fig. 7.21 *Comparison of experimental and simulation results for out-of-plane displacements along the compressed diagonal of the glass pane for specimens Type 1B (left) and Type 2B (right) under out-of-plane surface loading*

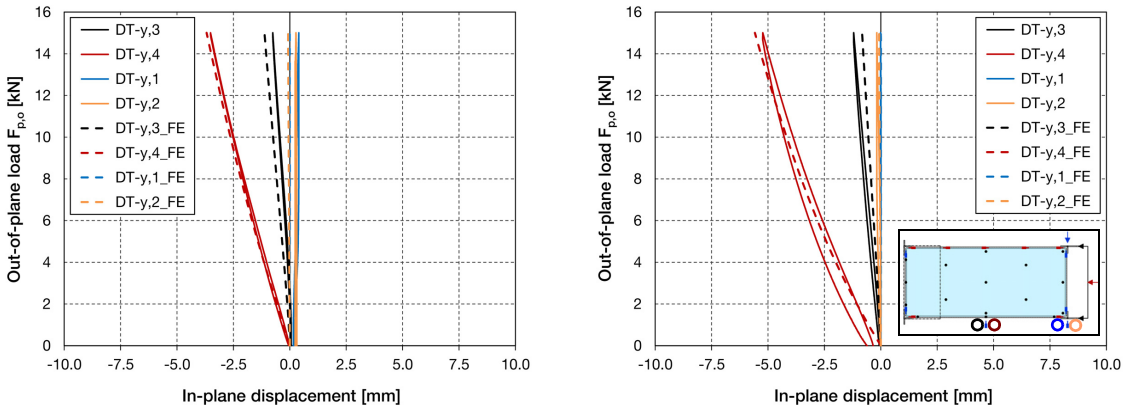

Fig. 7.22 *Comparison of experimental and simulation results for in-plane displacements in the middle of the bottom frame profile for specimens Type 1B (left) and Type 2B (right) under out-of-plane surface loading*

A summary of selected displacement and stress values obtained from the finite element simulations for the two investigated systems under an out-of-plane surface load equivalent to *15 kN* is provided in Tab. 7.3. It can be observed, that the stress values in all components are below the material strengths as well as below the yield stresses for materials exhibiting plasticity. However, it should be considered that the maximum out-of-plane displacements of the glass panes are larger than the limit of *L/100 = 15 mm* given in standards like [DIN 18008-2] or [ÖNORM B 3716-1] for linearly supported glazings.

Tab. 7.3 *Comparison of selected values obtained from the finite element simulations for the models of Type 1 and Type 2 under an out-of-plane surface loading equivalent to 15 kN*

Selected displacement and stress values	Unit	Model Type 1	Model Type 2
max. out-of-plane displacement of glass pane (+)	[mm]	35.2	26.7
max. principal stress in the glass pane	[MPa]	35.9	43.4
max. principal stress in the adhesive	[MPa]	0.75	7.89
max. Mises stress in the adhesive	[MPa]	0.75	4.73
max. Mises stress in the metal edge elements	[MPa]	199.8	178.9
max. Mises stress in the metal corner elements	[MPa]	140.3	127.4

The location of the maximum stresses is not evaluated in detail with contour plots for each component as it was done in the case of the failure tests in subchapter 7.2.2. The maximum Mises stresses in the framing components of both systems are occurring near the contact surfaces between fixed corner elements and longer edge elements. The maximum stresses in the adhesive joints are located at the inner edges of the contact surface between adhesive and glass pane.

Regarding the glass panes, different locations of the maximum principal stresses can be observed for the two systems. In the case of the system with silicone adhesive and grouting blocks, the maximum values are occurring on the front side of the glass pane in its centre, which is also the location of the maximum out-of-plane displacement, as well as near the two fixed corners in the vicinity of the grouting blocks (see Fig. 7.23, left). In the case of the system with acrylic adhesive, the maximum values are occurring on the back side of the glass pane near the adhesive joint to the fixed edge (see Fig. 7.23, right). These differences are caused by the different stiffness of the used adhesives.

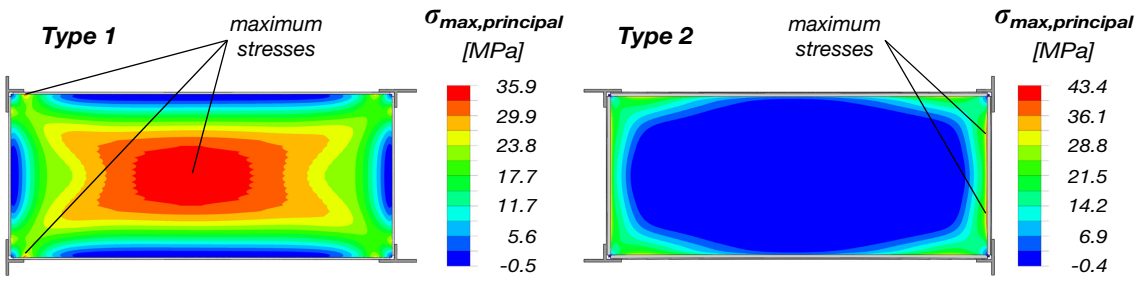

Fig. 7.23 *Maximum principal stresses in the glass panes from the models for specimens Type 1B (left) and Type 2B (right) under an out-of-plane surface load equivalent to 15 kN*

The same type of results are evaluated for the combined loading with an out-of-plane surface load equivalent to *10 kN* and an in-plane shear load of *30 kN*. The out-of-plane displacements in the selected points of the glass pane plotted *vs.* the in-plane shear load in Fig. 7.24 show a relatively good agreement between experimental and simulation results for both systems in terms of maximum values. However, it can be noticed that the experimentally determined curves for the examined load cycle show non-linear developments with a smaller inclination at the beginning of in-plane loading. This occurs probably due to the resilience of the air cushion used for out-of-plane loading in the tests, which is not considered in the simulation.

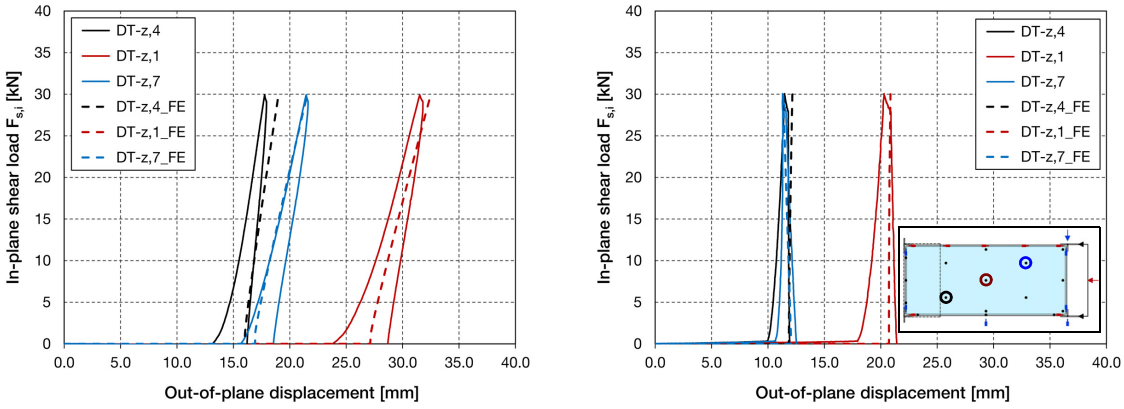

Fig. 7.24 *Comparison of experimental and simulation results for out-of-plane displacements along the compressed diagonal of the glass pane for specimens Type 1B (left) and Type 2B (right) under combined out-of-plane surface loading and in-plane shear loading*

The in-plane displacements examined at the bottom edge element of the framing, which are plotted vs. the in-plane shear load in Fig. 7.25, show as well a good general agreement between experimental and simulation values. Only in the case of the displacement in the middle of the framing element, recorded away from the glass pane ($DT_{y,4}$), a certain discrepancy can be noticed in the case of the system with acrylic adhesive (*Type 2*). A reason for this could be small deviations of the edge element dimensions between simulation and test.

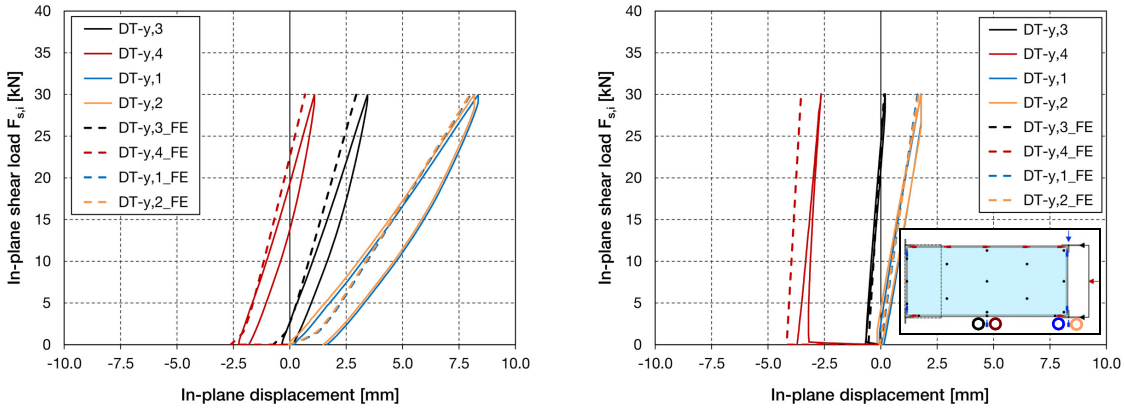

Fig. 7.25 *Comparison of experimental and simulation results for in-plane displacements in the middle of the bottom frame profile for specimens Type 1B (left) and Type 2B (right) under combined out-of-plane surface loading and in-plane shear loading*

The same selected displacement and stress values as in the case of out-of-plane loading alone are summarised in Tab. 7.4 for combined out-of-plane loading and in-plane shear loading. It can be generally noticed, that although the out-of-plane displacements of the glass pane are smaller, the in-plane shear loading leads to higher stress values in all components, except the glass pane of model *Type 2*. In the case of the model *Type 1* the increased stresses in the framing should be considered and lead to local yielding both in the top edge element and in the loaded corner element. The maximum stress values in the framing of model *Type 2* are rather singularities near the contact surfaces between edge elements and corner elements and therefore no yielding is expected in the metal framing.

Tab. 7.4 *Comparison of selected values obtained from the finite element simulations for the models of Type 1 and Type 2 under combined out-of-plane surface loading equivalent to 10 kN and in-plane shear loading of 30 kN*

Selected displacement and stress values	Unit	Model Type 1	Model Type 2
max. out-of-plane displacement of glass pane (+)	[mm]	32.4	20.9
max. principal stress in the glass pane	[MPa]	45.1	40.4
max. principal stress in the adhesive	[MPa]	1.23	12.34
max. Mises stress in the adhesive	[MPa]	1.51	6.21
max. Mises stress in the metal edge elements	[MPa]	255.6	298.4
max. Mises stress in the metal corner elements	[MPa]	392.6	380.3

The comparative studies between results from experimental testing and such obtained by finite element simulations prove that the proposed models including element types, material assumptions and interaction properties are suitable to a large extent for simulating the mechanical behaviour of glass-metal elements with composite structural behaviour by adhesive bonding. However, it should be considered that the validity of the models is limited to the boundary conditions investigated in this thesis, which address ambient conditions. Moreover, improvements of the models, especially in terms of material properties for the load transfer materials, are still possible and will be briefly pointed out in subchapter 9.2.

Based on the results of these comparative studies, the hyperelastic *Mooney-Rivlin* model will be used for the silicone and the fitted strain rate dependent plastic model will be used for the acrylic in the following two subchapters.

7.3 Parametric study on large-scale multi-component elements

In subchapter 7.2 the performed experimental failure tests along with other selected test series on large-scale multi-component elements are simulated with the finite element analysis software *Abaqus 6.14*. The assumptions made for the two models (*Type 1* and *Type 2*) regarding material properties, interaction between the components and boundary conditions lead to a generally good agreement between experimental results and simulation results. However, as already pointed out in subchapter 6.2.1, the dimensioning of the different components of the test specimens is carried out rather conservative in order to avoid undesired failure occurrence (e.g. fracture in the metal components). The main objective in this subchapter is to investigate how the mechanical behaviour of the glass-metal elements with composite structural behaviour by adhesive bonding and especially the deformation behaviour are influenced by modifying selected parameters. The tendencies obtained from the results of these parameter studies should improve the understanding for how the innovative structural elements function from a mechanical point of view. Furthermore, these tendencies will ease the initial dimensioning of the different components for preliminary designs.

Before varying parameters regarding the geometry of the components and the stiffness of the adhesives, two other studies are carried out. In subchapter 7.3.1 the influence of different support conditions of the elements on their deformation behaviour is investigated. In subchapter 7.3.2 the potential of the two glass-metal element types with composite structural behaviour is emphasized by comparing their first eigenmodes and eigenvalues to those of subsidiary systems consisting of the glass pane alone and of the framing alone, respectively. The parametric studies are divided into variation of the glass pane height and assembly, variation of the metal framing depth and metal corner thickness as well as variation of the adhesive joint geometry and stiffness (Young‘s modulus). A matrix with the varied parameters and the investigated values for the systems of *Type 1* and of *Type 2* is given in Tab. 7.5. Finally, the influence of different shapes and sizes of initial geometric imperfections is evaluated in subchapter 7.3.9

Tab. 7.5 *Parameter values investigated in finite element simulations for the large-scale multi-component glass-metal elements with composite structural behaviour*

Parameter		**Unit**	**Investigated values** [a]				
Glass pane height		[mm]	1 500	2 500	**3 500**	4 500	5 500
Glass pane assembly		[mm]	6	10	**6/1.52/6**	10/1.52/10	-
Framing - depth		[mm]	10	50	**100**	150	200
Framing - corner thickness		[mm]	5	10	15	20	**25**
Adhesive - cross section	Type 1	[mm]	10 x 6	15 x 6	**20 x 6**	20 x 3	20 x 9
	Type 2	[mm]	10 x 3	15 x 3	**20 x 3**	20 x 1	20 x 2
Adhesive - Young‘s modulus	Type 1	[MPa]	**2.4**	1	10	100	1 000
	Type 2	[MPa]	**250**	1	10	100	1 000

[a] Values used for the reference system are provided in bold

The varied parameters regarding the geometry of the different components are illustrated for a better understanding by the sketches in Fig. 7.26.

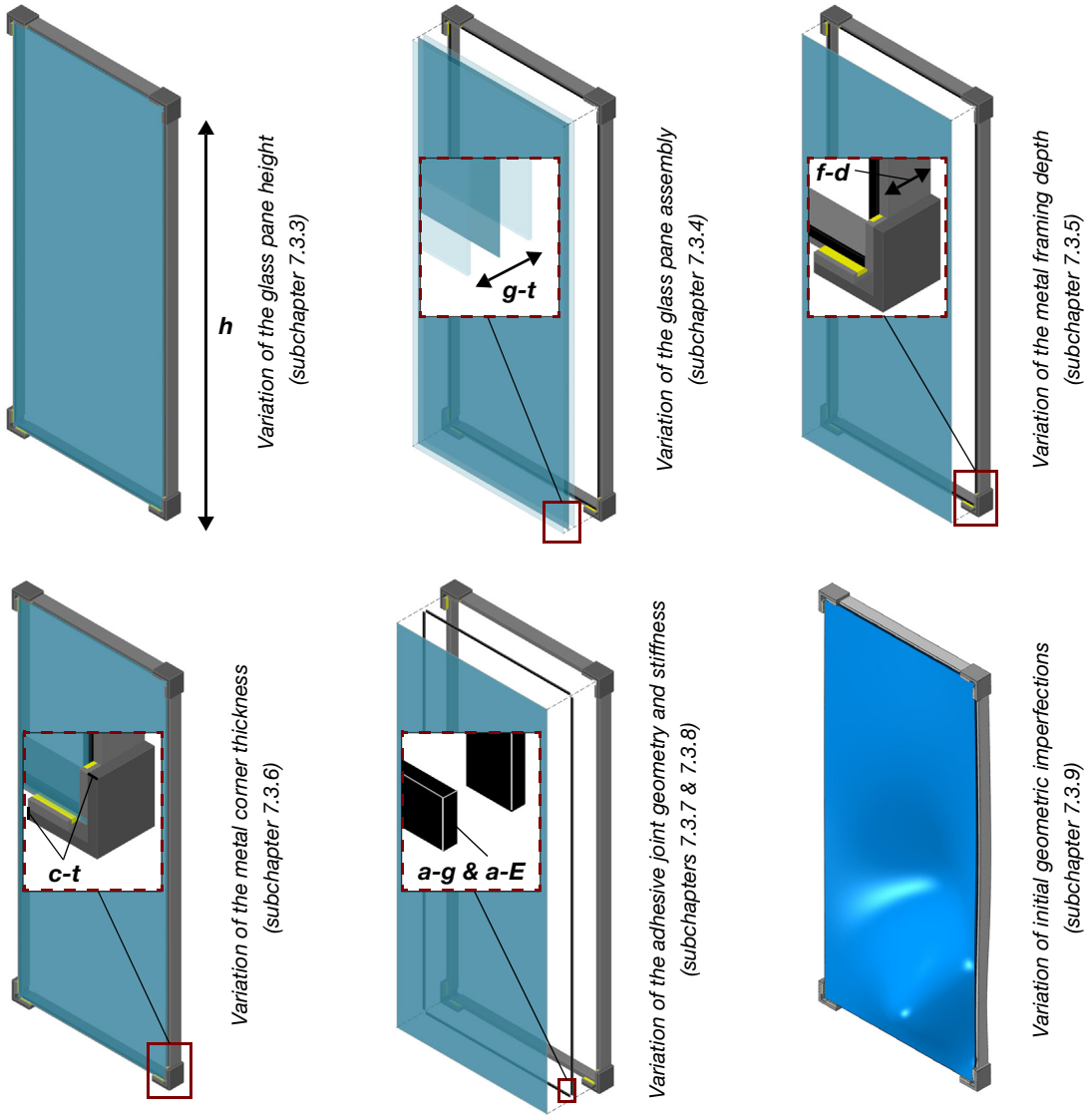

Fig. 7.26 *Sketches illustrating the varied parameters regarding the geometry of different components belonging to the glass-metal elements with composite structural behaviour based on the system with silicone adhesive bonding and grouting blocks (Type 1)*

7.3.1 Investigation of different support conditions

The support conditions for facade elements in general and implicitly for glass-metal elements of the type investigated in this thesis depend on the specific application and can have a significant influence on the deformation behaviour of the elements and subsequently on occurring stresses in their components. In the case of the experimentally investigated glass-metal elements, two corners of the framing, representing the two bottom corners of a standing facade element, are fixed (all degrees of freedom are locked). For the other two corners of the framing, representing the top corners of a standing facade element, the out-of-plane translational degree of freedom is locked. Such a situation would be obtained if pendulum rods for transferring out-of-plane loads would ensure the connection between the element‘s corners and the main structure behind the facade (see Fig. 3.2, right, in chapter 3). However, due to the design of the in-plane load application in the test setup, a free rotation of these two corner elements is restrained as well. In the finite element simulations from subchapter 7.2 this is taken into account by locking all rotational degrees of freedom for the load application reference points.

The support conditions used in the experimental tests can be assumed to be representative for single-storey facade elements. When considering a transparent facade consisting of several elements over its height (as illustrated in Fig. 3.1, left, and in Fig. 3.2, right), the support conditions used in the experimental tests are not representative for all elements, but only, with restrictions, for the bottom row. In the case of the elements positioned in higher rows, all element corners can be subjected to rotations as well. For the elements belonging to the bottom row only the top corners can be subjected to rotations. The influence of different support conditions on the eigenvalues and eigenmodes as well as on the occurring deformations in selected points is studied in this subchapter. Three additional support conditions (SC) to those used in the experimental tests are investigated:

- **SC of type (a):** are representative for the bottom row elements in a facade consisting of several elements over its height (see Fig. 7.27, top);

- **SC of type (b):** are representative for the elements not belonging to the bottom row of a facade consisting of several elements over its height (see Fig. 7.27, middle);

- **SC of type (c):** are representative for single-storey facade elements spanning from floor to floor (see Fig. 7.27, bottom).

The schematic representations in Fig. 7.27 show sketches of the meshed corners of the finite element models for the two systems (*Type 1* and *Type 2*). The position of the reference points (RP) and the corresponding surfaces used to apply the support conditions (SC) are illustrated for the three different mentioned alternatives. The reference points RP1, RP2, RP3 and RP4, when used, are connected to the rear overlap surface of the two legs of the corner elements. They are only used to restrain the out-of-plane translational degree of freedom (u_z). The reference points RP5 and RP6 are used to apply the boundary conditions on the two bottom corners and are connected with rigid body constraints to the blue-framed surfaces. The reference points RP7 and RP8 are connected to the orange-framed surfaces of the top corners when used for application of the in-plane axial load ($F_{n,i}$). When used for the application of the in-plane shear load ($F_{s,i}$), the reference point RP7 is connected to the dark-red-framed surfaces.

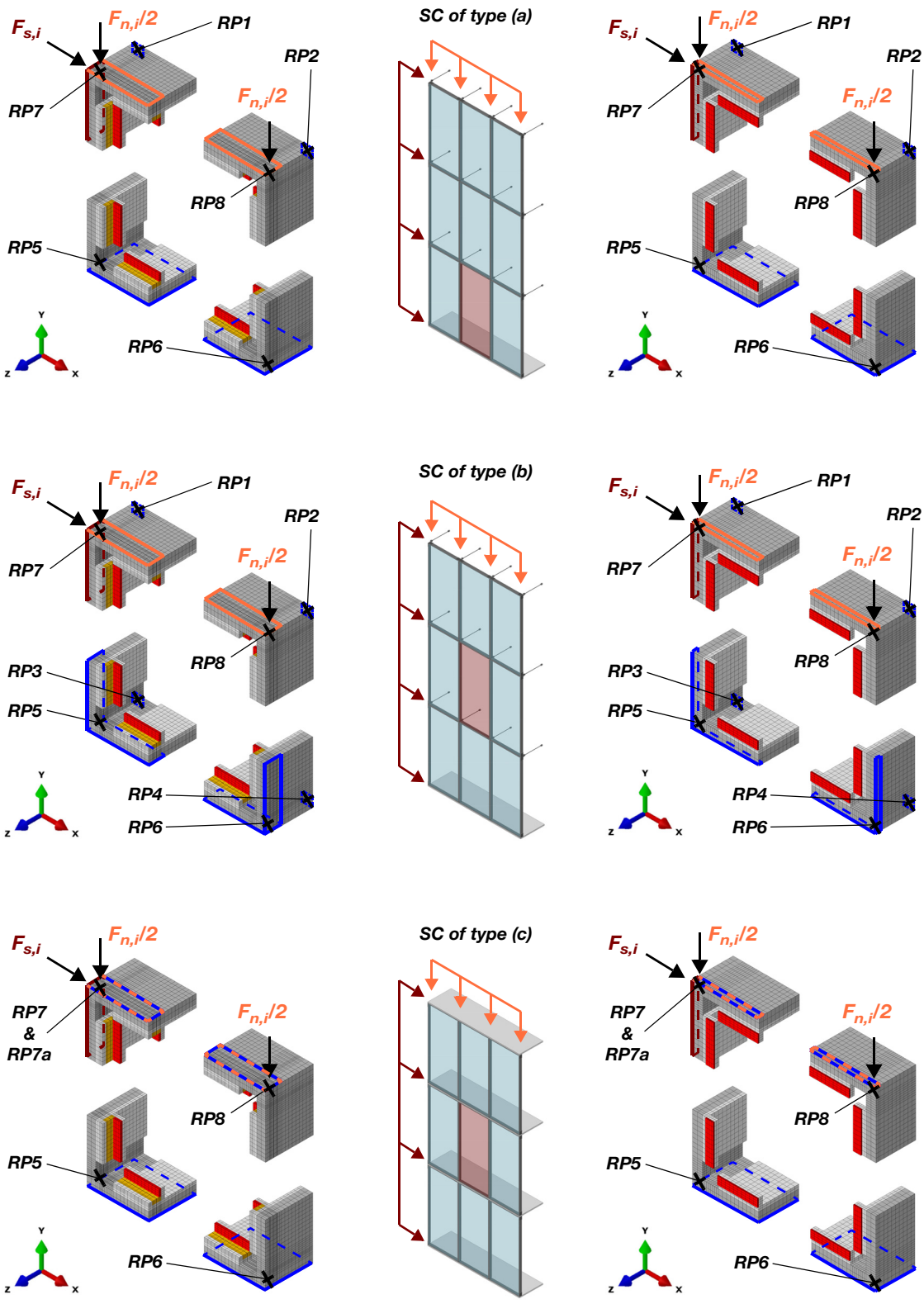

Fig. 7.27 *Schematic representation of the reference points and the constrained surfaces used for the support conditions of type (a), type (b) and type (c) in the models of Type 1 (left) and in the models of Type 2 (right)*

The finite element models are slightly modified for the parametric studies compared to those described in Fig. 7.1, Fig. 7.2 and Fig. 7.3. These modifications will be used throughout the following subchapters. Firstly, the glass-metal elements are modelled in a standing position, as they would be generally used in real applications instead of the landscape format used for the experimental testing due to the boundary conditions given in the laboratory. Secondly, the corner elements, which have a T-shaped geometry based on the test specimens, are reduced to an L-shaped geometry for the parametric studies. This simplification reduces the modelling and computational efforts and has negligible influence on the results from investigations on a single element. Thirdly, the depth of the corner elements is reduced to be equal to the depth of the edge elements in the case of the models for the system with perimetrical acrylic adhesive joints (*Type 2*). This modification is carried out considering the load transfer path between the framing and the glass pane over the one-sided adhesive joint. Furthermore, this design, which makes more sense with respect to a further development of the glass panes to insulating glass units, allows to reduce the length of the shorter leg of the framing edge elements from *40 mm* to *30 mm*.

The position of the reference points as well as the size and the position of the corresponding surfaces for the support conditions equivalent to those used in subchapter 7.2 are similar to those illustrated for SC of *type (a)*. The restrained degrees of freedom on each reference point for the support conditions equivalent to those used in the simulation of the failure tests and in subchapter 7.2 and for the support conditions of *type (a)*, *type (b)* and *type (c)* are summarized in Tab. 7.6.

Tab. 7.6 *Restrained degrees of freedom of the reference points for the support conditions equivalent to those used in subchapter 7.2 and those of type (a), type (b) and type (c)*

Reference point (RP)	**Investigated support conditions (SC)**			
	SC from tests	**SC of type (a)**	**SC of type (b)**	**SC of type (c)**
RP1	$u_z = 0$	$u_z = 0$	$u_z = 0$	*RP not used*
RP2	$u_z = 0$	$u_z = 0$	$u_z = 0$	*RP not used*
RP3	*RP not used*	*RP not used*	$u_z = 0$	*RP not used*
RP4	*RP not used*	*RP not used*	$u_z = 0$	*RP not used*
RP5	$u_x = u_y = u_z = 0$ $\varphi_x = \varphi_y = \varphi_z = 0$	$u_y = u_z = 0$ $\varphi_x = \varphi_y = \varphi_z = 0$	$u_y = 0$	$u_y = u_z = 0$ $\varphi_x = \varphi_y = \varphi_z = 0$
RP6	$u_x = u_y = u_z = 0$ $\varphi_x = \varphi_y = \varphi_z = 0$	$u_x = u_y = u_z = 0$ $\varphi_x = \varphi_y = \varphi_z = 0$	$u_x = u_y = 0$	$u_x = u_y = u_z = 0$ $\varphi_x = \varphi_y = \varphi_z = 0$
RP7	$u_z = 0$ $\varphi_x = \varphi_y = \varphi_z = 0$	only load application	only load application	$u_z = 0$ $\varphi_x = \varphi_y = \varphi_z = 0$
RP7a [a]	*RP not used*	*RP not used*	*RP not used*	only load application
RP8	$u_z = 0$ $\varphi_x = \varphi_y = \varphi_z = 0$	only load application	only load application	$u_z = 0$ $\varphi_x = \varphi_y = \varphi_z = 0$

[a] RP7a has the same position as RP7 and is only required in the case of the support condition of type (c) to apply the in-plane shear load since different surfaces are connected by rigid body constraints to RP7 (support) and RP7a (load application)

In a first step, the first eigenvalues obtained under in-plane axial loading ($F_{n,i}$) and under in-plane shear loading ($F_{s,i}$) with the different support conditions are compared to each other (see Tab. 7.7). Since a unit load is applied in both cases ($F_{s,i} = 1.0$ acting horizontally on RP7 and $F_{n,i}/2 = 0.5$ acting vertically on RP7 and on RP8, respectively), the obtained eigenvalues can be considered as a kind of critical buckling loads for the systems. For both loading types, the highest values are reached with the support conditions of *type (c)* in the case of the system *Type 1* and with the support conditions from tests in the case of the system *Type 2*. The lowest values result with the support conditions of *type (b)* for both systems. The eigenvalues determined for the support conditions used in the simulations of the experimental tests are situated in the range of the values obtained with support conditions of *type (c)*.

Tab. 7.7 *First eigenvalues determined under in-plane axial loading and under in-plane shear loading for the support conditions equivalent to those used in the simulations of the failure tests and for the support conditions of type (a), type (b) and type (c)*

Support conditions (SC)	**First eigenvalues [kN]**			
	In-plane axial load $F_{n,i}$		**In-plane shear load $F_{s,i}$**	
	Type 1	**Type 2**	**Type 1**	**Type 2**
SC from tests	208.742	281.985	76.577	140.854
SC of type (a)	198.245	260.302	73.987	136.406
SC of type (b)	155.076	208.947	65.580	111.904
SC of type (c)	210.330	280.023	79.647	139.149

In a second step, the displacement behaviour of the elements under in-plane shear loading is analysed. The shear load is applied displacement-controlled as it is the case in the experiments. A displacement rate of *5 mm/min* is chosen. The following diagrams are used to compare occurring displacement values for the different investigated parameters (support conditions):

- in-plane shear load *vs.* in-plane horizontal displacement measured at the reference point for shear load application (RP7);
- in-plane shear load *vs.* out-of-plane displacement measured at the top quarter-point of the compressed glass pane diagonal;
- in-plane shear load *vs.* out-of-plane displacement measured at the bottom quarter-point of the compressed glass pane diagonal;
- out-of-plane displacements along the compressed glass pane diagonal at a horizontal in-plane displacement of the reference point for shear load application of *20 mm* (a normalised length of the diagonal is used in the diagrams);
- in-plane shear load *vs.* maximum positive relative displacement between glass pane and metal framing (a positive displacement is considered when a gap is resulting between glass pane edge and grouting blocks in case of model *Type 1* or when the distance between glass pane edge and corner elements is increasing in case of model *Type 2*) - these displacements are measured at the bottom left corner in vertical direction between the exterior glass pane and the corner element;

- in-plane shear load *vs.* maximum negative relative displacement between glass pane and metal framing (a negative displacement is considered when the glass pane edge is pressed into the grouting blocks in case of model *Type 1* or when the distance between glass pane edge and corner elements is decreasing in case of model *Type 2*) - these displacements are measured in vertical direction between the interior glass pane and the corner element at the top left corner for model *Type 1* and at the bottom right corner for model *Type 2*.

Throughout the subchapters 7.3 and 7.4, the diagrams on the left show results obtained for the model of *Type 1*, while the diagrams on the right illustrate results for the model of *Type 2*. Generally, the same ranges are chosen for the axes to allow a direct comparison. In the case of the load *vs.* displacement diagrams, additional to the curves obtained without initial geometric imperfections (continuous curves) also curves obtained with an initial geometric imperfection of *L/500* (*L* being the longer edge length of the glass pane) are provided (dashed curves with short dashes). Furthermore, the critical buckling loads determined based on the first eigenvalues are indicated by dashed lines with long dashes. Moreover, on the curves without initial imperfections three different points are highlighted as follows:

- a black triangle with coloured filling (▲) represents the point at which a maximum principal stress of *70 MPa* is reached in the glass pane (characteristic strength for heat strengthened glass);
- a black diamond with coloured filling (♦) represents the point at which a maximum principal stress of *120 MPa* is reached in the glass pane (characteristic strength for thermally toughened glass);
- a coloured circle with grey filling (●) represents the point at which a maximum principal stress of *1 MPa* is reached in the silicone adhesive or a maximum Mises stress of *10 MPa* is reached in the acrylic adhesive.

In a third step, the out-of-plane displacements along the same diagonal as considered in the case of shear loading (compressed diagonal) are compared for an out-of-plane load of *2.0 kPa*, applied as a suction load on the full area of the exterior glass pane. The same type of results are evaluated in the subchapters 7.3.3 to 7.3.8 for the other investigated parameters.

The influence of the different support conditions on the mechanical behaviour of the glass-metal elements is evaluated under in-plane shear loading as findings regarding the in-plane global behaviour of the elements, the out-of-plane displacements of the glass panes and the relative in-plane displacements between the glass pane and the metal framing. Under out-of-plane surface loading, findings based on the out-of-plane displacements of the glass panes are given. The same type of evaluation is carried out in the subchapters 7.3.3 to 7.3.8 for the other varied parameters.

Findings regarding the influence of different **support conditions** on the **global in-plane behaviour** for the glass-metal elements under in-plane shear loading (see Fig. 7.28):

- the lowest in-plane stiffness is obtained for both model types with the support conditions of *type (b)* since a rotation of both the top and the bottom corner elements is allowed;

- for the model of *Type 2*, no significant differences regarding in-plane stiffness is noticed between the support conditions corresponding to the tests and those of *type (a)* and of *type (c)*;
- the results obtained with initial geometric imperfections (dashed curves) show no significant differences to those obtained without imperfections (continuous curves);
- the maximum principal stress of *1 MPa* in the silicone adhesive (model *Type 1*) is reached at approximately the same in-plane displacement (*~8 mm*) for all support conditions;
- the Mises stress of *10 MPa* in the acrylic adhesive (model *Type 2*) is reached for all support conditions at approximately the same in-plane displacement (*~10 to 12 mm*), at which also the change in in-plane stiffness of the system can be roughly observed;
- the critical loads determined based on eigenvalues are exceeded in the simulations for models of *Type 1*, which is not the case for models of *Type 2*;
- in the case of the models of *Type 2*, the framing starts to slide parallel to the glass pane after yielding of the acrylic adhesive, which leads to a kind of column buckling of the compressed edge element; this behaviour determines the reached maximum loads; the maximum principal stresses of *120 MPa* in the glass panes are reached after the column buckling starts.

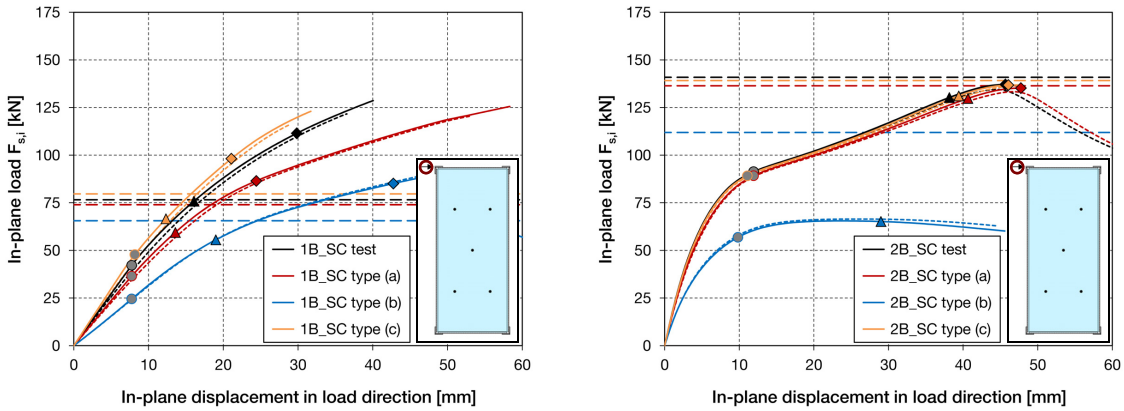

Fig. 7.28 *In-plane shear load vs. in-plane horizontal displacement measured at reference point RP7 for model Type 1 (left) and model Type 2 (right) with the different analysed support conditions*

Findings regarding the influence of different **support conditions** on the **out-of-plane displacements** of the glass panes for the glass-metal elements under in-plane shear loading (see Fig. 7.29, Fig. 7.30, Fig. 7.31 and Fig. 7.32):

- the out-of-plane displacements of the glass panes for the models with support conditions used in the tests as well as with support conditions of *type (a)* and of *type (c)* are oriented to opposite directions in the case of models of *Type 1* and of *Type 2*;
- the applied initial geometric imperfections reduce the out-of-plane deformations at the bottom quarter-point of the compressed diagonal for models of *Type 1* and slightly increase these displacements at both the top and the bottom quarter-points for models of *Type 2*;

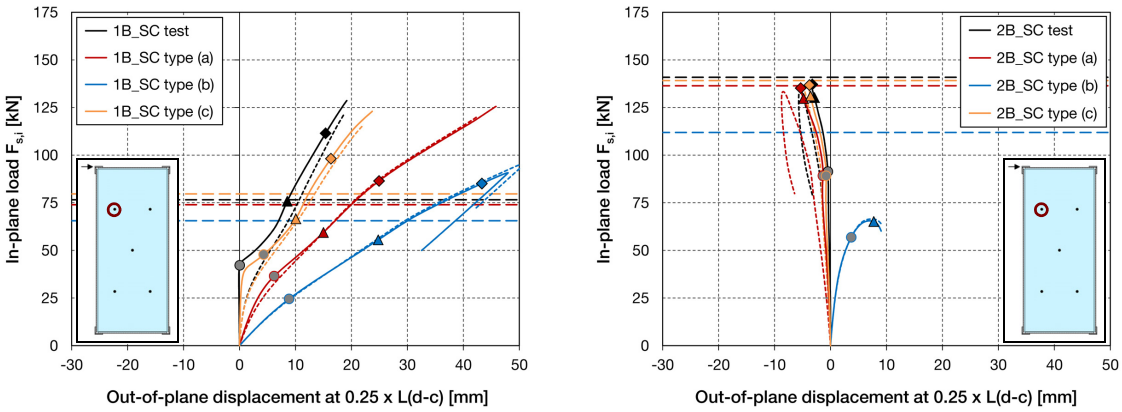

Fig. 7.29 *In-plane shear load vs. out-of-plane displacement measured at the top quarter-point of the compressed glass pane diagonal for model Type 1 (left) and model Type 2 (right) with the different analysed support conditions*

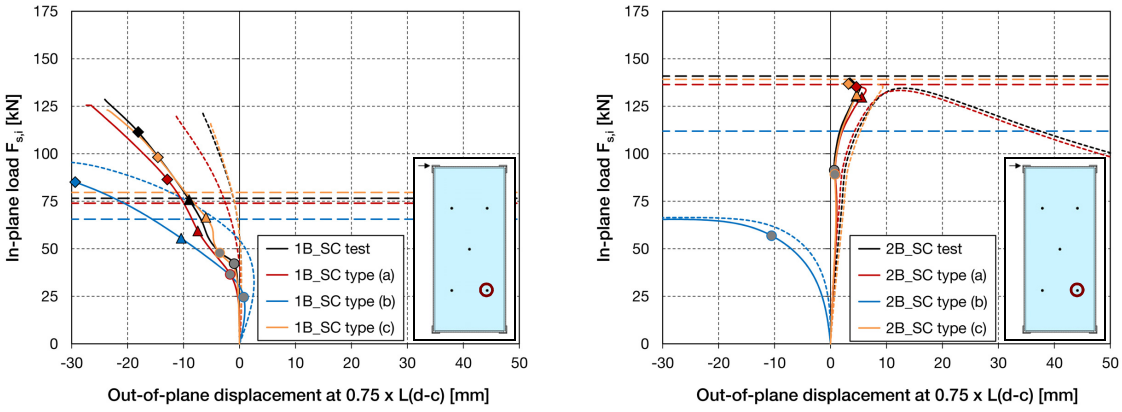

Fig. 7.30 *In-plane shear load vs. out-of-plane displacement measured at the bottom quarter-point of the compressed glass pane diagonal for model Type 1 (left) and model Type 2 (right) with the different analysed support conditions*

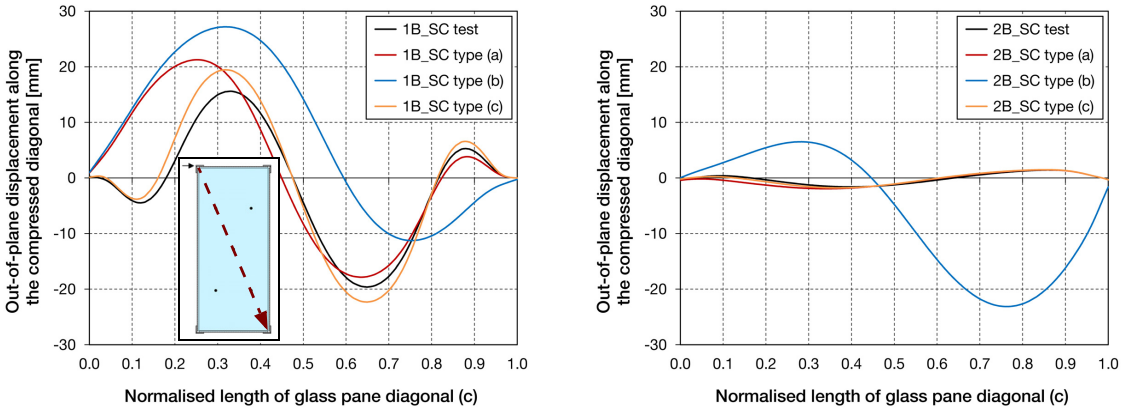

Fig. 7.31 *Out-of-plane displacements along the compressed glass pane diagonal at a horizontal in-plane displacement of the reference point for shear load application of 20 mm for model Type 1 (left) and model Type 2 (right) with the different analysed support conditions (no initial imperfections)*

- the out-of-plane displacements of the glass pane occur mainly due to plate buckling in the case of the models of *Type 1*, while they mainly start to increase due to buckling of the compressed edge element in its vicinity in the case of models of *Type 2*;
- the larger out-of-plane displacements of the glass panes indicate a better activation of this component in the case of the elements with silicone adhesive and grouting (*Type 1*).

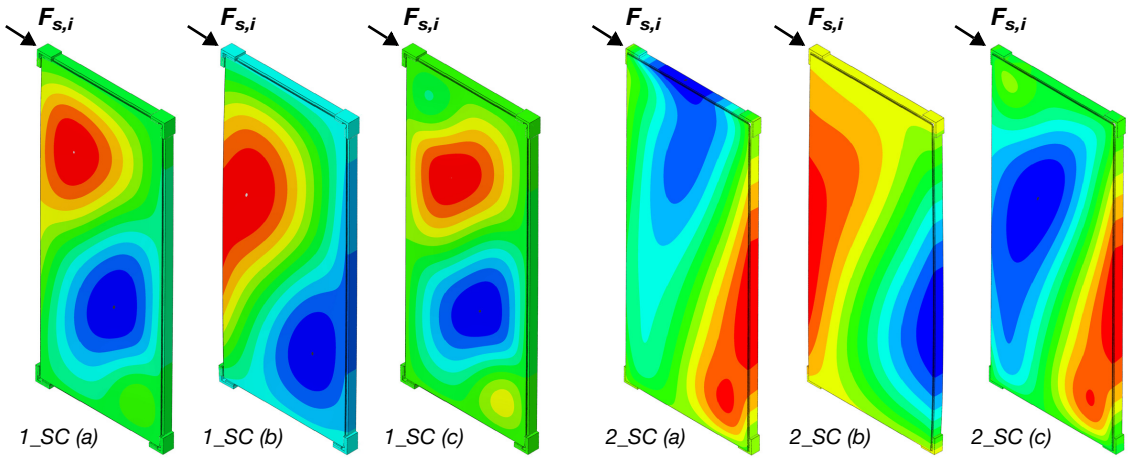

Fig. 7.32 *Qualitative out-of-plane displacements at a horizontal in-plane displacement of the reference point for shear load application of 20 mm with support conditions (SC) of type (a), of type (b) and of type (c) for model Type 1 (left) and model Type 2 (right)*

Findings regarding the influence of different **support conditions** on the **relative in-plane displacements** between glass pane and metal framing for the glass-metal elements under in-plane shear loading (see Fig. 7.33 and Fig. 7.34):

- the maximum positive relative in-plane displacements are significantly higher than the negative ones for models of *Type 1*, while they have similar sizes for models of *Type 2* - this is in accordance with the different load transfer concepts;
- initial geometric imperfections have almost no influence on relative in-plane displacements.

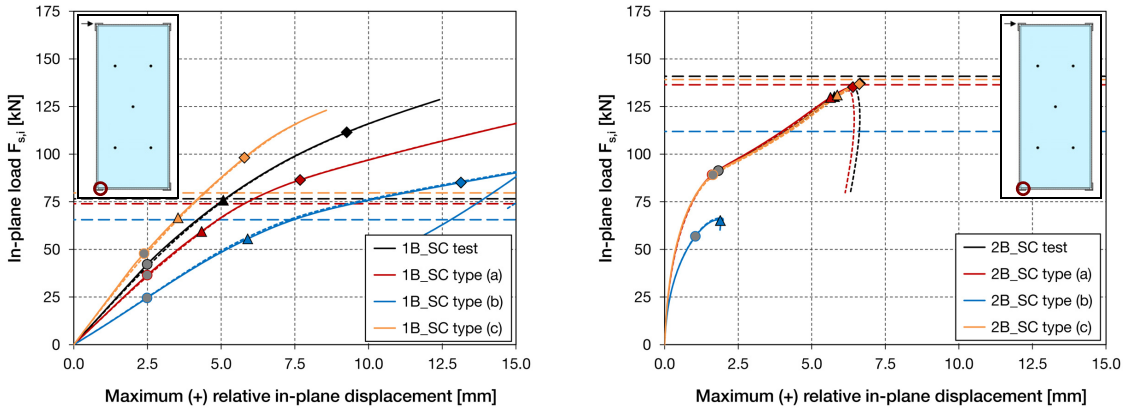

Fig. 7.33 *Maximum positive relative in-plane displacements between glass pane and metal framing for model Type 1 (left) and model Type 2 (right) with the different analysed support conditions*

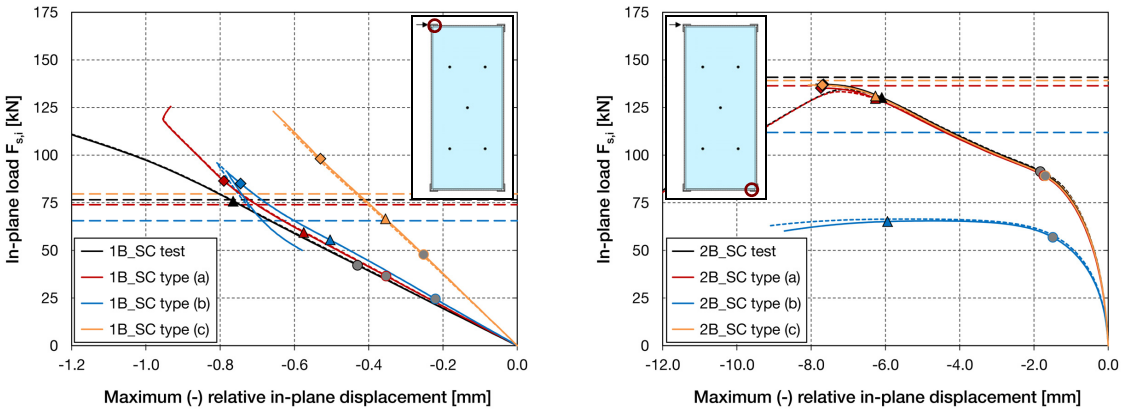

Fig. 7.34 *Maximum negative relative in-plane displacements between glass pane and metal framing for model Type 1 (left) and model Type 2 (right) with the different analysed support conditions (different ranges are used for the x-axis in the two diagrams)*

Findings regarding the influence of different **support conditions** on the **out-of-plane displacements** of the glass panes for the glass-metal elements under out-of-plane surface loading (see Fig. 7.35):

- the highest out-of-plane displacements result for the simulations with support conditions of *type (b)*, while in the case of the other support conditions only small differences are noticed.

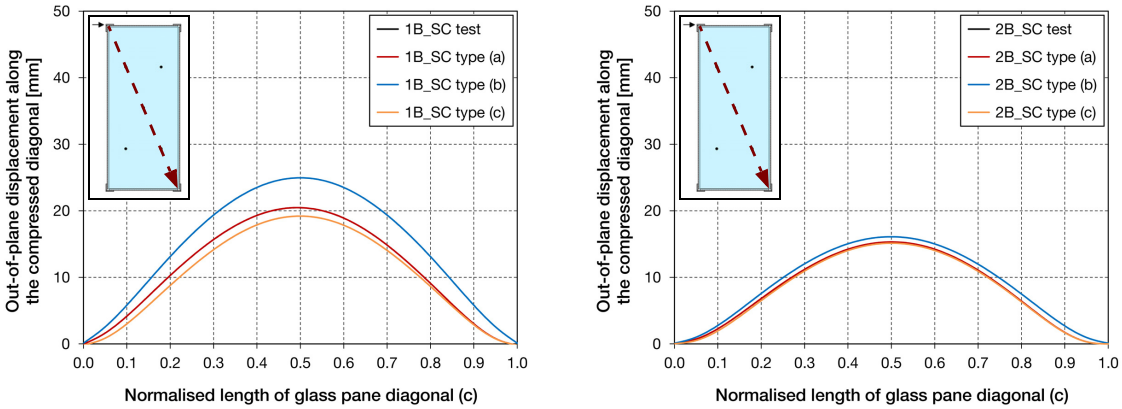

Fig. 7.35 *Out-of-plane displacements along one diagonal (compressed glass pane diagonal under shear loading) under a wind suction load of 2.0 kPa for model Type 1 (left) and model Type 2 (right) with the different analysed support conditions*

The influence of different parameters on the mechanical behaviour of the glass-metal elements with composite structural behaviour is investigated in the next subchapters (7.3.2 to 7.3.9 and 7.4.1 to 7.4.4) on systems with support conditions of *type (a)*. This decision is made based on the fact, that in a facade with several elements over its height, generally, the bottom row of elements would receive the highest loads.

7.3.2 Eigenmodes and eigenvalues of subsidiary systems

Before discussing the influence of the parameters listed in Tab. 7.5 on the mechanical performance of the glass-metal elements with structural composite behaviour, the potential of these elements is emphasised in this subchapter by comparing their first eigenvalues to those obtained for their subsidiary systems. Since the investigated glass-metal elements consist of a glass pane and a metal framing which are bonded together either by perimetrical silicone adhesive joints and local grouting blocks (*Type 1*) or by perimetrical acrylic adhesive joints (*Type 2*), the glass pane on its own and the metal framing on its own are considered their subsidiary systems. For the glass pane, two different alternatives are analysed. In the case of both alternatives the glass pane is supported in-plane by setting blocks, as in the system of *Type 1*. The loads and the boundary conditions are applied on reference points which are connected to the setting blocks by rigid body constraints. The difference between the two alternatives consists in the out-of-plane support of the glass pane, which in the first case is only local near the corners (see Fig. 7.36, left) and in the second one is along its whole perimeter (see Fig. 7.36, right).

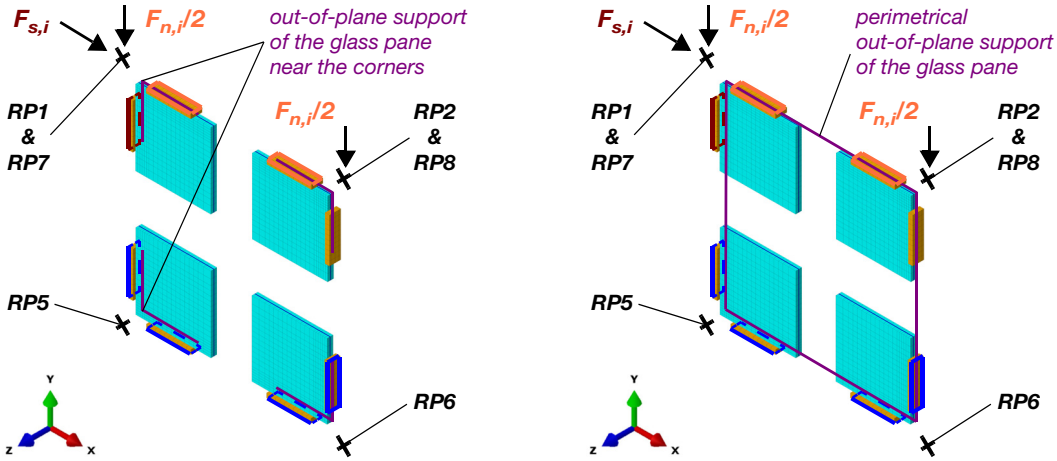

Fig. 7.36 *Schematic representation of the reference points, the constrained surfaces and the out-of-plane support conditions used for the system (i) (left) and for the system (ii) (right)*

Five different systems are included in this study, as listed below:

(i) glass pane with hinged out-of-plane support along the setting block length near all four corners and in-plane support over the setting block length near the two bottom corners (see Fig. 7.36, left);

(ii) glass pane with hinged perimetrical out-of-plane support (Navier) and in-plane support over the setting block length near the two bottom corners (see Fig. 7.36, right);

(iii) metal framing on its own with support conditions of *type (a)* according to subchapter 7.3.1 (the metal framing is modelled as used for the systems of *Type 2* without the supports for grouting blocks);

(iv) glass-metal element with composite structural behaviour by perimetrical silicone adhesive bonding and grouting blocks near the corners with support conditions of *type (a)* according to subchapter 7.3.1;

(v) glass-metal element with composite structural behaviour by perimetrical acrylic adhesive bonding with support conditions of *type (a)* according to subchapter 7.3.1.

The first eigenvalues and the corresponding eigenmodes are determined for two different geometries of the glass pane and under three different loading directions. In the case of the glass pane geometry, a rectangular shape with the size of *1.5 m x 3.5 m* and a quadratic shape with an edge length of *1.5 m* are used. For the loads, an in-plane vertical load (axial load), an in-plane horizontal load (shear load) and an in-plane diagonal load are considered. The diagonal loading is added to this study because it could be more appropriate than the shear loading as an equivalent load resulting in systems consisting of several elements. The resulting shapes of the eigenmodes for this type of loading are a combination of those observed under axial loading and under shear loading.

The first eigenvalues for all the different systems investigated in this subchapter are provided in Tab. 7.8, while the corresponding eigenmodes are depicted in Fig. 7.37, Fig. 7.38 and Fig. 7.39 for the rectangular glass pane geometry and in Fig. 7.40, Fig. 7.41 and Fig. 7.42 for the quadratic one. For both geometries, but especially for the rectangular one, it can be noticed that the eigenvalues determined for *system (i)* and *system (iii)* are significantly lower than those obtained for *system (iv)* and *system (v)*, without depending on the loading direction. A perimetrical hinged support of the glass pane as in the case of *system (ii)* allows for a substantial increase of the eigenvalues compared to *system (i)*. This fact is also indicated by the similar first eigenmodes determined for *system (ii)* and for the two investigated systems for glass-metal elements with composite structural behaviour (see *system (iv)* and *system (v)* in Fig. 7.37 to Fig. 7.42). However, a reduction of the framing depth and implicitly of its out-of-plane stiffness in the case of *system (iv)* and *system (v)* leads to a reduction of the eigenvalues and to a modification of the eigenmodes from shapes similar to the eigenmodes of *system (ii)* to shapes similar to the eigenmodes of *system (i)*.

Tab. 7.8 *First eigenvalues determined under in-plane axial loading, in-plane shear loading and in-plane diagonal loading for the two investigated element types and their subsidiary systems with rectangular geometry (1.5 m x 3.5 m) and quadratic geometry (1.5 m x 1.5 m) of the glass pane*

Subsidiary system	**First eigenvalues [kN]**					
	Rectangular geometry			**Quadratic geometry**		
	axial load	**shear load**	**diagonal load**	**axial load**	**shear load**	**diagonal load**
System (i)	14.842	8.129	14.906	36.407	22.763	29.118
System (ii)	108.928	48.736	100.511	166.650	96.260	108.018
System (iii)	14.431	10.453	13.998	78.251	67.460	76.791
System (iv)	198.245	73.987	138.227	362.660	137.664	155.760
System (v)	260.302	136.406	193.734	657.944	201.132	239.026

By an optimised dimensioning of the glass pane and the metal framing depending on each other, combined with the application of suitable load transfer mechanisms between them, the material consumption can be reduced and the mechanical performance of glass-metal elements with composite structural behaviour can be maximized.

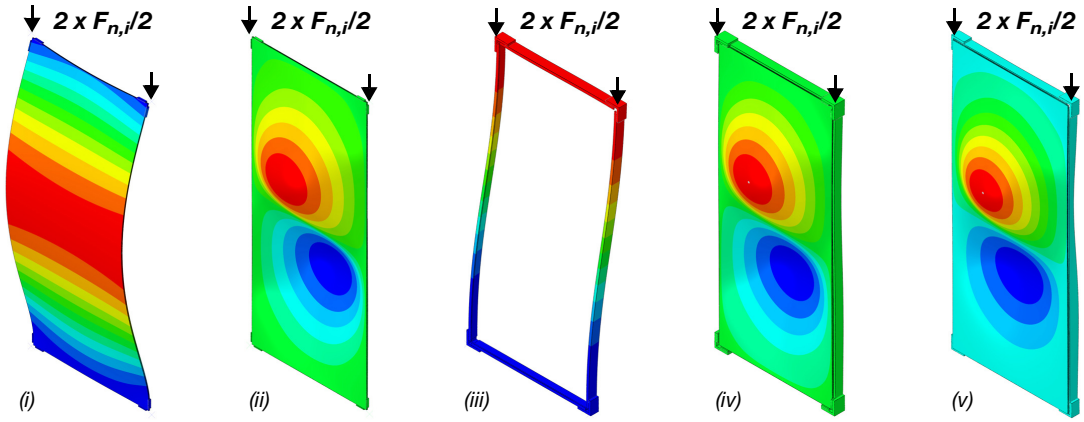

Fig. 7.37 *First eigenmodes determined under in-plane axial loading for the two investigated element types and their subsidiary systems with rectangular geometry of the glass pane (1.5 m x 3.5 m)*

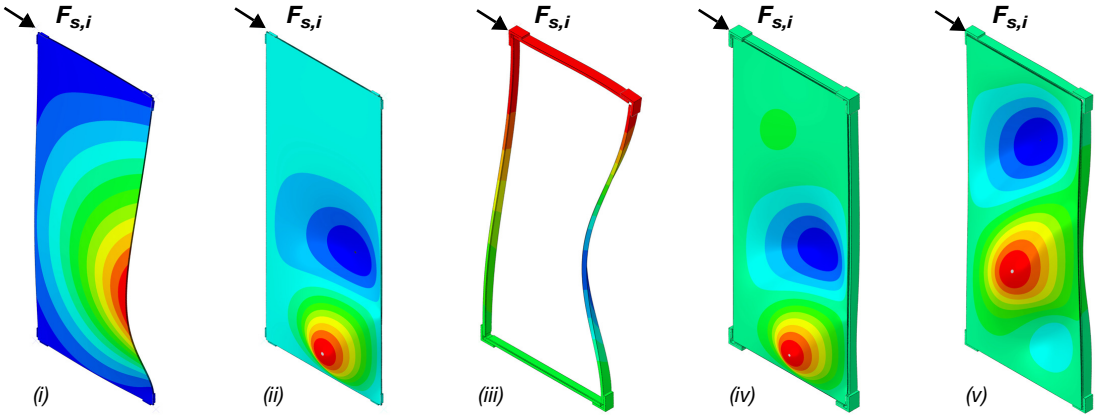

Fig. 7.38 *First eigenmodes determined under in-plane shear loading for the two investigated element types and their subsidiary systems with rectangular geometry of the glass pane (1.5 m x 3.5 m)*

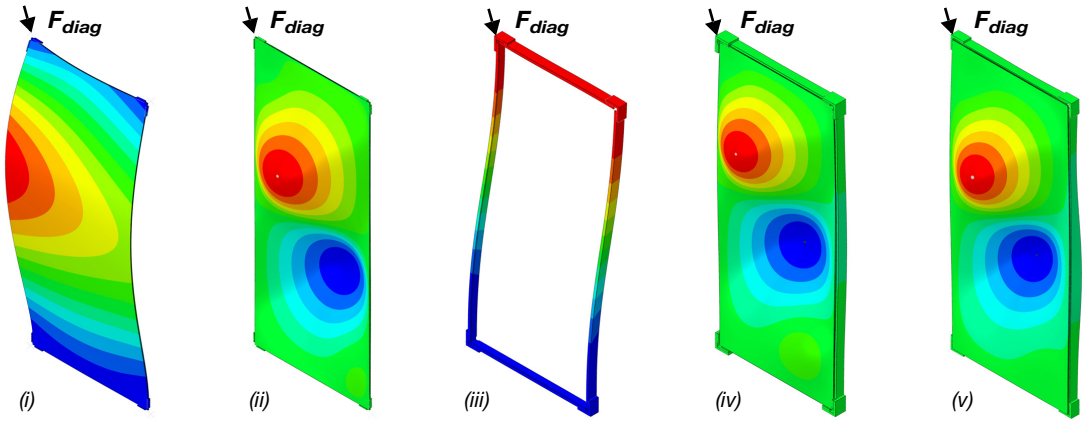

Fig. 7.39 *First eigenmodes determined under in-plane diagonal loading for the two investigated element types and their subsidiary systems with rectangular geometry of the glass pane (1.5 m x 3.5 m)*

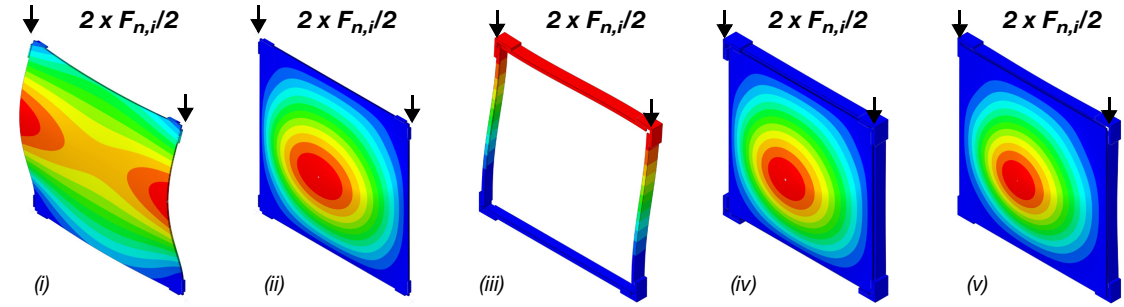

Fig. 7.40 *First eigenmodes determined under in-plane axial loading for the two investigated element types and their subsidiary systems with quadratic geometry of the glass pane (1.5 m x 1.5 m)*

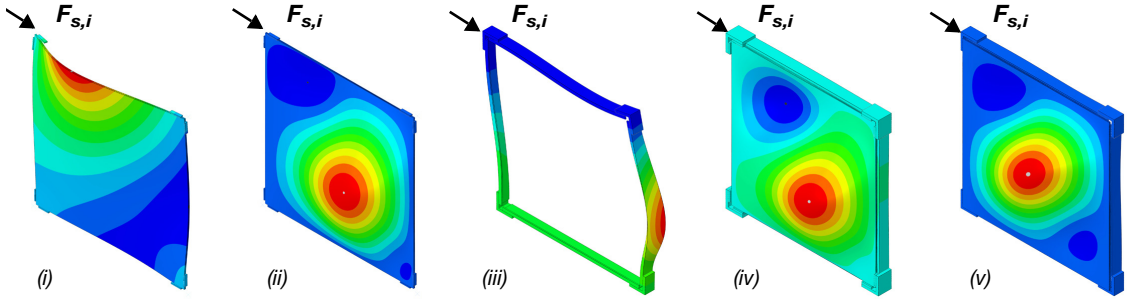

Fig. 7.41 *First eigenmodes determined under in-plane shear loading for the two investigated element types and their subsidiary systems with quadratic geometry of the glass pane (1.5 m x 1.5 m)*

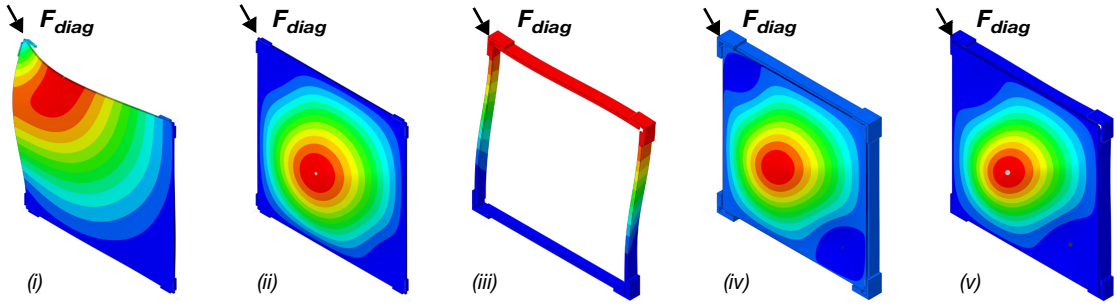

Fig. 7.42 *First eigenmodes determined under in-plane diagonal loading for the two investigated element types and their subsidiary systems with quadratic geometry of the glass pane (1.5 m x 1.5 m)*

7.3.3 Variation of the glass pane height

Considering the existing tendency for larger glass panes as well as the potential of the investigated systems for gridshells with quadratic glass panes, two larger and two smaller values for the glass pane height are analysed (see first column of Tab. 7.9). Not only the glass pane height, but also the other related components (edge elements and adhesive joint) are modified accordingly in height direction. The first eigenvalues determined under in-plane axial loading and under in-plane shear loading are decreasing with increasing height of the glass panes for both investigated element types, as pointed out by the values in Tab. 7.9.

Tab. 7.9 *Influence of the glass pane height on the first eigenvalues determined under in-plane axial loading and under in-plane shear loading*

Glass pane height	First eigenvalues [kN]			
	In-plane axial load $F_{n,i}$		In-plane shear load $F_{s,i}$	
	Type 1	Type 2	Type 1	Type 2
h = 1 500 mm	362.660	657.944	137.664	201.132
h = 2 500 mm	238.726	309.795	100.052	156.858
h = 3 500 mm	198.245	260.302	73.987	136.406
h = 4 500 mm	183.080	235.543	56.853	117.032
h = 5 500 mm	174.241	221.765	45.892	98.423

Findings regarding the influence of different **glass pane heights** on the **global in-plane behaviour** for the glass-metal elements under in-plane shear loading (see Fig. 7.43):

- higher elements lead to a lower in-plane stiffness, while reaching larger in-plane displacements at given load values;
- the applied initial geometric imperfections (see dashed curves) have only a negligible influence on the in-plane behaviour of both element types;

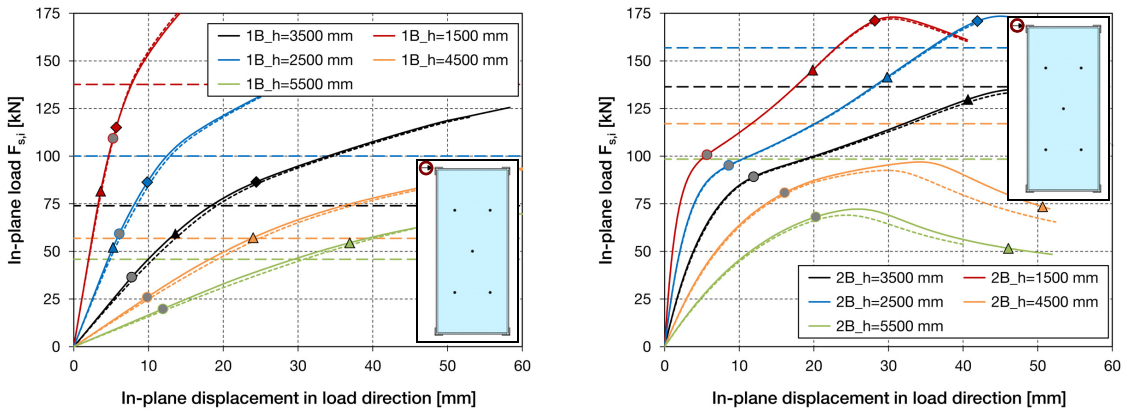

Fig. 7.43 *Influence of the glass pane height on the relationship between in-plane shear load and in-plane horizontal displacement measured at reference point RP7 for model Type 1 (left) and model Type 2 (right)*

- with increasing element height a certain stress in the adhesive (see coloured circles with grey filling) is reached at smaller loads and larger in-plane displacements;
- the maximum principal stresses in the glass panes occur at the glass edge near the grouting blocks at the load application corner for the models of *Type 1*, while for models of *Type 2*, they are first located near the adhesive joint in the area of the fixed corner of the tensioned diagonal and at higher loads in the area where the compressed edge element buckles.

Findings regarding the influence of different **glass pane heights** on the **out-of-plane displacements** of the glass panes for the glass-metal elements under in-plane shear loading (see Fig. 7.44, Fig. 7.45 and Fig. 7.46):

- higher elements lead to larger out-of-plane displacements at a given load value for both element types;
- for the models of *Type 1*, the influence of initial geometric imperfections is higher in the case of elements with smaller glass pane height (compare dashed curves with continuous ones);

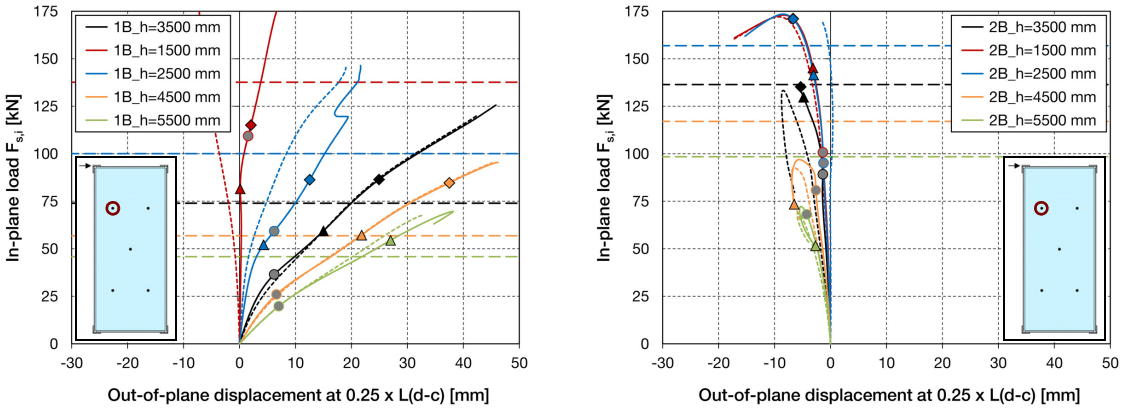

Fig. 7.44 *Influence of the glass pane height on the relationship between in-plane shear load and out-of-plane displacement measured at the top quarter-point of the compressed glass pane diagonal for model Type 1 (left) and model Type 2 (right)*

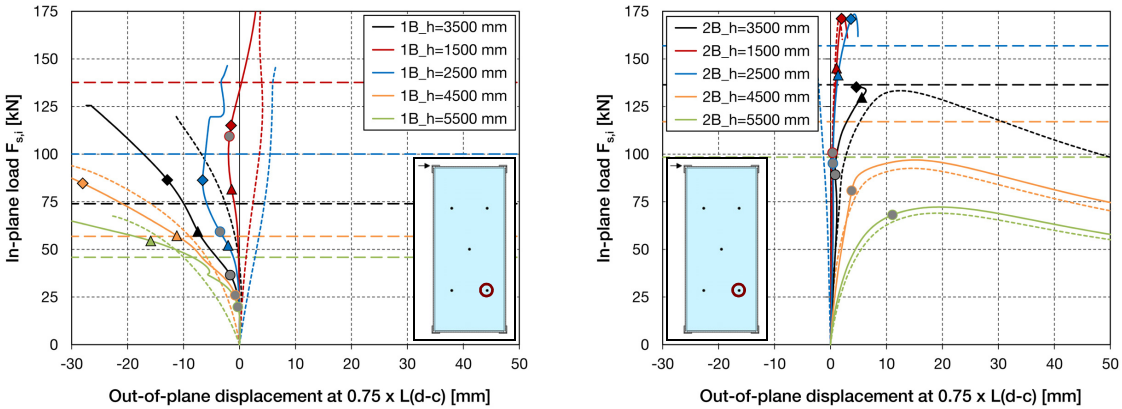

Fig. 7.45 *Influence of the glass pane height on the relationship between in-plane shear load and out-of-plane displacement measured at the bottom quarter-point of the compressed glass pane diagonal for model Type 1 (left) and model Type 2 (right)*

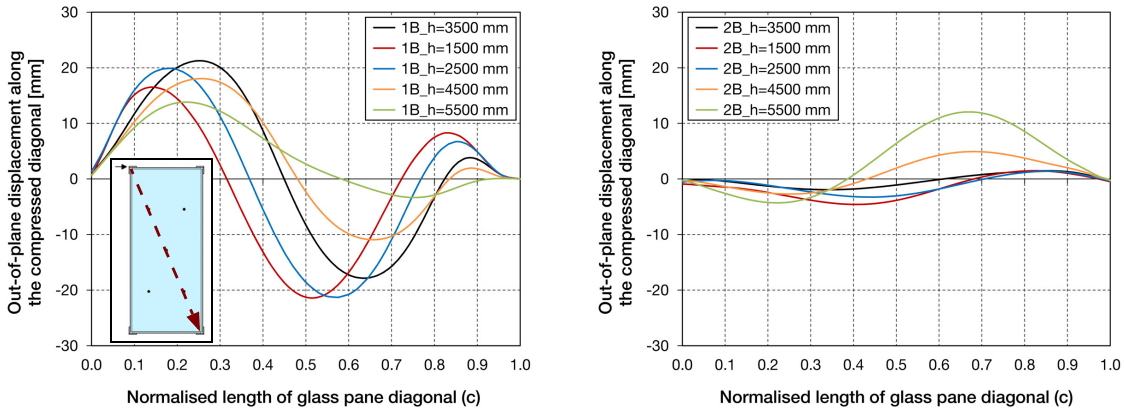

Fig. 7.46 *Influence of the glass pane height on the out-of-plane displacements along the compressed glass pane diagonal at a horizontal in-plane displacement of the reference point for shear load application of 20 mm for model Type 1 (left) and model Type 2 (right)*

Findings regarding the influence of different **glass pane heights** on the **relative in-plane displacements** between glass pane and metal framing for the glass-metal elements under in-plane shear loading (see Fig. 7.47 and Fig. 7.48):

- both the positive and the negative maximum relative in-plane displacements are increasing with larger height of the elements for both model types;
- the maximum positive relative in-plane displacements are significantly larger in the case of the models of *Type 1*, especially for loads at which the yielding of the acrylic adhesive did not start yet (see Fig. 7.47);
- the maximum negative relative in-plane displacements get significantly larger in the case of the models of *Type 2* after the acrylic adhesive starts to yield (see Fig. 7.48 - different ranges are used for the x-axis in the two diagrams);
- initial geometric imperfections have almost no influence on relative in-plane displacements.

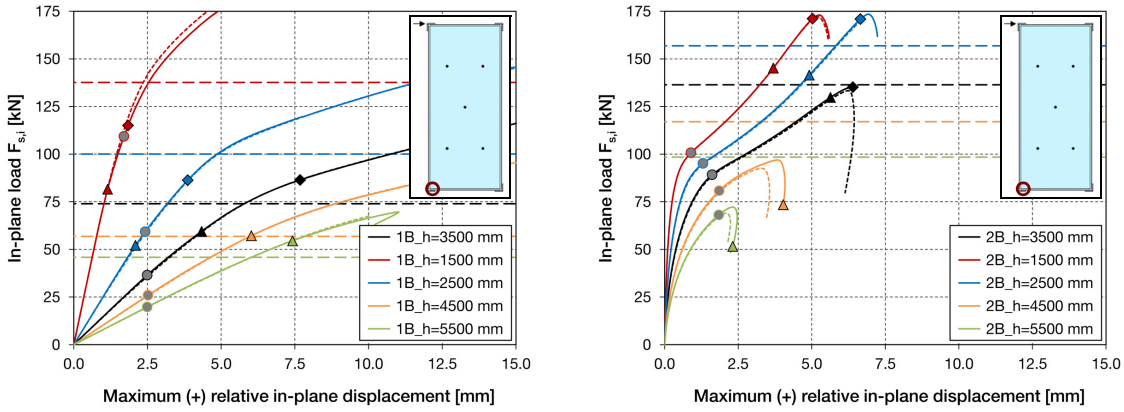

Fig. 7.47 *Influence of the glass pane height on the maximum positive relative in-plane displacements between glass pane and metal framing for model Type 1 (left) and model Type 2 (right)*

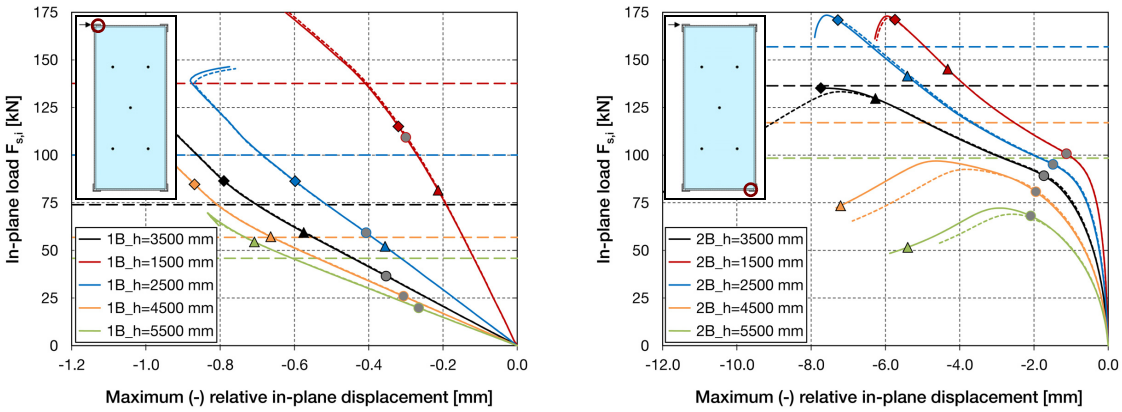

Fig. 7.48 *Influence of the glass pane height on the maximum negative relative in-plane displacements between glass pane and metal framing for model Type 1 (left) and model Type 2 (right)*

Findings regarding the influence of different **glass pane heights** on the **out-of-plane displacements** of the glass panes for the glass-metal elements under out-of-plane surface loading (see Fig. 7.49):

- higher elements lead to larger out-of-plane displacements because the span between the out-of-plane supports in height direction is increasing;
- the out-of-plane displacements for the elements with silicone adhesive and grouting are higher than those for the elements with acrylic adhesive in the case of equal glass pane heights due to the more pronounced clamping effect obtained with the acrylic adhesive joint.

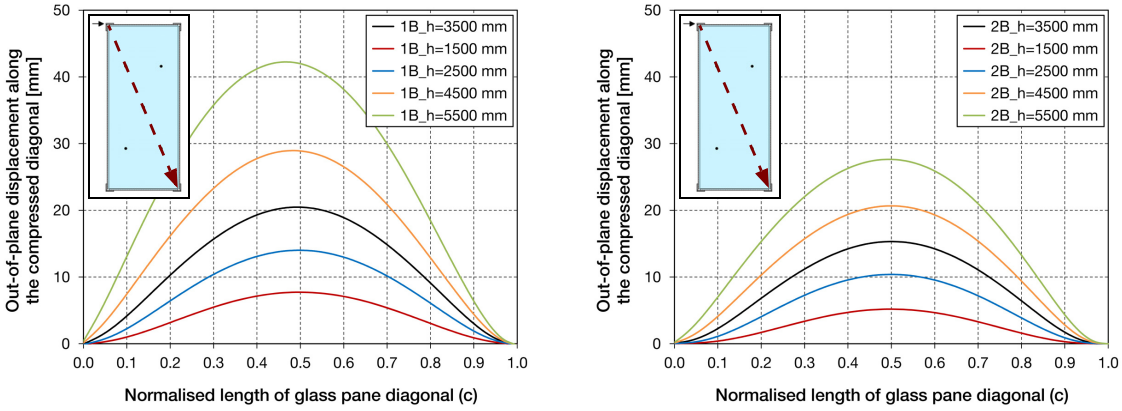

Fig. 7.49 *Influence of the glass pane height on the out-of-plane displacements along one diagonal (compressed glass pane diagonal under shear loading) under a wind suction load of 2.0 kPa for model Type 1 (left) and model Type 2 (right)*

7.3.4 Variation of the glass pane assembly

Two assemblies with monolithic glass panes (*6 mm* and *10 mm*) and two assemblies with laminated glass panes (*2 x 6 mm* and *2 x 10 mm*) are included in this study. Thicker glass panes are considered overdimensioned for elements with the investigated size. The first eigenvalues determined under in-plane axial loading and under in-plane shear loading are increasing with larger thickness of the monolithic glass panes and of the laminated glass panes for both investigated element types, as pointed out by the values in Tab. 7.10.

Tab. 7.10 *Influence of the glass pane assembly on the first eigenvalues determined under in-plane axial loading and under in-plane shear loading*

Glass pane assembly [mm]	First eigenvalues [kN]			
	In-plane axial load $F_{n,i}$		In-plane shear load $F_{s,i}$	
	Type 1	Type 2	Type 1	Type 2
6	92.573	114.516	34.826	63.573
10	313.560	354.608	136.618	213.749
6 / 1.52 / 6	198.245	260.302	73.987	136.406
10 / 1.52 / 10	595.076	786.287	254.546	393.370

Findings regarding the influence of different **glass pane assemblies** on the **global in-plane behaviour** for the glass-metal elements under in-plane shear loading (see Fig. 7.50):

- in the case of elements with silicone adhesive and grouting blocks (*Type 1*), a higher in-plane stiffness can be reached by increasing the thickness of monolithic glass panes or the thickness of the single sheets belonging to a laminated glass pane;
- in the case of elements with acrylic adhesive (*Type 2*), only a small influence of the glass pane assembly on the in-plane stiffness can be observed;
- initial geometric imperfections have a negligible influence on the in-plane displacements;

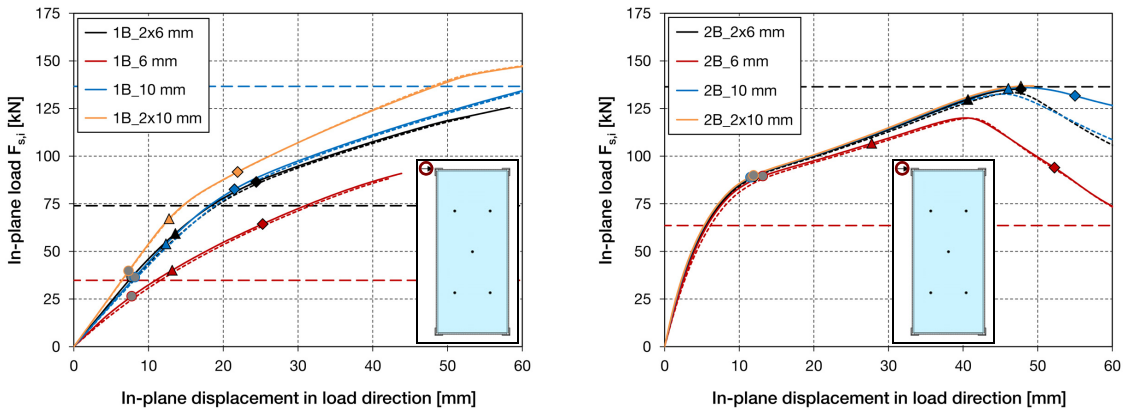

Fig. 7.50 *Influence of the glass pane assembly on the relationship between in-plane shear load and in-plane horizontal displacement measured at reference point RP7 for model Type 1 (left) and model Type 2 (right)*

- the in-plane displacement at which the stresses of *1 MPa* in the silicone adhesive and of *10 MPa* in the acrylic adhesive are reached, varies only little for different glass pane assemblies (see coloured circles with grey filling);
- an assembly with a *10 mm* thick monolithic glass pane and a laminated glass pane assembly with *2 x 6 mm* thick glass sheets lead to approximately the same global in-plane displacements for both system types.

Findings regarding the influence of different **glass pane assemblies** on the **out-of-plane displacements** of the glass panes for the glass-metal elements under in-plane shear loading (see Fig. 7.51, Fig. 7.52 and Fig. 7.53):

- thicker glass panes lead to smaller out-of-plane displacements due to plate buckling;
- the applied initial geometric imperfections have an influence on the out-of-plane displacements, especially on those recorded at the bottom quarter-point of the compressed diagonal for models of *Type 1* (see Fig. 7.52, left);

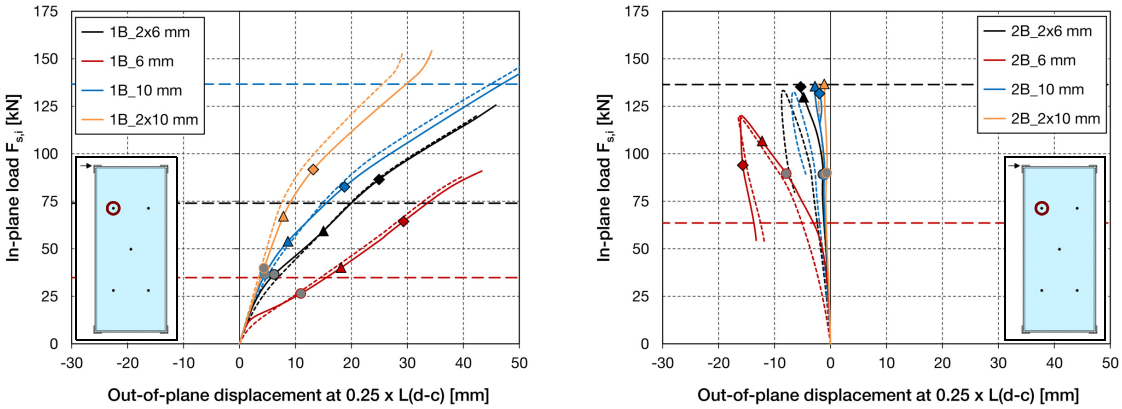

Fig. 7.51 *Influence of the glass pane assembly on the relationship between in-plane shear load and out-of-plane displacement measured at the top quarter-point of the compressed glass pane diagonal for model Type 1 (left) and model Type 2 (right)*

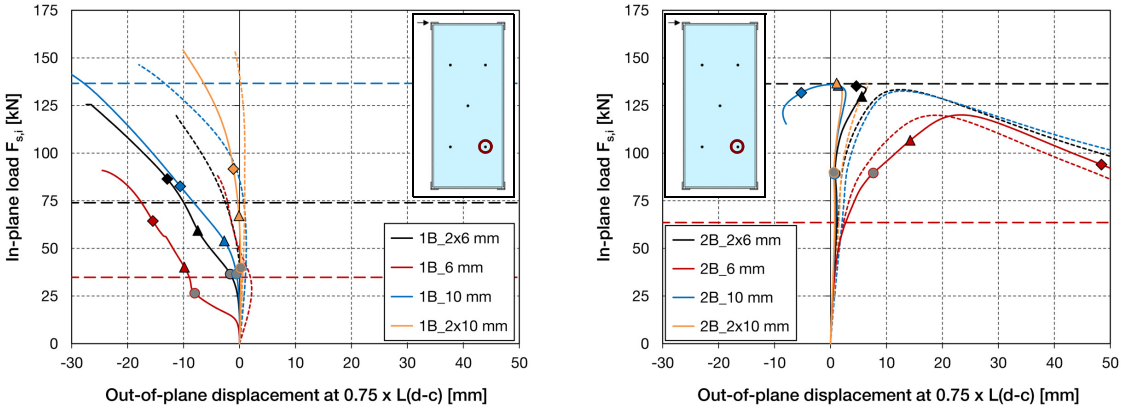

Fig. 7.52 *Influence of the glass pane assembly on the relationship between in-plane shear load and out-of-plane displacement measured at the bottom quarter-point of the compressed glass pane diagonal for model Type 1 (left) and model Type 2 (right)*

- for the model of *Type 2* with a *6 mm* thick monolithic glass pane, significantly higher out-of-plane displacements due to plate buckling are indicated by the diagram in Fig. 7.53, right, which proves a better activation of glass panes with smaller thickness.

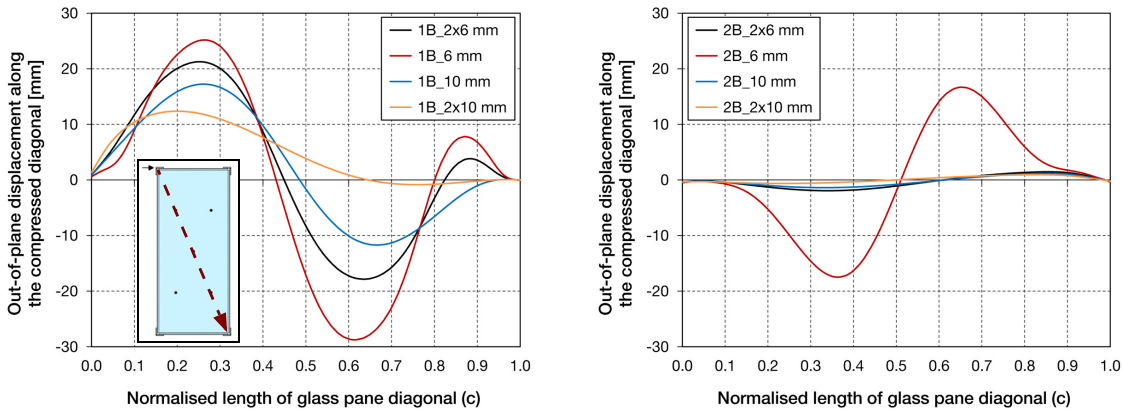

Fig. 7.53 *Influence of the glass pane assembly on the out-of-plane displacements along the compressed glass pane diagonal at a horizontal in-plane displacement of the reference point for shear load application of 20 mm for model Type 1 (left) and model Type 2 (right)*

Findings regarding the influence of different **glass pane assemblies** on the **relative in-plane displacements** between glass pane and metal framing for the glass-metal elements under in-plane shear loading (see Fig. 7.54 and Fig. 7.55):

- for the models of *Type 1*, thicker monolithic glass panes or thicker glass sheets in laminated assemblies lead to smaller relative in-plane displacements at a given shear load value;
- for the models of *Type 2*, the glass pane assembly has almost no influence on the relative in-plane displacements at a given shear load value, which indicates that this displacements are occurring due to shearing of the metal framing parallel to the glass pane;
- initial geometric imperfections have almost no influence on relative in-plane displacements for both element types and all investigated assemblies.

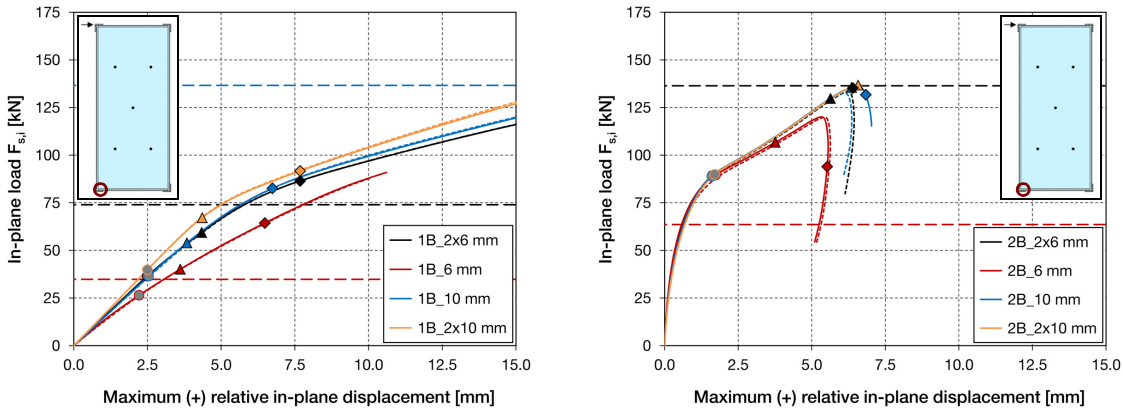

Fig. 7.54 *Influence of the glass pane assembly on the maximum positive relative in-plane displacements between glass pane and metal framing for model Type 1 (left) and model Type 2 (right)*

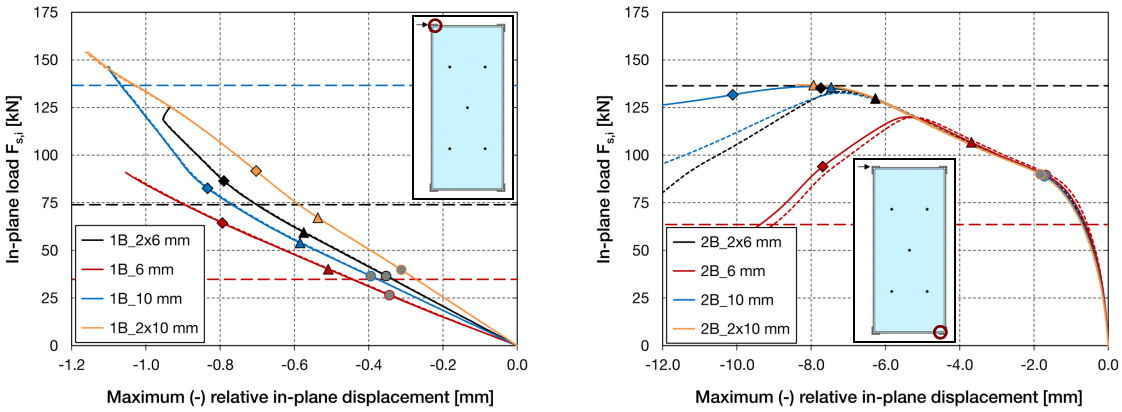

Fig. 7.55 *Influence of the glass pane assembly on the maximum negative relative in-plane displacements between glass pane and metal framing for model Type 1 (left) and model Type 2 (right)*

Findings regarding the influence of different **glass pane assemblies** on the **out-of-plane displacements** of the glass panes for the glass-metal elements under out-of-plane surface loading (see Fig. 7.56):

- thicker glass panes lead as expected to smaller out-of-plane displacements;
- the out-of-plane displacements for the system with silicone adhesive and grouting are higher than those for the system with acrylic adhesive in the case of similar glass pane assemblies due to the more pronounced clamping effect obtained with the acrylic adhesive joint;
- an assembly with a *10 mm* thick monolithic glass pane and a laminated glass pane assembly with *2 x 6 mm* thick glass sheets lead to approximately the same out-of-plane displacements of the glass panes for both system types.

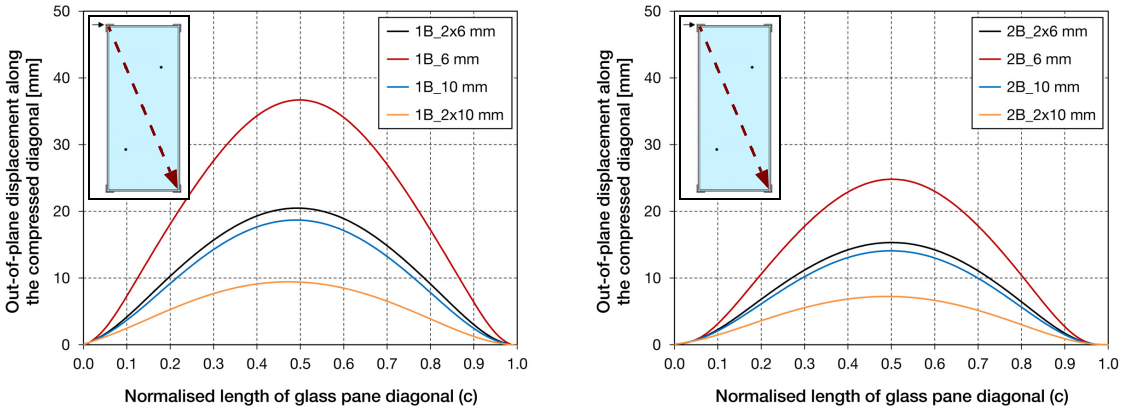

Fig. 7.56 *Influence of the glass pane assembly on the out-of-plane displacements along one diagonal (compressed glass pane diagonal under shear loading) under a wind suction load of 2.0 kPa for model Type 1 (left) and model Type 2 (right)*

7.3.5 Variation of the metal framing depth

The framing depth is on the one hand an important parameter for ensuring the out-of-plane support of the glass pane. On the other hand it is aimed to minimize this dimension in order to reduce material consumption. Two smaller and two larger values compared to the reference depth of *100 mm* are analysed (see first column of Tab. 7.11).The first eigenvalues determined under in-plane axial loading and under in-plane shear loading are increasing with larger metal framing depth for both investigated element types, as pointed out by the values in Tab. 7.11. A high difference is noticed between the eigenvalues determined with a depth of *10 mm* and those determined with a depth of *50 mm*. In the first case the eigenmodes are similar to those exhibited by *system (i)* in subchapter 7.3.2, while in the second case they are closer to the eigenmodes shown by *system (ii)* and by the reference systems.

Tab. 7.11 *Influence of the metal framing depth on the first eigenvalues determined under in-plane axial loading and under in-plane shear loading*

Metal framing depth	First eigenvalues [kN]			
	In-plane axial load $F_{n,i}$		In-plane shear load $F_{s,i}$	
	Type 1	Type 2	Type 1	Type 2
f-d = 10 mm	24.343	32.565	11.532	15.370
f-d = 50 mm	135.697	204.858	57.624	84.835
f-d = 100 mm	198.245	260.302	73.987	136.406
f-d = 150 mm	232.234	297.679	78.802	149.394
f-d = 200 mm	262.669	334.454	82.058	156.644

Findings regarding the influence of different **metal framing depths** on the **global in-plane behaviour** for the glass-metal elements under in-plane shear loading (see Fig. 7.57):

- the in-plane stiffness and the maximum bearable shear loads of both glass-metal element types increase with larger depths of the metal framing;

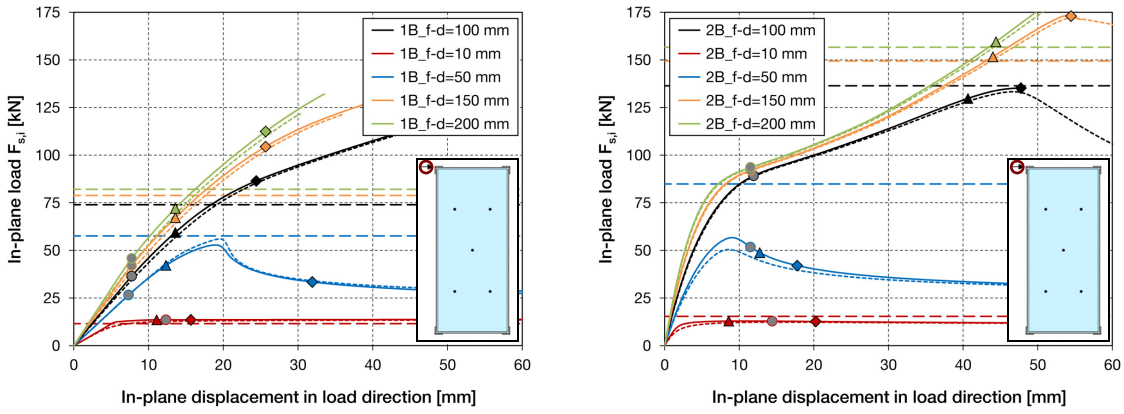

Fig. 7.57 *Influence of the metal framing depth on the relationship between in-plane shear load and in-plane horizontal displacement measured at reference point RP7 for model Type 1 (left) and model Type 2 (right)*

- almost no influence of the applied initial geometric imperfections on the in-plane displacements is observed without depending on the framing depth;
- for framing depths of *10 mm* and of *50 mm*, the global deformations in the case of both element types are qualitatively similar to the eigenmode obtained for a glass pane without perimetrical out-of-plane support (see *system (i)* under shear loading in Fig. 7.39);
- for depth values of *100 mm* and higher, the global deformations are qualitatively more similar to the eigenmode obtained for a glass pane with perimetrical out-of-plane support (see *system (ii)*, *system (iv)* and *system (v)* under shear loading in Fig. 7.39).

Findings regarding the influence of different **metal framing depths** on the **out-of-plane displacements** of the glass panes for the glass-metal elements under in-plane shear loading (see Fig. 7.58, Fig. 7.59 and Fig. 7.60):

- a general statement regarding the influence of the metal framing depth on the out-of-plane displacements is not possible due to the different deformation behaviours mentioned above;

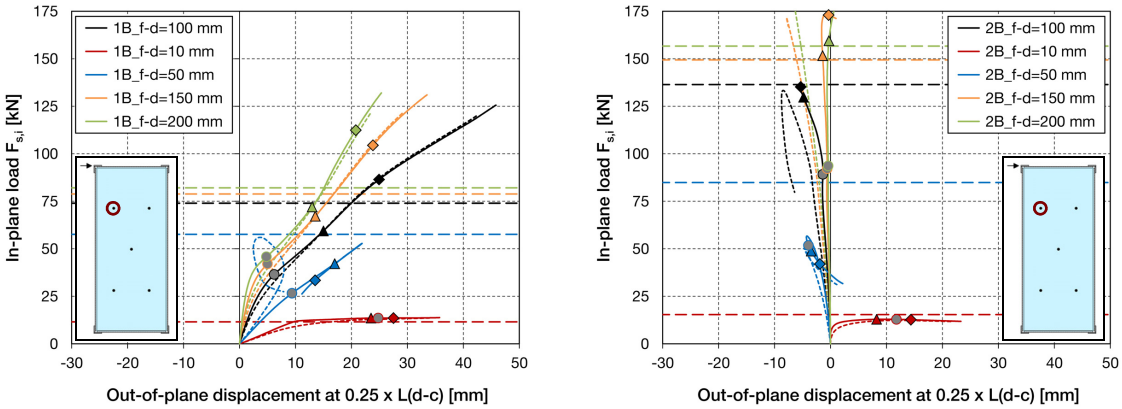

Fig. 7.58 *Influence of the metal framing depth on the relationship between in-plane shear load and out-of-plane displacement measured at the top quarter-point of the compressed glass pane diagonal for model Type 1 (left) and model Type 2 (right)*

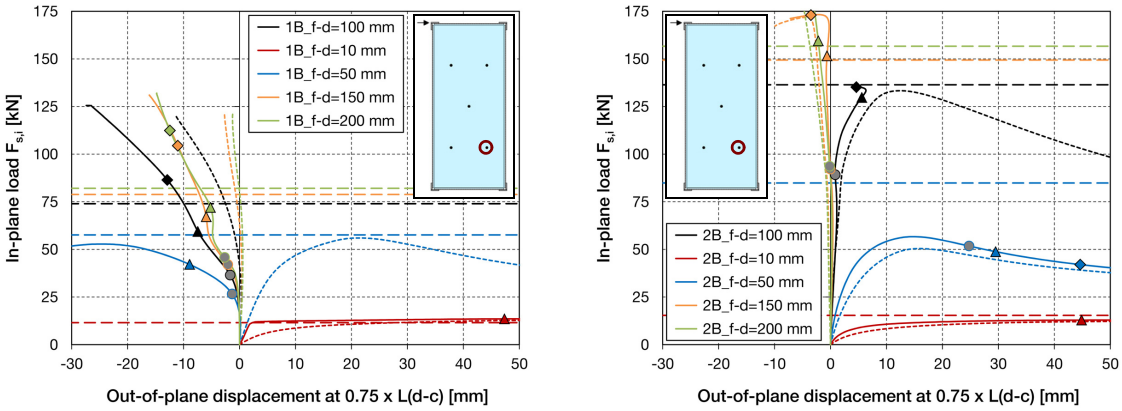

Fig. 7.59 *Influence of the metal framing depth on the relationship between in-plane shear load and out-of-plane displacement measured at the bottom quarter-point of the compressed glass pane diagonal for model Type 1 (left) and model Type 2 (right)*

- the applied initial geometric imperfections have an influence on the out-of-plane displacements under shear loading, especially for the elements of *Type 1* (in the case of a framing depth of *50 mm* even the direction of the out-of-plane displacements at the bottom quarter-point is different);
- framing depth values larger than *100 mm* have a relatively small influence on the out-of-plane displacements compared to values smaller than *100 mm*.

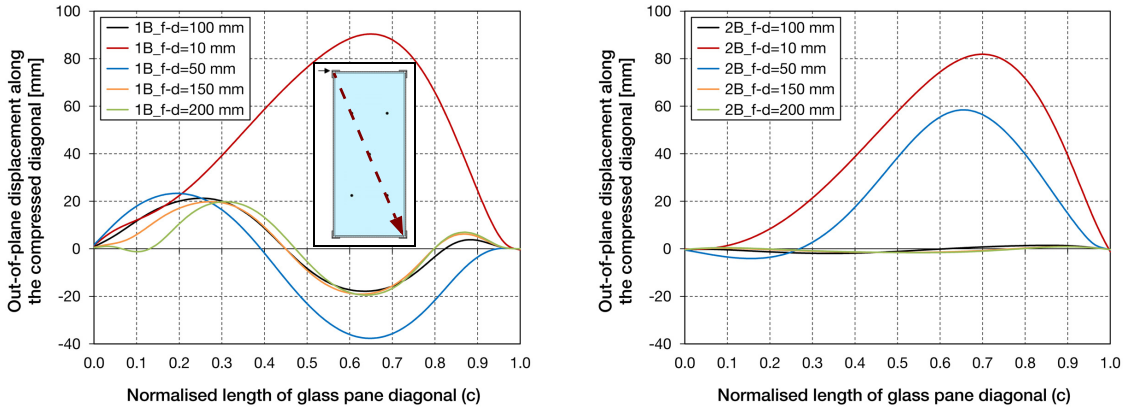

Fig. 7.60 *Influence of the metal framing depth on the out-of-plane displacements along the compressed glass pane diagonal at a horizontal in-plane displacement of the reference point for shear load application of 20 mm for model Type 1 (left) and model Type 2 (right)*

Findings regarding the influence of different **metal framing depths** on the **relative in-plane displacements** between glass pane and metal framing for the glass-metal elements under in-plane shear loading (see Fig. 7.61 and Fig. 7.62):

- the maximum positive relative in-plane displacements at a given load value slightly decrease with larger metal framing depths for both element types; for the maximum negative relative in-plane displacements this is only the case for elements of *Type 2*, while for those of *Type 1* almost no influence is observed;

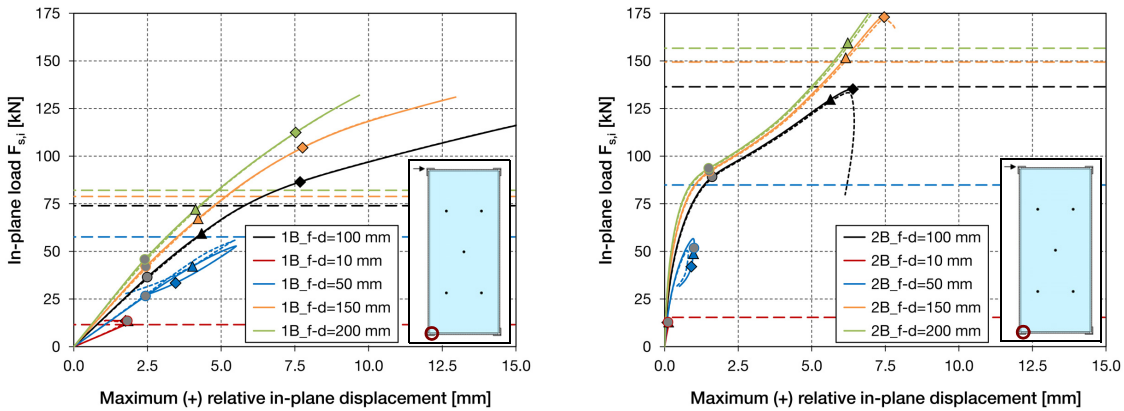

Fig. 7.61 *Influence of the metal framing depth on the maximum positive relative in-plane displacements between glass pane and metal framing for model Type 1 (left) and model Type 2 (right)*

- initial geometric imperfections have almost no influence on relative in-plane displacements, especially for metal framing depths of *100 mm* and larger.

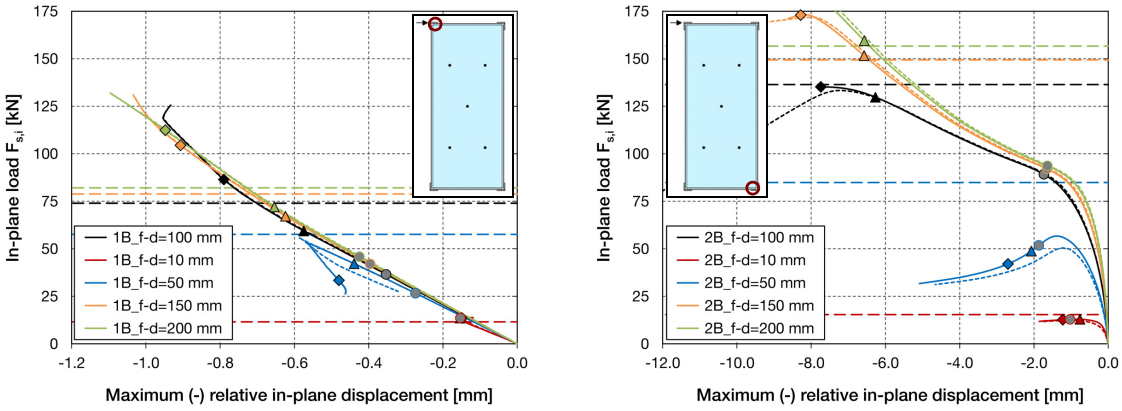

Fig. 7.62 *Influence of the metal framing depth on the maximum negative relative in-plane displacements between glass pane and metal framing for model Type 1 (left) and model Type 2 (right)*

Findings regarding the influence of different **metal framing depths** on the **out-of-plane displacements** of the glass panes for the glass-metal elements under out-of-plane surface loading (see Fig. 7.63):

- with smaller depths of the metal framing, the out-of-plane displacements under surface loading are increasing;
- for elements of *Type 1*, a metal framing depth of *10 mm* leads to significantly higher out-of-plane displacements than the other investigated depth values; for elements of *Type 2*, the simulation with a depth of *10 mm* does not converge up to a load of *2.0 kPa*;
- increasing the framing depth to values higher than *100 mm*, has a relatively reduced influence on the out-of-plane displacements under the applied surface loading.

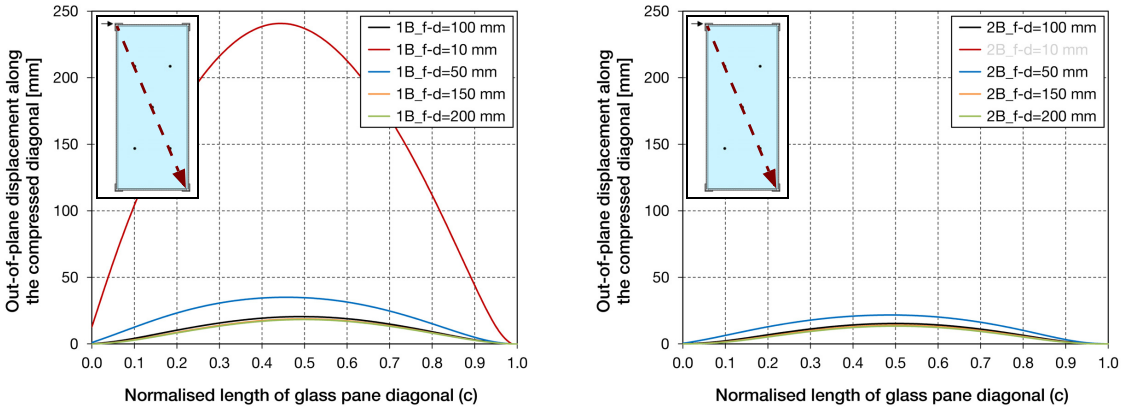

Fig. 7.63 *Influence of the metal framing depth on the out-of-plane displacements along one diagonal (compressed glass pane diagonal under shear loading) under a wind suction load of 2.0 kPa for model Type 1 (left) and model Type 2 (right)*

7.3.6 Variation of the metal corner thickness

The support and the loading of the glass-metal elements are located in the area of the corner elements, which have a certain bending stiffness. Therefore, the influence of smaller values for the metal corner thickness on the mechanical performance of the glass-metal elements is analysed (see values in first column of Tab. 7.12). The first eigenvalues determined under in-plane axial loading and under in-plane shear loading are only varying very little with decreasing metal corner thickness for both investigated element types, as pointed out by the values in Tab. 7.12.

Tab. 7.12 *Influence of the metal corner thickness on the first eigenvalues determined under in-plane axial loading and under in-plane shear loading*

Metal corner thickness	First eigenvalues [kN]			
	In-plane axial load $F_{n,i}$		In-plane shear load $F_{s,i}$	
	Type 1	Type 2	Type 1	Type 2
c-t = 5 mm	196.242	263.025	73.549	137.095
c-t = 10 mm	198.229	261.786	73.873	136.916
c-t = 15 mm	198.558	261.081	73.972	136.722
c-t = 20 mm	198.461	260.623	73.997	136.553
c-t = 25 mm	198.245	260.302	73.987	136.406

Findings regarding the influence of different **metal corner thicknesses** on the **global in-plane behaviour** for the glass-metal elements under in-plane shear loading (see Fig. 7.64):

- thicker corner elements lead to a higher in-plane stiffness and smaller in-plane displacements at given shear loads; for elements of *Type 2* this influence is only visible after yielding of the acrylic adhesive;
- the applied initial geometric imperfections (compare dashed curves to continuous ones) have only a negligible influence on the in-plane behaviour of both element types.

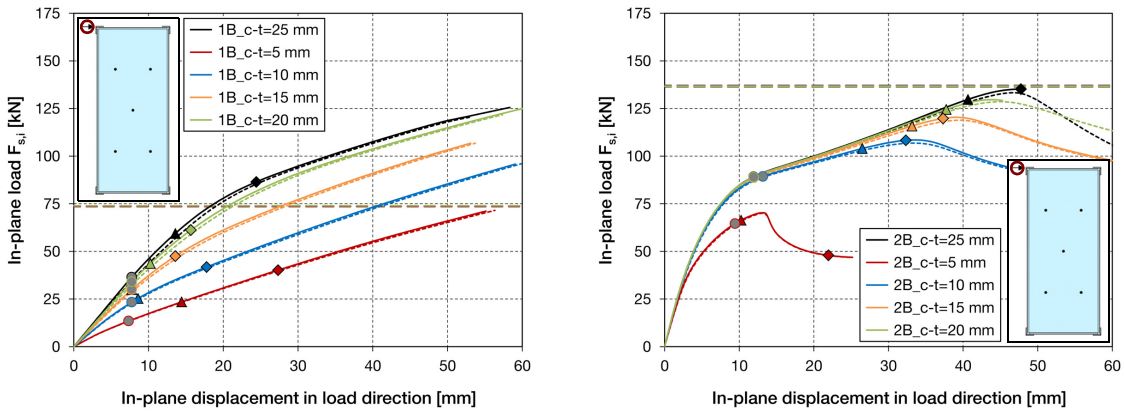

Fig. 7.64 *Influence of the metal corner thickness on the relationship between in-plane shear load and in-plane horizontal displacement measured at reference point RP7 for model Type 1 (left) and model Type 2 (right)*

- for the thickness of *5 mm*, the yielding in the corner elements belonging to the compressed diagonal is more pronounced, and therefore the curves for this thickness are qualitatively slightly different.

Findings regarding the influence of different **metal corner thicknesses** on the **out-of-plane displacements** of the glass panes for the glass-metal elements under in-plane shear loading (see Fig. 7.65, Fig. 7.66 and Fig. 7.67):

- for elements of *Type 1*, larger values of the corner thickness lead to larger out-of-plane displacements at the top quarter-point of the compressed diagonal for a given shear load (see Fig. 7.65, left); this is not the case at the bottom quarter-point for a given shear load (see Fig. 7.66, left), but it is the case for a given in-plane displacement (see Fig. 7.67, left);
- for elements of *Type 2*, only a small influence of the corner thickness on the out-of-plane displacements is noticed at both quarter-points of the compressed diagonal;

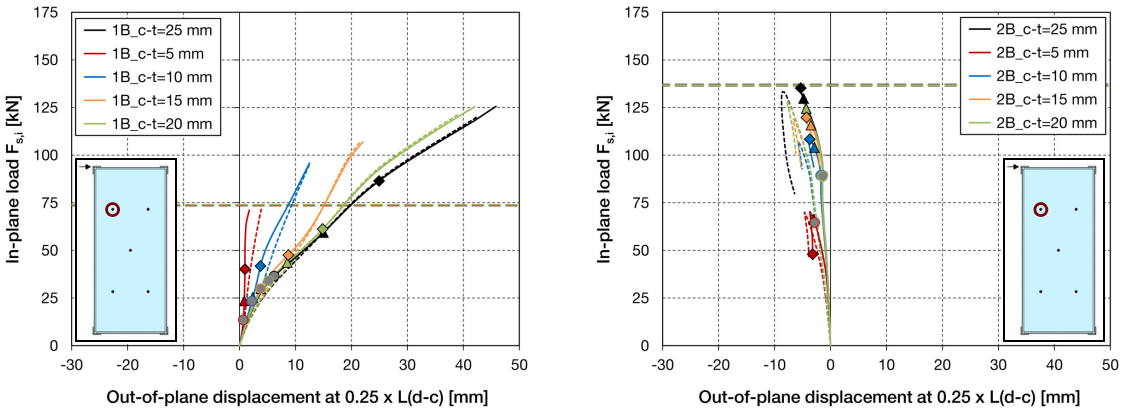

Fig. 7.65 *Influence of the metal corner thickness on the relationship between in-plane shear load and out-of-plane displacement measured at the top quarter-point of the compressed glass pane diagonal for model Type 1 (left) and model Type 2 (right)*

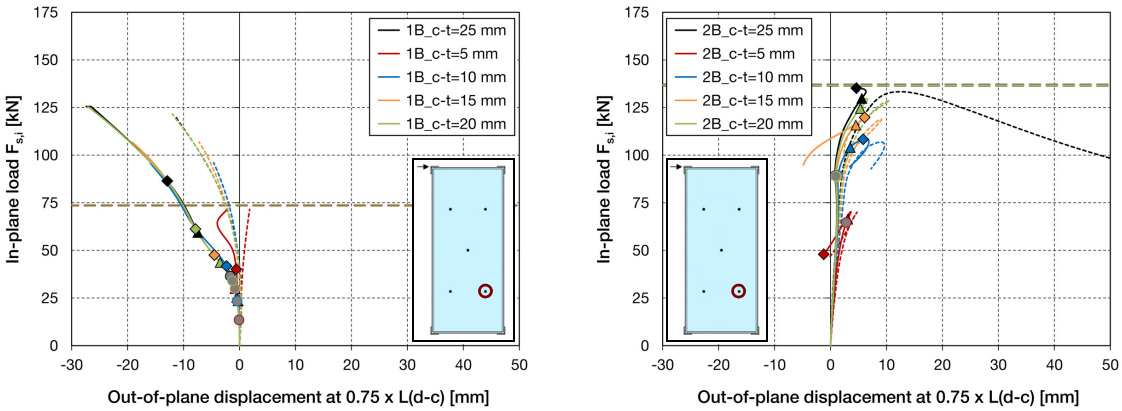

Fig. 7.66 *Influence of the metal corner thickness on the relationship between in-plane shear load and out-of-plane displacement measured at the bottom quarter-point of the compressed glass pane diagonal for model Type 1 (left) and model Type 2 (right)*

- the applied initial geometric imperfections have an influence on the out-of-plane displacements; the largest differences can be observed for the values recorded at the bottom quarter-point of the compressed diagonal for elements of *Type 1*.

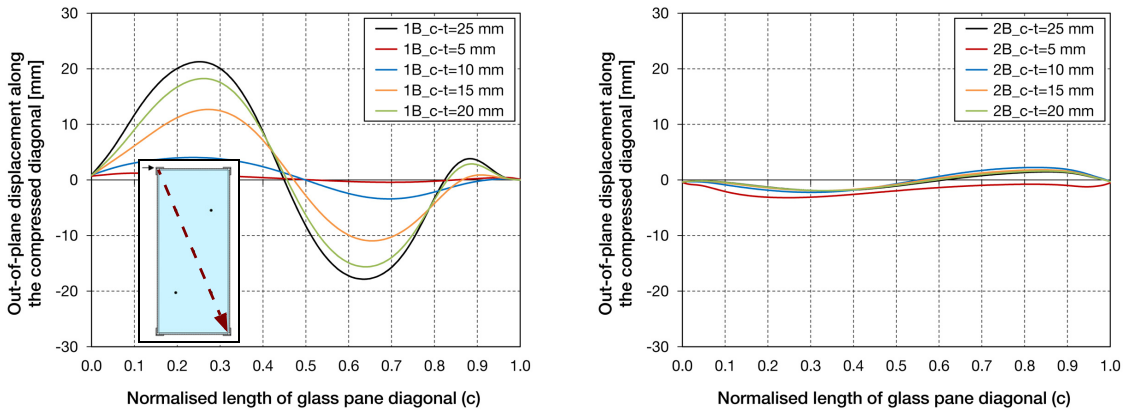

Fig. 7.67 *Influence of the metal corner thickness on the out-of-plane displacements along the compressed glass pane diagonal at a horizontal in-plane displacement of the reference point for shear load application of 20 mm for model Type 1 (left) and model Type 2 (right)*

Findings regarding the influence of different **metal corner thicknesses** on the **relative in-plane displacements** between glass pane and metal framing for the glass-metal elements under in-plane shear loading (see Fig. 7.68 and Fig. 7.69):

- for elements of *Type 1*, the maximum positive relative in-plane displacements at a given shear load are decreasing with increasing corner thickness; the same is noticed for the maximum negative relative in-plane displacements, except for thicknesses of *5 mm* and *10 mm*, for which a more pronounced yielding of the corner elements is occurring;
- for elements of *Type 2*, both the positive and the negative maximum relative in-plane displacements at a given shear load are slightly decreasing with increasing corner thickness only after yielding of the acrylic adhesive;

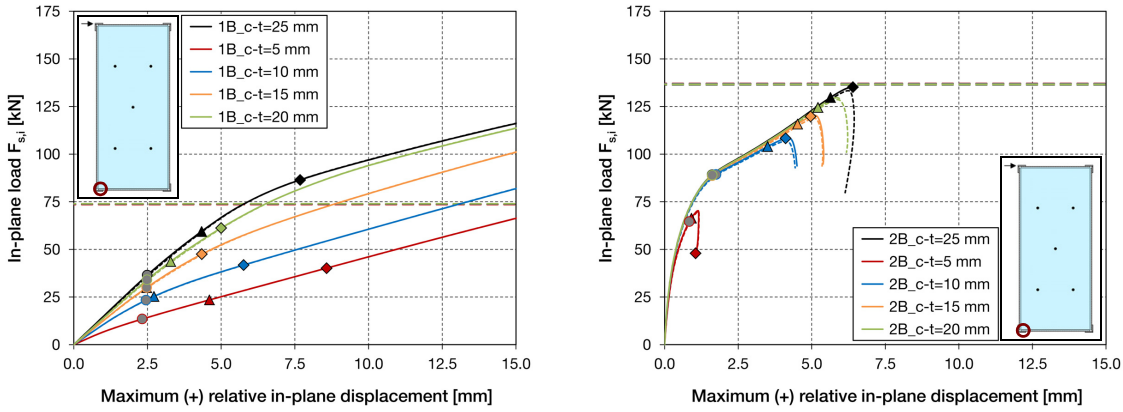

Fig. 7.68 *Influence of the metal corner thickness on the maximum positive relative in-plane displacements between glass pane and metal framing for model Type 1 (left) and model Type 2 (right)*

- initial geometric imperfections have almost no influence on relative in-plane displacements without depending on the metal corner thickness.

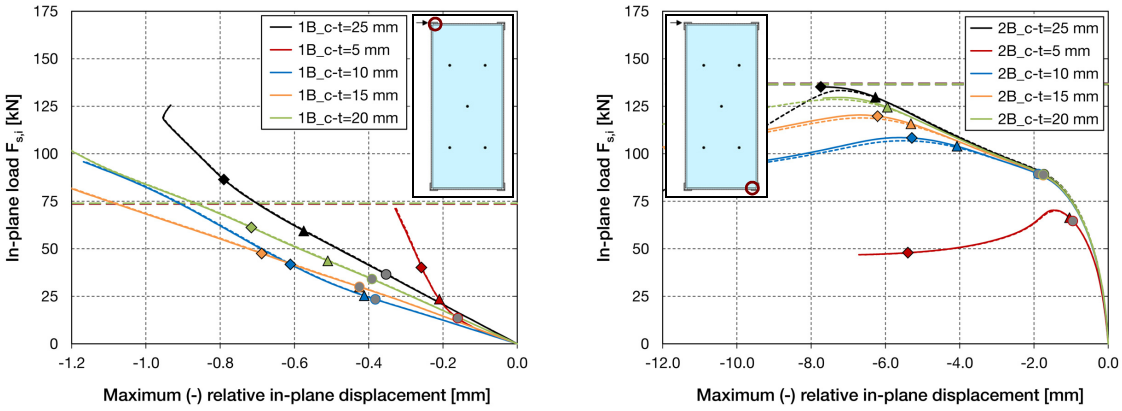

Fig. 7.69 *Influence of the metal corner thickness on the maximum negative relative in-plane displacements between glass pane and metal framing for model Type 1 (left) and model Type 2 (right)*

Findings regarding the influence of different **metal corner thicknesses** on the **out-of-plane displacements** of the glass panes for the glass-metal elements under out-of-plane surface loading (see Fig. 7.70):

- different values of the corner thickness have almost no influence on the out-of-plane displacements under the applied surface loading;

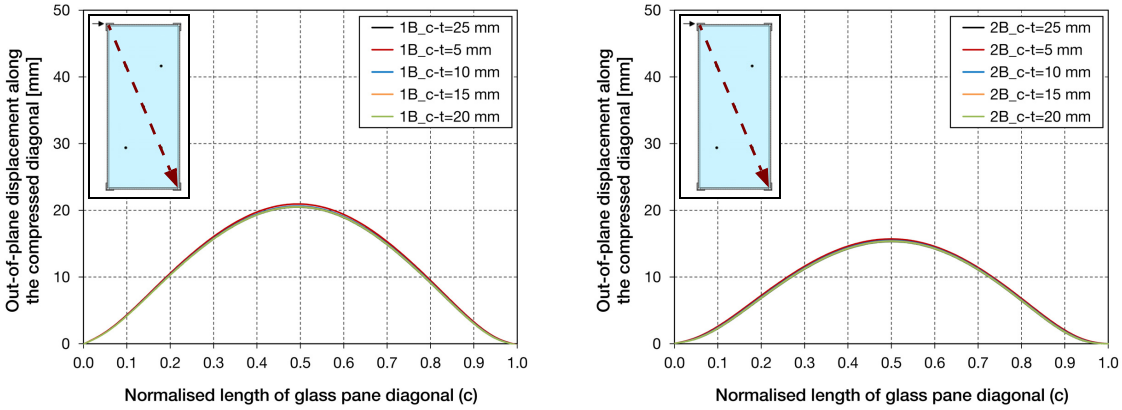

Fig. 7.70 *Influence of the metal corner thickness on the out-of-plane displacements along one diagonal (compressed glass pane diagonal under shear loading) under a wind suction load of 2.0 kPa for model Type 1 (left) and model Type 2 (right)*

7.3.7 Variation of the adhesive joint geometry

One of the main factors determining the visible width of the metal framing is the width of the adhesive joints. The influence of two smaller values (*10 mm* and *15 mm*) on the mechanical behaviour of the elements is analysed. Furthermore, the thickness of the adhesive joints determines the stiffness of these connections between glass pane and metal framing. Two additional values to the reference thicknesses are analysed (see values in the first two columns of Tab. 7.13). The first eigenvalues determined under in-plane axial loading and under in-plane shear loading are increasing with larger width of the joints for both investigated element types, as pointed out by the values in Tab. 7.13. With decreasing thickness of the joints, the determined first eigenvalues are increasing for models of *Type 1* and are decreasing for models of *Type 2*.

Tab. 7.13 *Influence of the adhesive joint geometry on the first eigenvalues determined under in-plane axial loading and under in-plane shear loading*

Adhesive joint geometry (width x thickness) [mm]		**First eigenvalues [kN]**			
		In-plane axial load $F_{n,i}$		**In-plane shear load $F_{s,i}$**	
Type 1	**Type 2**	**Type 1**	**Type 2**	**Type 1**	**Type 2**
10 x 6	10 x 3	183.105	254.118	67.708	129.265
15 x 6	15 x 3	190.510	257.485	71.092	134.066
20 x 6	**20 x 3**	198.245	260.302	73.987	136.406
20 x 3	20 x 1	204.416	241.273	77.948	133.316
20 x 9	20 x 2	194.338	250.967	71.837	135.180

Findings regarding the influence of different **adhesive joint geometries** on the **global in-plane behaviour** for the glass-metal elements under in-plane shear loading (see Fig. 7.71):

- wider adhesive joints lead to a higher in-plane stiffness for elements of *Type 1*, while this is only the case until yielding for elements of *Type 2*; after yielding the load-displacement curves for different joint widths in Fig. 7.71, right, show an almost parallel development;

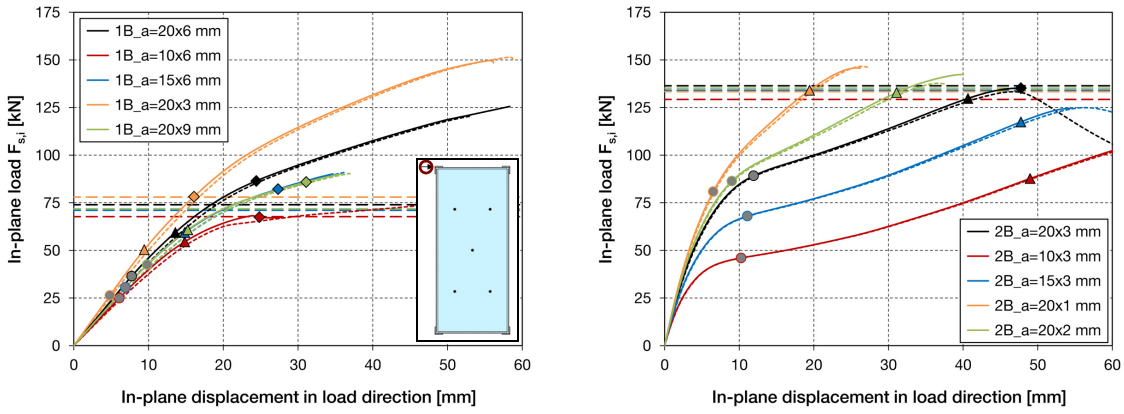

Fig. 7.71 *Influence of the adhesive joint geometry on the relationship between in-plane shear load and in-plane horizontal displacement measured at reference point RP7 for model Type 1 (left) and model Type 2 (right)*

- thinner adhesive joints lead to a higher in-plane stiffness for both investigated element types;
- the applied initial geometric imperfections (see dashed curves) have almost no influence on the in-plane displacements for both element types;
- with decreasing adhesive joint thickness a certain stress in the adhesive (see coloured circles with grey filling) is reached at smaller shear loads and smaller in-plane displacements; the same is the case for decreasing adhesive joint widths.

Findings regarding the influence of different **adhesive joint geometries** on the **out-of-plane displacements** of the glass panes for the glass-metal elements under in-plane shear loading (see Fig. 7.72, Fig. 7.73 and Fig. 7.74):

- by increasing the width or by reducing the thickness of the adhesive joint, the out-of-plane displacements under a certain shear load value can be reduced for elements of *Type 1*;

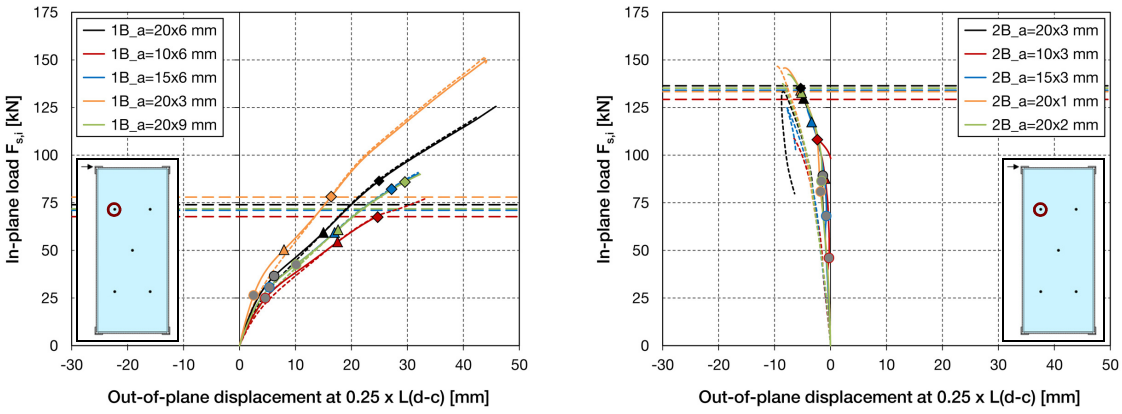

Fig. 7.72 *Influence of the adhesive joint geometry on the relationship between in-plane shear load and out-of-plane displacement measured at the top quarter-point of the compressed glass pane diagonal for model Type 1 (left) and model Type 2 (right)*

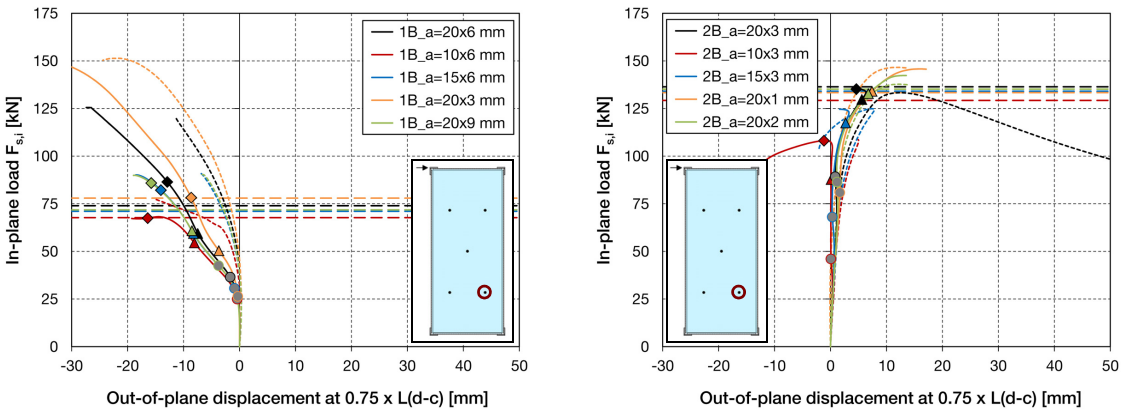

Fig. 7.73 *Influence of the adhesive joint geometry on the relationship between in-plane shear load and out-of-plane displacement measured at the bottom quarter-point of the compressed glass pane diagonal for model Type 1 (left) and model Type 2 (right)*

- from the diagrams in Fig. 7.72 and Fig. 7.73, right, plotting the in-plane shear loads *vs.* the out-of-plane displacements for elements of *Type 2*, only a small influence of the adhesive joint dimensions on the out-of-plane displacements is observed; the diagram in Fig. 7.74, right, however, shows that for a given global in-plane displacement, the out-of-plane displacements are increasing with decreasing thickness of the adhesive joint;
- the elements of *Type 1* with adhesive joint cross sections of *15 mm x 6 mm* and *20 mm x 9 mm* show a similar behaviour under in-plane shear loading.

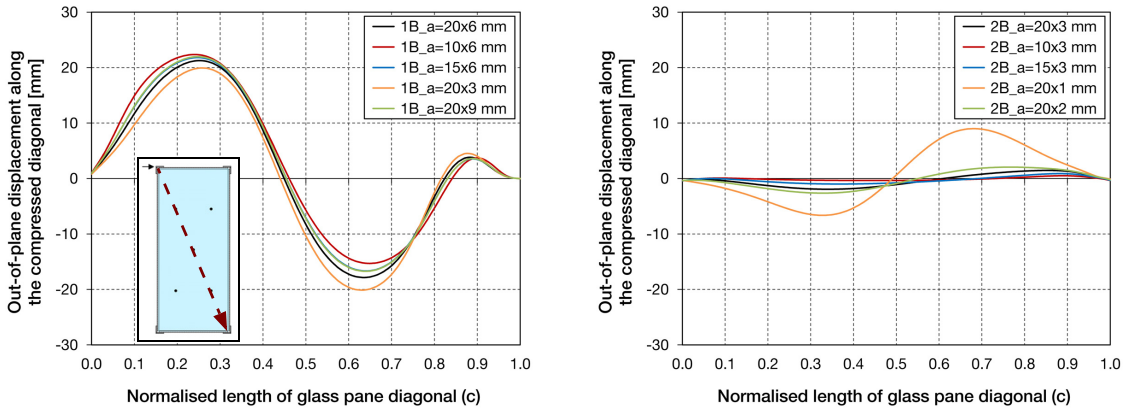

Fig. 7.74 *Influence of the adhesive joint geometry on the out-of-plane displacements along the compressed glass pane diagonal at a horizontal in-plane displacement of the reference point for shear load application of 20 mm for model Type 1 (left) and model Type 2 (right)*

Findings regarding the influence of different **adhesive joint geometries** on the **relative in-plane displacements** between glass pane and metal framing for the glass-metal elements under in-plane shear loading (see Fig. 7.75 and Fig. 7.76):

- with smaller width or with larger thickness of the adhesive joints, both the positive and the negative maximum relative in-plane displacements are increasing for a given shear load value in the case of both element types.

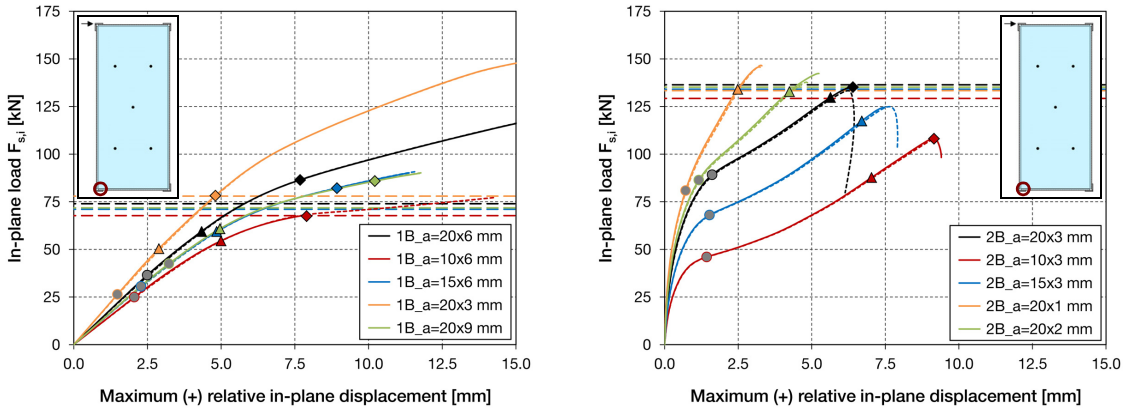

Fig. 7.75 *Influence of the adhesive joint geometry on the maximum positive relative in-plane displacements between glass pane and metal framing for model Type 1 (left) and model Type 2 (right)*

- initial geometric imperfections have almost no influence on relative in-plane displacements without depending on the adhesive joint geometry.

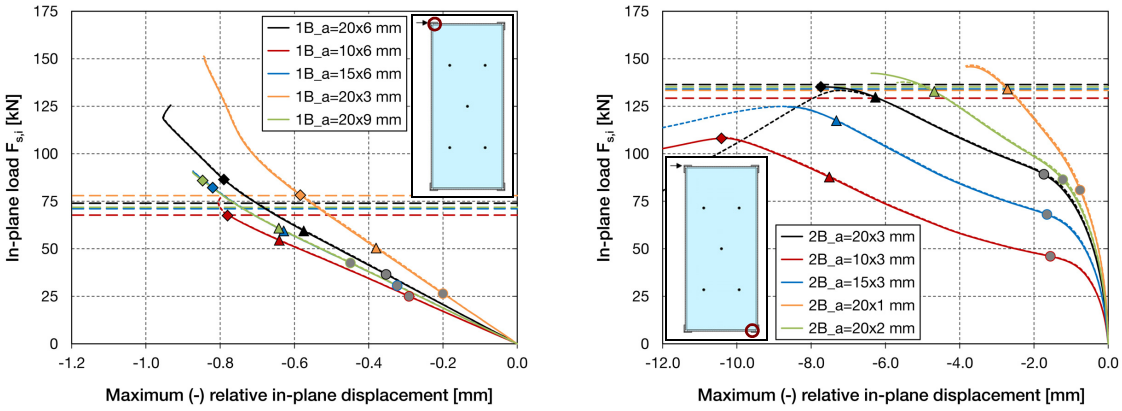

Fig. 7.76 *Influence of the adhesive joint geometry on the maximum negative relative in-plane displacements between glass pane and metal framing for model Type 1 (left) and model Type 2 (right)*

Findings regarding the influence of different **adhesive joint geometries** on the **out-of-plane displacements** of the glass panes for the glass-metal elements under out-of-plane surface loading (see Fig. 7.77):

- the different adhesive joint geometries have only a small influence on the out-of-plane displacements under the applied surface loading for both system types;
- the out-of-plane displacements are slightly increasing with smaller width as well as with larger thickness of the adhesive joints.

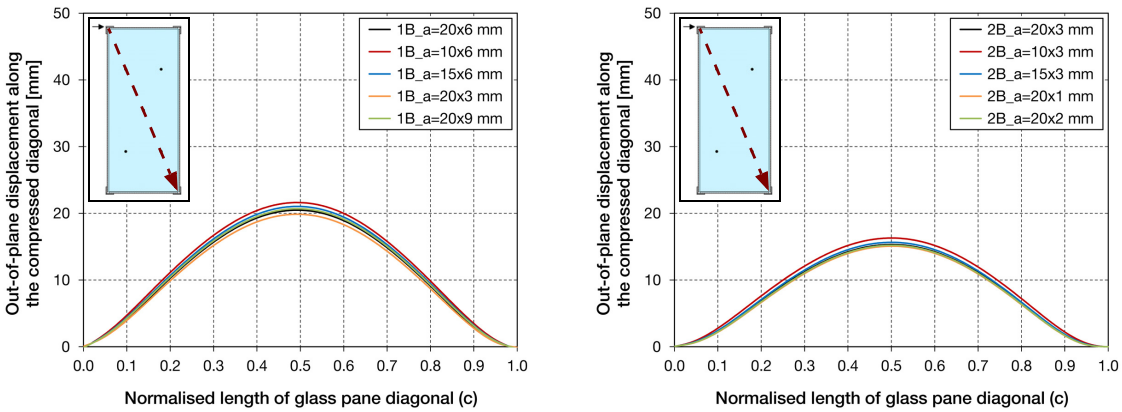

Fig. 7.77 *Influence of the adhesive joint geometry on the out-of-plane displacements along one diagonal (compressed glass pane diagonal under shear loading) under a wind suction load of 2.0 kPa for model Type 1 (left) and model Type 2 (right)*

7.3.8 Variation of the adhesive stiffness

To indicate how the two systems behave if adhesives with different stiffness values are used, simulations with linear-elastic material models for the adhesives are performed. The values from the first two columns in Tab. 7.14 are used for the Young's modulus in the simulations, which are carried out geometrically linear due to a better convergence behaviour. Furthermore, no simulations with initial geometric imperfections are performed for this parameter. The first eigenvalues under in-plane axial loading and under in-plane shear loading determined for the two investigated element types with different Young's moduli of the adhesives are given in Tab. 7.14.

Tab. 7.14 *Influence of the adhesive stiffness (Young's modulus) on the first eigenvalues determined under in-plane axial loading and under in-plane shear loading*

Adhesive stiffness (Young's modulus) [MPa]		**First eigenvalues [kN]**			
		In-plane axial load $F_{n,i}$		**In-plane shear load $F_{s,i}$**	
Type 1	**Type 2**	**Type 1**	**Type 2**	**Type 1**	**Type 2**
2.4	**250**	198.245	260.302	73.987	136.406
1	1	196.074	-	71.477	-
10	10	204.219	744.589	81.245	138.566
100	100	211.554	294.449	109.065	138.727
1000	1000	202.791	242.726	122.590	133.382

Findings regarding the influence of different **adhesive stiffness** values on the **global in-plane behaviour** for the glass-metal elements under in-plane shear loading (see Fig. 7.78):

- a higher Young's modulus of the adhesives lead to a higher in-plane stiffness, while reaching smaller global in-plane displacements at given load values;
- Young's moduli of *100 MPa* and *1000 MPa* lead to similar in-plane stiffnesses and displacements for both element types.

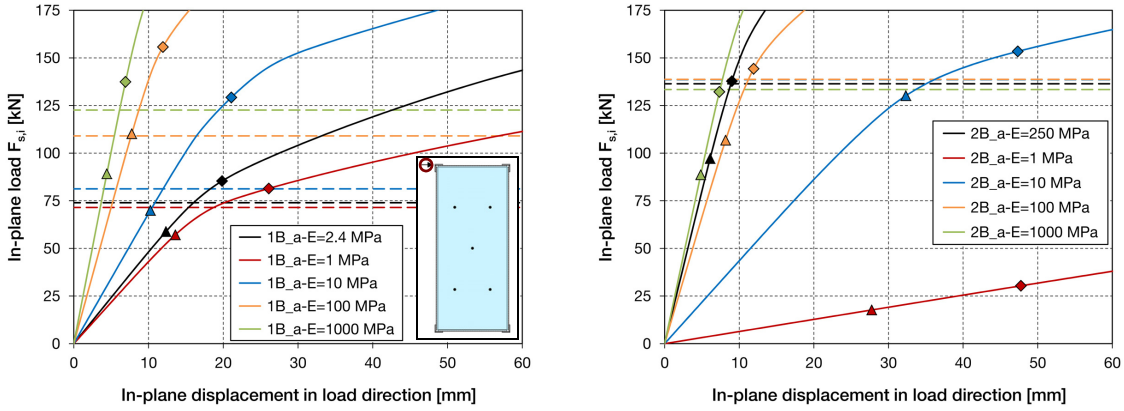

Fig. 7.78 *Influence of the adhesive stiffness on the relationship between in-plane shear load and in-plane horizontal displacement measured at reference point RP7 for model Type 1 (left) and model Type 2 (right)*

Findings regarding the influence of different **adhesive stiffness** values on the **out-of-plane displacements** of the glass panes for the glass-metal elements under in-plane shear loading:

- an evaluation of the out-of-plane displacements under shear loading is not carried out, since the simulations with different Young's moduli for the adhesives are performed geometrically linear and the real out-of-plane displacements are underestimated.

Findings regarding the influence of different **adhesive stiffness** values on the **relative in-plane displacements** between glass pane and metal framing for the glass-metal elements under in-plane shear loading (see Fig. 7.79 and Fig. 7.80):

- both the positive and the negative maximum relative in-plane displacements are decreasing with higher Young's moduli of the adhesives for both element types;
- for a Young's modulus of *1 MPa*, the maximum positive relative in-plane displacements at a given load value are larger for model *Type 2* than for model *Type 1*, while for Young's moduli of *10 MPa* and higher the opposite is the case.

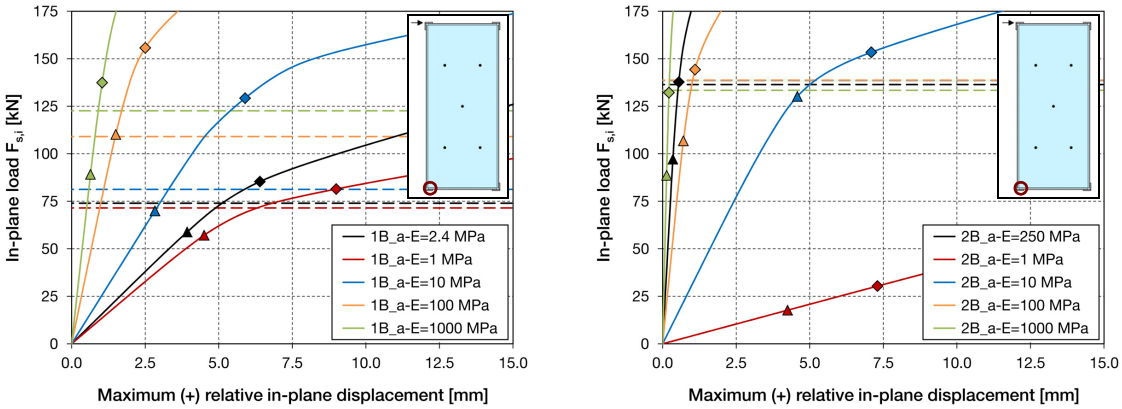

Fig. 7.79 *Influence of the adhesive stiffness on the maximum positive relative in-plane displacements between glass pane and metal framing for model Type 1 (left) and model Type 2 (right)*

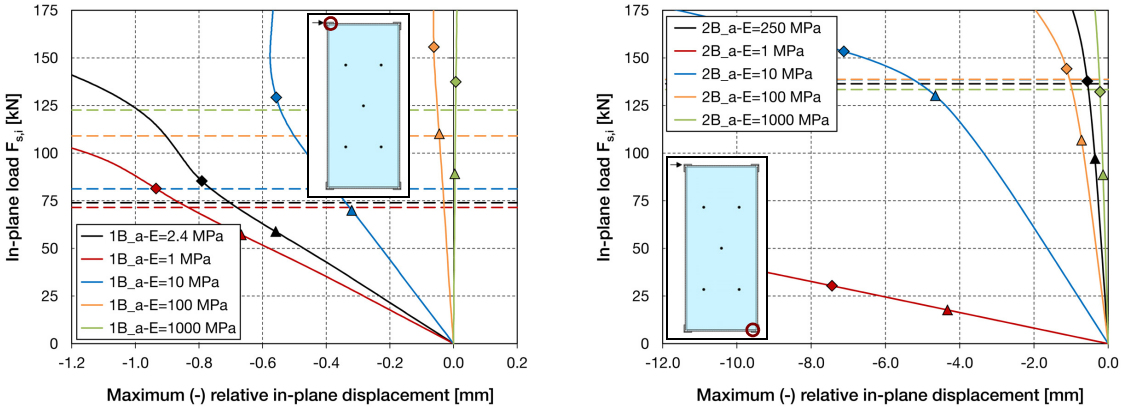

Fig. 7.80 *Influence of the adhesive stiffness on the maximum negative relative in-plane displacements between glass pane and metal framing for model Type 1 (left) and model Type 2 (right)*

Findings regarding the influence of different **adhesive stiffness** values on the **out-of-plane displacements** of the glass panes for the glass-metal elements under out-of-plane surface loading (see Fig. 7.81):

- with higher values for the Young's modulus of the adhesives the out-of-plane displacements under surface loading (suction) are decreasing;
- the out-of-plane displacements for the two system types with the same Young's modulus values for the silicone and the acrylic are almost equal, since linear-elastic materials are used in these simulations for the adhesives.

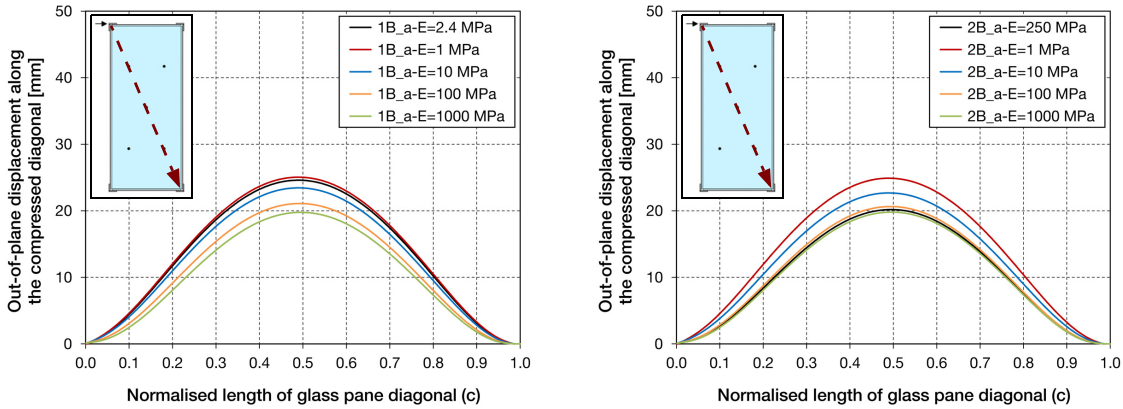

Fig. 7.81 *Influence of the adhesive stiffness on the out-of-plane displacements along one diagonal (compressed glass pane diagonal under shear loading) under a wind suction load of 2.0 kPa for model Type 1 (left) and model Type 2 (right)*

The results evaluated in this subchapter substantiate that the response of the glass-metal elements in terms of both in-plane and out-of-plane displacements is sensitive to different stiffness values of the adhesive. Considering that the in-plane shear load is applied on the metal framing, it is easily to understand how the adhesive stiffness influences the in-plane displacements. For the model *Type 2*, without an adhesive joint, the glass pane would not contribute to the bearing of the in-plane load and the framing would shear off, parallel to the glass pane. A behaviour close to this boundary case is given for low values of the adhesive stiffness. With higher stiffness values, the contribution of the glass pane increases. For the model *Type 1*, a similar effect of the adhesive stiffness is given. However, the glass pane would contribute to the bearing of the in-plane load also without an adhesive joint, due to the additional grouting blocks.

In terms of out-of-plane displacements, the perimetrical adhesive joints provide in the case of both model types a certain degree of composite action depending on their stiffness (see also subchapter 3.2). For the model *Type 1*, also the grouting blocks can have a contribution by preventing a slip between glass pane and framing. The results evaluated in Fig. 7.81 for a wind suction load of *2.0 kPa*, indicate that adhesives with higher stiffness help to reduce the size of the out-of-plane displacements. An additional assessment of the degree of composite action could be done by evaluating the out-of-plane displacements along the metal framing. However, this is not included within this thesis.

7.3.9 Variation of initial geometric imperfections

For the simulations under in-plane shear loading from the subchapters 7.3.1 and 7.3.3 to 7.3.7 alternatives with an initial geometric imperfection based on the first eigenmode scaled by a factor of *L/500*, *L* being in this case the glass pane height, are carried out. Generally, a negligible influence of this imperfections on the in-plane displacements and a relatively small influence on the out-of-plane displacements are observed. In this subchapter it is analysed if a larger imperfection with the same shape or imperfections with different shapes have a higher influence on in-plane and out-of-plane displacements. Initial geometric imperfection shapes based on the first eigenmode determined under shear loading ($F_{s,i}$) and the first eigenmode determined under axial loading ($F_{n,i}$) as well as on the deformation shape resulting under a wind suction load ($F_{p,o}$) are generated (see Fig. 7.82 for the different applied imperfection shapes). For each of these shapes the maximum deflection is scaled by factors of *L/500* and *L/100* to evaluate the influence of the imperfection size.

Findings regarding the influence of different **initial geometric imperfections** on the **global in-plane behaviour** for the glass-metal elements under in-plane shear loading (see Fig. 7.83):

- the initial geometric imperfections scaled by a factor of *L/500* based on the different shapes have almost no influence on the in-plane displacements for both element types (see dashed curves in Fig. 7.83);

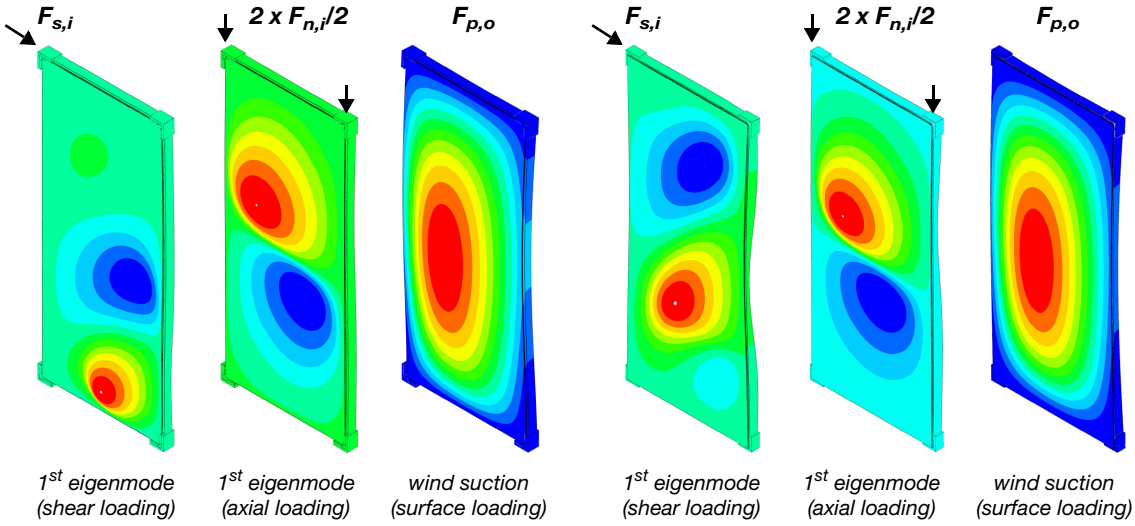

Fig. 7.82 *Investigated shapes of the initial geometric imperfections for model Type 1 (left) and model Type 2 (right)*

- the imperfections scaled by a factor of *L/100* based on the eigenmodes lead to an increase of the in-plane displacements for a given shear load; higher values are reached if the eigenmodes under shear loading are used;
- the imperfections scaled by a factor of *L/100* based on the deformation shape resulting under a wind suction load have no influence on the in-plane displacements for elements of *Type 2*, while for elements of *Type 1* they lead to slightly higher in-plane displacements for loads up to *~75 kN* and to slightly lower in-plane displacements above this load value.

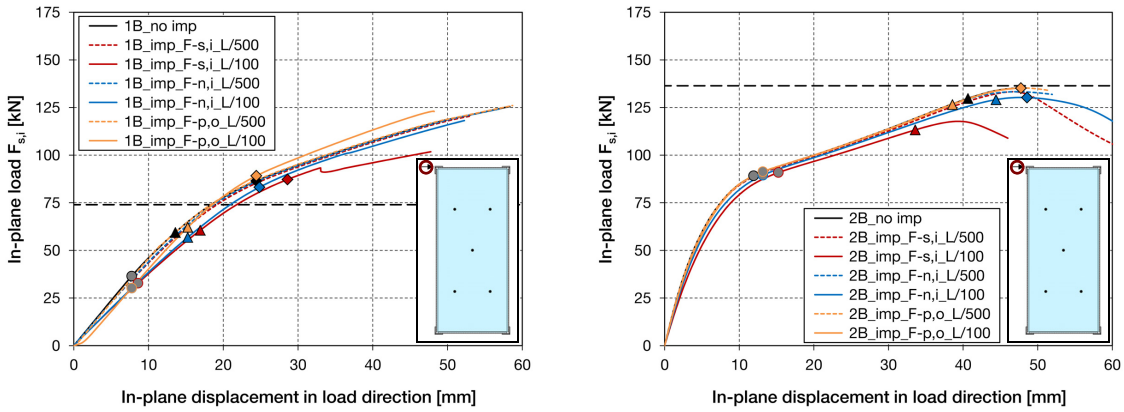

Fig. 7.83 *Influence of the initial geometric imperfection shape and size on the relationship between in-plane shear load and in-plane horizontal displacement measured at reference point RP7 for model Type 1 (left) and model Type 2 (right)*

Findings regarding the influence of different **initial geometric imperfections** on the **out-of-plane displacements** of the glass panes for the glass-metal elements under in-plane shear loading (see Fig. 7.84 and Fig. 7.85):

- for the elements of *Type 1* the imperfections scaled by a factor of *L/500* based on all the different shapes have a rather small influence on the out-of-plane displacements at the top quarter-point of the compressed diagonal, while their influence on the out-of-plane displacements at the bottom quarter-point varies depending on the size of the shear load;
- for elements of *Type 1* an increase of the imperfection size to the factor *L/100* has a higher impact on the out-of-plane displacements, if the eigenmode under axial loading or the deformation shape under a wind suction load is used, than in the case of the eigenmode under shear loading;

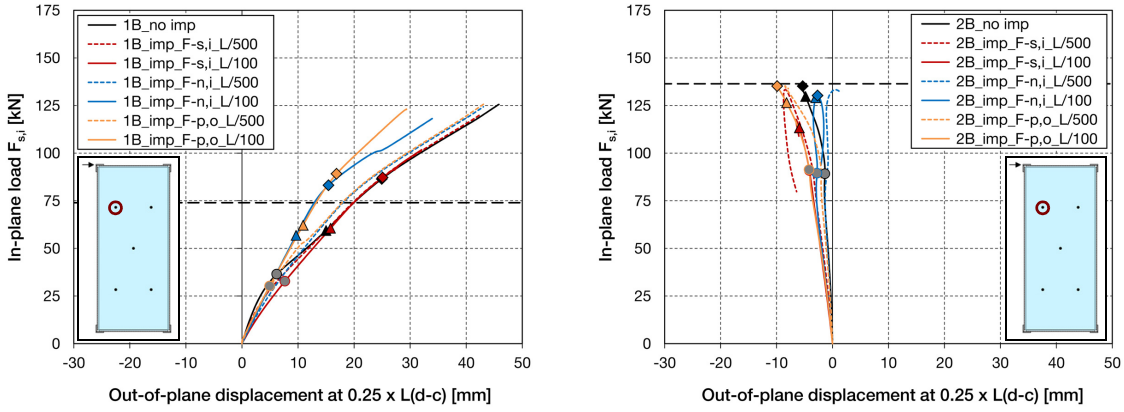

Fig. 7.84 *Influence of the initial geometric imperfection shape and size on the relationship between in-plane shear load and out-of-plane displacement measured at the top quarter-point of the compressed glass pane diagonal for model Type 1 (left) and model Type 2 (right)*

- for elements of *Type 2*, all the applied imperfections slightly increase the out-of-plane displacements at the top quarter-point of the compressed diagonal with a little higher values for

higher imperfection sizes; at the bottom quarter-point, imperfections based on the eigen-mode under shear loading increase the out-of-plane displacements, while the other two shapes decrease them or even orientate them in the opposite direction.

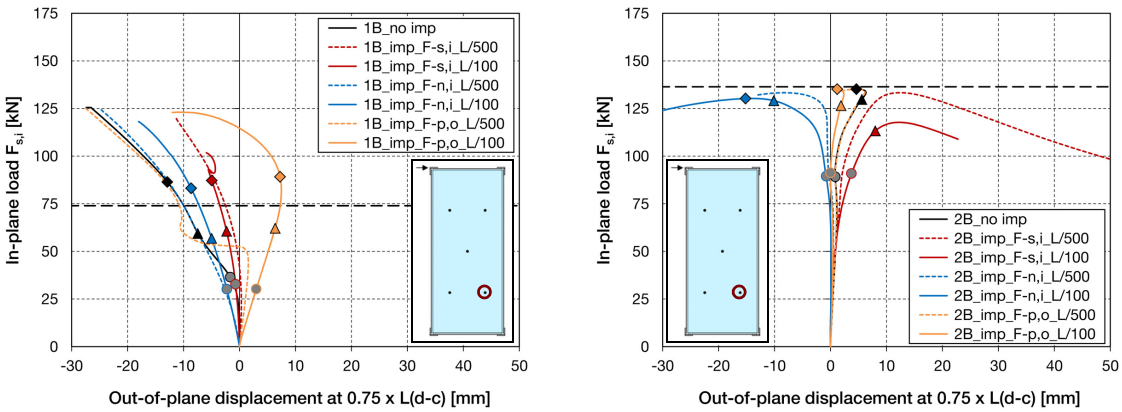

Fig. 7.85 *Influence of the initial geometric imperfection shape and size on the relationship between in-plane shear load and out-of-plane displacement measured at the bottom quarter-point of the compressed glass pane diagonal for model Type 1 (left) and model Type 2 (right)*

7.4 Investigation of different loading scenarios and levels

The finite element simulations in subchapter 7.3 focus mainly on the behaviour of the glass-metal elements under in-plane shear loading and provide also an insight on the behaviour of the elements under out-of-plane wind suction for most parameters. However, in the case of applications in facades, the elements would be subjected to a combination of in-plane shear loads ($F_{s,i}$), out-of-plane surface loads ($F_{p,o}$), in-plane axial loads ($F_{n,i}$) as well as additional temperature loads. Therefore, in this chapter the influence of an additional out-of-plane wind suction or wind pressure load and of an additional in-plane axial load on the behaviour of the elements under in-plane shear loading is assessed. Furthermore, the behaviour of the glass-metal elements under selected temperature loads is evaluated. Other potential extraordinary loads are not considered in this thesis.

7.4.1 Combined wind suction and shear loading

The wind suction loads are applied on the whole exterior surface of the glass pane in a first step and then the shear load is raised displacement-controlled as is done in subchapter 7.3. Values of the wind suction load (*w-s*) from *0.00 kPa* to *1.00 kPa* in steps of *0.25 kPa* are included in the study. Only the out-of-plane displacements are evaluated for this load combination, since the additional surface load has no influence on the in-plane displacements.

Findings regarding the influence of different **wind suction loads** on the **out-of-plane displacements** of the glass panes for the glass-metal elements under in-plane shear loading (see Fig. 7.86, Fig. 7.87 and Fig. 7.88):

- for the elements of *Type 1*, the shape of the out-of-plane displacements is dominated by the displacements resulting from the shear loading; a wind suction load, generally, increases the positive out-of-plane displacements, decreases the negative ones and shifts the maximum positive displacement towards the centre of the glass pane;

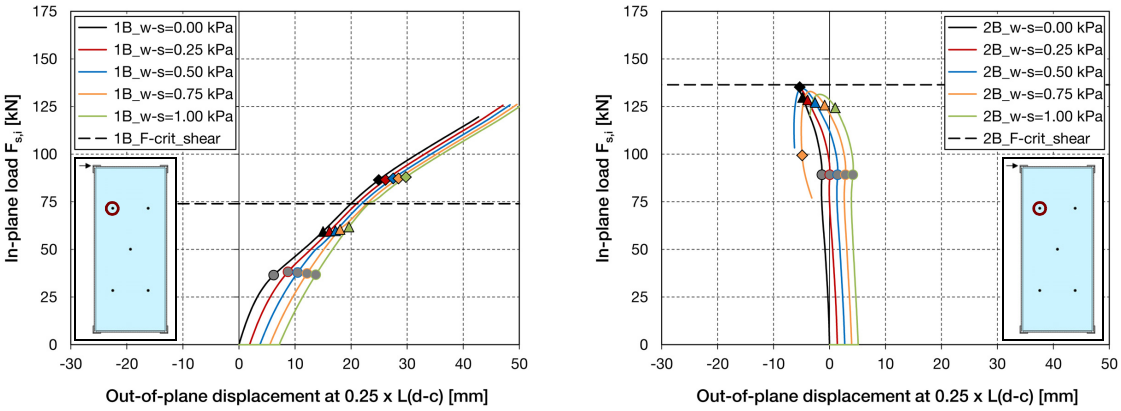

Fig. 7.86 *Influence of a wind suction surface load on the relationship between in-plane shear load and out-of-plane displacement measured at the top quarter-point of the compressed glass pane diagonal for model Type 1 (left) and model Type 2 (right)*

- for the elements of *Type 1* a kind of snap-through effect, which is more pronounced for

higher wind suction loads, can be observed at the bottom quarter-point of the compressed diagonal;

- for the elements of *Type 2*, the shape of the out-of-plane displacements is dominated by the displacements resulting from the wind suction load; such a load, generally, increases the positive out-of-plane displacements, decreases the negative ones or turns them into positive ones;
- the size of the wind suction load has almost no influence on the shear load value at which the maximum principal stress of *1 MPa* occurs in the silicone adhesive and the Mises stress of *10 MPa* occurs in the acrylic adhesive (see coloured circles with grey filling);
- the influence on the shear load value at which the marked maximum principal stresses of *70 MPa* and *120 MPa* occur in the glass panes is also small for both element types.

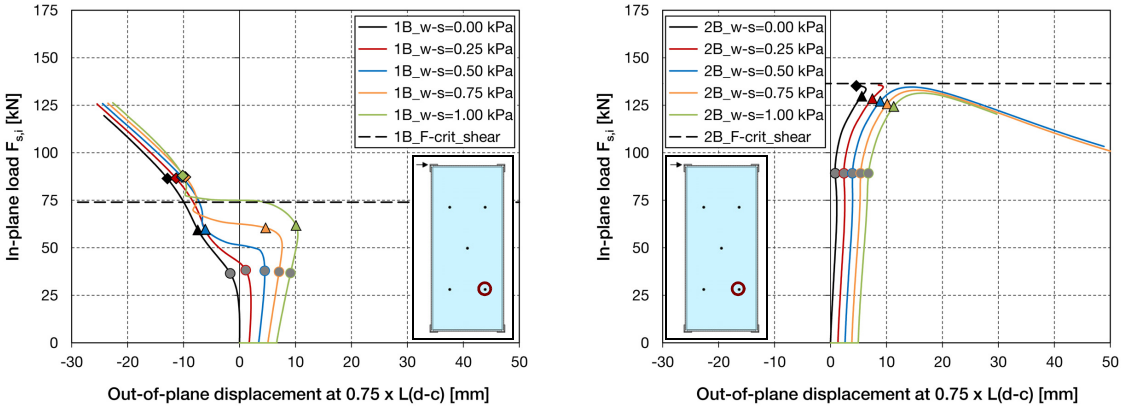

Fig. 7.87 *Influence of a wind suction surface load on the relationship between in-plane shear load and out-of-plane displacement measured at the bottom quarter-point of the compressed glass pane diagonal for model Type 1 (left) and model Type 2 (right)*

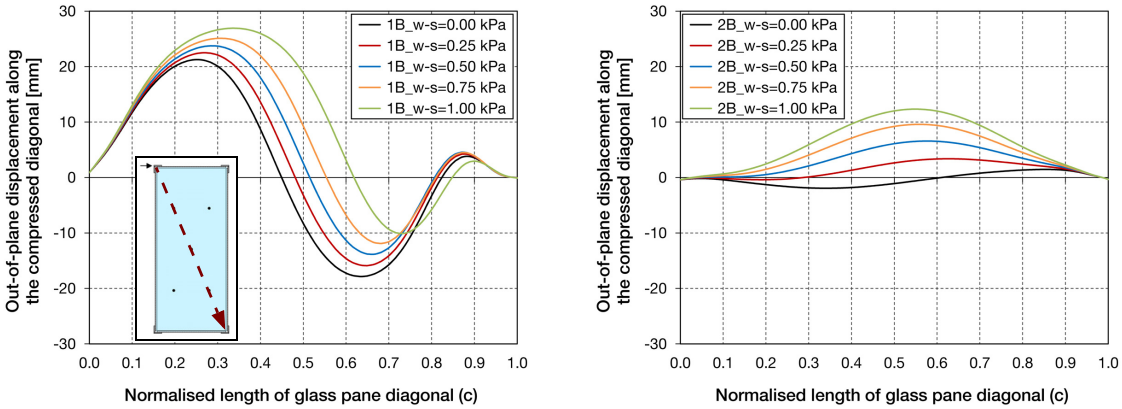

Fig. 7.88 *Influence of a wind suction surface load on the out-of-plane displacements along the compressed glass pane diagonal at a horizontal in-plane displacement of the reference point for shear load application of 20 mm for model Type 1 (left) and model Type 2 (right)*

7.4.2 Combined wind pressure and shear loading

The wind pressure loads are applied similar to the wind suction loads in the previous subchapter on the whole exterior surface of the glass pane. Values of the wind pressure load (*w-p*) from *0.00 kPa* to *1.00 kPa* in steps of *0.25 kPa* are included in the study. As in the case of the combination with a wind suction load, only the out-of-plane displacements are evaluated, since the additional surface load has no influence on the in-plane displacements.

Findings regarding the influence of different **wind pressure loads** on the **out-of-plane displacements** of the glass panes for the glass-metal elements under in-plane shear loading (see Fig. 7.89, Fig. 7.90 and Fig. 7.91):

- generally, a wind pressure load has an opposite effect on the out-of-plane displacements of the glass pane than a wind suction load, for both element types;

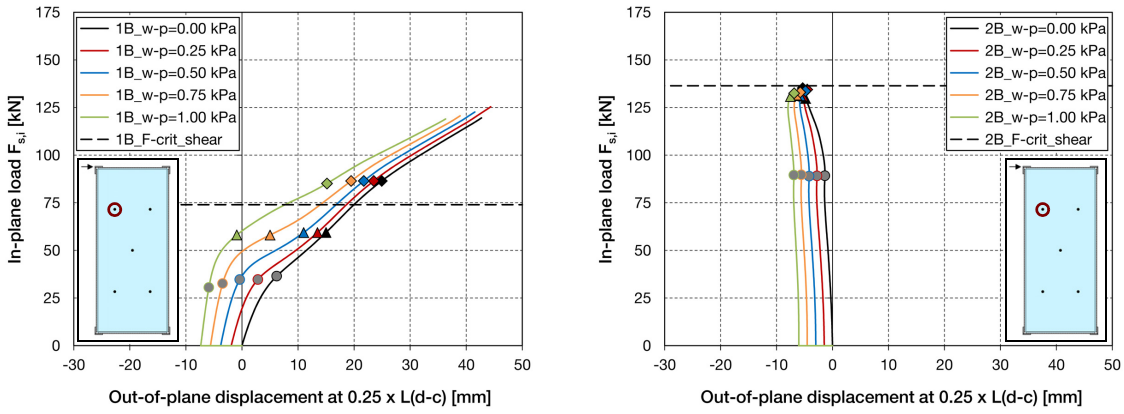

Fig. 7.89 *Influence of a wind pressure surface load on the relationship between in-plane shear load and out-of-plane displacement measured at the top quarter-point of the compressed glass pane diagonal for model Type 1 (left) and model Type 2 (right)*

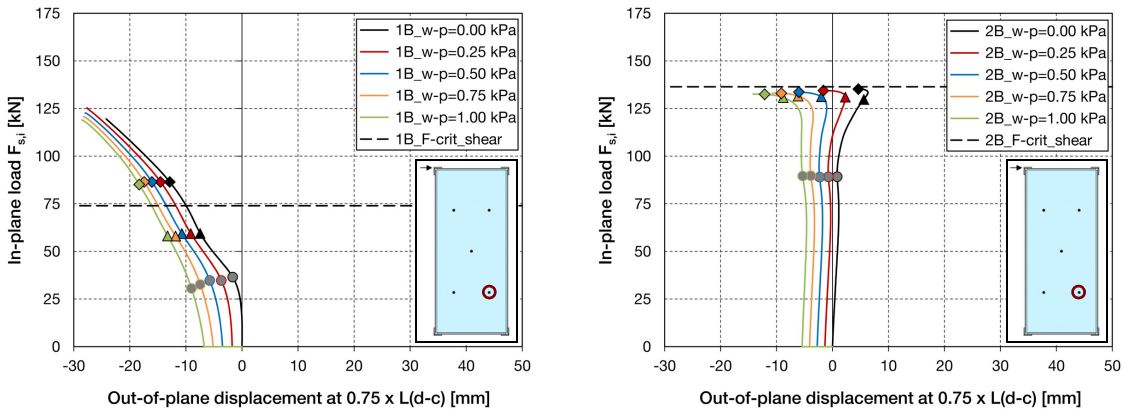

Fig. 7.90 *Influence of a wind pressure surface load on the relationship between in-plane shear load and out-of-plane displacement measured at the bottom quarter-point of the compressed glass pane diagonal for model Type 1 (left) and model Type 2 (right)*

- for the elements of *Type 1*, the shape of the out-of-plane displacements is dominated by the displacements resulting from the shear loading; a wind pressure load, generally, decreases the positive out-of-plane displacements, increases the negative ones and shifts the maximum negative displacement towards the centre of the glass pane;
- for the elements of *Type 2*, the shape of the out-of-plane displacements is dominated by the displacements resulting from the wind pressure load; such a load, generally, increases the negative out-of-plane displacements and decreases the positive ones or turns them into negative ones;
- the size of the wind pressure load has almost no influence on the shear load value at which the Mises stress of *10 MPa* occurs in the acrylic adhesive, but the shear load value at which the maximum principal stress of *1 MPa* occurs in the silicone adhesive is slightly reduced with higher wind pressure loads (see coloured circles with grey filling);
- there is almost no influence on the shear load value at which the marked stresses of *70 MPa* and *120 MPa* occur in the glass panes for both element types.

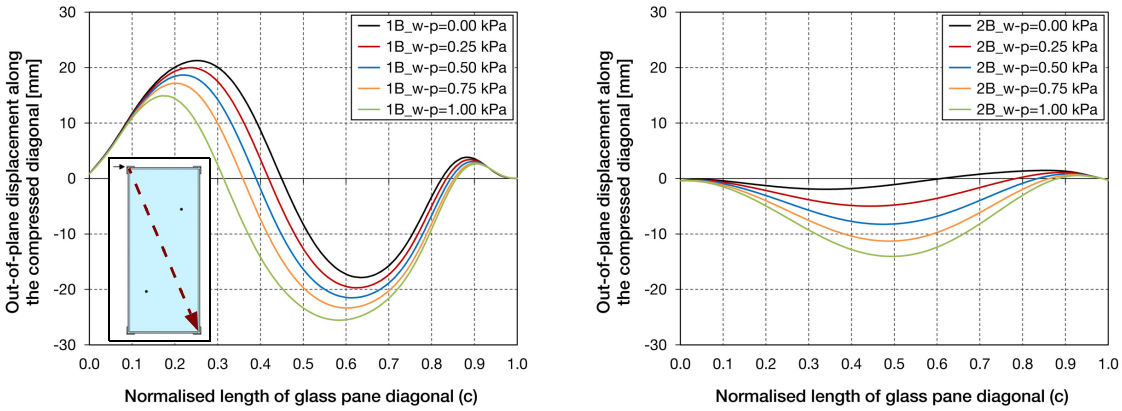

Fig. 7.91 *Influence of a wind pressure surface load on the out-of-plane displacements along the compressed glass pane diagonal at a horizontal in-plane displacement of the reference point for shear load application of 20 mm for model Type 1 (left) and model Type 2 (right)*

7.4.3 Combined axial loading and shear loading

The in-plane axial loads are applied in a first step as illustrated in Fig. 7.27 for support conditions of *type (a)* and then the shear load is raised displacement-controlled. Values of the axial load ($F_{n,i}$) from *0 kN* to *100 kN* in steps of *25 kN* are included in the study. The out-of-plane displacements of the glass pane and the relative in-plane displacements between glass pane and metal framing are evaluated for this load combination.

Findings regarding the influence of different **in-plane axial loads** on the **out-of-plane displacements** of the glass panes for the glass-metal elements under in-plane shear loading (see Fig. 7.92, Fig. 7.93 and Fig. 7.94):

- the influence of an axial load of the applied sizes on the out-of-plane displacements is significantly smaller than that of the surface loads applied in the previous two subchapters for both element types;

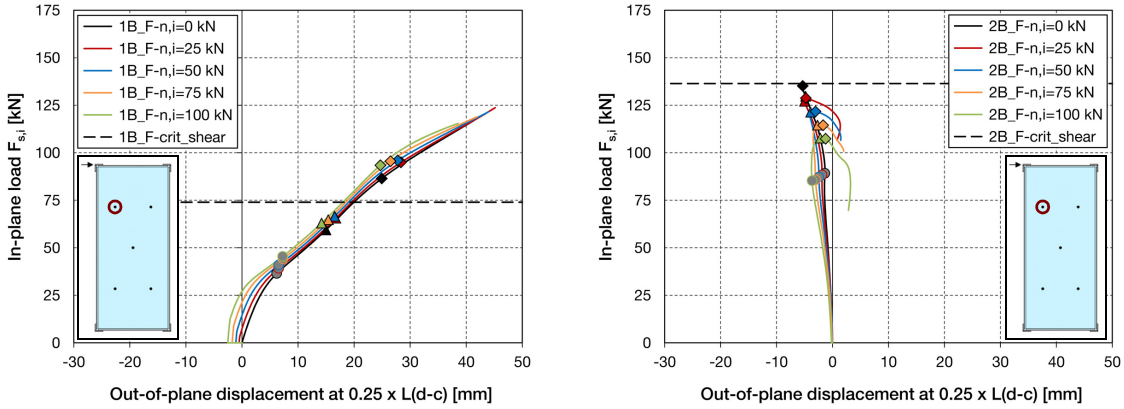

Fig. 7.92 *Influence of an axial load on the relationship between in-plane shear load and out-of-plane displacement measured at the top quarter-point of the compressed glass pane diagonal for model Type 1 (left) and model Type 2 (right)*

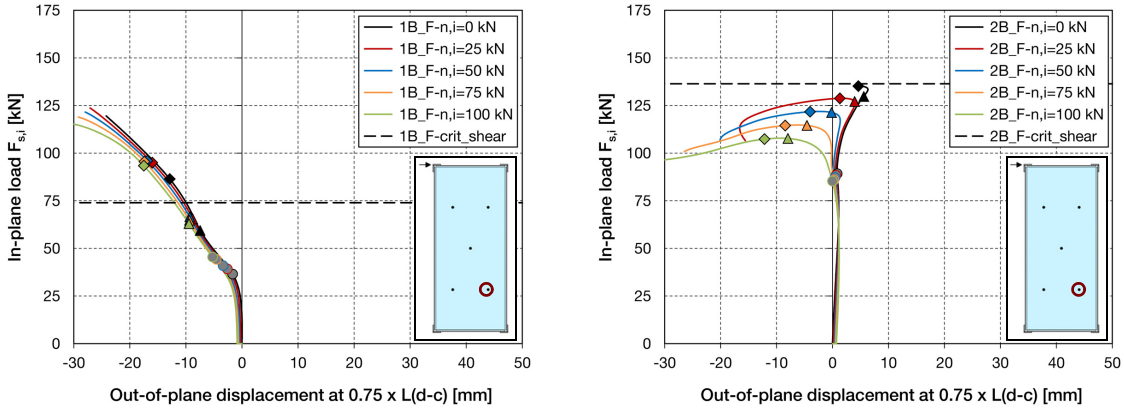

Fig. 7.93 *Influence of an axial load on the relationship between in-plane shear load and out-of-plane displacement measured at the bottom quarter-point of the compressed glass pane diagonal for model Type 1 (left) and model Type 2 (right)*

- for elements of *Type 1*, an additional axial load slightly reduces the positive out-of-plane displacements and increases the negative ones;
- for elements of *Type 2*, an additional axial load slightly increases the negative out-of-plane displacements, while in the case of the positive ones it reduces them and at a certain shear load they turn into negative ones; moreover, the maximum bearable shear load is reduced with increasing axial load;
- the shear load value at which the maximum principal stress of *1 MPa* occurs in the silicone adhesive is slightly increased with higher additional axial load, while the shear load value at which the Mises stress of *10 MPa* occurs in the acrylic adhesive is slightly reduced with higher additional axial load;
- for elements of *Type 2*, the shear load at which a maximum principal stress of *70 MPa* is reached in the glass pane is decreasing with higher additional axial load.

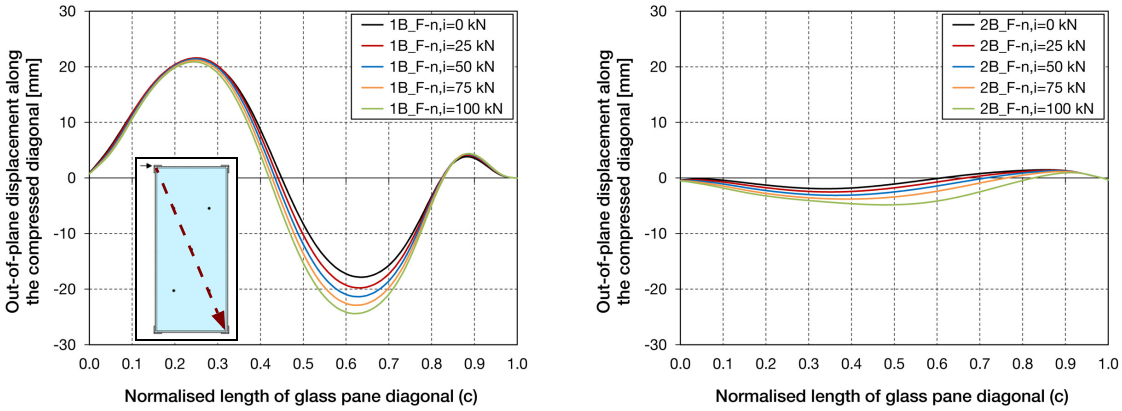

Fig. 7.94 *Influence of an axial load on the out-of-plane displacements along the compressed glass pane diagonal at a horizontal in-plane displacement of the reference point for shear load application of 20 mm for model Type 1 (left) and model Type 2 (right)*

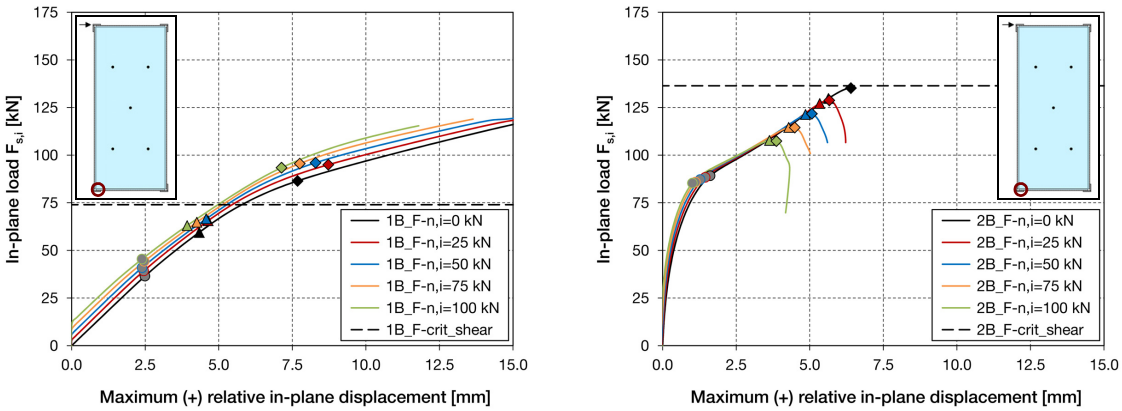

Fig. 7.95 *Influence of an axial load on the maximum positive relative in-plane displacements between glass pane and metal framing for model Type 1 (left) and model Type 2 (right)*

Findings regarding the influence of different **in-plane axial loads** on the **relative in-plane displacements** between glass pane and metal framing for the glass-metal elements under in-plane shear loading (see Fig. 7.95 and Fig. 7.96):

- for both element types, with increasing additional axial loads the maximum positive relative in-plane displacements are reduced, while the negative ones are increased.

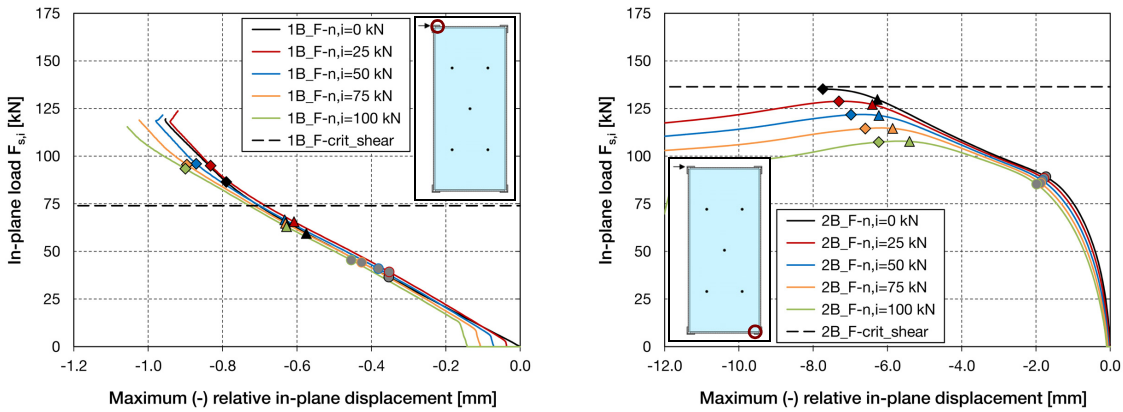

Fig. 7.96 *Influence of an axial load on the maximum negative relative in-plane displacements between glass pane and metal framing for model Type 1 (left) and model Type 2 (right)*

7.4.4 Performance under temperature loads

In subchapter 3.3.2 basic considerations for temperature loads are given assuming that the location where the investigated glass-metal elements are applied is Vienna. Based on the temperature differences determined in the mentioned subchapter, three load scenarios are analysed in this subchapter: *(i)* heating of the whole elements from *+20 °C* to *+38 °C* (ΔT_{gp} *= +18 °C* & ΔT_{mf} *= +18 °C*), *(ii)* heating of the metal framing from *+20 °C* to *+80 °C* and of all other components from *+20 °C* to *+38 °C* (ΔT_{gp} *= +18 °C* & ΔT_{mf} *= +60 °C*) and *(iii)* cooling of the whole elements from *+20 °C* to *-26 °C* (ΔT_{gp} *= -46 °C* & ΔT_{mf} *= -46 °C*). The temperature loads are applied as predefined fields in the software application *Abaqus/CAE*. For the different materials, the thermal expansion coefficients provided in Tab. 7.15 are used in the simulations.

Tab. 7.15 *Thermal expansion coefficients used in the finite element simulations for the different materials*

Material	Glass	Interlayer	Stainless steel	Structural steel	Grout	Adhesives
Thermal expansion coefficient α_T [1/K]	9×10^{-6}	200×10^{-6}	16×10^{-6}	12×10^{-6}	34×10^{-6}	100×10^{-6}

The resulting qualitative global displacements are illustrated in Fig. 7.97 for the two element types. In the case of heating, the different elongations of the framing and the glass panes have to be counterbalanced solely by the adhesives in both element types. This leads to a buckling of the elements of *Type 2* inwards due to the higher stiffness of the acrylic, which is not the case for elements of *Type 1*. In the case of cooling, the grouting blocks are activated for elements of *Type 1* and, therefore, both element types buckle outwards (metal framing expands more than glass pane). However, it can be noticed based on the deformation shapes, that a more uniform load transfer between framing and glass pane is accomplished for the elements of *Type 2*.

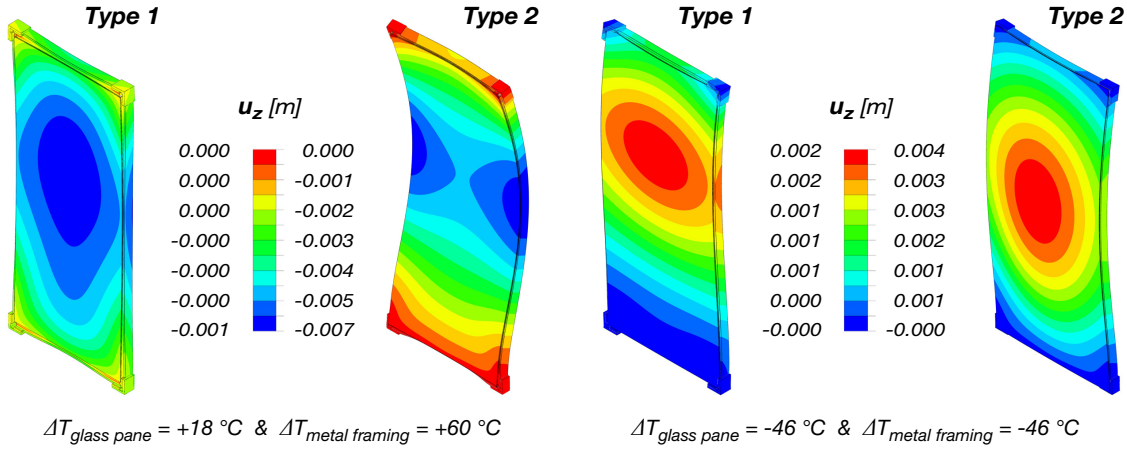

Fig. 7.97 *Out-of-plane displacements (scaled by a factor of 50) for model Type 1 and model Type 2 under temperature loads: heating (left) and cooling (right)*

Findings regarding the influence of different **temperature loads** on the **relative in-plane displacements** between glass pane and metal framing for the glass-metal elements under in-plane shear loading (see Fig. 7.98):

- for the heating load scenarios, the relative in-plane displacements are larger for elements of *Type 1* than for elements of *Type 2* both near the bottom and near the top edges;
- for the cooling load scenario, the relative in-plane displacements near the bottom edge are larger for elements of *Type 2*, while those near the top edge are larger for elements of *Type 1*.
- the maximum stresses in the adhesives are reached under load scenario *(ii)*: a maximum principal stress of *~0.62 MPa* in the silicone and a Mises stress of *~6.90 MPa* in the acrylic.

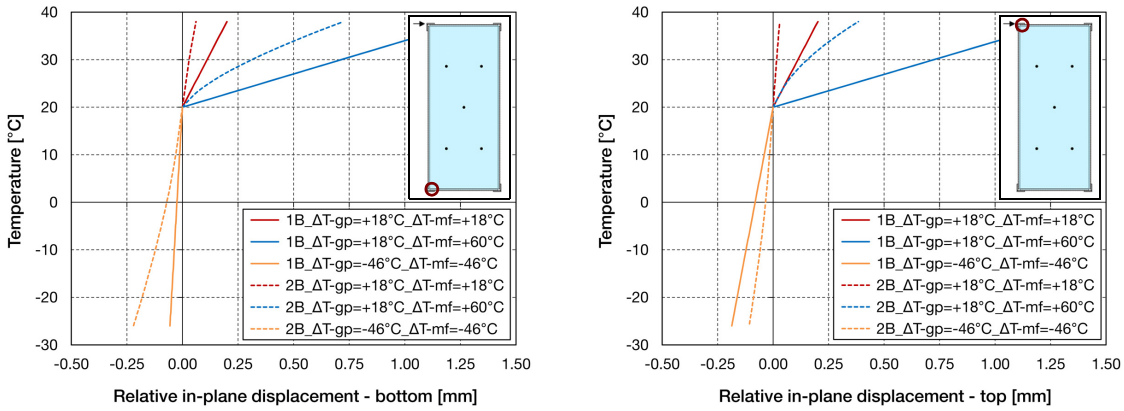

Fig. 7.98 *Influence of temperature loads on the relative in-plane displacements between glass pane and metal framing for model Type 1 and model Type 2 near the bottom edge (left) and near the top edge (right)*

7.5 Conclusions on the large-scale finite element simulations

As it is often the case in research projects dealing with investigations at real scale, the number of large-scale test specimens is limited by the available funding. In order to be able to evaluate the influence of different parameters and additional loading scenarios on the structural behaviour of the elements, finite element models are developed and validated by comparison to the available experimental results obtained from the small number of tested large-scale specimens. Geometrically non-linear simulations are performed on models with second order solid elements for all components. Among the assumptions made for the finite element models, a significant influence on the results have the properties assigned to the different materials, especially to the load transfer materials for which no generally valid material models are available.

Hyperelastic properties based on the *Mooney-Rivlin* parameters used also in subchapter 5.2.4 for the silicone adhesive *Dow Corning 993* and linear-elastic properties for the grouting lead to simulation results in good agreement with the experimental ones for the system of *Type 1*. For the system of *Type 2*, the strain rate dependent plastic model without consideration of porosity leads to simulation results in good agreement with the experimental ones in terms of system stiffness, but the yielding of the adhesive occurs delayed and the loads after yielding are overestimated by *~30%* in the simulation. The addition of the porous properties defined in subchapter 5.2.4 for the acrylic adhesive allow an improvement of this aspect, but do not lead to satisfying results. Therefore an additional fitting procedure of the plastic material data by reducing the yield stresses by *30%* is performed to obtain a model which allows a good prediction of the experimental results.

The influence of several parameters on the structural behaviour of the two glass-metal element types is assessed with the validated finite element models based on absolute and relative displacements. Support conditions, glass pane height and assembly, framing depth and corner thickness, adhesive cross section and Young‘s modulus as well as initial geometric imperfections are varied. The variation of support conditions simulates different positions of a glass-metal element in a facade. It illustrates that elements which are not fixed to the ground and for which a rotation of all four corner elements is allowed, can only bear smaller loads and experience larger displacements.

In the case of the glass pane height, larger values lead to an increase of all occurring displacements under a given load. Different glass pane assemblies mainly influence the resulting out-of-plane displacements, while only the alternative with a *6 mm* thin glass pane has an impact on in-plane displacements. In the case of the varied framing depths, only values smaller than *100 mm* have a significant influence on both absolute and relative resulting displacements, while larger values have only a small effect. Different corner thicknesses exercise an influence on in-plane and out-of-plane displacements resulting under in-plane shear loading, but have no influence on the displacements resulting under an out-of-plane surface load. Both the adhesive joint cross section and the adhesive Young‘s modulus determine the stiffness of the adhesive bonding and therefore, a variation of these parameters has an impact on both the resulting in-plane and out-of-plane displacements. However, in the case of the Young‘s modulus, values higher than *100 MPa* have a smaller influence, than lower values. Initial geometric imperfections

slightly reduce the in-plane stiffness of the systems and modifies the out-of-plane displacements under in-plane shear loading. However, their influence is not large, since the geometry, the supports and the loading of the glass-metal elements is non-symmetric.

The influence of additional loads on displacements resulting under in-plane shear loading is also investigated in finite element simulations with the validated models. Out-of-plane wind suction and wind pressure loads of up to *1.0 kPa* and in-plane axial loads of up to *100 kN* are added in separate studies. While the additional out-of-plane loads have a considerable effect on the size of resulting out-of-plane displacements, the influence of the additional in-plane axial loads is rather small. However, in the case of the system with acrylic adhesive, it is observed that with increasing additional axial load, the maximum bearable shear load is decreasing.

Considering the different thermal expansion coefficients of glass and of the metals used for the framing, the structural behaviour of the glass-metal elements under temperature loads is assessed in a case study. During heating scenarios, the framing is expanding more than the glass. Gaps are resulting between the glass pane and the grouting blocks and therefore only the adhesives are transferring loads between the glass pane and the framing. Higher relative in-plane displacements between the glass pane and the metal framing are resulting in the case of heating for the elements with silicone adhesive bonding and grouting blocks compared to those with acrylic adhesive. In the case of the latter ones, also an out-of-plane bending of the whole elements is occurring due to the higher stiffness of the acrylic adhesive compared to the silicone adhesive. During cooling scenarios, the framing contracts more than the glass and therefore the grouting blocks are activated. This leads to reduced relative in-plane displacements for the elements of *Type 1*. Cooling scenarios cause out-of-plane displacements of the glass pane for both element types.

8 Approaches for structural and functional design

Considerations on the transfer between research and practice
Simplified mechanical models
Design approach for composite structural glazing systems
Conceptual extensions regarding building physics requirements

1 Introduction 1

2 State of the art – theoretical framework

3 Transparent building envelopes with composite structural behaviour

4 Investigations on adhesives and their adhesion to metal substrates

5 Mechanical behaviour of adhesive joints between glass and stainless steel

6 Experimental investigations on large-scale multi-component elements

7 Finite element investigations on large-scale multi-component elements

8 Approaches for structural and functional design 8

9 Conclusions and future research 9

8.1 Considerations on the transfer between research and practice

Although the topic of this thesis is application driven, the investigations documented in the previous four chapters are based on scientific research methodologies. Accurate determination of material properties by experimental testing, derivation of adequate material models for predicting the mechanical behaviour of certain materials under specific conditions, experimental testing on conceptual innovative structural systems and parameter studies based on complex finite element simulations are used for these investigations. Structural and facade engineering offices being part of the building industry, however, are often driven primarily by cost and implicitly time efficiency. Therefore, especially for the preliminary design phases, adequate tools and appropriate simplified models are required for assessing if certain concepts are applicable for given tasks.

Another aspect which generally characterizes scientific research is setting the focus on a particular detailed task of a wider problem. This approach leads to a series of assumptions and simplifications which in most cases have the aim to exclude certain factors of influence on the investigated properties. In the case of the concept of glass-metal elements with composite structural behaviour by adhesive bonding, an application in transparent facades is envisaged. This application presumes beside the structural performance a series of functional requirements which are briefly discussed in subchapter 3.4. However, the investigations in this thesis focus on the structural behaviour of such elements, mainly under ambient conditions. The influence of more extreme temperatures on this behaviour as well as factors which influence the ageing, like moisture or UV-radiation, are not directly included in the investigations, but are considered in the material selection process. If an implementation of the studied structural concept in a real facade project is intended, the elements analysed experimentally and by finite element methods need to be further adapted to fulfil functional requirements, like water tightness and thermal insulation among several others.

The content of this chapter intends to provide approaches for bridging the gap between complexity and assumptions from scientific research and requirements from engineering offices regarding the investigated concept of glass-metal elements with composite structural behaviour by adhesive bonding. The presented approaches for structural and functional design should ease a future application of this concept.

8.2 Simplified mechanical models

Engineering offices, generally, prefer to use simplified mechanical models for structural design tasks, especially in early project phases. The reasons for this are, primarily, the aimed time and implicitly cost efficiency. Secondly, many structural design offices do not have access to software for complex finite element simulations like Abaqus or Ansys. Therefore, simplified mechanical models are derived in this subchapter for the two investigated systems with composite structural behaviour by adhesive bonding. The derived models should allow the prediction of the in- and the out-of-plane behaviour of the glass-metal elements regarding stiffness and deformations. The main simplification is the replacement of the solid elements used in chapter 7 for all materials with shell, beam or spring elements. This reduces significantly the computation time, but demands a thorough consideration of thicknesses and eccentricities for the different components. Further simplifications are considered in terms of replacing non-linear material behaviours with linear-elastic ones. However, it should be kept in mind that, generally, the more simplifications are made, the more inaccurate the obtained results will be.

For deriving the simplified mechanical models for the two investigated systems, the spring model proposed by [Huveners, 2009] and discussed by [Huveners et al., 2009] and by [Cruz et al., 2010] for a glass pane adhesively bonded along its perimeter to a rigid metal frame with an adhesive joint at the glass edge is used as a starting basis. The load transfer concept for the system investigated by [Huveners, 2009] is represented schematically in Fig. 8.1, left, while the concepts for the two systems investigated in this thesis are illustrated in the same figure, middle and right.

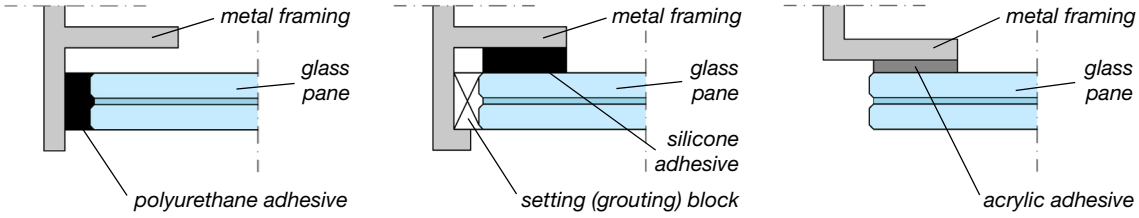

Fig. 8.1 *Schematic representations of the load transfer concepts between glass pane and framing for the system investigated by [Huveners, 2009] (left) as well as for the systems of Type 1 (middle) and of Type 2 (right) studied in this thesis*

The spring model proposed by [Huveners, 2009] is considered valid for predicting the in-plane behaviour of the system regarding stiffness and deformations and is based on several basic assumptions:

- rigid in-plane acting of the glass pane and no initial out-of-plane displacements;
- no bending and no deformation in axial direction of the steel profiles;
- linear distribution of the normal stresses in the adhesive joint;
- uniform distribution of the shear stresses in the adhesive joint.

The model consists of eight discrete normal springs and four discrete shear springs as shown in Fig. 8.2. The equations for determining the spring stiffnesses for an assumed linear material behaviour are given in Fig. 8.2 beside the sketch of the model. In case of a non-linear material

behaviour it is recommended to substitute the quotient of Young's modulus E_a and joint thickness t_a with a curve based on quotients of normal stress and relative in-plane displacement in normal direction, respectively the quotient of shear modulus G_a and joint thickness t_a with a curve based on quotients of shear stress and in-plane displacement in longitudinal direction.

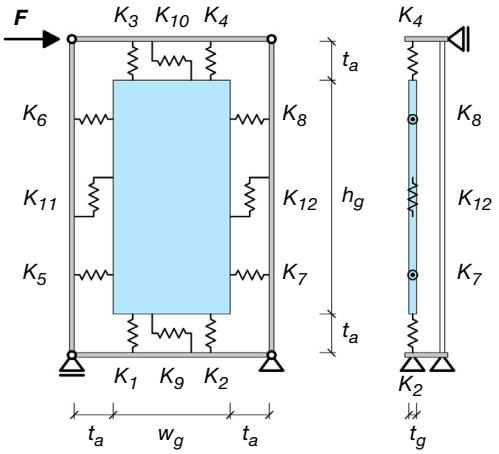

$$K_1 = K_2 = K_3 = K_4 = \frac{3}{8} \cdot \frac{E_a}{t_a} \cdot t_g \cdot w_g \qquad \text{(Eq. 8.1)}$$

$$K_5 = K_6 = K_7 = K_8 = \frac{3}{8} \cdot \frac{E_a}{t_a} \cdot t_g \cdot h_g \qquad \text{(Eq. 8.2)}$$

$$K_9 = K_{10} = \frac{G_a}{t_a} \cdot t_g \cdot w_g \qquad \text{(Eq. 8.3)}$$

$$K_{11} = K_{12} = \frac{G_a}{t_a} \cdot t_g \cdot h_g \qquad \text{(Eq. 8.4)}$$

Fig. 8.2 *Mechanical spring model proposed by [Huveners, 2009] for glass panes which are adhesively bonded at the glass edge along their perimeter*

8.2.1 Adaptation of existing mechanical models for the investigated systems

In [Huveners, 2009] the spring model is used to determine in-plane displacements of the system. In this subchapter, this is not the primary objective, but to derive mechanical models which can be implemented in finite element software used in structural design offices. First, the spring model is adapted for the system of *Type 2* with perimetrical acrylic adhesive bonding, since only the position of the adhesive is differing, but no additional materials are introduced. The adapted model is illustrated in Fig. 8.3. The formulas for determining the spring stiffnesses for transferring the in-plane loads are provided beside the model sketch. Different to the system treated by [Huveners, 2009], all twelve springs are discrete shear springs.

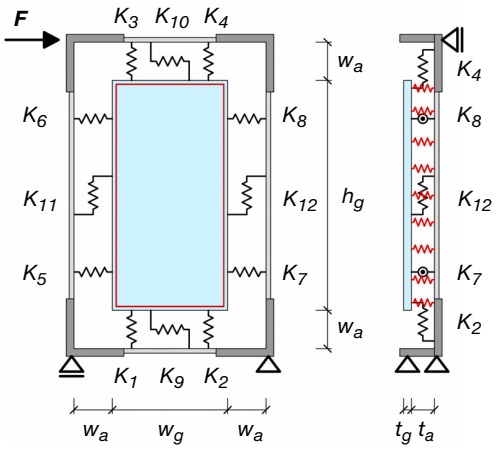

$$K_1 = K_2 = K_3 = K_4 = \frac{3}{8} \cdot \frac{G_a}{t_a} \cdot w_a \cdot w_g \qquad \text{(Eq. 8.5)}$$

$$K_5 = K_6 = K_7 = K_8 = \frac{3}{8} \cdot \frac{G_a}{t_a} \cdot w_a \cdot h_g \qquad \text{(Eq. 8.6)}$$

$$K_9 = K_{10} = \frac{G_a}{t_a} \cdot w_a \cdot w_g \qquad \text{(Eq. 8.7)}$$

$$K_{11} = K_{12} = \frac{G_a}{t_a} \cdot w_a \cdot h_g \qquad \text{(Eq. 8.8)}$$

Fig. 8.3 *Mechanical spring model proposed for the system of Type 2 with perimetrical adhesive bonding with acrylic*

The Young's modulus of the adhesive, E_a, used for the stiffnesses K_1 to K_8 by [Huveners, 2009] is replaced in the model for the system of *Type 2* by the shear modulus of the adhesive, G_a. Furthermore, different dimensions of the adhesive joint have to be considered, since the position of the joint is not at the glass edge, but on the glass surface. Going a step further than the model proposed by [Huveners, 2009], perimetrical normal spring elements are introduced for the transfer of out-of-plane loads between the glass pane and the framing (red spring elements in Fig. 8.3). These spring elements have to be positioned with such a frequency, that the glass pane is not able to buckle between the springs. The stiffness of these spring elements, K_{oop}, can be determined by (Eq. 8.9), where $l_{a,influence}$ is the influence length of one spring.

$$K_{oop} = \frac{E_a}{t_a} \cdot w_a \cdot l_{a,\,influence} \qquad \text{(Eq. 8.9)}$$

In the case of the system of *Type 1* with perimetrical silicone adhesive bonding and local grouting (setting blocks) at the glass corners, the behaviour of the adhesive joint can be represented by the same type of spring elements as in the case of the system of *Type 2*. This is valid both for the transfer of in-plane and out-of-plane loads. To represent the grouting (setting blocks) eight additional normal springs are introduced. The stiffness for one such spring can be determined by (Eq. 8.10). For a proper representation of the in-plane load transfer, these springs should only transfer compression loads, while in case of tension they should be ineffective.

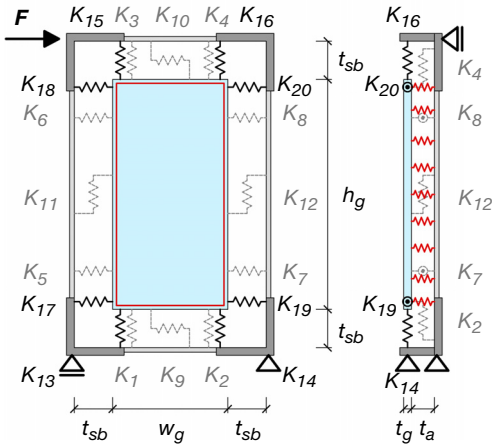

The spring stiffnesses K_1 to K_{12} can be determined with (Eq. 8.5) to (Eq. 8.8) as in the case of the model for the system of *Type 2*. However, since the in-plane loads are transferred mainly over the grouting (setting blocks), the contribution of the silicone adhesive can also be neglected.

$$K_{13} \text{ to } K_{20} = \frac{E_{sb}}{t_{sb}} \cdot t_g \cdot l_{sb} \qquad \text{(Eq. 8.10)}$$

Fig. 8.4 *Mechanical spring model proposed for the system of Type 1 with perimetrical adhesive bonding with silicone adhesive and additional grouting blocks*

The notations used in (Eq. 8.5) to (Eq. 8.10) have the following meanings:

K_i	spring stiffness
t_g	thickness of the glass pane
w_g	width of the glass pane
h_g	height of the glass pane
t_a	thickness of the perimetrical adhesive joint
w_a	width of the perimetrical adhesive joint

t_{sb}	thickness of the grouting (setting blocks)
l_{sb}	length of one grouting (setting block)
G_a	shear modulus of the adhesive material
E_{sb}	Young‘s modulus of the grouting (setting block) material

8.2.2 Evaluation at element level with a structural engineering software

To assess the suitability of the simplified mechanical models introduced in the previous subchapter for the investigated glass-metal elements, finite element simulations are carried out with a software application often used in structural engineering offices (*RFEM 5* from *Dlubal*). Monolithic glass panes with the dimensions of *1.5 m x 3.5 m* and a thickness of *10 mm* are used for the glass-metal elements in these simulations. The dimensions of all other components are similar to those of the reference models in subchapter 7.3 (see Tab. 7.5). The glass panes and the metal framing are modelled with shell elements having their midplanes as reference planes. For the two adhesives, beam elements with eccentricities (axial and lateral) are used instead of spring elements, since the latter type only allows for an axial stiffness in the used software application and for the adhesives the consideration of their shear stiffness is essential. The grouting blocks are modelled with compression struts with eccentricities (axial), which are not able to transfer tensile stresses. Representations of the corner area for the models of *Type 1* and those of *Type 2* are shown both in a full transparent style and in a wired style in Fig. 8.5.

For the length of both the beam elements and the compression struts, the thickness of the respective load transfer material (silicone adhesive, acrylic adhesive or grouting) is used. For the cross sections of these elements, one dimension is equivalent to the width of the respective load transfer material, while the other results from the number of such elements used along the length of the load transfer material. Each grouting block with a length of *100 mm* is represented by two compression strut elements with a length of *10 mm* and a cross section of *50 mm* x *22 mm*. The adhesive joints along the length of each grouting block are represented by two beam elements with a cross section of *50 mm x 20 mm*. Between the grouting blocks, ten beam elements with a cross section of *124 mm x 20 mm* are used along the width of the glass panes and thirty beam elements with a cross section of *108 mm x 20 mm* along the height of the glass panes. The length of the beam elements is *6 mm* for the model of *Type 1* (silicone adhesive) and *3 mm* for the model of *Type 2* (acrylic adhesive). The axial eccentricities applied in the case of the beam elements and of the compression struts are necessary for compensating the shell thicknesses of the glass panes and the framing edge elements. The lateral eccentricities applied in the case of the beam elements are responsible for translating the adhesive joints by half of their width towards the glass pane centre.

The connection between the corner elements and the edge elements of the metal framing are realised by rigid bars. A modelling of the metal framing with beam elements instead of shell elements would represent a further simplification of the model, but requires substantial additional effort in determining eccentricities. A consideration of laminated glass panes can be accomplished either by equivalent effective thicknesses or by modelling the interlayer with elements which can reproduce its shear stiffness (e.g. solid elements, beam elements or spring elements).

For the stainless steel and the structural steel of the metal framing, plastic material models with the properties given in Tab. 7.1 are used. The glass, the grouting and the adhesives are modelled with the linear-elastic properties according to Tab. 7.1. The addition of plastic properties for the acrylic adhesive is possible, however since strain rate dependency cannot be considered, this is not done for the present study. For the meshing an aimed finite element length of *20 mm* is used as input.

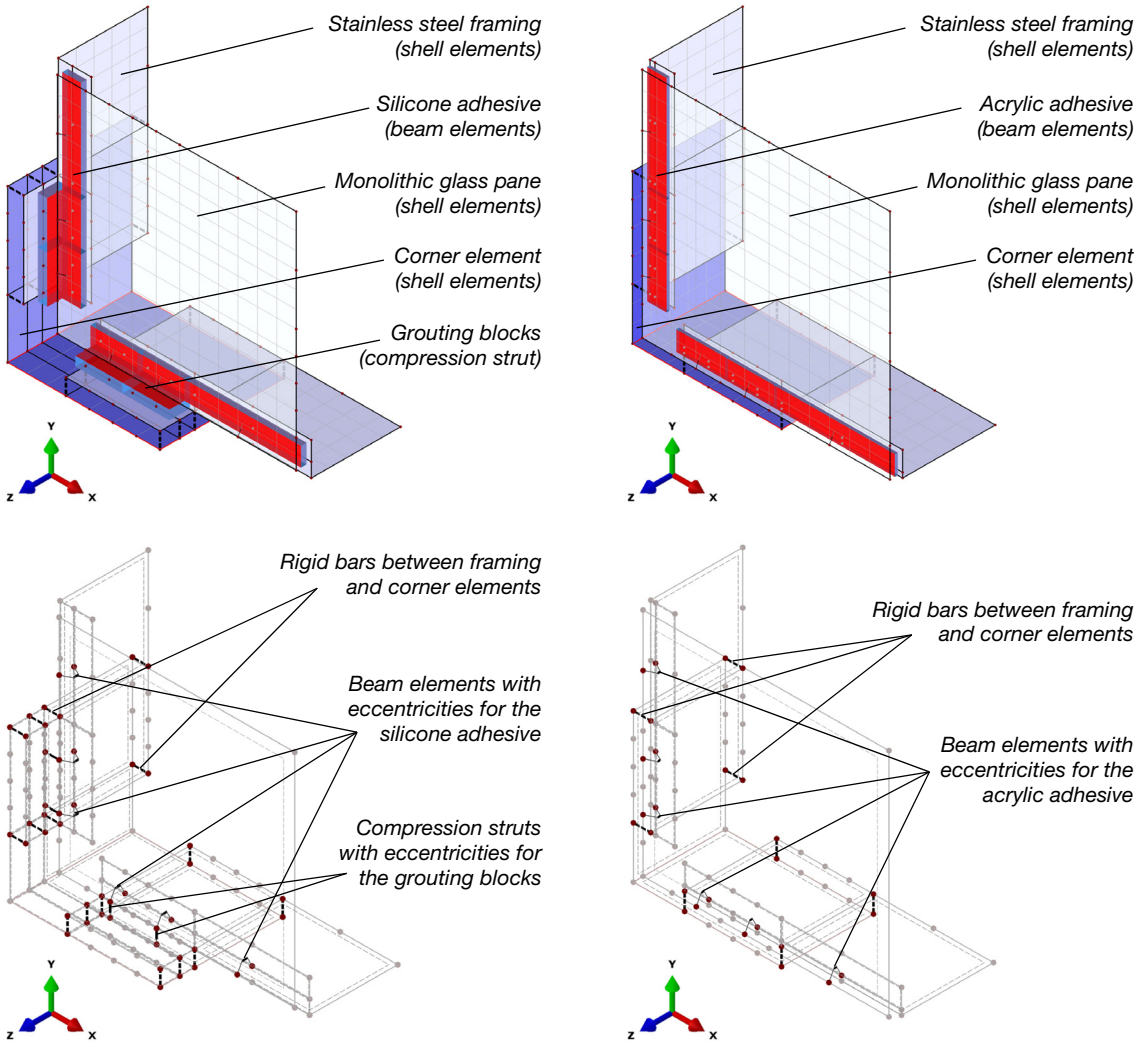

Fig. 8.5 *Sketches of the corner area for the simplified models of Type 1 (left) and of Type 2 (right) used in the structural engineering software RFEM - filled transparent representations (top) and wired representations (bottom)*

First, the eigenvalues and eigenmodes under in-plane axial loading and under in-plane shear loading are compared to those obtained for the two glass-metal element types with similar dimensions in subchapter 7.3.4. Afterwards, displacement results for two load scenarios are evaluated: *(i)* an in-plane shear load of *100 kN* and *(ii)* an out-of-plane wind suction load of *2.0 kPa*. The simulations are performed geometrically non-linear.

Eigenvalues and eigenmodes

The eigenvalues and eigenmodes are determined with the additional module *RF-STABIL* under unit loads applied as shown in Fig. 8.6 for in-plane axial loading ($2 \times F_{n,i}/2 = 1$) and in Fig. 8.7 for in-plane shear loading ($F_{s,i} = 1$). Based on the eigenmodes, initial geometric imperfections could be derived and transformed in a load case with a second additional module, *RF-IMP*. Since the results from chapter 7 show a rather small influence of imperfections on occurring displacements, this step is not included in this study. The first and the second eigenvalues determined with the simplified models under the two different loading directions are compared in Tab. 8.1 to those determined for similar glass-metal elements with the complex model used in subchapter 7.3.4. Furthermore, contour plots of the eigenmodes (out-of-plane displacements) obtained with the complex models in *Abaqus* and the simplified ones in *RFEM* for elements of *Type 1* and of *Type 2* are shown in Fig. 8.6 for in-plane axial loading and in Fig. 8.7 for in-plane shear loading.

Tab. 8.1 *Comparison between eigenvalues determined with the simplified models and eigenvalues obtained with the complex models used in chapter 7*

Finite element model	In-plane axial load $F_{n,i}$		In-plane shear load $F_{s,i}$	
	Type 1	Type 2	Type 1	Type 2
	First eigenvalues [kN]			
complex model (Abaqus)	313.560	354.608	136.618	213.749
simplified model (RFEM)	288.804	365.934	133.414	207.638
	Second eigenvalues [kN]			
complex model (Abaqus)	374.915	395.633	142.226	223.008
simplified model (RFEM)	333.976	401.598	137.862	222.675

The eigenvalues are in a relatively good agreement (differences of up to ~3%) for elements of *Type 2* under both loading directions. For elements of *Type 1*, a similar good agreement is reached under in-plane shear loading, but under in-plane axial loading higher discrepancies are noticed (eigenvalues determined with Abaqus are higher by ~10%).

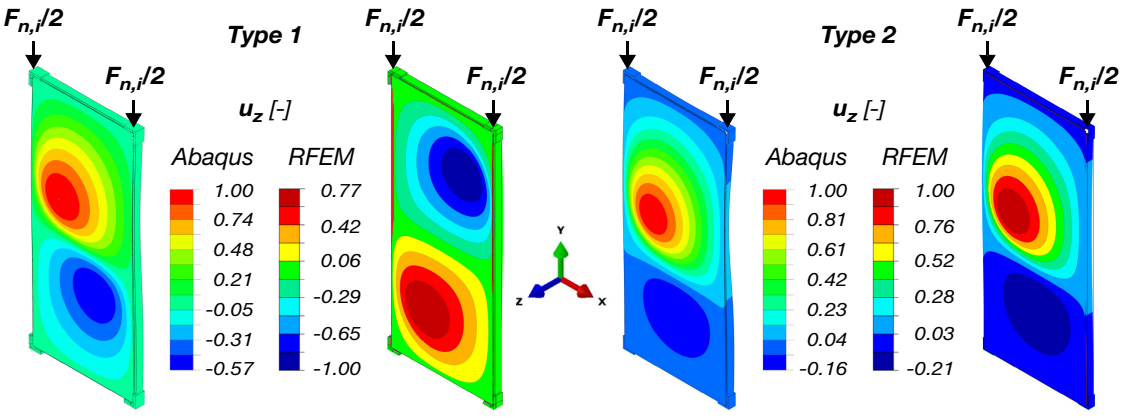

Fig. 8.6 *First eigenmodes determined for the element of Type 1 (left) and for the element of Type 2 (right) with the complex (Abaqus) and with the simplified (RFEM) models under in-plane axial loading*

The eigenmodes determined under in-plane axial loading with the complex and the simplified model show a good agreement for elements of *Type 2* (see Fig. 8.6, right). For elements of *Type 1*, the bulges resulting in the two models under in-plane axial loading are oriented in opposite directions (see Fig. 8.6, left). The eigenmodes determined under in-plane shear loading with the complex and the simplified model show a good agreement both for elements of *Type 1* and elements of *Type 2* (see Fig. 8.7).

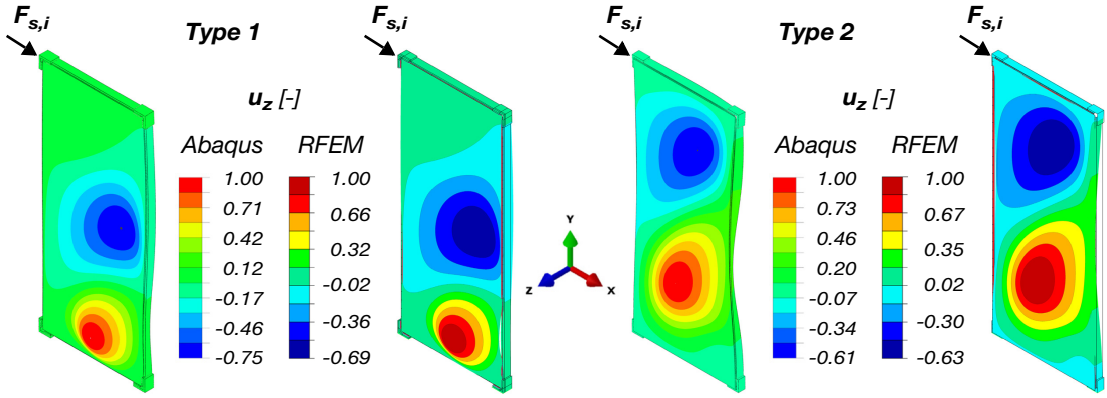

Fig. 8.7 *First eigenmodes determined for the element of Type 1 (left) and for the element of Type 2 (right) with the complex (Abaqus) and with the simplified (RFEM) models under in-plane shear loading*

A variation of the mesh density shows that the orientation of the bulges obtained with the module *RF-STABIL* is sensitive to the used finite element length, without reaching convergence in case of finer meshes. This is the case for both glass-metal element types and both applied load directions.

Structural behaviour under in-plane loading

The suitability of the simplified models under in-plane shear loading is assessed for both glass-metal element types under a load $F_{s,i} = 100$ *kN*. In the case of the simplified models, the simulations are carried out load-controlled in *RFEM*, with the load being applied in five increments. For the complex models, load-controlled simulations are performed in *Abaqus* in order to allow a direct comparison without influences from a displacement rate dependency.

For the elements of *Type 1*, a significant aspect is the lateral restrain of the grouting blocks, which leads to an additional out-of-plane support of the glass pane corner when it is pressed into the grouting. In the simplified model, this is taken into account by assigning the material properties of the grouting to the beam elements, which represent the silicone adhesive along the grouting blocks in the two corners belonging to the compressed diagonal. Without this modification, errors regarding instability of nodes in out-of-plane direction in the area of these two corners prevent the simulations from completing.

Contour plots of the out-of-plane displacements obtained with the complex models in *Abaqus* and the simplified ones in *RFEM* for elements of *Type 1* and of *Type 2* are shown in Fig. 8.8. A good qualitatively agreement can be noticed for both element types. Moreover, the out-of-plane

displacements determined with the simplified models are also quantitatively close to those obtained with the more complex models.

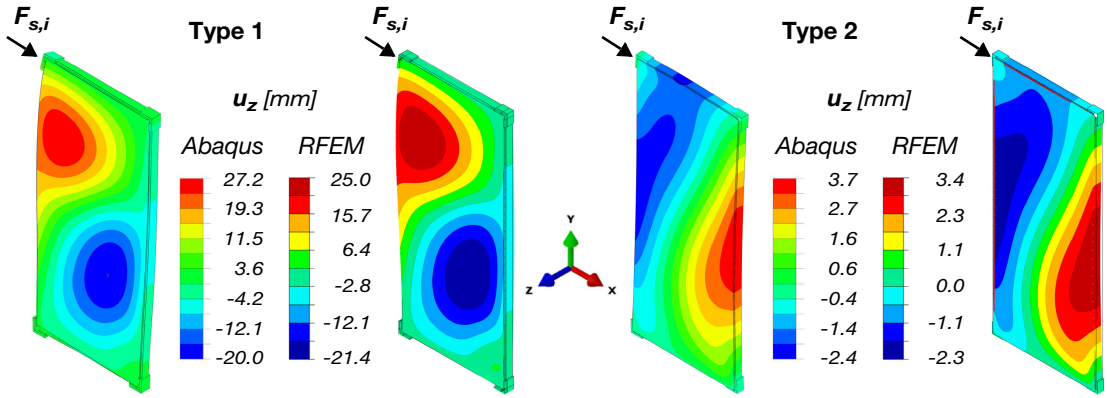

Fig. 8.8 *Out-of-plane displacements determined for the element of Type 1 (left) and for the element of Type 2 (right) with the complex (Abaqus) and with the simplified (RFEM) models under an in-plane shear load $F_{s,i}$ = 100 kN*

Selected displacement results determined for the two glass-metal element types under an in-plane shear loading of $F_{s,i}$ = *100 kN* with the complex models used in *Abaqus* and the simplified ones used in *RFEM* are summed up in Tab. 8.2. Additional to the maximum positive and negative out-of-plane displacements, which are also illustrated in Fig. 8.8, the maximum horizontal in-plane displacements of the elements and the maximum relative in-plane displacements between the glass pane and the metal framing are provided. For all these values a relatively good agreement can be observed.

Tab. 8.2 *Comparison of selected displacement values obtained from the finite element simulations for the models of Type 1 and the models of Type 2 with the complex (Abaqus) and with the simplified (RFEM) models*

Selected displacement	**Model Type 1 ($F_{s,i}$ = 100 kN)**		**Model Type 2 ($F_{s,i}$ = 100 kN)**	
	complex (Aabaqus)	**simplified (RFEM)**	**complex (Abaqus)**	**simplified (RFEM)**
max. out-of-plane displacement of the glass pane (+) [mm]	27.2	25.0	3.7	3.4
max. out-of-plane displacement of the glass pane (-)	-20.0	-21.4	-2.4	-2.3
max. horizontal in-plane displacement of the glass pane [mm]	32.4	27.2	7.7	8.0
max. positive relative in-plane displacement [mm]	10.1	8.4	0.8	0.8
max. negative relative in-plane displacement [mm]	-0.9	-0.8	-0.9	-0.9

Stress values in the glass pane and in the metal framing can be obtained from the models in order to evaluate the utilisation of these components. However, the occurrence of singularities needs to be considered, since punctual connections and implicitly load applications are used in

the simplified models. In order to conduct a simplified stress analysis for the load transfer materials based on the simplified models, the internal forces in the beam elements and in the compression struts can be used.

Structural behaviour under out-of-plane loading

In the interest of completeness, the suitability of the simplified models under out-of-plane loading is assessed for both glass-metal element types under a wind suction surface load of $F_{p,o} = 2.0$ *kPa*. Contour plots of the out-of-plane displacements obtained with the complex models in *Abaqus* and the simplified ones in *RFEM* for elements of *Type 1* and of *Type 2* are shown in Fig. 8.9. A good agreement, both qualitatively and quantitatively, can be noticed for both element types.

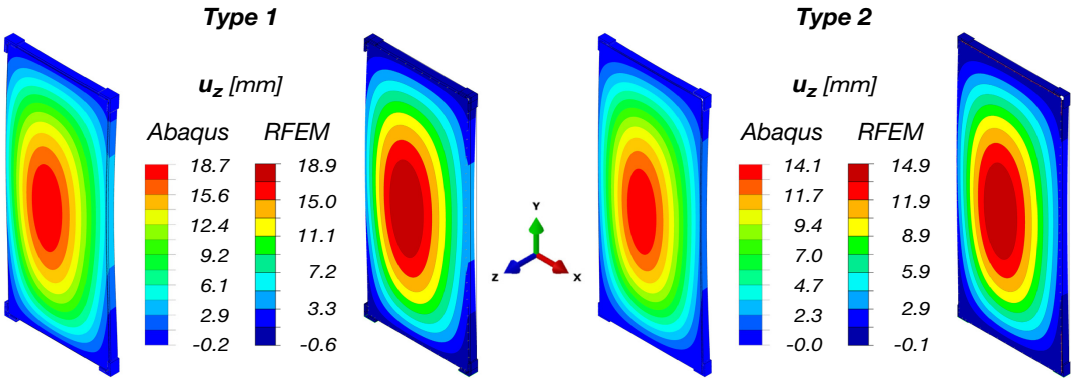

Fig. 8.9 *Out-of-plane displacements determined for the element of Type 1 (left) and for the element of Type 2 (right) with the complex (Abaqus) and with the simplified (RFEM) models under a wind suction load of $F_{p,o} = 2.0$ kPa*

Based on the comparisons between results obtained with the complex model used in *Abaqus* and validated in subchapter 7.2 and results obtained with the simplified model used in *RFEM*, it can be concluded that the latter model is suitable for predicting in-plane and out-of-plane displacements of systems consisting of the investigated glass-metal element types with composite structural behaviour.

8.2.3 Structural behaviour of several connected elements

Redundancy is a key aspect in structural design, especially when dealing with brittle materials like glass. In this subchapter the structural behaviour of a system consisting of six glass-metal elements of *Type 1* and of *Type 2* is analysed under in-plane shear loading by using the simplified models assessed in the previous subchapter. Three scenarios are included in the study:

- *Scenario A* - the glass panes of all six elements are intact;
- *Scenario B* - the glass pane of the middle element from the top row is assumed broken;
- *Scenario C* - the glass pane of the first bottom element from the left is assumed broken.

The supports at the bottom are applied on the underside of the corner elements and restrain all three rotations as well as translations in y-direction and in z-direction. The translation in x-direc-

tion is restrained only at the bottom right corner of the bottom right glass-metal element. The point supports of the corner elements in the middle and at the top restrain only the out-of-plane displacements (translation in z-direction). The in-plane shear loading is applied with concentrated forces as shown in Fig. 8.10 and Fig. 8.11 and sums up to a total of *300 kN*.

Results in the form of out-of-plane displacements are provided for *scenario A* in Fig. 8.10 and for *scenario B* and *scenario C* in Fig. 8.11. The results for *scenario A* show that the bottom element farthest away from the load application, which is also the one with the support in x-direction, is the one exhibiting the largest out-of-plane displacements. This element is acting as a kind of corner stone for the facade system. Similar to the investigations on single elements, larger out-of-plane displacements are occurring in the case of the system with elements of *Type 1* compared to the system with elements of *Type 2*.

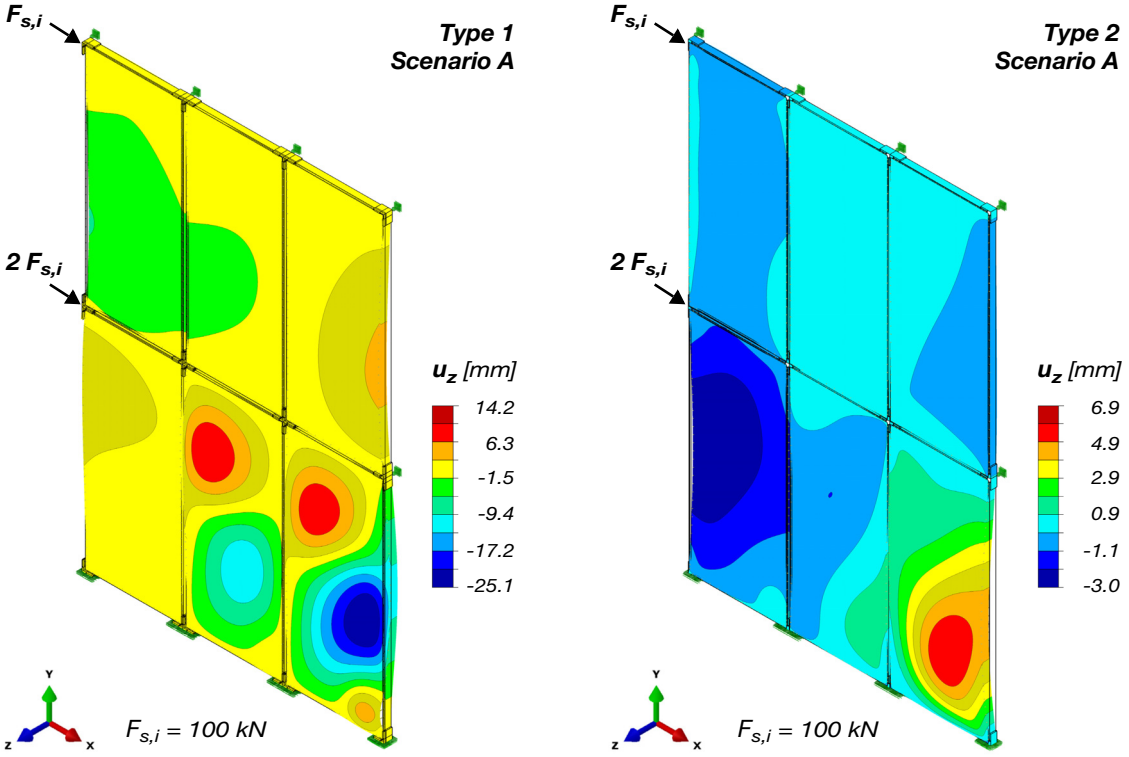

Fig. 8.10 *Mechanical behaviour in the form of out-of-plane displacements for a system consisting of six elements of Type 1 (left) and of Type 2 (right) under in-plane shear loading*

The *scenario B* and the *scenario C* illustrate the consequences of a possible broken glass pane. Assuming a proper dimensioning, a local glass failure still needs to be considered, since it can be caused either by an accidental load or by vandalism. Structurally efficient glass elements are nowadays designed as laminated glass panes, which exhibit a certain remaining lifting capacity even after breakage. Therefore, the two scenarios analysed in this subchapter, in which one glass pane is missing entirely, are overestimating the effects of a local glass failure. In the case of both scenarios with broken glass panes, the maximum out-of-plane displacements (both the positive and the negative ones) are increasing. The values are higher for the system with a broken glass pane in the bottom row than with one in the top row.

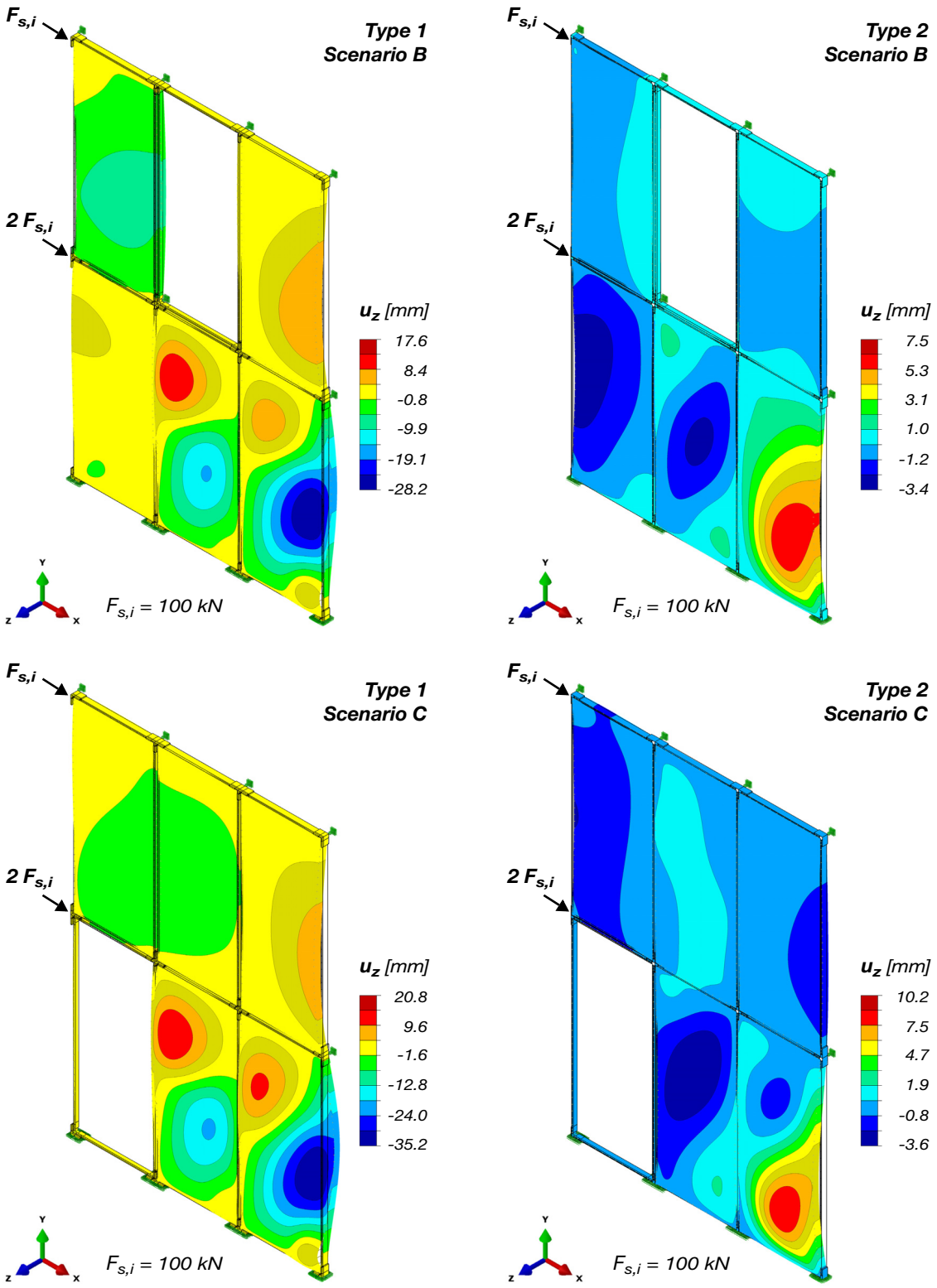

Fig. 8.11 *Two scenarios for the mechanical behaviour in the form of out-of-plane displacements for a system consisting of six elements of Type 1 (left) and of Type 2 (right) under in-plane shear loading with one broken glass pane*

The maximum in-plane horizontal displacements for the three scenarios with the two different element types are given in Tab. 8.3. Also in this case the values reached for the systems with elements of *Type 1* are higher than those reached for the systems with elements of *Type 2*. The maximum in-plane displacements are also increasing in the case of a broken glass pane. However, for the investigated scenarios, higher values are reached when a glass pane of the top row is broken, than in the case of a broken glass pane in the bottom row.

Tab. 8.3 *Maximum horizontal in-plane displacements for the different scenarios analysed for a system consisting of six elements of Type 1 and of Type 2 under in-plane shear loading*

Selected displacement	Model Type 1			Model Type 2		
	Scenario A	Scenario B	Scenario C	Scenario A	Scenario B	Scenario C
max. horizontal in-plane displ. [mm]	22.3	30.0	27.1	13.1	18.2	16.8

This study on a small system consisting of several elements shows that a redistribution of the loads on different paths in the case of single broken glass panes is possible. However, when the components are structurally designed, reserves should be planned by limiting their utilisation. Furthermore, framing elements located adjacent to broken glass panes and which are under compressive stress, show an increased susceptibility for stability failure (column buckling or lateral torsional buckling).

8.3 Design approach for composite structural glazing systems

Based on the experimental and finite element investigations performed in this thesis as well as following the design proposals for systems with in-plane loaded glass panes and different load transfer materials given in [Mocibob, 2008] and [Ebert, 2014], a general step-by-step approach is recommended in this subchapter for the structural design of facade systems made of glass-metal elements with composite structural behaviour by adhesive bonding. This approach is intended for the use in rather early project stages to determine the realizability of proposed architectural facade designs with the structural concepts investigated in this thesis. The same procedure can be followed both for the system with silicone adhesive bonding and grouting blocks as well as for the system with acrylic adhesive bonding alone. Certain steps which address the load transfer materials between glass pane and metal framing can be skipped depending on the selected system.

(a) **Architectural and functional design of the facade**
This step is generally completed either by architects alone or in a more ideal case in collaboration with structural and facade engineers. The geometry of the facade including the size of single elements as well as functional requirements are predefined by this design.

(b) **Preliminary decision for the load transfer concepts to be used**
Whether the system with (silicone) adhesive bonding and setting blocks or the system with (acrylic) adhesive bonding alone is planned to be used, needs to be decided at an early stage, since it has an influence on assumptions made for the structural system. Furthermore, the load transfer concept between several elements needs to be defined. Later modifications of these concepts require a reprocessing of the most steps to follow.

(c) **Development of a structural system**
Due to the complexity resulting from the composite structural behaviour of the glass-metal elements, generally, finite element methods are required for developing the structural systems. Depending on the stage of the project, whether a global or a local system is analysed and on the aimed accuracy of the results, different models can be used, ranging from more complex ones with solid elements and non-linear material properties (see chapter 7) to simplified ones with shell, beam and/or spring elements (see subchapter 8.2). For investigations at global level and often also for certain local analyses, simplified models require significantly less computation time and deliver accurate enough results.

(d) **Determination of loads and relevant load combinations acting on the facade**
The loads and the load combinations can be determined according to [EN 1990] and [EN 1991-1] by additionally considering the specifications given in standards for the material glass.

(e) **Definition of load paths for in-plane loading and for out-of-plane loading**
In this step it should be firstly defined whether both in-plane and out-of-plane loads are transferred between the glazing and the metal framing by adhesive bonding or only the out-of-plane loads are transferred by adhesive bonding, while the in-plane loads are

transferred by setting (grouting) blocks. This decision is important especially in the case of simplified models for defining the stiffness of eventual spring elements in the different directions. Secondly, the transfer of both the in-plane loads and the out-of-plane loads from the facade to the main structure or to the ground needs to be defined in order to add proper boundary conditions to the structural system.

(f) **Preliminary dimensioning of the glazing**
The glass assembly (monolithic glass, laminated glass or insulating glass units) and the thickness of the glass layers can be determined in a first step based on thermal insulation requirements and out-of-plane surface loading.

(g) **Preliminary dimensioning of the metal framing**
Based on the defined boundary conditions of the elements for out-of-plane loads, an approximate depth of the framing can be determined. Depending on the selected load transfer concepts between glazing and metal framing as well as between several elements, preliminary calculations of the profile thickness can be performed. The aim of this step is to provide initial dimensions of the metal framing for the finite element model.

(h) **Selection of suitable load transfer materials**
Depending on the chosen load transfer concept between glazing and metal framing, only a material for adhesive bonding or materials for both adhesive bonding and grouting (setting blocks) need to be selected in this step. Several requirements and properties need to be considered in the selection process, from which only a part are subject of investigation within this thesis. If for eligible materials, certain properties are unknown, experimental testing might be required in this step.

(h-1) **Selection of the material for adhesive bonding**
The following properties are relevant: Young‘s modulus, Poisson‘s ratio, short-term strength, relationship between stresses and strains (both tension and compression), temperature dependency, adhesion to the considered materials and surface treatments, creeping under the expected long-term loads, ageing behaviour under moisture and UV-radiation.

(h-2) **Selection of the material for the grouting (setting blocks)**
The following properties are relevant: Young‘s modulus under compression, Poisson‘s ratio under compression, short-term compressive strength, relationship between compressive stresses and strains, temperature dependency, creeping under the expected long-term loads, friction coefficient to glass.

(i) **Preliminary dimensioning of the load transfer materials**
The dimensions of the load transfer materials required for a first iteration in the finite element analysis can either be assumed based on experience from other projects or can be estimated by considering the material strength and the expected loads to be transferred. For the simplified models with spring elements, the dimensions are important for determining the spring stiffness.

(j) **Running of a geometric non-linear analysis on the structural system**
If initial geometric imperfections of the glazing or the framing are expected to have a high influence on the resulting stresses and displacements, an additional step can be included for determining the first eigenmode and implementing an initial imperfection based on it. However, the investigations in chapter 7 at element level show, that due to the position of the framing on the interior side of the glazing and the resulting eccentric load application, initial imperfections can be generally neglected.

(k) **Verification of global displacements of the structural system**
The in-plane and out-of-plane displacements of the whole facade structure need to be evaluated and compared to serviceability limits.

(l) **Structural design of the glazing**
For structural design, occurring stresses and displacements need to satisfy given limits. An insight on the determination of the design strength of glass was given in subchapter 2.2.1. The stresses due to out-of-plane displacements as well as due to local load application can be obtained from the global model. However, it needs to be considered that singularities can occur. The out-of-plane displacements of single glass panes need to be determined from separate subsystems.

(m) **Structural design of the framing**
The same approach as for the glazing needs to be carried out for structural design of the framing. While the stresses might be obtained from the global system, for the displacements subsystems are required.

(n) **Structural design of the load transfer materials**
If simplified models with spring or beam elements representing the load transfer materials are used, the structural design of these components can be carried out in early project stages by limiting the occurring relative displacements between glazing and metal framing. A structural design based on stresses requires at least the forces acting on the load transfer materials, which can be obtained from simplified models as internal forces. For an accurate determination of the occurring stresses, models with solid elements are necessary.

For the steps ***(j)*** to ***(n)*** an iterative process is recommended in order to optimise the dimensions of the different components of the glass-metal elements. It is once again emphasised that, due to the composite structural behaviour, changes made for the dimensions of one component can have an influence on stresses and displacements of other components.

8.4 Conceptual extensions regarding building physics requirements

In the two previous subchapters approaches and suggestions are provided for dealing with the novel glass-metal elements with composite structural behaviour by adhesive bonding from a structural point of view. In this subchapter, the focus lies on fulfilling selected requirements from a building physics point of view when connecting several elements together. Conceptual details are proposed, which can be very useful for elaborating functional solutions for aimed applications with the novel glass-metal elements during preliminary design phases. From the functional requirements highlighted in subchapter 3.4 the fulfilment of the following two is primarily aimed: *(i)* to ensure the resistance to weathering of a facade consisting of several glass-metal elements and *(ii)* to improve the thermal insulation by showing the possibility to implement the novel structural concept in facades with insulating glass units. Firstly, elements with single laminated glass panes, which can be used either for facades without heat-insulating demands or as the outer layer of double-skin facades, are treated. Secondly, the more interesting case of elements with insulating glass units is given attention to.

In all the conceptual details presented in the next two subchapters, the connections between the edge elements and the corner elements of the metal framing are represented with bolts. In the large-scale experimental tests discussed in chapter 6, welded connections are preferred in order to avoid an influence on the results of eventual slippage in bolted connections. Such slippage is difficult both to measure during testing and to consider during simulations. However, for facade applications, generally, bolted connections are preferred since they allow an easier replacement of single components in case of local damages. To obtain a smoother and more aesthetic appearance of the metal framing surfaces counter-sunk bolts can be used.

A key aspect for the connections in the novel proposed structural elements are production tolerances. Especially in the case of the metal components, tolerances characteristic for plant engineering should be aimed instead of the larger tolerances allowed according to standards for common steel structures. In the developed conceptual details neither hole tolerances nor slotted holes are depicted. Since the glass-metal elements are aimed to have a structural role, both hole tolerances and slotted holes should be avoided as far as possible. However, in certain locations they will be required to prevent undesired restraints.

The provided sketches do not include dimensions, but the different components are drawn in a realistic proportion to each other. In order to allow an estimation of certain thicknesses, the structurally efficient glass panes are assumed to be laminated glass made of two *6 mm* thick monolithic panes. Furthermore, the number and the size of the bolts included in the sketches are only schematic and will have to be determined in a more exact calculation based on the real occurring loads.

8.4.1 Considerations for elements with single laminated glass panes

In the case of elements with single laminated glass panes the most significant requirement to fulfil regarding building physics is to ensure the weather tightness. This is achieved in most cases with weather sealing materials or with gaskets. In Fig. 8.12 conceptual details with the position of weather seals in the corner area where four elements are connected together is illustrated in different sections. The detail is represented for elements of *Type 1* in the left sketches and for elements of *Type 2* in the right ones. The hinged connection to the main structure behind the facade, which is assumed in the experimental and finite element investigations from chapters 6 and 7, is not included in the details. A spherical joint or an eye bar could be welded to the corner element for this connection, depending on the desired degrees of freedom.

For single-skin facades without heat-insulating demands the weather tightness is especially important to protect the interior from both wind and rain. To the interior, the same sealing solution is adopted for both investigated element types. A covering strip is screwed to the interior face of the corner elements in threaded holes and closes the gap between two elements. Additional spacer blocks with the thickness of the corner elements could be added along the edge elements if necessary for their stabilisation or for intermediary connection points of the covering strips. Along the perimetrical adhesive joints a weather seal is applied to the interior to avoid the contact of the adhesive to moisture resulting from possible condensate (see sections *s_a1* and *s_a2* in Fig. 8.12). Furthermore, the gaps eventually resulting between horizontal and vertical edge elements at the glass pane corners, which might be caused by manufacturing tolerances, are closed as well with sealing materials (see sections *s_c1* and *s_c2* in Fig. 8.12).

To the exterior, different solutions are chosen for the two element types. In the case of systems with elements of *Type 2*, the corner parts and the edge parts of the metal framing have the same depth. Therefore, it is possible to apply a weather seal between the glass pane edges of adjacent elements, as illustrated in sections *s_a2* and *s_b2* from Fig. 8.12. In the case of systems with elements of *Type 1* it is not possible to use the same solution, because the corner elements have a larger depth in order to allow a direct in-plane load transfer between two elements over the grouting blocks (or setting blocks). This is illustrated in sections *s_a1* and *s_b1* from Fig. 8.12. The grouting blocks are partially enclosed in stainless steel brackets with milled notches. These brackets are welded to the edge elements. To close the gap between adjacent elements to the exterior and simultaneously to restrain the grouting blocks laterally to the exterior, clamping strips are screwed to the corner elements in a similar way as in the case of the covering strips on the interior side. Finally, a weather seal is applied along the perimeter between the glass panes and this clamping strips to ensure the water and air tightness to the exterior.

In the case of double-skin facades, the space between the two skins does not necessarily need to be completely air- and water-tight. However, it is important to at least keep the rain away from the materials on whose properties it can have a negative influence, which is the case for the acrylic adhesive. The properties of the silicone adhesive and of the resin-based grout, generally, do not degrade in case of contact with water. Therefore, the details in Fig. 8.12 could be further modified for an application as the outer layer of a double-skin facade. The gap between two elements extending from corner element to corner element could be left open, while enclosing the water-sensible load transfer materials with weather seals on each element separately.

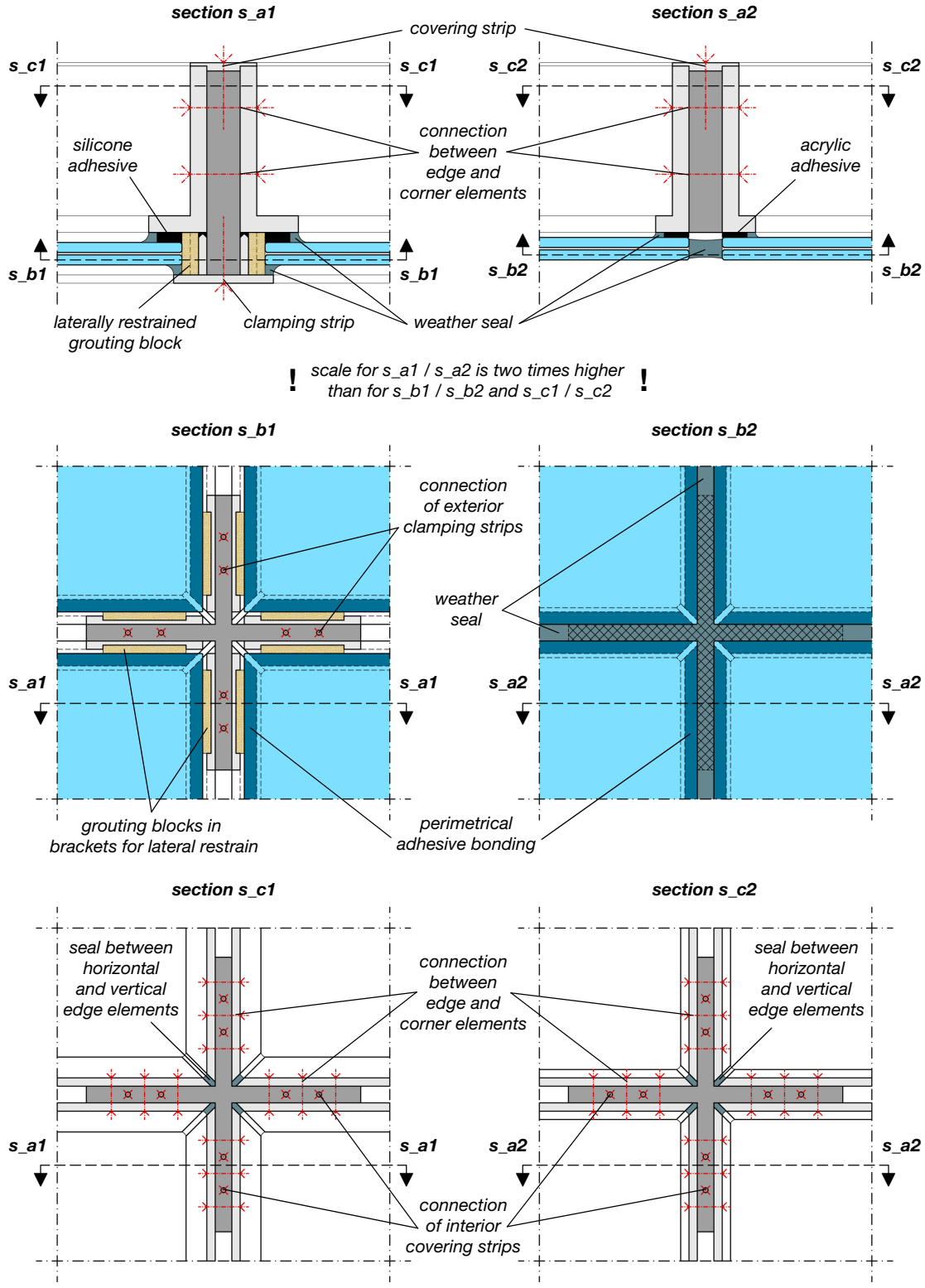

Fig. 8.12 *Conceptual details for ensuring weather tightness along the connections of several elements of Type 1 (left) and of Type 2 (right) with single laminated glass panes*

8.4.2 Considerations for elements with insulating glass units

Since the energy efficiency demands for buildings and implicitly for their facades are constantly increasing in recent years, the use of insulating glass units will be aimed for most future transparent building envelopes. Therefore, a special attention is given during the development of the novel structural facade elements investigated in this thesis to be applicable as insulating glass units as well. The conceptual details in this subchapter illustrate diverse possibilities of how the two investigated concepts for glass-metal elements with composite structural behaviour can be implemented in combination with insulating glass units (IGUs) and different out-of-plane supporting structures. Double IGUs are used in the sketches. However, the same concepts can be applied as well with triple IGUs. In all presented details, only the interior package of the IGU is activated for in-plane loads. A similar assembly of this package as in the case of the elements with single laminated glass panes is assumed in the sketches (2 x 6 mm).

First, the details discussed in the previous subchapter for elements with single laminated glass panes are adapted for insulating glass units (IGUs) in Fig. 8.13. For elements of *Type 2*, the differences are minor. The water and air tightness to both the interior and the exterior are solved in the same way as for elements with single laminated glass panes. The only difference is that the exterior weather seal is applied between the glass edges of the exterior packages of the IGUs (see section *s_b2* in Fig. 8.13). In the resulting space delimited by this weather seal, the IGU edges and the corner element of the framing, backer rods can be filled in to improve the heat-insulating properties by reducing the influence of linear thermal bridges. For elements of *Type 1*, slightly more adaptations are necessary. The weather seal to the interior is applied similar to the case of elements with single laminated glass panes. The water and air tightness to the exterior is ensured with a weather seal between the glass edges of the exterior packages of the IGUs (see section *s_b1* in Fig. 8.13) in the same way as for elements of *Type 2* with IGUs. This is possible, since only the interior glass package is activated for transferring in-plane loads and, therefore, the corner element of the framing does not have to extend in depth direction over the thickness of the exterior glass package. The brackets to enclose the grouting blocks (or setting blocks) have an L-shape as in the case of the experimental tests. Milled notches are planned as in the case of elements with single laminated glass panes to hold the blocks in position in longitudinal direction. The secondary seal of the IGUs has indentations in the area of the brackets to avoid eventual local stresses on the sealing material. Backer rods are placed in the resulting space between the exterior weather seal and the corner element of the framing to reduce heat losses in this area.

The spaces between the edge elements of the framing belonging to adjacent units can be filled with a heat insulating material to reduce the negative effect of linear thermal bridges (see section *s_c1* in Fig. 8.13). This can be done both for elements of *Type 1* and elements of *Type 2*. Furthermore, for both element types, additional local spacer blocks with the thickness of the corner elements can be added along the edge elements if necessary for their stabilisation or for intermediary connection points of the covering strips (see *s_c2* in Fig. 8.13). In the case of both element types, it is assumed that the out-of-plane loads are transferred by the adhesives. Furthermore, in the case of elements of *Type 2*, the adhesive is also responsible for carrying the dead weight of the IGU. Local mechanical retaining devices of the IGUs as they are provided by structural sealant glazing suppliers could be implemented in the conceptual details if required.

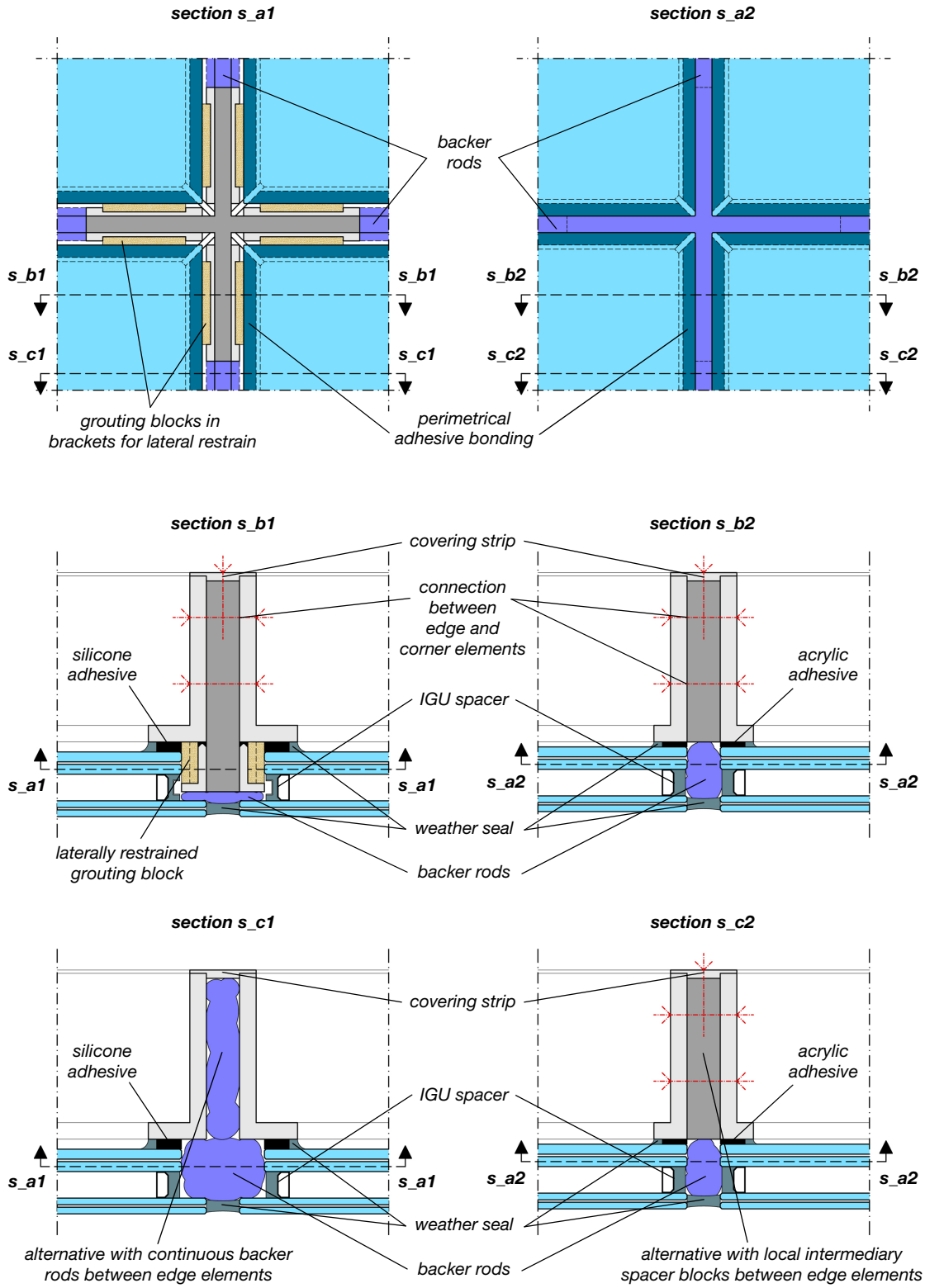

Fig. 8.13 *Conceptual details for the connection of several elements of Type 1 (left) and of Type 2 (right) with insulating glass units considering functional requirements*

In case there is no main structure behind the facade (e.g. concrete ceilings) to which the glass-metal elements can be connected point-wise in their corners with pendulum bars to transfer the out-of-plane loads, fins are a common solution. Dealing with a transparent facade, the use of glass fins is often aimed in order to increase the perception of transparency. Two innovative alternatives are proposed which combine the novel concept of glass-metal elements with composite structural behaviour with existing high-end engineering solutions for connecting structural sealant glazing units to glass fins or post-and-beam structures. The first one, which is illustrated in horizontal cross sections in Fig. 8.14 and in vertical cross sections in Fig. 8.15, brings no significant novelties to the glass-metal elements themselves.

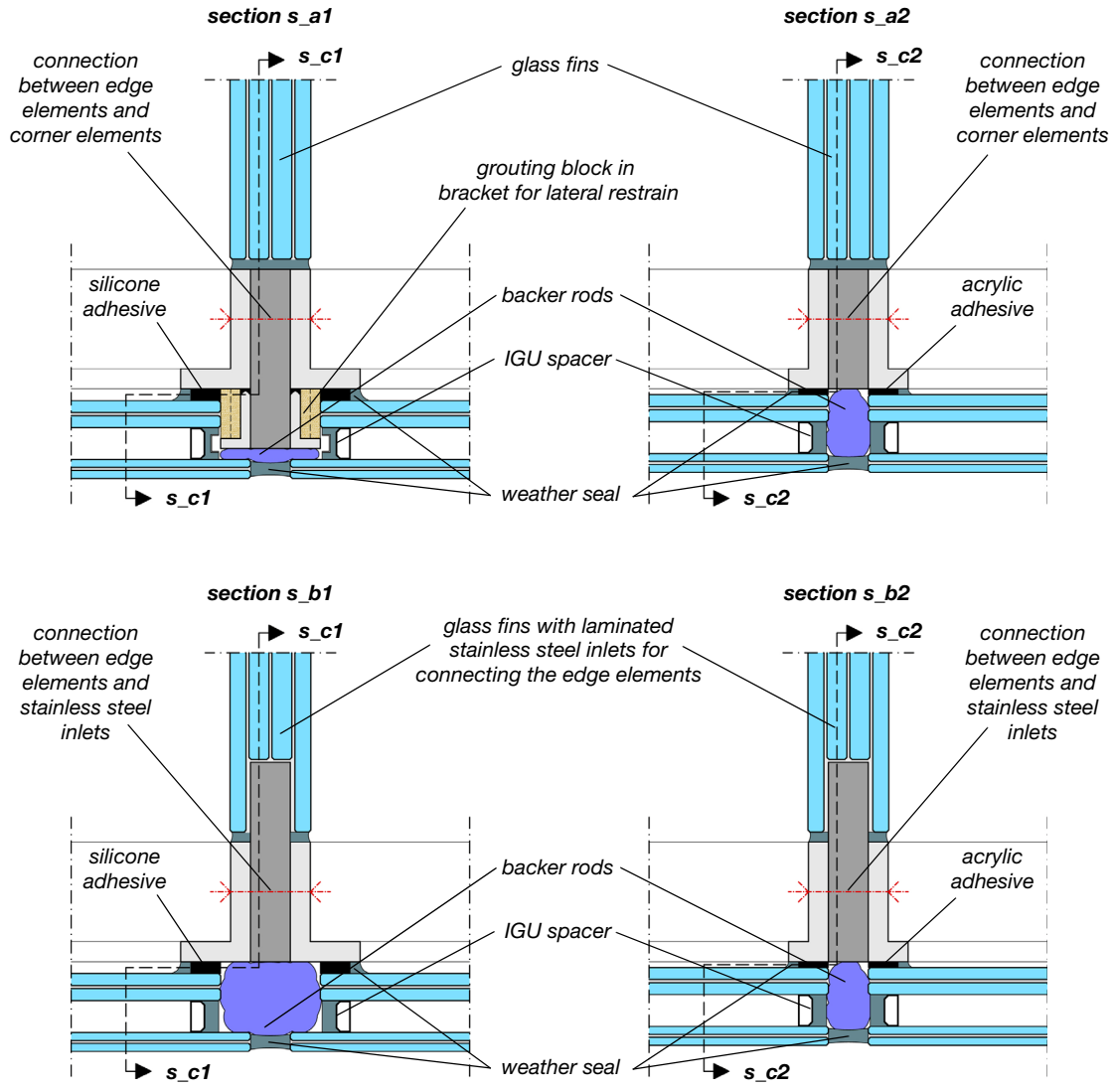

Fig. 8.14 *Conceptual details for an alternative with (vertical) glass fins for elements of Type 1 (left) and of Type 2 (right) - horizontal cross sections*

The depth of the edge elements and of the corner elements is aimed to be reduced if the required number and size of the bolts allows it (see sections *s_a1* and *s_a2* in Fig. 8.14). The connection between the facade elements and the glass fins is realized by bolted connections

between the edge elements and inlets which are laminated in the glass fins (see horizontal sections *s_b1* and *s_b2* in Fig. 8.14 and vertical sections in Fig. 8.15). These kind of inlets, which are made of stainless steel or titanium, have been used for connections in case of the glass cube at the Apple Store on Fifth Avenue in New York (see Fig. 1.3) and are investigated in [Santarsiero, 2015]. Interlayers with higher shear stiffness and strength as for example the ionoplast SentryGlas should be used for laminating the glass fins, since shear forces resulting from out-of-plane wind loads need to be transferred by this laminated connection. The number and the size of the inlets needs to be determined based on the required number of bolts.

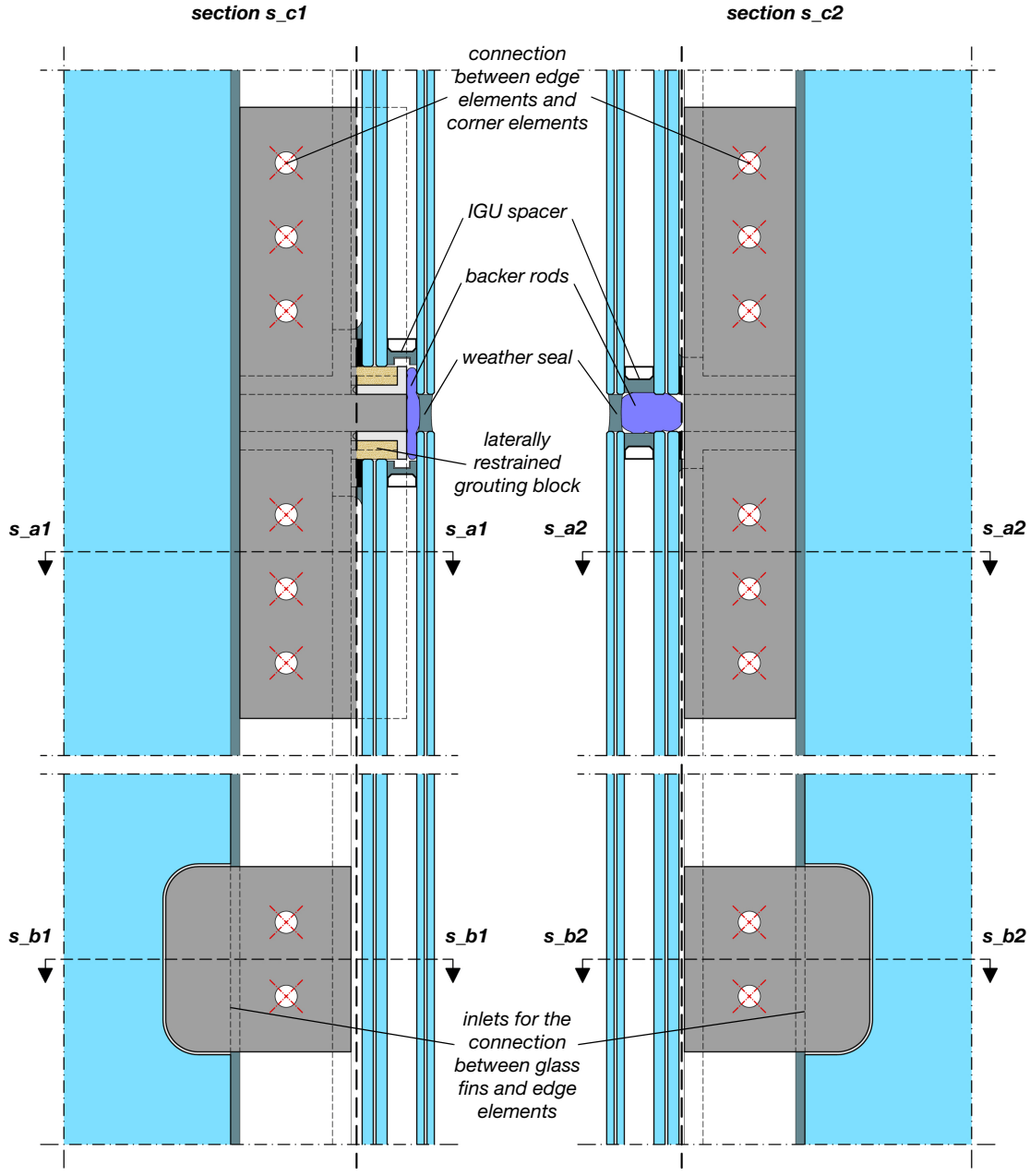

Fig. 8.15 *Conceptual details for an alternative with (vertical) glass fins for elements of Type 1 (left) and of Type 2 (right) - vertical cross sections*

The second alternative is illustrated in vertical and horizontal sections in Fig. 8.16 and pursues a further increase of transparency. To achieve this, the corner elements are removed and the depth of the edge elements is reduced to a minimum equal to the sheet thickness.

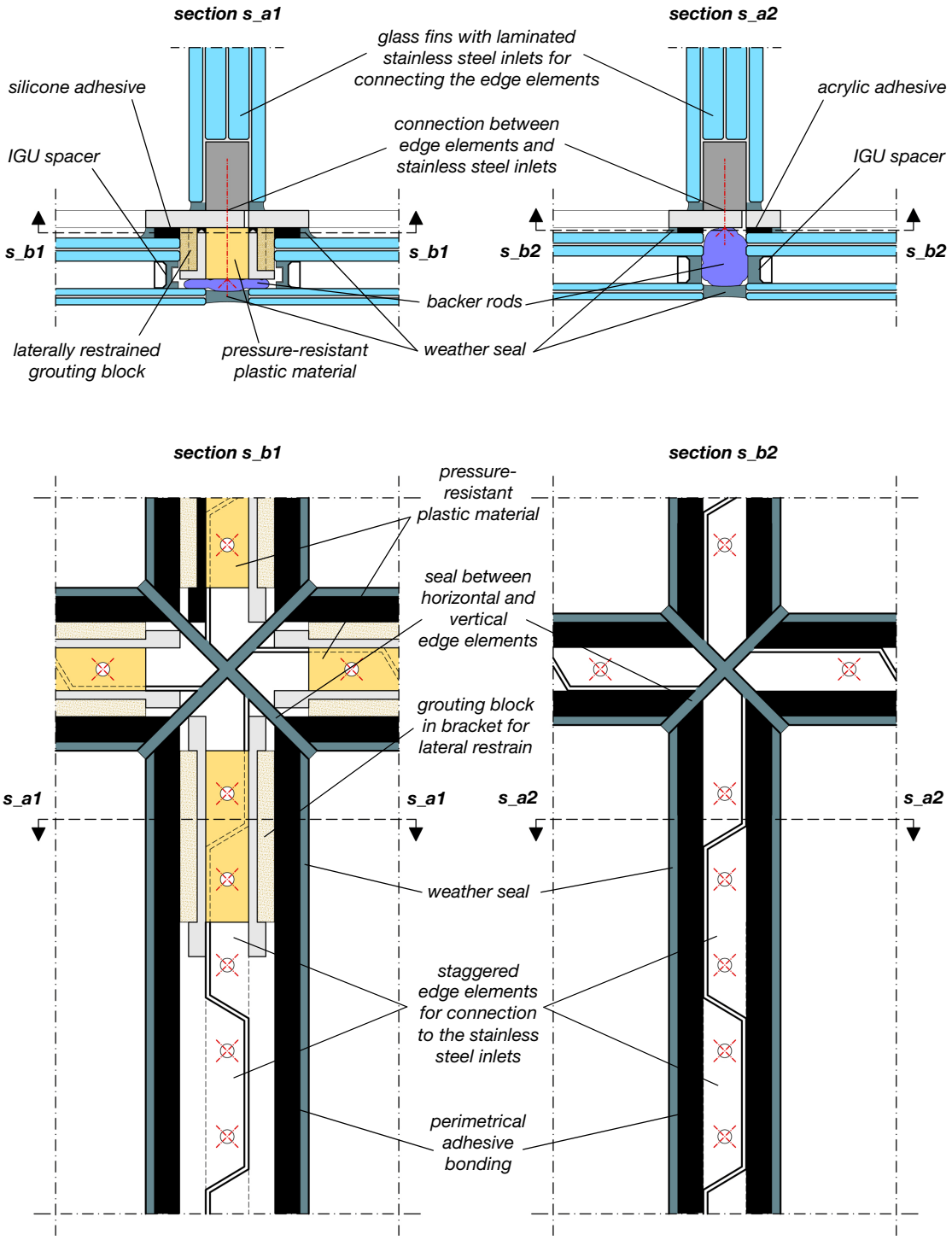

Fig. 8.16 *Conceptual details for an alternative with (vertical) glass fins and without corner elements for systems of Type 1 (left) and of Type 2 (right)*

The connection between the structural glass-metal facade elements and the glass fins is realized again by bolts between the edge elements of the metal framing and inlets laminated into the glass fin. However in this case, the bolts are fastened through the gap between two adjacent elements and the connection is therefore not visible. To be able to do this without having to increase the width of the gap to much, the edge elements of the framing are cut in a staggered pattern as shown by the sections *s_b1* and *s_b2* in Fig. 8.16 for the two different structural glass-metal element types. In this way it is possible to use only one row of bolts for connecting both adjacent elements to the glass fin inlets. This concept is applied successfully for timber-glass composite panels by [Neubauer, 2011] and by [Hochhauser, 2011]. The difficulty for this system in case of using metals instead of timber is that the holes need to be drilled in advance which requires a very exact production.

In the case of elements of *Type 1*, additional blocks are required between adjacent elements near their corners in order to allow a direct transfer of in-plane loads over the laterally restrained grouting blocks. In the sections on the left side in Fig. 8.16, blocks made of a pressure-resistant plastic material are drawn. These blocks can be fixed with the same screws used to connect the edge elements to the glass fin inlets. Whether single local inlets or linear inlets over the whole length of the glass fins are laminated depends of the required number of bolts. In both cases attention has to be paid to the thermal expansion coefficients of the laminated materials. Titanium has beside its high strength, the advantage of a similar thermal expansion coefficient to glass.

The last introduced concept is especially advantageous in the case of elements of *Type 2*, because the linear adhesive connection between the glass pane and the metal framing, which is responsible for the transfer of both in-plane and out-of-plane loads, is consequently achieved between the metal framing and the glass fins as well. For both described alternatives with glass fins, systems with vertical glass fins alone are illustrated in this subchapter. By developing a suitable connection between vertical and horizontal glass fins, the latter ones can be easily added to these conceptual details.

9 Conclusions and future research

Conclusions
Future research

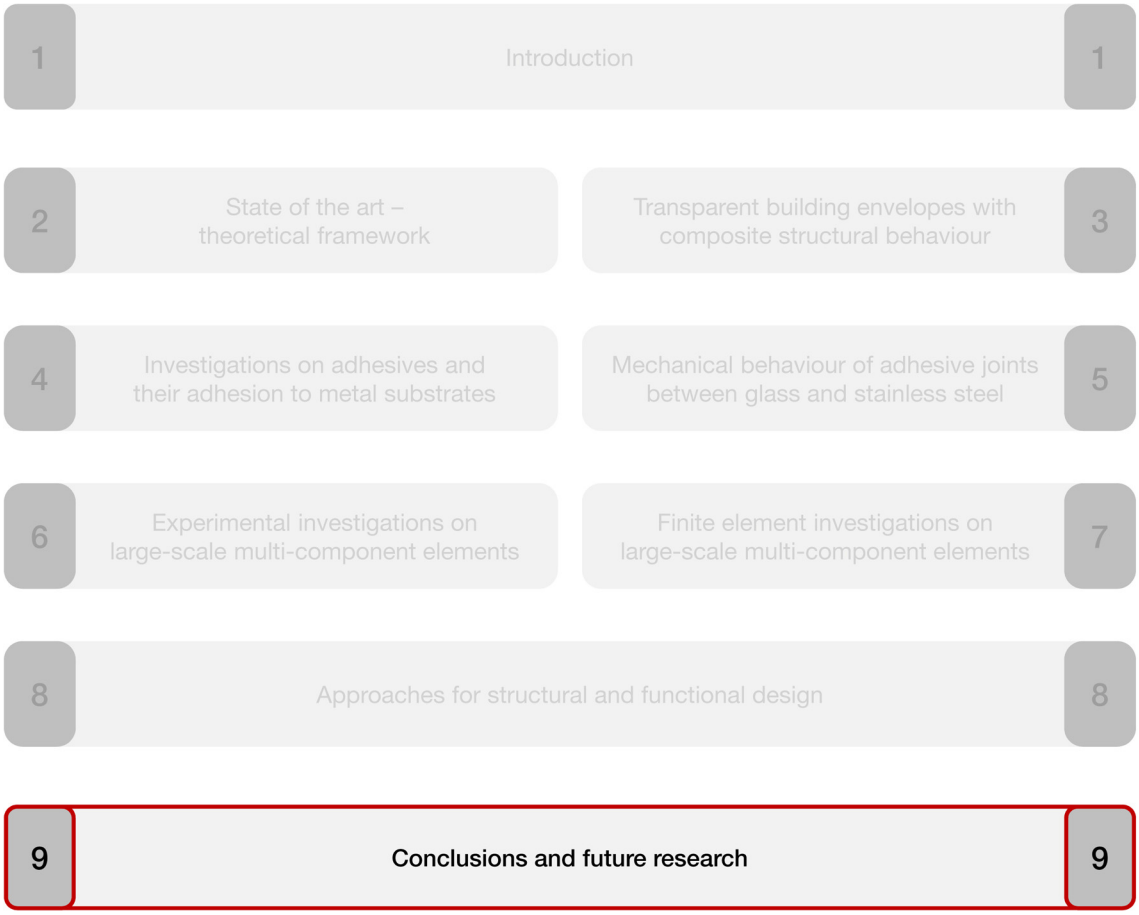

9.1 Conclusions

In this thesis novel concepts for glass-metal elements with composite structural behaviour by adhesive bonding subjected to both in-plane and out-of-plane loading are investigated. The main research questions stated in the introductory part are *(i)* to examine how and to what extent can adhesive bonding be used for connecting a glass pane with a filigree metal frame in order to obtain elements with composite structural behaviour, and *(ii)* to assess the structural performance and the failure limitations of such elements. After evaluating the state of the art regarding in-plane loaded glass panes and possible materials for transferring loads between glass panes and metal framing, the above mentioned objectives are addressed by extensive experimental, analytical and numerical investigations at material level, connection level and element level. Furthermore, approaches for structural and functional design are suggested with the aim to encourage a future application of the proposed concepts. The main conclusions drawn from the obtained results are highlighted in the next paragraphs.

Material behaviour and models for the investigated silicone adhesives

Two structural silicone adhesives (*Dow Corning 993* and *Sikasil SG-550*) are selected for investigations at material level. Their performance under uniaxial tensile loading is assessed by experimental tests on dumbbell specimens at room ambient conditions. Both materials exhibit a similar stress-strain relationship with a slight S-shaped development characteristic for elastomers when plotting engineering values. The determined engineering failure stresses average *2.25 MPa* for *Dow Corning 993* and *2.84 MPa* for *Sikasil SG-550*. Regarding stiffness, slightly higher values are observed for the second material. For both silicones hyperelastic material laws with a maximum of two parameters (*Neo-Hooke*, *Mooney-Rivlin*, *Arruda-Boyce* and *Ogden*) are analysed for their suitability to reproduce the stress-strain behaviour. Since silicones are considered almost incompressible, the volumetric parts of the strain energy formulations are neglected. All models lead to a good overall agreement between analytically and experimentally determined curves, but fail to reproduce the S-shaped development and therefore slightly underestimate stresses for small strains and overestimate them for larger strains. For the applications studied in this thesis, these models are considered sufficient and, in accordance with previous research, *Mooney-Rivlin* is suggested for *Dow Corning 993* and *Arruda-Boyce* for *Sikasil SG-550*.

Material behaviour and models for the investigated acrylic adhesive

Additional to the two silicones, the performance of a structural acrylic adhesive (*SikaFast-5221 NT*) is assessed under uniaxial tensile loading. The same conditions are used in terms of temperature (*~23°C*) and relative humidity (*~50%*). Other than for the silicones, also the influence of different displacement rates is analysed for the acrylic. The general stress-strain relationship differs significantly from those of the silicones. It exhibits a high stiffness at very small strains, followed by yielding and hardening. A strong dependency of the material behaviour on the applied displacement rate is observed. Yielding stress, failure stress and initial stiffness are all increasing with higher applied displacement rate. The mean values for the engineering failure stress vary between *8.47 MPa* for a loading speed of *1 mm/min* and *10.46 MPa* for a loading speed of *100 mm/min*. Considering the observed aspects regarding the stress-strain behaviour of the material, a strain rate dependent plastic model is derived. Stress-strain curves at constant strain

rates are determined by a 3D-fitting procedure with a novel proposed function, which shows good results for the available experimental data. The derived model allows a good prediction of the stress-strain behaviour of the acrylic adhesive at material level.

Adhesion to glass and metal substrates

The adhesion of the three investigated adhesives to selected metal surfaces is analysed experimentally by double-lap shear tests. An untreated finish and grinded surfaces with different corn sizes are included in the test programme for the stainless steel *no. 1.4404*, while for the aluminium *no. 3.3206* an untreated, an anodised and a powder-coated finish are studied. For the two silicones solely cohesive failures within the adhesive material are noticed, without depending on the substrate materials or their surface treatment. The joints with acrylic adhesive exhibit failures due to loss of adhesion or mixed failure modes for metal substrates with too smooth (aluminium surfaces) or too rough surfaces (stainless steel surfaces with untreated finish or grinded finish with large corn size). The best results in terms of an aimed cohesive failure are obtained on stainless steel surfaces grinded with an abrasive paper P150. All the failures due to loss of adhesion occur at shear displacements larger than *200%* for the analysed joint thickness of *3 mm*. For the adhesion to glass substrates no special test programme is carried out. Nevertheless, the failure modes noticed in the tests on glass-stainless steel connections are evaluated. For the silicones only cohesive failure is observed. In the case of the acrylic, failure due to loss of adhesion is noticed on the air side of the glass panes for the joints tested under shear loading. All the obtained results regarding adhesion are valid for adhesive joints under room ambient conditions.

Linear adhesive joints at the glass surface under tensile loading

Experimental tests on linear adhesive joints with rectangular cross section between stainless steel sheets and glass panes are carried out to evaluate the influence of different dimensions on the structural behaviour of the joints under tensile loading. Thickness, length and width of the joints are varied. Finite element simulations of the tests are performed to evaluate the suitability of the previously derived material models for joints under tensile loading. From the test results it is noticed for all three adhesives that the variation of the thickness has the biggest influence. Thinner joints allow the transfer of higher stresses which is illustrated by both the steeper stress-strain curves in the case of the silicones and the reached failure engineering stress values for all three adhesives. The recorded values can be found in subchapter 5.2.2 or in [Appendix C]. The proposed hyperelastic models for the silicone *Dow Corning 993* allows for a good overall reproduction of the experimental load *vs.* displacement curves with finite element simulations. For small displacement values the loads are slightly underestimated which could be improved by using hyperelastic material models with more than two parameters. In the case of the thinnest joint (*6 mm*), the experimentally determined loads are overestimated for larger displacements. This could be caused by a change in volume of the adhesive material due to the resistance provided by the stiffer substrate materials. Including the volumetric component to the strain energy formulation should lead to an improvement in this case. For the joints with *Sikasil SG-550* the agreement provided by the finite element simulations with the proposed hyperelastic model regarding load *vs.* displacement curves is a little poorer. Additionally to the observations made in the case of *Dow Corning 993*, an underestimation of the experimentally measured loads of up to *~20%* can be noticed depending of joint dimensions and applied displacement.

Additional experimental investigations on the bulk material and on joints should be carried out to determine the reasons for these discrepancies. In the case of the joints with the acrylic adhesive *SikaFast-5221 NT*, the simulations with the proposed strain rate dependent plastic model determined based on the uniaxial tensile tests lead to a significant overestimation of the maximum loads reached in the experiments. Despite this, qualitatively there is a good agreement in the development of the load *vs.* displacement curves. It is shown that by including in the material model a part which considers existing voids, a considerable quantitative improvement of the agreement regarding load values can be obtained. For further improvements regarding the inclination of the curves during yielding and for the load dropping after passing the maximum loads, a more complex cavitation model based on additional bulk material tests could be expedient.

Linear adhesive joints at the glass surface under shear loading

A similar procedure including experimental tests (double-lap shear) and finite element simulations as for tensile loading is carried out for linear adhesive joints with rectangular cross section between stainless steel sheets and glass panes under shear loading. However, only the thickness of the joints is varied in this case. For all three adhesives it is observed from the test results, that the inclination of the stress-strain curves and implicitly the stiffness of the joints are similar for the different thicknesses. The failure loads and the failure engineering stresses are increasing with decreasing thickness of the joints. For recorded values subchapter 5.2.3 or [Appendix C] should be referred to. In the case of the silicones, the load *vs.* displacement curves for the first loading cycle are almost linear. This development can be reproduced relatively well by the proposed hyperelastic material model for the specimens with *Dow Corning 993*. Only for small displacements the loads are slightly underestimated as in the case of tensile loading. Similar observations are made also in the case of the silicone *Sikasil SG-550* for the simulation results with the proposed hyperelastic model with the only difference, that the experimentally recorded loads are underestimated over the whole displacement range by up to *~15%*. This is in accordance with the simulations for tensile loading and for improvements additional investigations at material and connection level would be reasonable. For the acrylic adhesive *SikaFast-5221 NT*, the proposed strain rate dependent plastic model without consideration of porosity leads to a good agreement of the simulation results to the experimental ones. Both the inclination of the curves before and after yielding as well as the loads at which the yielding occurs are reproduced well. This indicates, that the influences of existing voids, void nucleation and coalescence can be neglected for simulations in which the adhesive is subjected to pure shear loading.

Linear adhesive joints at the edge of laminated glass

An alternative for a load transfer system between the metal framing and the glass pane are linear adhesive joints at the edge of laminated glass. To assess the structural performance and the failure modes of such joints under potential loading scenarios for the aimed glass-metal elements with composite load-bearing behaviour, tests under tensile, compressive and shear loading are carried out. Different joint cross sections (rectangular, L-shaped and U-shaped) are included in this experimental programme for the three adhesives. The specimens with U-shaped cross section allow the transfer of the highest loads, followed by those with L-shaped cross section and those with rectangular cross section. Nevertheless, joints with U-shaped or L-shaped cross section are more difficult to manufacture. For joints with the acrylic adhesive and

rectangular cross section under tensile and under shear loading, significantly lower loads are reached for joints positioned at the edge of laminated glass panes compared to joints positioned on the surface of glass panes. For joints with the silicone adhesives, only minimal differences are noticed. Regarding the failure modes, delamination between the interlayer and the glass panes is observed to be an issue under compressive loading for all three adhesives as well as under tensile and under shear loading for the acrylic adhesive. In the case of compressive loading, the delamination is preceded by cavitation effects indicated through bubble formation within the interlayer. Moreover, loss of adhesion to parts of the glass pane edges is occurring in the case of several specimens with the silicone *Sikasil SG-550* and the acrylic *SikaFast-5221 NT*.

Manufacturing of test specimens with structural adhesives

All the test specimens for the experimental investigations at connection level and at element level are manufactured by the author of this thesis either based on recommendations from the adhesive producers or with their assistance. Different procedures are applied leading to potentially useful recommendations for future test specimen production. The chosen auxiliary constructions needed for holding in place the different parts to be assembled prove to fulfil their scope and deliver good results in the case of all specimen types. The two most important steps in producing test specimens with adhesive joints are considered to be the pre-treatment of the substrate surfaces and the application of the adhesive including the mixing procedure. For the pre-treatment a proper cleaning of the surfaces and a wipe-over with recommended primers are essential. For the application of the adhesive, generally a gap-filling procedure is to be preferred. In the case of the specimens produced for the investigations within this thesis, this was not always possible due to the partially small thickness of the joints. Regarding the mixing procedure, different methods are available for the different adhesives. In the case of the acrylic, the mixing with the specially designed injection needle provided for the dual cartridges is used for all specimens and leads to good mixing results. For the silicones, dynamic mixers lead to the best mixing results and are therefore recommended. The mixing in cartridges in the case of *Dow Corning 993* or with a dissolver for *Sikasil SG-550* lead as well to generally satisfying results, but a risk for air inclusions is given and longer preparation and cleaning times are required.

Experimental investigations on glass-metal elements with composite structural behaviour

Based on the investigated adhesives and the results evaluated at material and at connection level, two novel concepts for elements with composite structural behaviour consisting of a glass pane and a metal framing are investigated experimentally and by finite element simulations. For the first concept (*Type 1*), a perimetrical adhesive bonding with the silicone *Dow Corning 993* is used to transfer the occurring out-of-plane loads. Additionally, grouting blocks positioned near the corners of the glass pane are responsible for transferring the in-plane loads. For the second concept (*Type 2*), a perimetrical adhesive bonding with the acrylic *SikaFast-5221 NT* is used for transferring both the out-of-plane and the in-plane loads. From tests under single and combined in-plane and out-of-plane loads raised up to levels at which no risk for an early failure is given, it is noticed that the elements can carry relatively high in-plane axial loads, as they would result from the dead weight of several elements positioned on top of each other. For loads up to *40 kN*, almost no displacements occur in the case of both concepts, neither relative ones between glass pane and framing nor absolute ones. Out-of-plane loads of up to *15 kN* (equiva-

lent to *~3.0 kPa*) lead, additionally to the expected out-of-plane displacements of the glass pane, also to a twisting of the framing elements due to their slenderness. The failure tests under shear loading performed on specimens with laminated glass panes for each of the two concepts show that the adhesives seem to be the weakest components in both cases. The system with acrylic adhesive exhibits a more than two times higher stiffness before the adhesive starts to yield, but the stiffness decreases significantly afterwards. Because of this decrease after yielding of the acrylic, the system with silicone adhesive and grouting allows for a better activation of the glass pane under in-plane loads. This is illustrated by the plate buckling, which is substantiated by the larger out-of-plane displacements measured for the system with silicone adhesive and grouting. In terms of failure load, the system with acrylic adhesive reached an approximately two times higher value (*~93 kN* for *Type 1* and *~133 kN* for *Type 2*). For both systems the failure is initiated by the adhesive. In the case of *Type 1*, cohesive failure occurs within the silicone adhesive, mainly because of the large out-of-plane displacements of the glass pane near the bonding, and is followed by glass failure. In the case of *Type 2*, both cohesive failure and loss of adhesion to the glass surface are occurring.

Finite element simulations on glass-metal elements with composite structural behaviour

Finite element non-linear simulations are performed to assess the influence of different parameters and loading scenarios on the structural behaviour of the two developed system types. By building models which replicate the performed tests, the suitability of the proposed material models for the two adhesives is first validated. For the system with silicone adhesive and grouting a good agreement is achieved with the proposed hyperelastic material model for the silicone and a linear-elastic model for the grouting. In the case of the system with acrylic adhesive, the proposed strain rate dependent plastic model reproduces well the stiffness of the system, but the yielding of the adhesive occurs delayed in the simulations. To improve the material model used for the parametric studies, an additional fitting of the material data is done. With the validated models, the influence of the following parameters on the structural behaviour of the two glass-metal element types under in-plane shear loading is evaluated: support conditions, glass pane height, glass pane assembly, framing depth, framing corner thickness, adhesive cross section, adhesive Young‘s modulus and initial geometric imperfection. For the effects caused by different values of these parameters on absolute in-plane and out-of-plane displacements of the elements as well as on relative in-plane displacements between glass pane and metal framing subchapter 7.3 should be referred to. Furthermore, the influence of additional loads on the structural behaviour of the elements under in-plane shear loading is analysed. Out-of-plane surface loads raised up to *1.0 kPa* have a visible increasing or decreasing effect on the out-of-plane displacements of the glass pane depending on the direction in which they are acting. In-plane axial loads raised up to *100 kN*, however, have a rather small influence on the out-of-plane displacements of the glass pane. A case study under heating and cooling scenarios shows that temperature loads cause as expected relative in-plane displacements between the glass pane and the metal framing for both element types, but also generates considerable out-of-plane displacements in the case of the elements with acrylic adhesive bonding.

Strengths and limitations of the two concepts for glass-metal elements

Both novel concepts for glass-metal elements with composite structural behaviour, which are introduced and investigated in this thesis, show a high potential for future application in trans-

parent facades. The concept with silicone adhesive and grouting (*Type 1*) has the advantage of using load transfer materials which have technical approvals for related applications: *(i)* the silicone *Dow Corning 993* is approved for structural sealant glazing systems, especially for transferring out-of-plane loads, and *(ii)* the resin-based grout *Hilti HIT HY270* is approved for transferring in-plane loads at the edge of glass panes, for example in the case of mechanical fixings as injection material between bushes and glass edge. Furthermore, the failure of this system, which is noticed to be initialized in the adhesive, is announced by large out-of-plane deformations of the glass pane. For structural design, relatively simple material models can lead to good predictions of the system stiffness and of occurring displacements. A limitation of this system can be given by creeping or by plastic deformations of the grouting material (these aspects are assessed in [Kolany, 2018]). Moreover, from a building physics point of view, the system of *Type 1* exhibits in most cases local thermal bridges in the area of the grouting. The concept with acrylic adhesive (*Type 2*) has the advantage of a perimetrical transfer of the in-plane loads between the glass pane and the framing. Furthermore, this system has a higher stiffness, until the point at which the adhesive starts to yield. From a building physics point of view, detail designs without thermal bridges are easily possible. The limitations for the concept of *Type 2* are given by finding an adequate adhesive. The acrylic *SikaFast-5221 NT* investigated in this thesis has no technical approval for applications in the area of facades and exhibits the following problematic aspects: *(i)* it is not able to activate the glass pane in such way that it causes plate buckling because of its low stiffness after yielding, *(ii)* its mechanical properties reduce significantly with increasing temperatures according to the producer (glass transition temperature of approximately *60°C*), and *(iii)* it exhibits a complex strain rate dependent material behaviour as well as cavitation effects under tensile stresses, which makes a structural design with relatively simple material models difficult. For both investigated concepts, temperature loads need to be considered as a possible factor for limiting the maximum element size.

Approaches for structural and functional design

To encourage a future application of the two proposed concepts for glass-metal elements with composite structural behaviour by adhesive bonding, basic approaches for structural and functional design are elaborated in this thesis. Especially the system with silicone adhesive bonding and grouting blocks can be considered for real projects, since the involved materials already have technical approvals for related applications. In the case of the system with acrylic adhesive bonding, there are higher limitations given and further investigations on the analysed adhesive or alternative ones are still required. The proposed simplified mechanical models with shell elements for the glass pane and the metal framing and linear elements for the load transfer materials (beam elements for the adhesives and compression struts for the grouting) show good results in predicting in-plane and out-of-plane deformations of single novel glass-metal elements. These models can be used as well for determining especially displacements, but also stresses and forces, in building envelopes consisting of several such elements. The proposed conceptual details to ensure the resistance to weathering of envelopes with single packages of laminated glass panes as well as with insulating glass units serve as a possible basis for functional design in future real projects.

9.2 Future research

The novel concepts for glass-metal elements with composite structural behaviour by adhesive bonding exhibit a high complexity given by the properties of the different involved materials, the interaction between the different components and the aimed application in building envelopes. For the investigations carried out in this thesis, certain delimitations, assumptions and simplifications are adopted. Taking this into account in correlation with the above mentioned complexity and based on the obtained results a wide spectrum of related future research topics can be formulated. The more significant ones for a further development of the concepts to building envelope system products are briefly described in the following paragraphs.

Extended investigations on the adhesive material properties

At material level, only uniaxial tensile tests at room ambient conditions are carried out in this thesis. Therefore also the derived material models rely only on the data obtained from these tests. However, when the adhesives are used as a component of the novel glass-metal elements with composite structural behaviour as well as in most other possible structural applications, they can be subjected to a combination of tensile, compressive and shear loading. Furthermore, an application in building envelopes requires for the adhesives to maintain their properties to a large extent at high and low temperatures as well as under ageing conditions generated by long-term loading, moisture or UV-radiation. An extension of the experimental investigations with regard to these aspects as well as an implementation of the obtained results in the material models is recommended. From the three adhesives studied in this thesis, only for the silicone *Dow Corning 993* published research results are available concerning the above mentioned regards. Furthermore, it is recommended to verify the assumption of a constant Poisson's ratio over the whole strain range for the investigated adhesives. This can be carried out by determining the true Poisson's ratio from additional uniaxial tensile tests in which both the longitudinal and the transverse strains are measured.

Development of material models with improved suitability for the adhesives

The performed finite element simulations at connection level indicate certain limitations of the material models used in this thesis for the three adhesives. Under shear loading, where mainly an isochoric deformation is occurring, the agreement between simulation results and experimental ones is relatively good, as summarised in the previous subchapter. Under tensile loading however, discrepancies are noticed for the joints with acrylic adhesive as well as for thin joints with silicone adhesive. In the case of the acrylic adhesive it is shown by adding simple porosity properties that existing voids as well as void nucleation and coalescence should be considered in a more exact model. Therefore, it is suggested to run additional experimental tests on bulk material specimens under compressive and shear loading in order to determine parameters required for a more complex cavitation model (see for example [NPL Manual, 2007]), which allows an improved prediction of the adhesive behaviour in joints under different load states. In the case of the thin joints with silicone adhesives, an improvement of the material models could be achieved by adding the volumetric component to the strain energy formulation. Furthermore, hyperelastic models with more than two parameters, as for example a higher order *Ogden* model, can improve the agreement between simulation results and experimental ones, especially for small strains, since they allow to reproduce the S-shaped stress-strain curve develop-

ment. In the case of the silicone *Sikasil SG-550* additional tests at material and connection level are recommended, since the size of the loads reached in the simulations with the derived hyperelastic model are both for tensile and for shear loading lower than those from the experiments.

Performance of the adhesive joints under different temperature and ageing conditions

All the experimental tests on adhesive joints performed within the framework of this thesis are carried out at room ambient conditions. Additional tests at different temperatures (ranging between *-20°C* and *+80°C* for facade applications) and under different ageing conditions (moisture, UV-radiation, long-term loading) are recommended for selected test series to evaluate the influence of these parameters on the results. While the two silicones have a technical approval for structural sealant glazing systems, which presumes that for some of the investigated joint configurations such tests have been carried out, in the case of the acrylic these type of tests are essential. Since the glass transition temperature lies at *~60°C* and based on specification of the producer, a significant decrease in strength and stiffness is expected at high temperatures. Furthermore, failure due to loss of adhesion can occur at lower strains after exposure of the joints to moisture. For the joints at the edge of laminated glass panes, investigations on the influence of temperature and moisture are suggested for all three adhesives.

Interaction between adhesives and interlayers for joints at the edge of laminated glass

The experimental investigations on adhesive joints at the edge of laminated glass panes show that delamination at the interfaces between interlayer and glass sheets can be an issue. Considering the potential of such joints in terms of reducing the visible width of non-transparent frame profiles, an extension of these investigations focusing on several aspects is suggested. Firstly, for the cavitation effect observed under compressive loading it should be analysed whether the bubbles are generated within the interlayer material or at the interface between interlayer and glass sheets. Secondly, a study on the influence of different interlayer materials on the cavitation effect under compressive loading as well as on the delamination of the interlayer noticed under tensile and under shear loading for the acrylic would be reasonable. Thirdly, since the properties of the interlayer materials and of many structural adhesives depend on load duration and temperature, experimental tests for these parameters should be carried out. Finally, an assessment of adhesive connections at the edge of laminated glass panes in comparison with embedded laminated connections (see [Santarsiero et al., 2017a]) would be interesting, since both types can be used in similar applications.

Extended adhesive selection for the concept with adhesive bonding alone

The concept for glass-metal elements with acrylic adhesive bonding alone shows several advantages compared to that with silicone adhesive bonding and grouting blocks. Among others, it allows for a more narrow visible width of the metal framing from the inside and it avoids the local thermal bridges, which are resulting due to the brackets required for laterally restraining the grouting. For the acrylic adhesive used in this thesis, its expected reduced performance under high temperatures and moisture influences can be a decisive factor for future applications. Therefore it would be reasonable to elaborate a detailed list of indispensable requirements for a more suitable adhesive and to conduct an experimental selection programme for identifying potential superior products. To avoid the necessity for a flexible adhesive which can com-

pensate different thermal elongations between the glass panes and the metal framing and implicitly to allow for thinner joints than those common in structural sealant glazing systems, a possible solution could be the consideration of glass fibre reinforced plastics (GFRP) as an alternative material for the framing (see [Peters, 2006] and [Pascual et al., 2017]).

Optimization of the connections between several elements

In subchapter 8.4 of this thesis conceptual details for connecting several glass-metal elements to each other with focus on fulfilling weather tightness requirements are provided. Bolted connections are chosen for these details considering their preferred use in metal facades. An optimization of these connections is due in following research steps in terms of size and number of required bolts correlated to the transferable loads between framing and glass panes for the two different concepts. Furthermore, the influence of eventual slippage due to hole tolerances and necessary slotted holes needs to be evaluated. Investigations for alternative connection types between the glass-metal elements are also a possible follow-up topic. A conceptual solution is proposed in this thesis with the staggered framing elements, which can transfer in-plane loads by contact in case of slippage of the bolted connections.

Simulations for evaluating the element performance regarding building physics

The conceptual details proposed in subchapter 8.4 are developed based on theoretical building physics requirements and existing solutions. However, no calculations are carried out to evaluate the performance of these concepts with regard to thermal and noise insulation or moisture proofing. Investigations for these aspects are proposed for future research either based on simulations or experimentally after developing a prototype facade element. For an initial assessment of the conceptual details, simulation results for heat and moisture transport could be compared to similar results for a conventional post-and-beam facade system.

Elaboration and analysis of redundancy concepts

The novel developed glass-metal elements with composite structural behaviour are intended to be optional parts of the primary load-bearing structure. Considering that one component of these elements is the glass pane and glass alone is a brittle material, redundancy concepts and preferred modes of failure need to be elaborated. The use of laminated glass is a must for structurally used glass elements nowadays because of the remaining lifting capacity after fracture. The structural capacity of a glass-metal element with a broken glass pane is, however, difficult to assess. Therefore, redundancy concepts allowing to redistribute the loads on alternative paths in case of glass failure in single elements should be aimed. An advantage of the novel glass-metal elements from a structural point of view is that, except for acts of vandalism, an emerging glass failure is generally predicted by out-of-plane deformations due to plate buckling.

Assessment of the two element concepts for curved building envelopes

Curved geometries are popular features in the architectural designs of iconic buildings from recent years. Several projects use triangular mesh structures made of steel or timber with in-filling flat glass panes to approximate free-form shapes. The glass-metal elements investigated in this thesis have a high structural potential under in-plane loading. Their application in curved building envelopes with quadrangular grids could lead to a reduction of material use for profiles

and an increased transparency compared to triangular meshes. The possibility to adapt both element concepts for the realization of curved shapes either with curved glass panes or with flat quadrangular glass panes joined at an angle is certainly worth to be investigated. At first view, the main challenges lie in the design of the framing elements and the connection between several elements.

Development of prototype facade elements based on the investigated concepts

The investigations in this thesis focus on the structural behaviour of the novel glass-metal elements with composite structural behaviour by adhesive bonding. An important step towards applying these concepts in real projects is considered to be the development of a prototype facade element. Some of the previous suggested research topics are necessary, especially for the concept with adhesive bonding alone, before being able to develop a prototype. However, in the case of the concept with silicone adhesive bonding and grouting blocks, due to the fact that existing products with technical approvals for related applications are used, only the optimization of the connections between several elements, the elaboration of a redundancy concept and eventually simulations regarding building physics aspects are essential. For a mock-up-like prototype at least two elements including their connection to each other need to be included. More representative would be a pavilion-like structure which could be established on a university campus or exhibited on a fair.

Bibliography

Books
Doctoral theses
Articles
Standards and Regulations
Technical Data Sheets
Online Links

Books

Abaqus, 2013a
Abaqus 6.13: *Analysis User's Guide - Volume III: Materials*, Dassault Systems Simulia, 2013.

Abaqus, 2013b
Abaqus 6.13: *Analysis User's Guide - Volume IV: Elements*, Dassault Systems Simulia, 2013.

Abaqus, 2013c
Abaqus 6.13: *Theory Guide*, Dassault Systems Simulia, 2013.

Abaqus, 2013d
Abaqus 6.13: *Getting Started with Abaqus: Interactive Edition*, Dassault Systems Simulia, 2013.

Adams, 2005
Adams R.D.: *Adhesive bonding: science, technology and applications*, Cambridge: Woodhead Publishing Limited, 2005.

Allen, 1969
Allen H.G.: *Analysis and design of structural sandwich panels*, London: Pergamon Press, 1969.

da Silva & Öchsner, 2008
da Silva L.F.M., Öchsner A. (Eds.): *Modeling of adhesively bonded joints*, Berlin Heidelberg: Springer-Verlag, 2008.

Dillard, 2010
Dillard D.A.: *Advances in structural adhesive bonding*, Cambridge: Woodhead Publishing Limited, 2010.

Ebnesajjad, 2014
Ebnesajjad S.: *Surface treatment of materials for adhesive bonding*, second edition, Waltham: Elsevier, 2014.

Feldmann et al., 2012
Feldmann M., Kasper R., Langosch K.: *Glas für tragende Bauteile*, Köln: Werner Verlag, 2012.

Habenicht, 2009
Habenicht G.: *Kleben - Grundlagen, Technologien, Anwendungen*, 6th updated edition, Berlin Heidelberg: Springer-Verlag, 2009.

Habenicht, 2012
Habenicht G.: *Kleben - erfolgreich und fehlerfrei*, 6th revised and supplemented edition, Wiesbaden: Vieweg+Teubner Verlag / Springer Fachmedien, 2012.

Haldimann et al., 2008
Haldimann M., Luible A., Overend M.: *Structural Use of Glass*, Zürich: IABSE-AIPC-IVBH, ETH Zürich, 2008.

Herzog et al., 2004
Herzog Th., Krippner R., Lang W.: *Fassaden Atlas*, Basel: Birkhäuser, 2004.

Knaack, 1998
Knaack U.: *Konstruktiver Glasbau*, Köln: Rudolf Müller, 1998.

Knaack et al., 2000
Knaack U., Führer W., Wurm J.: *Konstruktiver Glasbau 2 - Neue Möglichkeiten und Techniken*, Köln: Rudolf Müller, 2000.

Knaack et al., 2007
Knaack U., Klein T., Bilow M., Auer T.: *Facades - Principles of Construction*, Basel: Birkhäuser Verlag AG, 2007.

Ostermann, 2014
Ostermann F.: *Anwendungstechnologie Aluminium*, 3. neu bearbeitete Auflage, Berlin: Springer-Verlag, 2014.

Pottmann et al., 2010
Pottmann H., Asperl A., Hofer M., Kilian A.: *Architekturgeometrie*, Wien: Springer-Verlag, 2010.

Pottgiesser, 2009
Pottgiesser U.: *Prinzipien der Baukonstruktion*, Paderborn: Wilhelm Fink, 2009.

Schittich et al., 1998
Schittich Ch., Staib G., Balkow D., Schuler M., Sobek, W.: *Glasbau Atlas*, Basel: Birkhäuser, 1998.

Siebert & Maniatis, 2012
Siebert G., Maniatis I.: *Tragende Bauteile aus Glas - Grundlagen, Konstruktion, Bemessung, Beispiele*, 2. vollständig überarbeitete Auflage, Berlin: Ernst & Sohn Verlag, 2012.

Schneider et al., 2016
Schneider J., Kuntsche J., Schula S., Schneider F., Wörner J.-D.: *Glasbau - Grundlagen, Bemessung, Konstruktion*, 2. Auflage, Berlin: Springer-Verlag, 2016.

Schwarzl, 1990
Schwarzl F.: *Polymermechanik - Strukturen und mechanisches Verhalten von Polymeren*, Berlin: Springer-Verlag, 1990.

Watts, 2014
Watts A., Maniatis I.: *Modern Construction Envelopes*, second edition, Vienna: AMBRA/V, 2014.

Wetzell, 2009
Wetzell O.: *Wendehorst Bautechnische Zahlentafeln*, 33. vollständig überarbeitete und aktualisierte Auflage, Wiesbaden: Vieweg+Teubner, 2009.

Whitehouse, 2004
Whitehouse D.: *Surfaces and their measurement*, Elsevier, 2004.

Wurm, 2007
Wurm J.: *Glass Structures - Design and Construction of Self-supporting Skins*, Basel: Birkhäuser, 2007.

Zenkert, 1997
Zenkert D.: *The handbook of sandwich construction*, Cradley Heath: Engineering Materials Advisory Service Ltd., 1997.

Doctoral theses

Baitinger, 2009
Baitinger M.: *Zur Bemessung von SL-belasteten Anschlüssen im konstruktiven Glasbau*, Doctoral thesis, RWTH Aachen, Shaker Verlag, 2009.

Bao, 2014
Bao M.: *Structural and functional integrity of energy-efficient glazing units*, Doctoral thesis, University of Birmingham, 2014.

Becker, 2009
Becker F.: *Entwicklung einer Beschreibungsmethodik für das mechanische Verhalten unverstärkter Thermoplaste bei hohen Deformationsgeschwindigkeiten*, Doctoral thesis, Martin-Luther-Universität Halle-Wittenberg, 2009.

Carvalho, 2014
Carvalho P.: *(De)materializing Detail: Technology, Structure, Design. Development of a reinforced glass connection technique*, Doctoral thesis, Universidade do Minho, 2014.

Dias, 2013
Dias V.: *Development of adhesives constitutive material laws for the assessment of bonded steel to glass partial composite beams*, Doctoral thesis, Université du Luxembourg, 2013.

Ebert, 2014
Ebert J.: *The application of heavy loads into glass edges - A contribution to the use of solid plastics as a block material*, Doctoral thesis, TU Dresden, 2014.

Edl, 2008
Edl T.: Entwicklung von wandartigen verklebten Holz-Glas-Verbundelementen und Beurteilung des Tragverhaltens als Aussteifungsscheibe, Doctoral thesis, TU Vienna, 2008.

Englhardt, 2007
Englhardt O.: *Flächentragwerke aus Glas - Tragverhalten und Stabilität*, Doctoral thesis, University of Natural Resources and Life Sciences Vienna (BOKU), 2007.

Ensslen, 2005
Ensslen F.: *Zum Tragverhalten von Verbund-Sicherheitsglas unter Berücksichtigung der Alterung der Polyvinylbutyral-Folie*, Doctoral thesis, Ruhr-Universität Bochum, 2005.

Freytag, 2002
Freytag B.: *Die Glas-Beton-Verbundbauweise*, Doctoral thesis, TU Graz, 2002.

Haldimann, 2006
Haldimann M.: *Fracture strength of structural glass elements - analytical and numerical modelling, testing and design*, Doctoral thesis, EPFL Lausanne, 2006.

Haese, 2013

Haese A.: *Beitrag zur Bemessung scheibenbeanspruchter Stahl-Glas-Elemente*, Doctoral thesis, Universität der Bundeswehr München, 2013.

Härth-Großgebauer, 2013

Härth-Großgebauer K.: *Contribution to studies on the structural behaviour of hybrid beams made of glass and plastics*, Doctoral thesis, TU Dresden, 2013.

Hochhauser, 2011

Hochhauser W.: *A contribution to the calculation and sizing of glued and embedded timber-glass composite panes*, Doctoral thesis, TU Vienna, 2011.

Huveners, 2009

Huveners E.: *Circumferentially Adhesive Bonded Glass Panes for Bracing Steel Frames in Facades*, Doctoral thesis, Eindhoven University of Technology, University Press Facilities, 2009.

Kasper, 2005

Kasper R.: *Tragverhalten von Glasträgern*, Doctoral thesis, RWTH Aachen, Shaker Verlag, 2005.

Kintzel, 2007

Kintzel O.: *Modellierung elasto-plastischen Materialverhaltens und duktiler Porenschädigung metallischer Werkstoffe bei großen Deformationen*, Doctoral thesis, Ruhr-Universität Bochum, 2007.

Kolany, 2018

Kolany G.: *Glas-Stahl-Konstruktionen unter Nutzung hybrider Verbundtragwirkung mit Schwerpunkt der Lasteinleitung an der Glaskante*, Doctoral thesis, TU Graz, 2018, in preparation.

Kothe, 2013a

Kothe Ch.: *Surface Modification Methods for Improving Adhesive Joints in Glass Structures*, Doctoral thesis, TU Dresden, 2013.

Kothe, 2013b

Kothe M.: *Ageing Behaviour of Polymeric Interlayer Materials in Civil Engineering*, Doctoral thesis, TU Dresden, 2013.

Kuntsche, 2015

Kuntsche J.: *Mechanisches Verhalten von Verbundglas unter zeitabhängiger Belastung bei Explosionsbeanspruchung*, Doctoral thesis, TU Darmstadt, 2015.

Langosch, 2012

Langosch K.: *Das Tragverhalten von Glasstützen mit Mono- und Verbundquerschnitten*, Doctoral thesis, RWTH Aachen, Shaker Verlag, 2012.

Laufs, 2000

Laufs W.: *Ein Bemessungskonzept zur Festigkeit thermisch vorgespannter Gläser*, Doctoral thesis, RWTH Aachen, Shaker Verlag, 2000.

Louter, 2011

Louter Ch.: *Fragile yet Ductile - Structural Aspects of Reinforced Glass Beams*, Doctoral thesis, TU Delft, 2011.

Luible, 2004

Luible A.: *Stabilität von Tragelementen aus Glas*, Doctoral thesis, EPFL Lausanne, 2004.

Mocibob, 2008

Mocibob D.: *Glass Panel under Shear Loading - Use of Glass Envelopes in Building Stabilization*, Doctoral thesis, EPFL Lausanne, 2008.

Netusil, 2011
Netusil M.: *Hybrid Steel-Glass Beams*, Summary of Doctoral thesis, Czech Technical University, Prague, 2011.

Neubauer, 2011
Neubauer G.: *Entwicklung und Bemessung von statisch wirksamen Holz-Glas-Verbundkonstruktionen zum Einsatz im Fassadenbereich*, Doctoral thesis, TU Vienna, 2011.

Nhamoinesu, 2014
Nhamoinesu S.: *Steel glass composite structures*, Doctoral thesis, University of Cambridge, 2014.

Nicklisch, 2016
Nicklisch F.: *Ein Beitrag zum Einsatz von höherfesten Klebstoffen bei Holz-Glas-Verbundelementen*, Doctoral thesis, TU Dresden, 2016.

Niedermaier, 2005
Niedermaier P.: *Holz-Glas-Verbundkonstruktionen. Ein Beitrag zur Aussteifung von filigranen Holztragwerken*, Doctoral thesis, TU München, 2005.

Overend, 2002
Overend M.: *The appraisal of structural glass assemblies*, Doctoral thesis, University of Surrey, 2002.

Peters, 2006
Peters S.: *Kleben von GFK und Glas für baukonstruktive Anwendungen*, Doctoral thesis, Universität Stuttgart, 2006.

Puller, 2012
Puller K.: *Untersuchung des Tragverhaltens von in die Zwischenschicht von Verbundglas integrierten Lasteinleitungselementen*, Doctoral thesis, Universität Stuttgart, 2012.

Rühl, 2016
Rühl A.: *On the time and temperature dependent behaviour of laminated amorphous polymers subjected to low-velocity impact*, Doctoral thesis, TU Darmstadt, 2016.

Sackmann, 2008
Sackmann V.: *Untersuchungen zur Dauerhaftigkeit des Schubverbunds in Verbundsicherheitsglas mit unterschiedlichen Folien aus Polyvinylbutyral*, Doctoral thesis, TU München, 2008.

Santarsiero, 2015
Santarsiero M.: *Laminated Connections for Structural Applications*, Doctoral thesis, EPFL Lausanne, 2015.

Silvestru, 2012
Silvestru V.A.: *Numerische und versuchstechnische Untersuchung von hängenden Glasschwertern*, Master thesis, TU Graz, 2012.

Staudt, 2013
Staudt Y.: *Untersuchung des Materialverhaltens von Klebeverbindungen mit Silikon*, Master thesis, TU Darmstadt, 2013.

Vogt, 2009
Vogt I.: *Strukturelle Klebungen mit UV- und lichthärtenden Acrylaten*, Doctoral thesis, TU Dresden, 2009.

Weller, 2007
Weller C.P.: *Fenster und Fassaden aus GFK und Glas: Konstruktionskonzepte, wärmetechnische Untersuchungen, Anwendungsbeispiele*, Doctoral thesis, Universität Stuttgart, 2007.

Wellershoff, 2006
Wellershoff F.: *Nutzung der Verglasung zur Aussteifung von Gebäudehüllen*, Doctoral thesis, RWTH Aachen, Shaker Verlag, 2006.

Research Articles & Reports

Abeln et al., 2013

Abeln B., Preckwinkel E., Yandzio E., Heywood M., Eliasova M., Netusil M., Grenier C.: *Development of innovative steel-glass structures in respect to structural and architectural design (Innoglast)*, Technical report, Research Fund for Coal and Steel, Luxembourg: Publication office of the European Union, 2013.

Ali et al., 2010

Ali A., Hosseini M., Sahari B.B.: *A review of constitutive models for rubber-like materials*, American Journal of Engineering and Applied Sciences, 3, 232-239, 2010.

Amadio & Bedon, 2010

Amadio C., Bedon C.: *Buckling of laminated glass elements in out-of-plane bending*, Engineering Structures, 32, 3780-3788, 2010.

Amadio & Bedon, 2016

Amadio C., Bedon C.: *Effect of circumferential sealant joints and metal supporting frames on the buckling behaviour of glass panels subjected to in-plane shear loads*, Glass Structures & Engineering, 1, 353-373, 2016.

Bedon et al., 2014

Bedon C., Belis J., Luible A.: *Assessment of existing analytical models for the lateral torsional buckling analysis of PVB and SG laminated glass beams via viscoelastic simulations and experiments*, Engineering Structures, 60, 52-67, 2014.

Beer, 2015

Beer B.: *Structural Silicone Sealed Cold-Bent Glass - High-Rise Projects Experience Leading to a New Design Concept*, in: Glass Performance Days, Proceedings, Tampere, 235-240, 2015.

Belis et al., 2007

Belis J., Inghelbrecht B., Van Impe R., Callewaert D.: *Cold bending of laminated glass panels*, Heron, 52, 123-146, 2007.

Belis et al., 2011a

Belis J., Van Hulle A., Out B., Bos F., Callewaert D., Poulis H.: *Broad screening of adhesives for glass-metal bonds*, in: Glass Performance Days, Proceedings, Tampere, 286-289, 2011.

Belis et al., 2011b

Belis J., Mocibob D., Luible A., Vandebroek M.: *On the size and shape of initial out-of-plane curvatures in structural glass components*, Construction and Building Materials, 25, 2700-2712, 2011.

Besserud et al., 2012

Besserud K., Bergers M., Black A.J., Carbary L.D., Mazurek A., Misson D., Rubis K.: *Durability of Cold-Bent Insulating-Glass Units*, Journal of ASTM International, 9 (3), 1-26, 2012.

Bigwood & Crocombe, 1989

Bigwood D.A., Crocombe A.D.: *Elastic analysis and engineering design formulae for bonded joints*, International Journal of Adhesion and Adhesives, 9, 229-242, 1989.

Bonet et al., 2016

Bonet J., Gil A.J., Ortigosa R.: *On a tensor cross product based formulation of large strain solid mechanics*, International Journal of Solids and Structures, 84, 49-63, 2016.

Bucak & Hagl, 2006

Bucak O., Hagl A.: *Kleben im Bauwesen - gestern, heute, morgen*, Stahlbau, 75, 499-507, 2006.

Bucak, 2011

Bucak O.: *Gutachterliche Stellungnahme für die Verwendbarkeit von Hilti HIT-HY 70 im Glasbau*, Technical report, Hochschule München, 2011.

Callewaert et al., 2011

Callewaert D., Van Hulle A., Belis J., Bos F., Dispersyn J., Out B.: *The Problem of a Failure Criterion for Glass-Metal Adhesive Bonds*, in: Glass Performance Days, Proceedings, Tampere, 654-657, 2011.

Carbary, 2007

Carbary L.D.: *A review of the durability and of performance silicone structural glazing systems*, in: Glass Performance Days, Proceedings, Tampere, 190-193, 2007.

Clift et al., 2014

Clift Ch., Carbary L., Hutley P., Kimberlain J.: *Next generation structural silicone glazing*, Journal of Facade Design and Engineering, 2, 137-161, 2014.

Cruz & Pequeno, 2008

Cruz P., Pequeno J.: *Timber-glass composite beams: mechancial behaviour and architectural solutions*, in: Challenging Glass, Proceedings, Delft, 439-448, 2008.

Cruz et al., 2010

Cruz P., Pequeno J., Lebet J.-P., Mocibob D.: *Mechanical Modelling of In-Plane Loaded Glass Panes*, in: Challenging Glass 2, Proceedings, Delft, 309-319, 2010.

da Silva et al., 2009a

da Silva L.F.M., das Neves P.J.C., Adams R.D., Spelt J.K.: *Analytical models of adhesively bonded joints - Part I: Literature survey*, International Journal of Adhesion and Adhesives, 29, 319-330, 2009.

da Silva et al., 2009b

da Silva L.F.M., das Neves P.J.C., Adams R.D., Spelt J.K.: *Analytical models of adhesively bonded joints - Part II: Comparative study*, International Journal of Adhesion and Adhesives, 29, 331-341, 2009.

Datsiou & Overend, 2014

Datsiou K., Overend M.: *Behaviour of cold bent glass plates during the shaping process*, in: engineered transparency, Proceedings, Düsseldorf, 125-133, 2014.

Diani et al., 2009

Diani J., Fayolle B., Gilormini P.: *A review on the Mullins effect*, European Polymer Journal, 45, 601-612, 2009.

Dias et al., 2014

Dias V., Odenbreit C., Hechler O., Scholzen F., Ben Zineb T.: *Development of a constitutive hyperelastic material law for numerical simulations of adhesive steel-glass connections using structural silicone*, International Journal of Adhesion and Adhesives, 48, 194-209, 2014.

Dispersyn et al., 2017

Dispersyn J., Hertele S., De Waele W., Belis J.: *Assessment of hyperelastic material models for the application of adhesive point-fixings between glass and metal*, International Journal of Adhesion and Adhesives, 77, 102-117, 2017.

Doebbel et al., 2014

Doebbel F., Neubauer D., Rudolf B., Wagner W.: *Höherfeste Silikonverklebungen am Beispiel einer Glas-Fin-Anwendung*, in: Glasbau 2014, 47-56; Editors: Weller B. & Tasche S., Berlin: Ernst & Sohn Verlag, 2014.

Drass et al., 2017a

Drass M., Schwind G., Schneider J., Kolling S.: *Adhesive connections in glass structures - part I: experiments and analytics on thin structural silicone*, Glass Structures & Engineering, published online, 2017.

Drass et al., 2017b

Drass M., Schwind G., Schneider J., Kolling S.: *Adhesive connections in glass structures - part II: material parameter identification on thin structural silicone*, Glass Structures & Engineering, published online, 2017.

Drass et al., 2017c

Drass M., Schneider J., Kolling S.: *Damage effects of adhesives in modern glass facades: A micro-mechanically motivated volumetric damage model for poro-hyperelastic materials*, International Journal of Mechanics and Materials in Design, published online, 2017.

Drass et al., 2018

Drass M., Schneider J., Kolling S.: *Novel volumetric Helmholtz free energy function accounting for isotropic cavitation at finite strains*, Materials and Design, 138, 71-89, 2018.

Duncan & Dean, 2003

Duncan B., Dean G.: *Measurements and models for design with modern adhesives*, International Journal of Adhesion and Adhesives, 23, 141-149, 2003.

Englhardt, 2013

Englhardt O.: *Leichtbau 3.0: Material, Struktur, Energie*, Stahlbau, 82, 421-427, 2013.

Fildhuth & al., 2014

Fildhuth T., Knippers J., Bindji-Odzili F., Baldassini N., Pennetier S.: *Recovery behaviour of laminated cold bent glass - Numerical analysis and testing*, in: Challenging Glass 4 & COST Action TU0905 Final Conference, Proceedings, Lausanne, 113-121, 2014.

Freitag & Wörner, 2011

Freitag C., Wörner J.-D.: *Verwendung von Glas zur Aussteifung von Gebäuden*, in: Stahlbau Spezial 2011 - Glasbau/Glass in Building, 45-51; Berlin: Ernst & Sohn Verlag, 2011.

Galuppi et al., 2014a

Galuppi L., Massimiani S., Royer-Carfagni G.: *Buckling phenomena in double curved cold-bent glass*, International Journal of Non-Linear Mechanics, 64, 70-84, 2014.

Galuppi et al., 2014b

Galuppi L., Royer-Carfagni G.: *Rheology of cold-lamination-bending for curved glazing*, Engineering Structures, 61, 140-152, 2014.

Goeppert & Paech, 2008

Goeppert K., Paech C.: *Gläsernes Mahnmal zur Errinnerung an die Terrorattentate vom 11. März 2004 in Madrid*, in: Stahlbau Spezial 2008, 42-46, Berlin: Ernst & Sohn Verlag, 2008.

Griffith, 1920

Griffith A.A.: *The phenomena of rupture and flow in solids*, Philosophical Transactions, Series A, 221, 163-198, 1920.

Goland & Reissner, 1944

Goland M., Reissner E.: *The stresses in cemented joints*, Journal of Applied Mechanics, 66, 17-27, 1944.

Gurson, 1977

Gurson A.L.: *Continuum theory of ductile rupture by void nucleation and growth: Part I - Yield criteria and flow rules for porous ductile materials*, Journal of Engineering Materials and Technology, 99, 2-15, 1977.

G'Sell & Jonas, 1979

G'Sell C., Jonas J.: *Determination of the plastic behaviour of solid polymers at constant true strain rate*, Journal of Materials Science, 14, 583-591, 1979.

Hagl, 2006
Hagl A.: *Die Innovation - Kleben*, Stahlbau, 75, 508-520, 2006.

Hagl, 2007
Hagl A.: *Bemessung von strukturellen Silikon-Klebungen*, Stahlbau, 76, 569-581, 2007.

Hagl, 2008
Hagl A.: *Punktuelles Kleben mit Silikonen*, Stahlbau 77, 791-801, 2008.

Hagl, 2016
Hagl A.: *Development and test logics for structural silicone bonding design and sizing*, Glass Structures & Engineering, 1, 131-151, 2016.

Hartmann & Neff, 2003
Hartmann S., Neff P.: *Polyconvexity of generalized polynomial-type hyperelastic strain energy functions for near-incompressibility*, International Journal of Solids and Structures, 40, 2767-2791, 2003.

Huveners et al., 2009
Huveners E.M.P., van Herwijnen F., Soetens F., Hofmeyer H.: *Bracing Steel Frames with Adhesively Bonded Glass Panes - Mechanic Models*, Glass Performance Days, Proceedings, Tampere, 256-260, 2009.

Irwin, 1957
Irwin G.: *Analysis of stresses and strains near the end of a crack traversing a plate*, Journal of Applied Mechanics, 24, 361-364, 1957.

Jandl, 2015
Jandl M.: *Quadruple IG-Unit with thin glass membranes*, in: Glass Performance Days, Proceedings, Tampere, 61-63, 2015.

Johnson & Cook, 1985
Johnson G.R., Cook W.H.: *Fracture characteristics of three metals subjected to various strains, strain rates, temperatures and pressures*, International Journal of Engineering Fracture Mechanics, 21, 31-48, 1985.

Maniatis et al., 2016
Maniatis I., Nehring G., Siebert G.: *Studies on determining the bending strength of thin glass*, ICE Proceedings of the Institution of Civil Engineers - Structures and Buildings, 169, 393-402, 2016.

Martens et al., 2015
Martens K., Caspeele R., Belis J.: *Development of composite glass beams - A review*, Engineering Structures, 101, Issue 10, 1-15, 2015.

Menkenhagen & Koschecknick, 2012
Menkenhagen J., Koschecknick K.: *Experimentelle und numerische Untersuchungen zu geklebten Glas-Stahl-verbindungen*, in: Glasbau 2012, 206-214; Editors: Weller B. & Tasche S., Berlin: Ernst & Sohn Verlag, 2012.

Nardini & Doebbel, 2015
Nardini V., Doebbel F.: *Concept for seismic design of structural silicone joints in unitized curtain walling*, in: Glass Performance Days, Proceedings, Tampere, 281-286, 2015.

Nelder, 1966
Nelder J.A.: *Inverse polynomials, a useful group of multi-factor response functions*, Biometrics, 22, 128-141, 1966.

Neugebauer, 2014
Neugebauer J.: *Applications for curved glass in buildings*, Journal of Facade Design and Engineering, 2, 67-83, 2014.

Neugebauer, 2015
Neugebauer J.: *Movable Canopy*, in: Glass Performance Days, Proceedings, Tampere, 210-213, 2015.

Neugebauer, 2016
Neugebauer J.: *Investigation of different test set scenarios for determination of ultimate bending stress of thin glass*, in: engineered transparency, Proceedings, Düsseldorf, 501-512, 2016.

Neumann et al., 2013
Neumann L., Arnold A., Hochhauser W.: *Zur Stabilität von geklebten und geklotzten Glasscheiben: Beurteilung der Dunkerley'schen Geraden zur Beulwertbestimmung*, Bauingenieur, 88, 14-21, 2013.

Neumer & Siebert, 2016
Neumer D., Siebert G.: *Timber-glass composite shear wall*, in: engineered transparency, Proceedings, Düsseldorf, 253-260, 2016.

Nhamoinesu & Overend, 2012
Nhamoinesu S., Overend M.: *The Mechanical Performance of Adhesives for a Steel-Glass Composite Facade System*, in: Challenging Glass 3, Proceedings, Delft, 293-306, 2012.

Nhamoinesu et al., 2014
Nhamoinesu S., Overend M., Silvestru V.A., Englhardt O.: *The mechanical performance of adhesively bonded steel-glass composite panels - Medium-scale tests and numerical models*, in: Challenging Glass 4 & COST Action TU0905 Final Conference, Proceedings, Lausanne, 269-276, 2014.

Nicklisch et al., 2014
Nicklisch F., Dorn M., Weller B., Serrano E.: *Joint study on material properties of adhesives to be used in load-bearing timber-glass composite elements*, in: engineered transparency, Proceedings, Düsseldorf, 271-280, 2014.

O'Callaghan & Bostick, 2012
O'Callaghan J., Bostick C.: *The Apple Glass Cube: Version 2.0*, in: Challenging Glass 3, Proceedings, Delft, 57-65, 2012.

Oechsner et al., 2015
Oechsner M., Hof P., Beyer J., Buddenberg S.: *Dauerhaftigkeit und Dimensionierung des Randverbundes von Mehrscheibenisolierglas in Abhängigkeit der Klimalast bei Zweifach- und Dreifachisolierglas - DuraSeal*. Technical report, TU Darmstadt, 2015.

Oikonomopoulou et al., 2015
Oikonomopoulou F., Bristogianni T., Nijsse R., Veer F.: *Innovative structural applications of adhesively bonded solid glass blocks*, in: Glass Performance Days, Proceedings, Tampere, 256-261, 2015.

Oikonomopoulou et al., 2017
Oikonomopoulou F., Bristogianni T., Veer F., Nijsse R.: *The construction of the Crystal Glass Houses facade: challenges and innovations*, Glass Structures & Engineering, online first article, 2017.

Overend, 2010
Overend M.: *Recent developments in design methods for glass structures*, The Structural Engineer, 88(14), 18-26, 2010.

Overend et al., 2010
Overend M., Jin Q., Watson J.: *Investigations into steel-glass adhesive joints*, Technical report nr. CUED/D-STRUCT/TR231, University of Cambridge, 2010.

Overend et al., 2011
Overend M., Jin Q., Watson J.: *The selection and performance of adhesives for a steel-glass connection*, International Journal of Adhesion and Adhesives, 31, 587-597, 2011.

Overend & Zammit, 2012

Overend M., Zammit K.: *A computer algorithm for determining the strength of float glass*, Engineering Structures, 45, 68-77, 2012.

Pascual et al., 2017

Pascual C., Montali J., Overend M.: *Adhesively-bonded GFRP-glass sandwich components for structurally efficient glazing applications*, Composite Structures, 160, 560-573, 2017.

Piculin et al., 2016

Piculin S., Nicklisch F., Brank B.: *Numerical and experimental tests on adhesive bond behaviour in timber-glass walls*, International Journal of Adhesion and Adhesives, 70, 204-217, 2016.

Santarsiero et al., 2016a

Santarsiero M., Louter C., Nussbaumer A.: *The mechanical behaviour of SentryGlas ionomer and TSSA silicone bulk materials at different temperatures and strain rates under uniaxial tensile stress state*, Glass Structures & Engineering, 1, 395-415, 2016.

Santarsiero et al., 2016b

Santarsiero M., Louter C., Nussbaumer A.: *Laminated connections for structural glass applications under shear loading at different temperatures and strain rates*, Construction and Building Materials, 128, 214-237, 2016.

Santarsiero et al., 2017a

Santarsiero M., Louter C., Nussbaumer A.: *Laminated connections for structural glass components: a full-scale experimental study*, Glass Structures & Engineering, 2, 79-101, 2017.

Santarsiero et al., 2017b

Santarsiero M., Louter C., Nussbaumer A.: *Laminated connections under tensile load at different temperatures and strain rates*, International Journal of Adhesion and Adhesives, 79, 23-49, 2017.

Silvestru & Englhardt, 2015a

Silvestru V.A., Englhardt O.: *Stabilitätsverhalten von Kragträgern aus Verbundsicherheitsglas*, in: Glasbau 2015, 213-227; Editors: Weller B. & Tasche S., Berlin: Ernst & Sohn Verlag, 2015.

Silvestru & Englhardt, 2015b

Silvestru V.A., Englhardt O.: *Stability behaviour of cantilevered glass fins*, in: Glass Performance Days, Proceedings, Tampere, 373-376, 2015.

Sinclair, 1999

Sinclair F.: *Conoidal facade casts light on courthouse*, Modern Steel Construction, 1999, *https://www.aisc.org/globalassets/modern-steel/archives/1999/11/1999v11_conoidal_facade.pdf*, accessed 02.04.2017.

Sitte et al., 2011

Sitte S., Brasseur M., Carbary L., Wolf A.: *Preliminary Evaluation of the Mechanical Properties and Durability of Transparent Structural Silicone Adhesive (TSSA) for Point Fixing in Glazing*, Journal of ASTM International, Vol. 8, No.10, 1-27, 2011.

Staudt et al., 2014

Staudt Y., Schneider J., Odenbreit C.: *Investigation of the material behaviour of bonded connections with silicone*, in: engineered transparency, Proceedings, Düsseldorf, 393-402, 2014.

Tvergaard, 1981

Tvergaard V.: *Influence of voids on shear band instabilities under plane strain condition*, International Journal of Fracture Mechanics, 17, 389-407, 1981.

Van den Bergh et al., 2013

Vand den Bergh S., Hart R., Petter Jelle B., Gustavsen A.: *Window Spacers and Edge Seals in Insulating Glass Units: A State-of-the-Art Review and Future Perspectives*, Energy and Buildings, 58, 263-280, 2013.

Van Lancker et al., 2016

Van Lancker B., De Corte W., Belis J.: *Material properties of a structural silicone for linear adhesive glass-metal connections*, in: Challenging Glass 5, Proceedings, Ghent, 363-371, 2016.

Volkersen, 1938

Volkersen O., Luftfahrtforschung, 15, 41-47, 1938.

Wang et al., 2003

Wang R.X., Cui J., Sinclair A.N., Spelt J.K.: *Strength of adhesive joints with adherend yielding: I. Analytical model*, The Journal of Adhesion, 79, 23-48, 2003.

Weibull, 1951

Weibull, W.: *A statistical distribution function of wide applicability*, Journal of Applied Mechanics, 18(3), 293-297, 1951.

Weimann et al., 2015

Weimann G., Henriksen Th., Keri S.: *Glazed Link Library Walk - Manchester*, in: Glasbau 2015, 167-178; Editors: Weller B. & Tasche S., Berlin: Ernst & Sohn, 2015.

Weller et al., 2010

Weller B., Meier A., Weimar T., Menkenhagen J., Koschecknick K.: *Hybride Glasträger als Fassadenelemente*, in: Stahlbau Spezial 2010, 41-45; Berlin: Ernst & Sohn Verlag, 2010.

Weller et al., 2011

Weller B., Kothe M., Nicklisch F., Schadow T., Tasche S., Vogt I., Wünsch J.: *Kleben im konstruktiven Glasbau*, in: Stahlbau Kalender 2011, 585-646; Editor: Kuhlmann U., Berlin: Ernst & Sohn Verlag, 2011.

Weller & Weimar, 2011

Weller B., Weimar T.: Development of a new facade system with hybrid glass-steel elements, in: Glass Performance Days, Proceedings, Tampere, 522-524, 2011.

Weller & Engelmann, 2014

Weller B., Engelmann M.: *Spannglasträger - Glasträger mit vorgespannter Bewehrung*, in: Glasbau 2014, 193-203; Editors: Weller B. & Tasche S., Berlin: Ernst & Sohn Verlag, 2014.

Wellershoff & Sedlacek, 2003a

Wellershoff F., Sedlacek G.: *Glass Pavilion Rheinbach - Stability of Glass Columns*, in: Glass Processing Days, Proceedings, Tampere, 316-318, 2003.

Wellershoff & Sedlacek, 2003b

Wellershoff F., Sedlacek G.: *Structural use of glass in hybrid elements: steel-glass-beams, glass-GFRP-plates*, in: Glass Processing Days, Proceedings, Tampere, 268-270, 2003.

Wellershoff, 2007

Wellershoff F.: *Bemessungsschubmodulwerte für Verbundglasscheiben*, Stahlbau, 76, 177-188, 2007.

Wellershoff, 2008a

Wellershoff F.: *Aussteifung von Gebäudehüllen durch randverklebte Glasscheiben*, Stahlbau, 77, 5-16, 2008.

Wellershoff, 2008b

Wellershoff F.: *Aussteifung von Gebäudehüllen durch eckgeklotzte Glasscheiben*, Stahlbau, 77, 555-565, 2008.

Wellershoff et al., 2011

Wellershoff F., Sendelbach M., Schmitt F.: *Einsatz von tragenden Glaselementen in Glasbrücken und Glaspavilons*, in: Stahlbau Spezial 2011 - Glasbau/Glass in Buildings, 13-23; Berlin: Ernst & Sohn Verlag, 2011.

Standards and Regulations

ASTM C 1401-02, 2002

ASTM C 1401-02: Standard guide for structural sealant glazing, United States: American Society for Testing and Materials, 2002.

ASTM D412, 2013

ASTM D412: Standard Test Methods for Vulcanized Rubber and Thermoplastic Elastomers - Tension, United States: American Society for Testing and Materials, 2013.

DIN 18008-1

DIN 18008-1: Glass in Building - Design and construction rules - Part 1: Terms and general bases, Berlin: Deutsches Institut für Normung (DIN), 2010.

DIN 18008-2

DIN 18008-2: Glass in Building - Design and construction rules - Part 2: Linearly supported glazings, Berlin: Deutsches Institut für Normung (DIN), 2010.

DIN 53504, 2009

DIN 53504: Prüfung von Kautschuk und Elastomeren - Bestimmung von Reißfestigkeit, Zugfestigkeit, Reißdehnung und Spannungswerten im Zugversuch, Berlin: Deutsches Institut für Normung (DIN), 2009.

EN 755-2, 2016

EN 755-2: Aluminium and aluminium alloys - Extruded rod/bar, tube and profiles - Part 2: Mechanical properties, Vienna: Austrian Standards Institute, 2016.

EN 1990

ÖNORM EN 1990: Basis of structural design, Vienna: Austrian Standards Institute, 2013.

EN 1991-1

ÖNORM EN 1991-1: Actions on structures - Part 1 to Part 7, Vienna: Austrian Standards Institute, 2011-2016.

EN 10025-2, 2011

EN 10025-2: Hot rolled products of structural steels - Part 2: Technical delivery conditions for non-alloy structural steels, Vienna: Austrian Standards Institute, 2011.

EN 10088-4, 2009

EN 10088-4: Stainless steels - Part 4: Technical delivery conditions for sheet/plate and strip of corrosion resisting steels for construction purposes, Vienna: Austrian Standards Institute, 2009.

EN 13022, 2014

EN 13022: Glass in building - Structural sealant glazing, Vienna: Austrian Standards Institute, 2014.

EN ISO 527, 2012

ÖNORM EN ISO 527: Plastics - Determination of tensile properties, Vienna: Austrian Standards Institute, 2012.

EN ISO 604, 2003

ÖNORM EN ISO 604: Plastics - Determination of compressive properties, Vienna: Austrian Standards Institute, 2003.

ETAG 002, 2001

ETAG 002: Guideline for european technical approval for Structural Sealant Glazing Systems (SSGS), Brussels: European Organization for Technical Approvals (EOTA), 2001.

EUR 26439 EN, 2014

Guidance for European Structural Design of Glass Components - Support to the implementation, harmonization and further developments of the Eurocodes, JRC Scientific and policy report, Editors: Dimova S., Pinto A., Feldmann M., Denton S., Luxembourg: Publication Office of the European Union, 2014.

ISO 37, 2011

ISO 37: Rubber, vulcanized or thermoplastic - Determination of tensile stress-strain properties, International standard, Geneve: International Organization for Standardization (ISO), 2011.

ISO 8339, 2005

ISO 8339: Building construction - Sealants - Determination of tensile properties (Extension to break), International standard, Geneve: International Organization for Standardization (ISO), 2005.

ÖNORM B 1991-1-4

ÖNORM B 1991-1-4: Actions on structures - Part 1-4: General actions - Wind actions - National specifications concerning ÖNORM EN 1991-1-4 and national supplements, Vienna: Austrian Standards Institute, 2013.

ÖNORM EN 1991-1-4

ÖNORM EN 1991-1-4: Actions on structures - Part 1-4: General actions - Wind actions, Vienna: Austrian Standards Institute, 2011.

ÖNORM B 1991-1-5

ÖNORM B 1991-1-5: Actions on structures - Part 1-5: General actions - Thermal actions - National specifications concerning ÖNORM EN 1991-1-5 and national supplements, Vienna: Austrian Standards Institute, 2012.

ÖNORM EN 1991-1-5

ÖNORM EN 1991-1-5: Actions on structures - Part 1-5: General actions - Thermal actions, Vienna: Austrian Standards Institute, 2012.

ÖNORM B 3716-1

ÖNORM B 3716-1: Glass in building - Structural glass construction, Part 1: Basic principles, Vienna: Austrian Standards Institute, 2009.

Technical Data Sheets

Dow Corning, 2011

Dow Corning Silicone Structural Glazing Manual, Dow Corning Corporation, 2011.

Dow Corning R40, 2012

Dow Corning® R40 Universal Cleaner, Product Data Sheet, Dow Corning Corporation, 2012.

Dow Corning 1200 OS, 2012

Dow Corning® 1200 OS Primer, UV Traceable - Primer for silicone adhesives and sealants, Product Data Sheet, Dow Corning Corporation, 2012.

Dow Corning TSSA, 2013

Dow Corning® TSSA Transparent Structural Silicone Adhesive - High strength structural glazing silicone film adhesive, Product Data Sheet, Dow Corning Corporation, 2013.

Dow Corning 3363, 2014

Dow Corning® 3363 Insulating Glass Sealant - Two-part silicone sealant with high strength for use as a secondary seal in insulating glass units, Product Data Sheet, Dow Corning Corporation, 2014.

Dow Corning 993, 2014

Dow Corning® 993 Structural Glazing Sealant - Two part silicone rubber, Product Data Sheet, Dow Corning Corporation, 2014.

Glas Trösch Composite Glazing, 2012

Composite Glazing - The unique building skin made from glass-fibre elements and glass, Bützberg: Glas Trösch AG Insulating Glass, 2012.

Merkblatt 821, 2012
Merkblatt 821: Edelstahl Rostfrei - Eigenschaften, Düsseldorf: Informationsstelle Edelstahl Rostfrei, 2013.

Merkblatt 875, 2004
Merkblatt 875: Edelstahl Rostfrei im Bauwesen: Technischer Leitfaden, Düsseldorf: Informationsstelle Edelstahl Rostfrei, 2004.

NPL Manual, 2007
Manual for the calculation of elastic-plastic materials models parameters, National Physical Laboratory, United Kingdom, http://www.npl.co.uk/upload/pdf/elastic-plastic-materials-manual.pdf, 2007, accessed 22.08.2017.

Roto, 2015
Roto Frank AG Window and Door Technology: *The Glazing Guide - Principles of Professional Glazing*, 2015.

Sika ADPrep, 2013
Sika® ADPrep - Oberflächenvorbehandlung für Sika ADP Klebstoffsysteme, Product Data Sheet, Sika Schweiz AG, 2013.

Sika Aktivator-205, 2010
Sika® Aktivator-205 - Pretreatment agent for non porous substrates, Product Data Sheet, Version 1, Sika Schweiz AG, 2010.

Sika Cleaner P, 2015
Sika® Cleaner P - Cleaning agent for non-porous substrates, Product Data Sheet, Version 5, Sika Schweiz AG, 2015.

SikaFast-5211 NT, 2013
SikaFast®-5211 NT - Schnelles 2-K-Klebstoffsystem für strukturelle Verklebungen, Product Data Sheet, Sika Schweiz AG, 2013.

SikaFast-5221 NT, 2013
SikaFast®-5221 NT - Schnelles 2-K-Klebstoffsystem für strukturelle Verklebungen, Product Data Sheet, Sika Schweiz AG, 2013.

Sikasil SG-550, 2016
Sikasil® SG-550 - High strength structural silicone adhesive, Product Data Sheet, Sika Schweiz AG, 2016.

Tiger Drylac, 2016
Tiger Drylac® Powder Coatings. Series 68 highly durable - Highly weather resistant powder coating for architectural application on polyester basis, Product Data Sheet, Tiger Coatings GmbH & Co.KG, 2016.

Online Links

www.raico.de
Raico facade systems: *http://www.raico.de/en/Products/THERM.php*, accessed 28.10.2016.

www.schueco.com
Schüco facade systems: *https://www.schueco.com/web2/de-en/architects/products/facades*, accessed 28.10.2016.

www.wicona.com
Wicona facade systems: *http://www.wicona.com/en/uk/Range-of-systems/Facades/Unitised-curtain-walls/*, accessed 28.10.2016.

www.wunderground.com
Weather Underground: *https://www.wunderground.com/history*, accessed 04.01.2017.

www.vma-getzmann.de

VMA-Getzmann GmbH: *http://www.vma-getzmann.de/willkommen/willkommen_0_1900.html*, accessed 20.01.2017.

Curriculum Vitae

Name:	Vlad Alexandru SILVESTRU
Date & place of birth:	13th of July 1986, Cluj-Napoca, Romania
Nationality:	Romanian
Contact:	silvestru_vlad@yahoo.com

Education

2012 - 2018	PhD candidate in Structural Engineering at Graz University of Technology
2009 - 2012	MSc in Structural Engineering at Graz University of Technology, degree with honourable mention
2005 - 2009	BSc in Civil Engineering at Graz University of Technology

Professional and research experience

10/2012 - 03/2018	teaching and research assistant at the Institute of Building Construction, Graz University of Technology
06/2013	visiting researcher at the Glass & Facade Technology Research Group, University of Cambridge
05/2012 - 09/2012	research assistant at the Institute of Building Construction, Graz University of Technology
03/2011 - 01/2012	student tutor at the Institute of Building Construction, Graz University of Technology
06/2008 - 04/2012	freelancer as owner of a registered technical drawing office - collaboration with small architecture offices in Graz
09/2010	internship in the engineering office *Werner Consult*, Vienna

07/2010 - 08/2010	research assistant at the Institute of Timber Engineering and Wood Technology, Graz University of Technology
07/2007 - 09/2007	internship in the engineering office *Depisch*, Unterpremstätten

Awards and Memberships

Young Researchers 2nd Place Award at GlassCon Global 2016 for the contribution: *Lateral torsional buckling of suspended glass fins with different support designs*.

COST Action TU 1403 - Adaptive Facades Network:
Member of work group WG3 (*Whole building integration and whole-life evaluation methods of adaptive facades*).

COST Action TU 0905 - European Research Network on Structural Glass:
Member of work group WG4 (*Novel Glass Assemblies*) - TG13 (*Hybrid Components*).

Languages

Romanian (native speaker)
German (advanced)
English (advanced)
French (beginner)

Publications (other than those related to the doctoral thesis and included in the publication list)

Silvestru V.A., Englhardt O.: *Lateral torsional buckling of suspended glass fins with different support designs*, in: GlassCon Global, Proceedings, Boston, 265-273, 2016.

Silvestru V.A., Englhardt O.: *Stability behaviour of cantilevered glass fins*, in: Glass Performance Days, Proceedings, Tampere, 373-376, 2015.

Silvestru V.A., Englhardt O.: *Stabilitätsverhalten von Kragträgern aus Verbundsicherheitsglas*, in: Glasbau 2015, 213-227, Editors: Weller B. & Tasche S., Berlin: Ernst & Sohn Verlag, 2015.

Nhamoinesu S., Silvestru V.A., Overend M., Englhardt O.: *The mechanical performance of adhesively bonded steel-glass composite panels: medium-scale tests and numerical models*, in: Challenging Glass 4 & COST Action TU0905 Final Conference, Proceedings, Lausanne, 269-276, 2014.

Silvestru V.A., Englhardt O.: *Numerical and experimental analysis of suspended glass fins*, in: Advanced Building Skins, Proceedings, Graz, paper on CD, 2012.

Publication List

Published papers

Silvestru V.A., Englhardt O., Schneider J.: *Investigations on Linear Silicone Joints for Glass-Metal Elements with Composite Structural Behavior*, in: Challenging Glass 6, Proceedings, Delft, 2018, accepted.

Silvestru V.A., Englhardt O.: *Adhesion of a two-part structural acrylate to metal and glass surfaces*, in: Engineered Transparency, Proceedings, Düsseldorf, 611-622, 2016.

Kolany G.H.E., Silvestru V.A., Zellinger M., Englhardt O.: *Resin based mortar: Long term behaviour test compared with analytical and numerical models*, in: Glass Performance Days, Proceedings, Tampere, 262-265, 2015.

Silvestru V.A., Kolany G.H.E., Englhardt O.: *Glass Building Skins: Presentation of the research project and intermediary findings*, in: Advanced Building Skins, Proceedings, Graz, 118-126, 2015.

Silvestru V.A., Kolany G.H.E., Englhardt O.: *Analyses on loads and adhesives for hybrid glass-steel facade structures*, in: Engineered Transparency, Proceedings, Düsseldorf, 581-591, 2014.

Kolany G.H.E., Silvestru V.A., Englhardt O.: *Long-term behaviour of a synthetic resin mortar under compressive stress*, in: Engineered Transparency, Proceedings, Düsseldorf, 221-230, 2014.

Silvestru V.A., Kolany G.H.E., Englhardt O.: *Load transfer materials for hybrid glass-steel facade elements*, in: IABSE Symposium, Proceedings, Madrid, 1804-1811, 2014.

Silvestru V.A., Englhardt O.: *Application study for hybrid adhesively bonded glass-steel facade elements*, in: Challenging Glass 4 & COST Action TU0905 Final Conference, Proceedings, Lausanne, 277-284, 2014.

Silvestru V.A., Zellinger M., Englhardt O.: *Hybrid glass structures for building skins - actions and requirements*, in: COST Action TU0905 Mid-term Conference, Proceedings, Porec, 33-42, 2013.

Papers under review or in preparation

Silvestru V.A., Englhardt O., Schneider J.: *Linear adhesive connections at the edge of laminated glass panes: an experimental study under tensile, compressive and shear loading*, Glass Structures & Engineering, under review.

Silvestru V.A., Drass M., Englhardt O., Schneider J.: *Performance of a structural acrylic adhesive for linear glass-metal connections under shear and tensile loading*, International Journal of Adhesion and Adhesives, under review.

Silvestru V.A., Kolany G., Freytag B., Schneider J., Englhardt O.: *Performance of glass-metal elements with composite structural behaviour under in-plane and out-of-plane loading,* Engineering Structures, in preparation.

Appendix A

Test results for uniaxial tensile tests on adhesive dumbbell specimens

Real cross section dimensions of the dumbbell specimens
Mechanical values determined from the measured data

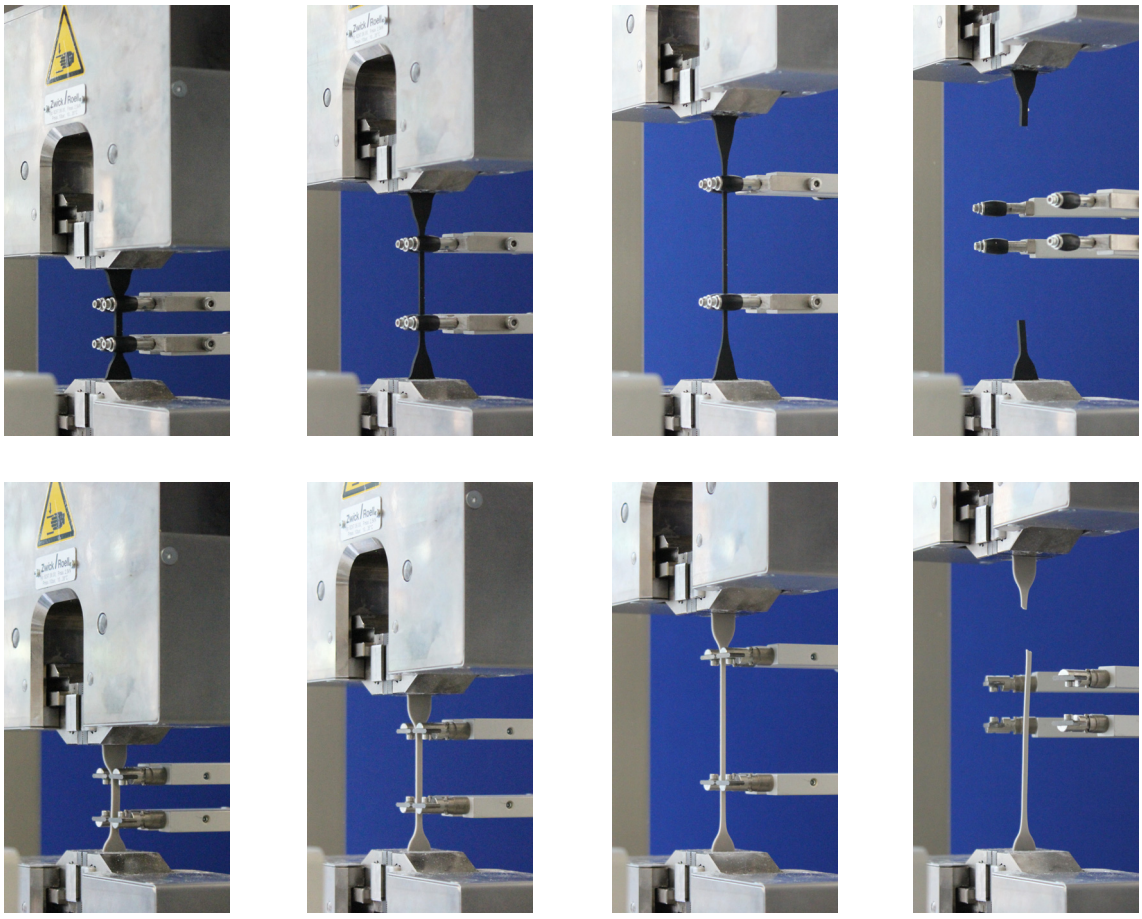

Real cross section dimensions and test results for the dumbbell specimens of *Dow Corning 993* tested under uniaxial tension:

Specimen	**Dimensions**		**Max. load** [N]	**Max. engin. stress** [MPa]	**Max. engin. strain** [%]	**Young's modulus 0.5-5%** [MPa]	**Young's modulus 0.5-50%** [MPa]
	width w [mm]	**thickness** t [mm]					
Series 1 - loading speed 5 mm/min							
1_DC 993_TS 01	6.47	1.81	23.7	2.03	198%	2.71	1.30
1_DC 993_TS 02	6.41	1.87	28.0	2.33	234%	3.14	1.33
1_DC 993_TS 03	6.45	1.86	26.3	2.19	206%	4.46	1.37
1_DC 993_TS 04	6.50	1.80	28.4	2.43	246%	1.87	1.36
Mean value	6.46	1.84	26.6	2.25	221%	3.05	1.34
Standard deviation	0.04	0.04	2.1	0.17	23%	1.08	0.03

Real cross section dimensions and test results for the dumbbell specimens of *Sikasil SG-550* tested under uniaxial tension:

Specimen	**Dimensions**		**Max. load** [N]	**Max. engin. stress** [MPa]	**Max. engin. strain** [%]	**Young's modulus 0.5-5%** [MPa]	**Young's modulus 0.5-50%** [MPa]
	width w [mm]	**thickness** t [mm]					
Series 1 - loading speed 5 mm/min							
1_SS SG-550_TS 01	3.85	2.32	26.5	2.96	259%	2.10	1.31
1_SS SG-550_TS 02	3.89	2.33	26.1	2.88	239%	1.85	1.34
1_SS SG-550_TS 03	3.83	2.22	23.4	2.75	228%	1.87	1.37
1_SS SG-550_TS 04	3.84	2.26	25.6	2.95	270%	1.48	0.89
Mean value	3.85	2.28	25.4	2.89	249%	1.83	1.23
Standard deviation	0.03	0.05	1.4	0.10	19%	0.26	0.23
Series 2 - loading speed 5 mm/min							
2_SS SG-550_TS 01	3.85	2.15	24.0	2.90	282%	3.07	1.47
2_SS SG-550_TS 02	3.87	2.02	22.7	2.91	281%	3.12	1.49
2_SS SG-550_TS 03	3.87	2.11	23.3	2.85	278%	3.19	1.47
2_SS SG-550_TS 04	3.87	1.99	22.2	2.89	282%	3.20	1.49
2_SS SG-550_TS 05	3.89	2.27	23.6	2.67	261%	3.04	1.40
Mean value	3.87	2.11	23.2	2.84	277%	3.12	1.46
Standard deviation	0.01	0.11	0.7	0.10	9%	0.07	0.04

Specimen	Dimensions		Max. load [N]	Max. engin. stress [MPa]	Max. engin. strain [%]	Young's modulus 0.5-5% [MPa]	Young's modulus 0.5-50% [MPa]
	width w [mm]	thickness t [mm]					
Series 2 - loading speed 200 mm/min							
2_SS SG-550_TS 06	3.87	2.60	31.5	3.13	275%	3.76	1.67
2_SS SG-550_TS 07	3.86	2.61	32.9	3.26	284%	3.78	1.62
2_SS SG-550_TS 08	3.85	2.57	30.6	3.09	260%	3.89	1.69
2_SS SG-550_TS 09	3.86	2.54	30.2	3.08	263%	3.73	1.61
2_SS SG-550_TS 10	3.88	2.69	35.1	3.36	299%	3.59	1.62
Mean value	3.86	2.60	32.1	3.18	276%	3.75	1.64
Standard deviation	0.01	0.06	2.0	0.12	16%	0.11	0.04

Real cross section dimensions and test results for the dumbbell specimens of *SikaFast-5211 NT* and *SikaFast-5221 NT* tested under uniaxial tension:

Specimen	Dimensions		Max. load [N]	Max. engin. stress [MPa]	Max. engin. strain [%]	Approx. yielding stress [MPa]	Young's modulus 0.5-1% [MPa]
	width w [mm]	thickness t [mm]					
Series 1 - loading speed 5 mm/min							
1_SF-5211 NT_TS 01	4.05	1.78	73.4	10.18	243%	8.10	239.93
1_SF-5211 NT_TS 02	4.04	1.65	63.9	9.58	216%	7.86	308.74
1_SF-5211 NT_TS 03	4.04	1.80	75.5	10.38	232%	8.12	199.92
1_SF-5211 NT_TS 04	4.00	1.80	74.0	10.28	227%	8.08	212.50
Mean value	4.03	1.76	71.7	10.11	230%	8.04	240.27
Standard deviation	0.02	0.07	5.3	0.36	11%	0.12	48.61
Series 2 - loading speed 5 mm/min							
2_SF-5221 NT_TS 01	4.04	1.74	71.0	10.10	256%	6.51	235.45
2_SF-5221 NT_TS 02	4.05	1.75	71.5	10.10	256%	6.56	227.86
2_SF-5221 NT_TS 03	4.06	1.76	67.2	9.40	242%	6.67	280.37
2_SF-5221 NT_TS 04	4.05	1.74	66.1	9.38	244%	6.63	255.49
2_SF-5221 NT_TS 05	4.05	1.73	65.7	9.37	243%	6.56	257.16
Mean value	4.05	1.74	68.3	9.67	248%	6.59	251.27
Standard deviation	0.01	0.01	2.8	0.39	7%	0.06	20.60

Specimen	Dimensions		Max. load [N]	Max. engin. stress [MPa]	Max. engin. strain [%]	Approx. yielding stress [MPa]	Young's modulus 0.5-1% [MPa]
	width w [mm]	**thickness** t [mm]					
Series 2 - loading speed 1 mm/min							
2_SF-5221 NT_TS 06	4.05	1.72	56.9	8.16	255%	4.77	159.66
2_SF-5221 NT_TS 07	4.05	1.71	57.6	8.31	250%	4.92	158.16
2_SF-5221 NT_TS 08	4.05	1.71	59.6	8.60	263%	5.03	164.06
2_SF-5221 NT_TS 09 *	4.05	1.70	59.7	8.67	252%	5.76	215.85
2_SF-5221 NT_TS 10 *	4.05	1.67	58.3	8.62	252%	5.75	204.39
Mean value	4.05	1.70	58.4	8.47	254%	5.25	180.42
Standard deviation	0.00	0.02	1.2	0.22	5%	0.47	27.50
* All five specimens were produced at the same time, but the specimens TS 09 and TS 10 were tested 10 days later than the other three (their results are not illustrated in Fig. 4.10)							
Series 2 - loading speed 10 mm/min							
2_SF-5221 NT_TS 11	4.05	1.74	68.3	9.69	243%	6.84	237.87
2_SF-5221 NT_TS 12	4.05	1.72	60.1	8.63	221%	6.81	255.48
2_SF-5221 NT_TS 13	4.06	1.76	57.2	8.00	197%	6.92	303.65
2_SF-5221 NT_TS 14	4.05	1.69	66.3	9.69	248%	6.72	241.63
2_SF-5221 NT_TS 15	4.05	1.69	65.5	9.57	241%	6.84	263.59
Mean value	4.05	1.72	63.5	9.12	230%	6.83	260.44
Standard deviation	0.00	0.03	4.6	0.77	21%	0.07	26.29
Series 2 - loading speed 100 mm/min							
2_SF-5221 NT_TS 16	4.04	1.67	71.4	10.58	238%	9.49	404.00
2_SF-5221 NT_TS 17	4.05	1.66	70.1	10.43	238%	9.64	356.80
2_SF-5221 NT_TS 18	4.05	1.68	70.9	10.43	231%	9.76	398.85
2_SF-5221 NT_TS 19	4.05	1.68	74.0	10.88	236%	9.84	397.00
2_SF-5221 NT_TS 20	4.05	1.65	66.6	9.97	225%	9.63	361.20
Mean value	4.05	1.67	70.6	10.46	234%	9.67	383.57
Standard deviation	0.00	0.01	2.7	0.33	6%	0.13	22.63

Appendix B

Test results for adhesive joints between metal substrates

Shear stress *vs.* shear displacement diagrams
Real cross section dimensions of the double-lap shear test specimens
Mechanical values determined from the measured data
Failure patterns of the double-lap shear test specimens

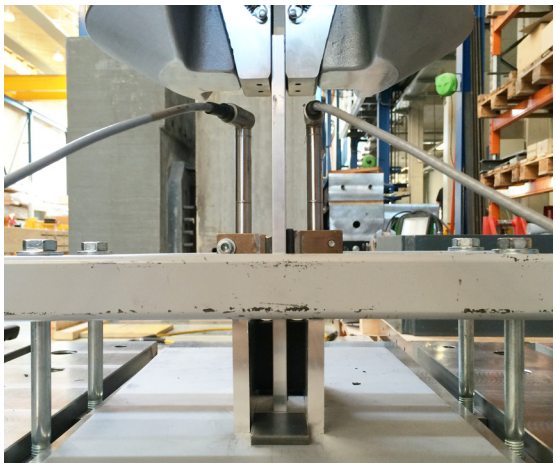

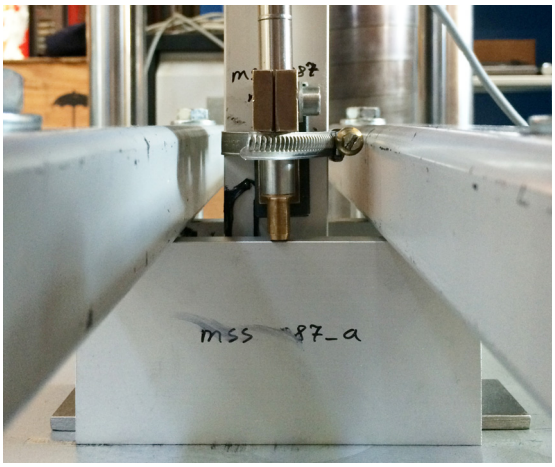

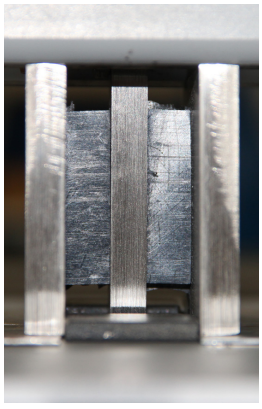

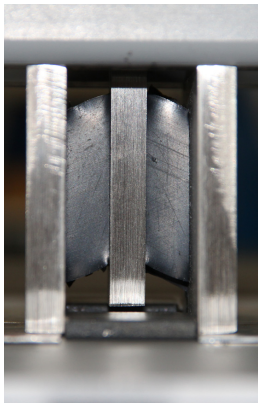

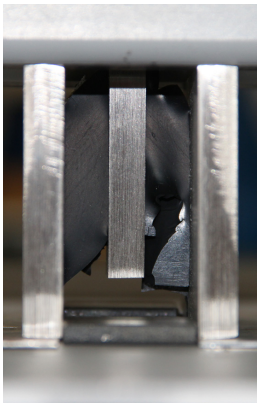

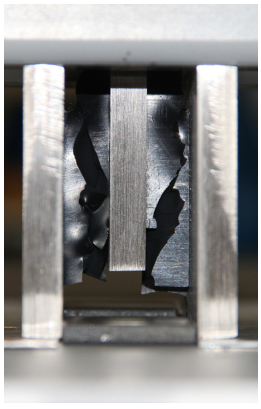

B.1 - Dow Corning 993 - adhesive joint dimensions: 50 mm x 12 mm x 12 mm

Shear stress *vs.* shear displacement diagrams from the double-lap shear tests on specimens with *Dow Corning 993*, stainless steel substrates and smaller joint geometry:

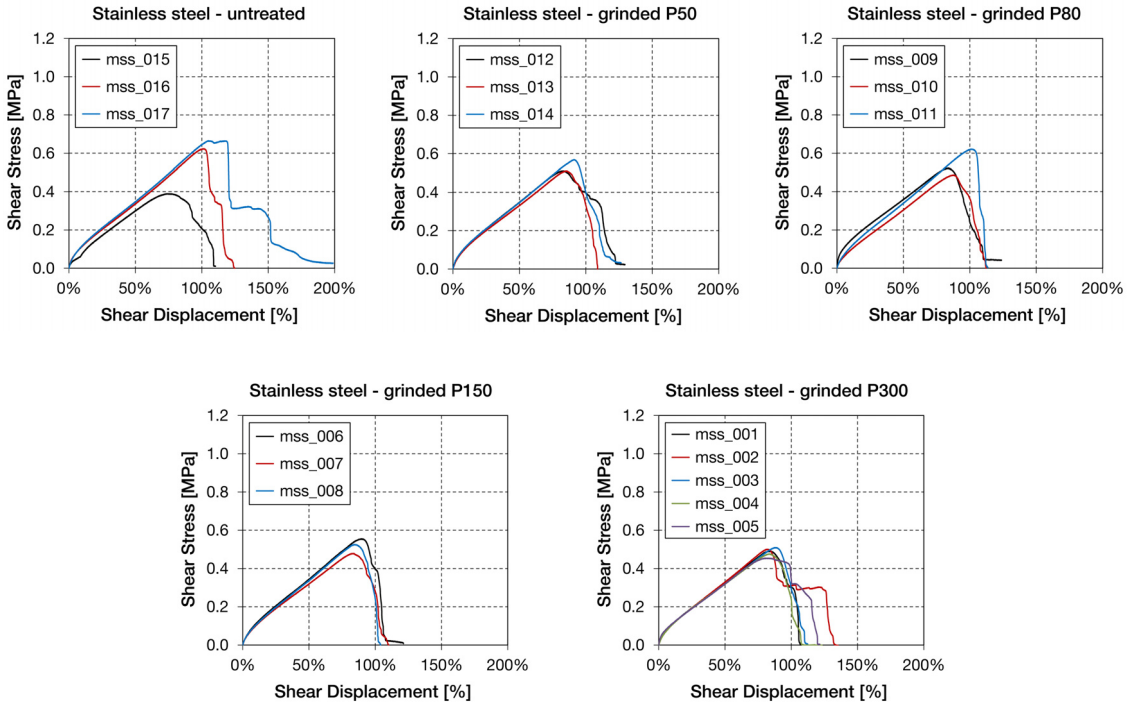

Shear stress *vs.* shear displacement diagrams from the double-lap shear tests on specimens with *Dow Corning 993*, aluminium substrates and smaller joint geometry:

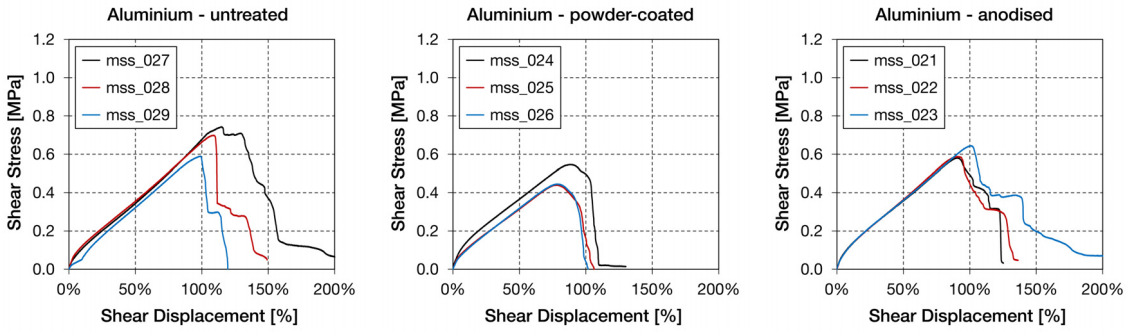

Real joint dimensions and test results for the double-lap shear specimens with *Dow Corning 993*, stainless steel substrates and smaller joint geometry:

Specimen		Joint dimensions			Max. load [N]	Corr. displ. [mm]	Max. shear stress [MPa]	Corr. shear displ. [-]
		length l [mm]	**width** w [mm]	**thickness** t [mm]				
mss_015	lap_a	48.2	13.6	13.1	494	10.1	0.39	0.77
	lap_b	48.1	12.7	13.1				
mss_016	lap_a	48.5	13.5	13.1	833	13.2	0.62	1.01
	lap_b	48.7	14.0	13.1				
mss_017	lap_a	47.9	12.7	13.0	802	13.7	0.67	1.05
	lap_b	47.4	12.6	13.0				
mss_012	lap_a	47.7	13.0	13.2	657	10.8	0.51	0.83
	lap_b	46.9	14.2	13.1				
mss_013	lap_a	48.6	14.7	13.1	707	11.2	0.51	0.85
	lap_b	49.3	13.5	13.1				
mss_014	lap_a	47.6	13.6	13.2	753	12.0	0.57	0.91
	lap_b	47.6	14.2	13.2				
mss_009	lap_a	49.3	14.3	13.1	723	10.9	0.52	0.84
	lap_b	49.9	13.6	13.1				
mss_010	lap_a	49.0	15.0	13.2	670	11.6	0.49	0.88
	lap_b	48.6	13.2	13.2				
mss_011	lap_a	48.5	12.6	13.1	810	13.2	0.62	1.01
	lap_b	48.7	14.2	13.1				
mss_006	lap_a	47.8	13.3	13.3	726	11.9	0.56	0.90
	lap_b	47.6	14.1	13.3				
mss_007	lap_a	49.3	13.9	12.9	683	10.8	0.48	0.83
	lap_b	49.0	15.1	12.9				
mss_008	lap_a	50.6	13.8	13.1	689	11.1	0.53	0.84
	lap_b	48.5	12.6	13.1				
mss_001	lap_a	50.2	14.6	13.3	680	11.1	0.49	0.83
	lap_b	49.7	13.1	13.3				
mss_002	lap_a	50.0	13.4	13.2	676	10.7	0.50	0.82
	lap_b	49.0	13.9	13.2				
mss_003	lap_a	49.4	14.8	13.1	726	11.5	0.51	0.87
	lap_b	49.9	13.9	13.1				
mss_004	lap_a	49.9	15.1	13.2	709	11.0	0.48	0.83
	lap_b	49.3	14.9	13.2				
mss_005	lap_a	46.5	14.5	13.1	622	10.5	0.46	0.80
	lap_b	47.6	14.6	13.2				
Mean value		48.7	13.9	13.1	704	11.5	0.52	0.87
Standard deviation		1.0	0.8	0.1	78	1.0	0.07	0.08

Real joint dimensions and test results for the double-lap shear specimens with *Dow Corning 993*, aluminium substrates and smaller joint geometry:

Specimen		**Joint dimensions**			**Max. load** [N]	**Corr. displ.** [mm]	**Max. shear stress** [MPa]	**Corr. shear displ.** [-]
		length l [mm]	**width** w [mm]	**thickness** t [mm]				
mss_027	lap_a	46.4	12.6	13.1	873	15.1	0.74	1.15
	lap_b	46.1	12.8	13.2				
mss_028	lap_a	48.6	13.0	13.1	897	14.3	0.70	1.09
	lap_b	48.3	13.5	13.2				
mss_029	lap_a	48.2	13.5	13.2	782	13.1	0.59	0.99
	lap_b	48.9	13.8	13.2				
mss_024	lap_a	48.8	14.0	13.2	739	11.7	0.55	0.88
	lap_b	48.1	13.9	13.2				
mss_025	lap_a	48.8	13.9	13.2	612	10.3	0.44	0.78
	lap_b	49.0	14.5	13.2				
mss_026	lap_a	48.1	13.0	13.2	595	10.3	0.45	0.78
	lap_b	48.2	14.7	13.2				
mss_021	lap_a	48.4	14.2	13.1	799	11.9	0.58	0.91
	lap_b	49.2	14.0	13.1				
mss_022	lap_a	49.4	12.1	13.1	747	11.8	0.59	0.90
	lap_b	49.5	13.6	13.1				
mss_023	lap_a	48.9	12.8	13.1	845	13.3	0.64	1.01
	lap_b	47.2	14.5	13.1				
Mean value		48.3	13.6	13.2	765	12.4	0.59	0.94
Standard deviation		0.9	0.7	0.1	106	1.7	0.10	0.13

Failure patterns from the double-lap shear tests on specimens with *Dow Corning 993*, stainless steel substrates and smaller joint geometry:

- stainless steel - untreated

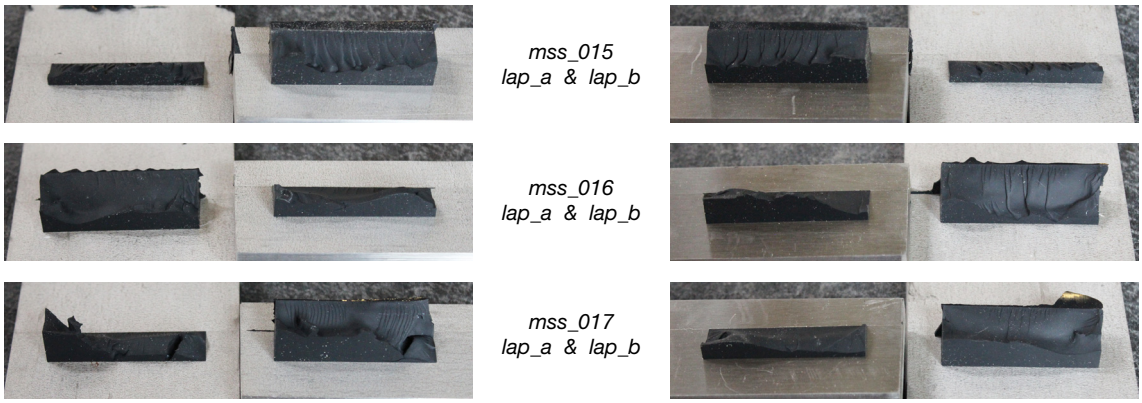

mss_015 lap_a & lap_b

mss_016 lap_a & lap_b

mss_017 lap_a & lap_b

- stainless steel - grinded P50

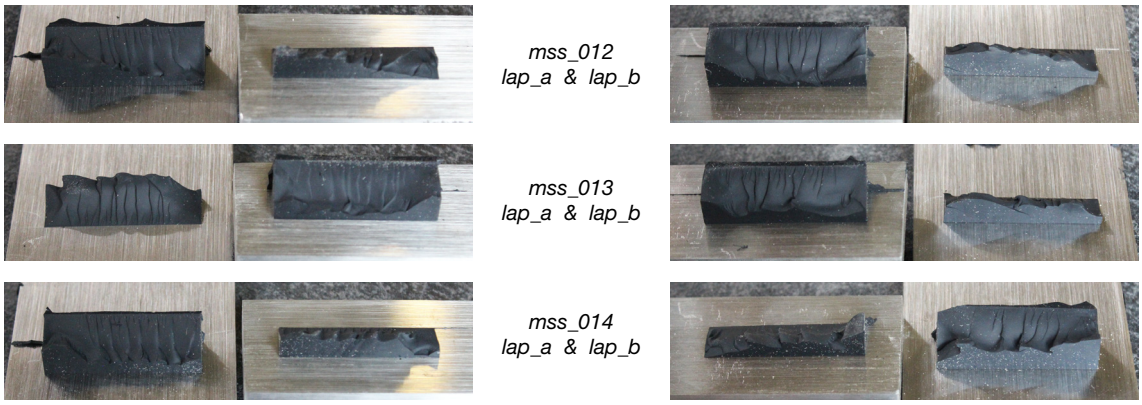

mss_012 lap_a & lap_b

mss_013 lap_a & lap_b

mss_014 lap_a & lap_b

- stainless steel - grinded P80

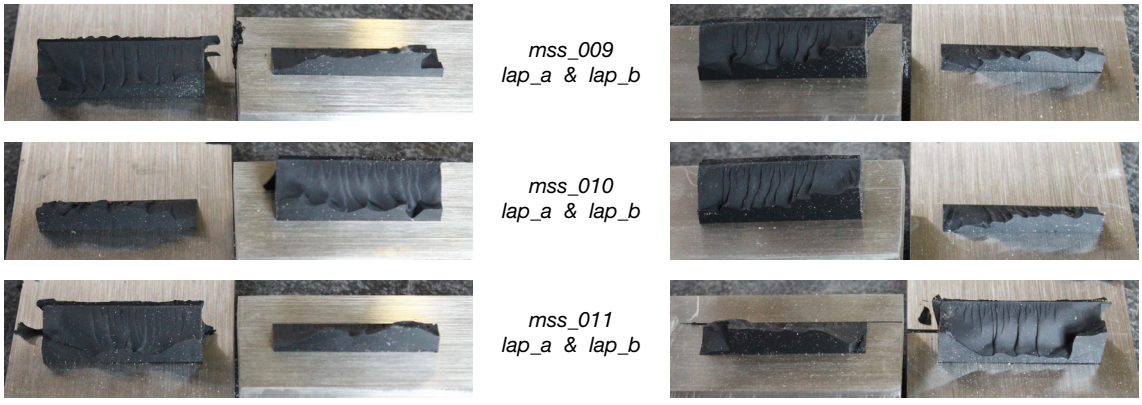

mss_009 lap_a & lap_b

mss_010 lap_a & lap_b

mss_011 lap_a & lap_b

- stainless steel - grinded P150

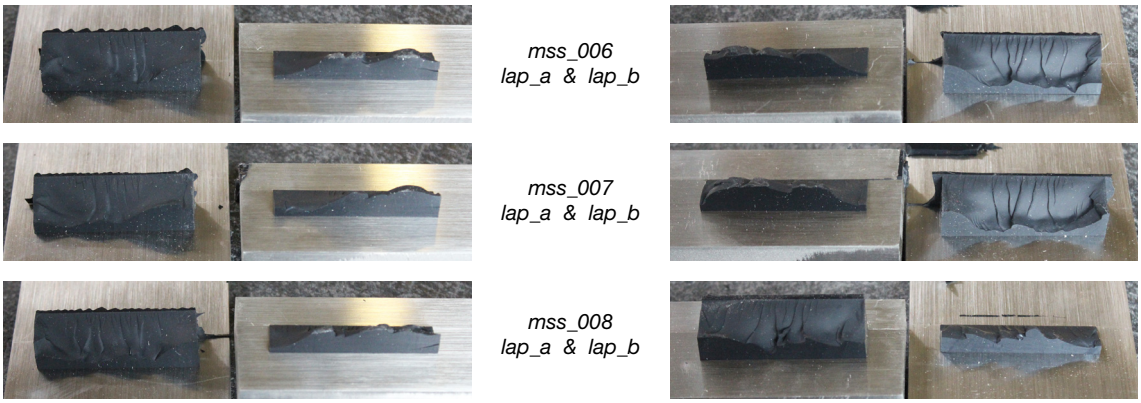

mss_006
lap_a & lap_b

mss_007
lap_a & lap_b

mss_008
lap_a & lap_b

- stainless steel - grinded P300

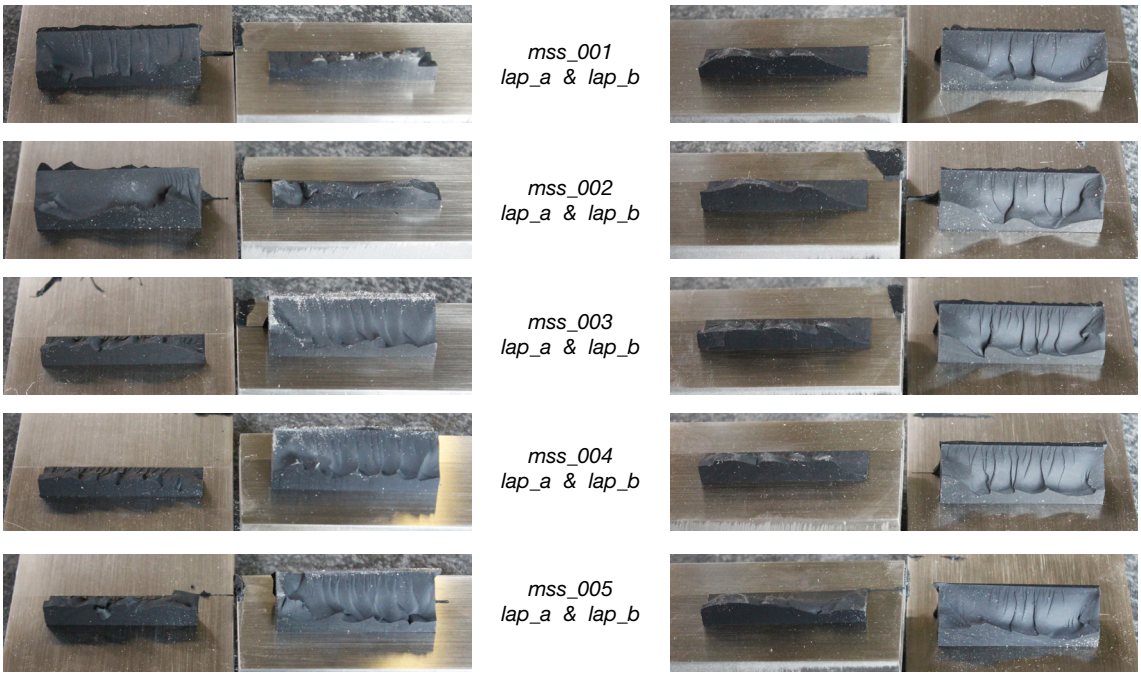

mss_001
lap_a & lap_b

mss_002
lap_a & lap_b

mss_003
lap_a & lap_b

mss_004
lap_a & lap_b

mss_005
lap_a & lap_b

Failure patterns from the double-lap shear tests on specimens with *Dow Corning 993*, aluminium substrates and smaller joint geometry:

- aluminium - untreated

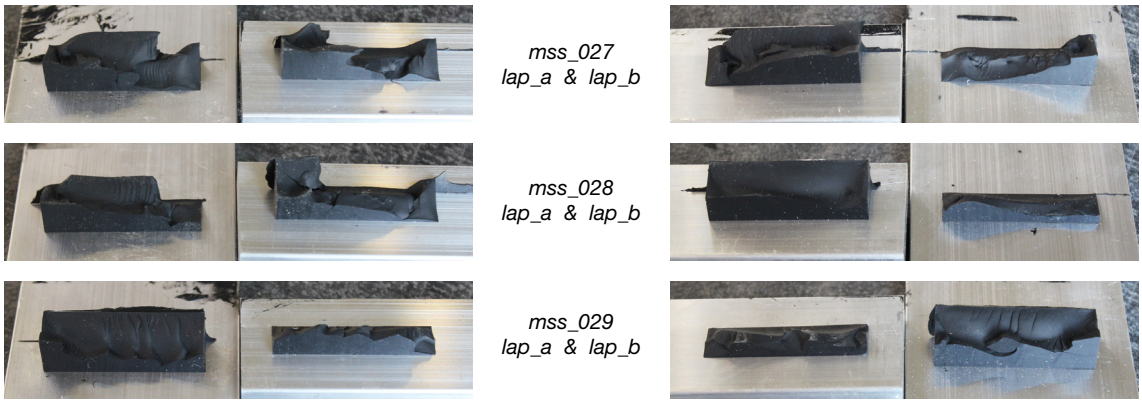

mss_027 lap_a & lap_b

mss_028 lap_a & lap_b

mss_029 lap_a & lap_b

- aluminium - powder-coated

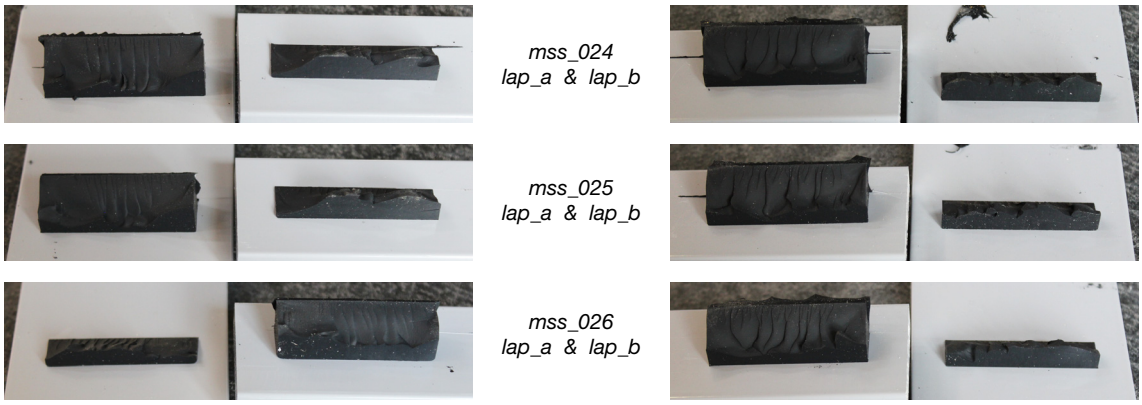

mss_024 lap_a & lap_b

mss_025 lap_a & lap_b

mss_026 lap_a & lap_b

- aluminium - anodised

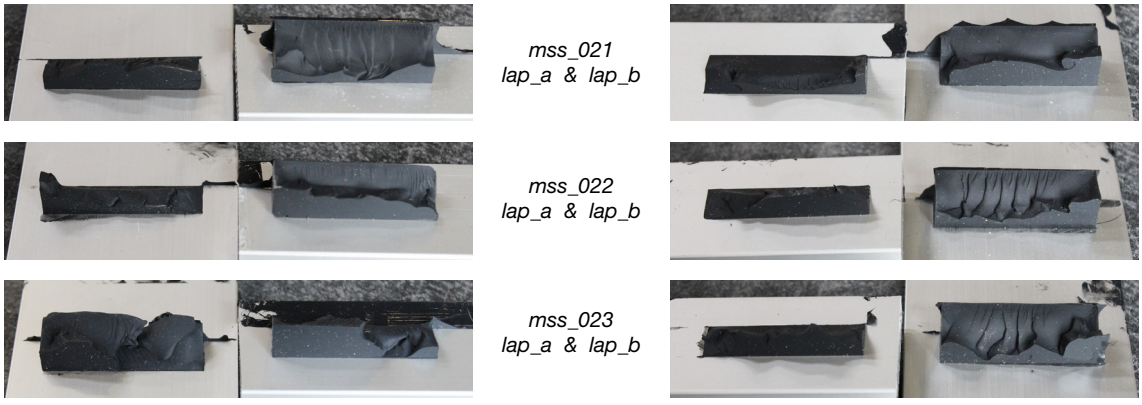

mss_021 lap_a & lap_b

mss_022 lap_a & lap_b

mss_023 lap_a & lap_b

B.2 - Dow Corning 993 - adhesive joint dimensions: 50 mm x 60 mm x 12 mm

Shear stress *vs.* shear displacement diagrams from the double-lap shear tests on specimens with *Dow Corning 993* and larger joint geometry:

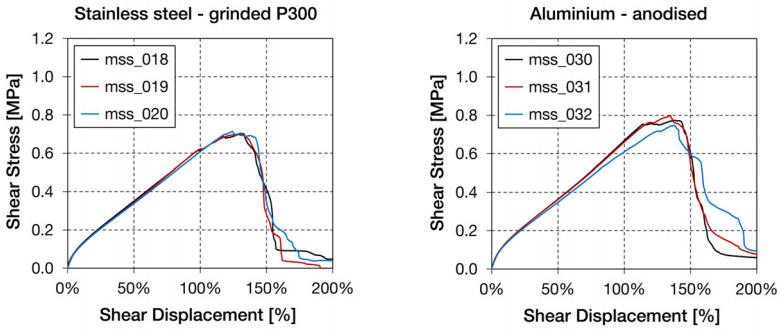

Real joint dimensions and test results for the double-lap shear specimens with *Dow Corning 993* and larger joint geometry:

Specimen		**Joint dimensions**			**Max. load** [N]	**Corr. displ.** [mm]	**Max. shear stress** [MPa]	**Corr. shear displ.** [-]
		length l [mm]	**width** w [mm]	**thickness** t [mm]				
mss_018	lap_a	54.2	57.6	12.5	4 245	16.5	0.70	1.32
	lap_b	52.0	56.2	12.5				
mss_019	lap_a	52.3	57.9	12.6	4 250	16.0	0.70	1.27
	lap_b	51.1	59.7	12.5				
mss_020	lap_a	54.6	59.0	12.7	4 474	15.9	0.71	1.24
	lap_b	52.4	58.1	12.9				
mss_030	lap_a	50.6	57.7	12.6	4 529	17.4	0.77	1.38
	lap_b	51.3	57.1	12.7				
mss_031	lap_a	50.8	59.0	12.8	4 788	17.3	0.80	1.35
	lap_b	51.8	57.8	12.8				
mss_032	lap_a	53.3	58.2	12.4	4 589	17.1	0.75	1.38
	lap_b	52.4	58.1	12.4				
Mean value		52.2	58.0	12.6	4 479	16.7	0.74	1.32
Standard deviation		1.3	0.9	0.2	208	0.7	0.04	0.06

Failure patterns from the double-lap shear tests on specimens with *Dow Corning 993* and larger joint geometry:

- stainless steel - grinded P300

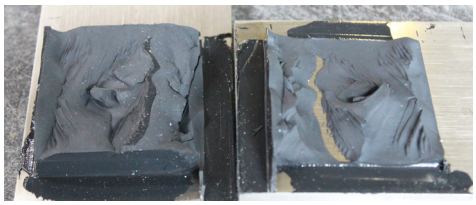
mss_018
lap_a & lap_b
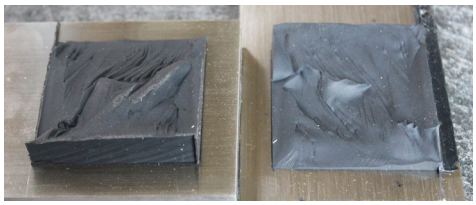

mss_019
lap_a & lap_b
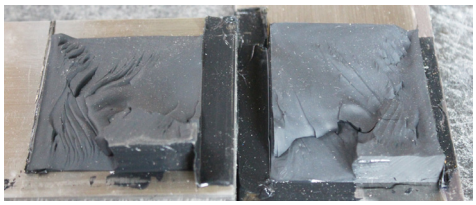

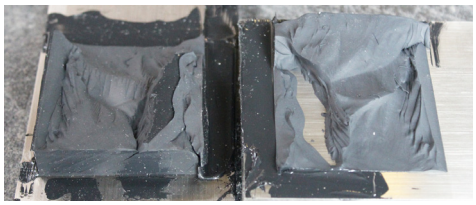
mss_020
lap_a & lap_b
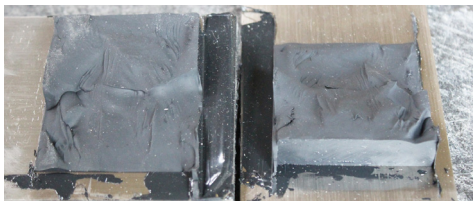

- aluminium - anodised

mss_030
lap_a & lap_b
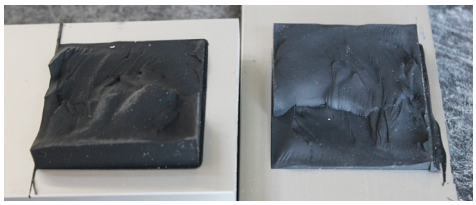

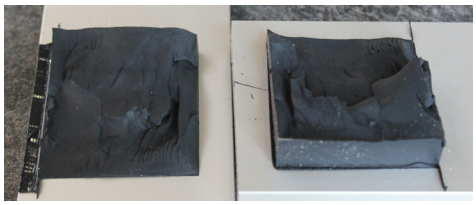
mss_031
lap_a & lap_b
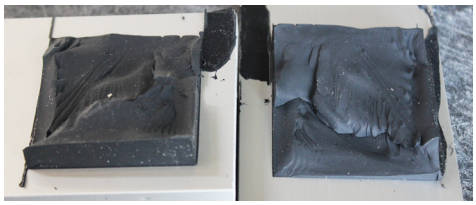

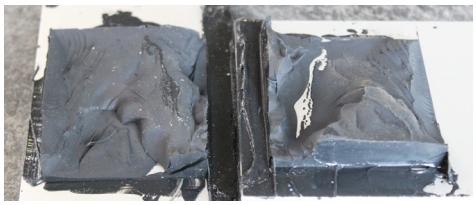
mss_032
lap_a & lap_b
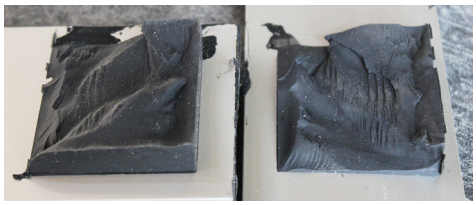

B.3 - Sikasil SG-550 - adhesive joint dimensions: 50 mm x 12 mm x 12 mm

Shear stress *vs.* shear displacement diagrams from the double-lap shear tests on specimens with *Sikasil SG-550*, stainless steel substrates and smaller joint geometry:

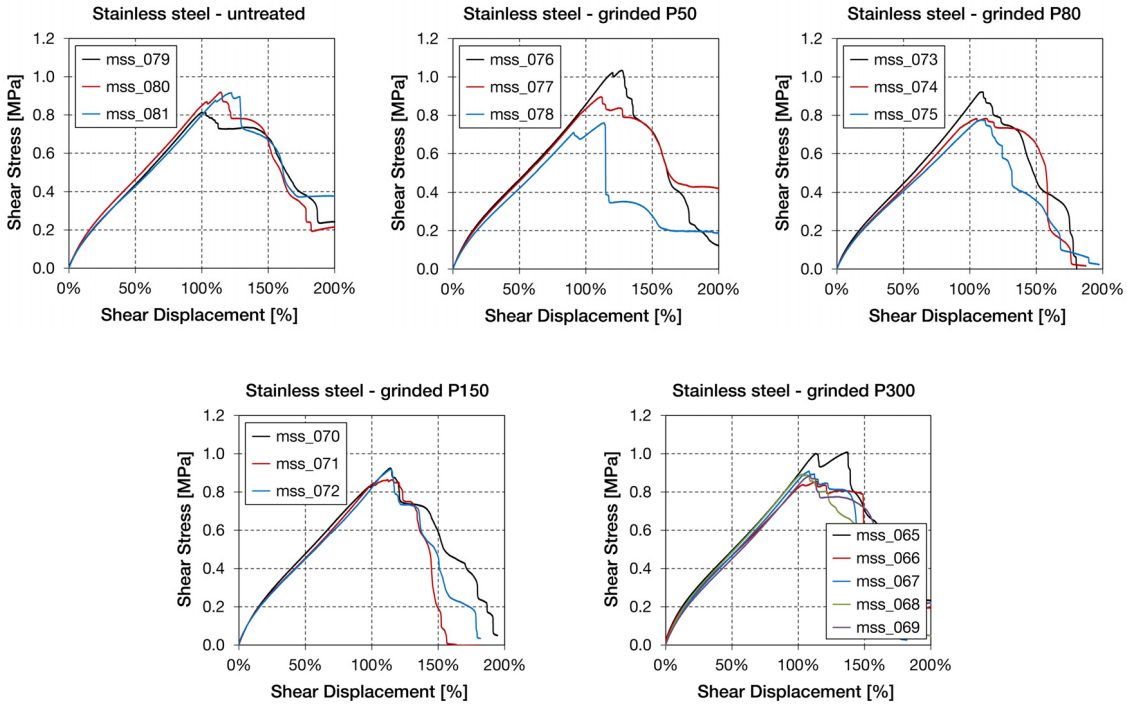

Shear stress *vs.* shear displacement diagrams from the double-lap shear tests on specimens with *Sikasil SG-550*, aluminium substrates and smaller joint geometry:

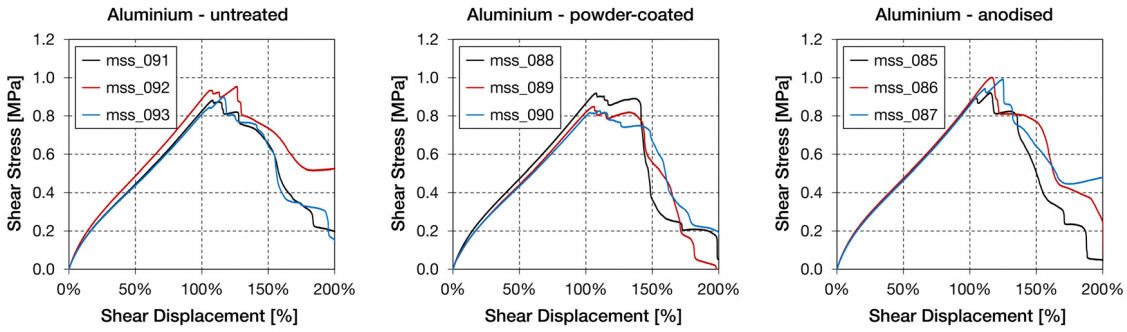

Note:
Specimens number *mss_033* to *mss_064* are missing from the results, since for these specimens the insulating glass sealant *Dow Corning 3363* is used. This adhesive is included in the experimental programme on the adhesion to metal substrates, but the results are not included in this thesis, because they are not directly relevant to the topic.

Real joint dimensions and test results for the double-lap shear specimens with *Sikasil SG-550*, stainless steel substrates and smaller joint geometry:

Specimen		Joint dimensions			Max. load [N]	Corr. displ. [mm]	Max. shear stress [MPa]	Corr. shear displ. [-]
		length l [mm]	**width** w [mm]	**thickness** t [mm]				
mss_079	lap_a	46.9	13.1	13.1	981	13.1	0.81	1.00
	lap_b	46.9	12.6	13.1				
mss_080	lap_a	51.7	12.8	13.1	1 214	14.9	0.92	1.14
	lap_b	51.0	12.9	13.1				
mss_081	lap_a	48.9	12.7	13.2	1 137	16.0	0.92	1.21
	lap_b	49.6	12.5	13.2				
mss_076	lap_a	46.8	14.0	13.1	1 358	16.6	1.04	1.27
	lap_b	47.9	13.7	13.1				
mss_077	lap_a	50.2	13.3	13.2	1 178	14.7	0.90	1.11
	lap_b	49.3	13.1	13.2				
mss_078	lap_a	49.7	12.6	13.1	971	14.8	0.76	1.13
	lap_b	49.7	13.1	13.1				
mss_073	lap_a	50.6	12.6	13.2	1 216	14.3	0.92	1.09
	lap_b	49.7	13.7	13.2				
mss_074	lap_a	50.8	12.5	12.8	1 001	14.3	0.78	1.11
	lap_b	49.4	13.0	12.9				
mss_075	lap_a	48.9	13.0	12.8	925	13.9	0.78	1.08
	lap_b	44.0	12.6	12.9				
mss_070	lap_a	47.9	11.9	13.2	1 044	15.0	0.93	1.14
	lap_b	42.9	13.0	13.2				
mss_071	lap_a	47.7	13.2	13.3	1 135	14.9	0.87	1.12
	lap_b	54.1	12.6	13.3				
mss_072	lap_a	47.8	13.7	13.2	1 178	15.1	0.92	1.14
	lap_b	48.2	13.0	13.2				
mss_065	lap_a	48.8	12.9	13.1	1 276	18.0	1.01	1.37
	lap_b	48.5	13.1	13.1				
mss_066	lap_a	50.5	12.4	13.1	1 088	14.9	0.86	1.13
	lap_b	51.2	12.6	13.1				
mss_067	lap_a	49.6	12.8	13.1	1 122	14.1	0.91	1.08
	lap_b	49.1	12.2	13.1				
mss_068	lap_a	49.4	12.8	13.2	1 153	13.5	0.89	1.03
	lap_b	50.3	13.1	13.2				
mss_069	lap_a	49.6	13.1	13.1	1 134	14.3	0.89	1.09
	lap_b	48.6	12.9	13.1				
Mean value		49.0	12.9	13.1	1 124	14.9	0.89	1.13
Standard deviation		2.1	0.4	0.1	114	1.2	0.08	0.09

Real joint dimensions and test results for the double-lap shear specimens with *Sikasil SG-550*, aluminium substrates and smaller joint geometry:

Specimen		Joint dimensions			Max. load [N]	Corr. displ. [mm]	Max. shear stress [MPa]	Corr. shear displ. [-]
		length l [mm]	**width** w [mm]	**thickness** t [mm]				
mss_091	lap_a	47.5	12.5	13.2	1 054	14.2	0.88	1.08
	lap_b	47.7	12.6	13.2				
mss_092	lap_a	47.6	11.9	13.2	1 095	16.6	0.96	1.26
	lap_b	47.2	12.3	13.2				
mss_093	lap_a	49.0	12.6	13.2	1 141	15.3	0.90	1.16
	lap_b	50.1	13.0	13.2				
mss_088	lap_a	49.0	12.7	13.2	1 170	14.3	0.92	1.08
	lap_b	48.9	13.3	13.2				
mss_089	lap_a	46.2	13.0	13.2	1 044	13.9	0.85	1.06
	lap_b	47.6	13.2	13.2				
mss_090	lap_a	49.7	12.9	13.2	1 046	14.6	0.83	1.10
	lap_b	48.4	12.9	13.2				
mss_085	lap_a	48.9	12.7	13.3	1 138	15.3	0.92	1.15
	lap_b	49.0	12.5	13.3				
mss_086	lap_a	49.6	13.0	13.3	1 301	15.4	1.00	1.16
	lap_b	50.3	13.0	13.3				
mss_087	lap_a	47.4	12.8	13.2	1 200	16.5	0.99	1.25
	lap_b	47.8	12.6	13.2				
Mean value		48.4	12.8	13.2	1 132	15.1	0.92	1.14
Standard deviation		1.1	0.3	0.0	85	1.0	0.06	0.07

Failure patterns from the double-lap shear tests on specimens with *Sikasil SG-550*, stainless steel substrates and smaller joint geometry:

- stainless steel - untreated

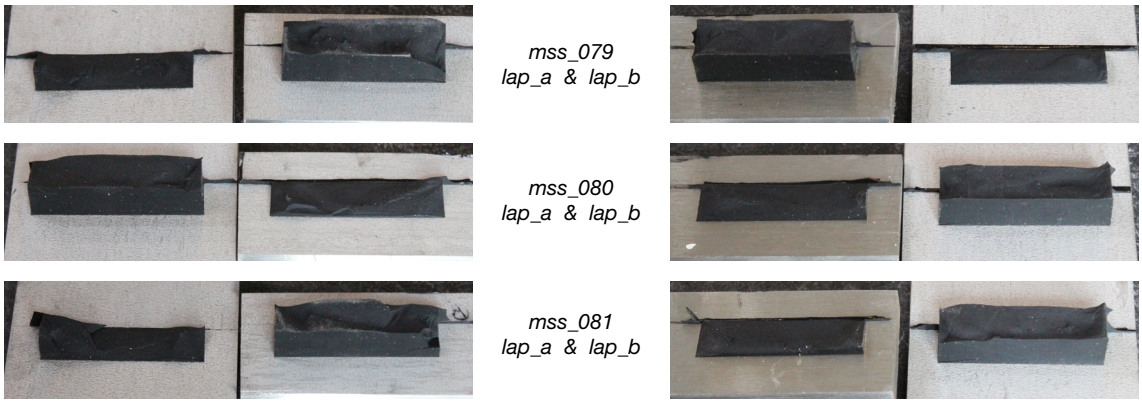

mss_079 lap_a & lap_b

mss_080 lap_a & lap_b

mss_081 lap_a & lap_b

- stainless steel - grinded P50

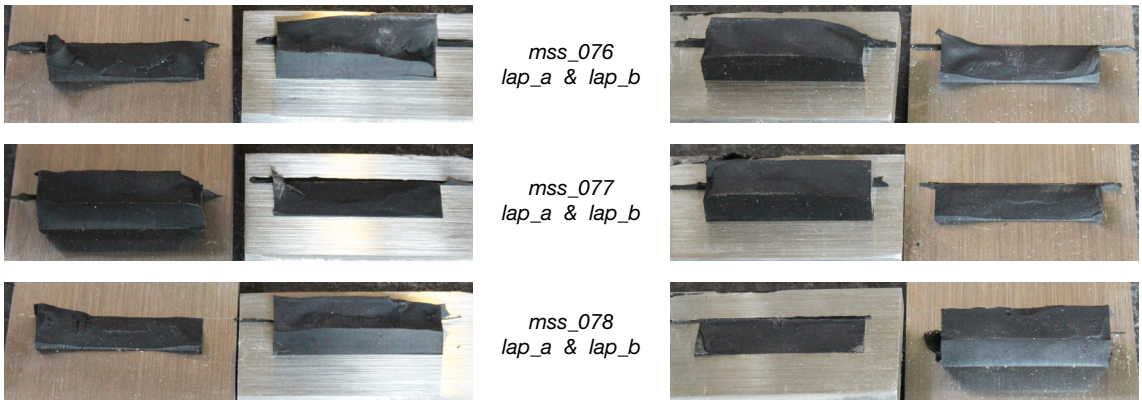

mss_076 lap_a & lap_b

mss_077 lap_a & lap_b

mss_078 lap_a & lap_b

- stainless steel - grinded P80

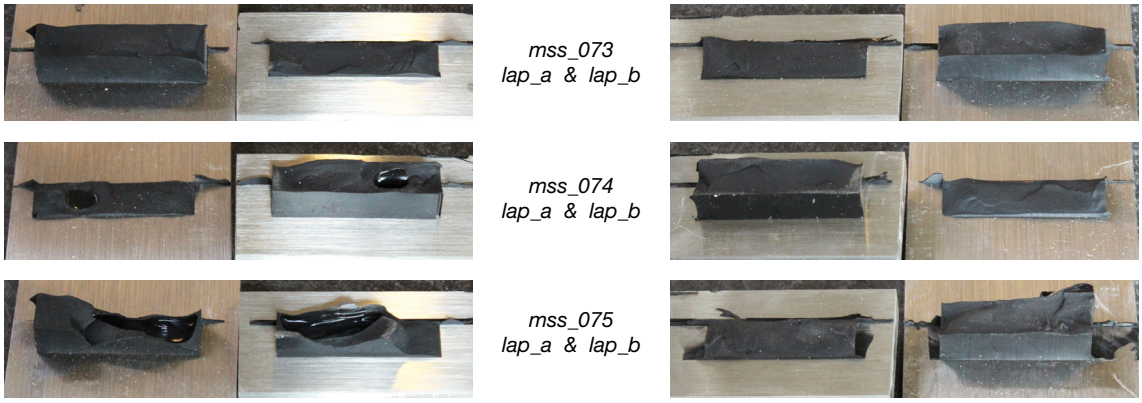

mss_073 lap_a & lap_b

mss_074 lap_a & lap_b

mss_075 lap_a & lap_b

- stainless steel - grinded P150

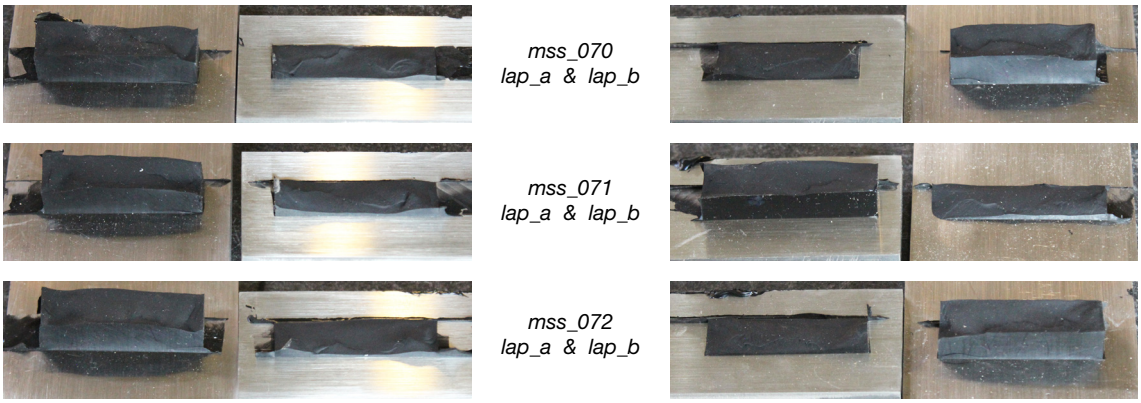

mss_070
lap_a & lap_b

mss_071
lap_a & lap_b

mss_072
lap_a & lap_b

- stainless steel - grinded P300

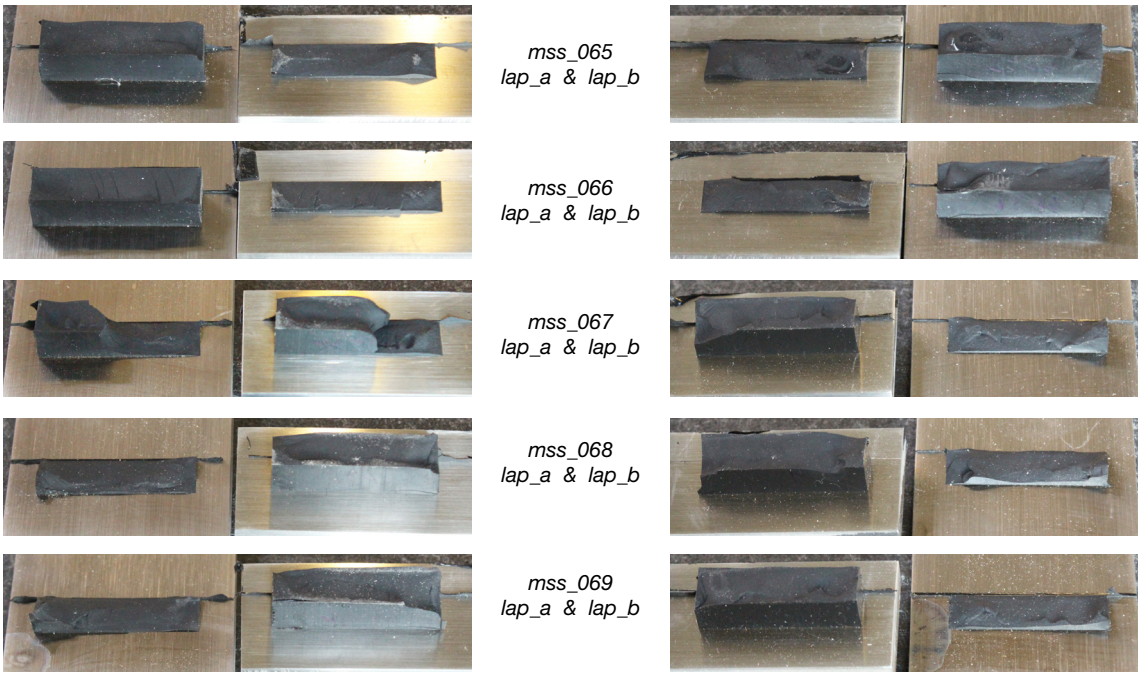

mss_065
lap_a & lap_b

mss_066
lap_a & lap_b

mss_067
lap_a & lap_b

mss_068
lap_a & lap_b

mss_069
lap_a & lap_b

Failure patterns from the double-lap shear tests on specimens with *Sikasil SG-550*, aluminium substrates and smaller joint geometry:

- aluminium - untreated

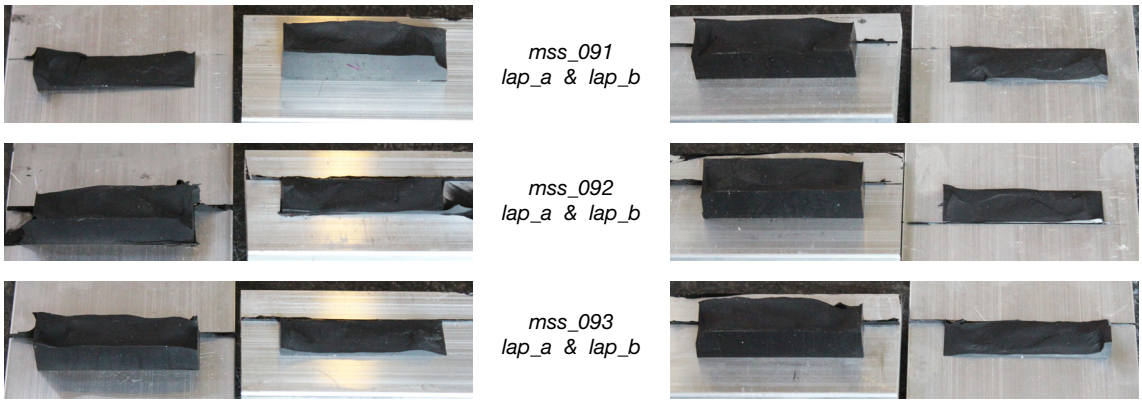

mss_091 lap_a & lap_b

mss_092 lap_a & lap_b

mss_093 lap_a & lap_b

- aluminium - powder-coated

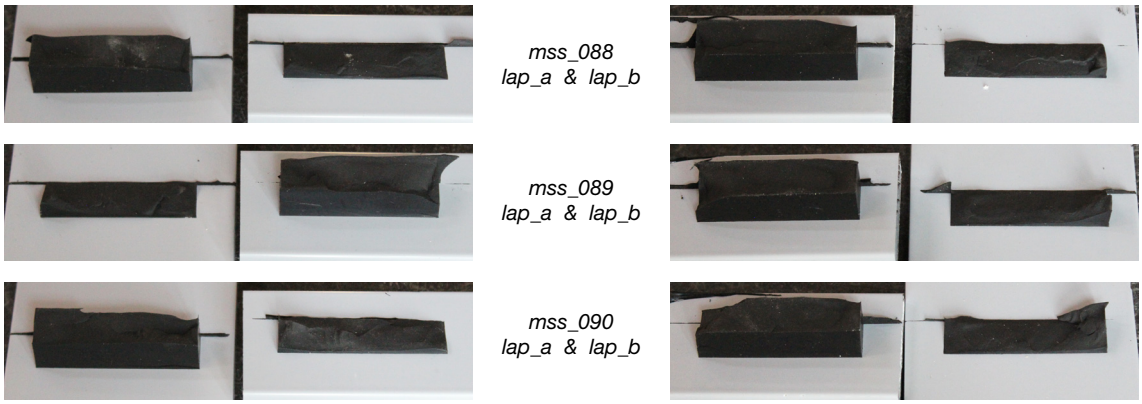

mss_088 lap_a & lap_b

mss_089 lap_a & lap_b

mss_090 lap_a & lap_b

- aluminium - anodised

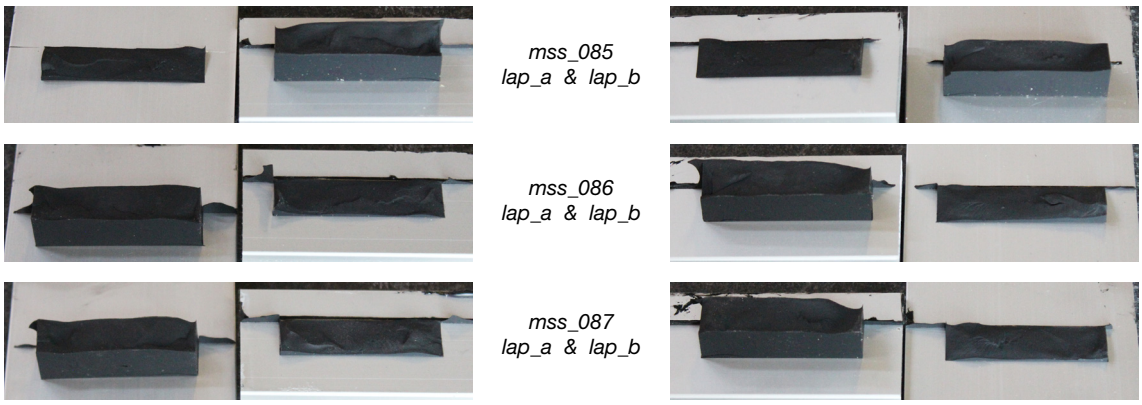

mss_085 lap_a & lap_b

mss_086 lap_a & lap_b

mss_087 lap_a & lap_b

B.4 - Sikasil SG-550 - adhesive joint dimensions: 50 mm x 60 mm x 12 mm

Shear stress *vs.* shear displacement diagrams from the double-lap shear tests on specimens with *Sikasil SG-550* and larger joint geometry:

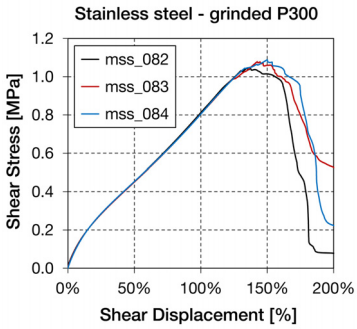

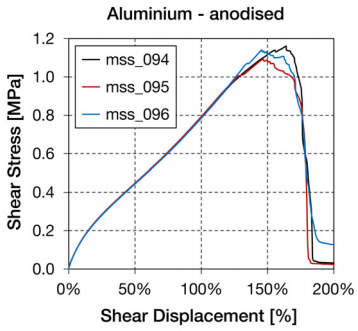

Real joint dimensions and test results for the double-lap shear specimens with *Sikasil SG-550* and larger joint geometry:

Specimen		Joint dimensions			Max. load [N]	Corr. displ. [mm]	Max. shear stress [MPa]	Corr. shear displ. [-]
		length l [mm]	width w [mm]	thickness t [mm]				
mss_082	lap_a	51.2	55.7	12.7	6 100	17.2	1.05	1.35
	lap_b	50.8	58.6	12.7				
mss_083	lap_a	50.5	56.6	12.8	6 289	18.3	1.08	1.43
	lap_b	51.0	58.3	12.8				
mss_084	lap_a	50.6	58.9	12.6	6 500	18.9	1.09	1.50
	lap_b	50.6	59.1	12.6				
mss_094	lap_a	50.9	59.0	12.6	6 964	20.7	1.16	1.64
	lap_b	50.8	59.0	12.7				
mss_095	lap_a	50.9	56.6	12.7	6 329	18.7	1.09	1.47
	lap_b	50.7	57.4	12.7				
mss_096	lap_a	51.0	58.0	12.7	6 796	18.5	1.14	1.46
	lap_b	51.0	58.8	12.8				
Mean value		50.8	58.0	12.7	6 496	18.7	1.10	1.48
Standard deviation		0.2	1.2	0.1	328	1.1	0.04	0.10

Failure patterns from the double-lap shear tests on specimens with *Sikasil SG-550* and larger joint geometry:

- stainless steel - grinded P300

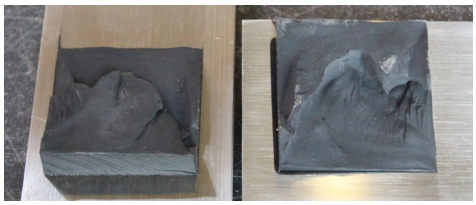
mss_082
lap_a & lap_b
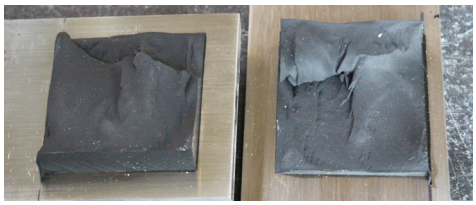

mss_083
lap_a & lap_b
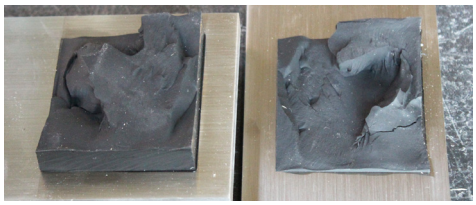

mss_084
lap_a & lap_b
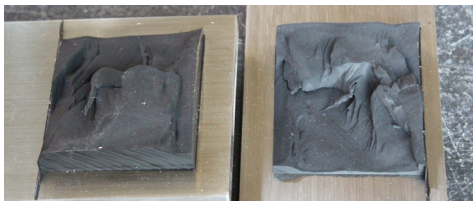

- aluminium - anodised

mss_094
lap_a & lap_b
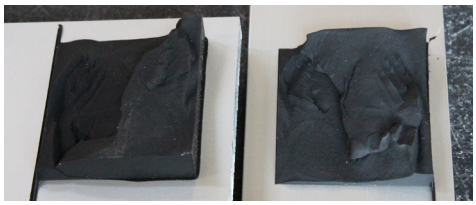

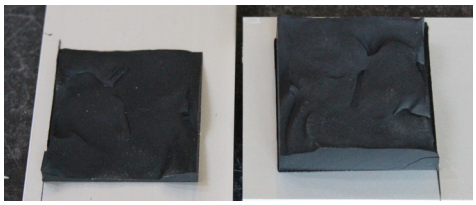
mss_095
lap_a & lap_b
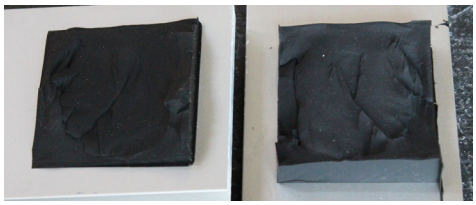

mss_096
lap_a & lap_b
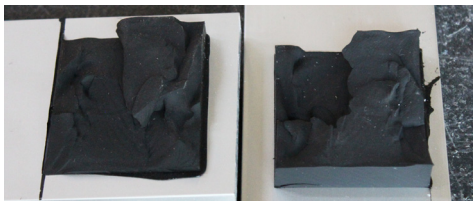

B.5 - SikaFast-5221 NT - adhesive joint dimensions: 50 mm x 12 mm x 3 mm

Shear stress *vs.* shear displacement diagrams from the double-lap shear tests on specimens with *SikaFast-5221 NT*, stainless steel substrates and smaller joint geometry:

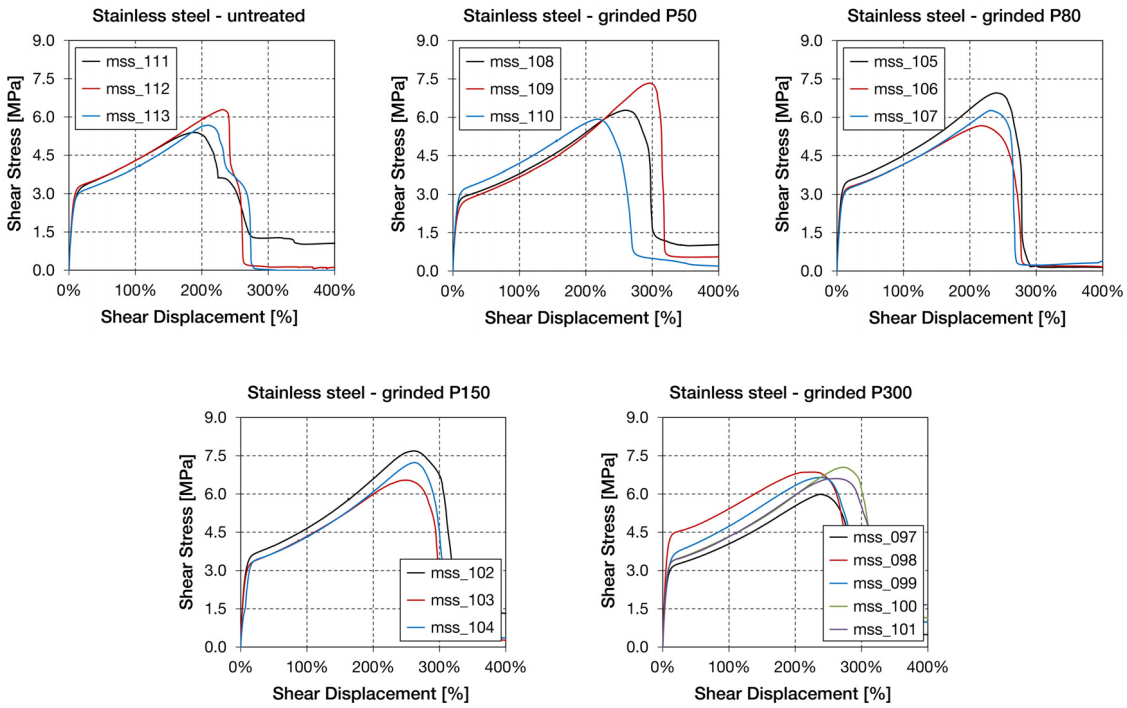

Shear stress *vs.* shear displacement diagrams from the double-lap shear tests on specimens with *SikaFast-5221 NT*, aluminium substrates and smaller joint geometry:

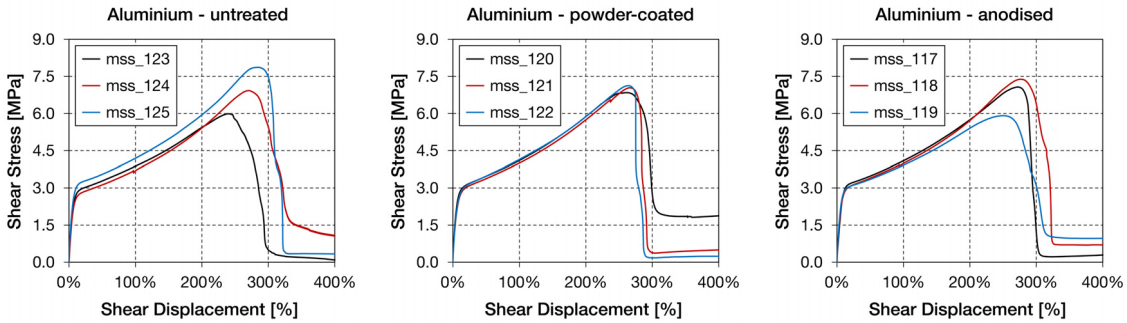

Real joint dimensions and test results for the double-lap shear specimens with *SikaFast-5221 NT*, stainless steel substrates and smaller joint geometry:

Specimen		Joint dimensions			Max. load [N]	Corr. displ. [mm]	Max. shear stress [MPa]	Corr. shear displ. [-]
		length l [mm]	**width** w [mm]	**thickness** t [mm]				
mss_111	lap_a	50.7	13.5	3.1	7 166	5.8	5.40	1.87
	lap_b	50.3	12.8	3.1				
mss_112	lap_a	48.9	12.9	3.1	7 890	7.2	6.28	2.31
	lap_b	48.8	12.8	3.1				
mss_113	lap_a	48.8	13.2	3.1	7 354	6.5	5.68	2.08
	lap_b	49.0	13.3	3.1				
mss_108	lap_a	49.4	13.4	3.1	8 465	8.1	6.28	2.60
	lap_b	50.5	13.6	3.1				
mss_109	lap_a	48.9	13.2	3.1	9 778	9.2	7.34	2.96
	lap_b	49.4	13.9	3.1				
mss_110	lap_a	50.3	12.9	3.1	7 638	6.8	5.93	2.18
	lap_b	49.2	13.0	3.1				
mss_105	lap_a	51.2	13.2	3.1	9 425	7.4	6.95	2.40
	lap_b	51.9	13.1	3.1				
mss_106	lap_a	47.7	13.8	3.1	7 255	6.7	5.67	2.17
	lap_b	48.5	12.8	3.1				
mss_107	lap_a	48.0	12.7	3.1	7 810	7.1	6.27	2.31
	lap_b	48.2	13.2	3.1				
mss_102	lap_a	47.1	13.5	3.1	9 606	8.1	7.69	2.61
	lap_b	46.8	13.1	3.1				
mss_103	lap_a	48.9	11.8	3.1	7 840	7.7	6.54	2.48
	lap_b	50.5	12.3	3.1				
mss_104	lap_a	47.5	12.9	3.1	8 872	8.1	7.23	2.62
	lap_b	46.5	13.2	3.1				
mss_097	lap_a	48.4	12.7	3.1	7 707	7.4	5.99	2.38
	lap_b	48.7	13.8	3.1				
mss_098	lap_a	47.9	13.5	3.1	8 731	7.0	6.86	2.27
	lap_b	47.1	13.3	3.1				
mss_099	lap_a	47.0	13.6	3.1	8 363	7.3	6.65	2.35
	lap_b	46.9	13.2	3.1				
mss_100	lap_a	46.9	13.5	3.1	9 038	8.5	7.05	2.73
	lap_b	47.4	13.7	3.1				
mss_101	lap_a	49.1	13.6	3.1	8 667	8.1	6.61	2.62
	lap_b	48.8	13.2	3.1				
Mean value		48.7	13.2	3.1	8 330	7.5	6.50	2.41
Standard deviation		1.4	0.4	0.0	831	0.8	0.64	0.27

Real joint dimensions and test results for the double-lap shear specimens with *SikaFast-5221 NT*, aluminium substrates and smaller joint geometry:

Specimen		**Joint dimensions**			**Max. load** [N]	**Corr. displ.** [mm]	**Max. shear stress** [MPa]	**Corr. shear displ.** [-]
		length l [mm]	**width** w [mm]	**thickness** t [mm]				
mss_123	lap_a	49.7	12.7	3.1	7 687	7.4	5.99	2.39
	lap_b	49.8	13.1	3.1				
mss_124	lap_a	50.4	13.9	3.1	9 712	8.4	6.93	2.70
	lap_b	50.1	14.0	3.1				
mss_125	lap_a	47.3	13.3	3.1	9 992	8.8	7.87	2.84
	lap_b	48.9	13.1	3.1				
mss_120	lap_a	48.4	12.8	3.1	8 740	8.1	6.85	2.60
	lap_b	49.4	13.3	3.1				
mss_121	lap_a	50.4	13.9	3.1	9 619	8.2	7.04	2.66
	lap_b	50.4	13.2	3.1				
mss_122	lap_a	49.1	13.1	3.1	9 269	8.2	7.13	2.64
	lap_b	48.7	13.5	3.1				
mss_117	lap_a	44.8	13.6	3.1	8 818	8.4	7.08	2.72
	lap_b	47.2	13.5	3.1				
mss_118	lap_a	48.9	13.8	3.1	9 789	8.5	7.39	2.75
	lap_b	48.9	13.3	3.1				
mss_119	lap_a	50.6	14.1	3.1	8 291	7.7	5.92	2.50
	lap_b	49.5	13.9	3.1				
Mean value		49.0	13.4	3.1	9 102	8.2	6.91	2.64
Standard deviation		1.4	0.4	0.0	775	0.4	0.62	0.14

Failure patterns from the double-lap shear tests on specimens with *SikaFast-5221 NT*, stainless steel substrates and smaller joint geometry:

- stainless steel - untreated

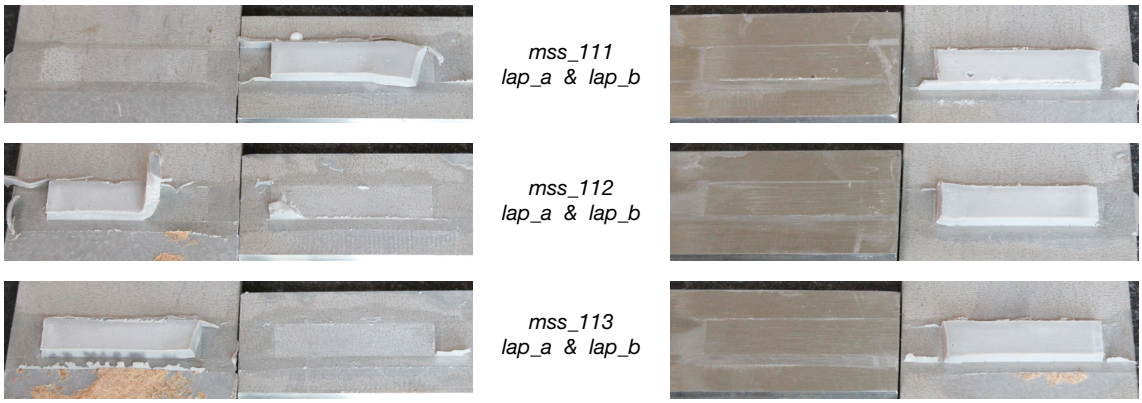

mss_111 lap_a & lap_b

mss_112 lap_a & lap_b

mss_113 lap_a & lap_b

- stainless steel - grinded P50

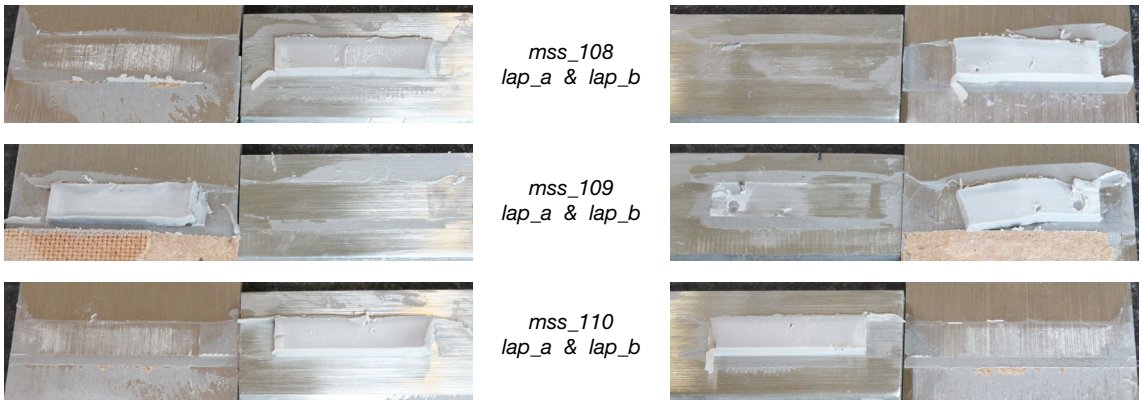

mss_108 lap_a & lap_b

mss_109 lap_a & lap_b

mss_110 lap_a & lap_b

- stainless steel - grinded P80

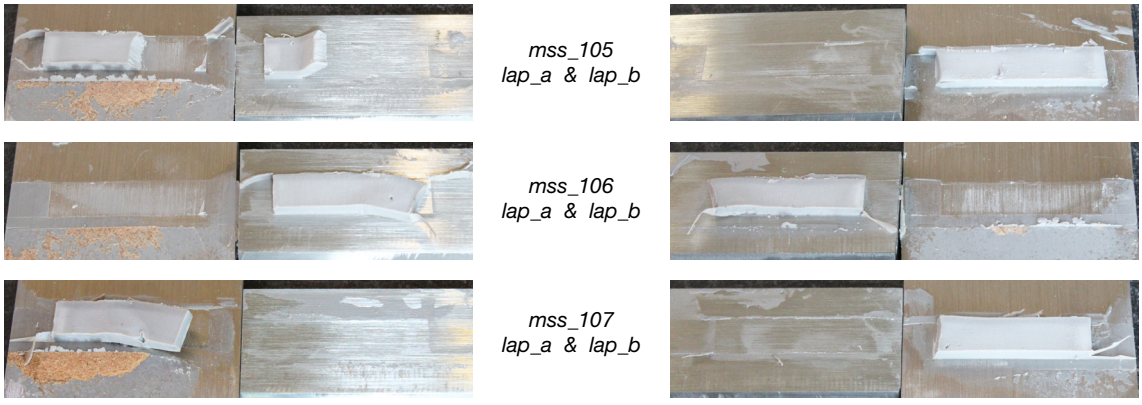

mss_105 lap_a & lap_b

mss_106 lap_a & lap_b

mss_107 lap_a & lap_b

- stainless steel - grinded P150

mss_102
lap_a & lap_b

mss_103
lap_a & lap_b

mss_104
lap_a & lap_b

- stainless steel - grinded P300

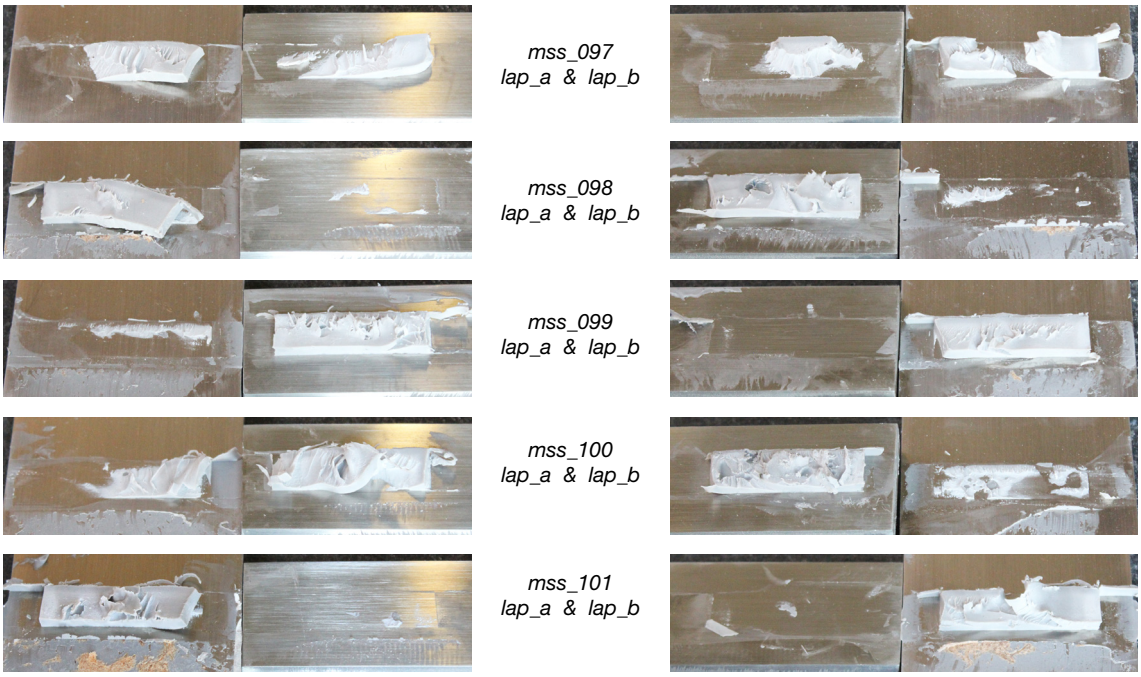

mss_097
lap_a & lap_b

mss_098
lap_a & lap_b

mss_099
lap_a & lap_b

mss_100
lap_a & lap_b

mss_101
lap_a & lap_b

Failure patterns from the double-lap shear tests on specimens with *SikaFast-5221 NT*, aluminium substrates and smaller joint geometry:

- aluminium - untreated

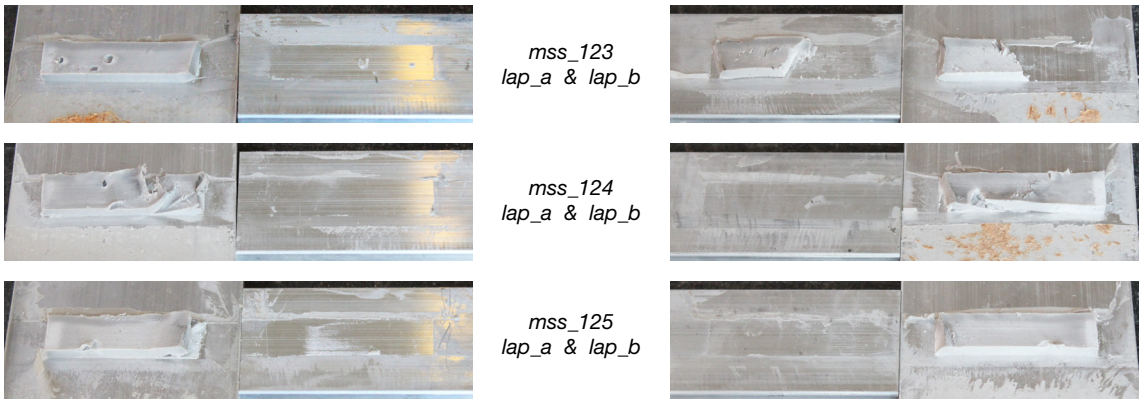

mss_123 lap_a & lap_b

mss_124 lap_a & lap_b

mss_125 lap_a & lap_b

- aluminium - powder-coated

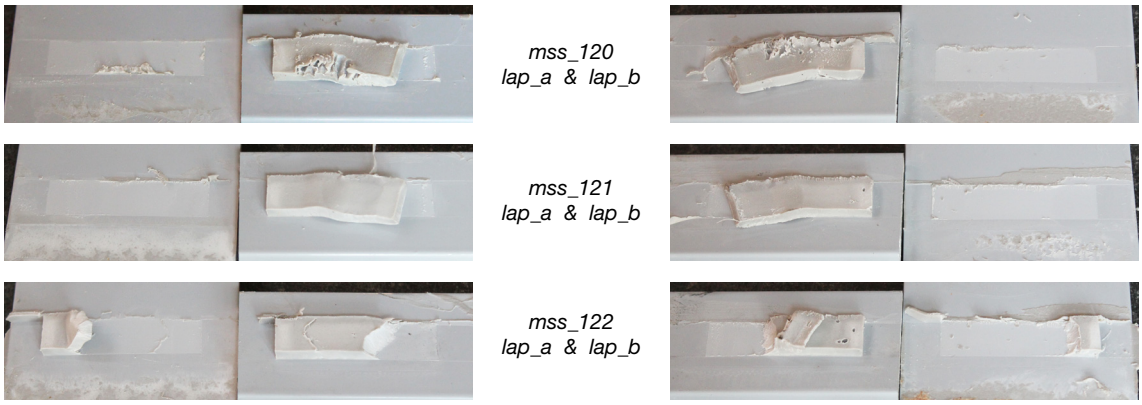

mss_120 lap_a & lap_b

mss_121 lap_a & lap_b

mss_122 lap_a & lap_b

- aluminium - anodised

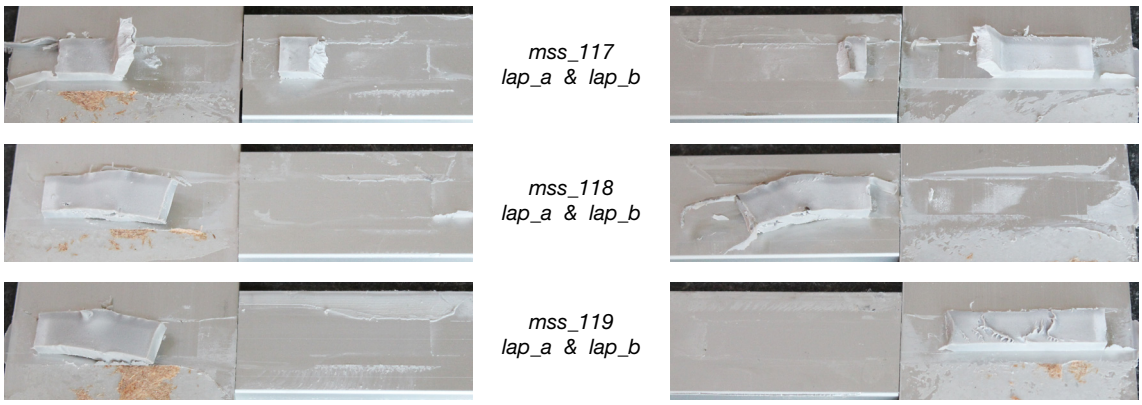

mss_117 lap_a & lap_b

mss_118 lap_a & lap_b

mss_119 lap_a & lap_b

B.6 - SikaFast-5221 NT - adhesive joint dimensions: 50 mm x 60 mm x 3 mm

Shear stress *vs.* shear displacement diagrams from the double-lap shear tests on specimens with *SikaFast-5221 NT* and larger joint geometry:

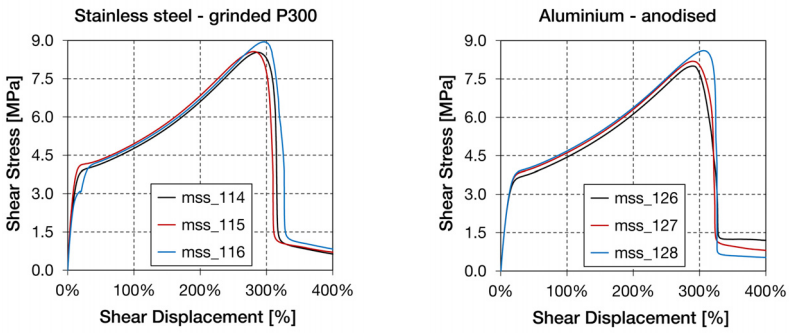

Real joint dimensions and test results for the double-lap shear specimens with *SikaFast-5221 NT* and larger joint geometry:

Specimen		Joint dimensions			Max. load [N]	Corr. displ. [mm]	Max. shear stress [MPa]	Corr. shear displ. [-]
		length l [mm]	**width** w [mm]	**thickness** t [mm]				
mss_114	lap_a	51.8	57.3	3.1	50 710	8.9	8.54	2.86
	lap_b	50.9	58.4	3.1				
mss_115	lap_a	50.9	58.9	3.1	50 158	8.7	8.56	2.80
	lap_b	50.6	56.5	3.1				
mss_116	lap_a	50.9	58.3	3.1	53 086	9.2	8.94	2.96
	lap_b	51.0	58.2	3.1				
mss_126	lap_a	50.5	56.7	3.1	46 518	9.0	8.00	2.90
	lap_b	51.1	57.7	3.1				
mss_127	lap_a	50.4	57.1	3.1	48 978	9.0	8.19	2.89
	lap_b	50.6	61.3	3.1				
mss_128	lap_a	50.1	61.5	3.1	51 327	9.5	8.61	3.06
	lap_b	50.3	57.3	3.1				
Mean value		50.8	58.3	3.1	50 130	9.1	8.47	2.91
Standard deviation		0.5	1.6	0.0	2 231	0.3	0.33	0.09

Failure patterns from the double-lap shear tests on specimens with *SikaFast-5221 NT* and larger joint geometry:

- stainless steel - grinded P300

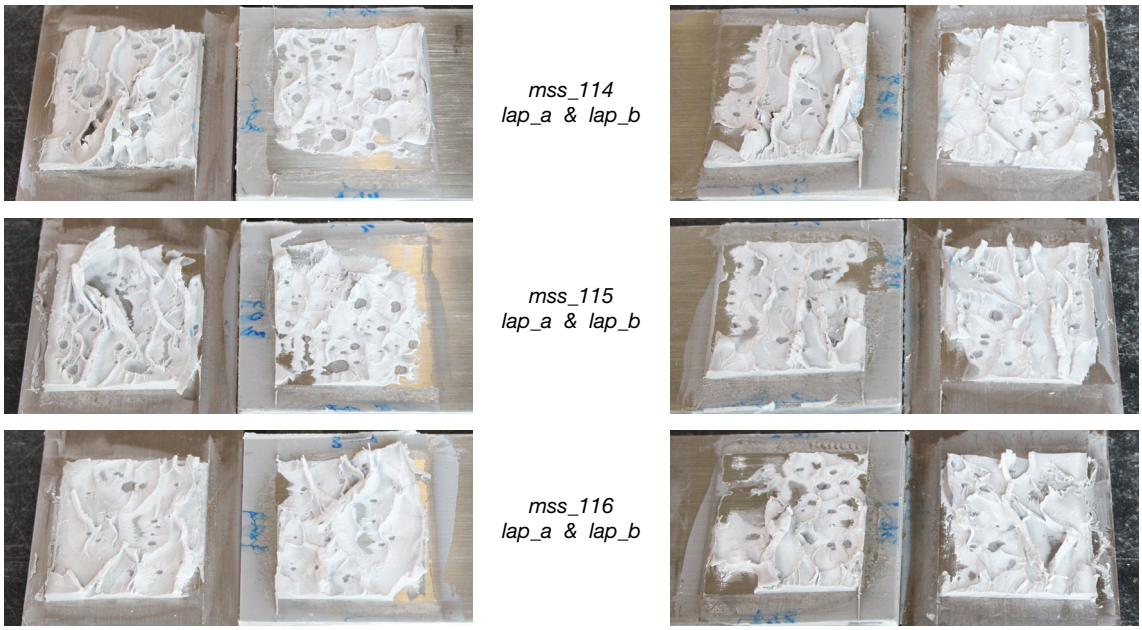

mss_114
lap_a & lap_b

mss_115
lap_a & lap_b

mss_116
lap_a & lap_b

- aluminium - anodised

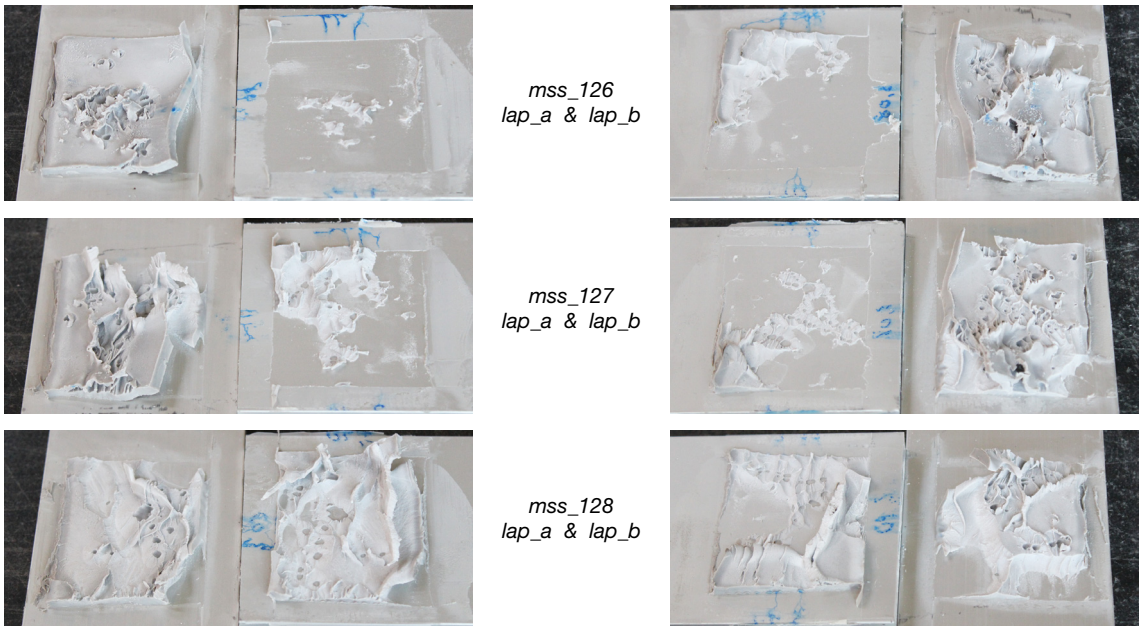

mss_126
lap_a & lap_b

mss_127
lap_a & lap_b

mss_128
lap_a & lap_b

Appendix C

Test results for linear adhesive joints at the glass surface

Engineering stress *vs.* engineering strain diagrams for the tensile tests
Shear stress *vs.* shear displacement diagrams for the shear tests
Real cross section dimensions of the test specimens
Mechanical values determined from the measured data
Failure patterns of the tensile and shear test specimens

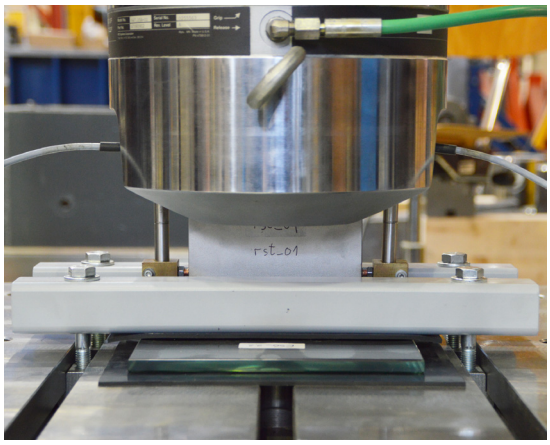

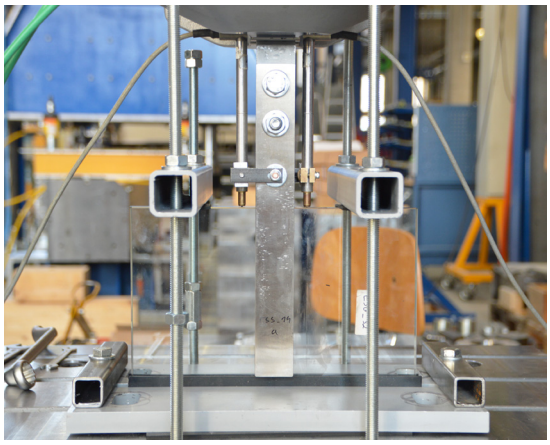

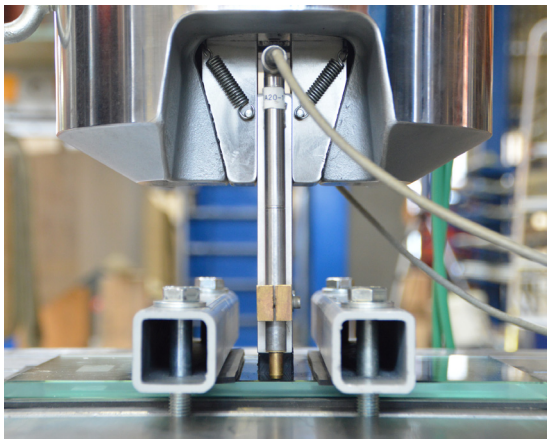

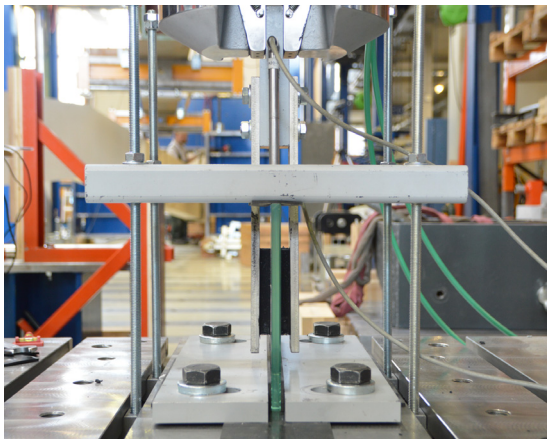

C.1 - Adhesive joints at the glass surface under tensile loading with Dow Corning 993

Engineering stress *vs.* engineering strain diagrams from the tensile tests on linear adhesive joints between glass and stainless steel substrates at the glass surface with *Dow Corning 993*:

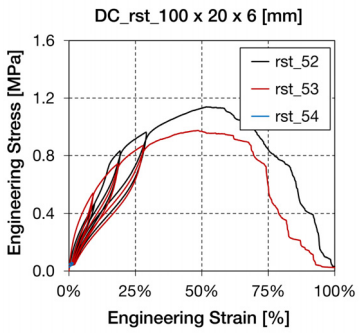

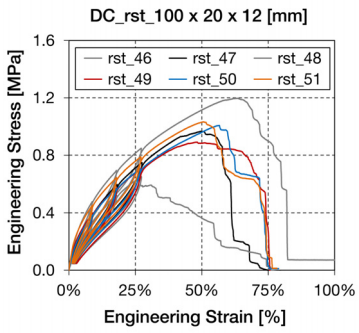

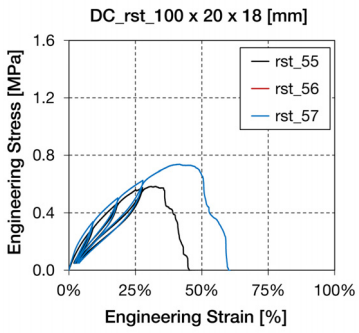

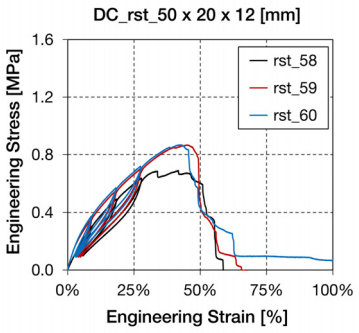

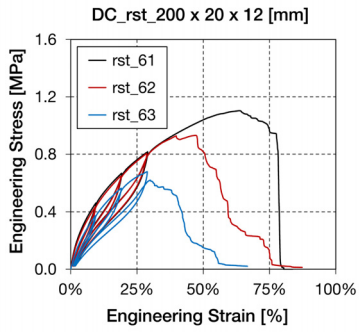

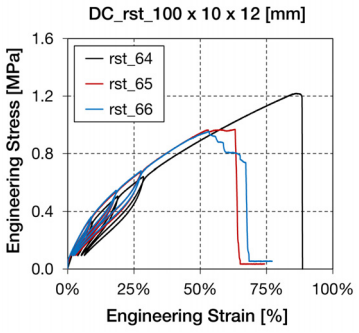

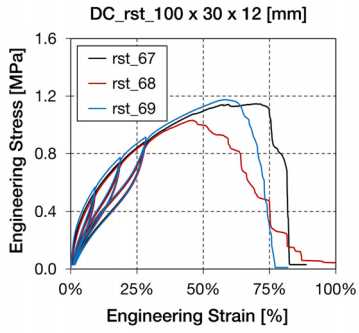

Real joint dimensions and test results from the tensile tests on linear adhesive joints between glass and stainless steel substrates at the glass surface with *Dow Corning 993*:

Specimen	Joint dimensions			Max. load [N]	Corr. displ. [mm]	Max. eng. stress [MPa]	Corr. eng. strain [-]
	length l [mm]	width w [mm]	thickness t [mm]				
target	100.0	20.0	12.0				
rst_46 *	101.1	20.2	12.8	2 445	8.1	1.20	0.63
rst_47	102.0	20.4	12.8	2 010	6.3	0.97	0.49
rst_48 *	101.5	20.7	12.9	1 370	3.5	0.65	0.27
rst_49	101.6	20.2	12.9	1 829	6.2	0.89	0.48
rst_50	97.7	19.7	13.1	1 939	7.4	1.01	0.57
rst_51	97.2	20.3	13.0	2 038	6.6	1.03	0.51
Mean value	99.6	20.2	13.0	1 954	6.6	0.98	0.51
Std. deviation	2.5	0.3	0.1	93	0.5	0.06	0.04
target	100.0	20.0	6.0				
rst_52	101.4	21.3	6.0	2 461	3.1	1.14	0.52
rst_53	98.9	20.8	6.2	2 006	3.0	0.98	0.48
rst_54 **	101.2	20.2	6.2	-	-	-	-
Mean value	100.5	20.8	6.1	2 234	3.1	1.06	0.50
Std. deviation	1.4	0.6	0.1	322	0.1	0.11	0.03
target	100.0	20.0	18.0				
rst_55	101.2	19.9	19.3	1 178	6.3	0.59	0.33
rst_56 **	101.0	20.2	18.8	-	-	-	-
rst_57	100.9	20.1	19.3	1 494	8.0	0.74	0.41
Mean value	101.0	20.1	19.1	1 336	7.2	0.67	0.37
Std. deviation	0.2	0.2	0.3	223	1.2	0.11	0.06
target	50.0	20.0	12.0				
rst_58	50.8	19.9	12.8	697	5.3	0.69	0.42
rst_59	51.6	20.9	12.8	935	5.8	0.87	0.45
rst_60	49.9	21.2	12.8	918	5.4	0.87	0.42
Mean value	50.8	20.7	12.8	850	5.5	0.81	0.43
Std. deviation	0.9	0.7	0.0	133	0.3	0.10	0.02

Specimen	Joint dimensions			Max. load [N]	Corr. displ. [mm]	Max. eng. stress [MPa]	Corr. eng. strain [-]
	length l [mm]	**width** w [mm]	**thickness** t [mm]				
target	200.0	20.0	12.0				
rst_61	202.0	20.7	12.2	4 614	7.8	1.10	0.64
rst_62	199.5	20.4	12.2	3 791	5.7	0.93	0.47
rst_63	199.0	20.3	12.2	2 749	3.5	0.68	0.29
Mean value	200.2	20.5	12.2	3 718	5.7	0.90	0.47
Std. deviation	1.6	0.2	0.0	935	2.2	0.21	0.18
target	100.0	10.0	12.0				
rst_64	101.7	10.2	12.4	1 264	10.6	1.22	0.86
rst_65	100.6	10.2	12.8	994	8.0	0.97	0.63
rst_66	101.0	10.2	12.7	984	6.7	0.96	0.53
Mean value	101.1	10.2	12.6	1 081	8.4	1.05	0.67
Std. deviation	0.6	0.0	0.2	159	2.0	0.15	0.17
target	100.0	30.0	12.0				
rst_67	101.7	29.8	12.6	3 475	8.8	1.15	0.70
rst_68	102.0	29.5	12.5	3 107	5.7	1.03	0.46
rst_69	101.2	29.7	12.4	3 534	7.2	1.18	0.58
Mean value	101.6	29.7	12.5	3 372	7.2	1.12	0.58
Std. deviation	0.4	0.2	0.1	231	1.6	0.08	0.12

Specimen	Eng. stress at 5% strain [MPa]		Eng. stress at 15% strain [MPa]		Eng. stress at 25% strain [MPa]	
	1st cycle	**2nd cycle**	**1st cycle**	**2nd cycle**	**1st cycle**	**2nd cycle**
rst_46 *	0.35	0.29	0.63	0.55	0.81	0.73
rst_47	0.27	0.20	0.54	0.45	0.71	0.62
rst_48 *	0.22	0.17	0.47	0.39	0.63	0.54
rst_49	0.29	0.21	0.52	0.43	0.68	0.59
rst_50	0.28	0.21	0.52	0.44	0.68	0.61
rst_51	0.34	0.25	0.59	0.49	0.76	0.66
Mean value	0.30	0.22	0.54	0.45	0.71	0.62
Std. deviation	0.03	0.02	0.03	0.03	0.04	0.03

Specimen	Eng. stress at 5% strain [MPa]		Eng. stress at 15% strain [MPa]		Eng. stress at 25% strain [MPa]	
	1st cycle	2nd cycle	1st cycle	2nd cycle	1st cycle	2nd cycle
rst_52	0.31	0.29	0.73	0.58	0.92	0.73
rst_53	0.40	0.28	0.69	0.54	0.84	0.70
rst_54 **	-	-	-	-	-	-
Mean value	0.36	0.29	0.71	0.56	0.88	0.72
Std. deviation	0.06	0.01	0.03	0.03	0.06	0.02
rst_55	0.20	0.15	0.41	0.35	0.56	0.47
rst_56 **	-	-	-	-	-	-
rst_57	0.23	0.16	0.45	0.36	0.59	0.50
Mean value	0.22	0.16	0.43	0.36	0.58	0.49
Std. deviation	0.02	0.01	0.03	0.01	0.02	0.02
rst_58	0.19	0.14	0.43	0.36	0.60	0.51
rst_59	0.25	0.17	0.49	0.41	0.67	0.57
rst_60	0.26	0.20	0.51	0.43	0.68	0.60
Mean value	0.23	0.17	0.48	0.40	0.65	0.56
Std. deviation	0.04	0.03	0.04	0.04	0.04	0.05
rst_61	0.32	0.24	0.59	0.48	0.76	0.63
rst_62	0.30	0.23	0.57	0.47	0.75	0.63
rst_63	0.25	0.19	0.50	0.40	0.64	0.51
Mean value	0.29	0.22	0.55	0.45	0.72	0.59
Std. deviation	0.04	0.03	0.05	0.04	0.07	0.07
rst_64	0.22	0.14	0.44	0.35	0.59	0.49
rst_65	0.25	0.20	0.48	0.41	0.64	0.57
rst_66	0.25	0.22	0.49	0.42	0.65	0.57
Mean value	0.24	0.19	0.47	0.39	0.63	0.54
Std. deviation	0.02	0.04	0.03	0.04	0.03	0.05

Specimen	Eng. stress at 5% strain [MPa]		Eng. stress at 15% strain [MPa]		Eng. stress at 25% strain [MPa]	
	1st cycle	2nd cycle	1st cycle	2nd cycle	1st cycle	2nd cycle
rst_67	0.40	0.30	0.67	0.56	0.84	0.73
rst_68	0.37	0.28	0.66	0.54	0.83	0.71
rst_69	0.43	0.31	0.71	0.57	0.87	0.73
Mean value	0.40	0.30	0.68	0.56	0.85	0.72
Std. deviation	0.03	0.02	0.03	0.02	0.02	0.01

Notes:

* These specimens are not considered in the calculation of the mean values.

** No measurement data from testing is available for these specimens.

Failure patterns from the tensile tests on linear adhesive joints between glass and stainless steel substrates at the glass surface with *Dow Corning 993*:

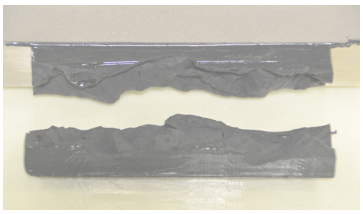

rst_46

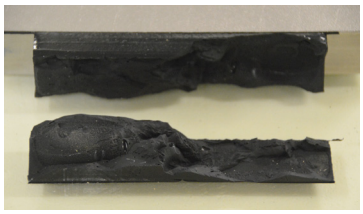

rst_47

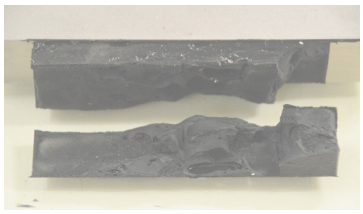

rst_48

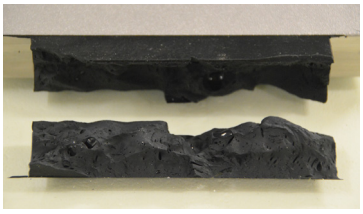

rst_49

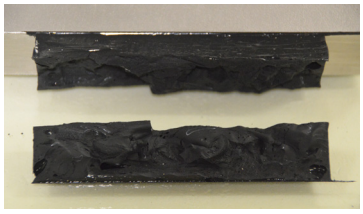

rst_50

rst_51

rst_52

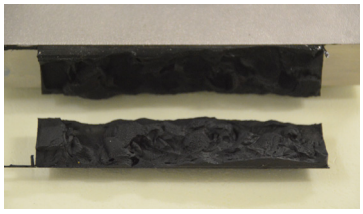

rst_53

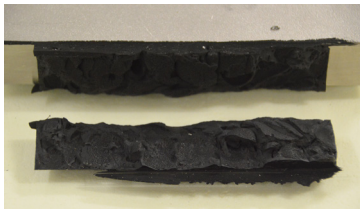

rst_54

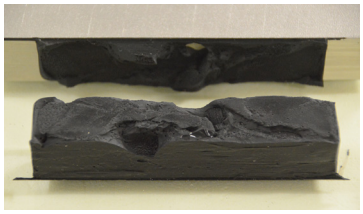

rst_55

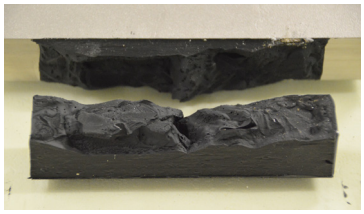

rst_56

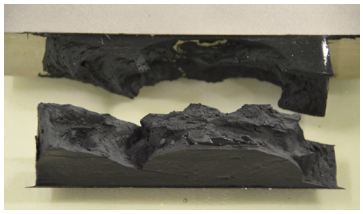

rst_57

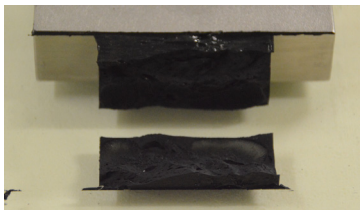

rst_58

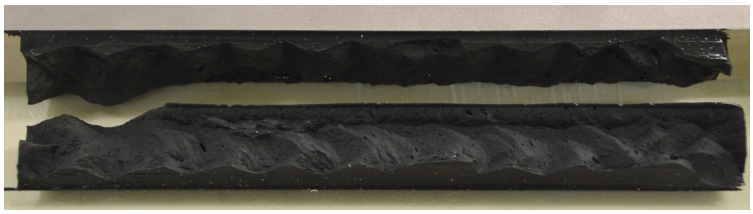

rst_61

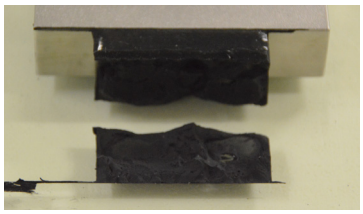

rst_59

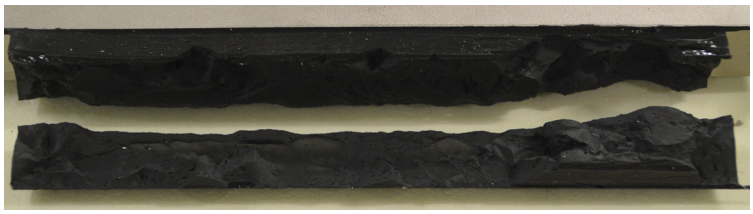

rst_62

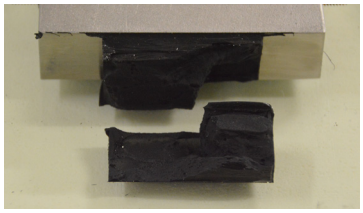

rst_60

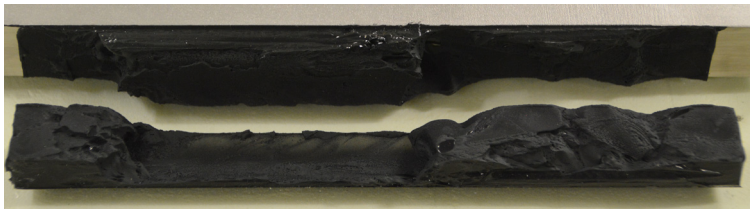

rst_63

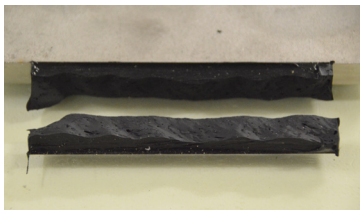

rst_64

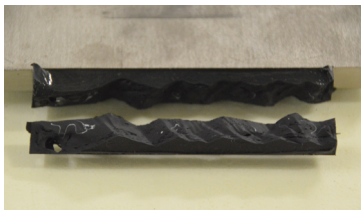

rst_65

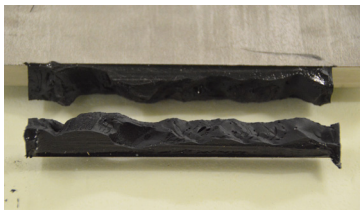

rst_66

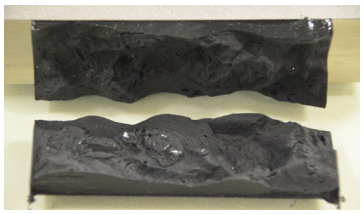

rst_67

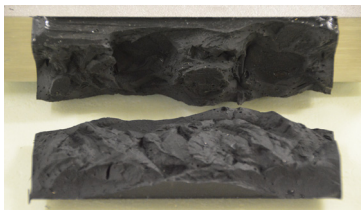

rst_68

rst_69

C.2 - Adhesive joints at the glass surface under tensile loading with Sikasil SG-550

Engineering stress *vs.* engineering strain diagrams from the tensile tests on linear adhesive joints between glass and stainless steel substrates at the glass surface with *Sikasil SG-550*:

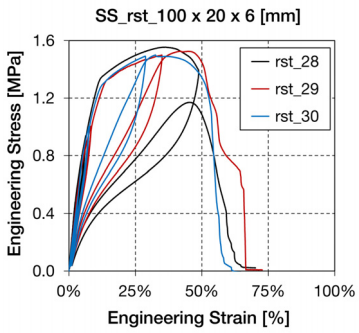

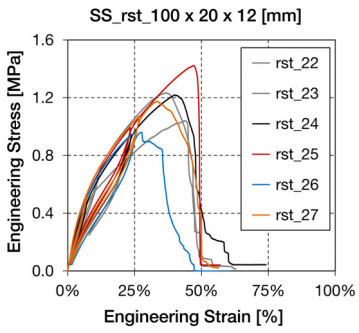

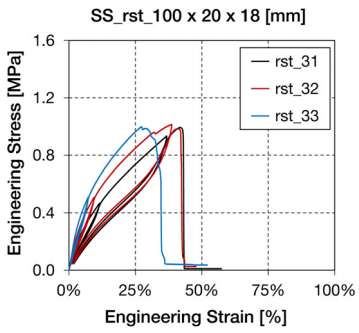

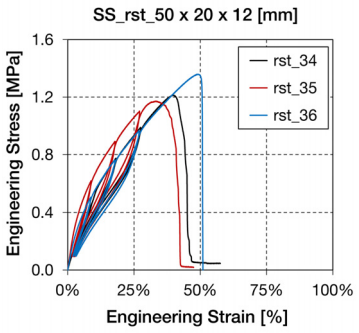

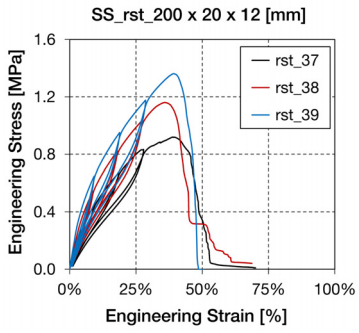

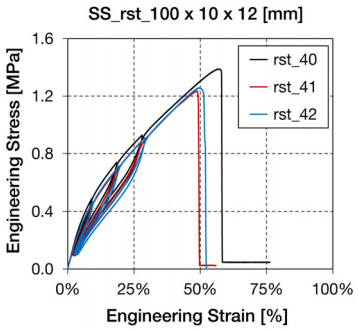

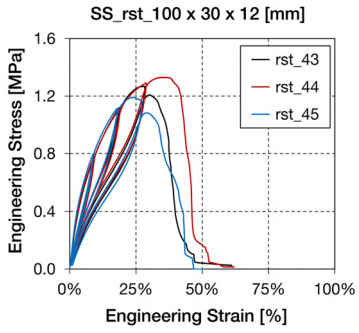

Real joint dimensions and test results from the tensile tests on linear adhesive joints between glass and stainless steel substrates at the glass surface with *Sikasil SG-550*:

Specimen	Joint dimensions			Max. load [N]	Corr. displ. [mm]	Max. eng. stress [MPa]	Corr. eng. strain [-]
	length l [mm]	width w [mm]	thickness t [mm]				
target	100.0	20.0	12.0				
rst_22 * **	100.6	19.8	12.8	2 072	5.6	1.04	0.44
rst_23 * **	100.8	20.7	12.4	2 573	4.5	1.23	0.37
rst_24 **	102.7	20.6	12.6	2 580	5.0	1.22	0.40
rst_25 **	98.7	20.4	12.9	2 865	6.1	1.42	0.47
rst_26	100.1	20.8	12.6	2 001	3.2	0.96	0.25
rst_27	100.4	18.6	12.8	2 191	4.2	1.17	0.33
Mean value	100.5	20.1	12.7	2 409	4.6	1.19	0.36
Std. deviation	1.7	1.0	0.2	388	1.2	0.19	0.09
target	100.0	20.0	6.0				
rst_28	102.4	21.0	6.0	3 342	2.1	1.55	0.36
rst_29	100.6	19.9	6.2	3 057	2.6	1.53	0.42
rst_30	101.1	19.9	6.2	3 018	2.0	1.50	0.32
Mean value	101.4	20.3	6.1	3 139	2.2	1.53	0.37
Std. deviation	0.9	0.6	0.1	177	0.3	0.03	0.05
target	100.0	20.0	18.0				
rst_31	98.8	21.7	18.8	2 130	7.9	0.99	0.42
rst_32	100.6	19.6	19.3	2 000	7.5	1.01	0.39
rst_33 **	101.1	19.4	19.3	1 957	5.3	1.00	0.27
Mean value	100.2	20.2	19.1	2 029	6.9	1.00	0.36
Std. deviation	1.2	1.3	0.3	90	1.4	0.01	0.08
target	50.0	20.0	12.0				
rst_34	49.3	20.1	12.8	1 202	5.1	1.21	0.40
rst_35	51.1	20.2	13.0	1 210	4.3	1.17	0.33
rst_36	49.3	20.3	13.1	1 360	6.4	1.36	0.49
Mean value	49.9	20.2	13.0	1 257	5.3	1.25	0.41
Std. deviation	1.0	0.1	0.2	89	1.1	0.10	0.08

Specimen	Joint dimensions			Max. load [N]	Corr. displ. [mm]	Max. eng. stress [MPa]	Corr. eng. strain [-]
	length l [mm]	**width** w [mm]	**thickness** t [mm]				
target	200.0	20.0	12.0				
rst_37	198.0	21.0	12.7	3 823	4.9	0.92	0.39
rst_38	200.0	20.2	12.8	4 690	4.6	1.16	0.36
rst_39	201.5	20.1	12.2	5 513	4.8	1.36	0.39
Mean value	199.8	20.4	12.6	4 675	4.8	1.15	0.38
Std. deviation	1.8	0.5	0.3	845	0.2	0.22	0.02
target	100.0	10.0	12.0				
rst_40	98.5	10.2	12.5	1 395	7.1	1.39	0.57
rst_41	98.6	10.5	12.8	1 280	6.2	1.24	0.49
rst_42	96.3	10.1	12.2	1 223	6.0	1.26	0.49
Mean value	97.8	10.3	12.5	1 299	6.4	1.30	0.52
Std. deviation	1.3	0.2	0.3	88	0.6	0.08	0.05
target	100.0	30.0	12.0				
rst_43	101.4	30.0	12.4	3 857	3.4	1.27	0.28
rst_44	101.6	30.2	12.2	4 081	4.3	1.33	0.35
rst_45	101.6	30.5	12.9	3 687	3.1	1.19	0.24
Mean value	101.5	30.2	12.5	3 875	3.6	1.26	0.29
Std. deviation	0.1	0.3	0.4	198	0.6	0.07	0.06

Specimen	Eng. stress at 5% strain [MPa]		Eng. stress at 15% strain [MPa]		Eng. stress at 25% strain [MPa]	
	1st cycle	**2nd cycle**	**1st cycle**	**2nd cycle**	**1st cycle**	**2nd cycle**
rst_22 * **	0.37	-	0.65	0.48	0.82	-
rst_23 * **	0.43	0.31	0.81	-	1.06	-
rst_24 **	0.38	0.32	0.74	0.56	0.97	-
rst_25 **	0.41	0.35	0.79	0.60	1.02	-
rst_26	0.41	0.35	0.76	0.52	0.96	0.90
rst_27	0.43	0.36	0.81	0.57	1.04	0.93
Mean value	0.41	0.35	0.78	0.56	1.00	0.92
Std. deviation	0.02	0.02	0.03	0.03	0.04	0.02

Specimen	Eng. stress at 5% strain [MPa]		Eng. stress at 15% strain [MPa]		Eng. stress at 25% strain [MPa]	
	1st cycle	2nd cycle	1st cycle	2nd cycle	1st cycle	2nd cycle
rst_28	0.81	0.68	1.39	0.57	1.50	0.78
rst_29	0.74	0.56	1.33	0.74	1.44	1.08
rst_30	0.78	0.60	1.34	0.89	1.46	1.31
Mean value	0.78	0.61	1.35	0.73	1.47	1.06
Std. deviation	0.04	0.06	0.03	0.16	0.03	0.27
rst_31	0.27	0.20	0.54	0.38	0.74	0.56
rst_32	0.34	0.26	0.65	0.40	0.85	0.58
rst_33 **	0.41	0.34	0.75	-	0.96	-
Mean value	0.34	0.27	0.65	0.39	0.85	0.57
Std. deviation	0.07	0.07	0.11	0.01	0.11	0.01
rst_34	0.28	0.26	0.69	0.59	0.93	0.83
rst_35	0.45	0.33	0.82	0.68	1.06	0.92
rst_36	0.36	0.27	0.69	0.59	0.93	0.82
Mean value	0.36	0.29	0.73	0.62	0.97	0.86
Std. deviation	0.09	0.04	0.08	0.05	0.08	0.06
rst_37	0.30	0.23	0.60	0.50	0.80	0.68
rst_38	0.38	0.30	0.74	0.63	0.99	0.87
rst_39	0.45	0.34	0.85	0.69	1.10	0.91
Mean value	0.38	0.29	0.73	0.61	0.96	0.82
Std. deviation	0.08	0.06	0.13	0.10	0.15	0.12
rst_40	0.33	0.27	0.66	0.56	0.87	0.76
rst_41	0.29	0.24	0.61	0.53	0.83	0.73
rst_42	0.30	0.22	0.61	0.50	0.83	0.69
Mean value	0.31	0.24	0.63	0.53	0.84	0.73
Std. deviation	0.02	0.03	0.03	0.03	0.02	0.04

Specimen	Eng. stress at 5% strain [MPa]		Eng. stress at 15% strain [MPa]		Eng. stress at 25% strain [MPa]	
	1st cycle	2nd cycle	1st cycle	2nd cycle	1st cycle	2nd cycle
rst_43	0.54	0.41	1.01	0.81	1.25	1.02
rst_44	0.55	0.41	1.00	0.80	1.25	1.05
rst_45	0.59	0.43	1.04	0.84	1.19	0.96
Mean value	0.56	0.42	1.02	0.82	1.23	1.01
Std. deviation	0.03	0.01	0.02	0.02	0.03	0.05

Notes:

* These specimens are not considered in the calculation of the mean values.

** No measurement data from testing is available or part of the data is missing for these specimens, since the load cycles are run up to a certain load instead of up to a certain strain.

Failure patterns from the tensile tests on linear adhesive joints between glass and stainless steel substrates at the glass surface with *Sikasil SG-550*:

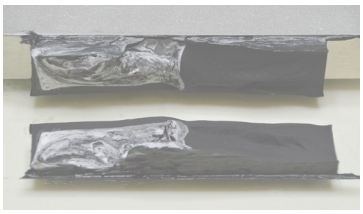

rst_22

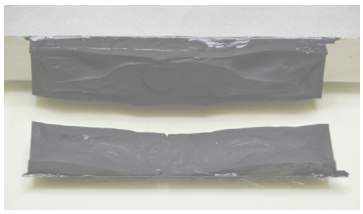

rst_23

rst_24

rst_25

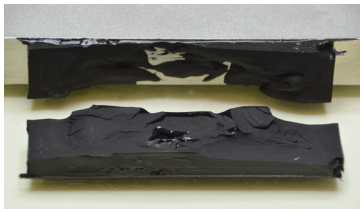

rst_26

rst_27

rst_28

rst_29

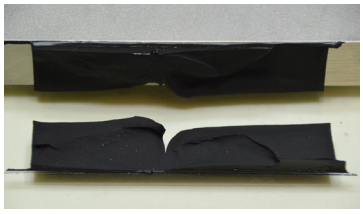

rst_30

rst_31

rst_32

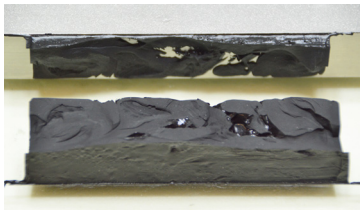

rst_33

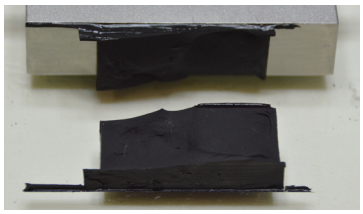

rst_34

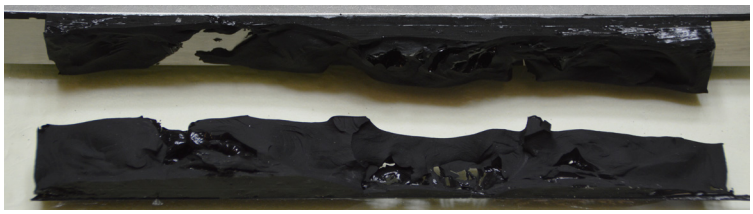

rst_37

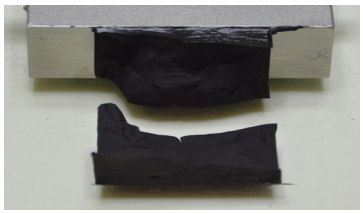

rst_35

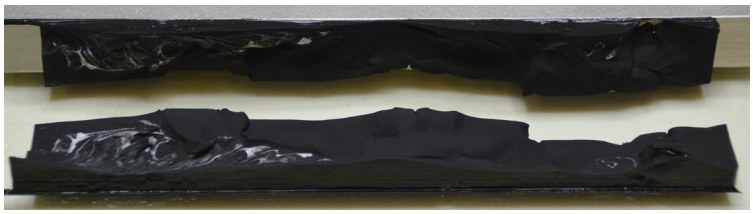

rst_38

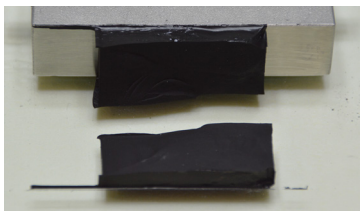

rst_36

rst_39

rst_40

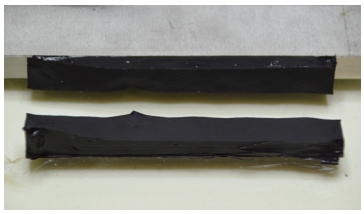

rst_41

rst_42

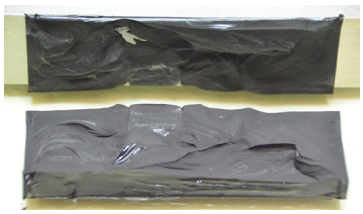

rst_43

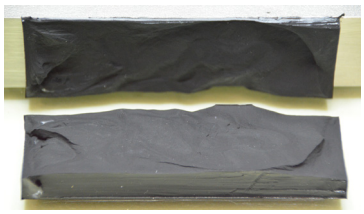

rst_44

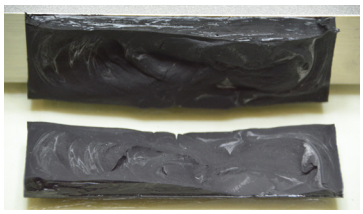

rst_45

C.3 - Adhesive joints at the glass surface under tensile loading with SikaFast-5221 NT

Engineering stress *vs.* engineering strain diagrams from the tensile tests on linear adhesive joints between glass and stainless steel substrates at the glass surface with *SikaFast-5221 NT*:

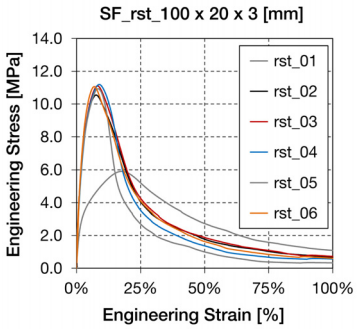

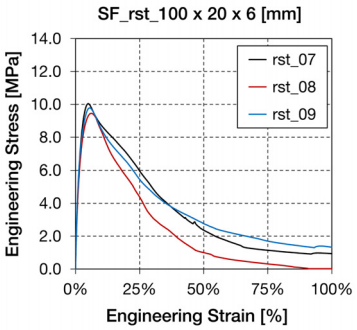

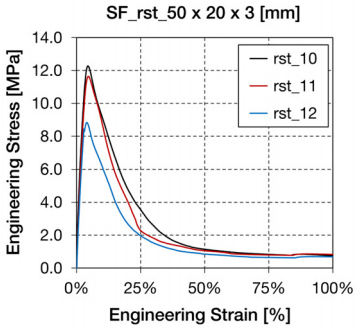

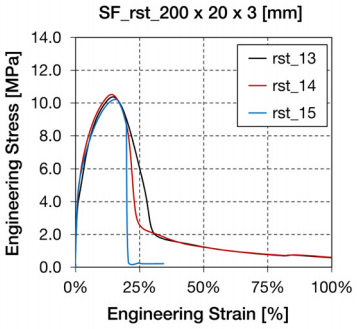

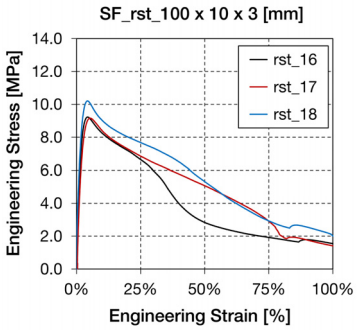

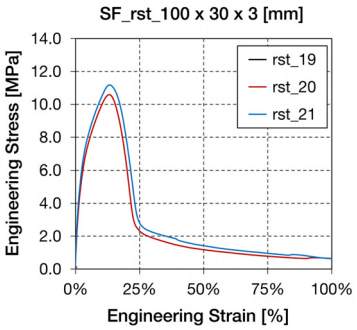

Real joint dimensions and test results from the tensile tests on linear adhesive joints between glass and stainless steel substrates at the glass surface with *SikaFast-5221 NT*:

Specimen	Joint dimensions			Max. load [N]	Corr. displ. [mm]	Max. eng. stress [MPa]	Corr. eng. strain [-]
	length l [mm]	width w [mm]	thickness t [mm]				
target	100.0	20.0	3.0				
rst_01 *	99.6	18.4	3.1	10 831	0.54	5.91	0.18
rst_02	99.1	19.0	3.1	19 861	0.23	10.55	0.08
rst_03	100.0	19.0	3.1	21 093	0.25	11.10	0.08
rst_04	100.9	18.4	3.1	20 773	0.27	11.19	0.09
rst_05 *	100.3	19.3	3.1	21 158	0.26	10.93	0.08
rst_06	100.4	18.6	3.1	20 652	0.21	11.06	0.07
Mean value	100.1	18.8	3.1	20.595	0.24	10.98	0.08
Std. deviation	0.8	0.3	0.0	523	0.03	0.29	0.01
target	100.0	20.0	6.0				
rst_07	99.0	18.2	6.1	18 091	0.31	10.04	0.05
rst_08	99.6	18.0	6.3	16 945	0.38	9.45	0.06
rst_09	98.9	17.9	5.9	17 312	0.32	9.78	0.05
Mean value	99.2	18.0	6.1	17 449	0.34	9.76	0.05
Std. deviation	0.4	0.2	0.2	585	0.04	0.30	0.01
target	50.0	20.0	3.0				
rst_10	50.9	18.2	3.1	11 368	0.14	12.27	0.04
rst_11	50.1	18.7	3.1	10 907	0.14	11.64	0.05
rst_12	50.0	19.2	3.1	8 481	0.12	8.83	0.04
Mean value	50.3	18.7	3.1	10 252	0.13	10.91	0.04
Std. deviation	0.5	0.5	0.0	1 551	0.01	1.83	0.01
target	200.0	20.0	3.0				
rst_13	200.0	18.9	3.1	39 199	0.45	10.37	0.15
rst_14	191.0	18.8	3.1	37 765	0.43	10.52	0.14
rst_15	192.0	19.2	3.1	37 651	0.48	10.21	0.16
Mean value	194.3	19.0	3.1	38 205	0.45	10.37	0.15
Std. deviation	4.9	0.2	0.0	863	0.03	0.16	0.01

Specimen	Joint dimensions			Max. load [N]	Corr. displ. [mm]	Max. eng. stress [MPa]	Corr. eng. strain [-]
	length l [mm]	width w [mm]	thickness t [mm]				
target	100.0	10.0	3.0				
rst_16	101.3	8.1	3.1	7 570	0.13	9.23	0.04
rst_17	99.4	8.5	3.1	7 738	0.16	9.16	0.05
rst_18	100.0	8.1	3.1	8 267	0.13	10.21	0.04
Mean value	100.2	8.2	3.1	7 858	0.14	9.53	0.04
Std. deviation	1.0	0.2	0.0	364	0.02	0.59	0.01
target	100.0	30.0	3.0				
rst_19 **	-	-	-	-	-	-	-
rst_20	101.5	27.7	3.1	29 771	0.41	10.59	0.13
rst_21	100.5	27.6	3.1	30 992	0.41	11.17	0.13
Mean value	101.0	27.7	3.1	30 382	0.41	10.88	0.13
Std. deviation	0.7	0.1	0.0	863	0.00	0.41	0.00

Notes:

* These specimens are not considered in the calculation of the mean values.

** No measurement data from testing is available for these specimens.

Failure patterns from the tensile tests on linear adhesive joints between glass and stainless steel substrates at the glass surface with *SikaFast-5221 NT*:

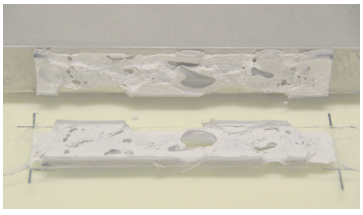

rst_01

rst_02

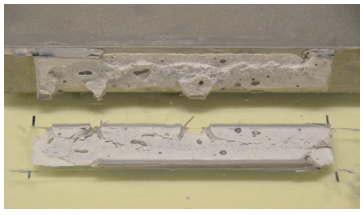

rst_03

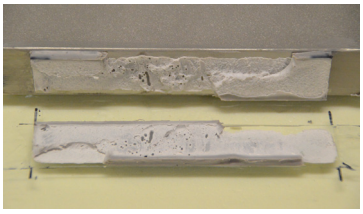

rst_04

rst_05

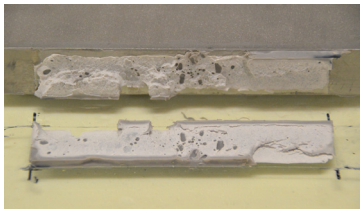

rst_06

rst_07

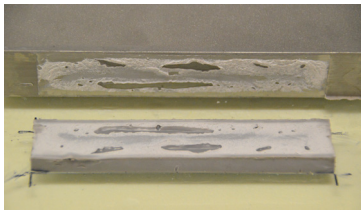

rst_08

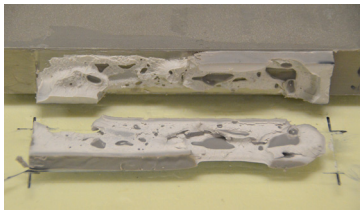

rst_09

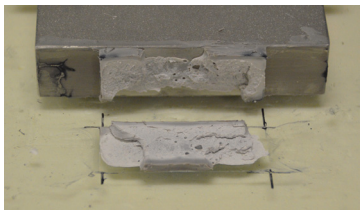

rst_10

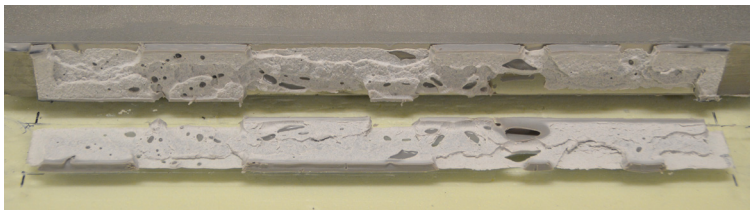

rst_13

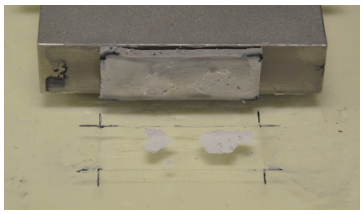

rst_11

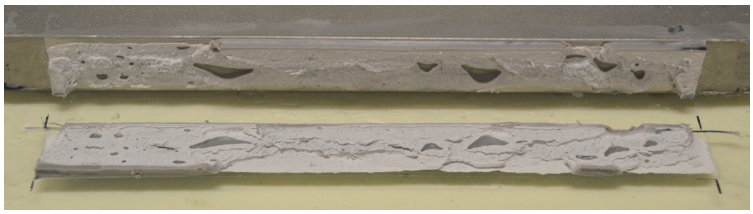

rst_14

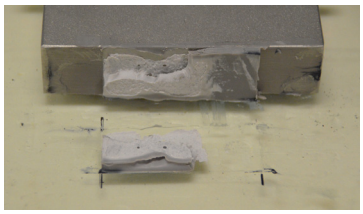

rst_12

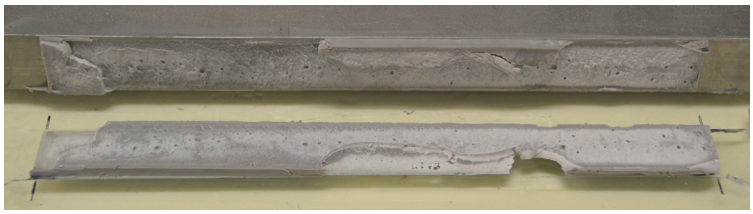

rst_15

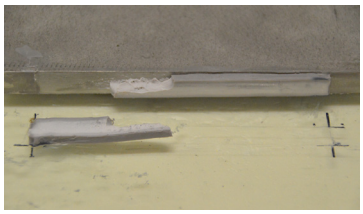

rst_16

rst_17

rst_18

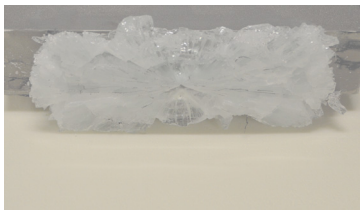

rst_19

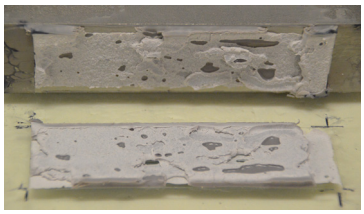

rst_20

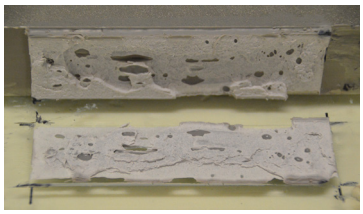

rst_21

C.4 - Adhesive joints at the glass surface under shear loading with Dow Corning 993

Shear stress *vs.* shear displacement diagrams from shear tests on linear adhesive joints between glass and stainless steel substrates at the glass surface with *Dow Corning 993*:

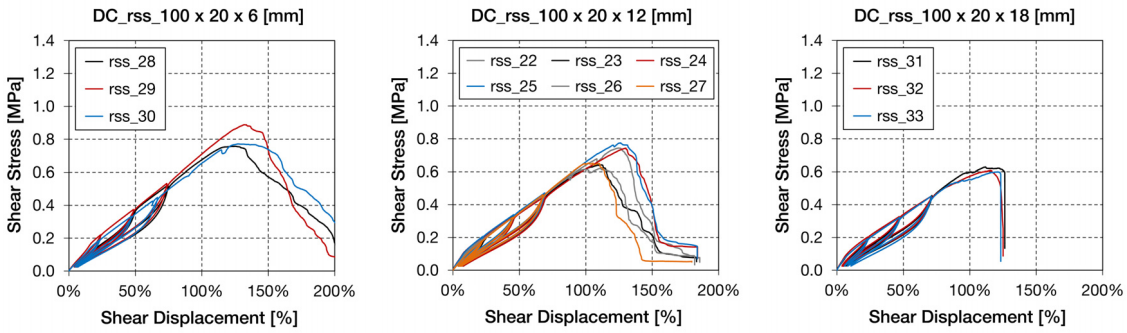

Real joint dimensions and test results from the shear tests on linear adhesive joints between glass and stainless steel substrates at the glass surface with *Dow Corning 993*:

Specimen		Joint dimensions			Max. load [N]	Corr. displ. [mm]	Max. shear stress [MPa]	Corr. shear displ. [-]
		length l [mm]	**width** w [mm]	**thickness** t [mm]				
target		100.0	20.0	12.0				
rss_22 *	lap_a	100.7	19.2	12.8	2 884	16.0	0.74	1.25
	lap_b	100.1	19.4	12.8				
rss_23	lap_a	101.0	19.6	12.8	2 526	14.3	0.64	1.12
	lap_b	102.7	19.1	12.8				
rss_24	lap_a	100.2	19.5	12.9	2 866	16.8	0.74	1.30
	lap_b	100.2	19.0	12.9				
rss_25	lap_a	100.7	19.2	12.9	3 018	16.3	0.78	1.26
	lap_b	101.1	19.4	12.9				
rss_26 *	lap_a	100.3	19.2	13.1	2 425	14.5	0.62	1.11
	lap_b	100.9	19.7	13.2				
rss_27	lap_a	99.4	20.1	13.2	2 598	13.5	0.65	1.02
	lap_b	100.4	19.8	13.2				
Mean value		100.7	19.5	13.0	2 752	15.2	0.70	1.18
Std. deviation		1.0	0.4	0.2	230	1.6	0.07	0.13

Notes:

* These specimens are not considered in the calculation of the mean values.

Specimen		Joint dimensions			Max. load [N]	Corr. displ. [mm]	Max. shear stress [MPa]	Corr. shear displ. [-]
		length l [mm]	width w [mm]	thickness t [mm]				
target		100.0	20.0	6.0				
rss_28	lap_a	101.5	19.7	5.9	3 016	7.4	0.76	1.25
	lap_b	101.2	19.6	6.0				
rss_29	lap_a	101.4	19.5	6.0	3 548	7.9	0.89	1.32
	lap_b	101.8	19.8	6.0				
rss_30	lap_a	100.0	19.6	6.2	3 045	7.9	0.77	1.27
	lap_b	100.3	19.8	6.2				
Mean value		101.0	19.7	6.1	3 203	7.7	0.81	1.28
Std. deviation		0.7	0.1	0.1	299	0.3	0.07	0.04
target		100.0	20.0	18.0				
rss_31	lap_a	99.8	19.0	18.8	2 394	21.1	0.63	1.12
	lap_b	99.8	19.2	18.9				
rss_32	lap_a	99.8	19.2	19.1	2 383	22.1	0.61	1.16
	lap_b	99.2	20.2	19.2				
rss_33	lap_a	99.1	19.6	19.1	2 334	23.0	0.60	1.21
	lap_b	100.0	19.5	19.0				
Mean value		99.6	19.5	19.0	2 370	22.1	0.61	1.16
Std. deviation		0.4	0.4	0.2	32	1.0	0.02	0.05

Specimen	Shear stress at 5% shear displacement [MPa]		Shear stress at 15% shear displacement [MPa]		Shear stress at 25% shear displacement [MPa]	
	1st cycle	2nd cycle	1st cycle	2nd cycle	1st cycle	2nd cycle
rss_22 *	0.058	0.034	0.146	0.118	0.211	0.153
rss_23	0.047	0.031	0.116	0.110	0.196	0.148
rss_24	0.069	0.034	0.158	0.121	0.215	0.149
rss_25	0.067	0.039	0.158	0.125	0.220	0.160
rss_26 *	0.054	0.037	0.141	0.116	0.205	0.154
rss_27	0.047	0.033	0.131	0.109	0.197	0.150
Mean value	0.058	0.034	0.141	0.116	0.207	0.152
Std. deviation	0.012	0.003	0.021	0.008	0.012	0.006

Specimen	Shear stress at 5% shear displacement [MPa]		Shear stress at 15% shear displacement [MPa]		Shear stress at 25% shear displacement [MPa]	
	1st cycle	2nd cycle	1st cycle	2nd cycle	1st cycle	2nd cycle
rss_28	0.045	0.030	0.110	0.105	0.167	0.157
rss_29	0.053	0.037	0.150	0.122	0.225	0.157
rss_30	0.046	0.031	0.131	0.109	0.200	0.146
Mean value	0.048	0.033	0.130	0.112	0.197	0.153
Std. deviation	0.004	0.004	0.020	0.009	0.029	0.006
rss_31	0.061	0.034	0.142	0.112	0.200	0.146
rss_32	0.071	0.041	0.154	0.123	0.212	0.156
rss_33	0.065	0.025	0.142	0.105	0.198	0.133
Mean value	0.066	0.033	0.146	0.113	0.203	0.145
Std. deviation	0.005	0.008	0.007	0.009	0.008	0.012

Failure patterns from the shear tests on linear adhesive joints between glass and stainless steel substrates at the glass surface with *Dow Corning 993*:

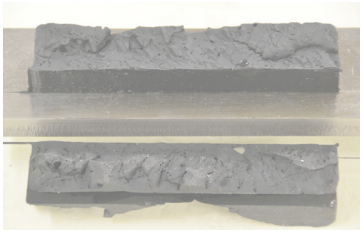

rss_22

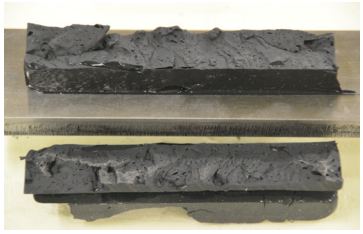

rss_23

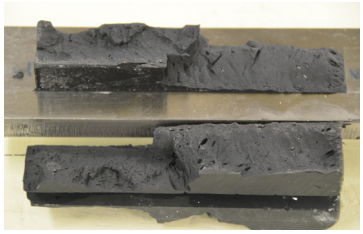

rss_24

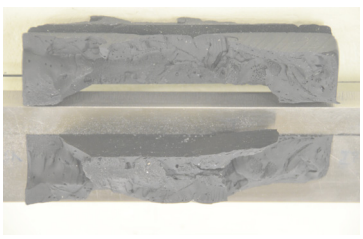

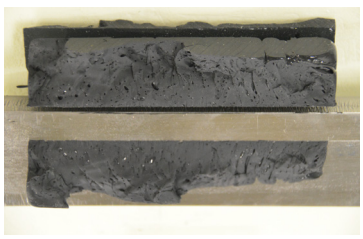

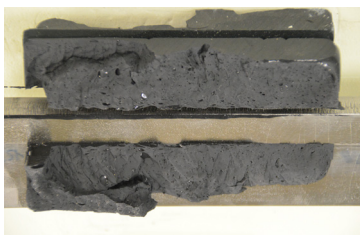

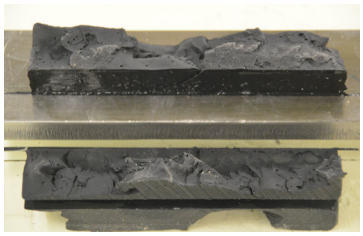

rss_25

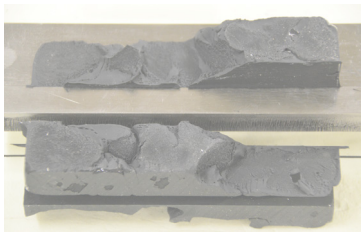

rss_26

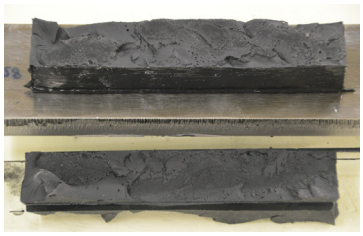

rss_27

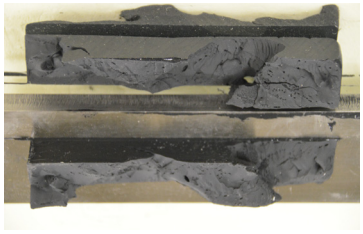

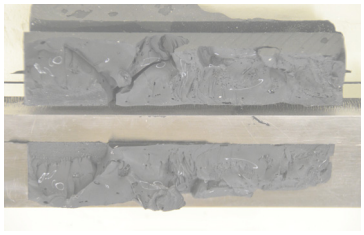

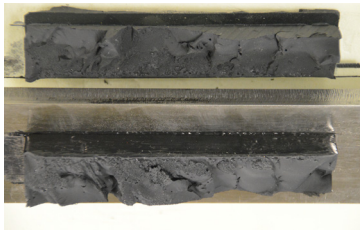

rss_28

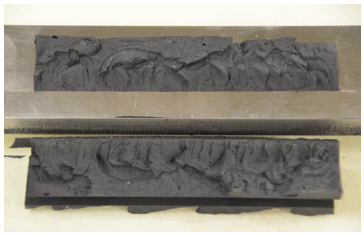

rss_29

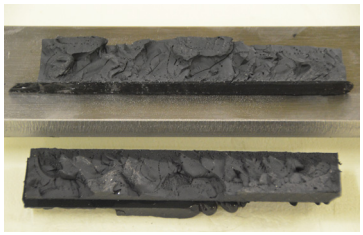

rss_30

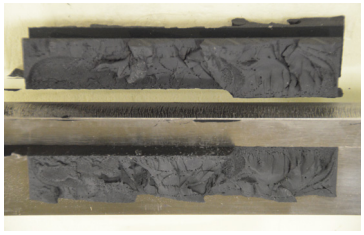

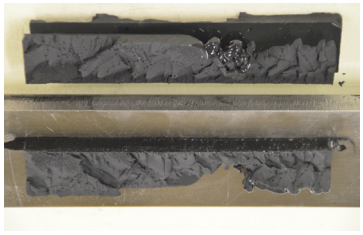

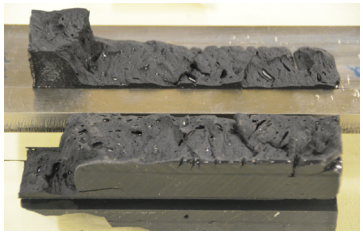

rss_31

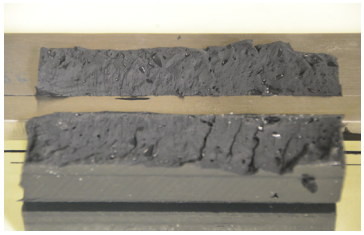

rss_32

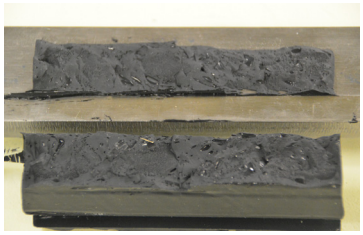

rss_33

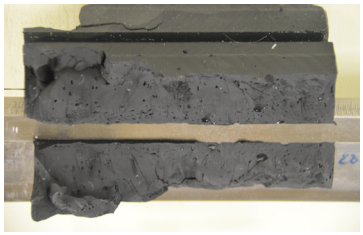

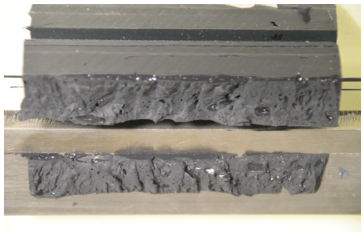

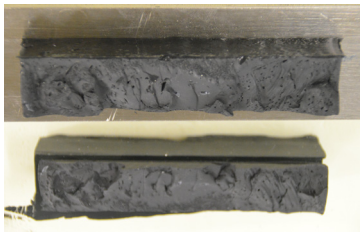

C.5 - Adhesive joints at the glass surface under shear loading with Sikasil SG-550

Shear stress *vs.* shear displacement diagrams from shear tests on linear adhesive joints between glass and stainless steel substrates at the glass surface with *Sikasil SG-550*:

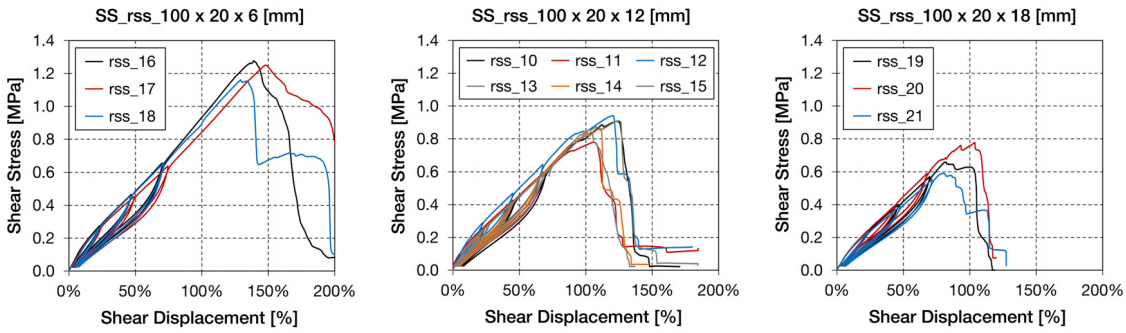

Real joint dimensions and test results from the shear tests on linear adhesive joints between glass and stainless steel substrates at the glass surface with *Sikasil SG-550*:

Specimen		Joint dimensions			Max. load [N]	Corr. displ. [mm]	Max. shear stress [MPa]	Corr. shear displ. [-]
		length l [mm]	**width** w [mm]	**thickness** t [mm]				
target		100.0	20.0	12.0				
rss_10	lap_a	99.3	19.5	12.8	3 478	15.8	0.91	1.23
	lap_b	98.0	19.4	12.8				
rss_11	lap_a	99.6	19.1	12.9	3 021	13.7	0.78	1.06
	lap_b	102.3	19.3	13.1				
rss_12	lap_a	99.5	18.9	13.2	3 552	15.9	0.94	1.21
	lap_b	99.7	19.0	13.2				
rss_13 *	lap_a	101.6	18.9	13.0	3 231	13.5	0.84	1.04
	lap_b	100.5	19.1	12.8				
rss_14	lap_a	101.1	19.1	12.9	3 357	14.4	0.86	1.11
	lap_b	101.4	19.3	13.2				
rss_15 *	lap_a	100.0	19.1	13.0	3 471	16.0	0.91	1.24
	lap_b	99.3	19.2	12.8				
Mean value		100.1	19.2	13.0	3 352	15.0	0.87	1.15
Std. deviation		1.4	0.2	0.2	235	1.1	0.07	0.08

Notes:

* These specimens are not considered in the calculation of the mean values.

Specimen		Joint dimensions			Max. load [N]	Corr. displ. [mm]	Max. shear stress [MPa]	Corr. shear displ. [-]
		length l [mm]	width w [mm]	thickness t [mm]				
target		100.0	20.0	6.0				
rss_16	lap_a	104.2	19.9	6.2	5 267	8.6	1.28	1.39
	lap_b	104.1	19.7	6.2				
rss_17	lap_a	102.7	19.7	5.9	4 967	8.7	1.25	1.48
	lap_b	101.5	19.2	5.9				
rss_18	lap_a	99.8	19.4	6.0	4 497	7.8	1.16	1.29
	lap_b	99.9	19.4	6.0				
Mean value		102.0	19.6	6.0	4 910	8.4	1.23	1.39
Std. deviation		2.0	0.3	0.1	388	0.5	0.06	0.10
target		100.0	20.0	18.0				
rss_19	lap_a	99.1	19.2	19.2	2 505	15.7	0.66	0.81
	lap_b	98.6	19.3	19.3				
rss_20	lap_a	99.7	18.9	18.9	2 910	19.7	0.78	1.04
	lap_b	99.4	18.7	19.1				
rss_21	lap_a	99.9	18.7	18.7	2 231	15.1	0.59	0.80
	lap_b	99.8	19.1	18.8				
Mean value		99.4	19.0	19.0	2 549	16.8	0.68	0.88
Std. deviation		0.5	0.3	0.2	342	2.5	0.10	0.14

Specimen	Shear stress at 5% shear displacement [MPa]		Shear stress at 15% shear displacement [MPa]		Shear stress at 25% shear displacement [MPa]	
	1st cycle	2nd cycle	1st cycle	2nd cycle	1st cycle	2nd cycle
rss_10	0.077	0.035	0.183	0.141	0.264	0.182
rss_11	0.100	0.066	0.199	0.163	0.277	0.203
rss_12	0.094	0.060	0.221	0.177	0.309	0.221
rss_13 *	0.072	0.048	0.181	0.151	0.266	0.200
rss_14	0.070	0.050	0.181	0.155	0.264	0.206
rss_15 *	0.072	0.053	0.177	0.161	0.262	0.244
Mean value	0.085	0.053	0.196	0.159	0.279	0.203
Std. deviation	0.014	0.014	0.019	0.015	0.021	0.016

Specimen	Shear stress at 5% shear displacement [MPa]		Shear stress at 15% shear displacement [MPa]		Shear stress at 25% shear displacement [MPa]	
	1st cycle	2nd cycle	1st cycle	2nd cycle	1st cycle	2nd cycle
rss_16	0.077	0.050	0.201	0.159	0.288	0.205
rss_17	0.070	0.046	0.194	0.148	0.273	0.191
rss_18	0.063	0.034	0.189	0.149	0.282	0.191
Mean value	0.070	0.043	0.195	0.152	0.281	0.196
Std. deviation	0.007	0.008	0.006	0.006	0.008	0.008
rss_19	0.070	0.043	0.169	0.138	0.247	0.181
rss_20	0.071	0.045	0.175	0.143	0.255	0.201
rss_21	0.068	0.047	0.168	0.137	0.236	0.176
Mean value	0.070	0.045	0.171	0.139	0.246	0.186
Std. deviation	0.002	0.002	0.004	0.003	0.010	0.013

Failure patterns from the shear tests on linear adhesive joints between glass and stainless steel substrates at the glass surface with *Sikasil SG-550*:

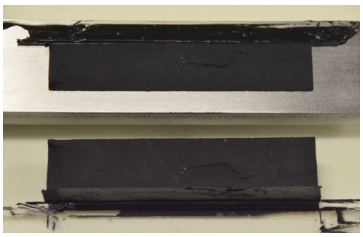

rss_10

rss_11

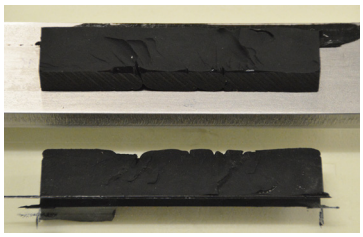

rss_12

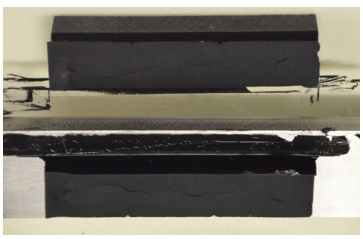

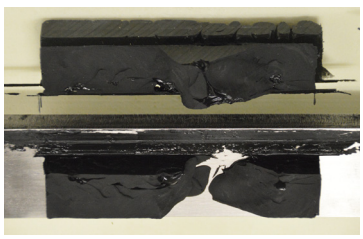

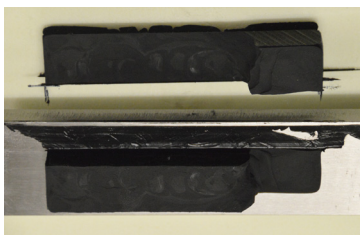

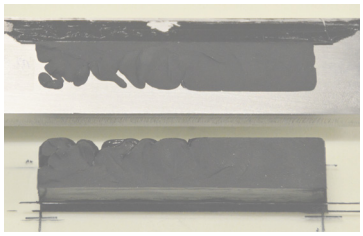

rss_13

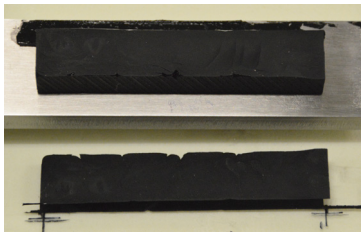

rss_14

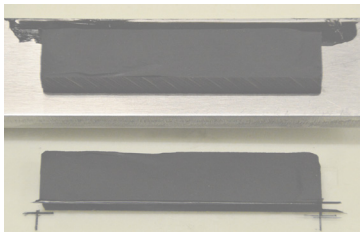

rss_15

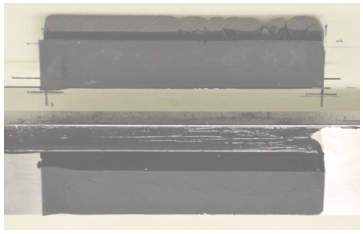

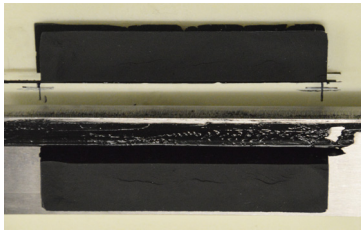

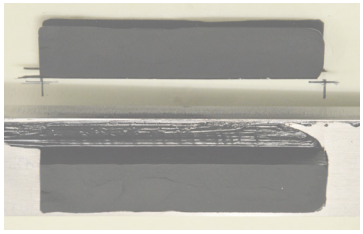

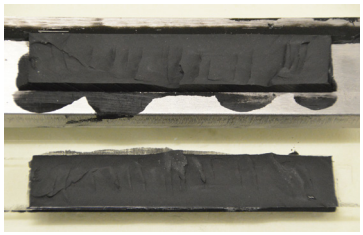

rss_16

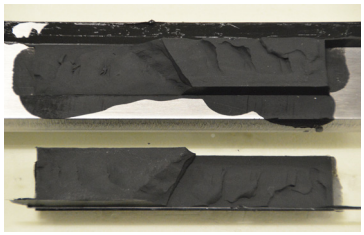

rss_17

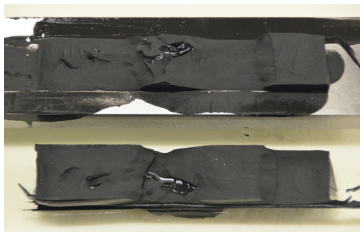

rss_18

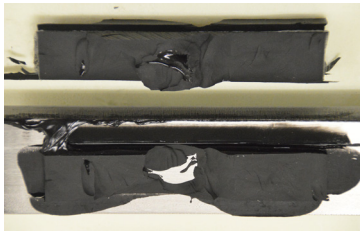

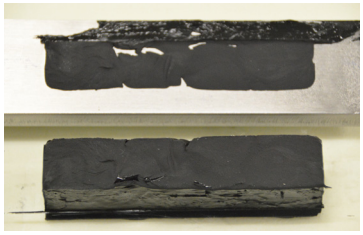

rss_19

rss_20

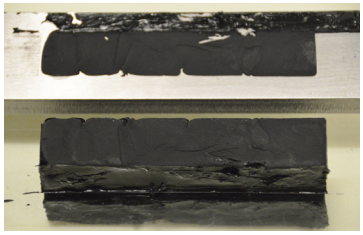

rss_21

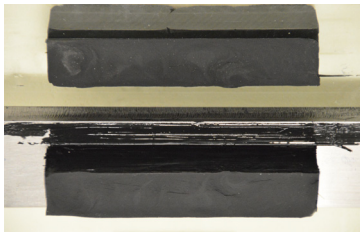

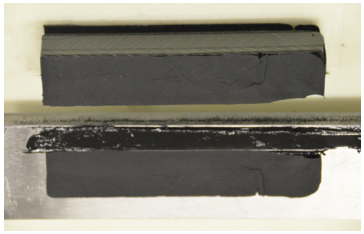

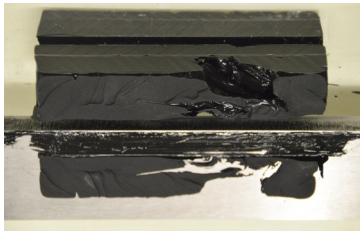

C.6 - Adhesive joints at the glass surface under shear loading with SikaFast-5221 NT

Shear stress *vs.* shear displacement diagrams from shear tests on linear adhesive joints between glass and stainless steel substrates at the glass surface with *SikaFast-5221 NT*:

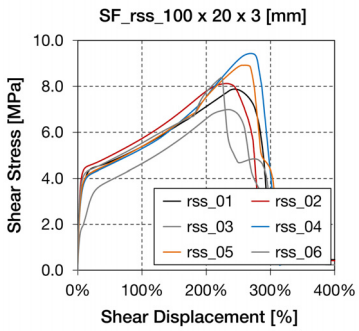

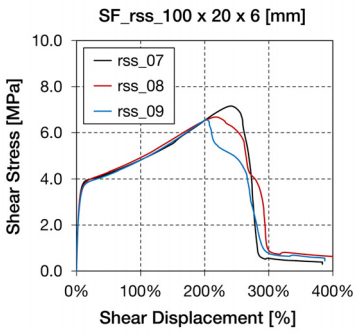

Real joint dimensions and test results from the shear tests on linear adhesive joints between glass and stainless steel substrates at the glass surface with *SikaFast-5221 NT*:

Specimen		Joint dimensions			Max. load [N]	Corr. displ. [mm]	Max. shear stress & (approx. yield. stress) [MPa]	Corr. shear displ. [-]
		length l [mm]	**width** w [mm]	**thickness** t [mm]				
target		100.0	20.0	3.0				
rss_01	lap_a	100.0	20.6	3.1	32 041	7.5	7.88	2.44
	lap_b	102.3	19.6	3.1			(4.2)	(0.15)
rss_02	lap_a	100.3	20.2	3.1	32 693	7.2	8.13	2.31
	lap_b	100.4	19.9	3.1			(4.4)	(0.09)
rss_03 *	lap_a	101.5	20.0	3.1	27 831	7.2	6.99	2.34
	lap_b	101.0	19.3	3.1			(3.4)	(0.26)
rss_04	lap_a	101.1	20.2	3.1	38 669	8.3	9.44	2.69
	lap_b	101.3	20.3	3.1			(4.0)	(0.12)
rss_05	lap_a	100.0	20.0	3.1	35 679	7.9	8.92	2.56
	lap_b	99.5	20.1	3.1			(4.1)	(0.14)
rss_06 *	lap_a	100.8	19.8	3.1	33 505	6.9	8.39	2.23
	lap_b	100.5	19.9	3.1			(4.2)	(0.12)
Mean value		100.6	20.1	3.1	34 771	7.7	8.59	2.50
							(4.2)	(0.13)
Std. deviation		0.9	0.3	0.0	3 044	0.5	0.72	0.16
							(0.2)	(0.03)

Notes:

* These specimens are not considered in the calculation of the mean values.

Specimen		Joint dimensions			Max. load [N]	Corr. displ. [mm]	Max. shear stress & (approx. yield. stress) [MPa]	Corr. shear displ. [-]
		length l [mm]	**width** w [mm]	**thickness** t [mm]				
target		100.0	20.0	6.0				
rss_07	lap_a	102.1	18.8	6.2	27 290	15.0	7.16	2.41
	lap_b	101.8	18.6	6.2			(3.9)	(0.13)
rss_08	lap_a	102.0	18.8	5.9	26 218	12.8	6.68	2.16
	lap_b	101.4	19.8	5.9			(3.8)	(0.13)
rss_09	lap_a	100.3	18.5	6.0	24 491	12.3	6.56	2.02
	lap_b	101.0	18.6	6.2			(3.8)	(0.14)
Mean value		101.4	18.9	6.1	26 000	13.4	6.80	2.20
							(3.8)	(0.13)
Std. deviation		0.7	0.5	0.2	1 412	1.4	0.32	0.20
							(0.1)	(0.01)

Failure patterns from the shear tests on linear adhesive joints between glass and stainless steel substrates at the glass surface with *SikaFast-5221 NT*:

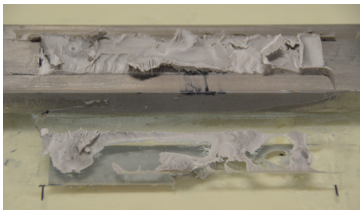

rss_01

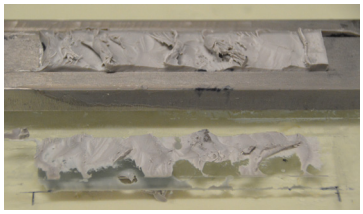

rss_02

rss_03

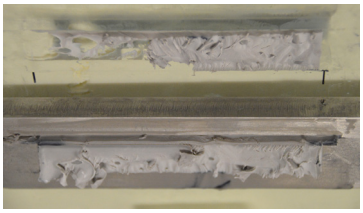

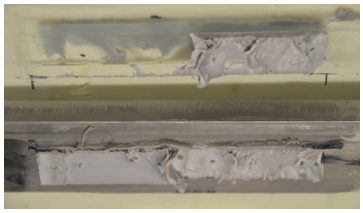

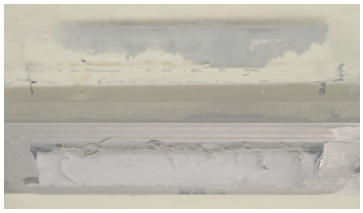

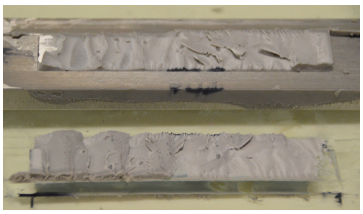

rss_04

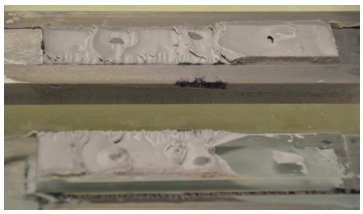

rss_05

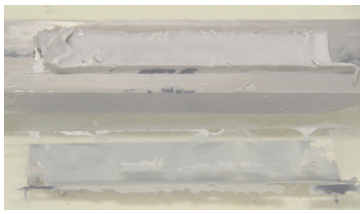

rss_06

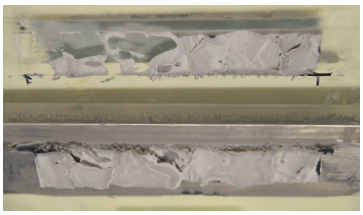

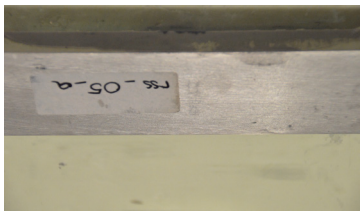

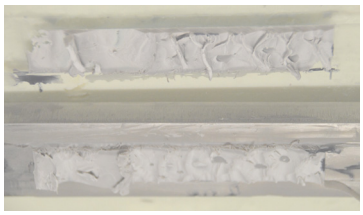

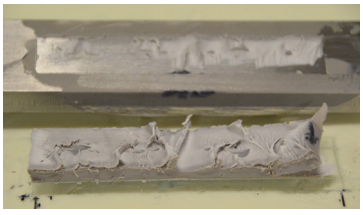

rss_07

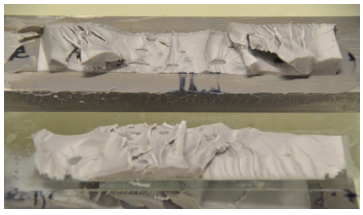

rss_08

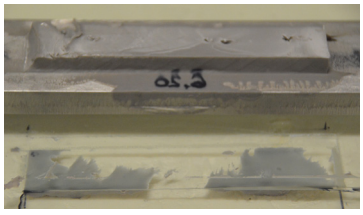

rss_09

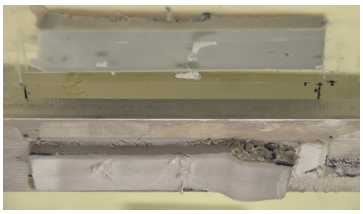

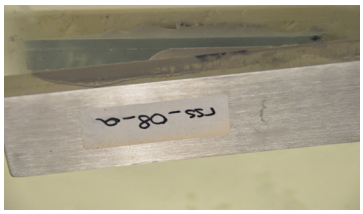

Appendix D

Test results for linear adhesive joints at the edge of laminated glass

Load *vs.* displacement diagrams for the tensile, compressive and shear tests
Real cross section dimensions of the test specimens
Mechanical values determined from the measured data
Failure patterns of the tensile, compressive and shear test specimens

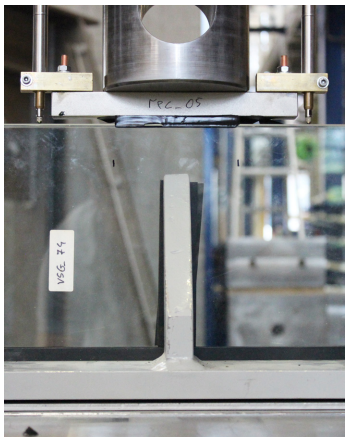
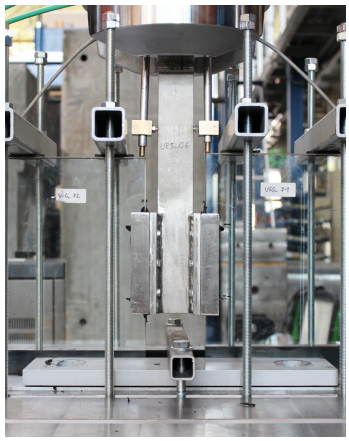
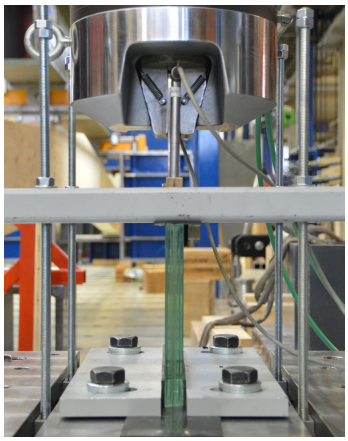
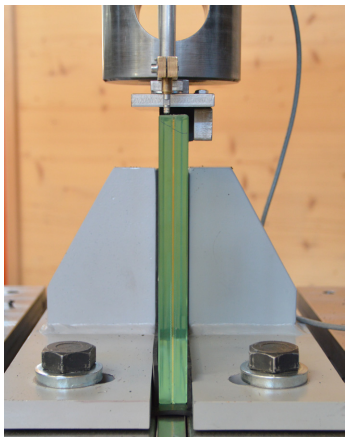
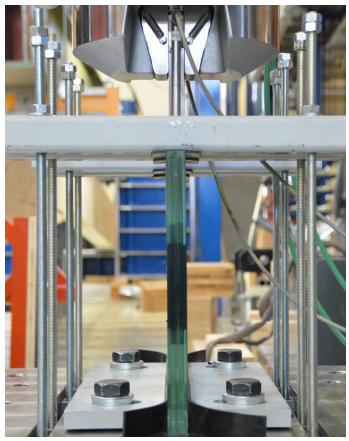

Sketches of the test setups and complementary exploded views of the test specimens for linear adhesive joints at the edge of laminated glass under tensile, compressive and shear loading:

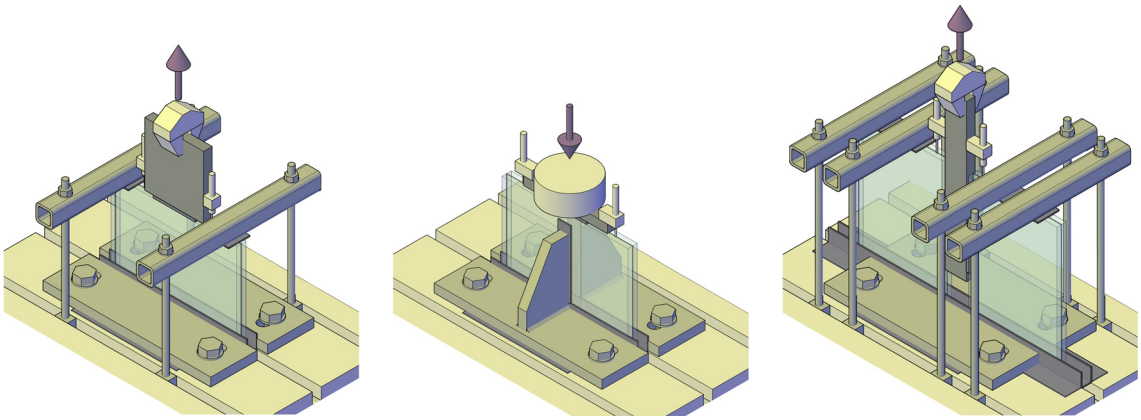

tensile loading *compressive loading* *shear loading*

Exploded view of the test specimens for adhesive joints with L-shaped (left) and U-shaped (right) cross section at the edge of laminated glass under compressive loading:

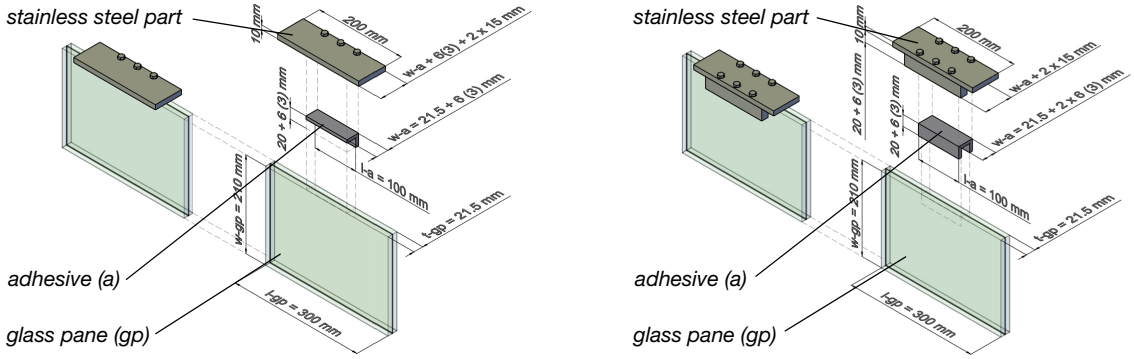

Exploded view of the test specimens for adhesive joints with L-shaped (left) and U-shaped (right) cross section at the edge of laminated glass under shear loading:

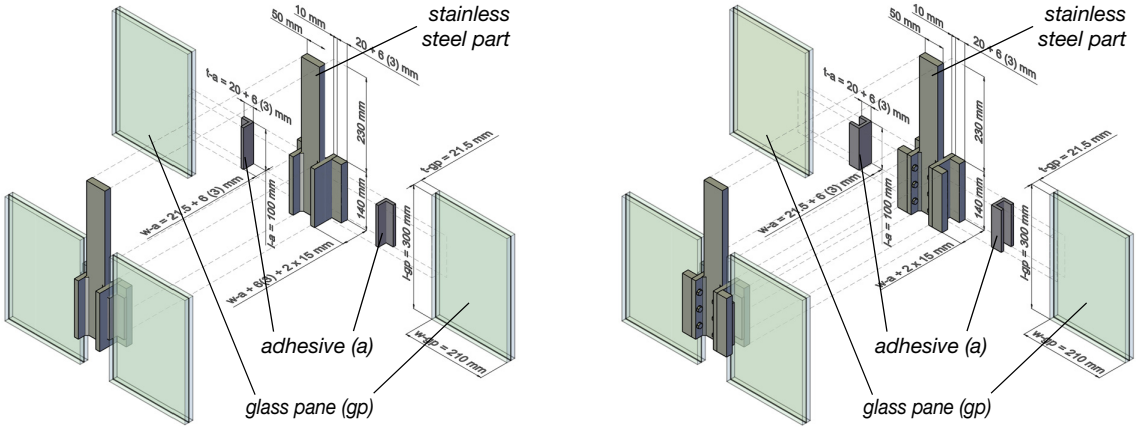

D.1 - Adhesive joints at the edge of laminated glass under tensile loading

Load *vs.* displacement diagrams from the tensile tests on linear adhesive joints between glass and stainless steel substrates at the edge of laminated glass:

Dow Corning 993 (DC):

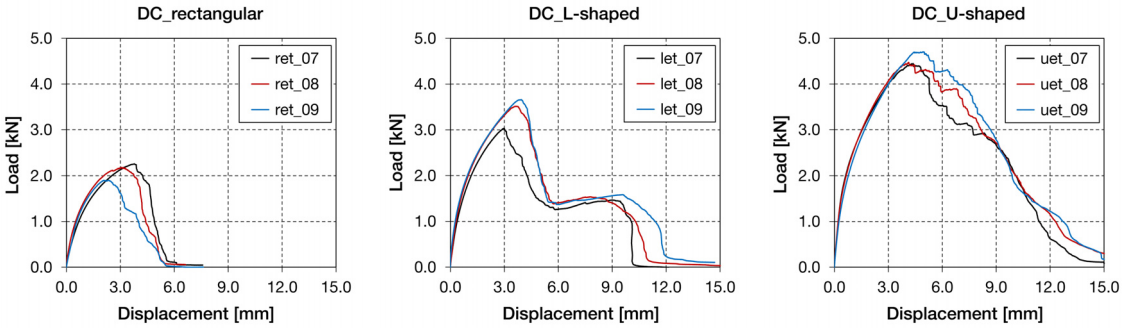

Sikasil SG-550 (SS):

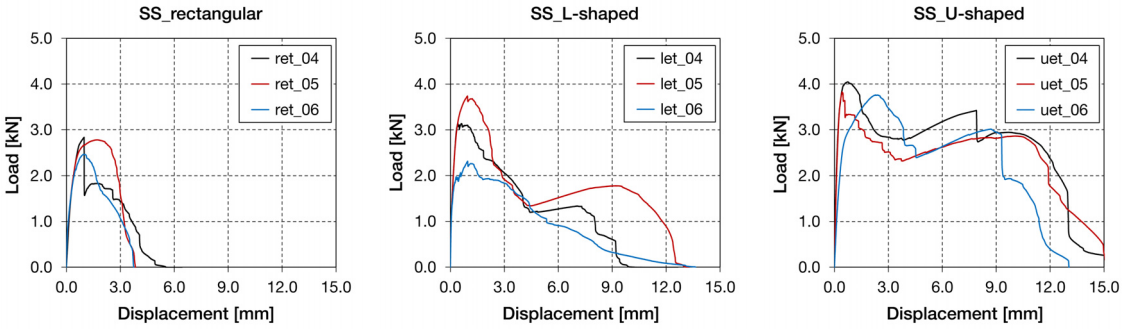

SikaFast-5221 NT (SF):

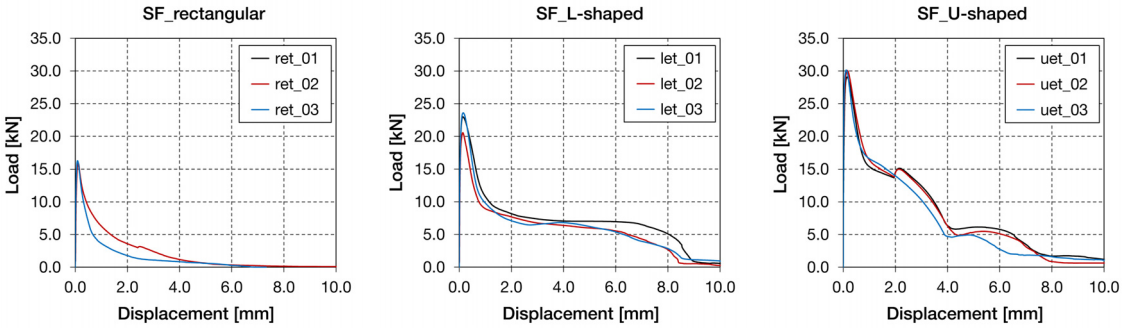

Real joint dimensions and test results from the tensile tests on linear adhesive joints between glass and stainless steel substrates at the edge of laminated glass:

Specimen	Joint dimensions			Max. load [N]	Corr. displ. [mm]	Max. eng. stress [MPa]	Corr. eng. strain [-]
	length l [mm]	**width** w [mm]	**thickness** t [mm]				
Dow Corning 993 - rectangular - 100 x 20 x 6 [mm]							
ret_07	100.1	20.1	6.25	2 253	3.79	1.12	0.61
ret_08	100.4	20.4	6.19	2 175	3.07	1.06	0.50
ret_09	100.4	20.1	6.16	1 901	2.09	0.94	0.34
Mean value	100.3	20.2	6.20	2 110	2.98	1.04	0.48
Dow Corning 993 - L-shaped - 100 x (21.5+20) x 6 [mm]							
let_07 *	102.8	-	6.36	3 035	2.98	-	0.47
let_08 *	102.8	-	6.13	3 517	3.65	-	0.60
let_09 *	102.8	-	6.18	3 660	3.94	-	0.64
Mean value	102.8	-	6.22	3 404	3.52	-	0.57
Dow Corning 993 - U-shaped - 100 x (21.5+2x20) x 6 [mm]							
uet_07 *	97.6	-	6.24	4 446	4.37	-	0.70
uet_08 *	103.7	-	6.33	4 474	4.13	-	0.65
uet_09 *	101.8	-	6.17	4 705	4.92	-	0.80
Mean value	101.0	-	6.25	4 542	4.47	-	0.72
Sikasil SG-550 - rectangular - 100 x 20 x 6 [mm]							
ret_04	101.9	20.5	5.93	2 834	0.98	1.36	0.17
ret_05	98.7	20.0	5.98	2 779	1.72	1.41	0.29
ret_06	98.6	20.1	6.26	2 460	0.95	1.24	0.15
Mean value	99.7	20.2	6.06	2 691	1.22	1.34	0.20
Sikasil SG-550 - L-shaped - 100 x (21.5+20) x 6 [mm]							
let_04 *	100.1	-	6.21	3 160	0.41	-	0.07
let_05 *	102.7	-	6.23	3 739	0.95	-	0.15
let_06 *	105.4	-	6.20	2 314	0.96	-	0.15
Mean value	102.7	-	6.21	3 071	0.77	-	0.12

Specimen	Joint dimensions			Max. load [N]	Corr. displ. [mm]	Max. eng. stress [MPa]	Corr. eng. strain [%]
	length l [mm]	width w [mm]	thickness t [mm]				
Sikasil SG-550 - U-shaped - 100 x (21.5+2x20) x 6 [mm]							
uet_04 *	107.9	-	6.23	4 046	0.75	-	0.12
uet_05 *	102.7	-	6.21	3 828	0.43	-	0.07
uet_06 *	99.3	-	6.09	3 760	2.29	-	0.38
Mean value	103.3	-	6.18	3 878	1.16	-	0.19
SikaFast-5221 NT - rectangular - 100 x 20 x 3 [mm]							
ret_01 **	100.5	20.1	3.09	-	-	-	-
ret_02	98.9	19.5	3.07	15 885	0.12	8.24	0.04
ret_03	99.2	19.4	3.09	16 252	0.09	8.44	0.03
Mean value	99.5	19.7	3.08	16 069	0.11	8.34	0.04
SikaFast-5221 NT - L-shaped - 100 x (21.5+20) x 3 [mm]							
let_01 *	100.7	-	3.06	22 994	0.14	-	0.05
let_02 *	100.1	-	3.07	20 567	0.14	-	0.05
let_03 *	102.1	-	3.08	23 594	0.15	-	0.05
Mean value	101.0	-	3.07	22 385	0.14	-	0.05
SikaFast-5221 NT - U-shaped - 100 x (21.5+2x20) x 3 [mm]							
uet_01 *	101.0	-	3.08	29 063	0.15	-	0.05
uet_02 *	100.8	-	3.07	30 064	0.16	-	0.05
uet_03 *	99.4	-	3.08	30 132	0.12	-	0.04
Mean value	100.4	-	3.08	29 753	0.14	-	0.05

Notes:

* In the case of the specimens for adhesive joints with L-shaped and U-shaped cross sections tested under tensile loading, the width of the joint is not measured. Furthermore the maximum engineering stress is not determined for these specimens, since one part of the joint is subjected to tensile stresses and the other part to shear stresses.

** No measurement data from testing is available for these specimens.

Failure patterns from the tensile tests on linear adhesive joints between glass and stainless steel substrates at the glass edge with *Dow Corning 993*, *Sikasil SG-550* and *SikaFast-5221 NT*:

ret_07

ret_08

ret_09

let_07

let_08

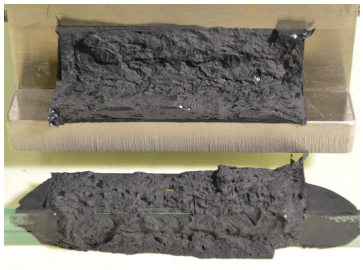

let_09

uet_07

uet_08

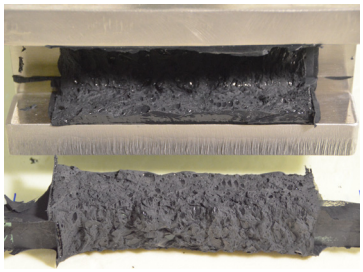

uet_09

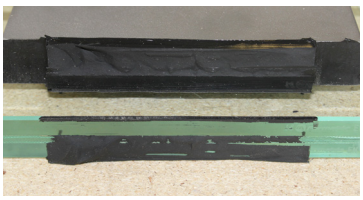

ret_04

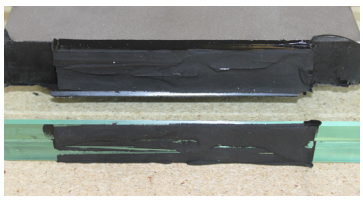

ret_05

ret_06

let_04

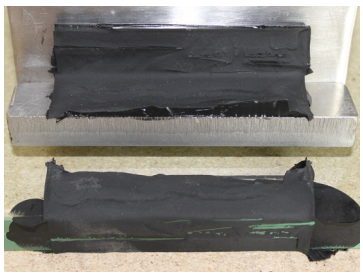

let_05

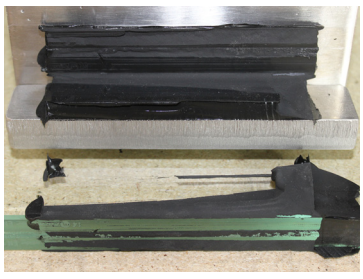

let_06

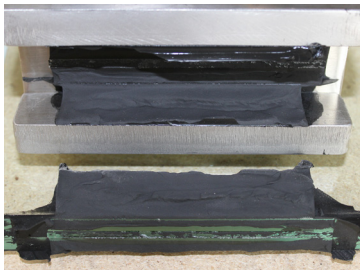

uet_04

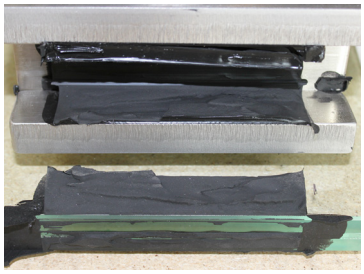

uet_05

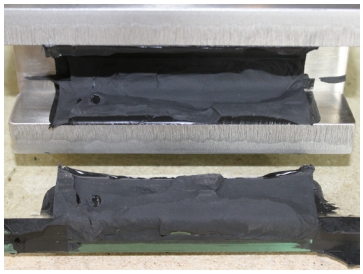

uet_06

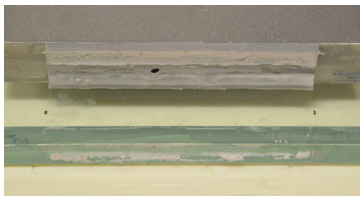

ret_01

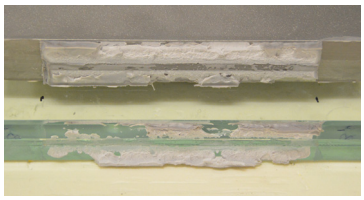

ret_02

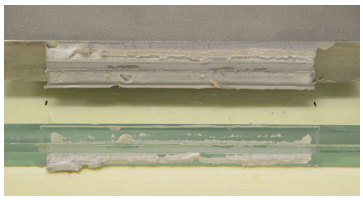

ret_03

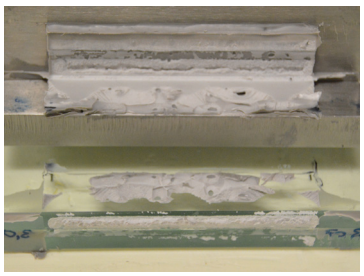

let_01

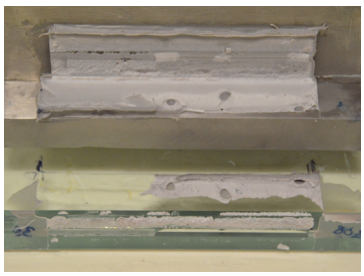

let_02

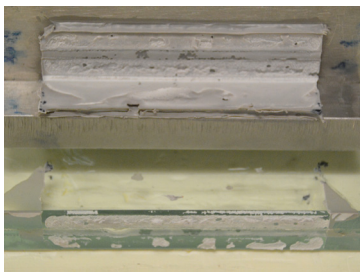

let_03

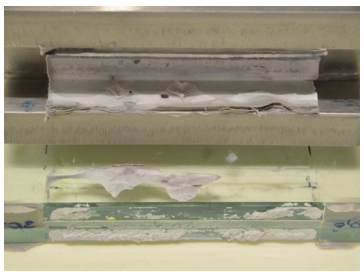

uet_01

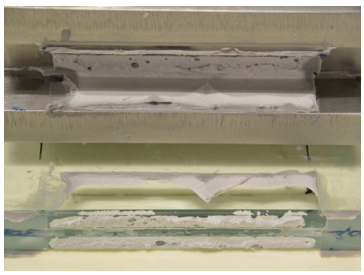

uet_02

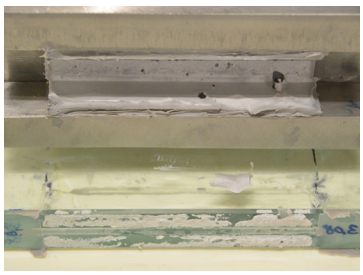

uet_03

D.2 - Adhesive joints at the edge of laminated glass under compressive loading

Load *vs.* displacement diagrams from the compressive tests on linear adhesive joints between glass and stainless steel substrates at the edge of laminated glass:

Dow Corning 993 (DC):

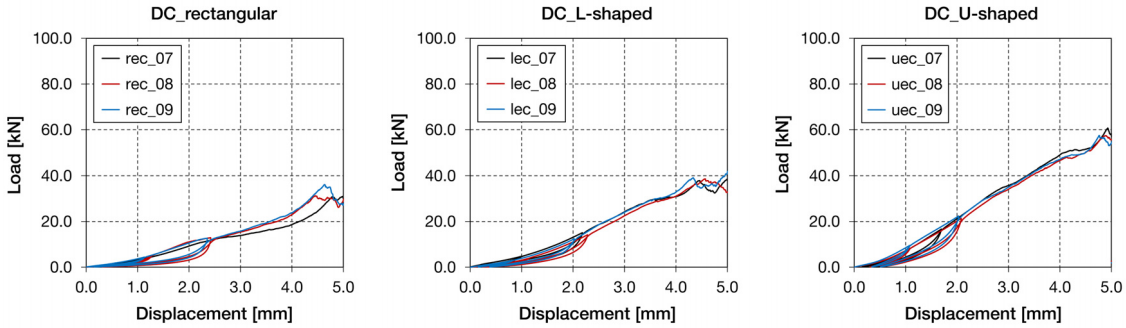

Sikasil SG-550 (SS):

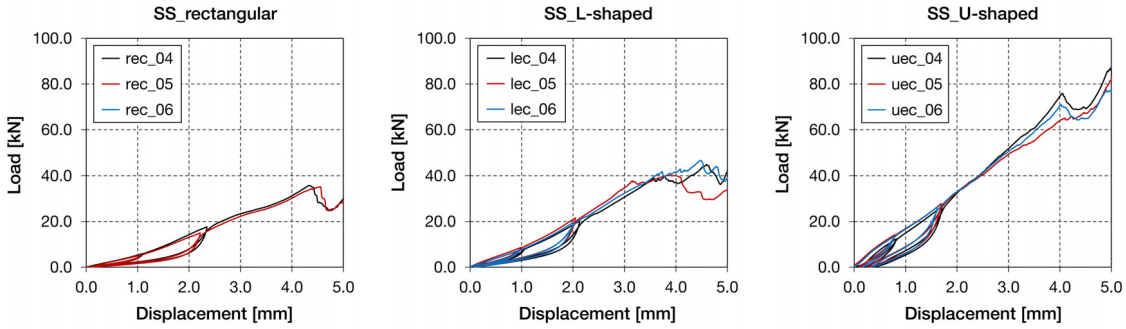

SikaFast-5221 NT (SF):

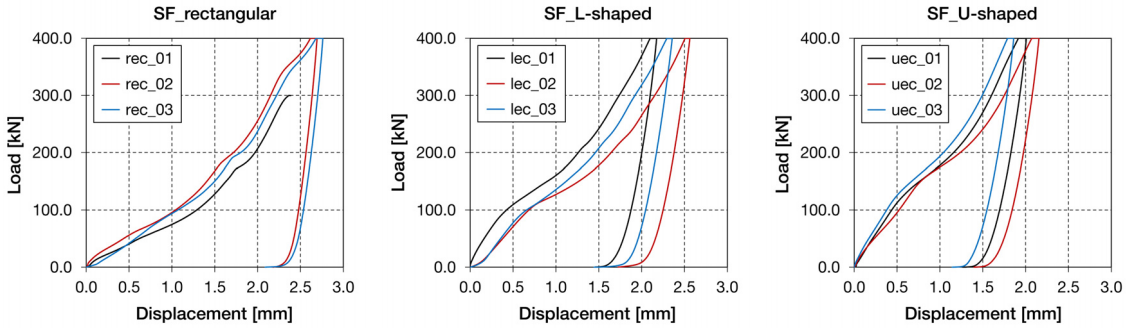

Real joint dimensions and test results from the compressive tests on linear adhesive joints between glass and stainless steel substrates at the edge of laminated glass:

Specimen	**Joint thickness** t [mm] *	**Load at 5% strain** [kN]	**Load at 15% strain** [kN]		**Load at 25% strain** [kN]		**Load at 50% strain** [kN]
			1st cycle	**last cycle**	**1st cycle**	**last cycle**	
Dow Corning 993 - rectangular - 100 x 20 x 6 [mm]							
rec_07	6.21	0.87	2.88	-	6.13	-	14.35
rec_08	5.92	0.61	2.05	1.09	6.75	2.46	15.19
rec_09	6.00	0.98	3.19	1.46	6.83	2.96	15.78
Mean value	6.04	0.82	2.71	1.28	6.57	2.71	15.11
Dow Corning 993 - L-shaped - 100 x (21.5+20) x 6 [mm]							
lec_07	6.20	1.60	4.38	2.67	8.75	5.77	25.40
lec_08	6.20	0.52	2.71	1.75	6.93	4.57	23.70
lec_09	6.23	1.08	3.52	2.02	7.87	5.22	25.24
Mean value	6.21	1.07	3.54	2.15	7.85	5.19	24.78
Dow Corning 993 - U-shaped - 100 x (21.5+2x20) x 6 [mm]							
uec_07	6.33	1.47	6.54	3.95	15.04	12.65	37.36
uec_08	6.16	1.45	6.39	2.94	13.98	8.62	35.15
uec_09	6.28	1.65	7.74	3.53	16.08	10.03	36.59
Mean value	6.26	1.52	6.89	3.47	15.03	10.43	36.37
Sikasil SG-550 - rectangular - 100 x 20 x 6 [mm]							
rec_04	6.01	1.60	4.67	2.02	9.17	4.08	23.37
rec_05	6.15	1.47	4.53	1.86	8.90	3.94	22.87
rec_06 **	6.06	2.20	5.63	2.79	10.69	6.68	27.22
Mean value	6.07	1.76	4.94	2.22	9.59	4.90	24.49
Sikasil SG-550 - L-shaped - 100 x (21.5+20) x 6 [mm]							
lec_04	6.37	2.46	7.30	3.54	13.41	7.51	33.15
lec_05	6.29	3.12	8.24	3.93	14.90	8.58	37.64
lec_06	6.31	2.51	7.42	3.77	13.88	8.57	34.30
Mean value	6.32	2.70	7.65	3.75	14.06	8.22	35.03

Specimen	Joint thickness t [mm] *	Load at 5% strain [kN]	Load at 15% strain [kN]		Load at 25% strain [kN]		Load at 50% strain [kN]
			1st cycle	last cycle	1st cycle	last cycle	
Sikasil SG-550 - U-shaped - 100 x (21.5+2x20) x 6 [mm]							
uec_04	6.25	3.88	13.97	6.52	24.07	17.74	54.31
uec_05	6.21	6.73	15.95	8.12	25.30	20.06	50.67
uec_06	6.21	6.16	15.66	7.90	25.26	21.88	52.10
Mean value	6.22	5.59	15.19	7.51	24.88	19.89	52.36

Specimen	Joint thickness t [mm] *	Load at 5% strain [kN]	Load at 15% strain [kN]	Load at 25% strain [kN]	Load at 50% strain [kN]
SikaFast-5221 NT - rectangular - 100 x 20 x 3 [mm]					
rec_01	3.00	16.11	36.83	58.62	127.99
rec_02	3.00	24.33	51.45	74.33	168.06
rec_03	3.00	8.02	36.51	69.90	150.38
Mean value	3.00	16.15	41.60	67.62	148.81
SikaFast-5221 NT - L-shaped - 100 x (21.5+20) x 3 [mm]					
lec_01	3.08	48.27	105.01	137.48	250.85
lec_02	3.08	12.55	64.36	110.22	183.25
lec_03	3.08	10.75	70.59	110.78	214.74
Mean value	3.08	23.86	79.99	119.49	216.28
SikaFast-5221 NT - U-shaped - 100 x (21.5+2x20) x 3 [mm]					
uec_01	3.07	35.99	104.84	150.55	279.55
uec_02	3.08	36.10	88.31	149.34	248.68
uec_03	3.07	46.21	118.23	162.85	313.00
Mean value	3.07	39.43	103.79	154.25	280.41

Notes:

* The length and the width of the adhesive joints tested under compressive loading are not measured before testing.

** After reaching *50%* strain one displacement transducer deliveres wrong data and therefore no curve is plotted for this specimen in the diagrams.

Failure patterns from the compressive tests on linear adhesive joints between glass and stainless steel substrates at the glass edge with *Dow Corning 993*, *Sikasil SG-550* and *SikaFast-5221 NT*:

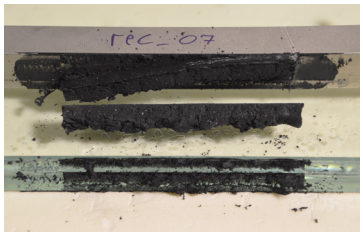

rec_07

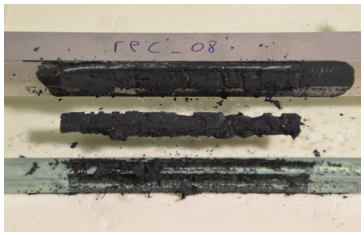

rec_08

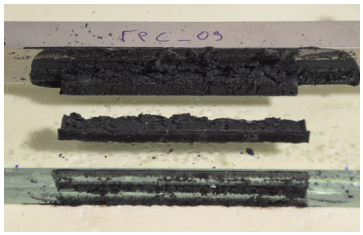

rec_09

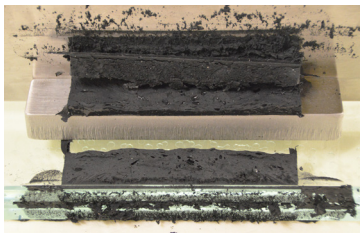

lec_07

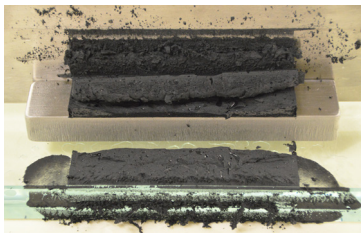

lec_08

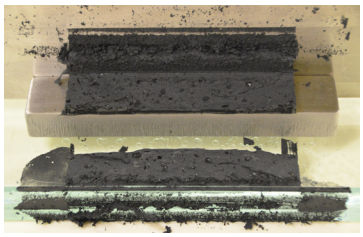

lec_09

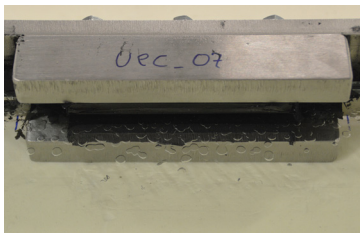

uec_07

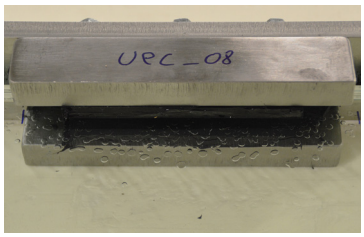

uec_08

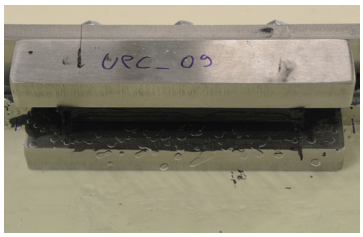

uec_09

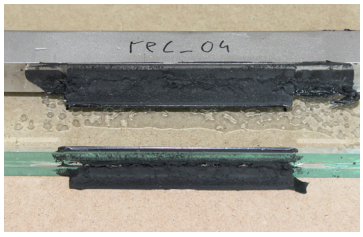

rec_04

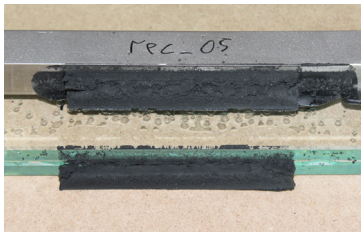

rec_05

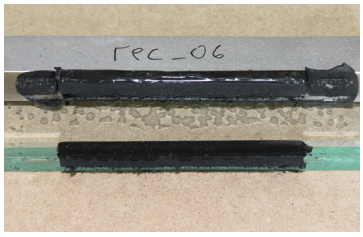

rec_06

lec_04

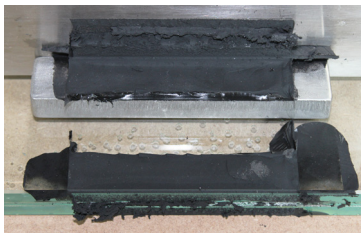

lec_05

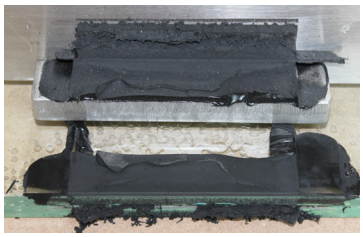

lec_06

uec_04

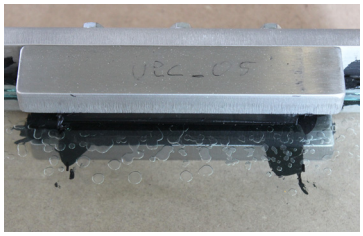

uec_05

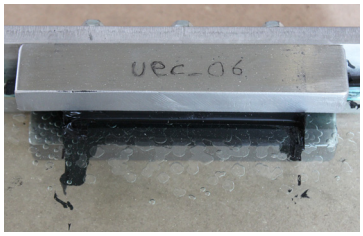

uec_06

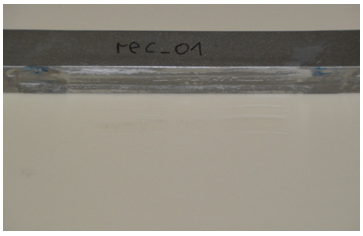

rec_01

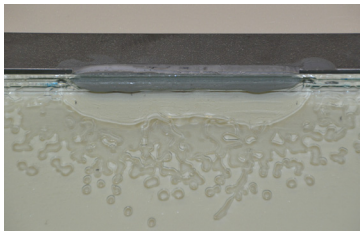

rec_02

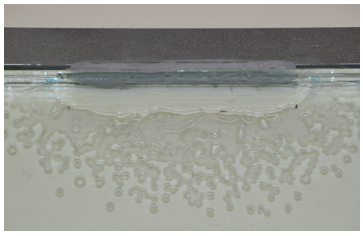

rec_03

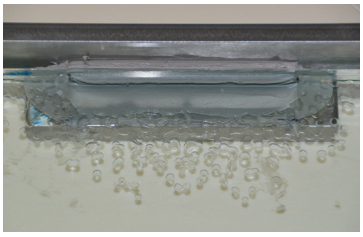

lec_01

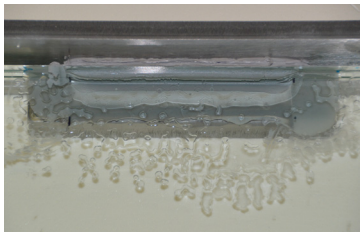

lec_02

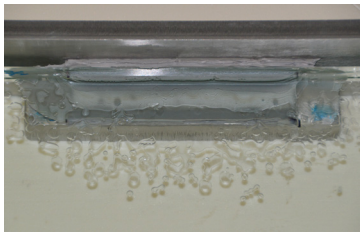

lec_03

uec_01

uec_02

uec_03

D.3 - Adhesive joints at the edge of laminated glass under shear loading

Load *vs.* displacement diagrams from the shear tests on linear adhesive joints between glass and stainless steel substrates at the edge of laminated glass:

Dow Corning 993 (DC):

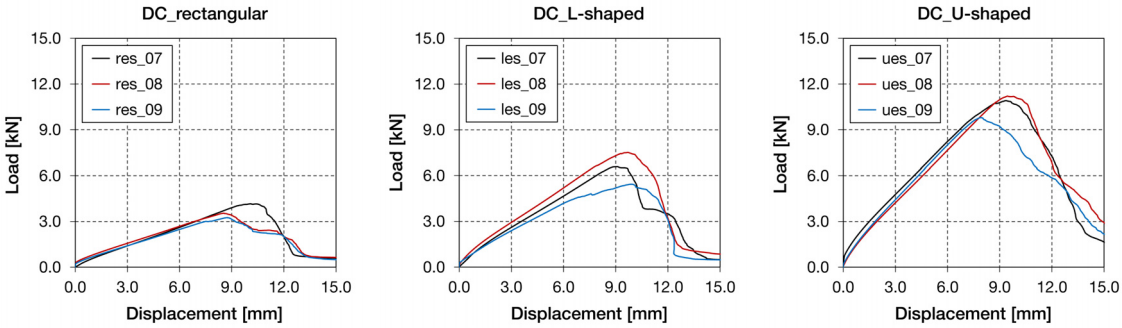

Sikasil SG-550 (SS):

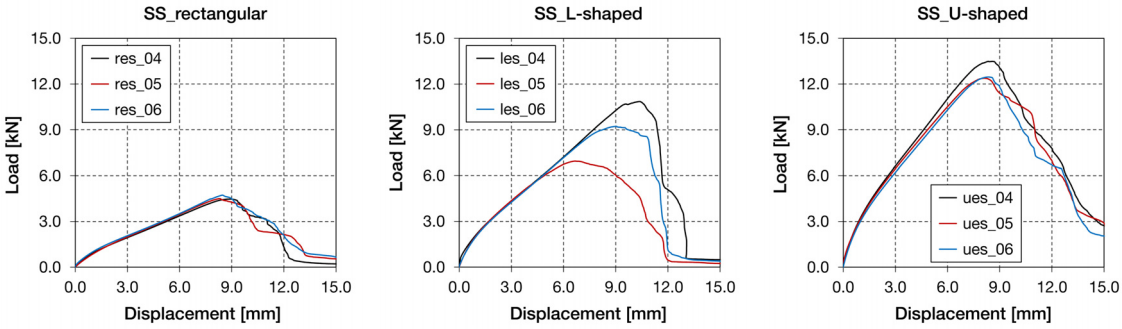

SikaFast-5221 NT (SF):

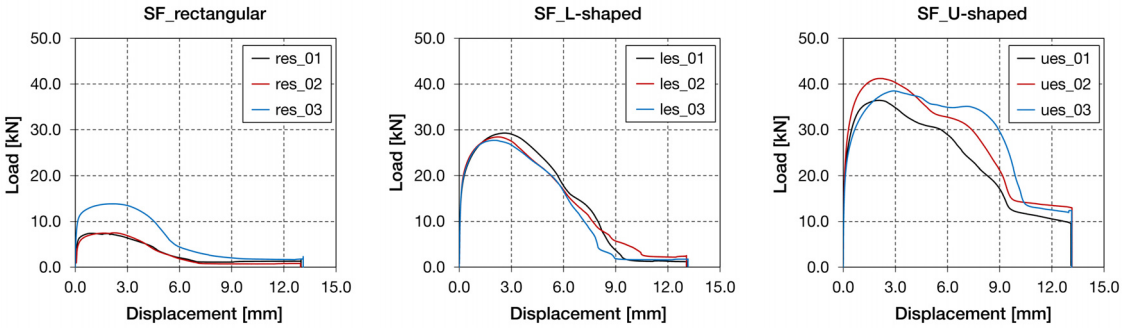

Real joint dimensions and test results from the shear tests on linear adhesive joints between glass and stainless steel substrates at the edge of laminated glass:

Specimen		Joint dimensions			Max. load [N]	Corr. displ. [mm]	Max. shear stress [MPa]	Corr. shear displ. [-]
		length l [mm]	**width** w [mm]	**thickness** t [mm]				
Dow Corning 993 - rectangular - 2 x [100 x 20 x 6] [mm]								
res_07	lap_a	103.6	20.6	6.08	4 162	10.07	0.99	1.64
	lap_b	100.9	20.6	6.17				
res_08	lap_a	103.2	20.4	6.11	3 541	8.53	0.83	1.40
	lap_b	103.8	20.9	6.06				
res_09	lap_a	101.2	20.6	6.10	3 257	8.75	0.79	1.45
	lap_b	100.6	20.3	5.99				
Mean value		102.2	20.6	6.09	3 653	9.12	0.87	1.50
Dow Corning 993 - L-shaped - 2 x [100 x (21.5+20) x 6] [mm]								
les_07 *	lap_a	100.1	-	6.16	6 592	9.04	0.78	1.47
	lap_b	103.2	-	6.18				
les_08 *	lap_a	100.2	-	6.17	7 517	9.67	0.90	1.59
	lap_b	101.1	-	6.02				
les_09 *	lap_a	98.8	-	6.17	5 435	9.90	0.65	1.59
	lap_b	103.3	-	6.32				
Mean value		101.1	-	6.17	6 515	9.54	0.78	1.55
Dow Corning 993 - U-shaped - 2 x [100 x (21.5+2x20) x 6] [mm]								
ues_07 *	lap_a	100.7	-	6.18	10 912	9.36	0.88	1.53
	lap_b	102.4	-	6.03				
ues_08 *	lap_a	101.5	-	6.25	11 209	9.45	0.91	1.52
	lap_b	98.2	-	6.18				
ues_09 *	lap_a	102.1	-	6.15	9 798	7.94	0.79	1.28
	lap_b	100.8	-	6.26				
Mean value		101.0	-	6.18	10 640	8.92	0.86	1.44

Notes:

* In the case of the specimens for adhesive joints with L-shaped and U-shaped cross sections tested under shear loading the width of the joint is not measured.

Specimen		Joint dimensions			Max. load [N]	Corr. displ. [mm]	Max. shear stress [MPa]	Corr. shear displ. [-]
		length l [mm]	width w [mm]	thickness t [mm]				
Sikasil SG-550 - rectangular - 2 x [100 x 20 x 6] [mm]								
res_04	lap_a	99.3	20.4	6.03	4 471	8.90	1.11	1.47
	lap_b	97.0	20.8	6.04				
res_05	lap_a	101.5	21.2	5.95	4 501	8.31	1.07	1.39
	lap_b	101.0	20.4	5.98				
res_06	lap_a	99.9	20.1	6.07	4 728	8.47	1.17	1.39
	lap_b	98.8	20.7	6.08				
Mean value		99.6	20.6	6.03	4 567	8.56	1.12	1.42
Sikasil SG-550 - L-shaped - 2 x [100 x (21.5+20) x 6] [mm]								
les_04 *	lap_a	103.3	-	6.18	10 859	10.38	1.27	1.69
	lap_b	102.6	-	6.10				
les_05 *	lap_a	113.0	-	6.12	6 953	6.66	0.78	1.07
	lap_b	102.3	-	6.27				
les_06 *	lap_a	100.3	-	6.33	9 227	9.04	1.10	1.45
	lap_b	102.2	-	6.12				
Mean value		104.0	-	6.19	9 013	8.69	1.05	1.40
Sikasil SG-550 - U-shaped - 2 x [100 x (21.5+2x20) x 6] [mm]								
ues_04 *	lap_a	97.9	-	6.27	13 485	8.35	1.08	1.34
	lap_b	104.2	-	6.18				
ues_05 *	lap_a	99.9	-	6.21	12 381	8.13	1.00	1.32
	lap_b	99.7	-	6.14				
ues_06 *	lap_a	99.5	-	6.21	12 459	8.34	1.01	1.34
	lap_b	99.1	-	6.23				
Mean value		100.1	-	6.21	12 775	8.27	1.03	1.33

Specimen		Joint dimensions			Max. load [N]	Corr. displ. [mm]	Max. shear stress [MPa]	Corr. shear displ. [-]
		length l [mm]	**width** w [mm]	**thickness** t [mm]				
SikaFast-5221 NT - rectangular - 2 x [100 x 20 x 3] [mm]								
res_01	lap_a	100.0	19.8	3.09	7 404	0.98	1.86	0.32
	lap_b	99.5	20.2	3.09				
res_02	lap_a	101.0	19.9	3.09	7 515	2.23	1.89	0.72
	lap_b	101.0	19.5	3.10				
res_03	lap_a	100.4	-	3.08	13 861	2.11	3.19	0.69
	lap_b	101.6	-	3.08				
Mean value		100.6	19.9	3.09	9 593	1.77	2.31	0.58
SikaFast-5221 NT - L-shaped - 2 x [100 x (21.5+20) x 3] [mm]								
les_01 *	lap_a	101.9	-	3.08	29 286	2.58	3.46	0.84
	lap_b	101.9	-	3.07				
les_02 *	lap_a	102.1	-	3.08	28 453	2.22	3.38	0.72
	lap_b	100.5	-	3.07				
les_03 *	lap_a	105.0	-	3.05	27 713	1.99	3.21	0.65
	lap_b	103.1	-	3.08				
Mean value		102.4	-	3.07	28 484	2.26	3.35	0.74
SikaFast-5221 NT - U-shaped - 2 x [100 x (21.5+2x20) x 3] [mm]								
ues_01 *	lap_a	97.4	-	3.07	36 423	2.08	3.01	0.68
	lap_b	98.9	-	3.07				
ues_02 *	lap_a	100.0	-	3.07	41 215	2.08	3.34	0.68
	lap_b	100.9	-	3.06				
ues_03 *	lap_a	97.9	-	3.08	38 492	2.89	3.19	0.94
	lap_b	97.0	-	3.07				
Mean value		98.7	-	3.07	38 710	2.35	3.18	0.77

Failure patterns from the shear tests on linear adhesive joints between glass and stainless steel substrates at the glass edge with *Dow Corning 993*, *Sikasil SG-550* and *SikaFast-5221 NT*:

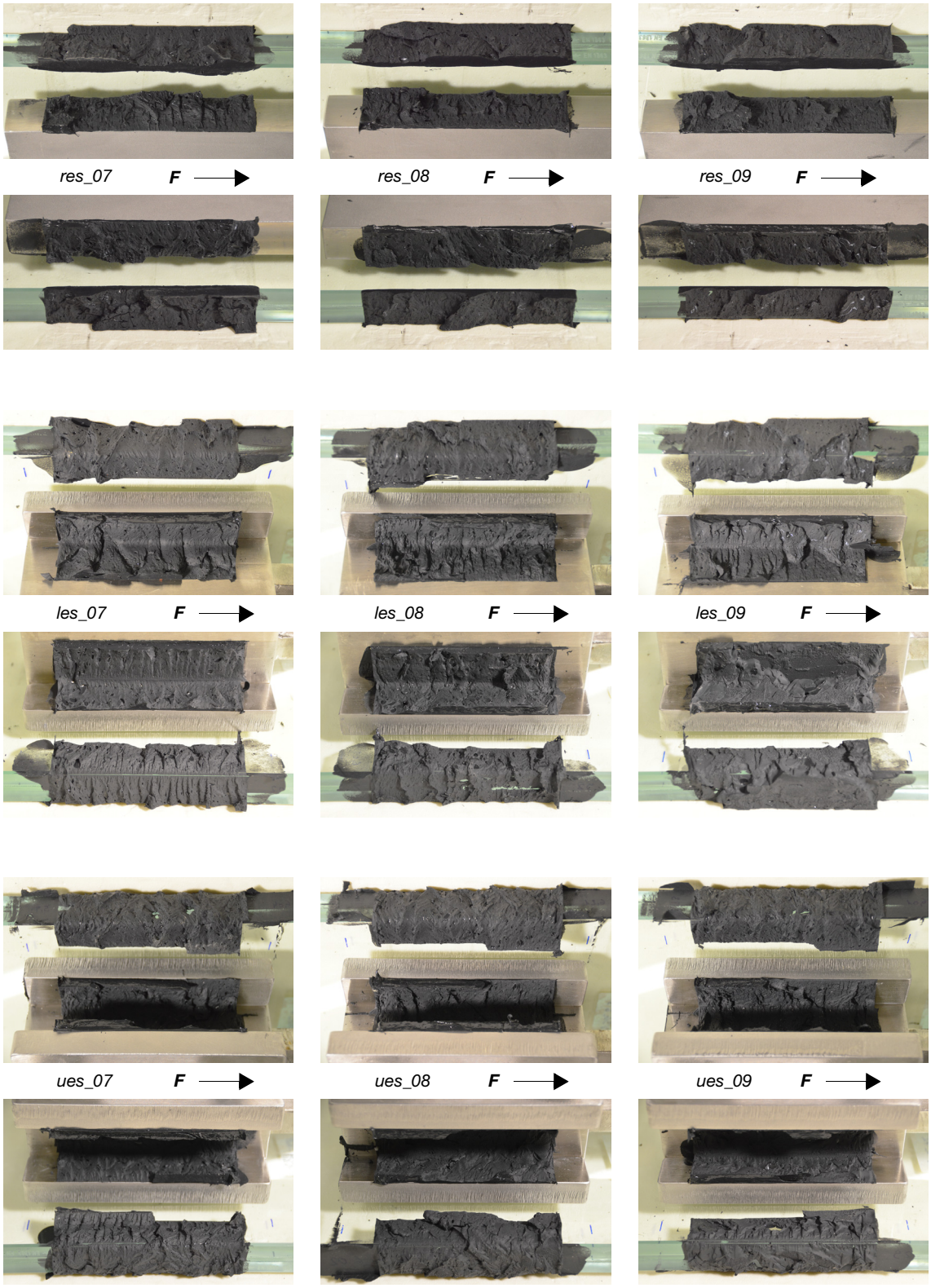

res_04 ***F*** →

res_05 ***F*** →

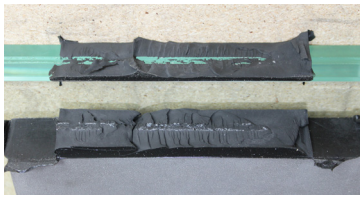

res_06 ***F*** →

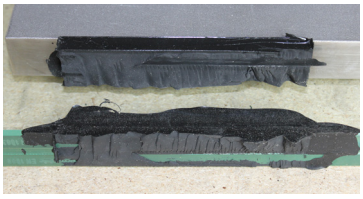

les_04 ***F*** →

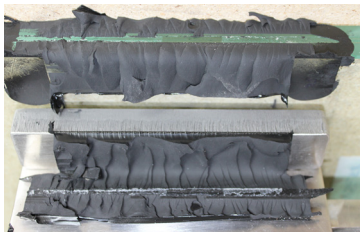

les_05 ***F*** →

les_06 ***F*** →

ues_04 ***F*** →

ues_05 ***F*** →

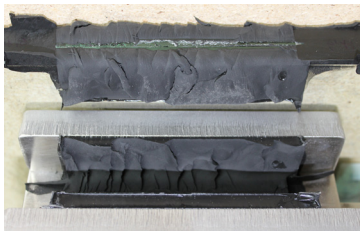

ues_06 ***F*** →

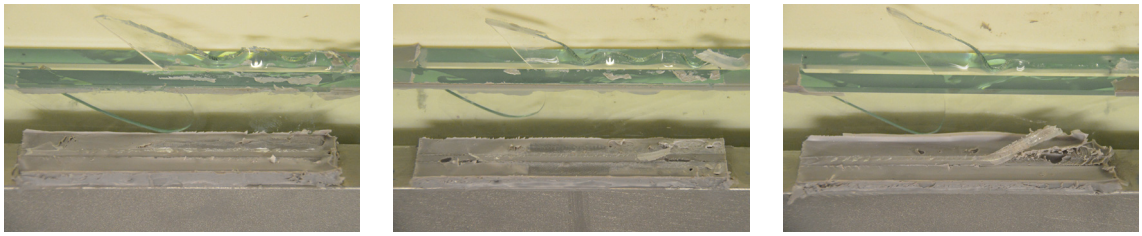

res_01 ***F*** → *res_02* ***F*** → *res_03* ***F*** →

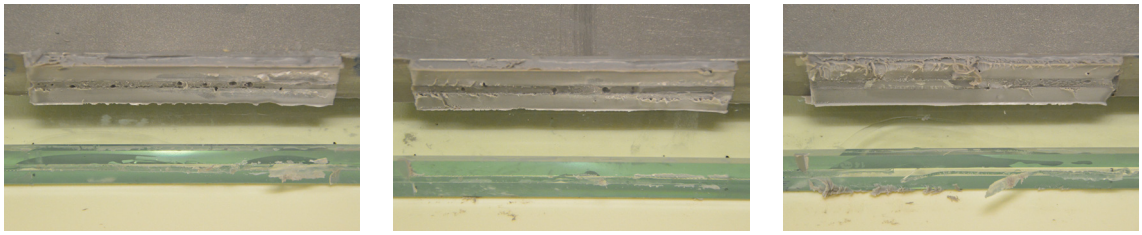

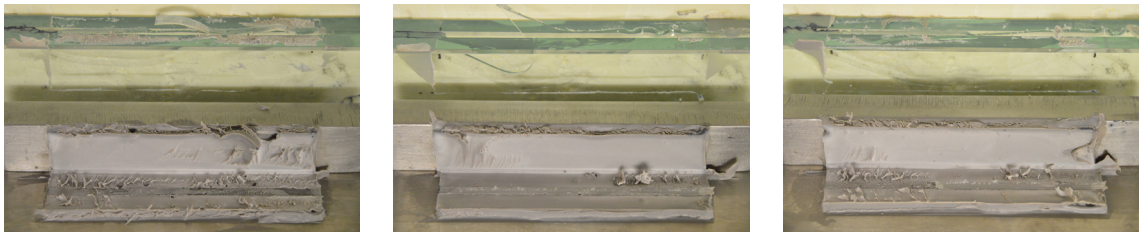

les_01 ***F*** → *les_02* ***F*** → *les_03* ***F*** →

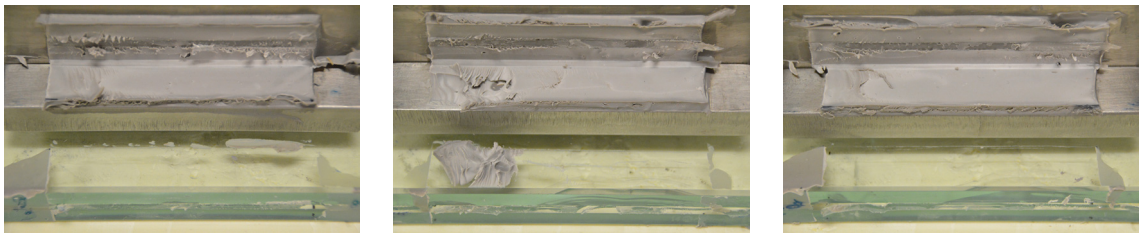

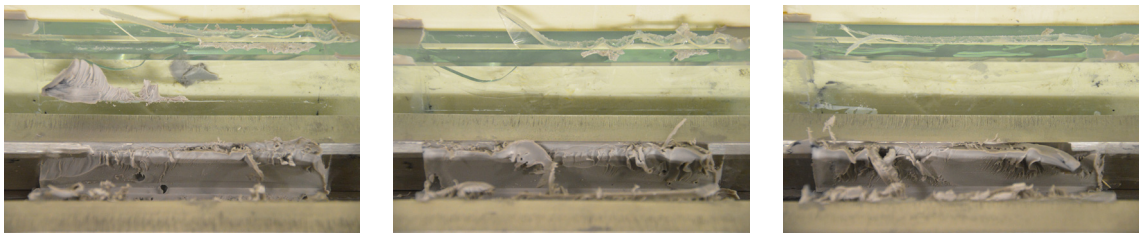

ues_01 ***F*** → *ues_02* ***F*** → *ues_03* ***F*** →

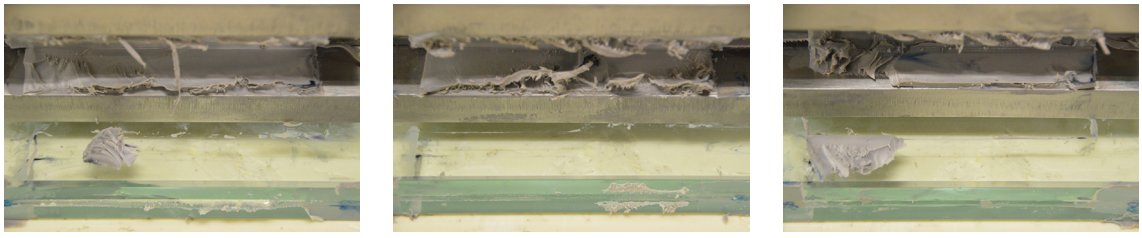

Appendix E

Additional results from tests on large-scale multi-component elements

Combined in-plane compressive axial loading and in-plane shear loading
Combined in-plane tensile axial loading and in-plane shear loading
Combined out-of-plane surface loading and in-plane shear loading
Combined out-of-plane surface loading with both axial and shear in-plane loading

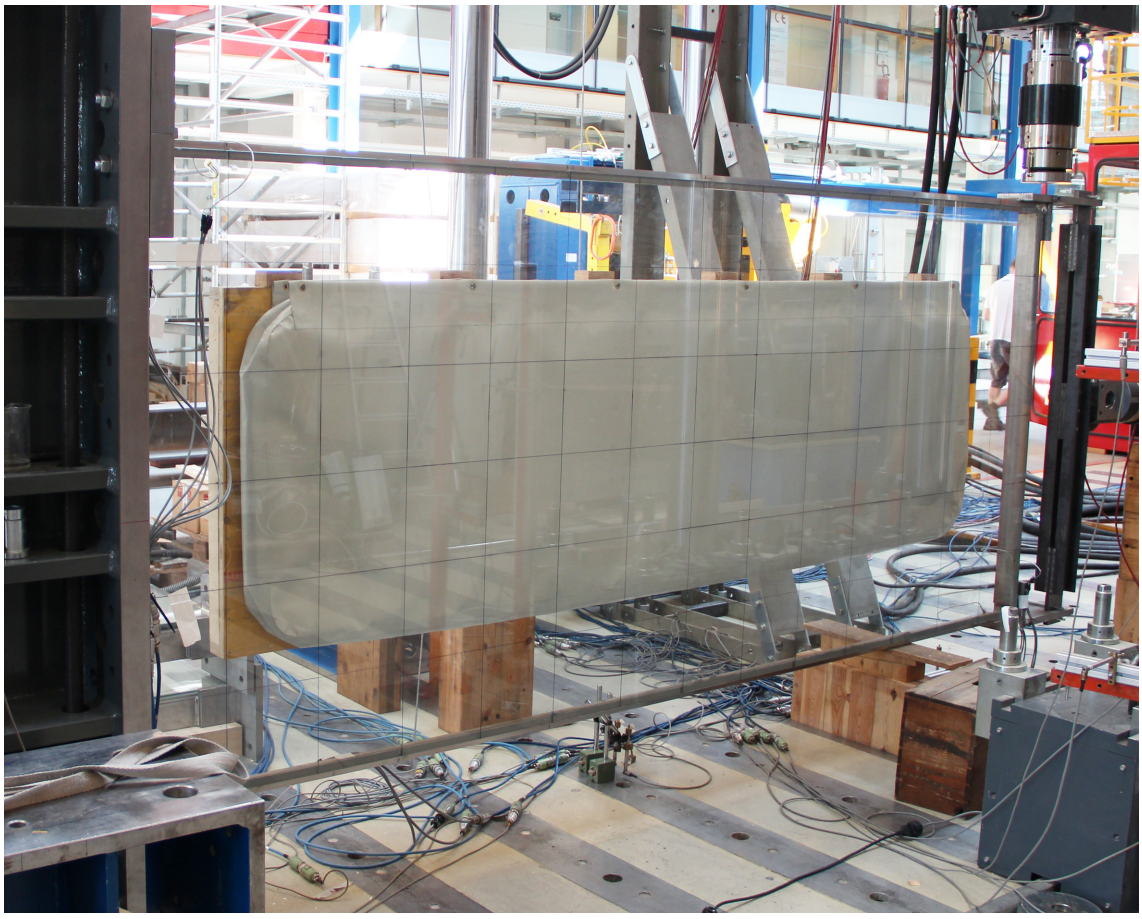

E.1 - Combined in-plane compressive axial loading and in-plane shear loading

The same diagrams as those discussed in subchapter 6.3.3 for specimens with laminated glass panes are provided for the specimens with monolithic glass panes (*Type 1A* and *Type 2A*).

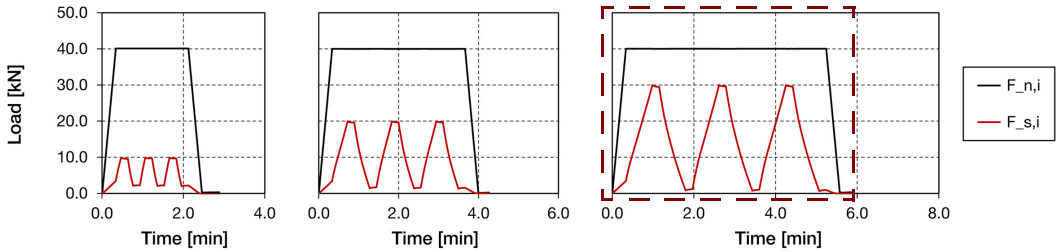

Fig. E.1 *Load vs. time diagram of the performed cycles for series with combined in-plane compressive axial loading and in-plane shear loading (Type 1A)*

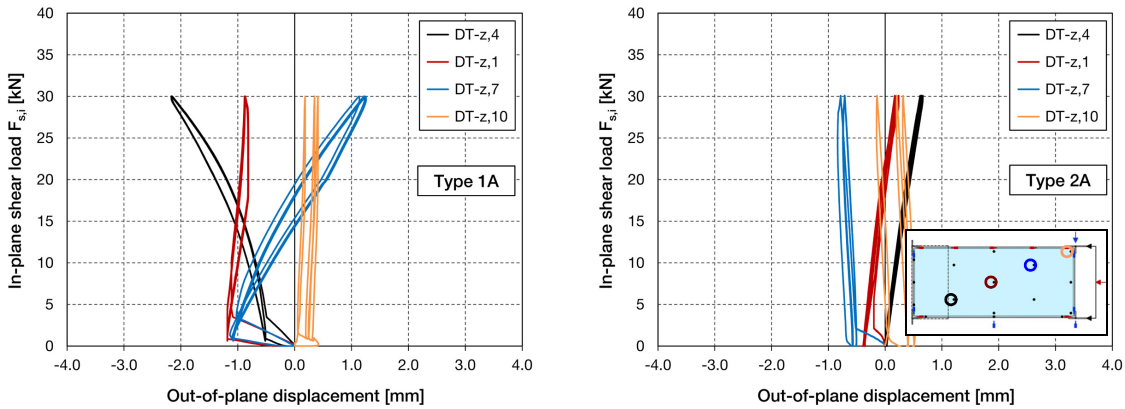

Fig. E.2 *Out-of-plane displacements of the monolithic glass pane along the compressed diagonal for specimens Type 1A (left) and Type 2A (right) under combined in-plane compressive axial loading and in-plane shear loading*

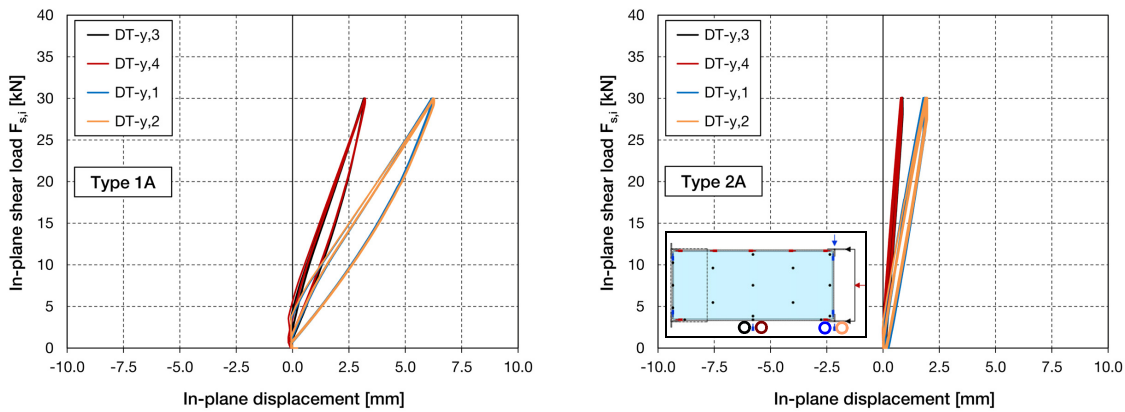

Fig. E.3 *In-plane displacements of the bottom frame profile in the middle and at the end of the element for specimens Type 1A (left) and Type 2A (right) under combined in-plane compressive axial loading and in-plane shear loading*

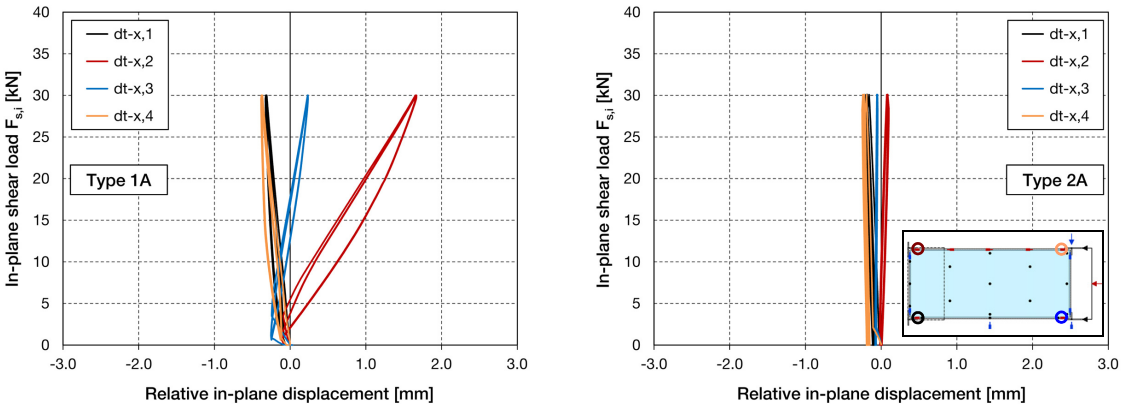

Fig. E.4 *Relative in-plane displacements between glass pane and framing in the four corners in x-direction for specimens Type 1A (left) and Type 2A (right) under combined in-plane compressive axial loading and in-plane shear loading*

E.2 - Combined in-plane tensile axial loading and in-plane shear loading

The same diagrams as those discussed in subchapter 6.3.3 for specimens with laminated glass panes are provided for the specimens with monolithic glass panes (*Type 1A* and *Type 2A*).

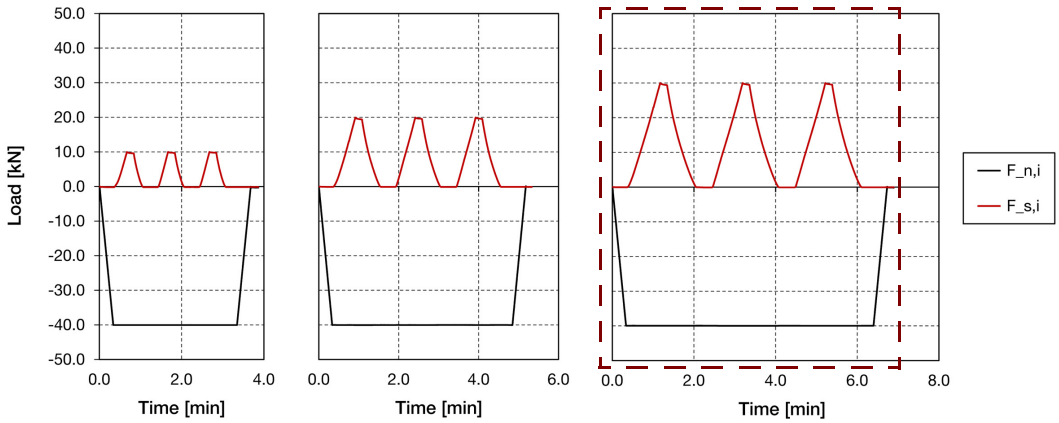

Fig. E.5 *Load vs. time diagram of the performed cycles for series with combined in-plane tensile axial loading and in-plane shear loading (Type 1A)*

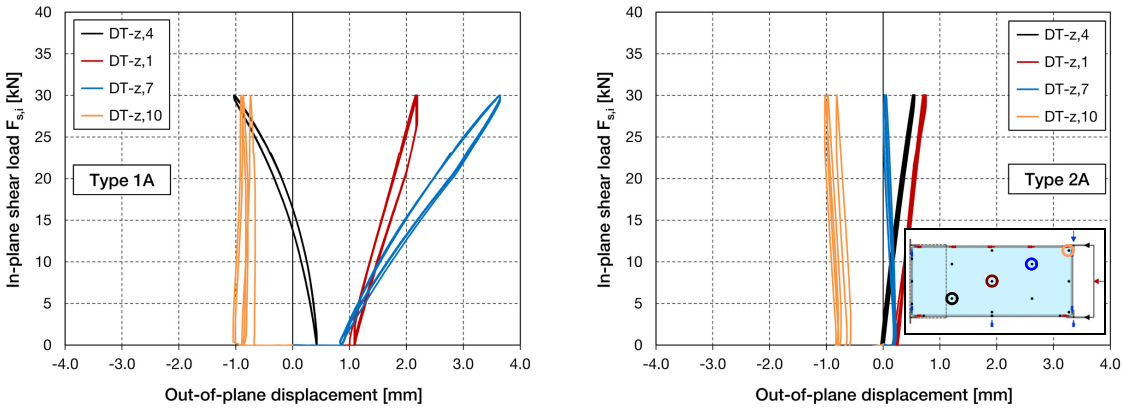

Fig. E.6 *Out-of-plane displacements of the monolithic glass pane along the compressed diagonal for specimens Type 1A (left) and Type 2A (right) under combined in-plane tensile axial loading and in-plane shear loading*

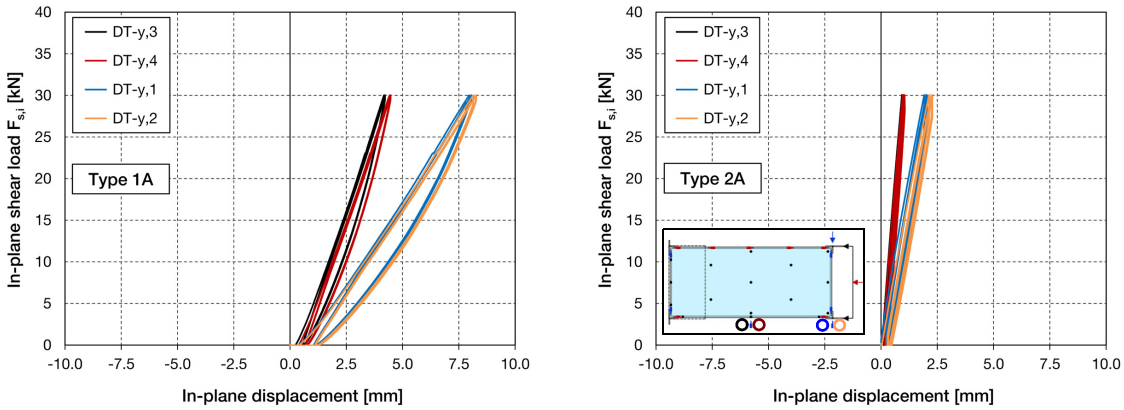

Fig. E.7 *In-plane displacements of the bottom frame profile in the middle and at the end of the element for specimens Type 1A (left) and Type 2A (right) under combined in-plane tensile axial loading and in-plane shear loading*

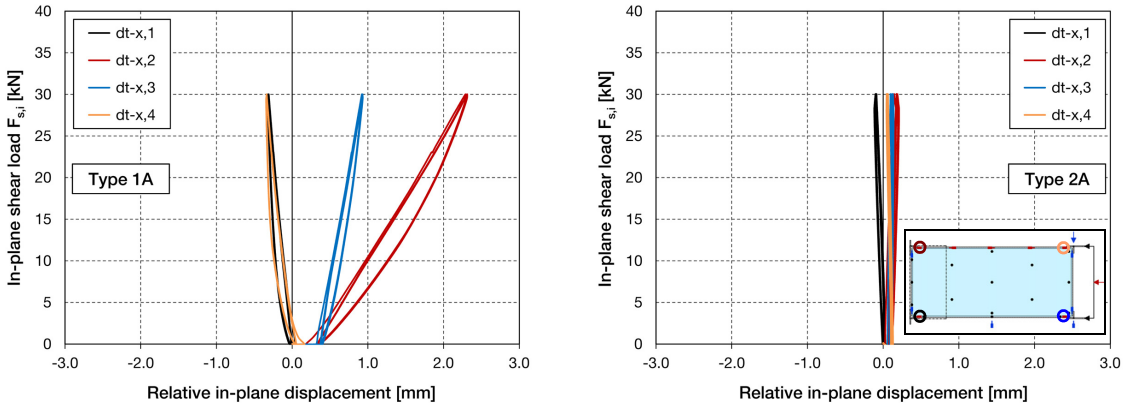

Fig. E.8 *Relative in-plane displacements between glass pane and framing in the four corners in x-direction for specimens Type 1A (left) and Type 2A (right) under combined in-plane tensile axial loading and in-plane shear loading*

E.3 - Combined out-of-plane surface loading and in-plane shear loading

The same diagrams as those discussed in subchapter 6.3.3 for specimens with laminated glass panes are provided for the specimens with monolithic glass panes (*Type 1A* and *Type 2A*).

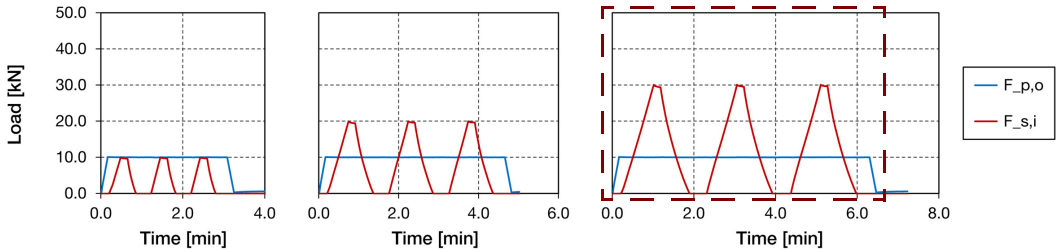

Fig. E.9 *Load vs. time diagram of the performed cycles for series with combined out-of-plane surface loading and in-plane shear loading (Type 1A)*

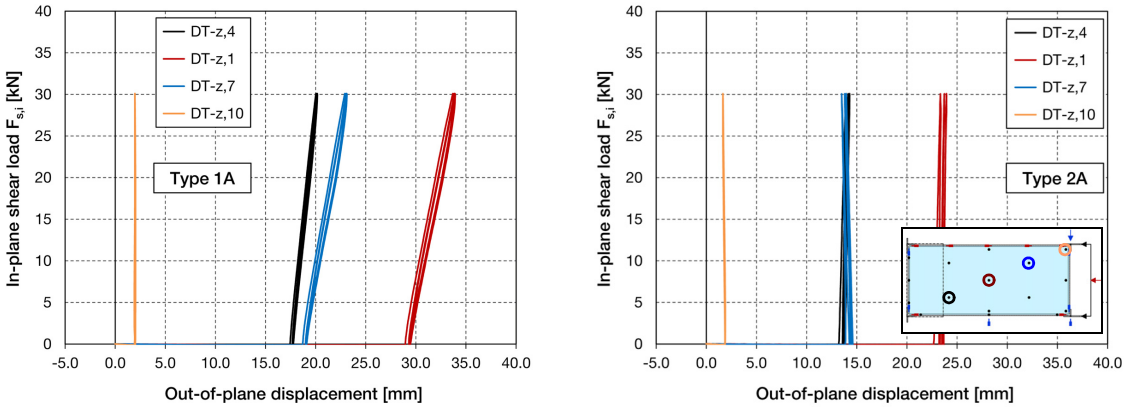

Fig. E.10 *Out-of-plane displacements of the monolithic glass pane along the compressed diagonal for specimens Type 1A (left) and Type 2A (right) under combined out-of-plane surface loading and in-plane shear loading*

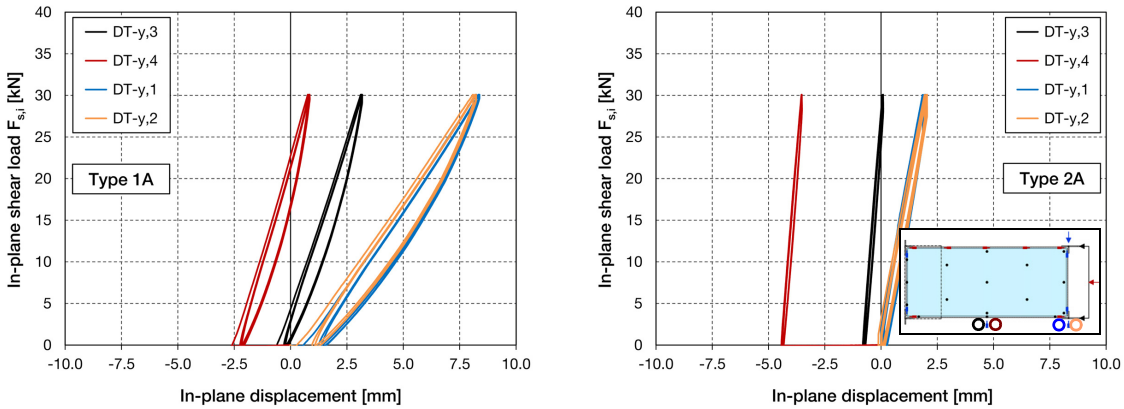

Fig. E.11 *In-plane displacements of the bottom frame profile in the middle and at the end of the element for specimens Type 1A (left) and Type 2A (right) under combined out-of-plane surface loading and in-plane shear loading*

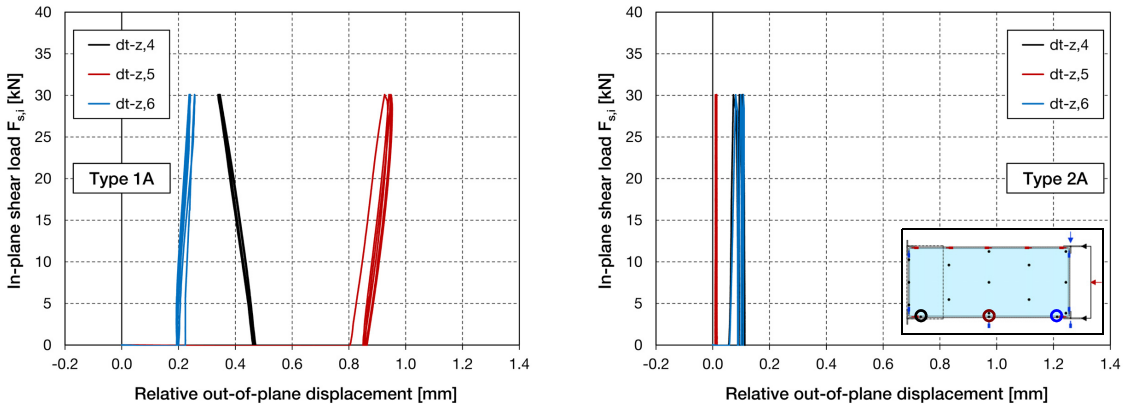

Fig. E.12 *Relative out-of-plane displacements between glass pane and framing along the bottom edge for specimens Type 1A (left) and Type 2A (right) under combined out-of-plane surface loading and in-plane shear loading*

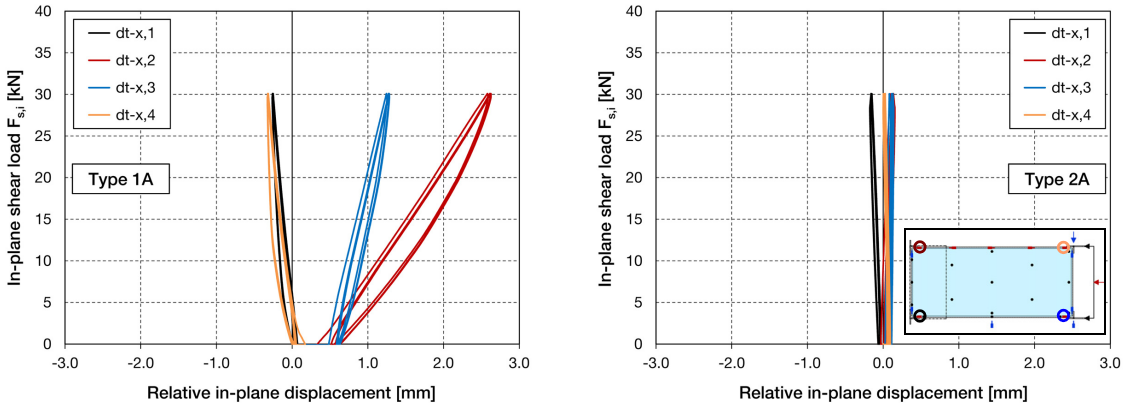

Fig. E.13 *Relative in-plane displacements between glass pane and framing in the four corners in x-direction for specimens Type 1A (left) and Type 2A (right) under combined out-of-plane surface loading and in-plane shear loading*

E.4 - Combined out-of-plane surface loading with both axial and shear in-plane loading

The same diagrams as those discussed in subchapter 6.3.4 for specimens with laminated glass panes are provided for the specimens with monolithic glass panes (*Type 1A* and *Type 2A*).

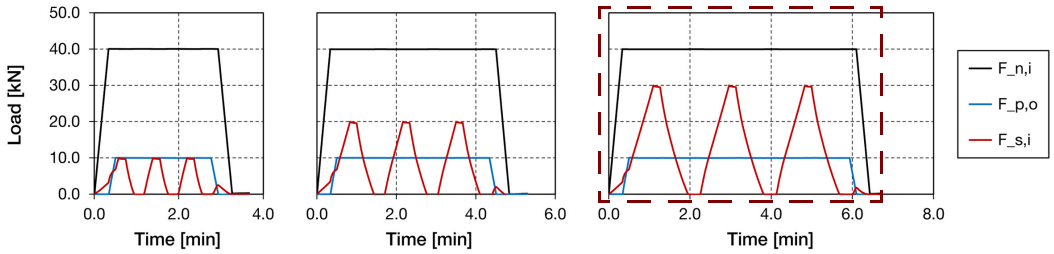

Fig. E.14 *Load vs. time diagram of the performed cycles for series with combined in-plane compressive loading, out-of-plane surface loading and in-plane shear loading (Type 1A)*

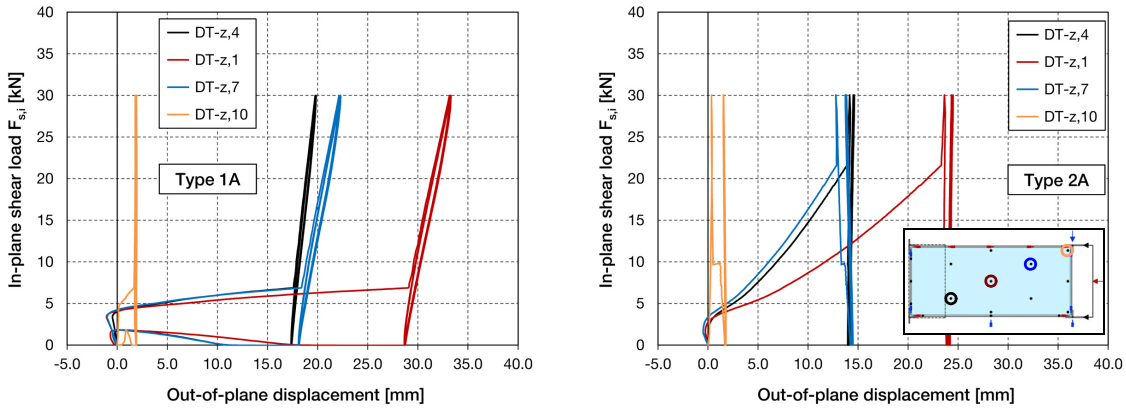

Fig. E.15 *Out-of-plane displacements of the monolithic glass pane along the compressed diagonal for specimens Type 1A (left) and Type 2A (right) under combined in-plane compressive axial loading, out-of-plane surface loading and in-plane shear loading*

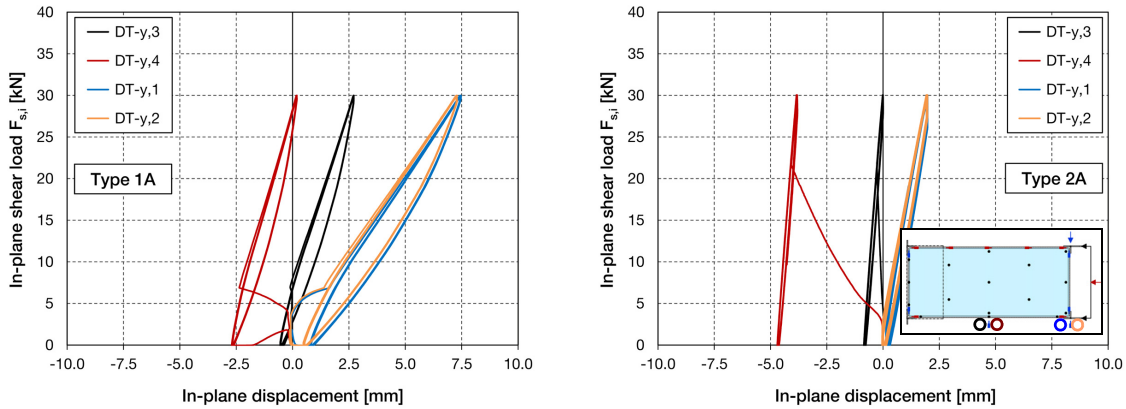

Fig. E.16 *In-plane displacements of the bottom frame profile in the middle and at the end of the element for specimens Type 1A (left) and Type 2A (right) under combined in-plane compressive axial loading, out-of-plane surface loading and in-plane shear loading*

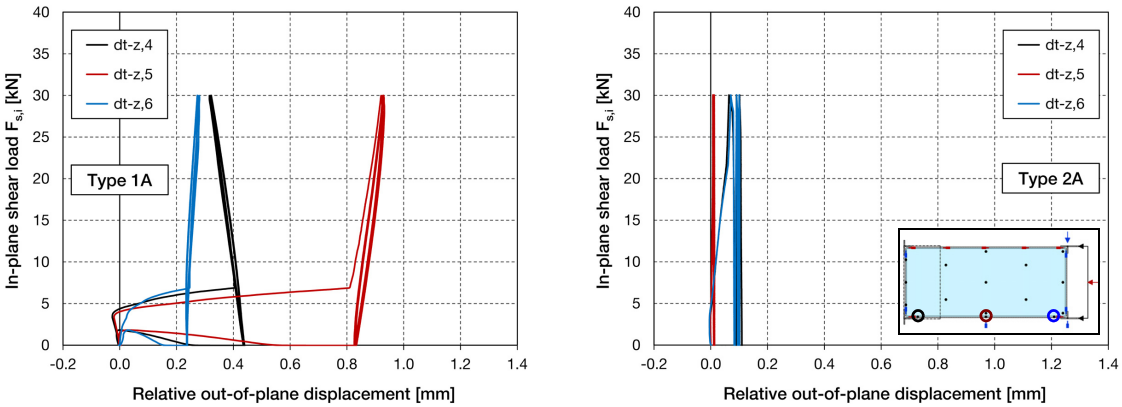

Fig. E.17 *Relative out-of-plane displacements between glass pane and framing along the bottom edge for specimens Type 1A (left) and Type 2A (right) under combined in-plane compressive axial loading, out-of-plane surface loading and in-plane shear loading*

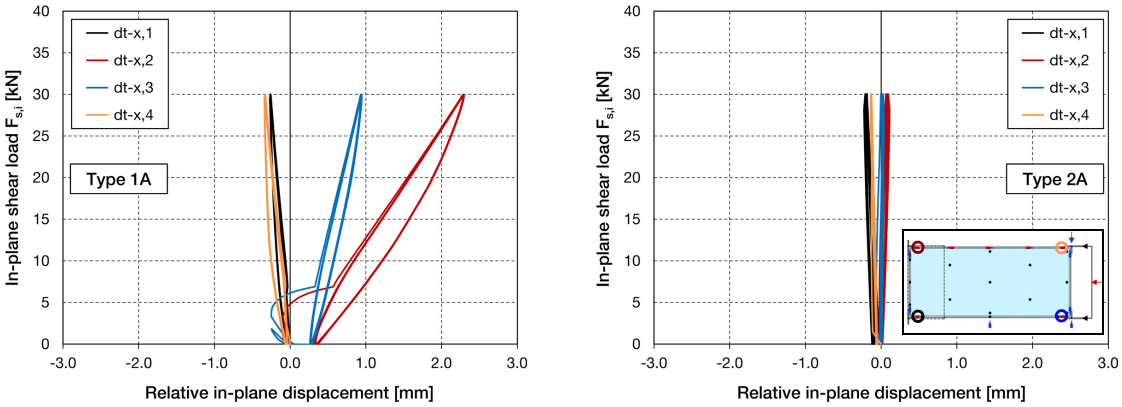

Fig. E.18 *Relative in-plane displacements between glass pane and framing in the four corners in x-direction for specimens Type 1A (left) and Type 2A (right) under combined in-plane compressive axial loading, out-of-plane surface loading and in-plane shear loading*